

**University Library**

Author/Filing Title ..... *ECK, T.* .....

Class Mark ..... *T* .....

Please note that fines are charged on ALL  
overdue items.

--	--	--

0403694663







# MEASUREMENT OF VIBRATIONAL ENERGY FLOW USING ELECTRONIC SPECKLE PATTERN INTERFEROMETRY

by

Thomas Eck

Department of Aeronautical and Automotive Engineering  
Loughborough University/England

Doctoral Thesis

Submitted in partial fulfilment of the requirements for the award of Doctor of  
Philosophy (Ph.D.) of Loughborough University

December 2007

© Thomas Eck 2007



Loughborough  
University  
Pilkington Library

Date 24/2/09

Class T

Acc  
No. 0403694663

# ABSTRACT

Vibrational energy flow (VEF) analysis (VEFA) is used to attain vibrational energy flow information within a vibrating structure of interest. Two essential pieces of information are provided, the direction of the energy flow as well as the magnitude of the energy flow. Once this information is available, vibration may be manipulated in order to suppress undesired vibrational phenomena.

The measurement of VEF is an important part in providing VEF information from real structures. In the past the measurement of VEF was restricted to single point measurements only. However, recent developments in advanced laser measurement techniques, such as electronic speckle pattern interferometry (ESPI), have gained interest in applying these measurement techniques to the measurement of VEF.

In this research VEF within transversally vibrating beam and plate structures was analytically studied and measured in detail. A measurement technique, denoted as measurement of VEF using ESPI (VEFESPI) was developed. A thorough error and sensitivity analysis of the VEFESPI method was carried out to highlight advantages and disadvantages. For validation purposes, measurements of VEF under usage of ESPI were undertaken. It was shown that VEF can be measured in beam and plate structures, even when a high standing wave environment and noise contamination is present.

In addition to the measurement of VEF using ESPI, a novel moment excitation technique was developed in order to measure moment induced point mobility and input energy of an experimental “infinite” beam. It was demonstrated that the technique worked well over a wide frequency range.

# ACKNOWLEDGEMENTS

The work reported in this thesis was financially granted by the Department of Aeronautical and Automotive Engineering, Loughborough University.

I would like to thank my supervisor, Dr. Stephen J. Walsh, for the guidance and encouragement he has given me throughout the duration of my research. I most certainly enjoyed the long discussions on a Friday afternoon about the fascinating world of structural dynamics and vibrational energy related phenomena.

Thanks also to Mr. Martin Dale for contributing to this research by providing the ESPI measurement system. Without his valuable advice and assistance this work could not have been completed.

Acknowledgement is due to Mr. Dennis Bönner for sharing my problems and being part of many discussions, academic or otherwise. His help is most appreciated.

Finally, my deepest thanks are to Ms. Tamara Braun for making sure everything I needed was available. Thanks also to my family, especially Mr. Norbert Braun, for believing in me and supporting me throughout this research. I am also grateful to my friends who shared time with me and made sure that I could occasionally relax.

# TABLE OF CONTENTS

<b>1</b>	<b>INTRODUCTION</b>	<b>1</b>
1.1	Motivation of Work	1
1.2	Objectives of Thesis	5
1.3	Structure of Thesis	7
<b>2</b>	<b>LITERATURE SURVEY</b>	<b>9</b>
2.1	Introduction	9
2.2	Introduction to Vibrational Energy Flow and Structural Intensity	9
2.3	Theory of Vibrational Energy Flow	11
2.4	Conventional Vibrational Energy Flow Measurements	17
2.5	Advanced Vibrational Energy Flow Measurements	20
2.6	Vibrational Energy Flow Measurements Using ESPI	27
2.7	Vibrational Energy Flow Measurements of Engineering Structures	28
2.8	Vibrational Energy Flow from Finite Element Method	30
2.9	Miscellaneous Applications in Vibrational Energy Flow Analysis	33
2.10	Moment Excitation of Structures	35
2.11	Summary and Conclusions	40

<b>3</b>	<b>DEFINITION OF VIBRATIONAL ENERGY FLOW AND ENERGETIC QUANTITIES</b>	<b>42</b>
3.1	Introduction	42
3.2	Vibrational Energy Relations	42
3.3	Definition of Mechanical Power	48
3.4	Definition of Structural Intensity	49
3.5	Vibrational Input Power	51
3.6	Vibrational Energy Flow and Energetic Quantities in Beams	54
3.6.1	Vibrational Energy Flow	54
3.6.2	Energetic Quantities	56
3.6.3	Energy Balance	57
3.7	Vibrational Energy Flow and Energetic Quantities in Thin Plates	59
3.7.1	Cartesian Coordinate Based Vibrational Energy Flow	59
3.7.2	Cartesian Coordinate Based Energetic Quantities	63
3.7.3	Energy Balance	65
3.7.4	Polar Coordinate Based Vibrational Energy Flow	66
3.8	Discussion	67
<b>4</b>	<b>VIBRATIONAL ENERGY DETERMINATION METHODS</b>	<b>70</b>
4.1	Introduction	70
4.2	Numerical Determination of Spatial Derivatives	71
4.2.1	Numerical Differentiation Using Finite Differences	71
4.2.2	Numerical Differentiation Using Spatial Fourier Transform	73
4.2.3	Numerical Differentiation Using B-Splines	77
4.3	Filter Methods	78
4.3.1	Spatial Domain Filtering	79
4.3.2	Wavenumber Domain Filtering	79
4.4	Vibrational Energy Determination Method	82
4.5	Summary	84

<b>5</b>	<b>THEORY OF VIBRATIONAL ENERGY IN BEAMS</b>	<b>86</b>
5.1	Introduction	86
5.2	Four-Wave Vibrational Energy Flow	87
5.3	Infinite Beam Analysis	89
5.3.1	Forced Vibration	90
5.3.1.1	Point Force Excitation	90
5.3.1.2	Moment Excitation	92
5.3.2	Vibrational Input Power	94
5.3.2.1	Point Force Excitation	94
5.3.2.2	Moment Excitation	95
5.3.3	Transmitted Vibrational Energy	96
5.3.3.1	Point Force Excitation	96
5.3.3.2	Moment Excitation	96
5.4	Simply Supported Beam Analysis	97
5.4.1	Forced Vibration	98
5.4.1.1	Point Force Excitation	100
5.4.1.2	Moment Excitation	102
5.4.2	Vibrational Input Power	104
5.4.2.1	Point Force Excitation	104
5.4.2.2	Moment Excitation	105
5.4.3	Transmitted Vibrational Energy	105
5.4.3.1	Four-Wave Vibrational Energy Flow Including Damping	107
5.4.3.2	Coupled Vibrational Energy Flow Including Damping	110
5.4.3.3	Point Force Excitation	112
5.4.3.4	Moment Excitation	119
5.5	Unconstrained Layer Damping	123
5.6	Discussion	127

<b>6</b>	<b>NUMERICAL ANALYSIS OF VIBRATIONAL ENERGY IN BEAMS</b>	<b>132</b>
6.1	Introduction	132
6.2	Numerical Infinite Beam Analysis	133
6.2.1	Non-Periodic Data Input	133
6.2.2	Vibrational Energy Flow Excluding Noise	137
6.2.3	Vibrational Energy Flow Including Noise	147
6.2.3.1	Ideal 2D Spectral Filtering	148
6.2.3.2	Oval 2D Spectral Butterworth Filtering	153
6.2.4	Vibrational Energy Flow Including ESPI Noise	156
6.3	Numerical Simply Supported Beam Analysis	161
6.3.1	Vibrational Energy Flow Excluding Noise	162
6.3.1.1	Vibrational Energy Flow Using the VEFESPI Method	162
6.3.1.2	Vibrational Energy Flow from Energetic Quantities	171
6.3.2	Vibrational Energy Flow Including Noise	177
6.3.2.1	Ideal 2D Spectral Filtering	178
6.3.2.2	Oval 2D Spectral Butterworth Filtering	190
6.3.3	Vibrational Energy Flow Including ESPI Noise	199
6.4	Discussion and Summary	203
<b>7</b>	<b>MEASUREMENT OF VIBRATIONAL ENERGY IN BEAMS: EXPERIMENTAL APPARATUS</b>	<b>207</b>
7.1	Introduction	207
7.2	Electronic Speckle Pattern Interferometry	207
7.2.1	Principle of Electronic Speckle Pattern Interferometry	208
7.2.2	ESPI Measurement System	210
7.3	Experimental Beam Apparatus	214
7.3.1	"Infinite" Beam Rig	215



7.3.1.1	Force Excited "Infinite" Beam Setup	215
7.3.1.2	Moment Excited "Infinite" Beam Setup	217
7.3.2	Simply Supported Beam Rig	219
7.3.2.1	Force Excited Simply Supported Beam Setup	219
7.3.2.2	Moment Excited Simply Supported Beam Setup	221
7.4	Summary	222
<b>8</b>	<b>MEASUREMENT OF VIBRATIONAL ENERGY IN BEAMS: MEASUREMENT METHODS</b>	<b>224</b>
8.1	Introduction	224
8.2	Force Excited Beam Measurements	225
8.2.1	Point Mobility Measurements	225
8.2.2	Vibrational Input Power Measurements	225
8.2.3	Accelerometer Based Transmitted Vibrational Energy Measurements	227
8.2.4	Vibrational Energy Flow Measurements Using ESPI	228
8.2.5	Application of the Measurement Methods to a Beam	229
8.3	Moment Excited Beam Measurements	230
8.3.1	Finite Difference Approximation of the Angular Velocity	230
8.3.2	Moment Point Mobility Measurements	231
8.3.3	Input Energy Measurements	233
8.3.4	Consideration of Moment Arm Inertia	234
8.3.5	Application of the Measurement Methods to a Beam	235
8.4	Summary	237
<b>9</b>	<b>MEASUREMENT OF VIBRATIONAL ENERGY IN BEAMS: EXPERIMENTAL RESULTS</b>	<b>238</b>
9.1	Introduction	238

9.2	Force Excited Beam Measurements	238
9.2.1	“Infinite” Beam Measurements	239
9.2.1.1	Point Mobility, Vibrational Input Power and Accelerometer Based Transmitted Vibrational Energy Measurements	239
9.2.1.2	Vibrational Energy Flow Measurements Using ESPI	241
9.2.1.3	Energy Balance	245
9.2.1.4	Discussion	246
9.2.2	Simply Supported Beam Measurements	249
9.2.2.1	Point Mobility, Vibrational Input Power and Accelerometer Based Transmitted Vibrational Energy Measurements	249
9.2.2.2	Vibrational Energy Flow Measurements Using ESPI	252
9.2.2.3	Energy Balance	257
9.2.2.4	Discussion	261
9.3	Moment Excited Beam Measurements	267
9.3.1	“Infinite” Beam Measurements	267
9.3.1.1	Moment Point Mobility Measurements	269
9.3.1.2	Input Energy Measurements	270
9.3.1.3	Comparison of Input Energy and Transmitted Energy Measurements	272
9.3.1.4	Discussion	273
<b>10</b>	<b>THEORY OF VIBRATIONAL ENERGY IN PLATES</b>	<b>275</b>
10.1	Introduction	275
10.2	Infinite Plate Analysis	276
10.2.1	Point Force Excitation	276
10.2.2	Vibrational Input Power	277
10.2.3	Transmitted Vibrational Energy Using Hankel Functions	277

10.2.4	Transmitted Vibrational Energy Using Asymptotic Expansion Functions	278
10.2.4.1	Polar Expressions	279
10.2.4.2	Cartesian Expressions	282
10.3	Simply Supported Plate Analysis	286
10.3.1	Point Force Excitation	287
10.3.2	Vibrational Input Power	288
10.3.3	Transmitted Vibrational Energy	289
10.4	Unconstrained Layer Damping	291
10.5	Discussion	296
<b>11</b>	<b>NUMERICAL ANALYSIS OF VIBRATIONAL ENERGY IN PLATES</b>	<b>299</b>
11.1	Introduction	299
11.2	Numerical Infinite Plate Analysis	301
11.2.1	Vibrational Energy Flow Excluding Noise	301
11.2.2	Vibrational Energy Flow Including Noise	311
11.2.3	Vibrational Energy Flow Including ESPI Noise	316
11.3	Numerical Simply Supported Plate Analysis	321
11.3.1	Vibrational Energy Flow Excluding Noise	321
11.3.2	Vibrational Energy Flow Including Noise	334
11.3.2.1	Ideal 2D Spectral Filtering	334
11.3.2.2	Oval 2D Spectral Butterworth Filtering	344
11.3.3	Vibrational Energy Flow Including ESPI Noise	350
11.4	Discussion and Summary	358
<b>12</b>	<b>MEASUREMENT OF VIBRATIONAL ENERGY IN PLATES: EXPERIMENTAL APPARATUS</b>	<b>366</b>
12.1	Introduction	366
12.2	Experimental Plate Apparatus	366
12.2.1	"Infinite" Plate Rig	367

---

12.2.2	Simply Supported Plate Rig	369
12.3	Summary	372
<b>13</b>	<b>MEASUREMENT OF VIBRATIONAL ENERGY IN PLATES: MEASUREMENT METHODS</b>	<b>373</b>
13.1	Introduction	373
13.2	Force Excited Plate Measurements	374
13.2.1	Point Mobility Measurements	374
13.2.2	Vibrational Input Power Measurements	375
13.2.3	Vibrational Energy Flow Measurements Using ESPI	377
13.2.4	Application of the Measurement Methods to a Plate	377
13.3	Summary	378
<b>14</b>	<b>MEASUREMENT OF VIBRATIONAL ENERGY IN PLATES: EXPERIMENTAL RESULTS</b>	<b>379</b>
14.1	Introduction	379
14.2	Force Excited Plate Measurements	379
14.2.1	"Infinite" Plate Measurements	380
14.2.1.1	Point Mobility and Vibrational Input Power Measurements	380
14.2.1.2	Vibrational Energy Flow Measurements Using ESPI	382
14.2.1.3	Energy Balance	387
14.2.1.4	Discussion	389
14.2.2	Simply Supported Plate Measurements	393
14.2.2.1	Point Mobility and Vibrational Input Power Measurements	393
14.2.2.2	Vibrational Energy Flow Measurements Using ESPI	395
14.2.2.3	Energy Balance	402
14.2.2.4	Discussion	405

<b>15 CONCLUSIONS AND FUTURE WORK</b>	<b>417</b>
15.1 General Conclusions	417
15.2 Future Work	421
<b>REFERENCES</b>	<b>423</b>
<b>APPENDICES</b>	<b>437</b>

# NOMENCLATURE

## Arabic Letters

$a$	Translational acceleration
$a_x$	Filter parameter of oval filter to adjust in $x$ direction
$a_y$	Filter parameter of oval filter to adjust in $y$ direction
$a_0$	Transverse acceleration at the excitation location
$a_1$	Transverse acceleration from accelerometer one
$a_2$	Transverse acceleration from accelerometer two
$a_3$	Transverse acceleration from accelerometer three
$a_4$	Transverse acceleration from accelerometer four
$A$	Cross-sectional area
$A(x, y)$	Measured two-dimensional ESPI amplitude
$A_B$	Cross-sectional area of beam
$A_D$	Cross-sectional area of damping material
$A_{Eh}$	Abbreviation used in layer attachment analysis of the plate
$A_{F_\infty}$	Simplification of hysteretic damping expression in force excited beam due to infinite waves
$A_{M_\infty}$	Simplification of hysteretic damping expression in moment excited beam due to infinite waves
$A_n$	Ingoing wave amplitude
$A_{PD}$	Abbreviated numerator used in layer attachment analysis of the plate
$A_+$	Complex evanescent wave amplitude to the right
$A_-$	Complex evanescent wave amplitude to the left

$b_B$	Width of beam
$b_D$	Width of damping material
$B_{Eh}$	Abbreviation used in layer attachment analysis of the plate
$B_{F_\infty}$	Simplification of hysteretic damping expression in force excited beam due to infinite waves
$B_{M_\infty}$	Simplification of hysteretic damping expression in moment excited beam due to infinite waves
$B_n$	Outgoing wave amplitude
$B_+$	Complex travelling wave amplitude to the right
$B_-$	Complex travelling wave amplitude to the left
$C$	Constant
$C_{F_\infty}$	Constant of time-averaged transmitted energy in hysteretically damped beam due to infinite waves and force excitation
$C_i$	Modal constant
$C_{i_0}$	Modal constant
$C_{k_i}$	Modal constant
$C_{k_0}$	Modal constant
$C_n$	Modal constant
$C_{n_0}$	Modal constant
$C_{M_\infty}$	Constant of time-averaged transmitted energy in hysteretically damped beam due to infinite waves and moment excitation
$C_n$	Modal constant
$C_{n_0}$	Modal constant
$C_{PD}$	Abbreviated denominator used in layer attachment analysis of the plate
$C_1$	Complex evanescent wave amplitude of infinite beam
$C_2$	Complex travelling wave amplitude of infinite beam
$C_{4W}$	Constant of time-averaged transmitted energy based on four waves
$C_+$	Complex evanescent wave amplitude to the right
$C_-$	Complex evanescent wave amplitude to the left
$d$	Distance between impact force $F_1$ and $F_2$

$D$	Flexural rigidity of plate
$D_{PD}$	Combined flexural rigidity
$\underline{D}_{PD}$	Complex combined flexural rigidity
$D_+$	Complex travelling wave amplitude to the right
$D_-$	Complex travelling wave amplitude to the left
$e_{kin}$	Kinetic energy density
$e_{pot}$	Potential energy density
$e_{tot}$	Total energy density
$E$	Young's modulus
$\underline{E}$	Complex Young's modulus
$E_B$	Young's modulus of beam
$\underline{E}_B$	Complex Young's modulus of beam
$E_D$	Young's modulus of damping material
$\underline{E}_D$	Complex Young's modulus of damping material
$E_P$	Young's modulus of plate
$\underline{E}_P$	Complex Young's modulus of plate
$f$	Frequency
$f_0$	Excitation frequency
$F$	Force
$F(k_x, k_y)$	Two-dimensional filter function
$F\{ \}$	Forward Fourier transform
$F^{-1}\{ \}$	Backward Fourier transform
$F_n$	Complex wave amplitude of moment excited infinite beam
$F_s$	Internal shear force in beam
$F_0$	Excitation force
$F_1$	Impact force at location one
$F_2$	Impact force at location two
$g(x)$	One-dimensional spatial signal
$G(k)$	One-dimensional wavenumber spectrum
$G(a_1, a_2)$	Cross-spectral density of transverse acceleration $a_1$ and $a_2$
$G(a_2, a_2)$	Auto spectral density of transverse acceleration $a_2$ and $a_2$
$G(a_2, a_4)$	Cross-spectral density of transverse acceleration $a_2$ and $a_4$



---

$G(a_3, a_1)$	Cross-spectral density of transverse acceleration $a_3$ and $a_1$
$G(a_3, a_2)$	Cross-spectral density of transverse acceleration $a_3$ and $a_2$
$G(a_3, a_3)$	Auto spectral density of transverse acceleration $a_3$ and $a_3$
$G(F, F)$	Force auto spectral density
$G(F_0, a_0)$	Cross-spectral density of force and transverse acceleration at the excitation location
$G(F_1, a_1)$	Cross-spectral density of impact force $F_1$ and transverse acceleration $a_1$
$G(F_2, a_2)$	Cross-spectral density of impact force $F_2$ and transverse acceleration $a_2$
$G(F_0, F_0)$	Force auto spectral density at the excitation location
$G(F_0, v_0)$	Cross-spectral density of force and transverse velocity at the excitation location
$G(F, \partial\theta/\partial t)$	Cross-spectral density of force and angular velocity
$G(M, M)$	Moment auto spectral density
$G(M_0, \alpha_0)$	Cross-spectral density of moment and rotational acceleration at the excitation location
$G(M_0, \omega_0)$	Cross-spectral density of moment and rotational velocity at the excitation location
$G(M, \partial\theta/\partial t)$	Cross-spectral density of moment and angular velocity
$h$	Thickness of plate
$h_i$	Inner product of zeroth order Bessel function
$h_D$	Thickness of unconstrained damping layer
$h_p$	Thickness of plate
$H_n^{(2)}$	Hankel function of second kind and order $n$
$H_0^{(2)}$	Hankel function of second kind and zeroth order
$H_1(f)$	Frequency response function estimator
$I$	Second moment of area of cross section
$\vec{I}$	Structural intensity vector
$\nabla \cdot \vec{I}$	Divergence of structural intensity
$I_B$	Second moment of area of the beam's cross section
$I_D$	Second moment of area of the damping material's cross section

$I_{mod}$	Modulation intensity of the observed speckle
$I_r$	Reference light beam intensity
$I_x$	Structural intensity component in $x$ direction
$I_y$	Structural intensity component in $y$ direction
$I_z$	Structural intensity component in $z$ direction
$I_0$	Object light beam intensity
$I_\alpha$	Intensity correlation fringe function of the $\alpha$ pulse
$I_\beta$	Intensity correlation fringe function of the $\beta$ pulse
$j$	Complex unity, i.e. $j = \sqrt{-1}$
$J$	Rotary inertia of the I-piece
$J_0$	Zeroth order Bessel function
$k$	Angular wavenumber
$\underline{k}$	Complex angular wavenumber
$\underline{k}_{BD}$	Complex angular wavenumber due to an unconstrained layer attachment onto a beam
$k_{c_x}$	Cut-off wavenumber in $x$ direction
$k_{c_y}$	Cut-off wavenumber in $y$ direction
$k_r$	Radial wavenumber component
$k_x$	$X$ component wavenumber
$\Delta k_x$	Spectral wavenumber resolution
$k_{x_0}$	Excitation wavenumber in $x$ direction
$k_y$	$Y$ component wavenumber
$k_0$	Fundamental wavenumber component
$K_{c_x}$	Cut-off wavenumber vector in $x$ direction
$K_{c_y}$	Cut-off wavenumber vector in $y$ direction
$K_n$	Complex wave amplitude of force excited infinite beam
$K_x$	$X$ component wavenumber vector
$K_y$	$Y$ component wavenumber vector
$l$	Surface contour of the plate
$L$	Length of beam
$L_x$	Length of plate or signal length in $x$ direction
$L_y$	Width of plate

$m$	Mass, modal number in $x$ direction
$M$	Moment
$M_B$	Internal bending moment in beam
$M_{cr}$	True moment
$M_{j,l+1}$	Normalised B-spline function
$M_r$	Internal plate bending moment per unit length in polar coordinates
$M_{r,\theta}$	Internal plate twisting moment per unit length in polar coordinates
$M_{xx}$	Internal plate bending moment per unit length about the $y$ -axis
$M_{xy}$	Internal plate twisting moment per unit length about the $x$ -axis
$M_{yx}$	Internal plate twisting moment per unit length about the $y$ -axis
$M_{yy}$	Internal plate bending moment per unit length about the $x$ -axis
$M_0$	Excitation moment
$M_\theta$	Internal plate bending moment per unit length in polar coordinates
$n$	Order, modal number in $y$ direction
$N$	Number of cycles or number of samples
$N_{i,k+1}$	Normalised B-spline function
$N_x$	Number of samples in $x$ direction
$N_y$	Number of samples in $y$ direction
$p(x,y)$	Applied load
$P$	Mechanical power
$\overline{\vec{P}}$	Time-averaged vector field of transmitted energy per unit length in the plate
$P(x_n)$	Complex transmitted energy from the IEDI method
$(P_a)_{F_\infty}$	Active time-averaged total transmitted vibrational energy in an infinite plate due to force excitation
$P_{in}$	Time-averaged input power
$\underline{P}_{in}$	Complex input power
$(P_{in})_F$	Time-averaged input power due to force excitation
$(P_{in})_{Fa}$	Transducer measured input power due to force excitation

$(P_{in})_{F_s}$	Time-averaged input power due to force excitation of a simply supported structure
$(P_{in})_{F_\infty}$	Time-averaged input power due to force excitation of an infinite structure
$(P_{in})_M$	Time-averaged input power due to moment excitation
$(P_{in})_{M_{cr}}$	Corrected energy input to a moment excited structure
$(P_{in})_{M_s}$	Time-averaged input power due to moment excitation of a simply supported structure
$(P_{in})_{M_\infty}$	Time-averaged input power due to moment excitation of an infinite structure
$P_{in}(t)$	Instantaneous input power
$P_{in}(\omega)_F$	Spectral input power due to force excitation
$P_{in}(\omega)_M$	Spectral input power due to moment excitation
$\overline{P}_r$	Time-averaged transmitted energy per unit length in the plate in polar coordinates
$(\overline{P}_r)_{F_\infty}$	Active time-averaged transmitted energy per unit length in an infinite plate due to force excitation in polar coordinates
$(\overline{P}_r)_{F_\infty}$	Reactive time-averaged transmitted energy per unit length in an infinite plate due to force excitation in polar coordinates
$P_{tr_2}$	Complex transmitted vibrational energy using 2 accelerometers
$(P_{tr_2})_{cr}$	Corrected complex transmitted vibrational energy using 2 accelerometers
$P_{tr_4}$	Complex transmitted vibrational energy using 4 accelerometers
$P_x$	Time-averaged transmitted energy in the beam
$(P_x)_{app}$	Approximated transmitted energy of the CW technique
$(\widetilde{P}_x)_{even}$	Even-numbered curve wrap of approximated transmitted energy of the CW technique
$(\widetilde{P}_x)_{odd}$	Odd-numbered curve wrap of approximated transmitted energy of the CW technique

$(P_x)_c$	Time-averaged transmitted energy due to coupling of reflection waves and infinite waves in the beam
$(P_x)_r$	Time-averaged transmitted energy due to reflection waves in the beam
$(P_x)_{r,\infty}$	Time-averaged transmitted energy due to internal reflection wave loads and respective infinite wave velocities in the beam
$(P_x)_\infty$	Time-averaged transmitted energy due to infinite waves in the beam
$(P_x)_{\infty,r}$	Time-averaged transmitted energy due to internal infinite wave loads and respective reflection wave velocities in the beam
$\overline{P_x}$	Time-averaged transmitted energy per unit length in the plate in $x$ direction
$(\overline{P_x})_{F_{ss}}$	Time-averaged complex transmitted energy per unit length in the simply supported plate due to force excitation in $x$ direction
$(\underline{P_x})_\infty$	Time-averaged transmitted energy in an infinite beam including hysteretic damping
$(P_x)_{4W}$	Time-averaged transmitted energy in a beam based on four waves including hysteretic damping
$P_{x_a}$	Active time-averaged transmitted energy in a beam
$(P_{x_a})_{F_\infty}$	Active time-averaged transmitted energy in an infinite beam due to force excitation
$(\overline{P_{x_a}})_{F_\infty}$	Active time-averaged transmitted energy per unit length in an infinite plate due to force excitation in $x$ direction
$(\overline{P_{y_a}})_{F_\infty}$	Active time-averaged transmitted energy per unit length in an infinite plate due to force excitation in $y$ direction
$(\underline{P_{x_a}})_{F_\infty}$	Active time-averaged transmitted energy in an infinite beam due to force excitation and hysteretic damping
$(P_{x_a})_{M_\infty}$	Active time-averaged transmitted energy in an infinite beam due to moment excitation
$(\underline{P_{x_a}})_{M_\infty}$	Active time-averaged transmitted energy in an infinite beam due to moment excitation and hysteretic damping

$(P_{x_a})_{4W}$	Active time-averaged transmitted energy based on four waves in a beam
$(\underline{P}_x)_c$	Time-averaged coupled complex transmitted energy in a finite beam
$(P_x)_{c_a}$	Active time-averaged coupled transmitted energy in a finite beam when $\eta = 0$
$(P_x)_{c_r}$	Reactive time-averaged coupled transmitted energy in a finite beam when $\eta = 0$
$(P_x)_{butter}$	Butterworth filtered transmitted energy
$(P_x)_{ideal}$	Ideal filtered transmitted energy
$(\overline{P}_x)_{exact}$	Exact transmitted energy per unit length
$(P_{x_i})_{exact}$	Exact transmitted energy
$(\overline{P}_x)_{VEFESPI}$	VEFESPI computed transmitted energy per unit length
$(P_{x_i})_{VEFESPI}$	VEFESPI computed transmitted energy
$P_{x_r}$	Reactive time-averaged transmitted energy in the beam
$(P_{x_r})_{F_\infty}$	Reactive time-averaged transmitted energy in an infinite beam due to force excitation
$(\overline{P}_{x_r})_{F_\infty}$	Reactive time-averaged transmitted energy per unit length in an infinite plate due to force excitation in $x$ direction
$(P_{x_r})_{F_\infty}$	Reactive time-averaged transmitted energy in an infinite beam due to force excitation and hysteretic damping
$(P_{x_r})_{M_\infty}$	Reactive time-averaged transmitted energy in an infinite beam due to moment excitation
$(\underline{P}_{x_r})_{M_\infty}$	Reactive time-averaged transmitted energy in an infinite beam due to moment excitation and hysteretic damping
$(P_{x_r})_{4W}$	Reactive time-averaged transmitted energy based on four waves in a beam
$P_{x_M}$	Time-averaged transmitted bending moment energy in the beam
$P_{x_s}$	Time-averaged transmitted shear force energy in the beam

---

$\overline{P}_y$	Time-averaged transmitted energy per unit length in the plate in $y$ direction
$(\overline{P}_y)_{F_s}$	Time-averaged complex transmitted energy per unit length in the simply supported plate due to force excitation in $y$ direction
$(\overline{P}_{y_r})_{F_\infty}$	Reactive time-averaged transmitted energy per unit length in an infinite plate due to force excitation in $y$ direction
$\overline{P}_\theta$	Time-averaged transmitted energy per unit length in the plate in polar coordinates
$Q_r$	Internal plate shear force per unit length in polar coordinates
$Q_x$	Internal plate shear force per unit length in $z$ direction
$Q_y$	Internal plate shear force per unit length in $z$ direction
$Q_\theta$	Internal plate shear force per unit length in polar coordinates
$r$	Radius or general displacement
$S$	Surface area or original signal
$S_L(n)_{left}$	Left-hand side link function of the MP technique
$S_L(n)_{right}$	Right-hand side link function of the MP technique
$S_{mirr}(n)_{left}$	Left-hand side mirror image of the original signal
$S_{mirr}(n)_{right}$	Right-hand side mirror image of the original signal
$t$	Time
$t_B$	Thickness of beam
$t_D$	Thickness of damping material
$T$	Temporal period
$u$	Beam displacement
$\vec{u}$	Displacement vector
$u(x)$	One-dimensional spatial signal
$u(x)_{F_\infty}$	Infinite beam displacement due to force excitation
$u(x)_{M_\infty}$	Infinite beam displacement due to moment excitation
$u(x)_r$	Reflection waved beam displacement
$u(x)_\infty$	Infinite waves beam displacement
$u(x, t)$	Spatial and temporal beam displacement
$u(x, t)_{F_s}$	Spatial and temporal displacement of simply supported beam due to force excitation

$u(x, t)_{M_s}$	Spatial and temporal displacement of simply supported beam due to moment excitation
$u(x, y)_{ESPI}$	Measured two-dimensional ESPI beam displacement
$u_+(x, t)_{F_\infty}$	Force excited spatial and temporal infinite beam displacement to the right
$u_+(x, t)_{M_\infty}$	Moment excited spatial and temporal infinite beam displacement to the right
$u_+(x, t)_\infty$	Spatial and temporal infinite beam displacement to the right
$u_-(x, t)_{F_\infty}$	Force excited spatial and temporal infinite beam displacement to the left
$u_-(x, t)_{M_\infty}$	Moment excited spatial and temporal infinite beam displacement to the left
$u_-(x, t)_\infty$	Spatial and temporal infinite beam displacement to the left
$U(k)$	One-dimensional wavenumber spectrum
$U(k_x, k_y)_{filt}$	Filtered two-dimensional wavenumber spectrum
$U(k_x, k_y; \omega)$	Two-dimensional wavenumber spectrum
$U_r$	Rotational mechanical work
$v$	Translational velocity
$v_n(t)$	Instantaneous translational velocity component
$V$	Volume of interest
$V_{im}$	Modified output voltage
$w$	Plate displacement
$w(r, \theta, t)$	Plate displacement in polar coordinates
$w(x, y)_{ESPI}$	Measured two-dimensional ESPI plate displacement
$w(x, y, t)$	Plate displacement in Cartesian coordinates
$w(x, y; \omega)$	Surface function
$\tilde{w}(x, y; \omega)$	B-spline fitted surface function
$W$	Total mechanical work
$W_t$	Translational mechanical work
$x$	Spatial variable
$\Delta x$	Spacing between two accelerometers or spatial resolution
$x_0$	Excitation location in $x$ direction



$X$	Filter length of the oval 2D Butterworth filter in $K_x$ direction
$y$	Spatial variable
$y_0$	Excitation location in $y$ direction
$Y$	Filter length of the oval 2D Butterworth filter in $K_y$ direction
$Y_F$	Point mobility due to force excitation
$Y_{F_s}$	Point mobility due to force excitation of simply supported beam
$Y_{E_0, \omega_0}$	Complex force point mobility
$Y_{F_\infty}$	Point mobility due to force excitation of infinite beam
$Y_M$	Point mobility due to moment excitation
$(Y_M)_{cr}$	Corrected point mobility due to moment excitation
$Y_{M_s}$	Point mobility due to moment excitation of simply supported beam
$Y_{M_0, \omega_0}$	Complex moment point mobility
$Y_{M_\infty}$	Point mobility due to moment excitation of infinite beam
$z$	Spatial variable
$z_B$	Neutral axis offset of beam due to unconstrained layer attachment
$Z_{E_0, \omega_0}$	Complex mechanical point impedance

## Greek Letters

$\alpha$	Slope of the CCD camera
$\delta$	Dirac delta function
$\Delta \varepsilon$	Relative error
$\Delta \varepsilon_x$	Relative error in $x$ direction
$\Delta \varepsilon_y$	Relative error in $y$ direction
$\eta$	Hysteretic loss factor
$\bar{\eta}$	$\eta/4$
$\eta_B$	Hysteretic loss factor of beam
$\eta_{BD}$	Combined hysteretic loss factor of beam and damping material
$\eta_D$	Hysteretic loss factor of damping material

$\eta_P$	Hysteretic loss factor of plate
$\eta_{PD}$	Combined hysteretic loss factor of plate and damping material
$\theta$	Angle
$\theta_0$	Angular displacement at the excitation location
$\lambda$	Wavelength
$\lambda_i$	B-spline knots
$\mu_j$	B-spline knots
$\nu$	Poisson's ratio
$\pi_{in}$	Input power density
$\pi_{diss}$	Dissipated power density
$\Pi$	Complex relative mean squared error
$\Pi_{diss}$	Total dissipated energy
$\Pi_x$	Complex relative mean squared error in $x$ direction
$\Pi_y$	Complex relative mean squared error in $y$ direction
$\rho$	Mass density
$\rho_B$	Mass density of beam
$\rho_D$	Mass density of damping material
$\sigma$	Stress
$\vec{\sigma}$	Stress tensor
$\phi(x, y)$	Measured two-dimensional ESPI phase
$\phi_{mn}(x, y)$	Eigenfunctions of a rectangular plate
$\phi_x$	Total transmitted energy in $x$ direction across a perpendicular line parallel to the plate's edge
$(\phi_x)_{exact}$	Exact total transmitted energy in $x$ direction across a perpendicular line parallel to the plate's edge
$(\phi_x)_{VEFESPI}$	VEFESPI computed total transmitted energy in $x$ direction across a perpendicular line parallel to the plate's edge
$\phi_y$	Total transmitted energy in $y$ direction across a perpendicular line parallel to the plate's edge
$(\phi_y)_{exact}$	Exact total transmitted energy in $y$ direction across a perpendicular line parallel to the plate's edge

$(\phi_y)_{VEFESPI}$	VEFESPI computed total transmitted energy in $y$ direction across a perpendicular line parallel to the plate's edge
$\phi_\alpha$	Phase map of $\alpha$ pulse
$\phi_\beta$	Phase map of $\beta$ pulse
$\varphi$	General rotation
$\Upsilon$	Squared residual error
$\omega$	Circular frequency
$\omega_{ki}$	Modal eigenfrequency
$\omega_{mn}$	Modal eigenfrequency
$\omega_k(t)$	Instantaneous rotational velocity component
$\partial\theta_0/\partial t$	Angular velocity at the excitation location
$\partial\theta/\partial t$	Angular velocity
$\partial^2\theta/\partial t^2$	Angular acceleration

## Special Symbols

$\Re$	Real part
$\Im$	Imaginary part
$\vec{\mathbb{I}}$	Identity tensor
$\langle \rangle_t$	Time-averaged quantity
$\nabla$	Nabla operator
$\nabla^2$	Laplace operator
$\cdot$	Time-averaged quantity

## Acronyms

BAHIM	Broadband acoustic holography from intensity measurement
CCD	Charge coupled device
CW	Curve wrap
ESPI	Electronic speckle pattern interferometry

FEM	Finite element method
FFT	Fast Fourier transform
FIR	Finite impulse response
FT	Fourier transform
HI	Holographic Interferometry
IEDI	Incremental energy density integration
IFFT	Inverse fast Fourier transform
KSD	$k$ -space derivation
LDV	Laser Doppler vibrometry
MP	Mirror-processing
MRS	Mirror-reverse-shear
MSE	Mean squared error
NAH	Nearfield acoustic holography
PZT	Piezo-electrical transducer
SD	Spatial derivative
SFT	Spatial Fourier transform
SI	Structural intensity
SIMAP	Structural intensity from the measurement of acoustic pressure
SNR	Signal-to-noise ratio
SWR	Standing wave ratio
TTVE	Total transmitted vibrational energy
TVE	Transmitted vibrational energy
VE	Vibrational energy
VEF	Vibrational energy flow
VEFA	Vibrational energy flow analysis
VEFESPI	Vibrational energy flow measurement using electronic speckle pattern interferometry
VIP	Vibrational input power
VPA	Vibrational power flow analysis

# LIST OF APPENDICES

<b>A1</b>	Partial Differential Beam Equation	438
<b>A2</b>	Time-Averaging of Complex Instantaneous Quantities	441
<b>A3</b>	Partial Differential Plate Equation	444
<b>A4</b>	Numerical Differentiation Using Finite Differences	449
<b>A5</b>	Spatial Derivatives of General Four-Wave Equation	454
<b>A6</b>	Four-Wave Vibrational Energy Flow Equation	456
<b>A7</b>	Forced Vibration of an Infinite Beam due to Point Force Excitation	459
<b>A8</b>	Forced Vibration of an Infinite Beam due to Moment Excitation	461
<b>A9</b>	Forced Vibration of a Simply Supported Beam due to Point Force Excitation	463
<b>A10</b>	Forced Vibration of a Simply Supported Beam due to Moment Excitation	468
<b>A11</b>	Force Point Mobility of a Simply Supported Beam	473
<b>A12</b>	Moment Point Mobility of a Simply Supported Beam	475
<b>A13</b>	Four-Wave Vibrational Energy Flow Equation Including Damping	477
<b>A14</b>	Coupled Transmitted Vibrational Energy	480
<b>A15</b>	Transmitted Vibrational Energy in a Simply Supported Beam due to Point Force Excitation Excluding Structural Damping	488

A16	Transmitted Vibrational Energy in a Simply Supported Beam due to Moment Excitation Excluding Structural Damping	491
A17	Unconstrained Layer Damping of Beams	494
A18	Signal-To-Noise Ratio	497
A19	Tables of Predicted Cut-Off Points and Relative Mean Square Error of Three Differently Damped Simply Supported Beam Structures Using Extracted ESPI Noise and Measured Force Magnitude	499
A20	Figures of Truncated ESPI Displacement and ESPI Measured Vibrational Energy Flow of "Infinite" Beam	504
A21	Transducer Measured Vibrational Input Power, Measured Four-Accelerometer and Two-Accelerometer Transmitted Energy of the Simply Supported Beam	507
A22	ESPI Measured Vibrational Energy Flow of Experimental Simply Supported Beams Using the VEFESPI Method	510
A23	ESPI Measured Vibrational Energy Flow of Experimental Simply Supported Beams Using the Incremental Energy Density Integration Method	513
A24	Forced Vibration of an Infinite Plate due to Point Force Excitation	516
A25	Transmitted Vibrational Energy in an Infinite Plate Using Polar Coordinates	518
A26	Transmitted Vibrational Energy in an Infinite Plate Using Cartesian Coordinates	520
A27	Transmitted Vibrational Energy in a Simply Supported Plate	524
A28	Unconstrained Layer Damping of Plates	529
A29	Tables of Predicted Cut-Off Points and Relative Mean Square Error of Three Differently Damped Simply Supported Plate Structures Using Extracted ESPI Noise and Measured Force Magnitude	534

<b>A30</b>	Figures of Truncated ESPI Displacement and ESPI Measured Vibrational Energy Flow of “Infinite” Plate	541
<b>A31</b>	Measured Vibrational Input Power of the Experimental Simply Supported Plates	554
<b>A32</b>	Measured Vibrational Energy Flow Maps of the Experimental Simply Supported Plates Using the VEFESPI Method	556
<b>A33</b>	Analytical Vibrational Energy Flow Maps of Simply Supported Plate	565

# LIST OF FIGURES

<b>Figure 1.1</b>	Examples of vibroacoustic analysis.	3
<b>Figure 3.1</b>	Energy balance on a steady state element volume.	47
<b>Figure 3.2</b>	Flexural beam vibration.	54
<b>Figure 3.3</b>	Sign convention of forces and moments on an infinitesimal plate element.	61
<b>Figure 4.1</b>	Four accelerometer setup.	71
<b>Figure 4.2</b>	Spectral derivation process: (a) sine wave $u(x) = \sin(k_0 x)$ with $k_0 = 20\pi$ , (b) wavenumber spectrum $U(k)$ of $u(x)$ .	75
<b>Figure 4.3</b>	Spectral derivation process: (a) cosine wave $g(x) = du(x)/dx = k_0 \cos(k_0 x)$ with $k_0 = 20\pi$ , (b) wavenumber spectrum $G(k)$ of $g(x)$ .	75
<b>Figure 4.4</b>	Illustration of the KSD method.	76
<b>Figure 4.5</b>	Oval 2D Butterworth filter.	82
<b>Figure 4.6</b>	VEFESPI method.	83
<b>Figure 5.1</b>	Four wave components in a rectangular beam.	87
<b>Figure 5.2</b>	Positive sign conventions.	90
<b>Figure 5.3</b>	Waves in a point force or moment excited infinite beam.	91
<b>Figure 5.4</b>	Waves in a point force or moment excited simply supported beam.	98
<b>Figure 5.5</b>	Transmitted infinite wave energy along a force excited simply supported beam at different damping levels: (a) active VEF, (b) reactive VEF.	114



<b>Figure 5.6</b>	Transmitted reflection wave energy along a force excited simply supported beam at different damping levels: (a) active VEF, (b) reactive VEF.	116
<b>Figure 5.7</b>	Transmitted coupled wave energy along a force excited simply supported beam at different damping levels: (a) active VEF, (b) reactive VEF.	118
<b>Figure 5.8</b>	Transmitted total wave energy along a force excited simply supported beam at different damping levels: (a) active VEF, (b) reactive VEF.	118
<b>Figure 5.9</b>	Transmitted infinite wave energy along a moment excited simply supported beam at different damping levels: (a) active VEF, (b) reactive VEF.	121
<b>Figure 5.10</b>	Transmitted reflected wave energy along a moment excited simply supported beam at different damping levels: (a) active VEF, (b) reactive VEF.	121
<b>Figure 5.11</b>	Transmitted coupled wave energy along a moment excited simply supported beam at different damping levels: (a) active VEF, (b) reactive VEF.	122
<b>Figure 5.12</b>	Transmitted total wave energy along a moment excited simply supported beam at different damping levels: (a) active VEF, (b) reactive VEF.	123
<b>Figure 5.13</b>	Unconstrained damping layer attached to a beam.	124
<b>Figure 5.14</b>	Combined linear hysteretic loss factor of an unconstrained layer damped beam in dependency on the thickness ratio $t_D/t_B$ .	126
<b>Figure 5.15</b>	Combined flexural stiffness of an unconstrained layer damped beam in dependency on the thickness ratio $t_D/t_B$ .	127
<b>Figure 6.1</b>	Periodisation of a non-periodic sinusoidal signal using the MRS periodisation technique: (a) original signal, (b) original signal + mirrored and reversed signal, (c) sheared original + mirrored and reversed signal.	135

- Figure 6.2** Periodisation of a non-periodic sinusoidal signal using the MP periodisation technique: (a) original signal, (b) truncated mirrored signals + original signal, (c) continuously linked mirrored signals + original signal. 136
- Figure 6.3** Complex infinite beam displacement to the right: (a) 2D real part, (b) 2D imaginary part, (c) 1D real part, (d) 1D imaginary part. 138
- Figure 6.4** Wavenumber spectrum of the infinite beam displacement shown in Figure 6.3: (a) real part, (b) imaginary part. 139
- Figure 6.5** KSD determined and exact solution of the 3<sup>rd</sup> spectral derivative of the displacement shown in Figure 6.3: (a) real part using KSD, (b) imaginary part using KSD, (c) real part exact solution, (d) imaginary part exact solution. 140
- Figure 6.6** Exact and VEFESPI determined energy flow of the infinite beam displacement shown in Figure 6.3: (a) active energy flow, (b) reactive energy flow. 141
- Figure 6.7** Periodised infinite beam displacement shown in Figure 6.3: (a) real part MP method, (b) imaginary part MP method, (c) real part MRS method, (d) imaginary part MRS method. 142
- Figure 6.8** Exact and VEFESPI determined energy flow of the infinite beam displacement shown in Figures 6.3 and 6.7: (a) active energy flow, (b) reactive energy flow. 143
- Figure 6.9** Exact and VEFESPI determined energy flow of the infinite beam displacement shown in Figure 6.7: (a) active energy flow, (b) reactive energy flow. 144
- Figure 6.10** Relative error of VEFESPI determined energy flow and exact solution of the infinite beam displacement shown in Figure 6.7: (a) relative active flow error, (b) relative reactive flow error. 145
- Figure 6.11** Infinite complex beam displacement to the right of the excitation location contaminated by normally distributed

	noise with $\text{SNR} = 108.2$ : (a) 2D real part, (b) 2D imaginary part, (c) 1D real part, (d) 1D imaginary part.	148
<b>Figure 6.12</b>	Wavenumber spectrum of the infinite beam displacement shown in Figure 6.11: (a) real part, (b) imaginary part.	149
<b>Figure 6.13</b>	Relative MSE of the infinite beam displacement shown in Figure 6.11 using ideal filtering: (a) real MSE, (b) imaginary MSE.	150
<b>Figure 6.14</b>	Exact and ideal filtered VEF of the infinite beam displacement shown in Figure 6.11 using ideal filtering at optimum cut-off points: (a) active energy flow, (b) reactive energy flow.	151
<b>Figure 6.15</b>	Relative MSE of the infinite beam displacement shown in Figure 6.11 using a Butterworth filter: (a) real MSE, (b) imaginary MSE.	153
<b>Figure 6.16</b>	Exact and Butterworth filtered VEF of the infinite beam displacement shown in Figure 6.11 using a Butterworth filter at optimum cut-off wavenumbers: (a) active energy flow, (b) reactive energy flow.	154
<b>Figure 6.17</b>	Comparison of noise: (a) extracted ESPI noise of 801 Hz vibration, (b) normally distributed artificially generated noise.	157
<b>Figure 6.18</b>	KSD determined and exact solution of the 3 <sup>rd</sup> spectral derivative of the ESPI noise contaminated infinite beam displacement at 801 Hz: (a) real part using KSD, (b) imaginary part using KSD, (c) real part exact solution, (d) imaginary part exact solution.	158
<b>Figure 6.19</b>	Real relative MSE of the ESPI noise contaminated infinite beam displacement at 801 Hz using different types of filter: (a) ideal filter, (b) Butterworth filter.	159
<b>Figure 6.20</b>	Exact and filtered VEF of the ESPI noise contaminated infinite beam displacement at 801 Hz: (a) real part of active energy flow, (b) real part of relative error.	160

- Figure 6.21** Magnitude of complex wave amplitudes to the right of the excitation location for different loss factors: (a) infinite evanescent wave, (b) infinite travelling wave, (c) reflecting evanescent wave, (d) reflecting travelling wave. 163
- Figure 6.22** Infinite waves and reflection waves beam displacement of a simply supported beam: (a) real part infinite waves, (b) imaginary part infinite waves, (c) real part reflection waves, (d) imaginary part reflection waves. 164
- Figure 6.23** Complex and hysteretically damped simply supported beam displacement at the 6<sup>th</sup> mode: (a) 2D real part, (b) 2D imaginary part, (c) 1D real part, (d) 1D imaginary part. 165
- Figure 6.24** KSD determined and exact solution of the 3<sup>rd</sup> spectral derivative of the beam displacement shown in Figure 6.23: (a) real part using KSD, (b) imaginary part using KSD, (c) real part exact solution, (d) imaginary part exact solution. 166
- Figure 6.25** Exact and determined VEF of the simply supported beam displacement shown in Figure 6.23: (a) active energy flow, (b) reactive energy flow. 167
- Figure 6.26** Relative error of determined VEF of the simply supported beam displacement shown in Figure 6.23: (a) relative active flow error, (b) relative reactive flow error. 168
- Figure 6.27** Complex and hysteretically damped simply supported beam displacement at the 7<sup>th</sup> mode: (a) 2D real part, (b) 2D imaginary part, (c) 1D real part, (d) 1D imaginary part. 169
- Figure 6.28** Exact and VEFESI determined VEF of the simply supported beam displacement shown in Figure 6.27: (a) active energy flow, (b) reactive energy flow. 170

- Figure 6.29** Relative error of determined VEF of the simply supported beam displacement shown in Figure 6.27: (a) relative active flow error, (b) relative reactive flow error. 170
- Figure 6.30** Energy densities of the simply supported beam displacement shown in Figure 6.23: (a) kinetic, potential, and total energy density, (b) Lagrangian energy density. 173
- Figure 6.31** Exact and determined VEF from the incremental energy density integration method of the simply supported beam displacement shown in Figure 6.23: (a) active energy flow, (b) reactive energy flow. 174
- Figure 6.32** Relative error of determined VEF from the incremental energy density integration method of the simply supported beam displacement shown in Figure 6.23: (a) relative active flow error, (b) relative reactive flow error. 174
- Figure 6.33** Relative error of determined VEF from the incremental energy density integration method of the simply supported beam displacement shown in Figure 6.23 for different levels of damping: (a) relative active flow error, (b) relative reactive flow error. 175
- Figure 6.34** Exact and determined VEF from the incremental energy density integration method of the simply supported beam displacement shown in Figure 6.27: (a) active energy flow, (b) reactive energy flow. 176
- Figure 6.35** Relative error of determined VEF from the incremental energy density integration method of the simply supported beam displacement shown in Figure 6.27: (a) relative active flow error, (b) relative reactive flow error. 176
- Figure 6.36** Noise contaminated displacement of Figure 6.23 with SNR = 50 &  $\eta = 5 \cdot 10^{-3}$ : (a) 2D real part, (b) 2D imaginary part, (c) 1D real part, (d) 1D imaginary part. 179
- Figure 6.37** Wavenumber spectrum of the displacement shown in Figure 6.36: (a) real part, (b) imaginary part. 179

- Figure 6.38** Relative MSE of ideal filtered VEF of the simply supported beam displacement shown in Figure 6.36 at  $\eta = 5 \cdot 10^{-3}$ : (a) real MSE, (b) imaginary MSE. 181
- Figure 6.39** Exact and ideal filtered VEF of the simply supported beam displacement shown in Figure 6.36 at  $\eta = 5 \cdot 10^{-3}$ : (a) active energy flow, (b) reactive energy flow. 181
- Figure 6.40** Relative MSE of ideal filtered VEF of the simply supported beam displacement shown in Figure 6.36 at  $\eta = 2.5 \cdot 10^{-2}$ : (a) real MSE, (b) imaginary MSE. 182
- Figure 6.41** Exact and ideal filtered VEF of the simply supported beam displacement shown in Figure 6.36 at  $\eta = 2.5 \cdot 10^{-2}$ : (a) active energy flow, (b) reactive energy flow. 182
- Figure 6.42** MP and MRS periodised noise contaminated beam displacement shown in Figure 6.27: (a) real part MP, (b) imaginary part MP, (c) real part MRS, (d) imaginary part MRS. 183
- Figure 6.43** Relative MSE of ideal filtered VEF of the simply supported beam displacement shown in Figure 6.42: (a) active MSE, (b) reactive MSE ( $\eta = 2.5 \cdot 10^{-2}$ ). 184
- Figure 6.44** Exact and ideal filtered VEF of the simply supported beam displacement shown in Figure 6.42: (a) active energy flow, (b) reactive energy flow ( $\eta = 2.5 \cdot 10^{-2}$ ). 184
- Figure 6.45** Relative MSE of ideal filtered VEF from the incremental energy density integration method of the beam displacement shown in Figure 6.36 at  $\eta = 5 \cdot 10^{-3}$ : (a) real MSE, (b) imaginary MSE. 186
- Figure 6.46** Exact VEF and ideal filtered VEF from the incremental energy density integration method of the beam displacement shown in Figure 6.36 at  $\eta = 5 \cdot 10^{-3}$ : (a) active energy flow, (b) reactive energy flow. 186
- Figure 6.47** Relative MSE of ideal filtered VEF from the incremental energy density integration method of the beam

- displacement shown in Figure 6.36 at  $\eta = 2.5 \cdot 10^{-2}$ : (a) real MSE, (b) imaginary MSE. 187
- Figure 6.48** Exact VEF and ideal filtered VEF from the incremental energy density integration method of the beam displacement shown in Figure 6.36 at  $\eta = 2.5 \cdot 10^{-2}$ : (a) active energy flow, (b) reactive energy flow. 187
- Figure 6.49** Relative MSE of ideal filtered VEF from the incremental energy density integration method of the simply supported beam displacement shown in Figure 6.42: (a) active MSE, (b) reactive MSE ( $\eta = 2.5 \cdot 10^{-2}$ ). 189
- Figure 6.50** Exact VEF and ideal filtered VEF from the incremental energy density integration method of the simply supported beam displacement shown in Figure 6.42: (a) active energy flow, (b) reactive energy flow ( $\eta = 2.5 \cdot 10^{-2}$ ). 189
- Figure 6.51** Relative MSE of Butterworth filtered VEF of the simply supported beam displacement shown in Figure 6.36 at  $\eta = 5 \cdot 10^{-3}$ : (a) real MSE, (b) imaginary MSE. 191
- Figure 6.52** Exact and Butterworth filtered VEF of the simply supported beam displacement shown in Figure 6.36 at  $\eta = 5 \cdot 10^{-3}$ : (a) active energy flow, (b) reactive energy flow. 191
- Figure 6.53** Relative MSE of Butterworth filtered VEF of the simply supported beam displacement shown in Figure 6.36 at  $\eta = 2.5 \cdot 10^{-2}$ : (a) real MSE, (b) imaginary MSE. 192
- Figure 6.54** Exact and Butterworth filtered VEF of the simply supported beam displacement shown in Figure 6.36 at  $\eta = 2.5 \cdot 10^{-2}$ : (a) active energy flow, (b) reactive energy flow. 192
- Figure 6.55** Relative MSE of Butterworth filtered VEF of the simply supported beam displacement shown in Figure 6.42: (a) active MSE, (b) reactive MSE ( $\eta = 2.5 \cdot 10^{-2}$ ). 194
- Figure 6.56** Exact and Butterworth filtered VEF of the simply supported beam displacement shown in Figure 6.42: (a) active energy flow, (b) reactive energy flow ( $\eta = 2.5 \cdot 10^{-2}$ ). 194

- Figure 6.57** Relative MSE of Butterworth filtered VEF from the incremental energy density integration method of the beam displacement shown in Figure 6.36 at  $\eta = 5 \cdot 10^{-3}$ : (a) real MSE, (b) imaginary MSE. 196
- Figure 6.58** Exact VEF and Butterworth filtered VEF from the incremental energy density integration method of the beam displacement shown in Figure 6.36 at  $\eta = 5 \cdot 10^{-3}$ : (a) active energy flow, (b) reactive energy flow. 196
- Figure 6.59** Relative MSE of Butterworth filtered VEF from the incremental energy density integration method of the beam displacement shown in Figure 6.36 at  $\eta = 2.5 \cdot 10^{-2}$ : (a) real MSE, (b) imaginary MSE. 197
- Figure 6.60** Exact VEF and Butterworth filtered VEF from the incremental energy density integration method of the beam displacement shown in Figure 6.36 at  $\eta = 2.5 \cdot 10^{-2}$ : (a) active energy flow, (b) reactive energy flow. 197
- Figure 6.61** Relative MSE of Butterworth filtered VEF from the incremental energy density integration method of the simply supported beam displacement shown in Figure 6.42: (a) active MSE, (b) reactive MSE ( $\eta = 2.5 \cdot 10^{-2}$ ). 198
- Figure 6.62** Exact VEF and Butterworth filtered VEF from the incremental energy density integration method of the simply supported beam displacement shown in Figure 6.42: (a) active energy flow, (b) reactive energy flow ( $\eta = 2.5 \cdot 10^{-2}$ ). 198
- Figure 6.63** VEF of ESPI noise contaminated 11<sup>th</sup> mode beam displacement using the VEFESPI method: (a) active flow, (b) reactive flow. 202
- Figure 6.64** VEF of ESPI noise contaminated 11<sup>th</sup> mode beam displacement using integrated energy densities: (a) active flow, (b) reactive flow. 202
- Figure 7.1** Speckle effect on a laser illuminated surface. 209



<b>Figure 7.2</b>	ESPI system employed in this work for vibration measurements.	211
<b>Figure 7.3</b>	Timing of stroboscopic illumination (modified from [119]).	212
<b>Figure 7.4</b>	Modulation intensities and unwrapped phase.	214
<b>Figure 7.5</b>	Anechoic termination.	215
<b>Figure 7.6</b>	Force excited experimental “infinite” beam setup: (a) side view, (b) top view.	216
<b>Figure 7.7</b>	Moment excited “infinite” beam setup: top view (not to scale).	217
<b>Figure 7.8</b>	Photograph of the moment actuator.	218
<b>Figure 7.9</b>	Simply supported beam rig including the ESPI beam.	219
<b>Figure 7.10</b>	Transducer locations on the simply supported ESPI beam.	220
<b>Figure 7.11</b>	Simply supported beam rig including the moment excitation beam.	221
<b>Figure 9.1</b>	Modulus of the measured and theoretical point mobility of the force excited “infinite” ESPI beam: (a) 10 Hz-6.4 kHz, (b) 750-1450 Hz.	239
<b>Figure 9.2</b>	ESPI image of measured beam displacement at 801 Hz: (a) amplitude, (b) phase.	242
<b>Figure 9.3</b>	Complex and truncated ESPI displacement of the “infinite” beam at 801 Hz: (a) 2D real part, (b) 2D imaginary part, (c) 1D real part, (d) 1D imaginary part.	243
<b>Figure 9.4</b>	Complex filtered and truncated ESPI displacement of the “infinite” beam at 801 Hz: (a)-(b) 2D ideal filtered, (c)-(d) 2D Butterworth filtered.	243
<b>Figure 9.5</b>	Active VEF of the “infinite” ESPI beam at 801 Hz filtered with the ideal filter and Butterworth filter.	244
<b>Figure 9.6</b>	Comparison of measured input power $(P_{in})_{Fa}$ , measured corrected transmitted energy $(P_{t2})_{cr}$ and measured ESPI based energy flow at 801 Hz.	245
<b>Figure 9.7</b>	Relative difference in percent between ESPI measured VEF and transducer measured energy values.	246

- Figure 9.8** Relative change of measured ESPI based VEF in dependency upon the relative change of wavelength span in percent of the ideal filtered ESPI based VEF measurement at 801 Hz. 248
- Figure 9.9** Modulus of the measured point mobility of the force excited simply supported ESPI beams: (a) 10 Hz-3.2 kHz, (b) 500-3000 Hz. 250
- Figure 9.10** ESPI image of the single-layer damped simply supported beam vibrating at the 11<sup>th</sup> mode and 2745 Hz: (a) amplitude, (b) phase. 253
- Figure 9.11** Complex ESPI displacement of the single-layer damped simply supported beam vibrating at the 11<sup>th</sup> mode and 2745 Hz: (a) 2D real part, (b) 2D imaginary part, (c) 1D real part, (d) 1D imaginary part. 253
- Figure 9.12** Complex filtered ESPI displacement of the single-layer damped simply supported beam vibrating at the 11<sup>th</sup> mode and 2745 Hz: (a)-(b) 2D ideal filtered, (c)-(d) 2D Butterworth filtered. 254
- Figure 9.13** ESPI measured VEF of the 11<sup>th</sup> mode single-layer damped beam displacement at 2745 Hz using the VEFESPI method: (a) active VEF, (b) reactive VEF. 255
- Figure 9.14** ESPI measured VEF of the 11<sup>th</sup> mode single-layer damped simply supported beam at 2745 Hz using the IEDI method: (a) active VEF, (b) reactive VEF. 256
- Figure 9.15** Filtered ESPI measured potential energy density of the 11<sup>th</sup> mode single-layer damped beam displacement at 2745 Hz. 257
- Figure 9.16** Complex simply supported beam displacement of the 9<sup>th</sup> mode non-layer damped vibration: (a) real part, (b) imaginary part. 263

<b>Figure 9.17</b>	Filtered ESPI measured Lagrangian energy density of the 11 <sup>th</sup> mode single-layer damped beam displacement at 2745 Hz.	267
<b>Figure 9.18</b>	Measured force signals: (a) time history, (b) auto spectral density.	268
<b>Figure 9.19</b>	Ratio of actual to measured moment signals.	268
<b>Figure 9.20</b>	Modulus of the measured and theoretical moment point mobility of the moment excited “infinite” beam.	269
<b>Figure 9.21</b>	Ratio of extraneous force to measured moment.	270
<b>Figure 9.22</b>	Vibrational energy input to the experimental “infinite” beam measured using moment and rotational velocity compared with measured energy calculated using force and transverse velocity on the moment arms.	271
<b>Figure 9.23</b>	Comparison of input and transmitted energies in the experimental “infinite” beam.	272
<b>Figure 9.24</b>	Comparison of input and doubled transmitted energy to the right of the excitation location.	273
<b>Figure 10.1</b>	Different integration contours in the VEF field of an infinite plate.	281
<b>Figure 10.2</b>	Unconstrained damping layer attached to a plate.	292
<b>Figure 10.3</b>	Combined linear hysteretic loss factor of an unconstrained layer damped plate in dependency on the thickness ratio $h_D/h_P$ .	295
<b>Figure 10.4</b>	Combined flexural rigidity of an unconstrained layer damped plate in dependency on the thickness ratio $h_D/h_P$ .	295
<b>Figure 11.1</b>	Complex infinite plate displacement at $f_0 = 986.7$ Hz: (a) 2D real part, (b) 2D imaginary part, (c) real part at $y = 0$ , (d) imaginary part at $y = 0$ .	302
<b>Figure 11.2</b>	Top view image of the complex infinite plate displacement shown in Figure 11.1: (a) real part, (b) imaginary part.	303
<b>Figure 11.3</b>	Modulus of 2D FFT spectrum of the complex infinite plate displacement shown in Figure 11.1.	304

- Figure 11.4** VEFESPI determined and exact solution of the 3<sup>rd</sup> spectral derivative with respect to  $k_x$  of the displacement shown in Figure 11.1: (a) 2D modulus - VEFESPI, (b) 2D modulus - exact solution, (c) 1D modulus at  $k_y = 0$  - VEFESPI, (d) 1D modulus at  $k_y = 0$  - exact solution. 305
- Figure 11.5** VEFESPI determined and exact solution of the 3<sup>rd</sup> spatial derivative with respect to  $x$  of the displacement shown in Figure 11.1 at  $y = 0$ : (a) real part - VEFESPI, (b) imaginary part - VEFESPI, (c) real part - exact solution, (d) imaginary part - exact solution. 306
- Figure 11.6** Determined VEF in the  $x$  and  $y$  directions of the infinite plate displacement shown in Figure 11.1 using the VEFESPI + CW method: (a) active VEF in  $x$  direction, (b) reactive VEF in  $x$  direction, (c) active VEF in  $y$  direction, (d) reactive VEF in  $y$  direction. 308
- Figure 11.7** VEF maps of the infinite plate displacement shown in Figure 11.1 from the VEFESPI + CW method: (a) active VEF, (b) reactive VEF. 308
- Figure 11.8** Relative error of VEF of the infinite plate displacement shown in Figure 11.1: (a) relative active error in  $x$  direction, (b) relative reactive error in  $x$  direction, (c) relative active error in  $y$  direction, (d) relative reactive error in  $y$  direction. 310
- Figure 11.9** Comparison of total transmitted active vibrational energy and vibrational input power of the infinite plate displacement shown in Figure 11.1. 311
- Figure 11.10** Noise contaminated infinite plate displacement of Figure 11.1 with a SNR = 110.4: (a) 2D real part, (b) 2D imaginary part, (c) real part at  $y = 0$ , (d) imaginary part at  $y = 0$ . 312
- Figure 11.11** Filtered and exact 3<sup>rd</sup> spectral derivative of the displacement shown in Figure 11.10: (a) 2D - VEFESPI,

(b) 2D - exact solution, (c) 1D at  $k_y = 0$  - VEFESPI, (d) 1D at  $k_y = 0$  - exact solution. 313

**Figure 11.12** Butterworth filtered and exact solution of the 3<sup>rd</sup> spatial derivative with respect to  $x$  of the displacement shown in Figure 11.10 at  $y = 0$ : (a) real part - VEFESPI, (b) imaginary part - VEFESPI, (c) real part - exact solution, (d) imaginary part - exact solution. 314

**Figure 11.13** Relative error of total transmitted energy flow of the infinite plate displacement shown in Figure 11.10: (a) active MSE ideal filter, (b) active MSE Butterworth filter. 315

**Figure 11.14** VEF maps of the infinite plate displacement shown in Figure 11.10: (a) active ideal filtered VEF, (b) reactive ideal filtered VEF, (c) active Butterworth filtered VEF, (d) reactive Butterworth filtered VEF. 315

**Figure 11.15** Comparison of ideal filtered and Butterworth filtered total transmitted active vibrational energy and vibrational input power of the infinite plate displacement shown in Figure 11.10. 316

**Figure 11.16** Noise contaminated infinite plate displacement and extracted ESPI noise at 1503.2 Hz: (a) 2D real displacement part, (b) 2D imaginary displacement part, (c) 2D real noise part, (d) 2D imaginary noise part. 318

**Figure 11.17** Relative active error of total transmitted energy flow of the infinite plate displacement shown in Figure 11.16: (a) active MSE ideal filter, (b) active MSE Butterworth filter. 318

**Figure 11.18** VEF maps of the infinite plate displacement shown in Figure 11.16: (a) active ideal filtered VEF, (b) reactive ideal filtered VEF, (c) active Butterworth filtered VEF, (d) reactive Butterworth filtered VEF. 319

**Figure 11.19** Comparison of ideal filtered and Butterworth filtered total transmitted active vibrational energy and vibrational

- input power of the infinite plate displacement shown in Figure 11.16. 320
- Figure 11.20** Complex simply supported plate displacement: (a) 2D real part, (b) 2D imaginary part, (c) real part at  $y = L_y/2$ , (d) imaginary part at  $y = L_y/2$ . 323
- Figure 11.21** Top view image of the complex simply supported plate displacement shown in Figure 11.20: (a) real part, (b) imaginary part. 323
- Figure 11.22** Modulus of the 2D FFT spectrum of the complex simply supported plate displacement shown in Figure 11.20. 324
- Figure 11.23** VEFESPI determined and exact solution of the 3<sup>rd</sup> spectral derivative with respect to  $k_x$  of the displacement shown in Figure 11.20: (a) 2D modulus - VEFESPI, (b) 2D modulus - exact solution, (c) 1D modulus at  $k_y = 0$  - VEFESPI, (d) 1D modulus at  $k_y = 0$  - exact solution. 325
- Figure 11.24** VEFESPI determined and exact solution of the 3<sup>rd</sup> spatial derivative of the displacement shown in Figure 11.20 at  $y = 0$ : (a) real part - VEFESPI, (b) imaginary part - VEFESPI, (c) real part - exact solution, (d) imaginary part - exact solution. 326
- Figure 11.25** Computed VEF in  $x$  and  $y$  direction of the simply supported plate displacement shown in Figure 11.20 from analytical data: (a) active VEF in  $x$  direction, (b) reactive VEF in  $x$  direction, (c) active VEF in  $y$  direction, (d) reactive VEF in  $y$  direction. 327
- Figure 11.26** VEF maps of the simply supported plate displacement shown in Figure 11.20: (a) exact active VEF, (b) exact reactive VEF, (c) active VEF - VEFESPI + CW, (d) reactive VEF - VEFESPI + CW. 328
- Figure 11.27** VEF maps of the simply supported plate displacement shown in Figure 11.20: (a) active VEF - VEFESPI + MP,

- (b) reactive VEF - VEFESPI + MP, (c) active VEF - VEFESPI + MRS, (d) reactive VEF - VEFESPI + MRS. 329
- Figure 11.28** Total transmitted vibrational energy  $\phi_x$  of the simply supported plate displacement shown in Figure 11.20: (a) active  $\phi_x$ , (b) reactive  $\phi_x$ . 331
- Figure 11.29** Total transmitted vibrational energy  $\phi_y$  of the simply supported plate displacement shown in Figure 11.20: (a) active  $\phi_y$ , (b) reactive  $\phi_y$ . 332
- Figure 11.30** Relative error  $\Delta\epsilon_x$  of the simply supported plate displacement shown in Figure 11.20: (a) relative active flow error, (b) relative reactive flow error. 333
- Figure 11.31** Relative error  $\Delta\epsilon_y$  of the simply supported plate displacement shown in Figure 11.20: (a) relative active flow error, (b) relative reactive flow error. 333
- Figure 11.32** Noise contaminated simply supported plate displacement: (a) 2D real part, (b) 2D imaginary part, (c) real part at  $y = L_y/2$ , (d) imaginary part at  $y = L_y/2$ , ( $\eta = 10^{-3}$ ). 336
- Figure 11.33** Top view image of the complex simply supported plate displacement shown in Figure 11.32: (a) real part, (b) imaginary part, ( $\eta = 10^{-3}$ ). 336
- Figure 11.34** Relative MSE of ideal filtered TTVE of the plate displacement shown in Figure 11.32: (a) active MSE in  $x$  direction, (b) active MSE in  $y$  direction, (c) reactive MSE in  $x$  direction, (d) reactive MSE in  $y$  direction, ( $\eta = 10^{-3}$ ). 337
- Figure 11.35** Exact and ideal filtered total transmitted vibrational energy of the simply supported plate displacement shown in Figure 11.32: (a) active  $\phi_x$ , (b) reactive  $\phi_x$ , ( $\eta = 10^{-3}$ ). 338
- Figure 11.36** Relative MSE of ideal filtered total transmitted energy of a simply supported plate: (a) active MSE in  $x$  direction, (b) active MSE in  $y$  direction, (c) reactive MSE in  $x$  direction, (d) reactive MSE in  $y$  direction, (mode (5,3),  $\eta = 10^{-2}$ ). 339

- Figure 11.37** Exact and ideal filtered total transmitted vibrational energy of a simply supported plate: (a) active  $\phi_x$ , (b) reactive  $\phi_x$ , (mode (5,3),  $\eta = 10^{-2}$ ). 340
- Figure 11.38** Ideal filtered and exact VEF maps of the plate displacement shown in Figure 11.32: (a) exact active VEF, (b) exact reactive VEF, (c) active VEF - VEFESPI, (d) reactive VEF - VEFESPI, ( $\eta = 10^{-3}$  & SNR = 2685). 341
- Figure 11.39** Ideal filtered and exact VEF maps of a simply supported plate: (a) exact active VEF, (b) exact reactive VEF, (c) active VEF - VEFESPI, (d) reactive VEF - VEFESPI, ((mode (5,3) &  $\eta = 10^{-2}$  & SNR = 103). 341
- Figure 11.40** Relative MSE of ideal filtered total transmitted energy of a simply supported plate: (a) active MSE in  $x$  direction, (b) active MSE in  $y$  direction, (c) reactive MSE in  $x$  direction, (d) reactive MSE in  $y$  direction, ( $\eta = 10^{-2}$ , SNR = 94). 343
- Figure 11.41** Ideal filtered VEF maps of a simply supported plate: (a) active VEF - VEFESPI+MP, (b) reactive VEF - VEFESPI+MP, (c) active VEF - VEFESPI+MRS, (d) reactive VEF - VEFESPI+MRS, ( $\eta = 10^{-2}$  & SNR = 94). 343
- Figure 11.42** Relative MSE of Butterworth filtered total transmitted energy of a simply supported plate: (a) active MSE in  $x$  direction, (b) active MSE in  $y$  direction, (c) reactive MSE in  $x$  direction, (d) reactive MSE in  $y$  direction, (mode (5,3),  $\eta = 10^{-3}$ ). 345
- Figure 11.43** Exact and Butterworth filtered total transmitted vibrational energy of a simply supported plate: (a) active  $\phi_x$ , (b) reactive  $\phi_x$ , (mode (5,3),  $\eta = 10^{-3}$ ). 345
- Figure 11.44** Relative MSE of Butterworth filtered total transmitted energy of a simply supported plate: (a) active MSE in  $x$  direction, (b) active MSE in  $y$  direction, (c) reactive MSE



- in  $x$  direction, (d) reactive MSE in  $y$  direction, (mode (5,3),  $\eta = 10^{-2}$ ). 346
- Figure 11.45** Exact and Butterworth filtered total transmitted vibrational energy of a simply supported plate: (a) active  $\phi_x$ , (b) reactive  $\phi_x$ , (mode (5,3),  $\eta = 10^{-2}$ ). 347
- Figure 11.46** Butterworth filtered and exact VEF maps of simply supported plate: (a) exact active VEF, (b) exact reactive VEF, (c) active VEF - VEFESPI, (d) reactive VEF - VEFESPI, ((mode (5,3) &  $\eta = 10^{-3}$  & SNR = 2896). 348
- Figure 11.47** Butterworth filtered and exact VEF maps of simply supported plate: (a) exact active VEF, (b) exact reactive VEF, (c) active VEF - VEFESPI, (d) reactive VEF - VEFESPI, ((mode (5,3) &  $\eta = 10^{-2}$  & SNR = 106). 348
- Figure 11.48** Relative MSE of Butterworth filtered total transmitted energy of a simply supported plate: (a) active MSE in  $x$  direction, (b) active MSE in  $y$  direction, (c) reactive MSE in  $x$  direction, (d) reactive MSE in  $y$  direction, ( $\eta = 10^{-2}$  & SNR = 104). 349
- Figure 11.49** Butterworth filtered VEF maps of a simply supported plate: (a) active VEF - VEFESPI+MP, (b) reactive VEF - VEFESPI+MP, (c) active VEF - VEFESPI+MRS, (d) reactive VEF - VEFESPI+MRS, ( $\eta = 10^{-2}$  & SNR = 104). 350
- Figure 11.50** ESPI noise contaminated, single layer damped, simply supported plate displacement: (a) 2D real part, (b) 2D imaginary part, (c) real part at  $y = L_y/2$ , (d) imaginary part at  $y = L_y/2$ , ((mode (5,7) &  $\eta = 1.67 \cdot 10^{-2}$  & SNR = 145). 354
- Figure 11.51** Butterworth filtered and exact VEF maps of the simply supported plate displacement shown in Figure 11.50: (a) exact active VEF, (b) exact reactive VEF, (c) active VEF - VEFESPI, (d) reactive VEF - VEFESPI. 354

<b>Figure 11.52</b>	Exact and Butterworth filtered total transmitted vibrational energy of the simply supported plate displacement shown in Figure 11.50: (a) active $\phi_x$ , (b) reactive $\phi_x$ .	355
<b>Figure 11.53</b>	Top view image of the simply supported plate displacement shown in Figure 11.50 however, truncated to an integer number of wavelengths: (a) real part, (b) imaginary part.	356
<b>Figure 11.54</b>	Butterworth filtered and exact VEF maps of the simply supported plate displacement shown in Figure 11.53: (a) exact active VEF, (b) exact reactive VEF, (c) active VEF - VEFESPI, (d) reactive VEF - VEFESPI.	356
<b>Figure 11.55</b>	Exact and Butterworth filtered total transmitted vibrational energy of the simply supported plate displacement shown in Figure 11.53: (a) active $\phi_x$ , (b) reactive $\phi_x$ .	357
<b>Figure 11.56</b>	Computed MSE of periodised simply supported plate displacement using the MP technique, excited at the natural (3,3) mode in dependency on the product of $\eta \times$ SNR: (a) active MSE, (b) reactive MSE.	362
<b>Figure 12.1</b>	Experimental "infinite" plate rig including the ESPI plate.	367
<b>Figure 12.2</b>	Cross-sectional view of the force excited experimental "infinite" plate setup.	368
<b>Figure 12.3</b>	Experimental simply supported plate rig including the ESPI plate.	370
<b>Figure 12.4</b>	Explosion view of half cut experimental simply supported plate rig including the ESPI plate.	370
<b>Figure 12.5</b>	Side view of half cut experimental simply supported plate rig including the ESPI plate.	371
<b>Figure 14.1</b>	Modulus of the measured and theoretical point mobility of the force excited "infinite" ESPI plate: (a) 10 Hz-6.4 kHz, (b) 500-3200 Hz.	380

- Figure 14.2** ESPI image of the measured “infinite” plate displacement at 1503 Hz: (a) amplitude, (b) phase. 383
- Figure 14.3** ESPI image of the measured and truncated “infinite” plate displacement at 1503 Hz: (a) 2D real part, (b) 2D imaginary part, (c) real part at  $y = 0$ , (d) imaginary part at  $y = 0$ . 383
- Figure 14.4** Top view image of the complex “infinite” plate displacement shown in Figure 14.3: (a) real part, (b) imaginary part. 384
- Figure 14.5** Filtered complex “infinite” plate displacement at 1503 Hz: (a)-(b) ideal 2D filtered, (c)-(d) 2D Butterworth filtered. 385
- Figure 14.6** Filtered VEF maps of the “infinite” plate displacement at 1503 Hz: (a) active VEF – ideal filter, (b) reactive VEF – ideal filter, (c) active VEF – Butterworth filter, (d) reactive VEF – Butterworth filter. 386
- Figure 14.7** Filtered VEF maps of the “infinite” plate displacement at 605.6 Hz: (a) active VEF – ideal filter, (b) reactive VEF – ideal filter, (c) active VEF – Butterworth filter, (d) reactive VEF – Butterworth filter. 386
- Figure 14.8** Comparison of total transmitted ESPI measured active VEF and vibrational input power at 1503 Hz. 387
- Figure 14.9** Comparison of total transmitted ESPI measured active VEF and vibrational input power at 605.6 Hz. 388
- Figure 14.10** Relative difference in percent between total transmitted ESPI measured power and measured VIP at 1503 Hz. 388
- Figure 14.11** Relative difference in percent between total transmitted ESPI measured power and measured VIP at 605.6 Hz. 389
- Figure 14.12** Modulus of the measured point mobility of the force excited simply supported ESPI plates: (a) 10 Hz-3.2 kHz, (b) 350-2100 Hz. 394

- Figure 14.13** ESPI image of the measured fully covered single-layer damped simply supported plate displacement at 1459 Hz & mode (7,5): (a) amplitude, (b) phase. 395
- Figure 14.14** ESPI image of the measured and non-periodically truncated simply supported plate displacement at 1459 Hz & mode (7,5): (a) 2D real part, (b) 2D imaginary part, (c) real part at  $y = L_y/2$ , (d) imaginary part at  $y = L_y/2$ . 397
- Figure 14.15** ESPI image of the measured and periodically truncated simply supported plate displacement at 1459 Hz & mode (7,5): (a) 2D real part, (b) 2D imaginary part, (c) real part at  $y = L_y/2$ , (d) imaginary part at  $y = L_y/2$ . 397
- Figure 14.16** Top view image of the complex simply supported periodically truncated plate displacement shown in Figure 14.15: (a) real part, (b) imaginary part. 398
- Figure 14.17** Filtered and periodically truncated complex simply supported plate displacement at 1459 Hz & mode (7,5): (a)-(b) ideal 2D filtered, (c)-(d) oval 2D Butterworth filtered. 399
- Figure 14.18** Filtered VEF maps of the non-periodically truncated simply supported plate at 1459 Hz & mode (7,5): (a) active VEF - ideal filter, (b) reactive VEF - ideal filter, (c) active VEF - Butterworth filter, (d) reactive VEF - Butterworth filter. 400
- Figure 14.19** Filtered VEF maps of the periodically truncated simply supported plate at 1459 Hz & mode (7,5): (a) active VEF - ideal filter, (b) reactive VEF - ideal filter, (c) active VEF - Butterworth filter, (d) reactive VEF - Butterworth filter. 400
- Figure 14.20** Filtered VEF maps of the non-periodically truncated simply supported plate at 658 Hz & mode (5,3): (a) active VEF - ideal filter, (b) reactive VEF - ideal filter, (c) active VEF - Butterworth filter, (d) reactive VEF - Butterworth filter. 401

- Figure 14.21** Filtered VEF maps of the periodically truncated simply supported plate at 658 Hz & mode (5,3): (a) active VEF - ideal filter, (b) reactive VEF - ideal filter, (c) active VEF - Butterworth filter, (d) reactive VEF - Butterworth filter. 401
- Figure 14.22** Butterworth filtered energy densities of the periodically truncated, single-layer damped simply supported plate at 1459 Hz & mode (7,5): (a) 2D potential energy density, (b) top view image of  $e_{pot}$  (c) 2D kinetic energy density, (d) top view image of  $e_{kin}$ . 403
- Figure 14.23** Comparison of VIP and radiated sound power at both sides of a baffled non-layer damped simply supported plate using a force magnitude of  $F_0 = 0.141$  N and a loss factor of  $\eta = 5.22 \cdot 10^{-3}$ . 410
- Figure 14.24** Radiation efficiency of a baffled non-layer damped simply supported plate using a force magnitude of  $F_0 = 0.141$  N and a loss factor of  $\eta = 5.22 \cdot 10^{-3}$ . 411
- Figure 14.25** Butterworth filtered VEF divergence of the periodically truncated, single-layer damped simply supported plate at 1459 Hz & mode (7,5): (a) 2D divergence of VEF, (b) contour plot of VEF divergence. 413
- Figure 14.26** Butterworth filtered VEF divergence of the periodically truncated non-layer damped simply supported plate at 1536 Hz & mode (7,5): (a) 2D divergence of VEF, (b) contour plot of VEF divergence. 414
- Figure 14.27** Butterworth filtered total dissipated energy in the  $x$  direction of the periodically truncated single-layer damped simply supported plate at 1459 Hz & mode (7,5). 415

# LIST OF TABLES

<b>Table 5.1</b>	Simply supported beam properties.	115
<b>Table 6.1</b>	“Infinite” beam properties.	137
<b>Table 6.2</b>	Noise sensitivity study of non-periodised beam displacement data filtered with an ideal 2D filter.	152
<b>Table 6.3</b>	Filter slope sensitivity study of non-periodised beam displacement data filtered with an oval 2D Butterworth filter.	155
<b>Table 6.4</b>	Noise sensitivity study of non-periodised beam displacement data filtered with an oval 2D Butterworth filter.	156
<b>Table 6.5</b>	Vibrational parameters of “infinite” beam.	158
<b>Table 6.6</b>	Optimum “infinite” beam cut-off points and predicted VEF.	161
<b>Table 6.7</b>	Simply supported beam properties.	161
<b>Table 6.8</b>	Vibration parameters of experimental non-layer damped simply supported beam.	199
<b>Table 6.9</b>	Vibration parameters of experimental single-layer damped simply supported beam.	200
<b>Table 6.10</b>	Vibrational parameters of experimental double-layer damped simply supported beam.	200
<b>Table 9.1</b>	Measured input power and transmitted energy (all values given in Watts).	241

<b>Table 9.2</b>	Measured input power and transmitted energy (all power values given in Watts).	247
<b>Table 9.3</b>	Comparison of measured VIP and integrated ESPI measured potential energy density of the non-layer damped beam (all power values given in Watts).	258
<b>Table 9.4</b>	Comparison of measured VIP and integrated ESPI measured potential energy density of the single-layer damped beam (all power values given in Watts).	259
<b>Table 9.5</b>	Comparison of measured VIP and integrated ESPI measured potential energy density of the double-layer damped beam (all power values given in Watts).	259
<b>Table 9.6</b>	Comparison of VEF measured by the two-accelerometer method and the IEDI method within the non-layer damped beam (all power values given in Watts).	260
<b>Table 9.7</b>	Comparison of VEF measured by the two-accelerometer method and the IEDI method within the single-layer damped beam (all power values given in Watts).	260
<b>Table 9.8</b>	Comparison of VEF measured by the two-accelerometer method and the IEDI method within the double-layer damped beam (all power values given in Watts).	260
<b>Table 11.1</b>	“Infinite” plate properties.	301
<b>Table 11.2</b>	Vibrational parameters of “infinite” plate.	317
<b>Table 11.3</b>	Optimum “infinite” plate cut-off points of square truncated data.	320
<b>Table 11.4</b>	Simply supported plate properties.	322
<b>Table 11.5</b>	Vibration parameters of the experimental non-layer damped simply supported plate.	351
<b>Table 11.6</b>	Vibration parameters of the experimental single-layer damped simply supported plate.	351
<b>Table 11.7</b>	Vibration parameters of the experimental checkerboard-layer damped simply supported plate.	352

<b>Table 11.8</b>	Comparison of the theoretical input power $(P_{in})_{F_s}$ with the total transmitted energy within the plate computed from the integrated potential energy density of the non-layer damped simply supported plate.	363
<b>Table 11.9</b>	Comparison of the theoretical input power $(P_{in})_{F_s}$ with the total transmitted energy within the plate computed from the integrated potential energy density of the single-layer damped simply supported plate.	364
<b>Table 11.10</b>	Comparison of the theoretical input power $(P_{in})_{F_s}$ with the total transmitted energy within the plate computed from the integrated potential energy density of the checkerboard-layer damped simply supported plate.	364
<b>Table 13.1</b>	Operational parameters employed during the point mobility measurements.	374
<b>Table 13.2</b>	Operational parameters employed during the input power measurements.	376
<b>Table 14.1</b>	Measured vibrational input power (all power values given in units of Watts).	381
<b>Table 14.2</b>	Comparison of transducer measured VIP and ESPI measured Butterworth filtered TTVE of the non-layer damped experimental simply supported plate.	404
<b>Table 14.3</b>	Comparison of transducer measured VIP and ESPI measured Butterworth filtered TTVE of the single-layer damped experimental simply supported plate.	405
<b>Table 14.4</b>	Comparison of transducer measured VIP and ESPI measured Butterworth filtered TTVE of the checkerboard pattern-layer damped experimental simply supported plate.	405



# 1 INTRODUCTION

## 1.1 Motivation of Work

Noise can be annoying. Noise can be hazardous. Noise is a burden of modern life every one has to cope with. The growing environmental impact of noise demands counteractive measures that diminish noise exposure, which may result in serious illness or at least in an additional level of stress.

Noise is caused by dynamic processes due to the presence of vibration. Vibration processes are numerous and an inherent part of modern societies. Everybody experiences vibrations and its causes every day. In addition to the human factor of discomfort, the occurrence of noise may result in fatigue damage and, hence, system failure of structures. Quite often both the human factor and the structural factor are involved in serious problems related to noise phenomena. A prominent example is the squealing noise of train wheels that sometimes produce a strong noisy sound while braking. Not only is the squealing train wheel sound painful to the human ear, the vibrational interactions between the wheel and the brake also cause undesirable damage due to fatigue and, hence, passenger safety is at risk.

The generation and transmission process of vibrations can generally be divided into a source and a receiver, or a number of each. Both, the generation and transmission processes are fairly complex. There are two approaches to reduce noise. The first approach is the most obvious one, the minimisation of vibrations at the source. The second approach is the minimisation of vibrations between the source and the receiver, while

transmitting. Noise can be transmitted within different mediums. It can be transmitted within structures, in this case structure-borne processes are considered. Noise can also be transmitted through air, hence, airborne processes are present. These two processes are the most common. Noise can also be transmitted through water and soil, or a mixture of all. Within this research, structure-borne processes are considered only.

To increase or maintain comfort and safety, undesired vibrations need to be minimised simply through control. The control mechanism can be passive or active. Effective control of vibration is achieved most often by analysing and understanding the vibrational behaviour of a certain structure. Once the vibration phenomena is analysed and understood, the control of vibration using appropriate countermeasures can be undertaken efficiently. Thus, it is essential to develop techniques, analytical or experimental in nature, which can cope with this objective.

Vibrations can be felt as well as heard. The interactions between vibration and acoustics are analysed in the field of vibroacoustics. Many analysis techniques have been developed over the years to serve different purposes. Their usage relies mainly on the range of frequencies considered, as well as the quantity of interest to be determined. Figure 1.1 displays a selected range of techniques, which are most commonly used in vibroacoustic analysis.

The finite element method (FEM) and the boundary element method (BEM) are well known and well established techniques. Both techniques are suited for low frequency range analysis. With low frequency range an area in the frequency response function (FRF) is meant where the modal overlap is small, i.e. the frequency gap from one resonant frequency to a surrounding resonant frequency.

Techniques to cope with vibration phenomena in a mid or high frequency range are also available. Modal analysis (MA) is a common technique to determine so-called modal parameters of a vibrating system, e.g. resonant frequencies, modal damping, and relative modal displacement shape. Noise path analysis (NPA) can be used to predict dominant paths of vibrating structures, which may result in undesired sound radiation.

At the high frequency range, techniques such as the statistical energy analysis (SEA) or energy mean mobility approach (EMMA) may be used. These techniques can be characterised as energy based methods, since the primary variable employed here is energy. Energy as the primary variable is

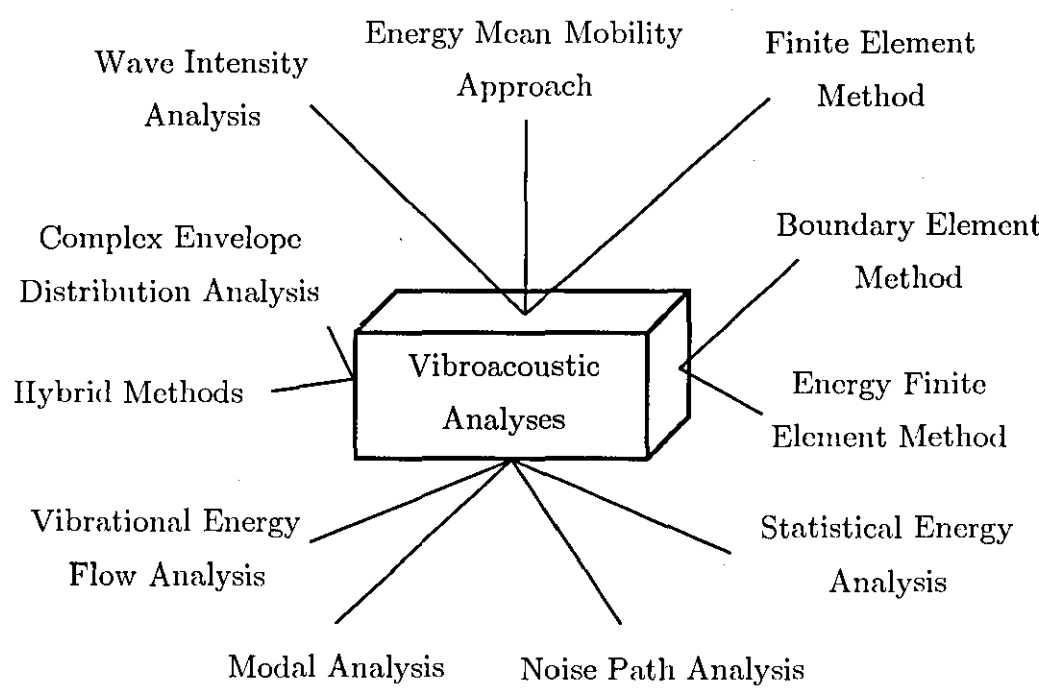


**Figure 1.1** Examples of vibroacoustic analysis.

chosen because the high modal overlap at high frequencies makes it rather difficult to distinguish between certain modes. In contrast, at low frequency range displacement, force and velocity are the primary variables. It is not the objective here to explain these techniques in detail as most literature sources do this. However, it is the intention to remind the reader that a huge number of techniques are available.

In Figure 1.1, vibrational energy flow (VEF) analysis is shown as a vibroacoustic analysis applicable in the mid frequency region. VEF analysis (VEFA) is used within this work. It employs the well known quantity energy and in the case of energy transmission per unit time, power. Energy and

power are universal measures applicable within almost every discipline. Electrical power, mechanical power or vibrational power all are given in units of Watts. This quantity is easy to understand and multidisciplinary.

VEFA provides energy flow information within a structure of interest. Energy-based quantities are derived as vector quantities containing two essential pieces of information, energy magnitude, and energy flow direction. Because of the vector property, it is possible to construct energy flow maps, which contain arrows that visualise the energy flow within a structure. Once this information is available, paths of high energy flow can be identified and, hence, manipulated in order to suppress undesired sound radiation.

VEF can also be used to develop abstract models, which allow a better understanding and handling of complex vibrational processes by employing energy balances. Imagine a transversally vibrating plate. The excitation of the plate is achieved by electrically powering an electrodynamic shaker. The electrical energy is transformed into mechanical energy and this mechanical energy is injected into the plate. Further, the mechanical energy is transformed into vibrational energy while transmitting through the plate. The point of energy injection is known as the energy source. Within the plate there might be points or regions, which are able to dissipate the injected vibrational energy. These points are called energy sinks. Due to a difference in vibrational potential, an energy flow occurs within the plate. Vibrational energy dissipation may appear due to the attachment of external dampers, internal structural dissipation, and sound radiation into surrounding mediums. Thus, by employing energy based quantities such as input energy, transmitted energy and dissipated energy, complicated processes within the structure of interest can easily be related to each other simply by applying the conservation of energy law.

VEFA has some advantages over alternative techniques, such as MA or SEA. With the aid of a MA, relative modal displacement information can be obtained. However, the modal displacement does not give information about energy source and energy sinks, since the modal spatial displacement distribution is not necessarily proportional to the spatial distribution of VEF within a structure. Thus, MA is not suitable when control of vibration is an

objective. SEA divides a structure into coupled substructures where stored and transmitted energies are computed. However, no information on the local energy distribution within the substructure can be obtained. This information is sometimes essential, however, when tackling vibrational problems.

There is also a major drawback to applying VEFA in solid structures. To determine VEF, the structural dynamics of the structure to be analysed needs to be known. In the case of simple beam and plate structures, the partial differential equations and, hence, internal force and moment definitions are well known. However, when the structure is more complex, an analytical definition of VEF is hardly possible without introducing erroneous approximation methods. Thus, VEFA is still restricted to simple built-up structures. However, this problem has been overcome recently by combining VEFA with the FEM method.

## 1.2 Objectives of Thesis

VEF can be analysed analytically. VEF can also be measured. There are numerous measurement techniques available on the market, spanning from accelerometer based measurements to the use of holographic interferometry. Electronic speckle pattern interferometry (ESPI), an advanced two-dimensional laser measurement technique, is a measurement tool used in the past to record modal displacement shapes of vibrating structures. Recent developments in ESPI, however, have gained interest in the applicability of this measurement technique to indirectly measure VEF. The main advantage of using such a system is the possibility to electronically acquire two-dimensional vibration amplitude and phase data. Thus, the recorded ESPI data are digitally provided, ready for further processing. Furthermore, most ESPI systems are delivered as compact modules and with increasing computation efficiency, real time processes could be applicable.

The aim of this research was to develop a measurement technique to measure VEF within beam and plate structures under use of an ESPI

measurement system (VEFESPI). Since dominant sound radiation is related mainly to flexural vibration, only this mechanism was considered herein.

The development process can be divided into four stages. In stage one, the theoretical base of VEF in beams and plates was set. In stage two, a technique was selected, which provides the spatial derivative information obtained from a set of displacement data. This information is essential as it is required by the VEF definitions set in stage one. An elaborate investigation in terms of VEF computation accuracy and VEF computation sensitivity was carried out in stage three. Here, the measurement method was investigated in detail using synthetic data. Advantages and disadvantages of the method were revealed. Stage four can be seen as the validation of the measurement technique as it uses real measured ESPI amplitude and phase data to compute VEF from experimental structures. Within this research infinite and finite beam and plate structures were analysed and measured.

However, it should be mentioned that in this research focus was drawn to the theoretical fundamentals and the numerical evaluation of the measurement with synthetic generated data, i.e. stage one to stage three. The reason focus was mainly drawn to the theoretical development and the numerical implementation of the measurement technique was that the practical validation could only be conducted with an ESPI measurement system, which was not state of the art and still at experimental stage. Thus, accuracy indications were given only, which are related to the performance of the employed ESPI measurement system. Modern systems may be much more capable.

In addition to the VEFESPI measurement technique, another measurement technique was developed in this research enabling the measurement of moment point mobility and input energy of a moment excited “infinite” beam. Although this measurement technique is not related to the VEFESPI method, it is part of the overall subject of measurement of VEF in structures.

### 1.3 Structure of Thesis

The dissertation presented here is divided into three parts. Chapters 2 to 4 deal with the general theory of VEF in beams and plates, as well as the introduction of the VEFESPI measurement technique. Chapters 5 to 9 address the theoretical and practical application of the VEFESPI method on beam structures. Furthermore, the measurement technique to measure moment point mobility and input energy is presented. Chapters 10 to 14 present the theoretical and practical application of the VEFESPI method on plate structures.

An extensive literature review is given in chapter 2. Literature sources on the theory of VEF, conventional and advanced measurements of VEF as well as moment excitation of structures are introduced and briefly summarised. Attention is drawn to literature related to the subject of this thesis and gaps in published research, leading to the objective of this work.

Chapter 3 reports a thorough introduction to VEF and energetic quantities in beams and plates. General energy based definitions and relations are presented and discussed.

Chapter 4 presents in detail the proposed measurement technique to measure VEF in beam and plate structures under use of ESPI. Therefore, VEFESPI and its components are described.

Chapter 5 introduces the theory of vibrational energy in beams, especially infinite beams and simply supported beams. The results of this chapter are used as reference quantities when validating the VEFESPI method numerically with synthetically generated beam displacement data.

Chapter 6 demonstrates the numerical validation of the VEFESPI method for infinite beams and simply supported beams. The computation accuracy and the computation sensitivity of the VEFESPI method in beam structures are taken into account. Hence, a fundamental feasibility investigation is carried out herein.

Chapters 7 and 8 present the measurement methods of vibrational energy in beams. The ESPI method is introduced briefly and the experimental beam apparatus employed during the beam experiments are

displayed. Furthermore, all the techniques used to measure point mobility, vibrational input power (VIP), and VEF in beams are reported in chapter 8. The measurement theory of the proposed moment excitation measurement technique is given here in detail.

Chapter 9 provides detailed results obtained on the ESPI based VEF measurements conducted on an “infinite” and simply supported beam. Furthermore, experimental validation of the proposed moment excitation measurement technique is given.

Chapter 10 introduces the theory of VEF in plates. Input and transmitted energy expressions are presented for infinite plate and simply supported plate structures. Also here, the results of this chapter are then used as a reference quantity when validating the VEFESPI method numerically with synthetic data.

Chapter 11 presents the numerical validation of the proposed VEFESPI measurement technique on infinite plates and simply supported plates. Also here, synthetic data are used and numerical VEFESPI computation results are compared with exact analytical solutions presented in chapter 10.

Chapters 12 and 13 provide information on the measurement of vibrational energy in plates. The experimental apparatus used throughout the “infinite” and simply supported plate experiments are displayed. All the measurement techniques used to compute point mobility, energy input, and transmitted energy employed during the experimental stage are given in detail.

Chapter 14 reports on the results obtained during the measurement of ESPI based VEF in an “infinite” and a simply supported plate. Furthermore, the gained results are discussed in detail.

Chapter 15 concludes on the results and cognitions obtained within this research. General conclusions on the measurement of VEF in beams and plates are given. An outlook of further work suggests actions that may be undertaken in order to improve the measurement of VEF in structures using ESPI.



## **2 LITERATURE SURVEY**

### **2.1 Introduction**

In this chapter literature related to the subject of this research is surveyed. A vast amount of literature can be found on vibrational power flow and its measurement techniques carried out over the last four decades. The most essential studies of conventional, typically accelerometer based, vibrational energy flow (VEF) measurements as well as more advanced, typically wavenumber based, VEF measurements are considered in greater detail. Less attention has been drawn to case studies derived from these fundamental researches. However, a few were included in this literature survey.

A literature review on the second subject of this thesis, moment excitation of structures, is also presented herein. However, focus has been drawn only to a few selected papers, which the author considers as the most important in relation to the moment excitation research conducted herein.

### **2.2 Introduction to Vibrational Energy Flow and Structural Intensity**

Mechanical structures exposed to external excitation within its elastic boundaries result in assumed linear stress-strain relations forcing the structure to a certain response (displacement, velocity or acceleration). Internal forces and moments occur within the structure due to elastic

deformation. Work is done when forces and moments move through the so-called displacement cycle [1, 1998]. In the existing literature many terms are related to vibrational power flow analysis (VPA). These are mainly vibrational energy flow, vibrational power flow, structural intensity, divergence of structural intensity and vibrational energy densities of any kind, such as total energy density, potential and kinetic energy density. The energy density quantities are important to carry out local energy distribution studies.

When vibrational power flow is mentioned, vibrational energy transmission is meant. The term vibrational power flow is somehow not correct in a physical sense, since it is not vibrational power that is flowing through a structure but vibrational energy that is flowing through a structure per unit time. However, a vast number of researchers use the physically wrong expression power flow, though. Within this work the expression vibrational energy flow per unit time is used instead, which is equivalent to vibrational power not vibrational power flow.

Another widely used important quantity is structural intensity (SI). This quantity is defined in a physically correct sense as vibrational energy flow per unit time per unit cross-sectional area, which is equivalent to vibrational power per unit cross-sectional area. The cross-sectional area is located perpendicular to the VEF direction. Most often this quantity is used in VEF analysis (VEFA) for beam and plate vibration equally, which is not entirely correct. From the occurring internal forces and moments within a beam that may be vibrating in flexure, vibrational power expressions can be derived directly. Often the derived vibrational power or VEF is wrongfully denoted as SI. However, herein the term VEF or transmitted vibrational energy (TVE) is preferred.

In terms of flexural plate vibration, energy flow equations derived from the arising internal forces and moments yield to a quantity, which is vibrational energy flow per unit time per unit width of cross-sectional area. In the existing literature this quantity is often denoted as SI of a plate. Sometimes this quantity is denoted as intensity resultant. Within this thesis the expression VEF per unit width or TVE per unit width is preferred

instead. Quite often VEF within a structure is computed as a complex quantity. The real part of it, which in a physical sense is the true TVE, is often denoted as active VEF or active SI. The imaginary part, which is less clear in a physical sense, is often denoted as reactive VEF or reactive SI.

In the following the term power flow and its derivatives will be used within the literature survey, since the surveyed literature sources use these terms. It will be however, dropped at the following chapters of this thesis.

## **2.3 Theory of Vibrational Energy Flow**

Locating energy sources and sinks, ranking paths of high transmitted energy that may cause strong sound radiation and identifying the resulting potential areas of vibration control are the main objectives of VEFA. There are many approaches in order to reduce vibration in structures. One can be the isolation or minimisation of unwanted vibration induced by machines and passed on to structures [2, 1991]. Another approach may be the manipulation of vibration in order to achieve predefined performance measures often used in sound design of products. All approaches presume a complete understanding of the dynamic process itself. In the past vibration has been defined in terms of modal behaviour of the structure. However, the modal amplitude distribution is not proportional to the net energy flow. A more effective way of describing a dynamic process is the use of the universal quantity power.

There are numerous publications dealing with theory of VEFA and the measurement of energy flow in structures such as beams, plates, pipes, or shells. A good general introduction to the topic VEFA can be found in reference [3, 2005]. The authors gave a critical review about the research undertaken within the field of VEFA. A categorisation of VEF measurements into three groups was given. These groups were denoted as contact methods, non-contact methods and computation methods. A similar approach is used here in sections 2.4, 2.5, and 2.6 of this chapter distinguishing between the

conventional VEF measurement techniques, advanced VEF measurement techniques and FEM based VEF computation, respectively.

Earlier work on VEFA was reported by Noiseux in 1970 [4, 1970]. He proposed mechanical intensity, defined as power per unit width of cross section, flowing through a structure. One and two-dimensional intensity formulations were derived. The structures have been assumed to be lossless, uniform and only in flexural vibration. Since Euler-Bernoulli theory has been applied, shear deformation and rotational inertia were neglected. Using biaxial accelerometers and assuming that the shear component of intensity in the farfield region is equal to the moment component of intensity the moment component has been measured only, since it was easier to acquire.

Goyder and White studied vibrational power flow from machines through isolators into built-up structures [5, 1980]. An introduction to power flow analysis was given considering several types of built-up structures. Mobility and power expressions were derived when exciting by a point force or torque an "infinite" beam and "infinite" plate. It was shown that the beam carries all the power away from the point of excitation. Also, the transmitted flexural power in an infinite beam is independent of distance and is equal to half the input power. The input power of an infinite plate is independent of frequency when excited by a harmonic point force and is proportional to increasing frequency when excited by a unit torque. The motion at the driving point of a foundation composed of a beam stiffened plate has also been investigated and was largely controlled by the beam. It was pointed out that flexural wave power radiates into the plate from the beam's excitation point whilst power transmitted by torsional waves in the beam does not radiate into the plate [6, 1980]. Vibrational power flow through isolators into the supporting foundations was also studied and it was concluded that power reduction can be achieved if the resonance frequency of the machine mass on the stiffness of the isolator is less than the excitation frequency [7, 1980]. Two stage isolation systems resulted in an increased power flow reduction. However, when dealing with broadband excitation the isolator will not be effective because resonant frequencies are included in the broadband excitation frequency range.

Walsh and White derived vibrational power transmission in a curved beam with constant curvature [8, 2000]. Four sets of power transmission equations have been presented using four different theories of wave motion, whereas one was based on the reduction of Love's thin shell equations, one was based on the reduction of Flügge's thin shell theory, and both were extended to corrections for rotary inertia and shear deformation. It has been demonstrated that three main frequency regions for predominantly extensional and flexural waves may be classified. One region below the ring frequency, one region above the ring frequency and one region above the shear wave cut-on frequency. It could be shown that rotary inertia and shear deformation can be neglected up to frequencies where the wavelength approaches the thickness of the curved beam.

Wohlever and Bernhard studied mechanical energy in rods and beams in analogy to the flow of the thermal energy model [9, 1992]. The authors showed that the rod was behaving approximately according to the thermal energy analogy. However, the beam solutions differed from the thermal analogy unless locally space-averaged energy and power was considered. Approximation models for longitudinally vibrating rods and transversally vibrating beams were derived relating the time-averaged local power to the time-averaged energy density. However, Caracterra and Sestieri have demonstrated later on that the thermal heat analogy is generally not applicable to vibration in mechanical systems. This is because energy transmission among finite sub-structures cannot be extended into a differential level using the thermal analogy to describe energy transmission within elemental volumes [10, 1995].

Bouthier and Bernhard modelled the energetics of transversally vibrating plates using the combination of three different relationships, namely the energy balance equation, a dissipation energy model and an approximation of energy propagation in the farfield [11, 1995]. The relation between energy density, input power density and dissipated power density in infinite plates were derived using the asymptotic expansion of the Hankel function of the farfield. It was shown that the presented energy expression is an excellent approximation in the farfield. In the case of finite plates a plane

wave farfield approximation was employed. After a spatial smoothing a relationship between energy density and intensity of the finite plate could be found. Comparison results to classical energy computation using modal descriptions revealed that the approximated quantities were in better agreement when internal damping increased. A rather similar study of transversally vibrating finite orthotropic plates was carried out in reference [12, 2003]. It was found that the approximate solutions agree well with the classical modal based energy distribution solutions at global and local levels.

Bobrovnitskii derived an exact expression of the energy conservation law and vibrational power in thin plates when vibrating in flexure [13, 1996]. A correction to reference [14, 1995] was given where scattering of flexural waves by circular inhomogeneities was investigated. The full energy density is defined as the sum of potential and kinetic energy density. Since three independent mechanisms cause energy transportation through a plate's cross section, effective shear force, bending moment and twisting moment components need to be taken into account when defining power quantities in plates. Thus, the initial power flow expression of reference [14, 1995] was corrected to one containing effective shear force (Kirchhoff-Kelvin edge condition), bending moment, and twisting moment terms. It was shown that the local energy conservation law as well as the integrated energy conservation law is valid, whereas the local energy conservation law of reference [14, 1995] fails.

It is widely accepted that evanescent waves do not transmit energy due to their exponentially decaying nature in space. However, Bobrovnitskii showed in [15, 1992] and Kurze in the following discussion [16, 1993] that evanescent waves can transmit energy. Bobrovnitskii demonstrated that two opposite evanescent waves (incident and reflected) at one end of a semi-infinite beam, which are neither in phase nor in counter phase, produce a uniform flow of energy along the structure. Although the net power flow through the beam's cross section was zero in this example this phenomenon has significance in many engineering structures where discontinuities or constraints occur.

The modelling of diffuse wavefields was investigated by Langley and Shorter in 2002 [17, 2002]. The authors have shown that diffuse wavefields can be modelled by using a summation of statistically independent outgoing and incoming cylindrical bending waves. These waves can be described in terms of  $n^{\text{th}}$ -order Bessel functions of the first kind or Hankel functions of the first and second kind. It has been reported that each cylindrical wave carries the same amount of power. These relations also hold true for diffuse longitudinal and diffuse shear waves in a plate.

Lande and Langley derived energy flow expressions of cylindrical bending waves in thin plates [18, 2005]. Inspired by Bobrovnikskii's results that evanescent waves can transmit energy, the interaction of energy flow related to evanescent cylindrical bending waves as well as cylindrical propagating wave components was investigated. If the displacement of a thin plate is composed of outgoing and incoming propagating wave components, which are defined by Hankel functions of order  $n$  of the first and second kind, energy flow is independent of the radius of consideration and there is no interactive energy flow between both wave components. Using modified Bessel functions for a description of the evanescent field showed that energy flow can occur through interaction of the two waves, if certain conditions are fulfilled. Using Hankel functions for the evanescent field description, the Hankel function of order  $n$  and of the second kind was the only one that permitted energy flow.

Xiong et al. [19, 2005] developed a damping based power flow mode method that is a derivative of the mobility based power flow mode method proposed in extended form in reference [20, 2003] for multi-excitation systems. Motivated by the conclusion that time-averaged power flow is equal to the power dissipated within a system [21, 1999] damping is chosen to be the primary quantity for power transmission definition. Reference [21, 1999] gave a thorough definition of power flow in mechanical continuums using the concept of an energy flow density vector. The damping based method utilises a characteristic damping matrix of the system to determine time-averaged transmitted power. The eigenvalues and eigenvectors of the characteristic damping matrix represent energy dissipated per unit power flow response. In

contrast to this, the mobility based power flow mode approach uses a characteristic mobility matrix. The eigenvalues and eigenvectors of this quantity represent the energy dissipated per unit power flow excitation. Transmitted power is predicted from the product of response vector and damping matrix eigenvalues and excitation force vector and mobility matrix eigenvalues, respectively.

Pavić investigated the importance of structural damping in mechanical systems in reference [22, 2005]. General relationships have been derived for local and global perceptions. It was concluded that on a global level the temporal mean total vibrational input power is proportional to the product of loss factor and global potential energy, assuming the damping is isotropic and uniformly distributed. If the damping is not uniformly distributed over the structure, volume integration of the product of loss factor and potential energy can be carried out. Identified relations on a local level are that the mean intensity divergence (spatial partial derivative of stress velocity intensity) is proportional to the product of internal material damping and potential energy density. In case the intensity is a complex quantity the imaginary part of the intensity divergence is proportional to the mean Lagrangian energy density, which means the difference between kinetic and potential energy density at the point of interest.

Two following articles of Pavić are also mentionable. As a subsequent study of reference [22, 2005], Pavić studied the energy characteristics of damped semi-infinite rods and beams [23, 2006]. Energy density and energy flow equations were presented and discussed when considering force and moment excitations. It has been shown that an acoustically long finite beam can approximate an equivalent semi-infinite beam well. Also, at the excitation location the potential energy is discontinuous for a rod or a moment excited beam. A computational study on a damped beam-plate system [24, 2006] gave an example of vibrational energy and vibrational energy flow in a beam attached to a plate.



## 2.4 Conventional Vibrational Energy Flow Measurements

Noiseux's attempt to measure vibrational power was limited by the lack of measurement equipment at that time. In 1976 Pavić introduced a wave intensity measurement method using an array of 4 (one-dimensional structure) or 8 (two-dimensional structure) velocity transducers measuring in the far and nearfield [25, 1976]. Using a finite difference approximation to obtain the spatial derivatives, the power flow distribution in the structure when in flexure was determined. A complete description of structural wave intensity for both, one and two-dimensional structures employing the Euler-Bernoulli theory was derived.

Verheij proposed in 1980 the cross-spectral density method to measure one-dimensional power flow for bending, longitudinal, and torsional waves [26, 1980]. The cross-spectral density method uses the theory of Fourier transform and applies frequency domain signal processing rather than time domain processing as used in Parvić's work [25, 1976]. The acceleration as the measured quantity is used instead of displacement or velocity. Employing a finite difference approximation to obtain spatial derivatives of the lateral acceleration, cross-spectral density formulations have been derived. Thus, readily available accelerometers can be applied for power flow measurements by using widespread multi-channel fast Fourier transform (FFT) analyser. The cross-spectral density method is widely employed as the standard power flow measurement technique.

Vibrational power flow outgoing from a source through a spring-like vibration isolator with complex stiffness to a finite beam (free at one end and arbitrary terminated at the other) was studied by Pinnington and White [27, 1981]. It was found that for force excitation, power is input to a structure at its resonant frequencies and for velocity source excitation power is input to a structure in the region of the anti-resonant frequencies. A finite beam model has been derived for beam mobility field taking reflection coefficient and damping attenuation into account. This model is used to derive simple

expressions for peak and average power transmission from a mass to a finite beam via spring-like isolators. Two measurement methods considering power input and power transmission have been used to verify the derived mobility model.

The finite difference approximation technique introduces errors to the power flow measurement, since the spatial derivatives are approximated by finite differences. The true value is underestimated and the error of this underestimation increases with increasing accelerometer spacing  $\Delta$ . Thus, the spacing should lie in the range between 0.15 and 0.2 of a wavelength. To avoid errors due to underestimation, Redman-White suggested a correction factor [28, 1984]. Applying this factor to the power flow measurement procedure compensates for the finite difference approximation error. Different error sources were investigated and recommendations for reliable power flow measurements were suggested.

Additional to the error introduced by the finite difference approximation further error sources need to be taken into account when measuring power in structures. Ming and Craik [29, 1997] investigated three types of bias errors in one-dimensional structures assuming that physical and material properties of the test structure are exactly known. It was shown that shear deformations and rotary inertia resulted in a large bias error at high frequency when using the Euler-Bernoulli wave theory. At frequencies far below a critical frequency where the decaying bending wave component became a travelling component, shear deformations and rotary inertia may be neglected. The presence of incoherent longitudinal waves during the measurement of bending wave power flow resulted in a non-bias error when measuring with biaxial accelerometers. However, when the longitudinal waves are coherent, the bias error increases with increasing longitudinal to bending wave power ratio, especially when employing the two-accelerometer power flow technique. Also, when measuring longitudinal wave power the presence of bending waves can be crucial to accuracy. Large bias errors may occur when the bending waves are incoherent with longitudinal waves and, thus, the error increases with increasing bending to longitudinal wave power ratio, the distance to beam thickness and the coherence.

Linjama and Lahti formulated a comprehensive derivation of cross-spectral density formulations when measuring the bending wave intensity in a beam including both, the near and the farfield [30, 1992]. The cross-spectral density method was extended utilising frequency response functions to estimate three cross-spectral densities required to predict the total bending wave intensity for the near and the farfield. With this method only two pairs of transducers were needed to predict the entire power flux including near- and farfield. However, one pair of transducers was needed when measuring in the farfield only. This method also cancelled phase errors of the instrumentation, since the cross-spectral density components were estimated. Good results were reported under controlled laboratory conditions.

Since the structural impedance and intensity are closely related to each other, Linjama and Lahti also investigated the measurement of the mechanical impedance and the reflection coefficient in beams [31, 1993]. Two methods were introduced to determine the reflection coefficient of bending waves in the farfield. One method was based on a finite difference approximation and the other was based on a direct analogy of the technique to measure the reflection of sound waves in ducts. The impedance may be estimated using three techniques. They are based on the finite difference approximation, the well known wave impedance, or the estimated reflection coefficient.

Bauman analysed five different estimation techniques to measure power flow in a damped beam using a finite difference approximation [32, 1993]. Two, three and four-position linear transducer configurations as well as single-position and three-position linear/rotational transducer configurations were taken into account. Effects on transducer spacing and transducer positioning were also included in this investigation. It has been found that all measurements based on farfield assumptions (two and three-positioning linear and single positioning linear/rotational transducer) performed reasonable well, even when locating the transducers within the nearfield. The three-positioning linear transducer technique delivered best results. Further, it has been pointed out that the four-position linear and three-position linear/rotational transducer technique, formulated to consider full field

conditions (near and farfield) delivered no acceptable results. It was assumed that positioning errors had been introduced. Since the single point linear/rotational transducer method was easily extendable to two dimensions and did not introduce positioning errors plus enabled direct and quick measurements, this method was proposed to be the most practical in situ measurement technique.

Walsh and White measured vibrational power transmission in an experimental “semi-infinite” curved beam with constant curvature using a finite-difference approximation [33, 2001]. An array of six accelerometers can be used to measure transmitted power, four in radial direction and two in circumferential direction. When exciting the beam in radial direction and when flexural waves are predominantly the main energy carrying mechanism, the traditional four accelerometer technique can be used. When exciting in the circumferential direction and extensional waves are the predominately energy carrying mechanism then straight beam extensional and curved beam extensional power components may be summed up.

## **2.5 Advanced Vibrational Energy Flow Measurements**

Accelerometer based power flow measurements and the usage of a finite difference approximation suffer from some drawbacks. Most mentionable are the influence on the structure’s dynamic response due to added transducer masses, unwanted phase mismatch between two or more transducer channels and the errors of the finite difference approximation while determining spatial derivatives. Thus, alternative measurement and processing techniques are desired in order to reduce the conventional accelerometer based method errors.

An alternative approach to the finite difference approximation is the wavenumber domain approach that was suggested by Williams, Dardy, and Fink in references [34, 1985; 35, 1985]. This approach was applied by a

method called structural intensity from the measurement of acoustic pressure (SIMAP), which is an outgrowth from nearfield acoustic holography (NAH) [36, 1985]. The acoustic pressure in a plane close to the surface of a vibrating underwater plate was measured. However, this method can be applied to any surrounding medium (e.g. air). From this two-dimensional pressure information, the normal surface velocity of the plate has been extracted, which is required for SI determination. To obtain the spatial derivatives of the plate's surface velocity a technique relying on the spatial Fourier transform has been applied and was denoted as a wavenumber domain approach. The wavenumber domain approach employed a derivation process of the transformed velocity signals in the wavenumber domain. After employing an inverse Fourier transform the spatial derivatives are found. SIMAP also provides the user with additional vibrational power and energy quantities such as acoustic intensity, injected power, radiated power, and energy densities.

The concept of the wavenumber domain approach to compute spatial derivatives of a structure's surface displacement or velocity was analytically applied to a beam in flexure by Unglenieks and Bernard [37, 1993]. Here, the wavenumber domain approach was addressed as spatial derivative (SD) technique [37, 1993]. Other references denote this technique  $k$ -space method [38, 1996]. The authors also investigated a second technique denoted as a travelling wave technique and carried out an error analysis for both techniques. It could be shown that the primary advantage of employing the SD-technique, in contrast to the finite difference approximation technique, is the ability to handle noise corrupted data. Problems using the SD-technique arose due to spatial leakage when a non-integer number of periods from the signal are to be analysed.

The need of alternative power flow measurement techniques led to the development of several other techniques. Most mentionable is the nearfield acoustic holography [34, 1985; 35, 1985; 36, 1985]. An outgrowth of NAH is the broadband acoustic holography from intensity measurement (BAHIM) method, introduced by Pascal et al. [39, 1990]. The authors proposed a method, which determined SI in plates using nearfield acoustic intensity and

quadratic pressure measurements under broadband frequency excitation. The Fourier transformed pressure field phase gradient, obtained from the measured acoustic intensity and the measured quadratic pressure modulus, formed a recalculated complex pressure expression. NAH can now be employed to calculate the spatial Fourier transformed plate velocity, required for further intensity calculation of the plate to predict the energy flowing through the structure.

Another approach to measure the surface deformation of vibrating structures is the use of an optical measurement apparatus using monochromatic laser light. Laser Doppler vibrometry (LDV) as a potential non-contacting optical measurement tool for power flow measurements has been widely studied. Hayek, Pechersky and Suen measured near and farfield SI using a scanning laser vibrometer on a vibrating beam, free at one end and terminated by a sand-filled box at the other (i.e. a semi-infinite beam) [40, 1990]. The finite difference approximation method was used to determine spatial derivatives of the surface velocity. A LDV scans the surface of a structure pointwise over a certain mesh size. Amplitude and phase of the structure's response to excitation (velocity) are measured and stored in a computer ready for post-processing. The acquired amplitude and phase are used to construct a complex vibration velocity field needed for power flow determination.

Kojima et al. measured SI in a U-shaped shell using two laser vibrometers and compared the measured results with SI results obtained from the finite element method (FEM) [41, 1998]. The two laser vibrometers were used to detect out-of-plane and in-plane deformation, which were defined in derived SI formulations of curved shells. A ratio of curve radius and bending wavelength has been introduced in order to show the amount of curve-term intensity in relation to the total intensity. It has been concluded that in case of large ratios the intensity of the curved structure can be measured with one laser vibrometer only, since in-plane deformations can be neglected.

Morikawa, Ueha, and Nakamura numerically and experimentally applied a scanning laser vibrometer to a finite damped beam and damped plate [38, 1996]. Here, the wavenumber domain approach was used to obtain

the spatial derivatives. Since noise in the acquired signal will be amplified during the derivation process in the  $k$ -space or wavenumber domain, the authors removed these noise components under usage of a low-pass filter. Filter parameters such as filter shape and cut-off wavenumber have been investigated in an error analysis. It was shown that the  $k$ -space method produced better results than the finite difference approximation.

Blotter and West introduced a three-step experimental power flow method [42, 1996]. This method utilised a scanning laser Doppler vibrometer to acquire the dynamic response of the structure at three different laser vibrometer positions. With the recorded data a continuous 3D complex-valued velocity field model was constructed using quintic B-splines. To obtain spatial derivatives, a  $9 \times 9$  Jacobian matrix was computed and inverted. Having the inverted Jacobian matrix, all the complex-valued generalised force terms can be determined (shear force, bending moment, twisting moment). Calculating the dot product between the force terms and velocities (transverse velocity, angular velocity) the vibrational power flow in a simply supported thin steel plate at three frequencies has been determined. It was demonstrated that at resonant and off-resonant frequencies energy transmission can be identified using this method.

Zhang and Mann III [43, 1996] investigated two different intensity formulations. One was earlier introduced by Pavić [25, 1976] and one was introduced by Romano [44, 1990]. Both formulations were applied to a viscoelastic damped plate using a laser vibrometer. Romano's intensity formulation relied on the three-dimensional elasticity definition. This formulation was simplified here by using the assumptions of Mindlin's plate theory (1951) [45, 1951]. Thus, longitudinal forces and in-plane shear forces corresponding to longitudinal and in-plane shear waves have been taken into account. The classical plate theory did not produce good results for sharp transients or at high frequency modes. A force distribution expression was used to identify vibration sources, based on Mindlin's plate equation of motion. The authors also investigated signal processing techniques such as windowing in the spatial domain and filtering in the wavenumber domain to overcome difficulties when analysing discrete data using a FFT. It could be

shown that at low frequencies both formulations produced almost identical results. Furthermore, the effect of windowing may be corrected, whereas the effect of filtering cannot be corrected.

Nejade and Singh applied a two-dimensional spatial Fourier transform in combination with a  $k$ -space filtering procedure to compute flexural intensity from a grid of lightweight accelerometers in finite plates with arbitrary boundary conditions in 2002 [46, 2002]. The authors employed a wavenumber domain filtering procedure, which was related to the well known modal superposition principle to remove noisy spectral components. Not all the vibration modes were included in the intensity calculation, since many modes contained unwanted information such as uncorrelated noise. Therefore, an ideal band-pass filter, centred at the wavenumber of the vibrating structure, was applied. Reactive and active flexural intensity maps were studied. Based on experimental results it was concluded that the reactive bending moment and shear force intensity components represented the deformation shape of the vibrating structure. Calculated active intensity components were used to detect source, absorption locations and transfer paths of energy. The shear force component has been identified as the most useful quantity to identify sources, since moments on the point of excitation are negligible. It was also concluded that at resonant frequencies of undamped plates where high standing waves were present, energy source localisation may be hampered.

Pascal et al. employed a two laser vibrometer system to measure SI in plates, whereas no reference signal was used [47, 1993]. The focus on this work was drawn to develop a measurement technique suitable for industrial application. Below the critical frequency of the plate, processing of evanescent waves is not an easy task, if one is interested in measuring intensity quite close to points of excitation locations or discontinuities. The technique proposed in this paper used the same principle as the BAHIM method. Thus, the complex velocity was obtained from the inverse Fourier transformed phase gradient of the velocity field and the modulus of the measured velocity by the two laser vibrometers. The finite difference approximation technique was then applied to find the first spatial derivative.



Another non-contacting laser based measurement method is the usage of holographic interferometry (HI). HI is a measurement technique, which utilises monochromatic laser light to construct a hologram that is based on the principles of interference and producible in a Michelson interferometer. However, whole-field measurements rather than pointwise scanning (LDV) measurements can be carried out. Pascal et al. applied HI to measure SI in an aluminium plate by measuring the flexural complex velocity of the whole vibration field [48, 1993]. Double-exposure and double-reference interferometry were employed to measure the velocity magnitude and the phase using a pulsed ruby laser. Two almost identical temporal exposures were recorded on the same photosensitive medium. The laser light reflected by the specimen interfered with the reference beam light for each exposure. The velocity information was then obtained due to an optical path change between the two exposures, assuming the surface state of the specimen had altered. Taking two holograms at one period in time, the complex vibrational field was found [49, 1995].

In high standing wave vibration fields the finite difference approximation method reduces its accuracy, since non-propagating wave components that form the standing wave field, result in measurement errors [49, 1995]. Using the  $k$ -space method in combination with HI it was possible to measure very weak energy flows close to the structure's resonant modes. For comparison reasons an energy transfer indicator was employed to compare measured intensity with the theoretical intensity present in an infinite plate due to flexural wave propagation. A 2D-FIR filter was used to reduce measurement noise that contaminated the signal prior to downsampling the image to 32 or 64 points [50, 1996]. Additionally, a low-pass filter was applied in the wavenumber domain to minimise the noise amplification during the derivation process.

It is well known that discontinuities in signals to be processed by a FFT result in a spectral leakage effect. The signal discontinuities may occur due to a non-periodic signal truncation. However, the computation of SI relies on the exact determination of the spatial derivatives obtained from the inverse transformed spectral derivatives. Thus, truncated signals will

introduce errors into the computation. Pascal et al. introduced a novel mirror processing technique to overcome the problem of leakage in 2002 [51, 2002]. This mirror technique created a continuous and periodic signal from the acquired original signal simply by mirroring the original signal at its ends. To ensure a smooth connection to either side of the original signal while mirroring, a link function (linear and cosine based) was employed. It has been demonstrated that this technique produced better results than applying either the spatial Fourier transform directly or padding the signals by zeros. Numerical examples were given for a free-free beam measured by using a scanning laser Doppler vibrometer.

Theoretical estimation of SI in naturally orthotropic plates has been carried out by Mandal et al. [52, 1998]. A two-transducer measurement method, which employed one cross spectra only, similar to the conventional two-accelerometer measurement technique of isotropic structures, was presented to predict SI at a single point within the structure. As an extension to this study, Mandal et al. investigated theoretically structure borne power transmission in thin naturally orthotropic plates [53, 2003]. Stress-strain relations were defined by using Young's modulus and the Poisson ratio in the  $x$  and  $y$  directions of the plate. Vibrational power expressions were derived using the complex power method. Employing the frequency response technique, as proposed by Linjama and Lahti [30, 1992], it was demonstrated that 15 cross-spectra of accelerometer signals are required to measure vibrational power in thin orthotropic plates when including the nearfield. This study has been extended by measuring the vibrational energy transfer in naturally thin orthotropic plates using the two-accelerometer method [54, 2005]. It could be shown that the two-accelerometer method can be used when measuring SI in thin orthotropic plates. The author applied the method of elastic equivalence [55, 1976] to quantify vibrational power flow in naturally orthotropic plates. In addition to this, experimental study on quasi longitudinal waves was carried out in 2006 [56, 2006]. Also here, the two-accelerator method and the method of elastic equivalence were employed in order to measure quasi-longitudinal wave power in rectangular and trapezoidal corrugated plates.

## 2.6 Vibrational Energy Flow Measurements Using ESPI

Petzing et al. measured surface intensity using electronic speckle pattern interferometry (ESPI) [57, 1996]. The surface intensity was predicted by measuring the vertical in-plane surface displacement on a resonant aluminium alloy beam free at one end and anchored in a damping sand box at the other end. The results were compared to vibrational power measurements using strain gauges and accelerometers. A close agreement has been found. The authors concluded that ESPI may be a potential measurement tool to measure vibrational power, especially when dealing with two intensity dimensions.

Alves et al. measured intensity in a free-free plate using a double pulsed ruby-laser to illuminate the vibrating object [58, 2000]. Amplitude and phase were determined by using a system of transcendental equations that corresponded to the acquired measurement information at two instants in time. Spatial derivatives were computed by employing regressive discrete Fourier series [59, 1992] in the wavenumber domain. A smoothing technique to smooth measured ESPI data using the two-dimensional discrete Fourier series was applied and noise spikes were filtered out by using a median filter. Measured structural intensity maps have been presented in terms of active and reactive intensity of the shear force, bending moment and twisting moment. Results were compared with computed intensity using finite element modelling. Despite good agreement at some cases no comparison to conventional measured power data were given nor were the measured and computed results compared in an example.

Chambard et al. applied TV-Holography to different mechanical structures (clamped plate, washing machine and cylinder) [60, 2002]. With the use of a special software called VIPART software [61, 2000] amplitude, phase, intensity, divergence and force distribution maps have been produced. This software was developed to determine SI and acoustic radiation of planar structures. Data input from holographic and scanning laser vibrometer

measurements was also possible. Image processing of holographic data enabled the correction of amplitude and phase if geometrical distortions were present. The wavenumber spectrum of a two-dimensional Fourier transform was used to compute spatial derivatives and SI divergence required for determining vibrational energy flow, energy sources and energy sinks. Acoustical radiation calculation can also be calculated by the program. It was shown that TV-holography is a new and valuable tool for engineers working in the field of vibration and noise, targeting structural behaviour improvement.

Eck and Walsh applied ESPI to measure vibrational power in a heavily damped beam using the SIMESPI method [62, 2003; 63, 2004 and 64, 2006]. A continuous 150 mW frequency doubled Nd:Yag laser was applied by a stroboscopic pulse that was synchronised to the excitation frequency of the structure. At a frequency rate of 25 Hz, the surface displacement of a transversally vibrating beam has been recorded at three different excitation frequencies. The wavenumber processing technique of the measured beam displacement was employed to determine the spatial derivatives required for energy flow computation. Comparisons with conventional acquired input power and transmitted energy data using transducers were made. It has been shown that measurements at local minima and local medium magnitude of the frequency response function showed a good agreement to the conventional measured vibrational power. However, at local maxima of the frequency response measurement errors occurred, mainly due to parasitic torsional motion within the beam.

## **2.7 Vibrational Energy Flow Measurements of Engineering Structures**

VEFA is still restricted to built up structures such as beams and plates having different boundary conditions or different material properties. However, there are also a few applications to engineering structures.

Kwon and Ih [65, 1998] measured vibrational power flow in a two-span belt-pulley system using two closely spaced laser velocity sensors. Vibrational power flow was obtained in the farfield only using a finite-difference approximation of the measured velocity signal. It has been concluded that the total vibrational power is the sum of true power flow and the power flow related to the belt motion.

Lee and Kim applied the concept of vibrational power flow analysis and multi-dimensional transfer path analysis to a compressor system, which was mounted in an air conditioner chassis [66, 2004]. Three major paths of high energy flow were identified and their individual contributions to the total power were investigated. Sound pressure level measurements were compared with acceleration level measurements on the structure surfaces and it was shown that VEFA can be used to qualitatively predict the level of noise radiation.

Hussein and Hunt applied a power flow method to evaluate the mean power flow generated by underground railways, which radiated sound into nearby buildings [67, 2006]. An infinite train that moved with constant speed within a thin shell, which represented the tunnel surrounded by an infinite medium was used in the modelling process. A track model and a tunnel soil model were derived. Wavenumber-frequency domain coupling between Euler-Bernoulli beams (track system) and a thin shell (tunnel) embedded within an infinite medium (soil) was employed in order to investigate different effects of different model parameters on power flow.

Lee measured vibrational power through 18 isolators located on different positions in a passenger car to identify high power transmission paths generating a booming noise in the back [68, 2004]. Vibrational power expressions of isolators were derived using an isolator apparent mass matrix and cross spectrum information between source and receiver accelerations. Acoustic transfer function measurements and experimental modal analysis were used to visualise the relationship between vibrational power of the isolators and interior noise. The transmission path identified as the major power path generating the booming noise was then modified and a decrease in interior sound pressure level could be achieved.

## 2.8 Vibrational Energy Flow from Finite Element Method

Computing vibrational power or SI with the aid of the finite element method (FEM) has been a concern to many researchers. The advantage of this method is that the structural response information of vibrating complex structures can be obtained numerically for each discretised structure element. Element forces and motion quantities, such as displacement and velocity, can be used to calculate vibrational power at each grid point. This information enables the localisation of vibrational power or SI in magnitude and direction in the structure itself.

Outgoing from studies referenced in [69, 1990], Hambric determined vibrational power and SI of a simple truss structure and a beam-stiffened cantilever plate at low frequencies [69, 1990]. Vibrational power flow and input power equations due to lateral, longitudinal, and torsional structure motion were derived. An analytical FEM study of the simple truss structure revealed different flow scenarios at different frequencies between the truss members. Also, different power flow pattern at different frequencies of the beam-stiffened cantilever plate were revealed.

Continuative from [69, 1990], Hambric and Taylor applied a FEM power flow analysis to real structures [70, 1994]. A straight steel beam excited at one side and attached to a rigid rubber mount at the other side was investigated. Rubber mounts with different end impedances were used. The different termination impedances symbolised different damping levels at the beam's end. Two cases, low and high damping were considered. The measured beam termination impedance was then used as an input to the FEM model to characterise the boundary condition of the rubber mount. Comparison to conventional measured flexural power using three accelerometers was made. It has been concluded that FEM based power flow predictions can be carried out if the boundary condition input to the FEM model is accurate enough.

Gavrić and Pavić used the normal mode approach to compute SI under use of the FEM [71, 1993]. SI expressions of beam, plate and shell structures were derived using variables often employed in finite element computation such as internal forces and moments as well as translational and angular displacements. A dissipation free simply supported plate with an attached viscous damper was investigated in order to estimate the convergence of the modal superposition principle. It has been shown that a large number of modes are required to achieve a good approximation of SI, particular at discontinuities, sources and sinks. Therefore, modal analysis cannot be used directly for SI predictions, since this procedure is limited to lower modes. However, the problem was overcome by using a swept static solution to provide additional mode information.

Li and Lai employed the FEM to calculate SI and surface mobility in a simply supported aluminium plate [72, 2000]. The full method for harmonic response solution was applied rather than using the mode superposition approach. This method used full matrices of the system to be analysed without any simplifications. The first and third bending modes were investigated. SI plots of both modes were presented for three different scenarios. The scenarios were a point force excitation of a lossless plate having an attached damper, a point force excitation of a non-lossless plate without viscous damping and a force excitation of a non-lossless plate over a finite area. It has been shown that the excitation locations as well as energy sinks and the position of the attached viscous damper could be identified in the SI plot. However, the root-mean-square (rms) velocity distribution from FEM prediction did not give any identification about energy sources and sinks. Furthermore, it was demonstrated that the FEM determined surface mobility agreed well with the analytically determined mobility.

Xu et al. investigated vibrational power flow behaviour in a beam stiffened plate system under usage of the FEM [73, 2005]. A simply supported rectangular steel plate, stiffened by an unsymmetrical eccentric flat stiffener was analysed. It could be shown that the stiffener had the effect of localising the amount of energy flux in the plate at the stiffener position as well as changing the directions of the flow itself in the stiffener vicinity. It has been

shown further that the total power flow was depending on the natural vibration frequency of the whole plate-beam structure. Also, the relative percentage of power flowing through the plate and the stiffener was depending upon the ratio of the two structure flexural rigidities.

Mace and Shorter employed the FEM to create an energy flow model that can be efficiently computed [74, 2000]. Two approaches a global and a local approach were presented. The latter one can be related to the procedure used in statistical energy analysis (SEA) where the FEM based analysis is performed on a subsystem level. This information was then coupled with each other in order to gain global energy information of the complete system. Damping was included in terms of applying the loss factor approach. A numerical example of a coupled three plate structure was presented.

SI in plates using a range of springs and dampers has been of interest in [75, 2004]. A simply supported plate was investigated using the FEM. It could be shown that VEF for single as well as multiple damper positions was identified, enabling control of VEF. When using dampers with a large damping coefficient, a damper with less damping coefficient located in the proximity of this damper had less effect in dissipating vibrational energy.

Lee et al. applied the FEM in combination with the SI technique to detect cracks in a simply supported plate [76, 2006]. The detection process was due to changes in intensity pattern at vicinity of the crack. Different crack positions and damper locations have been investigated. It was found that cracks can be detected with the aid of the SI technique if the location of the crack was not parallel to the intensity flow. Smaller cracks were more difficult to detect than larger ones. It was also shown that intelligent positioning of dampers close to the crack tips may divert the energy flow around the crack. Thus, this method may be used to protect the structure on a temporary basis from further damage.



## 2.9 Miscellaneous Applications in Vibrational Energy Flow Analysis

Wang et al. applied a least-square B-spline approximation to a vibrational velocity field to determine SI [77, 2006]. This method can be seen as an alternative to the SD-technique. It was demonstrated that the use of B-splines resulted in a low-pass filtering, similar to the  $k$ -space filtering procedure, to remove unwanted noise components. It was also shown that the B-spline approximation technique did not require periodic and equally spaced velocity data. However, this requirement is essential when using the spatial Fourier transform to compute spatial derivatives. The B-spline method was applied on a simply supported aluminium plate that was excited by two shakers.

Arruda introduced a regressive discrete Fourier series method (RDFS) as an alternative to the two-dimensional spatial Fourier transform [59, 1992], which is suitable for SI computation. This method was employed to smooth data used for partial spatial derivative computation from measured data contaminated by noise. The RDFS method estimated coefficients using the two-dimensional discrete Fourier series of data having an arbitrary period and an arbitrary frequency resolution in a least-square way. It was shown that the RDFS method is computationally more efficient and precise than the smoothing process using a common 2D FFT. It has also been shown that this method may also be applicable to data that are non-equally spaced and stored in a non-rectangular form.

Energy source localisation using the reactive SI has been a concern in a study of Alves and Arruda [78, 2001]. It was demonstrated that using the divergence of the reactive SI in combination with the potential and kinetic energy densities, the source of a vibrating aluminium beam (simulated numerically using FEM) could be localised in a reverberant environment. Usually in high reverberant structures active SI is hard to measure, since the net energy flow tends towards zero due to high discontinuity reflections.

Control of vibrating structures in either a passive or active way is of great concern to many researches in order to suppress unwanted vibration, especially at resonant frequencies. The SI method can be employed as a control input measure once the dominant paths of a vibrating structure are identified.

Fuller and Burdisso suggested the use of a feedforward controller applied in the wavenumber domain to minimise sound radiation by minimising the appropriate structural wavenumber component of the spectral acceleration [79, 1991].

Arruda presented extended results on the active control of power flow in plates outgoing from previous studies referenced in the same publication [80, 1998]. The principle of these studies was to use controlling forces to dissipate input power as a measure to reduce vibrational power transmission.

Mace et al. introduced a real-time measurement method to measure near and farfield wave components in a beam. The measured wave components were estimated by digital filtering, designed in the frequency domain by employing a wave decomposition approach [81, 1998] and implemented in time domain as finite impulse response (FIR) filters [82, 2005].

Liu and Lu applied the SI method to attenuate the interior noise level of a simple box using passive and active control methods [83, 2006]. The SI method was used as a measure to detect dominant paths, which can then be manipulated in magnitude using dampers or controlling forces. The results of numerical simulations were presented using the FEM.

Wu and White presented a wave based approach to analyse vibrational power transmission applicable to a finite multi-supported beam with different support and end conditions [84, 1995]. Input power and transmitted power expressions were derived and different scenarios such as excitation location or internal damping magnitude were investigated. A subsequent paper extended this study by investigating the manipulation of vibrational power using a hysterical damped single degree of freedom (SDOF) mass-spring system, known as a neutraliser [85, 1995].

A similar study has been carried out by El-Khatib et al. in 2005 investigating the influence of a tuned vibration absorber (TVA) to minimise vibrational energy transmission or maximise vibrational energy absorption [86, 2005]. Near and farfield positions of the TVA were taken into account and the influence of different tuning parameters was analysed.

Zhu et al. studied the vibrational power flow behaviour of an infinite open cracked Timoshenko beam in dependency upon different geometrical parameters. The numerical study was compared to perfect beam structures. It has been found that the vibrational power flow method can be used as crack identification procedure however, the method is not very sensitive to small cracks.

Wang et al. focused on the study of a coupled plate-cylindrical shell system using VPFA [87, 2004]. Receptance functions for both structures were determined using modal analysis. The coupling of both structures was carried out using dynamic information from the externally excited substructures and reactions at the interface. Power flow results have been presented within the substructures and at the interfaces. The proposed method enabled simple and efficient calculations at higher modes, since the modes are defined by hyperbolic and trigonometric functions, which had continuous derivatives.

## **2.10 Moment Excitation of Structures**

Moment excitation has been neglected within power flow analysis over the last decades as it was assumed that power input to structures due to moment excitation is more essential in the high frequency region [88, 1996]. However, recently it has been shown that moment induced power at low frequencies is important to be included in analysis when sources are in proximity of discontinuities [89, 1993; 90, 1999; 91, 1999]. Also, difficulty in measuring the moment and its appropriate rotational response was one reason to exclude moment excitation in structural analysis. Here, problems arose in the attempt to induce a pure excitation moment to a structure. The then measured moment point mobility differed from the true moment point mobility due to

the presence of non-zero cross mobility terms. [92, 1998; 93, 1995]. However, with the knowledge of these non-zero mobility terms the measured moment point mobility can then be corrected in order to obtain the true mobility.

Petersson investigated the acoustic power transmission in a combined moment and force excited beam and frame-like structure [89, 1993] as well as plate-like structures [94, 1993]. Spatial variations near discontinuities were the focus of the work. Complex eccentricity, allowing for a phase shift between force and moment has been used to express the moment itself. Since force and moment derived quantities are dimensionally incompatible, transmitted power has been used as a comparison measure. Therefore, force and velocity expressions needed to be known. Asymptotic expressions of point- and cross-mobilities due to force and moment excitation were presented. Numerical results have shown that moments are important to include in the power transmission analysis at all frequencies if the translatory motion at discontinuities is constraint. On the other hand moment induced transmitted power can be neglected if the discontinuities are free from translatory constraints.

Two giant magnetostrictive rods used as a moment actuator was proposed by Petersson [95, 1987]. The use of two electrodynamic shakers to induce a moment to a structure was restricted due to physical shaker dimensions and a difficulty in matching the exact phase between the two shakers. Problems with stability, heating the coils due to the high current required to generate the magnetic field were the drawbacks of this technique, which may also be applied to other forms of excitation.

Jianxin and Gibbs [92, 1998] demonstrated that in principle a twin-shaker excitation system cannot induce a pure excitation moment to a structure. The reason for this is that the magnitudes of the shaker forces are mainly driven by the structure response. Furthermore, a correction is difficult to make, since the shakers do not match with each other. Therefore, true moment mobility cannot be determined directly from measured data. The use of magnetostrictive rods overcomes the matching problem of twin-shakers. However, the measured mobility may be corrected in order to obtain true moment point mobility.

Vibrational power transmissions to machinery supporting structures subjected to multi-excitation systems has been of interest in Koh's and White's study [88, 1996]. Since mobility can be related to power in relation with force, the authors have derived driving point mobility functions of uniform beams and rectangular plates. Measured mobilities on a clamped-simply supported beam and clamped-free-simply supported-free rectangular plate were compared to theoretical solutions. The theoretical response of the plate has been derived using the Raleigh-Ritz method. It was found that for finite beams and rectangular plates the driving point coupling mobility always exists. Exceptions occurred when the excitation point was located at the same position of mode shape symmetry. High frequency behaviour of finite structures in terms of moment and force excitation was in good agreement with theoretical finite structures when using higher hysterical loss factors. However, difficulties occurred with the measurement of rotational response at lower frequencies and the measurement of moment excitation. Especially the latter one raised questions of measurement accuracy. Mass load issues have also been of real concern.

VEFA and control schemes of structures was the subject in references [96, 1996; 97, 1996] when exposing the structures to multi-excitation. It has been shown that in situations in which the driving point coupling mobility exists (see [88, 1996]) all three mobilities contribute to vibrational power. The real part of the driving force mobility and moment mobility was always positive. However, the real part of the driving point coupling mobility can be both positive and negative depending on the mode shapes of vibration. If this real part is negative vibrational power will be diminished and this cancellation effect was employed as a basis for the proposed vibration control technique.

Moment excitation of structures raises problems in accurate measuring of the different dynamic quantities. Sanderson and Fredö investigated moment excited beam structures using a T and I-shape exciter configuration [93, 1995]. A method was derived to investigate the effects of loading due to moment exciter mass and transducer mass. Different force and force-moment ratios were derived in order to assess the quality of the measurement such as

the exciters adjustment or the quality of excitation. It has been shown that two main bias errors when measuring moment mobility with T and I-shape configurations occurred. One error was caused by wrong moment measurement due to exciter inertia. The other was caused by unwanted excitation and, thus, errors occurred in the rotational velocity measurement. The latter one can be divided further into the measurement object's sensitivity due to false excitation and the quality of moment excitation. Both are represented by different mobility and force-moment ratios. These errors mainly arose due to adding mass of the moment exciter, which introduced unwanted force excitation (especially at resonant frequencies) and differences between the exciting force couple to form the moment. Errors in measuring the moment can be tackled at best by subtracting the rotational inertia term of the moment exciter configuration or using a proper design to keep the inertia very low. At low frequencies rotational inertia loading may be neglected. It has also been shown that the I-shape exciter configuration was the better choice when exciting structures by a moment.

Measurement of moment mobility using a T and I-shape exciter configuration has been carried out by Sanderson [98, 1995] using direct two-channel measurements. Two dynamic exciters were used to apply a moment to a free-free steel and L-shaped steel free-free beam structure. As shown in theory, the bias error due to the exciter rotational inertia was compensated simply by subtracting the inertia term from the measured moment. Upper frequency limits were driven by the moment exciter resonance frequency. It has been demonstrated that I-shape configurations are slightly better in moment excitation measurements due to a lower mass and the direction of the applied force. However, both configurations can produce significant measurement errors, which are mostly caused by the total mass attached to the vibrating structure.

Champoux et al. applied an almost pure moment excitation to a simply supported aluminium plate [99, 2003]. The authors employed two impact hammers to generate a force couple, separated by a certain distance and were acting parallel to each other and in opposite direction. Theoretical investigations have been undertaken to investigate the limits and validity of

this approach. The coupling between plate and impact hammers was studied in theory using a plate-hammer model. The impact hammers were driven by two electric motors. These motors were controlled by a digital signal processor. The theoretical calculated quantities translational moment accelerance and rotational moment mobility were compared to the equivalent experimental quantities. An almost identical force impact had been achieved. It was realised that different force separation distances may be taken into account to measure a wide range of frequency, since large force separations excited low frequency modes better and vice versa.

Yap and Gibbs measured force [90, 1999] and moment [91, 1999] induced power at the interface of machine and receiver using the reciprocal method. The principle of reciprocity states that source and receiver positions are interchangeable. Under use of this principle power equations using transfer mobilities of excitation and selected remote points were derived. Therefore, the necessity to measure force and moment at point of contact between machine and receiver could be excluded. This exclusion was necessary as most interfaces could not be disconnected to directly measure force, nor was a moment transducer available. Since the moment could not be measured at the footage of the machine, reciprocal relationships were used to replace moment cross-transfer mobilities by associated force cross-transfer mobilities. Applying this indirect method measurement of a centrifugal fan connected to a concrete plate were carried out for single-point force and multi-point force contact [90, 1999] as well as for single-point force and moment contact [91, 1999]. It was shown that away from discontinuities the transmitted power is mainly dominated by the vertical input force at low frequencies. At higher frequencies moment induced power became more important. However, in proximity to discontinuities moment induced power became also essential at low frequencies.

## 2.11 Summary and Conclusions

This literature survey has introduced the most important research carried out in the field of VEFA, which is related to the work undertaken within this thesis. Additional to the references given above a huge amount of VEFA literature can be found from published proceedings of the international congresses on intensity techniques hosted four times in Senlis (France) by the Centre Technique des Industries Mécaniques (CETIM) [100, 1993].

Section 2.3 has introduced the theory of VEF briefly. Some of the most important publications were summarised. Because a huge amount of literature on the theory of VEF can be found, this section gives only a short introduction into the subject. However, the basic theory of VEF is developed in detail in chapter 3.

Different types of measurement techniques to measure VEF, considered as a main objective within this work, were introduced within section 2.4 to section 2.6. VEF measurements are categorised here into three groups namely conventional VEF measurements using accelerometer probes, advanced VEF measurements introducing NAH, BAHIM and LDV based measurements and previous work done on ESPI based VEF measurements.

Additional to the measurement technique the use of FEM based VEF methods were highlighted. FEM based VEF computation is considered as an alternative to the VEF measurement techniques, which still are restricted to simple build-up structures such as beams, plates, shells, or pipes. Thus, FEM based energy computation may be a potential tool in many engineering fields especially on a pre-development stage of products subjected to vibrational environments.

Some case studies on VEF related measurements on real engineering structures were also reported. Additionally, miscellaneous applications of VEFA were presented in order to give a more complete overview about the work done within this research area.

It should be mentioned that almost every study reporting on VEF in beams and plates did not include an error analysis, energy balance or sensitivity study. Most conclusions found in the literature were restricted to



subjective comments such as the measurement of VEF was feasible, applicable or seemed to work well. An objective validation of these subjective conclusions were often neglected. Therefore, within this thesis attention was mainly drawn to the theoretical and numerical implication of the measurement technique to be proposed. Thus, an error and sensitivity analysis was taken into account for each type of structure to be investigated.

Further, literature reporting on the VEF measurement using ESPI was restricted to case studies only. No reference was found that studied the application of ESPI to measure VEF in structures on a fundamental level.

It was also shown within this literature survey that the application of the  $k$ -space technique has certain advantages over the finite difference approximation, especially when two-dimensional signal processing is required. Hence, this method was chosen as an essential part of the VEF measurement technique proposed within this research.

Section 2.10 reported on literature, which investigated the subject of moment excitation of structures. Because this subject was almost neglected in the past only a few essential publications were found. However, most proposed moment excitation measurement techniques are either fairly complicated or potentially erroneous. Thus, focus was drawn within this research to develop a novel, simple and easy to implement moment measurement technique.

# **3 DEFINITION OF VIBRATIONAL ENERGY FLOW AND ENERGETIC QUANTITIES**

## **3.1 Introduction**

The aim of this chapter is to introduce the concept of vibrational energy flow (VEF) and its related quantities used throughout this work, for one-dimensional (beam) and two-dimensional (plate) structures. Thus, in section 3.2 general energy based balance equations are presented in order to point out relations between vibrational energy flow, structural intensity (SI), energy dissipation, and vibrational input power (VIP). Section 3.3 introduces a practical general mechanical power definition applicable to most vibration scenarios in VEF analysis (VEFA). The general definition of SI as an essential measure in VEFA is introduced in section 3.4. Input power and VEF expressions derived from internal forces and moments occurring during transverse harmonic force excitation of beam and plate-like structures are presented in the remaining sections.

## **3.2 Vibrational Energy Relations**

In the existing literature a huge amount of vibrational energy and vibrational power based definitions are used. So far no standardisation of energy based

expressions has been achieved. There is now a huge amount of literature sources available that provide energy based quantities and its derivatives on a fundamental level. Most mentionable are references [9, 11, 19, 21, 22, 101, and 102]. The energy balance of different types of energy densities within a structure present in a given volume of interest can be written as [11]:

$$\int_V \frac{\partial e_{tot}}{\partial t} dV + \int_V \pi_{diss} dV = \int_A \vec{\sigma} \frac{\partial \vec{u}}{\partial t} dA + \int_V \pi_{in} dV. \quad (3.1)$$

Here,  $e_{tot}$  is the total energy density (energy per unit volume),  $V$  is the volume,  $A$  is the cross-sectional area,  $t$  denotes the variable time,  $\vec{\sigma}$  is the stress tensor,  $\vec{u}$  is the displacement vector,  $\pi_{in}$  denotes the input power density (energy input per unit time per unit volume) and  $\pi_{diss}$  represents dissipated power density (energy dissipated per unit time per unit volume). It can be noted from equation (3.1) that the sum of total energy density flow (energy density rate) and dissipated power density is equal to the sum of energy intensity flow and input power density that is injected into the system. The first integral on the right-hand side of equation (3.1) represents an energy density flow within the region of interest and its kernel is known as SI. This quantity is introduced later in section 3.4. Taking into account that the outflow of SI is negative and using the divergence theorem of the SI equation (3.1) can be rewritten as:

$$\frac{\partial e_{tot}}{\partial t} = \pi_{in} - \pi_{diss} - \nabla \cdot \vec{I}. \quad (3.2)$$

Herein,  $\vec{I} = \vec{\sigma} \partial \vec{u} / \partial t$  denotes the SI vector and  $\nabla \cdot \vec{I}$  represents the divergence of the SI, defined later on by equation (3.19). This equation is known as the power balance equation for all elastic media and is true for steady state or transient analysis [11]. In the case of a steady state analysis spatial variation is considered only. Thus, the temporal differential of the total energy density is zero. Taking this into account equation (3.2) rearranged can be reduced to:

$$\pi_{in} = \nabla \cdot \vec{I} + \pi_{diss}. \quad (3.3)$$

The power balance shown in equation (3.3) states that the power input density supplied by an external source is equal to the energy flow (although here divergence of SI is shown) moving out of the volume through the volume boundaries and power density dissipated within the volume. This is a very important definition. If equation (3.3) is applied to infinite structures, often the dissipation process is neglected and, hence, input power is equal to the outflow of energy. If equation (3.3) is applied to finite structures that have a small or negligible energy outflow, the outflow divergence of SI can be neglected and, thus, only the dissipation process becomes essential.

The dissipation process within the volume can be seen primarily as a conversion of vibrational energy flow into heat. There are also losses due to sound radiation into the surrounding medium. Within this work a hysteretic damping approach is used to account for structural losses. The structural loss factor is defined in reference [103] as:

$$\eta = \frac{1}{2\pi} \frac{\pi_{diss}}{e_{rev}}. \quad (3.4)$$

Here,  $e_{rev}$  is the reversible mechanical energy density. Due to the ratio of dissipated energy and reversible energy density, the loss factor indicates the fraction of energy lost during one cycle of vibration. Another definition of the loss factor, quite similar to (3.4), is given in reference [1] as:

$$\eta = \frac{1}{2\pi} \frac{\text{energy dissipated per cycle}}{\text{max energy stored during the cycle}}. \quad (3.5)$$

It can be seen from equations (3.4) and (3.5) that the structural loss factor defines the amount of energy lost during one cycle of vibration. Thus,  $0 \leq \eta \leq 1$ . In statistical energy analysis (SEA) it is often assumed that the energy injected into an isolated subsystem is equal to the energy dissipated within

the isolated subsystem. Further, it is also assumed that this dissipated energy is proportional to the total energy such that [104]:

$$\pi_{in} = \pi_{diss} = \omega \eta e_{tot}. \quad (3.6)$$

In equation (3.6),  $\omega$  is the corresponding circular frequency that accounts for energy dissipated per cycle of vibration. Equation (3.6) shows a simple relationship between dissipated energy density and total energy density. It can be noted that the dissipated energy density is proportional to the product of total energy density, circular frequency, and structural loss factor. However, for many structures the total energy density is not distributed uniformly across a vibrating structure. Thus, equation (3.6) cannot be applied at a local level [22]. Time-averaged energetic quantities such as potential and kinetic energy density are derived within this thesis on a local basis providing information about their spatial distribution across the structure. Pavic presented in [22] a fundamental relationship that relates the complex divergence of SI with the energy densities of finite hysteretically damped structures as:

$$\langle \nabla \cdot \vec{l} \rangle_t = -2\omega \left( j \langle e_{kin} \rangle_t - (j - \eta) \langle e_{pot} \rangle_t \right). \quad (3.7)$$

Here,  $j$  is the complex unity, i.e.  $j = \sqrt{-1}$  and the chevrons  $\langle \rangle_t$  denote time-averaged quantities. The hysteretic loss factor  $\eta$  in equation (3.7) is assumed to be constant within the volume of interest. In this thesis divergence of SI is a complex scalar field, whereas SI is a complex vector field. From equation (3.7) it can be seen that the real part of SI divergence is proportional to the product of structural loss factor and potential energy density. The imaginary part of SI divergence is proportional to the Lagrangian energy density, which is defined as:

$$l_e = e_{kin} - e_{pot}. \quad (3.8)$$

Herein,  $e_{kin}$  is the kinetic energy density and  $e_{pot}$  is the potential energy density. The sum of both is simply the total energy density  $e_{tot}$ . Pavic also presented a relationship between the total time-averaged complex input power to SI and to the divergence of SI as:

$$\langle \underline{P}_{in} \rangle_t = - \int_S \langle \vec{I} \rangle_t dS = - \int_V \langle \nabla \cdot \vec{I} \rangle_t dV. \quad (3.9)$$

Here,  $S$  is the surface perpendicular to the direction of energy injection (see Figure 3.). It can be seen from equation (3.9) that the surface integral of SI and the volume integral of SI divergence are equal to the time-averaged input power. The negative sign in equation (3.9) accounts for outgoing flows. Hence, the sum of time-averaged input power and one of the SI based integrals is zero. If one substitutes equation (3.7) into the SI divergence integral of equation (3.9), the local energy density quantities may be transferred to global energy quantities and, thus, related to input power. Within a volume that contains no vibrational outflow of energy across its boundaries it has been shown in [105] that the real part of the complex, time-averaged power  $\langle \underline{P}_{in} \rangle_t$  is equal to the time-averaged dissipated power as:

$$\Re \{ \langle \underline{P}_{in} \rangle_t \} = \langle \Pi_{diss} \rangle_t. \quad (3.10)$$

Further, Alfredsson also showed that the imaginary part of  $\langle \underline{P}_{in} \rangle$  in an outflow-free volume is proportional to the negative Lagrangian density  $l_e$  given by:

$$\Im \{ \langle \underline{P}_{in} \rangle_t \} = 2j\omega \int_V (\langle e_{kin} \rangle_t - \langle e_{pot} \rangle_t) dV. \quad (3.11)$$

Using equations (3.7), (3.9), and (3.10) it can be shown that time-averaged dissipated power within a structure is proportional to the product of potential energy, the structural loss factor, and angular frequency as:

$$\langle \Pi_{diss} \rangle_t = 2\omega\eta \int_V \langle e_{pot} \rangle_t dV. \quad (3.12)$$

Equation (3.12) displays a simple relationship between dissipated power and potential energy if hysteretic damping is regarded. If one applies equation (3.2) to a lossless and load free volume element, it can be realised that the SI divergence is equal to the temporal change in total energy density, i.e.  $\partial e_{tot} / \partial t = \nabla \cdot \vec{I}$ . However, within this thesis a steady state analysis is

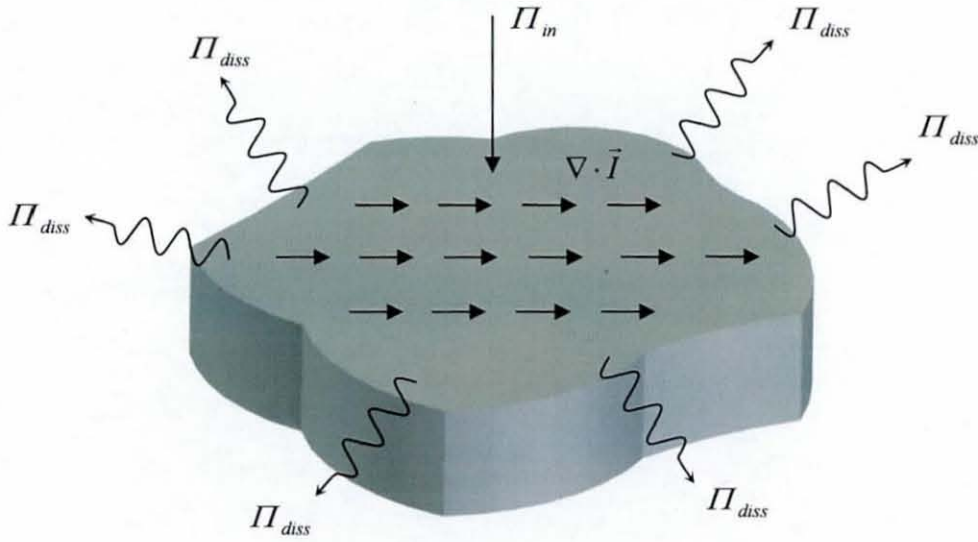


**Figure 3.1** Energy balance on a steady state element volume.

employed. The temporal derivative of the instantaneous total energy density is then zero and, thus, in a lossless and load free volume, the divergence of SI becomes zero. A contrast to this non-zero divergence of SI can be found if a source of energy supply is located within the volume of interest or if a source of energy dissipation is located within the volume of interest as indicated by equation (3.3) that defines the complete power balance of a volume in steady state motion. Thus, SI divergence can be used to locate energy sources (points of energy input) and energy sinks (points of energy dissipation). The

energy sinks may arise due to local damping or local radiation. Figure 3. displays the power balance shown in equation (3.3).

### 3.3 Definition of Mechanical Power

Mechanical work is done when a constant force  $F$  or a constant moment  $M$  act on a certain mass  $m$  and provoke a displacement  $r$  or a rotation  $\varphi$  of the mass. Herein,  $r$  is denoted as the translational displacement vector, and  $\varphi$  is denoted as the rotational displacement vector. Forces and moments can be seen as external or internal quantities. The differential of mechanical work due to forces is given by  $dW_t = \sum F dr$  and due to moments is given by  $dU_r = \sum M d\varphi$ . The summation accounts for the number of forces and moments to be considered that act on the mass  $m$ . Note, the subscript  $t$  denotes translational quantities, and the subscript  $r$  denotes rotational quantities. Integrating and summing the appropriate work's differentials defines the general total mechanical work as:

$$W = \sum_n \int_{R_n} F_n dr_n + \sum_k \int_{\varphi_k} M_k d\varphi_k. \quad (3.13)$$

It is evident from equation (3.13) that the sum of two integral expressions may form total mechanical work. Using the first integral sum kinetic energy and potential energy due to forces may be derived depending upon the direction of action. The second integral sum can be related to rotational motion. One or both terms may be considered in a vibration system depending on the structure to be analysed.

Mechanical power  $P$  is defined as mechanical work per unit time and, thus,  $P = dW/dt$ . Differentiating equation (3.13) with respect to time instantaneous mechanical power is given by:

$$P(t) = \sum_n F_n(t) v_n(t) + \sum_k M_k(t) \omega_k(t). \quad (3.14)$$



Herein,  $v_n(t)$  is the  $n^{\text{th}}$  translational velocity component and  $\omega_k(t)$  is the  $k^{\text{th}}$  rotational velocity component. In practice it is not useful to deal with instantaneous quantities. More often time-averaged quantities are employed, since a particular instant in time may not be of great interest. Hence, a time-averaged quantity needs to be defined. The time-averaged mechanical power of a time-depending signal is given as:

$$P = \langle P(t) \rangle_t = \lim_{T \rightarrow \infty} \left\{ \frac{1}{T} \left( \sum_n \int_T F_n(t) v_n(t) dt + \sum_k \int_T M_k(t) \omega_k(t) dt \right) \right\}. \quad (3.15)$$

Also here, the chevrons in equation (3.14) indicate time-averaged mechanical power. Equation (3.14) is a general expression of time-averaged mechanical power within a vibrating mechanical system. If the instantaneous time signals are sinusoidal, the limit of the integral can be neglected, since the period  $T$  is of finite length. When dealing with random time signals the limit needs to be taken into account. To derive power expressions for vibrating continuums as investigated herein the internal vibration mechanisms need to be analysed by defining internal forces and internal moments and their respective velocities.

### 3.4 Definition of Structural Intensity

The term SI is widely used in vibrational energy flow analysis (VEFA). Within this section a brief fundamental definition of SI is given. The integral product of the first right-hand side term in equation (3.1) can be identified as SI. In general the instantaneous field intensity vector is given by [44]:

$$\vec{I} = -\vec{\sigma} \frac{\partial \vec{u}}{\partial t}. \quad (3.16)$$

The intensity vector  $\vec{I}$  physically means energy transmission per unit time through a unit area of the structure. It can also be seen as the product of

energy density  $e$  and its propagation velocity. The negative sign states intensity flow out of the structural volume. The partial temporal derivative  $\partial \vec{u} / \partial t$  denotes the velocity vector  $\vec{v}$  at a certain point in the medium. The stress tensor is defined as [44]:

$$\vec{\sigma} = \lambda [\nabla \cdot \vec{u}] \vec{\mathbb{I}} + \mu [\nabla \vec{u} + \vec{u} \nabla]. \quad (3.17)$$

Here,  $\lambda$  and  $\mu$  are the Lamé constants of the lossless material and  $\vec{\mathbb{I}}$  is the identity tensor. A positive value of the SI indicates energy transmission from the outside to the inside of the medium. Using a three-dimensional Cartesian coordinate system, equation (3.15) can also be written as:

$$\vec{I}(x, y, z, t) = - \begin{bmatrix} \sigma_{xx} & \sigma_{xy} & \sigma_{xz} \\ \sigma_{yx} & \sigma_{yy} & \sigma_{yz} \\ \sigma_{zx} & \sigma_{zy} & \sigma_{zz} \end{bmatrix} \begin{bmatrix} v_x \\ v_y \\ v_z \end{bmatrix}. \quad (3.18)$$

The 3×3 matrix in equation (3.18) contains the stress components of the stress tensor on a three-dimensional solid element. The 1×3 vector denotes its corresponding velocity components in the  $x$ ,  $y$  and  $z$  direction, respectively. The stress components  $\sigma_{xx}$ ,  $\sigma_{yy}$  and  $\sigma_{zz}$  represent normal stress components and the remaining components denote tangential (shearing) stress components. The unit of SI, as defined by equation (3.18), is Watts/m<sup>2</sup>. In equations (3.2) and (3.3) the divergence of the SI has been used, which is given by:

$$\nabla \cdot \vec{I} = \frac{\partial I_x}{\partial x} + \frac{\partial I_y}{\partial y} + \frac{\partial I_z}{\partial z}. \quad (3.19)$$

The divergence of SI is a scalar field, which defines the strength of SI at each point due to summation of the SI slope for each direction to be considered. As mentioned before divergence of SI is an important indicator to visualise a

surface density of injected and dissipated energy flow in a structure [106]. Thus, with the computed rate of VEF or SI change points of energy supply or energy dissipation can be identified.

### 3.5 Vibrational Input Power

Vibrational energy injected into a structure per unit time is denoted here as vibrational input power (VIP). Points of vibrational energy injection are known as sources. VEF occurs if the structure dissipates the injected power in some way at some point. Usually vibrational energy is dissipated by internal and external damping mechanisms. Internal damping mechanisms could be of hysteretic or of viscous nature. External damping mechanisms may be achieved by attached dampers somewhere on the structure or at the boundary. Points of energy dissipation are known as sinks. General VIP can be defined according to the dot product of equations (3.14) and (3.15) given in section 3.3. An applied load (force or moment) may induce energy to a system by forcing the structure to a certain velocity response at an excitation location. Thus, the dot product between load and its appropriate velocity components at the excitation location is defined as input power. Load can be a force or a moment. Velocity response can be lateral velocity or rotational velocity. Using equation (3.13) the general total instantaneous input power injected into a system under applied sinusoidal varying loads is:

$$P_{in}(t) = \sum_n F(r_{0_n}, t) v(r_{0_n}, t) + \sum_k M(r_{0_k}, t) \omega(r_{0_k}, t). \quad (3.20)$$

Here, the subscript 0 represents excitation location quantities. In equation (3.20),  $r_0$  is the excitation location vector. The input power is strictly a real valued expression. However, in this work structural response measures are presented by complex quantities. Assuming a complex displacement solution and a complex, sinusoidal varying load, one may write equation (3.20) as:

$$P_{in}(t) = \sum_n \Re \{ \underline{F}_{0n} e^{j\omega t} \} \Re \{ \underline{v}_{0n} e^{j\omega t} \} + \sum_k \Re \{ \underline{M}_{0k} e^{j\omega t} \} \Re \{ \underline{\omega}_{0k} e^{j\omega t} \}. \quad (3.21)$$

The underbar of expressions  $\underline{F}_{0n}$ ,  $\underline{v}_{0n}$ ,  $\underline{M}_{0k}$  and  $\underline{\omega}_{0k}$  denote complex amplitudes and  $\Re$  denotes the real part of the complex quantities. Using equation (3.21) and relation (A2.10), the time-averaged total input power at the excitation location is given by:

$$P_{in} = \frac{1}{2} \sum_n \Re (\underline{F}_{0n} \underline{v}_{0n}^*) + \frac{1}{2} \sum_k \Re (\underline{M}_{0k} \underline{\omega}_{0k}^*). \quad (3.22)$$

Here, the asterisk  $*$  denotes a conjugate complex quantity. Note, the conjugate complex operation is commutative. Equation (3.22) is the general input power description of the time-averaged input power using multiple force and moment excitation. The usual chevron notation is dropped. Usually most structures are loaded only by one type of load.

It is well known that the mobility at the excitation location may be used to define input power when a force load is applied. This is presented as [103]:

$$(P_{in})_F = \frac{1}{2} |\underline{F}_0|^2 \Re \{ Y_{\underline{F}_0, \underline{v}_0} \}. \quad (3.23)$$

Similarly, input power due to moment excitation may be written as:

$$(P_{in})_M = \frac{1}{2} |\underline{M}_0|^2 \Re \{ Y_{\underline{M}_0, \underline{\omega}_0} \}. \quad (3.24)$$

Herein,  $Y_{\underline{F}_0, \underline{v}_0}$  is the complex force point mobility and  $Y_{\underline{M}_0, \underline{\omega}_0}$  is the complex moment point mobility. Most measurements in structural dynamics are carried out using an  $n$ -channel FFT analyser, which provides with different types of spectral density quantities such as auto spectral density and cross-spectral density. By employing the one-sided auto spectral and cross-spectral

densities of the force and its velocity component, equation (3.23) can be rewritten as [107]:

$$P_{in}(\omega)_F = G(F, F) \Re \left\{ \frac{G(F_0, v_0)}{G(F, F)} \right\} = \Re \{ (F_0, v_0) \}. \quad (3.25)$$

Also here, the subscript 0 denotes excitation location quantities. Similarly, the moment input power is given as:

$$P_{in}(\omega)_M = G(M, M) \Re \left\{ \frac{G(M_0, \omega_0)}{G(M, M)} \right\} = \Re \{ G(M_0, \omega_0) \}. \quad (3.26)$$

$G(F, F)$  and  $G(M, M)$  are the auto spectral densities of the force and moment, respectively. Note, the input powers  $P_{in}(\omega)_F$  and  $P_{in}(\omega)_M$  are in units of Watts/Hz and, hence, the spectral density quantities too.  $G(F_0, v_0)$  and  $G(M_0, \omega_0)$  are the cross-spectral densities between force and moment and respective velocity components. However, in practice most response quantities are acquired as accelerations. Using the temporal relation between velocity and acceleration  $v = a/j\omega$ , equations (3.25) and (3.26) may be rewritten as:

$$P_{in}(\omega)_F = \frac{1}{\omega} \Im \{ G(F_0, a_0) \}, \quad (3.27)$$

$$P_{in}(\omega)_M = \frac{1}{\omega} \Im \{ G(M_0, \alpha_0) \}. \quad (3.28)$$

All the given spectral expressions define the input power as a function of frequency, since all the employed spectral densities are functions of frequency.

### 3.6 Vibrational Energy Flow and Energetic Quantities in Beams

#### 3.6.1 Vibrational Energy Flow

Sound radiation due to flexural wave motion is considered to be the most effective mechanism [103]. Thus, mainly lateral force excitation is considered within this thesis. Figure 3.3 illustrates lateral load excitation of a beam, forcing the structure to a flexural response. The applied load can be a distributed force or an applied moment. The derivation of the beam's partial

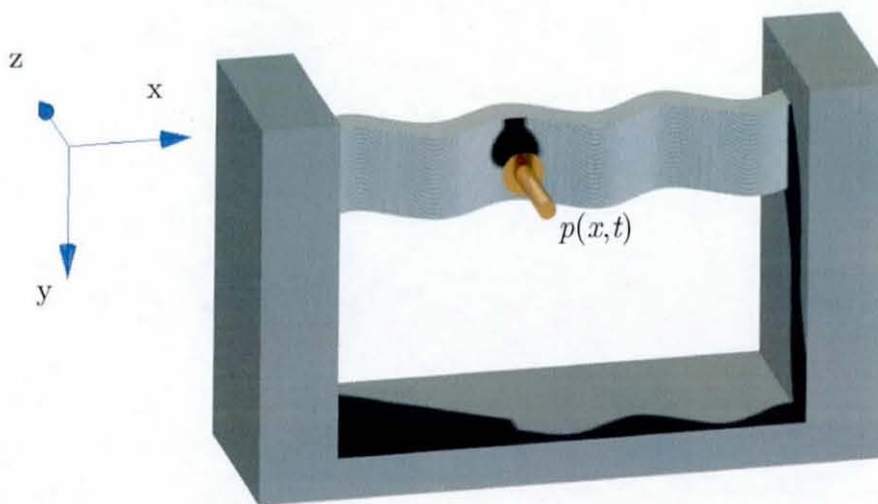


**Figure 3.2** Flexural beam vibration.

differential equation of motion and its dynamic quantities can be found in detail in Appendix A1. Euler-Bernoulli bending theory is used to derive vibrational energy transmission in a beam.

Flexural wave propagation in a beam is caused by the occurrence of internal shear forces and internal bending moments as a stress-strain reaction to external lateral load excitation. The shear force and bending moment that act on a small element are described by partial derivatives of the beams

lateral displacement  $u(x,t)$ . From Appendix A1, the bending moment is given by [103]:

$$M_B = -EI \frac{\partial^2 u(x,t)}{\partial x^2}. \quad (3.29)$$

Note, the negative sign is due to the fact that the normal stress  $\sigma_{xx}$  arises opposite to the positive  $x$  direction. Taking moment equilibrium of the small beam element, the shear force  $F_s$  can be found to be [103]:

$$F_s = EI \frac{\partial^3 u(x,t)}{\partial x^3}. \quad (3.30)$$

Having defined the internal forces and moments due to flexural wave propagation in beams, the number of force and moment components in equation (3.3) is thus, one. When a beam is vibrating in flexure the shear force causes the lateral velocity motion  $\partial u(x,t)/\partial t$ . On the other hand the bending moment causes element rotation, which results in an angular velocity component  $\partial u^2(x,t)/\partial t/\partial x$ . If one substitutes equations (3.29) and (3.30) into equation (3.15) by using the previously given velocity expressions, complex VEF within a beam can be written as:

$$P_x = \frac{EI}{T} \left( \int_0^T \frac{\partial^3 u(x,t)}{\partial x^3} \frac{\partial u(x,t)}{\partial t} dt - \int_0^T \frac{\partial^2 u(x,t)}{\partial x^2} \frac{\partial^2 u(x,t)}{\partial x \partial t} dt \right). \quad (3.31)$$

In equation (3.31) a time-harmonic load excitation and a complex beam displacement was assumed. Equation (3.31) may be simplified to:

$$P_x = \frac{1}{T} \left( \int_0^T F_s v_s dt - \int_0^T M_B \omega_B dt \right). \quad (3.32)$$

Using relation (A2.10) given in Appendix A2, the complex, time-averaged VEF within a beam is given by:

$$P_x = \frac{EI}{2} \left( \frac{\partial^3 u(x,t)}{\partial x^3} \left( \frac{\partial u(x,t)}{\partial t} \right)^* - \frac{\partial^2 u(x,t)}{\partial x^2} \left( \frac{\partial^2 u(x,t)}{\partial x \partial t} \right)^* \right). \quad (3.33)$$

The real part of equation (3.33) is addressed in this work as the active VEF, i.e.  $P_{x_a} = \Re\{P_x\}$ , where  $\Re$  denotes the real part. This part is the most interesting one, since it represents the net energy flow in the beam. The imaginary part is denoted in this work as reactive VEF of a beam, i.e.  $P_{x_r} = \Im\{P_x\}$ , where  $\Im$  denotes the imaginary part of the time-averaged complex VEF. Physically, the meaning of the reactive VEF is less obvious.

### 3.6.2 Energetic Quantities

In sections 3.2 and 3.4 SI, the divergence of SI and energy based quantities were derived as density quantities of a three-dimensional volume element. However, the beam's internal forces and moments are not derived as force and moment density quantities. The derived VEF in a beam has units equal to vibrational power (Watts). Thus, definition of SI in a beam is also in units of Watts. If one substitutes equation (3.33) into equation (3.19), the divergence of VEF in a beam can be found to be:

$$\langle \nabla \cdot P_x \rangle_t = \frac{EI}{2} \left( \frac{\partial^4 u(x,t)}{\partial x^4} \left( \frac{\partial u(x,t)}{\partial t} \right)^* - \frac{\partial^3 u(x,t)}{\partial x^3} \left( \frac{\partial^2 u(x,t)}{\partial x \partial t} \right)^* \right). \quad (3.34)$$

It can be seen from equation (3.34) that up to the 4th order spatial derivatives are required in order to determine the divergence of VEF (in W/m) in a beam. The time-averaged kinetic energy density (in J/m) of a beam is simply defined as:



$$\langle e_{kin} \rangle_t = \frac{1}{4} \rho A \frac{\partial u(x,t)}{\partial t} \left( \frac{\partial u(x,t)}{\partial t} \right)^* \quad (3.35)$$

Herein,  $\rho$  is the mass density and  $A$  is the cross-sectional area of the beam. The time-averaged potential energy density (in J/m) in a beam is given by:

$$\langle e_{pot} \rangle_t = \frac{EI}{4} \frac{\partial^2 u(x,t)}{\partial x^2} \left( \frac{\partial^2 u(x,t)}{\partial x^2} \right)^* \quad (3.36)$$

Summing equations (3.35) and (3.36) the time-averaged total energy density (in J/m) in a beam can be written as:

$$\langle e_{tot} \rangle_t = \frac{1}{4} \left( \rho A \omega^2 u(x,t) u(x,t)^* + EI \frac{\partial^2 u(x,t)}{\partial x^2} \left( \frac{\partial^2 u(x,t)}{\partial x^2} \right)^* \right) \quad (3.37)$$

### 3.6.3 Energy Balance

Some simple energy balance of infinite and finite beam structures employing equation (3.3) will be given next. Most of the experimentally determined energy based data are energy densities and, hence, density expressions are employed for energy balance. Equation (3.3) states that input power is equal to the sum of energy outflow through the structure's boundary and the vibrational energy dissipated within the structure. Within this work both infinite and finite structures are investigated. Infinite beam structures do not have any boundaries. Supplied energy is flowing from the point of excitation towards the infinite ends. If one assumes that the VEF is much higher than the internal dissipation and, hence, neglects internal energy dissipation, one can find a simple energy balance within infinite beam structures from equation (3.9) as:

$$\langle P_{in} \rangle_t = -\langle \tilde{I} \rangle_t \quad (3.38)$$

Equation (3.38) states that the input power is equal to the determined VEF. A true actual VEF (active VEF) balance can be obtained by taking the real parts of equation (3.38) assuming complex quantities. In contrast to VEF in infinite beams, finite structures are assumed in this research to have adiabatic boundaries, which means no energy is flowing out of the structure nor is energy dissipated at the boundary. Hence, the SI divergence term in equation (3.3) can be set to zero and equation (3.10) holds true stating that the real part of input power is equal to dissipated power. Substituting equation (3.7) into equation (3.9) one can obtain energy balance within a hysteretically damped finite beam as:

$$\langle \underline{P}_{in} \rangle_t = 2\omega\eta \int_L \langle e_{pot} \rangle_t dx + 2j\omega \int_L (\langle e_{kin} \rangle_t - \langle e_{pot} \rangle_t) dx. \quad (3.39)$$

Here,  $L$  is denoted as the beam length. Of course there is VEF within the structure. However, all the energy flowing away from the external energy source per cycle is dissipated within one cycle of vibration. Due to the modal behaviour of finite beams net VEF in a finite structure only appears due to internal damping mechanism, assuming no external damping process is added. From equation (3.10) it can be seen that the dissipated power is equal to the real part of the left-hand side expression in equation (3.39), which is given by:

$$\Re \{ \langle \underline{P}_{in} \rangle_t \} = 2\omega\eta \int_L \langle e_{pot} \rangle_t dx. \quad (3.40)$$

### 3.7 Vibrational Energy Flow and Energetic Quantities in Thin Plates

Thin plates are defined as structures having a much larger length and width than thickness, i.e.  $h \ll L_x$  and  $h \ll L_y$ , where  $L_x$  is the plate's length,  $L_y$  is the plate's width and  $h$  is the plate's thickness. Also here, the plate is considered to be homogeneous and isotropic. Euler-Bernoulli theory is employed to derive the partial differential plate equation of motion as well as the dynamic quantities. The derivation of it can be found in Appendix A3.

It is well known that a thin plate, although being a three-dimensional structure, is treated as a two-dimensional vibration problem. Since the plate's thickness is considered to be thin in comparison to its length and width, the dynamic quantities derived in Appendix A3 are quantities per unit length due to moment integration over the plate's thickness rather than the plate's cross-sectional area. Thus, the presented vibrational energy expressions are derived as vibrational energy flow per unit time per unit length. This quantity is denoted as SI in most literature though it is not SI as per given definition in section 3.4. In this work it will be denoted as VEF per unit length or simply VEF. Since infinite plate structures are considered in this work also, VEF per unit length expressions are presented in Cartesian and polar coordinates.

#### 3.7.1 Cartesian Coordinate Based Vibrational Energy Flow

A thin plate under lateral load excitation responds internally by shear forces  $Q_x$  and  $Q_y$ , internal bending moments  $M_{xx}$  and  $M_{yy}$  as well as internal twisting moments  $M_{xy}$  and  $M_{yx}$ . Bending moments arise due to the occurrence of normal stresses. Twisting moments arise due to the occurrence of horizontal shearing stresses in the  $x$ - $z$  and  $y$ - $z$  plane, respectively. Shear forces arise due to the vertical shear stresses in the  $x$ - $z$  and  $y$ - $z$  plane, respectively. From Appendix A3, the bending moments per unit length about the  $y$  and  $x$ -axis are given by:

$$M_{xx} = -D \left( \frac{\partial^2 w}{\partial x^2} + \nu \frac{\partial^2 w}{\partial y^2} \right), \quad (3.41)$$

$$M_{yy} = -D \left( \frac{\partial^2 w}{\partial y^2} + \nu \frac{\partial^2 w}{\partial x^2} \right). \quad (3.42)$$

Here, the two-dimensional plate displacement is denoted as  $w$ ,  $\nu$  is Poisson's ratio and  $D$  is the flexural rigidity of the plate given as [108]:

$$D = \frac{Eh^3}{12(1-\nu^2)}. \quad (3.43)$$

The negative sign in the moment equations are due to negative strain (see Appendix A3). Herein, the displacement  $w$  is a function of two-dimensional space and time thus,  $w(x,y,t)$ . The twisting moments per unit length can be found to be [108]:

$$M_{xy} = -M_{yx} = D(1-\nu) \frac{\partial^2 w}{\partial x \partial y}. \quad (3.44)$$

From Appendix A3, the shear forces per unit length in the  $z$  direction are:

$$Q_x = -D \frac{\partial}{\partial x} \left( \frac{\partial^2 w}{\partial x^2} + \frac{\partial^2 w}{\partial y^2} \right) = -D \frac{\partial}{\partial x} (\nabla^2 w), \quad (3.45)$$

$$Q_y = -D \frac{\partial}{\partial y} \left( \frac{\partial^2 w}{\partial y^2} + \frac{\partial^2 w}{\partial x^2} \right) = -D \frac{\partial}{\partial y} (\nabla^2 w). \quad (3.46)$$

Note, the negative sign in equations (3.45) and (3.46) is because of moment equilibrium on the plate's infinitesimal element. Thus, the shear forces act in the opposite direction to that displayed by Figure 3.3. To define the time-averaged VEF per unit length one may employ equation (3.14).

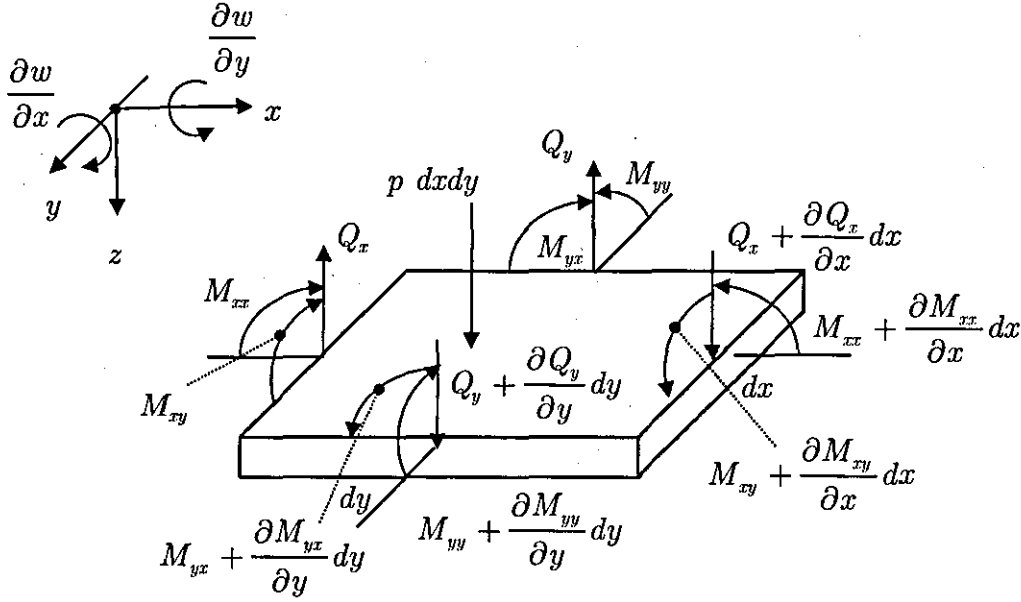


**Figure 3.3** Sign convention of forces and moments on an infinitesimal plate element.

With the number of forces being one and the number of moments being two, time-averaged VEF per unit length in the  $x$  and  $y$  directions are given as:

$$\overline{P}_x = \left\langle -Q_x \frac{\partial w}{\partial t} \right\rangle_t + \left\langle M_{xx} \frac{\partial^2 w}{\partial x \partial t} \right\rangle_t + \left\langle M_{xy} \left( -\frac{\partial^2 w}{\partial y \partial t} \right) \right\rangle_t, \quad (3.47)$$

$$\overline{P}_y = \left\langle -Q_y \frac{\partial w}{\partial t} \right\rangle_t + \left\langle M_{yy} \frac{\partial^2 w}{\partial y \partial t} \right\rangle_t + \left\langle M_{yx} \frac{\partial^2 w}{\partial x \partial t} \right\rangle_t. \quad (3.48)$$

Herein, the overbar denotes quantity per unit length in order to distinguish it from the respective quantities in the beam. Note, the quantity  $\overline{P}_x$  and  $\overline{P}_y$ , respectively is of two-dimensional nature. However, herein the mathematical more correct notation  $\overline{P}_x(x, y)$  and  $\overline{P}_y(x, y)$ , respectively is dropped due to shortage reasons. It can be seen that the product of shear force, bending moment and twisting moment in combination with their respective velocities form a VEF per unit length expression.

If one assumes a time harmonic varying load and substitutes equations (3.41) to (3.46) into equation (3.47) and (3.48), respectively, and takes relations (A2.10) and (A2.11) into account, time-averaged VEF per unit length in the  $x$  and  $y$  direction, respectively, may be found to be:

$$\overline{P}_x = \frac{D}{2} \begin{pmatrix} \frac{\partial}{\partial x} (\nabla^2 w) \left( \frac{\partial w}{\partial t} \right)^* - \left( \frac{\partial^2 w}{\partial x^2} + \nu \frac{\partial^2 w}{\partial y^2} \right) \left( \frac{\partial^2 w}{\partial x \partial t} \right)^* \\ -(1-\nu) \frac{\partial^2 w}{\partial x \partial y} \left( \frac{\partial^2 w}{\partial y \partial t} \right)^* \end{pmatrix}, \quad (3.49)$$

$$\overline{P}_y = \frac{D}{2} \begin{pmatrix} \frac{\partial}{\partial y} (\nabla^2 w) \left( \frac{\partial w}{\partial t} \right)^* - \left( \frac{\partial^2 w}{\partial y^2} + \nu \frac{\partial^2 w}{\partial x^2} \right) \left( \frac{\partial^2 w}{\partial y \partial t} \right)^* \\ -(1-\nu) \frac{\partial^2 w}{\partial x \partial y} \left( \frac{\partial^2 w}{\partial x \partial t} \right)^* \end{pmatrix}. \quad (3.50)$$

Also here, the real part of equations (3.49) and (3.50) is denoted as active VEF per unit length (in W/m) and the imaginary part is denoted as reactive VEF per unit length (in W/m). Equations (3.49) and (3.50) can be seen as complex vector fields that contain two-dimensional information of active and reactive energy flow of the plate in the  $x$  direction and  $y$  direction, respectively. The complex VEF shown in equations (3.49) and (3.50) is often denoted as the plate's SI.

As mentioned before, due to the complex displacement input a complex energy transmission per unit length is assumed and, hence, the plate's time-averaged VEF per unit length vector field is given as:

$$\overrightarrow{\overline{P}} = \begin{pmatrix} \Re \{ \overline{P}_x \} + j \Im \{ \overline{P}_x \} \\ \Re \{ \overline{P}_y \} + j \Im \{ \overline{P}_y \} \end{pmatrix}. \quad (3.51)$$

Herein,  $j$  is the complex unity, i.e.  $j = \sqrt{-1}$  and the arrow denotes a vector quantity. Note, although  $\overline{P}_x$  and  $\overline{P}_y$  are both two-dimensional complex

vector fields the subscript is used only to indicate the direction of the energy that flows into the  $x$  and  $y$  direction, respectively.

### 3.7.2 Cartesian Coordinated Based Energetic Quantities

The plate's energetic quantities may be found in a similar manner to that, as demonstrated in section 3.6.2. Since the plate is simplified to a two-dimensional structure, the units of the energy based quantities are different to units used in section 3.2. If one substitutes equation (3.49) into the spatial  $x$ -derivative of equation (3.19) the spatial  $x$ -derivative of the divergence of the plate's VEF is:

$$\frac{\partial \overline{P}_x}{\partial x} = \frac{D}{2} \left[ \left( \frac{\partial^4 w}{\partial x^4} + \frac{\partial^4 w}{\partial x^2 \partial y^2} \right) \left( \frac{\partial w}{\partial t} \right)^* + \left( \frac{\partial^3 w}{\partial x^3} + \frac{\partial^3 w}{\partial x \partial y^2} \right) \left( \frac{\partial^2 w}{\partial x \partial t} \right)^* - \left( \frac{\partial^3 w}{\partial x^3} + \nu \frac{\partial^3 w}{\partial x \partial y^2} \right) \left( \frac{\partial^2 w}{\partial x \partial t} \right)^* - \left( \frac{\partial^2 w}{\partial x^2} + \nu \frac{\partial^2 w}{\partial y^2} \right) \left( \frac{\partial^3 w}{\partial x^2 \partial t} \right)^* - (1-\nu) \frac{\partial^3 w}{\partial x^2 \partial y} \left( \frac{\partial^2 w}{\partial y \partial t} \right)^* - (1-\nu) \frac{\partial^2 w}{\partial x \partial y} \left( \frac{\partial^3 w}{\partial x \partial y \partial t} \right)^* \right]. \quad (3.52)$$

It can be seen from equation (3.52) that also for the plate up to 4<sup>th</sup> order spatial derivatives need to be determined. Due to differentiating of a functional product, expression (3.52) is substantially larger than equation (3.50). Analogously, the divergence component of the spatial  $y$ -derivative of the divergence of the plate's VEF can be found by substituting equation (3.50) into (3.19), as:

$$\frac{\partial \overline{P}_y}{\partial y} = \frac{D}{2} \left[ \left( \frac{\partial^4 w}{\partial y^4} + \frac{\partial^4 w}{\partial x^2 \partial y^2} \right) \left( \frac{\partial w}{\partial t} \right)^* + \left( \frac{\partial^3 w}{\partial y^3} + \frac{\partial^3 w}{\partial y^2 \partial x} \right) \left( \frac{\partial^2 w}{\partial y \partial t} \right)^* - \left( \frac{\partial^3 w}{\partial y^3} + \nu \frac{\partial^3 w}{\partial y \partial x^2} \right) \left( \frac{\partial^2 w}{\partial y \partial t} \right)^* - \left( \frac{\partial^2 w}{\partial y^2} + \nu \frac{\partial^2 w}{\partial x^2} \right) \left( \frac{\partial^3 w}{\partial y^2 \partial t} \right)^* - (1-\nu) \frac{\partial^3 w}{\partial y^2 \partial x} \left( \frac{\partial^2 w}{\partial x \partial t} \right)^* - (1-\nu) \frac{\partial^2 w}{\partial x \partial y} \left( \frac{\partial^3 w}{\partial x \partial y \partial t} \right)^* \right]. \quad (3.53)$$

The complete divergence of the plate's VEF is simply the summation of equations (3.52) and (3.53) that yields to a two-dimensional scalar field (in  $W/m^2$ ), given by:

$$\nabla \cdot \vec{\bar{P}} = \frac{\partial \bar{P}_x}{\partial x} + \frac{\partial \bar{P}_y}{\partial y}. \quad (3.54)$$

It can be realised that the plate's divergence takes only  $x$ - and  $y$ -components into account. Equations (3.52) and (3.53) combined can be reduced to a more simple form using the plate's lateral velocity component as [39]:

$$\nabla \cdot \vec{\bar{P}} = \frac{D}{2\omega} \Im(\nabla^4 v v^*). \quad (3.55)$$

Here,  $\nabla^4$  is the double Laplacian and  $v$  is the plate's transverse velocity component. Analogously to the beam, the time-averaged kinetic energy density (in  $J/m^2$ ) of a plate may be written as:

$$\langle e_{kin} \rangle_t = \frac{\rho h}{4} \frac{\partial w}{\partial t} \left( \frac{\partial w}{\partial t} \right)^*. \quad (3.56)$$

The time-averaged potential energy density (in  $J/m^2$ ) in a plate is defined as:

$$\langle e_{pot} \rangle_t = \frac{D}{4} \left[ \frac{\partial^2 w}{\partial x^2} \left( \frac{\partial^2 w}{\partial x^2} \right)^* + \frac{\partial^2 w}{\partial y^2} \left( \frac{\partial^2 w}{\partial y^2} \right)^* + \right. \\ \left. 2\nu \frac{\partial^2 w}{\partial x^2} \left( \frac{\partial^2 w}{\partial y^2} \right)^* + 2(1-\nu) \frac{\partial^2 w}{\partial x \partial y} \left( \frac{\partial^2 w}{\partial x \partial y} \right)^* \right]. \quad (3.57)$$

Summing equations (3.56) and (3.57), time-averaged total energy density (in  $J/m^2$ ) in a plate can be written as:



$$\langle e_{tot} \rangle_t = \frac{D}{4} \left[ \frac{\rho h}{D} \frac{\partial w}{\partial t} \left( \frac{\partial w}{\partial t} \right)^* + \frac{\partial^2 w}{\partial x^2} \left( \frac{\partial^2 w}{\partial x^2} \right)^* + \frac{\partial^2 w}{\partial y^2} \left( \frac{\partial^2 w}{\partial y^2} \right)^* + \right. \\ \left. 2\nu \frac{\partial^2 w}{\partial x^2} \left( \frac{\partial^2 w}{\partial y^2} \right)^* + 2(1-\nu) \frac{\partial^2 w}{\partial x \partial y} \left( \frac{\partial^2 w}{\partial x \partial y} \right)^* \right]. \quad (3.58)$$

### 3.7.3 Energy Balance

Analogously to the procedure in section 3.6.3, the energy balance of an infinite plate structure can be found by neglecting the dissipated energy and employing equation (3.9) as:

$$\langle \underline{P}_{in} \rangle_t = - \oint_l \langle \vec{I} \rangle_t dl. \quad (3.59)$$

Here,  $l$  is a closed contour on the plate's surface. Equation (3.59) states that the line integration of the plate's VEF at each position in the plate is equal to the vibrational input power. Because of the derivation of internal forces and moments within the plate in units per width contour integration needs to be carried out. Also here, the real part of equation (3.59) represents active energy flow. In the case of finite plates the input power is related to the kinetic and potential energy densities as:

$$\langle \underline{P}_{in} \rangle_t = 2\omega\eta \int_S \langle e_{pot} \rangle_t dxdy + 2j\omega \int_S (\langle e_{kin} \rangle_t - \langle e_{pot} \rangle_t) dxdy. \quad (3.60)$$

Herein,  $S$  is the surface area that is enclosed by the contour line. Taking the real part of equation (3.60), dissipated vibrational energy is balanced with vibrational input energy as:

$$\Re \{ \langle \underline{P}_{in} \rangle_t \} = 2\omega\eta \int_S \langle e_{pot} \rangle_t dxdy. \quad (3.61)$$

### 3.7.4 Polar Coordinate Based Vibrational Energy Flow

Flexural vibration in circular and infinite plates results in circular wave motion. The Cartesian coordinates  $x$  and  $y$  are a function of the radius  $r$  and the angle  $\theta$ , which is measured between the radius  $r$  and the  $x$ -axis. The two-dimensional Cartesian Laplace operator  $\nabla^2 = \partial^2/\partial x^2 + \partial^2/\partial y^2$  can be written in polar form as [109]:

$$\nabla^2 = \frac{\partial^2}{\partial r^2} + \frac{1}{r} \frac{\partial}{\partial r} + \frac{1}{r^2} \frac{\partial^2}{\partial \theta^2}. \quad (3.62)$$

Using the Laplace operator  $\nabla^2$  of polar coordinates the radial shear force  $Q_r$  and the angular shear force  $Q_\theta$  are given by [110]:

$$Q_r = -D \frac{\partial}{\partial r} \left( \frac{\partial^2 w}{\partial r^2} + \frac{1}{r} \frac{\partial w}{\partial r} + \frac{1}{r^2} \frac{\partial^2 w}{\partial \theta^2} \right) = -D \frac{\partial}{\partial r} (\nabla^2 w), \quad (3.63)$$

$$Q_\theta = -D \frac{1}{r} \frac{\partial}{\partial \theta} \left( \frac{\partial^2 w}{\partial r^2} + \frac{1}{r} \frac{\partial w}{\partial r} + \frac{1}{r^2} \frac{\partial^2 w}{\partial \theta^2} \right) = -D \frac{1}{r} \frac{\partial}{\partial \theta} (\nabla^2 w). \quad (3.64)$$

Analogously to the bending moment definition of Cartesian coordinates, the bending moments  $M_r$  and  $M_\theta$  are given in polar coordinates as [110]:

$$M_r = -D \left( \frac{\partial^2 w}{\partial r^2} + \nu \left( \frac{1}{r} \frac{\partial w}{\partial r} + \frac{1}{r^2} \frac{\partial^2 w}{\partial \theta^2} \right) \right), \quad (3.65)$$

$$M_\theta = -D \left( \frac{1}{r} \frac{\partial w}{\partial r} + \frac{1}{r^2} \frac{\partial^2 w}{\partial \theta^2} + \nu \frac{\partial^2 w}{\partial r^2} \right). \quad (3.66)$$

The twisting moment of a plate in polar coordinates is defined as [110]:

$$M_{r\theta} = D(1-\nu) \frac{\partial}{\partial r} \left( \frac{1}{r} \frac{\partial w}{\partial \theta} \right). \quad (3.67)$$

When considering the above equations that show polar quantities it can be realised that the number of forces in each direction is one and the number of moments is two. If one substitutes equations (3.63) to (3.67) into equation (3.47) and (3.48), respectively, and assumes sinusoidal varying load and takes relations (A2.10) and (A2.11) into account the time-averaged VEF per unit length in the radial and angular directions can be found to be:

$$\overline{P}_r = \frac{D}{2} \left[ \frac{\partial}{\partial r} (\nabla^2 w) \left( \frac{\partial w}{\partial t} \right)^* - \left( \frac{\partial^2 w}{\partial r^2} + \nu \left( \frac{1}{r} \frac{\partial w}{\partial r} + \frac{1}{r^2} \frac{\partial^2 w}{\partial \theta^2} \right) \right) \left( \frac{\partial^2 w}{\partial r \partial t} \right)^* - \right. \\ \left. (1 - \nu) \frac{\partial}{\partial r} \left( \frac{1}{r} \frac{\partial w}{\partial \theta} \right) \left( \frac{\partial^2 w}{\partial \theta \partial t} \right)^* \right], \quad (3.68)$$

$$\overline{P}_\theta = \frac{D}{2} \left[ \frac{1}{r} \frac{\partial}{\partial \theta} (\nabla^2 w) \left( \frac{\partial w}{\partial t} \right)^* - \left( \frac{1}{r} \frac{\partial w}{\partial r} + \frac{1}{r^2} \frac{\partial^2 w}{\partial \theta^2} + \nu \frac{\partial^2 w}{\partial r^2} \right) \left( \frac{\partial^2 w}{\partial \theta \partial t} \right)^* - \right. \\ \left. (1 - \nu) \frac{\partial}{\partial r} \left( \frac{1}{r} \frac{\partial w}{\partial \theta} \right) \left( \frac{\partial^2 w}{\partial r \partial t} \right)^* \right]. \quad (3.69)$$

### 3.8 Discussion

Within this chapter an introduction to the theory of VEF in simple beam and plate-like structures and their energy related quantities has been given. The general energy balance, given by equation (3.1), of a three-dimensional body element was presented. This important equation outlined that the total energy flow within the body volume is equal to the sum of mechanical intensity (SI) flowing per unit cross-sectional area plus the injected energy flow minus the flow losses occurring within the volume of interest. Further, a general energy balance, given by equation (3.3), was presented when a steady state motion of the body is regarded.

In order to apply a simple energy balance on real finite structures information about the dissipation within the structure is desired. Hence, a

simple relation has been derived, using equation (3.12), which states that the time-averaged dissipated energy flow is proportional to the product of loss factor and time-averaged potential energy. Thus, the dissipated VEF within a finite structure can be obtained from the knowledge of the loss factor and the potential energy.

SI and the divergence of SI were introduced briefly. It has been pointed out that the SI is a vector field that contains information about the magnitude and direction of vibrational energy flow at each point in the volume. Divergence of SI can be used to localise energy sources and sinks. Energy sources are points of energy inflow into a structure and energy sinks are points of energy outflow out of the structure due to energy dissipation or sound radiation. Since the outflow is defined as negative in this work, divergence of SI less than zero indicates energy sinks.

A general definition of mechanical power from the dot product of forces and moments with their respective velocities was also derived. This practical and useful expression, as shown by equations (3.14) and (3.15), was then applied to define time-averaged VEF in rectangular beams and rectangular plates. In beams flexural VEF is caused by a one-dimensional lateral and rotational velocity response due to the occurrence of an internal shear force and bending moment, respectively. Flexural VEF in plates is caused by the two-dimensional lateral and rotational velocity response due to the occurrence of a shear force, bending moment and twisting moment, respectively.

The integration of SI over the structure's cross-sectional area would provide vibrational power information. The generally defined SI or VEF per unit cross-sectional area was presented in sections 3.1 and 3.4 as a quantity that depended on three spatial variables and time. Within this work mainly time-averaged VEF and energy based measures are employed. Thus, the VEF expressions were presented as the temporal mean value of the instantaneous flow. In rectangular beams the derivation of SI yielded directly to vibrational power due to the fact that the forces and moments on the infinitesimally small beam element were not derived as density functions by means of unit force and moment per area. The derivation of SI in a plate led to vibrational

energy flow per unit length due to the fact that internal forces and moments were derived as density function per unit length only. Although the derivation of VEF in beams and plates is comparable to SI, as shown in the energy balance equation (3.1), the expression SI is not used in this work due to the difference in units between generally defined SI and VEF derived for beams and plates.

The application of the energy balance, as shown by equation (3.3), generally requires a volume integration of the respective energy flow densities in order to transfer local energy quantities to a global energy level. Within this thesis, total vibrational input power to a structure is always considered. Thus, energy balance will be carried out on a global level. The equations presented in sections 3.6.3 and 3.7.3 have shown that from the knowledge of the locally distributed potential energy density and the hysteretic loss factor a global energy balance can be established. In the case of finite beam vibration the potential energy density needs to be integrated along the beam length and in the plate's case integration along the plate's surface needs to be carried out.

## **4 VIBRATIONAL ENERGY FLOW DETERMINATION METHODS**

### **4.1 Introduction**

Vibrational energy flow (VEF) can be determined in numerous ways. The procedure of VEF determination can be divided into three stages. In stage one the structure's response to an excitation load is acquired. Usually displacement, velocity, or acceleration information will be employed. This information can be measured on a real structure or synthetically generated within a numerical analysis.

Stage two provides partial spatial derivatives required for VEF or energetic quantity computation. If the data to be processed are contaminated by noise, the application of filtering is also included at this stage. Therefore, section 4.2 introduces different techniques to compute spatial derivatives from a set of tabulated data. Section 4.3 introduces spatial domain and wavenumber domain filtering in order to reduce errors in VEF computation due to noise contamination.

The final stage utilises the determined spatial derivatives to compute vibrational energy (VE) based quantities using the VE expressions derived in chapter 3. The herein proposed measurement method, called vibrational energy flow measurements using electronic speckle pattern interferometry (VEFESPI), is presented in section 4.4 using methods introduced previously.

## 4.2 Numerical Determination of Spatial Derivatives

### 4.2.1 Numerical Differentiation Using Finite Differences

The most common method to determine spatial derivatives from tabulated data is the use of finite differences. A short introduction can be found in Appendix A4. Within this work the numerical determination of spatial derivatives using finite differences will be addressed as finite difference approximation. Herein, this technique is used to approximate spatial derivatives required to measure VEF with the aid of accelerometers. From Appendix A4 it can be seen that at least 4 points are required to find spatial derivatives up to the third order. Figure 4.1 displays the setup of 4 accelerometers. The spatial distance is denoted as  $h$ , the transverse

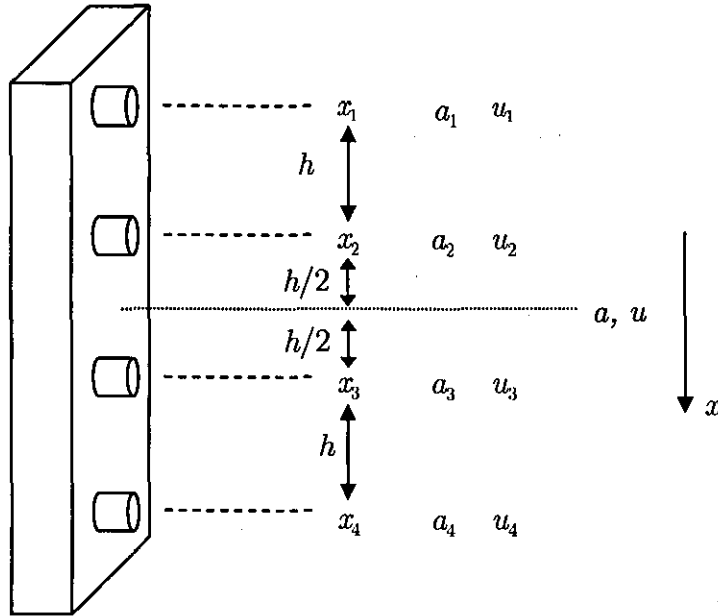


**Figure 4.1** Four accelerometer setup.

displacement is denoted as  $u$  and the transverse acceleration is denoted as  $a$ . The spatial derivatives of the transverse displacement using the finite difference approximation can be found by employing the central difference

based equations given in Appendix A4. Thus, using equation (A4.10) the first spatial derivative of the displacement  $u(x,t)$  is given by:

$$\frac{\partial u(x,t)}{\partial x} \approx \left( \frac{u_3 - u_2}{h} \right). \quad (4.1)$$

Since only beam VEF has been measured, the method is demonstrated for a one-dimensional displacement function only. However, it can easily be extended into two dimensions simply by adding another variable. Analogously, using equation (A4.14) the second derivative can be found as:

$$\frac{\partial^2 u(x,t)}{\partial x^2} \approx \left( \frac{u_4 - u_3 - u_2 + u_1}{2h^2} \right). \quad (4.2)$$

Employing equation (A4.17), the third spatial partial derivative is given as:

$$\frac{\partial^3 u(x,t)}{\partial x^3} \approx \left( \frac{u_4 - 3u_3 + 3u_2 - u_1}{h^3} \right). \quad (4.3)$$

The approximated displacement at position  $x = 0$  simply is:

$$u(x,t) \approx \frac{1}{2}(u_3 + u_2). \quad (4.4)$$

Note, to substitute the acceleration into the above given equations, the displacement has to be temporal differentiated twice. However, in practice often velocity signals are substituted into the spatial partial derivatives, since force and moments are multiplied with their appropriate velocities in order to obtain VEF. The practical use of these derivatives to measure one-dimensional VEF using measured spectral quantities will be presented in section 8.2.3.



### 4.2.2 Numerical Differentiation Using Spatial Fourier Transform

It has been pointed out in Appendix A4 that the finite difference approximation technique introduces errors when computing spatial derivatives from tabulated data due to the truncation of the Taylor series. Additionally, the technique is fairly cumbersome if more than one point of spatial derivatives is required. Thus, a different technique is employed within this research, which utilises the spatial Fourier transform (SFT) and wavenumber domain processing in order to obtain spatial derivatives. In this work this technique is addressed as  $k$ -space derivation (KSD) method. This method is sometimes denoted as wavenumber technique or spatial derivative (SD) technique.

As mentioned, the KSD method utilises the SFT to transform spatially sampled data into the wavenumber domain to detect the wavenumber content of the signal. This procedure is similar to the temporal Fourier transform. Mathematically, the forward two-dimensional SFT is given by:

$$U(k_x, k_y; \omega) = F\{u(x, y; \omega)\} = \frac{1}{4\pi^2} \int_{-\infty}^{\infty} \int_{-\infty}^{\infty} u(x, y; \omega) e^{-j(k_x x + k_y y)} dx dy. \quad (4.5)$$

Analogously, the inverse two-dimensional SFT can be expressed as:

$$u(x, y; \omega) = F^{-1}\{U(k_x, k_y; \omega)\} = \int_{-\infty}^{\infty} \int_{-\infty}^{\infty} U(k_x, k_y; \omega) e^{j(k_x x + k_y y)} dk_x dk_y. \quad (4.6)$$

Herein,  $F$  denotes a forward Fourier transform (FT) and  $F^{-1}$  denotes an inverse (backward) FT. In practice the above shown equations are evaluated numerically by a fast Fourier transform (FFT) algorithm [111].

Spatial derivatives from tabulated data of the original signal are obtained by applying the KSD method. The KSD method can be divided into three steps, as shown in Figure 4.4. At the first step the spatial tabulated

data are transformed into the wavenumber domain by applying a forward FFT. Within the wavenumber domain step two is employed. Herein, a multiplication of the wavenumber spectrum  $U(k_x, k_y; \omega)$  with the product of complex unity  $j = \sqrt{-1}$  and the respective wavenumber vector  $K_x$  and  $K_y$  is carried out. The use of the wavenumber vector  $K_x$  and  $K_y$  depends on which coordinate needs to be differentiated. This simple multiplication procedure results in spectral derivatives.

An example of spectral differentiation is given next with aid of Figure 4.2 and Figure 4.3. Figure 4.2 displays a simple one-dimensional spatial sine function  $u(x) = \sin(k_0 x)$ , with  $k_0 = 20\pi$  being the wavenumber and  $U(k)$  being the wavenumber spectrum. Here,  $x$  is the spatial distance and  $k$  is the wavenumber. Figure 4.3 displays the spatial derivative of  $u(x)$ , i.e.  $g(x) = k_0 \cos(k_0 x)$  and  $G(k)$  its respective wavenumber spectrum. Substituting  $u(x)$  and  $g(x)$  into equation (4.5), one can obtain their spectra as:

$$U(k) = F\{u(x)\} = \frac{j}{2} \{\delta(k + k_0) - \delta(k - k_0)\}, \quad (4.7)$$

$$G(k) = F\{g(x)\} = 10\pi \{\delta(k + k_0) + \delta(k - k_0)\}. \quad (4.8)$$

As evident from equations (4.7) and (4.8),  $G(k) = -jk_0 U(k)$  for  $k < 0$  and  $G(k) = jk_0 U(k)$  for  $k > 0$ . Thus, the left-hand side of the spectrum is multiplied by  $-k_0$  and the right-hand side of the spectrum is multiplied by  $k_0$ . Herein,  $\delta$  is the Dirac delta function. In practice the multiplication of the spectrum is not just carried out at the two wavenumber components of interest. It is carried out over the entire wavenumber vector  $K$  containing positive and negative wavenumber components of the signal to be processed. Of course the same relation holds for complex signals to be processed. Thus, spectral derivatives can be obtained simply due to the above described spectral multiplication process. Transforming these spectral derivatives back into the spatial domain will complete step three and one can obtain spatial derivatives.

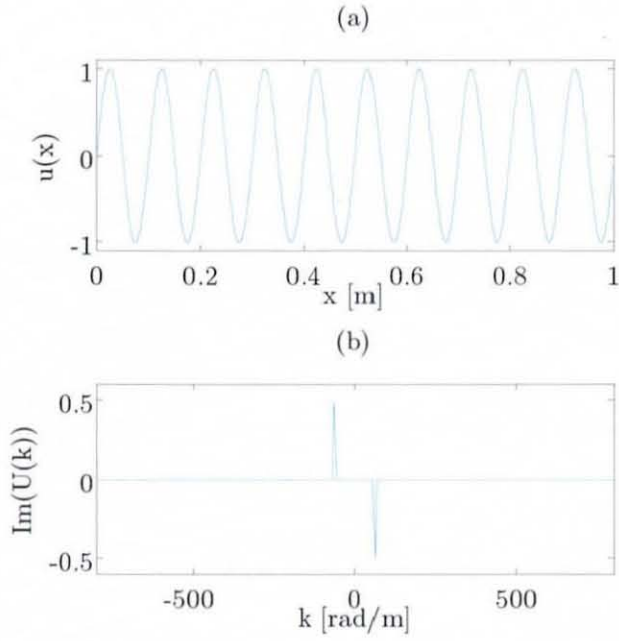


**Figure 4.2** Spectral derivation process: (a) sine wave  $u(x) = \sin(k_0 x)$  with  $k_0 = 20\pi$ , (b) wavenumber spectrum  $U(k)$  of  $u(x)$ .

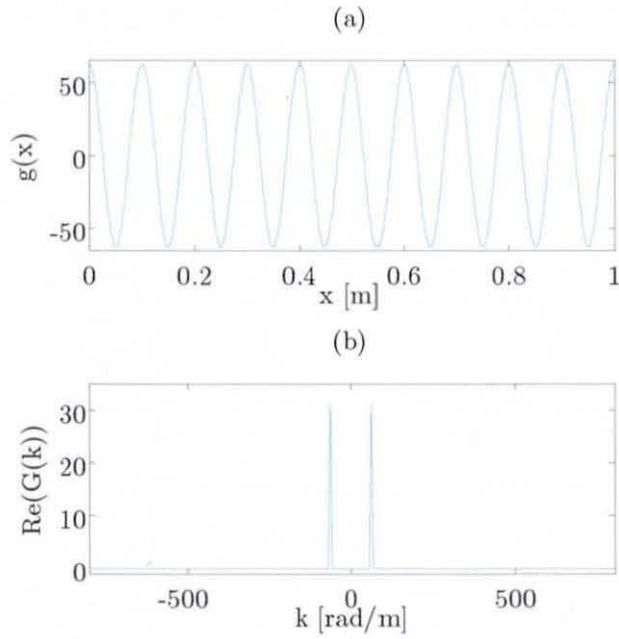


**Figure 4.3** Spectral derivation process: (a) cosine wave  $g(x) = \frac{du(x)}{dx} = k_0 \cos(k_0 x)$  with  $k_0 = 20\pi$ , (b) wavenumber spectrum  $G(k)$  of  $g(x)$ .

The entire KSD method can be mathematically expressed for two-dimensional differentiation as:

$$\frac{\partial^m \partial^n}{\partial x^m \partial y^n} [u(x, y)] = F^{-1} \left\{ (jK_x)^m (jK_y)^n F \{ u(x, y) \} \right\}. \quad (4.9)$$

Equation (4.9) contains wavenumber vectors denoted by  $K_x$  and  $K_y$  required to differentiate numerically. The order of the respective spatial derivative is driven by integer  $m$  and  $n$ , respectively. Also here, when dealing with one-dimensional functions equation (4.9) can easily be reduced to one variable

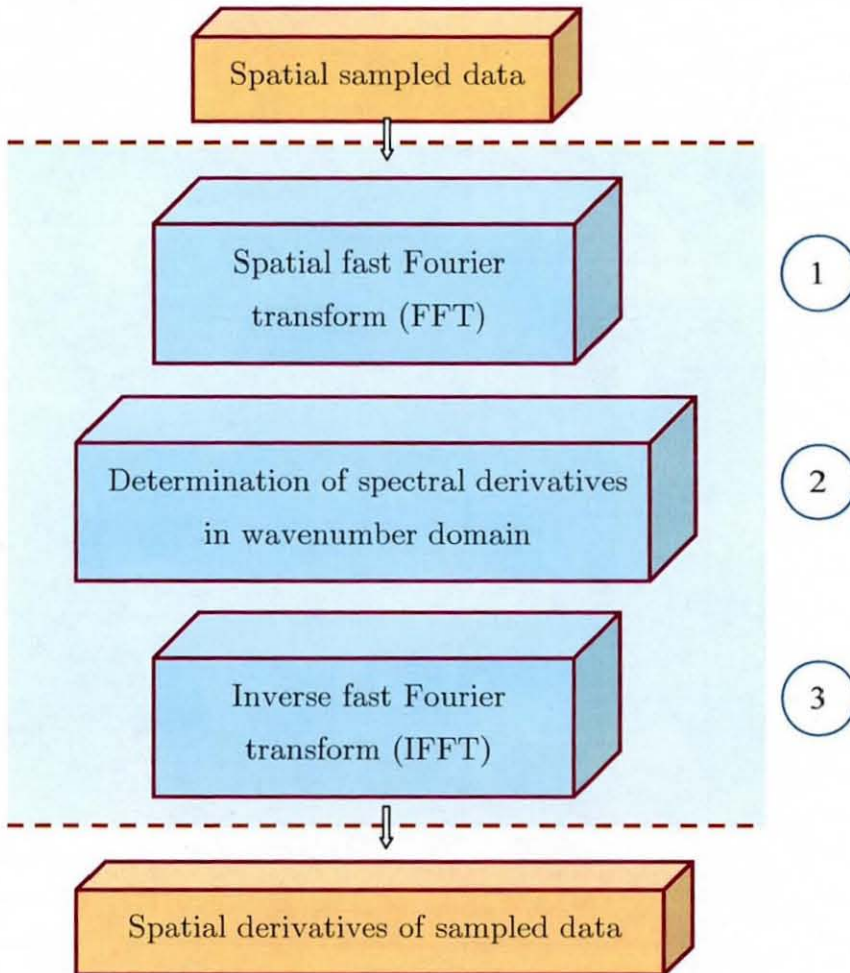


**Figure 4.4** Illustration of the KSD method.

only simply by setting the other variable equal to zero. The above demonstrated KSD method is more accurate than the finite difference approximation [37]. A drawback of this method stems from the property of the Fourier transform when transforming non-periodic signals [51], which are often present within a set of measurements. In this case spectral leakage will affect the accuracy of the spectrum and, thus, the leakage error will be amplified when multiplying in the wavenumber domain to compute spectral derivatives. Figure 4.4 displays the stages of the KSD technique.

### 4.2.3 Numerical Differentiation Using B-Splines

An alternative method to find spatial derivatives is the use of B-Splines. This technique has been used by Fuller [79] and later in more detail by Wang [77]. The main idea is to interpolate a curve or surface by a set of piecewise polynomials known as splines. As the curve or surface is then described by the approximation function one can obtain derivatives from it.

One could argue that for this technique simple polynomials might be adequate. However, when approximating tabulated data with a high number of points, complex curve shaped polynomial functions tend to oscillate heavily as the number of degrees is increased in order to achieve a better curve fit. Using a set of piecewise polynomial segments joined together under predefined conditions and keeping the polynomial order low can compensate for this drawback. Thus, a much greater flexibility can be achieved when interpolating complex curves and surfaces. The area of spline functions is fairly vast. Introducing its entire scope would be inappropriate for this work. There are several textbooks such as [112, 113] available.

However, the basic mathematical descriptions used in approximating two-dimensional surfaces and its derivatives in order to obtain VEF will be introduced briefly. The least square criterion of scattered surface data (i.e. measured two-dimensional ESPI displacement data contaminated by optical noise) in a rectangular approximation domain is given by [112]:

$$\mathcal{R} = \sum \sum (w(x, y; \omega) - \tilde{w}(x, y; \omega))^2. \quad (4.10)$$



Herein, the squared residual error  $\mathcal{I}$  needs to be minimised. The fitted surface function  $\tilde{w}(x, y; \omega)$  fitted by B-splines is given by [112]:

$$\tilde{w}(x, y; \omega) = \sum_{i=-k}^g \sum_{j=-l}^h (c_{i,j} N_{i,k+1}(x) M_{j,l+1}(y)). \quad (4.11)$$

The above shown tensor product spline is fitted in the two-dimensional space  $R = [a, b] \times [c, d]$ , where  $a$ ,  $b$ ,  $c$  and  $d$  are the spatial dimensions.  $N_{i,k+1}$  and  $M_{j,l+1}$  are the normalised B-spline functions of degree  $k$  and  $l$ , respectively. The spline knots are defined as  $\lambda_i$ ,  $i = 0, \dots, g + 1$  and  $\mu_j$ ,  $j = 0, \dots, h + 1$ , respectively with  $\lambda_0 = a$ ,  $\lambda_{g+1} = b$ ,  $\mu_0 = c$  and  $\mu_{h+1} = d$ . The B-spline coefficients  $c_{i,j}$  need to be computed. Once the two-dimensional tensor product spline has been determined, derivatives of the spatial approximation function can be computed. Derivatives from B-spline functions are continuous up to  $(k-1)^{\text{th}}$  and  $(l-1)^{\text{th}}$  order, respectively [77]. In order to obtain smooth derivatives in practice,  $(k-2)^{\text{th}}$  and  $(l-2)^{\text{th}}$  orders are chosen, respectively. Thus, to obtain smooth 3<sup>rd</sup> order derivatives from interpolated B-spline surface data a five degree B-spline function is at least required.

### 4.3 Filter Methods

As previously mentioned, data acquired by a non-contacting optical measurement method, such as ESPI, contain optical noise. It can be seen from equation (4.9) that especially the high frequency noise components may be amplified in the wavenumber domain due to the multiplication process between spectral noise amplitude and wavenumber of power  $n$ . Thus, the spatial derivatives computed by the KSD method are potentially very erroneous. In order to minimise the effect of noise data filtering either in spatial domain or wavenumber domain is indispensable.

### 4.3.1 Spatial Domain Filtering

Spatial domain filtering can be carried out by interpolating sampled data with different interpolation techniques, such as the previously described B-spline approximation method. If the sampled data contain noise, they can be smoothed by an interpolation technique. Wang et al. demonstrated in reference [77] that this smoothing process is similar to a low-pass filtering in the wavenumber domain. It has been shown that the discrete evaluation of the function to be approximated is equal to a discrete convolution between the sampled data and a cardinal spline function that is evaluated at integer values. The frequency response of this cardinal spline converges to an ideal low-pass filter as the degree of the spline function tends to infinity. Thus, spatially sampled data can be filtered without transforming data into other domains.

### 4.3.2 Wavenumber Domain Filtering

Since the KSD method employs a SFT as part of the spatial derivative computation, it is practical to remove undesired noise components in the wavenumber domain. Usually the filtered wavenumber spectrum  $U(k_x, k_y)_{filt}$  is simply manipulated as:

$$U(k_x, k_y)_{filt} = U(k_x, k_y) F(k_x, k_y). \quad (4.12)$$

Herein,  $U(k_x, k_y)$  is the wavenumber spectrum of the sampled data to be filtered and  $F(k_x, k_y)$  is the filter function multiplied within the spectral domain. For each filter the design of  $k$ -space filter characteristics underlies some requirements. The filter has to be of two-dimensional nature, since the recorded data within this work for VEF computation are two-dimensional. The filter should allow adjustments to be made in the  $x$  and  $y$  direction separately. Thus, the filter design should enable shape alterations between a circular and an oval filter shape that depends on the respective spatial

frequency components in the  $x$  and  $y$  directions. Also an alteration in filter slope is desirable.

The simplest filter to be employed in spectral filter design is the use of an ideal filter. Within this work the ideal filter is programmed as an algorithm. The discrete noise contaminated wavenumber spectrum  $U(k_x, k_y)$  is searched element wise for components that are smaller or equal to the product of a carefully selected constant  $C$  and the maximum magnitude of the wavenumber spectrum, i.e.  $C \cdot |U(k_x, k_y)|_{\max}$ . If this condition is satisfied, the particular wavenumber spectrum component is simply multiplied by zero. Vice versa, the particular wavenumber spectrum component is multiplied by one.

Thus, the ideal filter process acts like a multiplication of the wavenumber spectrum with zeros and ones at specifically defined positions. This filter can be implemented as:

$$F(k_x, k_y) = \begin{cases} 1 & \text{for } |U(k_x, k_y)| > C |U(k_x, k_y)|_{\max} \\ 0 & \text{for } |U(k_x, k_y)| < C |U(k_x, k_y)|_{\max} \end{cases} \quad (4.13)$$

Herein,  $C$  is a constant between  $0 \leq C \leq 1$  and  $C \in \mathbb{R}$ . The filtering process is applied, as shown in equation (4.12). The advantage of this method is its straightforward implementation at different programming platforms. The optimum cut-off point can be found by running an automated trial and error computation to find the optimum filter parameter  $C$  to remove a sufficient amount of noise and retain a sufficient amount of signal information in the spectrum. This is the main objective of  $k$ -space filtering employed for VEF measurements.

Another filter type widely used by research community is the so-called oval filter given as [43]:



$$F(k_x, k_y) = \begin{cases} 1 - \frac{1}{2} e^{\frac{\left(1 - \frac{K_r}{K_c}\right)}{S}}, & \text{for } K_r < K_c \\ \frac{1}{2} e^{\frac{\left(1 - \frac{K_r}{K_c}\right)}{S}}, & \text{for } K_r > K_c \end{cases}. \quad (4.14)$$

Here,  $K_r = \sqrt{K_x^2 + K_y^2}$  is the radial wavenumber vector,  $K_c = \sqrt{K_{c_x}^2 + K_{c_y}^2}$  is the radial cut-off wavenumber and the condition  $(K_{c_x}^2 / a_x^2 + K_{c_y}^2 / a_y^2) = 1$  needs to be satisfied. Note, the lower case letter  $k$  is used in this work to define the wavenumber as a variable and capital  $K$  is used in this work to define a discrete wavenumber quantity (vector). The parameter  $S$  controls the filter slope. Adjustments of the filter in the  $x$  and  $y$  directions can be made simply by manipulating the two quantities  $a_x$  and  $a_y$ . This filter involves a trial and error in process in order to find the optimum filter shape.

An alternative filter type may be the implementation of an oval 2D Butterworth filter. Also here, its advantage is a much easier implementation within software packages. The oval Butterworth filter shape is given by:

$$F(k_x, k_y) = \frac{1}{1 + \left(\frac{r}{K_c}\right)^{2n}} = \frac{1}{1 + \left[\left(\frac{X}{K_{c_x}}\right)^2 + \left(\frac{Y}{K_{c_y}}\right)^2\right]^{2n}}. \quad (4.15)$$

It can be seen by equation (4.15) that the oval Butterworth filter is the magnitude of the well known two-dimensional Butterworth filter. The coordinates  $X$  and  $Y$  are the filter length in the  $K_x$  and  $K_y$  direction, respectively, and  $n$  is the order of the filter that changes the filter slope at the cut-off frequencies  $k_{c_x}$  and  $k_{c_y}$ . Figure 4.5 displays the oval 2D Butterworth filter in the spectral domain with a filter slope of  $n = 8$ . Clearly, the low pass filter shape can be seen. It can also be noted that due to  $X$  and  $Y$  adjustments an oval shape can be produced. It will be shown in chapter 11 that this procedure becomes very useful if a two-dimensional finite plate

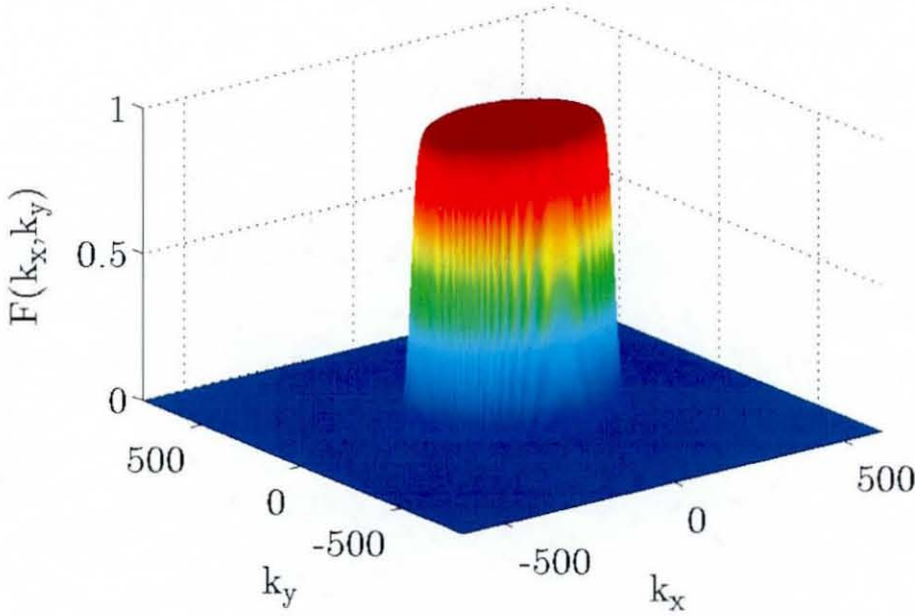


**Figure 4.5** Oval 2D Butterworth filter.

displacement with different mode shapes in the  $x$  and  $y$  directions is required to be filtered.

#### 4.4 Vibrational Energy Determination Method

With the information given in the previous sections a complete flow chart of the VEF method can be drawn in order to visualise the VEF computation process. Figure 4.6 displays each step of the VEF determination method employed in this research.

Spatial displacement data are sampled with the aid of an ESPI system. This system is introduced in chapter 7 in detail. After truncating the recorded displacement data to a useable size, a 2D FFT is applied in order to transform the samples into the wavenumber domain or  $k$ -space. In the wavenumber domain unwanted optical noise components are filtered out by employing a two-dimensional filtering technique as introduced above. After the  $k$ -space filtering desired spectral derivatives are then obtained simply by

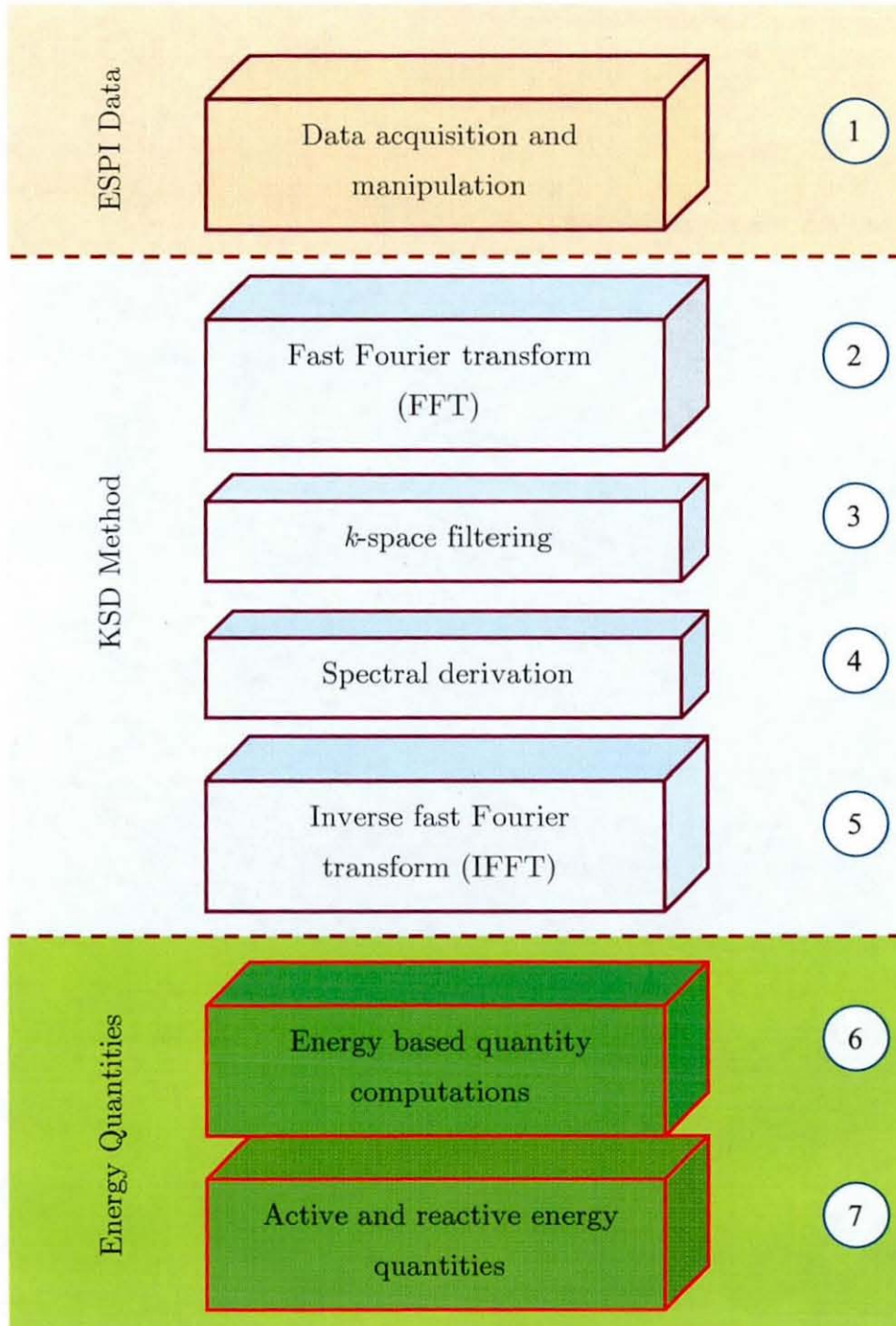


Figure 4.6 VEFESPI method.

multiplying the wavenumber spectra by the complex unity of order  $n$  and  $m$ , respectively, with its appropriate wavenumber component vectors of order  $n$



and  $m$ , respectively. The filtered spectral derivatives of order  $n$  and  $m$  are then transformed back into the spatial domain by employing an inverse 2D fast Fourier transform (IFFT). Once in the spatial domain the desired spatial derivatives are used to calculate the energy based quantities such as VEF, the divergence of VEF, kinetic energy density, potential energy density, and total energy density.

## 4.5 Summary

This chapter presented the procedure to obtain VEF and energy based quantities essential in VEF analysis. As shown in chapter 3, all vibrational energy based quantities are described by partial derivatives of the structural transverse displacement. The determination of these derivatives from sampled data is one of the primary objectives of the VEF determination method. If the data in stage one are acquired by ESPI, the method will be addressed as VEFESPI method. Throughout this work the KSD method is employed. It has the advantage that once accurate spectra are determined derivatives of each order can be obtained easily. It employs the forward and backward FFT a tool, which may be found in almost every software package. Thus, the KSD method can be implemented on many platforms. In contrast, application of the B-spline method demands some mathematical knowledge prior to implementation. Furthermore,  $k^{\text{th}}$  and  $l^{\text{th}}$  degree tensor product splines need to be created in order to find  $(k-2)^{\text{th}}$  and  $(l-2)^{\text{th}}$  order smooth derivatives. Thus, with ascending derivative order the determination of spatial derivatives becomes more delicate when B-splines are employed. The advantage of this method is that the interpolation of the noisy samples can be compared to a filtering process because of the data smoothing. Thus, additional filtering of the data does not need to be carried out. Also the computation of VEF from non-periodic input data can be carried out without expecting VEF computation errors due to spectral leakage.

Filtering of data acquired by an optical system is indispensable. Hence, a filtering procedure in the wavenumber domain is carried out in this

work. Two filter mechanisms, the ideal 2D  $k$ -space filter and the oval 2D Butterworth  $k$ -space filter are employed in order to remove unwanted noise components within the wavenumber domain. The ideal 2D  $k$ -space filter has the advantage of an easy implementation. However, due to its sharp filter slope at the cut-off frequency location false frequencies components are introduced once the spectral derivatives are transformed back into spatial domain (Gibb's phenomenon). Employing an oval 2D Butterworth  $k$ -space filter with a much smoother filter slope may diminish this problem.

# **5        THEORY        OF        VIBRATIONAL ENERGY IN BEAMS**

## **5.1        Introduction**

The aim of this chapter is the analytical study of vibrational energy of uniform, linear-elastic and isotropic beam structures that are assumed to be either lossless (infinite case) or hysteretically damped (finite case). In this study a harmonic load excitation is assumed and the solution to the harmonic load excitation is presented using a steady state wave-based approach. The wave-based method takes evanescent and travelling waves into account. The Euler-Bernoulli beam theory is employed.

Along with the wave-based solution of the partial differential beam equation specific analytical vibrational energy flow (VEF) expressions are derived for infinite and simply supported boundaries when exciting the structure with two different load forms, point force excitation, and moment excitation. Thus, section 5.2 presents a general four-wave VEF equation employing complex wave amplitudes to define vibrational net energy transport. This solution is then applied to the special boundary cases. Hence, section 5.3 presents time-averaged vibrational input power (VIP) and VEF expressions of an infinite beam using prior determined complex wave amplitudes. The same procedure is carried out for a simply supported beam in section 5.4. Section 5.5 introduces the theory of unconstrained layer damping on beams. Most of the presented expressions herein are derived from original work on the study of the beam.



## 5.2 Four-Wave Vibrational Energy Flow

The derivation of a general wave-based expression of VEF in a beam is useful when investigating beam structures that have different boundary conditions. It is then easier to substitute the appropriate complex wave amplitudes into the general VEF expression, once they are determined by the particular solution of the beam's differential equation of motion. Consider Figure 5.1, where a transversely vibrating finite beam is shown having four wave components in it. By applying a wave-based approach it is evident from Figure 5.1 that a near field wave component  $A_+e^{-kx}$  and a travelling

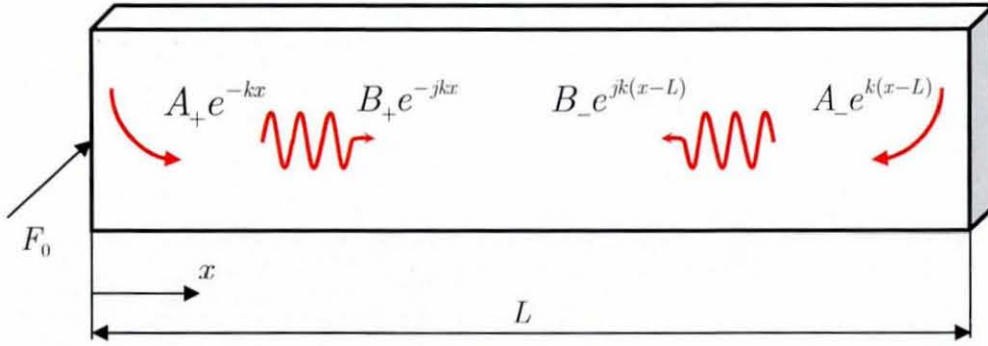


**Figure 5.1** Four wave components in a rectangular beam.

component  $B_+e^{-jkx}$  arise at the left-hand side discontinuity, which might be driven by an excitation force  $F_0$ . Because the beam is of finite nature reflections occur at the right-hand discontinuity. Thus,  $A_-e^{k(x-L)}$  and  $B_-e^{jk(x-L)}$  are the reflection components heading towards the excitation location. All four waves superimpose with each other and form the beam displacement. Thus, the general beam displacement may be assumed as [1]:

$$u(x, t) = \left( A_+e^{-kx} + B_+e^{-jkx} + B_-e^{jk(x-L)} + A_-e^{k(x-L)} \right) e^{j\omega t}. \quad (5.1)$$

Here,  $A_+$  and  $A_-$  are complex, evanescent wave amplitudes  $B_+$  and  $B_-$  are complex, travelling wave amplitudes, the subscript  $+$  denotes waves travelling into the positive  $x$  direction and the subscript  $-$  denotes wave components travelling into the negative  $x$  direction. Equation (5.1) can also be seen as the general solution of the beam's partial differential equation of motion given in equation (A1.8).

To derive time-averaged VEF expressions one can substitute equation (5.1) into equation (3.33). Note, the temporal term  $e^{j\omega t}$  was omitted. By doing so the real part of the complex, time-averaged VEF in a rectangular beam is given by:

$$(P_{x_a})_{4W} = EIk^3\omega(B_+B_+^* - B_-B_-^* - 2e^{-kL}\Im\{A_+A_+^*\}). \quad (5.2)$$

The asterisk  $*$  denotes complex conjugate of the respective complex wave amplitude and the subscript  $4W$  denotes four wave-based quantity. Analogously, the imaginary part of the time-averaged VEF in a rectangular beam can be found to be:

$$(P_{x_r})_{4W} = jEIk^3\omega \left[ \begin{aligned} & e^{-kx} \left( \cos(k(x-L))\Im\{A_+B_+^*\} + \cos(kx)\Im\{B_+A_+^*\} - \right. \\ & \left. \sin(k(x-L))\Re\{A_+B_+^*\} - \sin(kx)\Re\{B_+A_+^*\} \right) - \\ & e^{k(x-L)} \left( \cos(kx)\Im\{A_-B_-^*\} + \cos(k(x-L))\Im\{B_-A_-^*\} + \right. \\ & \left. \sin(kx)\Re\{A_-B_-^*\} + \sin(k(x-L))\Re\{B_-A_-^*\} \right) + \\ & e^{-kx} \left( \cos(k(x-L))\Re\{A_+B_+^*\} + \cos(kx)\Re\{B_+A_+^*\} + \right. \\ & \left. \sin(k(x-L))\Im\{A_+B_+^*\} + \sin(kx)\Im\{B_+A_+^*\} \right) - \\ & e^{k(x-L)} \left( \cos(kx)\Re\{A_-B_-^*\} + \cos(k(x-L))\Re\{B_-A_-^*\} - \right. \\ & \left. \sin(kx)\Im\{A_-B_-^*\} - \sin(k(x-L))\Im\{B_-A_-^*\} \right) \end{aligned} \right]. \quad (5.3)$$

Herein,  $\Re$  denotes the real part and  $\Im$  denotes the imaginary part of a complex quantity. Equations (5.2) and (5.3) display the net VEF in a beam if four wave components are present. Expression (5.2) is known as the active



VEF. This part gives information about net energy transmitted through the structure. Equation (5.3) is known as the reactive VEF and this part gives information about energy stored in the beam in dependency upon the amount of standing waves forming the displacement. From equation (5.2) it becomes evident that the active net energy flow is contributed mostly by the difference of squared wave magnitude  $|B_+|^2 = B_+ B_+^*$  and squared wave magnitude  $|B_-|^2 = B_- B_-^*$ . It is also shown that the nearfield components  $A_+$  and  $A_-$  can contribute to energy flow if they have a significant imaginary part, the beam length is short, or the frequency given by the wavenumber  $k$  is low. Of course both nearfield components need to be present.

### 5.3 Infinite Beam Analysis

The concept of infinite structures is pure hypothetical. It is often used in analytical dynamic analysis to simplify the solution by neglecting reflections from the boundaries. Hence, the structure boundaries are extended theoretically to infinity. The advantage of this procedure is that a simple and fast insight into the physical behaviour of any vibrating structure can be obtained. In practice, infinite structures are simulated by a very high boundary damping. Thus, almost the entire vibrational energy injected into the system at the excitation location is dissipated at the end of the structure. Within this analysis internal structural damping, usually modelled by a hysteretic damping model, is neglected, since the damping at the boundary is considered much higher than the internal structural damping.

Within this section a fully infinite beam is analysed when excited by a point force or a moment. Simple results of transverse beam displacement are derived in section 5.3.1. From these results VIP expressions are presented in section 5.3.2. In section 5.3.3 VEF expressions are derived employing the derived four wave-based VEF equations.

### 5.3.1 Forced Vibration

The solution of the beam's inhomogeneous partial differential equation of motion (A1.8) is the response of the beam to an applied load. In this research a harmonic excitation is assumed. The inhomogeneous differential beam

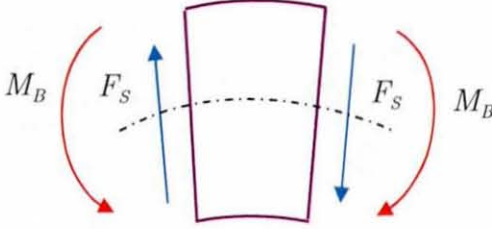


**Figure 5.2** Positive sign conventions.

equation can be solved by using different techniques. Applying a finite Fourier transform [108], using a modal approach [114] or utilising the Laplace transform [108] are just a few of them. In this work a wave-based approach is employed. This approach is relatively new. It has the advantage of a simple implementation in computational systems. Wave-based analysis uses exponential travelling and decaying waves to describe the beam's response to a harmonic load. The sign conventions are shown in Figure 5.2.

#### 5.3.1.1 Point Force Excitation

Consider a fully infinite beam, excited in the middle by a harmonically varying load, as shown in Figure 5.3. It is convenient to distinguish between a positive and a negative beam displacement location. Thus, the beam displacement is given by [1]:

$$u_+(x, t)_\infty = (A_+ e^{-kx} + B_+ e^{-jkx}) e^{j\omega t} \text{ for } x \geq 0, \quad (5.4)$$

$$u_-(x, t)_\infty = (C_- e^{kx} + D_- e^{jkx}) e^{j\omega t} \text{ for } x \leq 0. \quad (5.5)$$

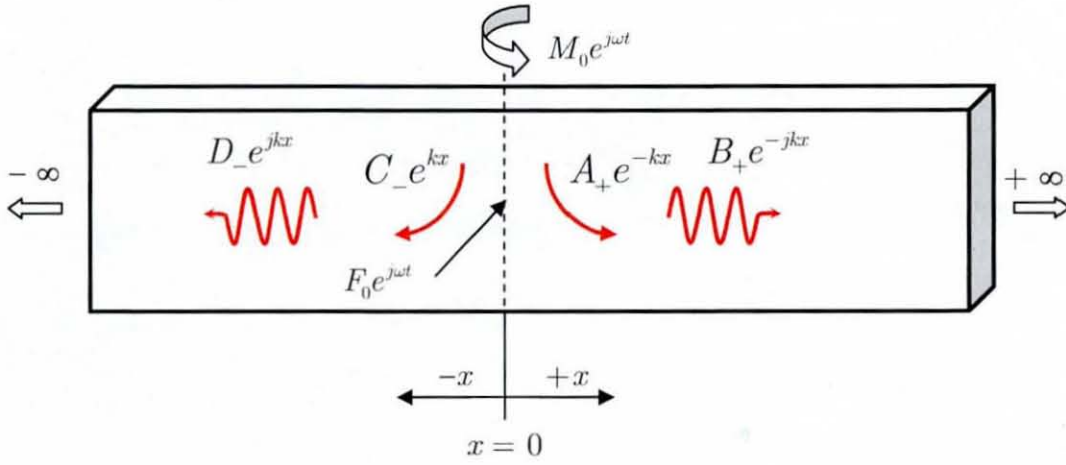


**Figure 5.3** Waves in a point force or moment excited infinite beam.

There are 4 unknown complex wave amplitudes and, thus, 4 boundary conditions need to be defined at the excitation location,  $x = 0$ . Two boundary conditions can be related to the geometrical condition on the beam at the excitation location given by:

$$u_+(0)_{F_\infty} = u_-(0)_{F_\infty}, \quad (5.6)$$

$$\frac{\partial u_+(0)_{F_\infty}}{\partial x} = \frac{\partial u_-(0)_{F_\infty}}{\partial x}. \quad (5.7)$$

Further, two more boundary conditions can be derived. One is related to the equilibrium of the internal bending moments at the excitation location  $x = 0$  and one is related to the equilibrium of the internal shear forces with the applied excitation force at the excitation location  $x = 0$ . Thus:

$$EI \frac{\partial^2 u_+(0)_{F_\infty}}{\partial x^2} = EI \frac{\partial^2 u_-(0)_{F_\infty}}{\partial x^2}, \quad (5.8)$$

$$\frac{\partial^3 u_+(0)_{F_\infty}}{\partial x^3} - \frac{\partial^3 u_-(0)_{F_\infty}}{\partial x^3} = \frac{F_0}{EI}. \quad (5.9)$$

A complete derivation of this analysis can be found in Appendix A7. From Appendix A7, the complex wave amplitudes are found to be:

$$\begin{Bmatrix} A_+ \\ B_+ \\ C_- \\ D_- \end{Bmatrix} = \begin{Bmatrix} -\frac{F_0}{4EI k^3} \\ -\frac{jF_0}{4EI k^3} \\ \frac{F_0}{4EI k^3} \\ -\frac{jF_0}{4EI k^3} \end{Bmatrix}. \quad (5.10)$$

If one substitutes equation (5.10) into equation (5.4) and (5.5), respectively, the infinite beam's response to a harmonically varying point force can be found to be [1]:

$$u_+(x, t)_{F_\infty} = -\frac{F_0}{4EI k^3} (e^{-kx} + j e^{-jkx}) e^{j\omega t} \text{ for } x \geq 0, \quad (5.11)$$

$$u_-(x, t)_{F_\infty} = -\frac{F_0}{4EI k^3} (e^{kx} + j e^{jkx}) e^{j\omega t} \text{ for } x \leq 0. \quad (5.12)$$

Here, the flexural wavenumber  $k$  is given as  $k^4 = \rho A \omega^2 / (EI)$ .

### 5.3.1.2 Moment Excitation

If the load is considered to be a harmonically varying moment, the transverse displacements  $u_+(0, t)_\infty$  and  $u_-(0, t)_\infty$  at the excitation location  $x = 0$  must be zero. Also, the slope of both displacements at the excitation location must be equal. The first two boundary conditions are satisfied by equations (5.6) and (5.7). Furthermore, the sum of the internal bending moments on either side at the excitation location  $x = 0$  must be equal to the applied moment



and the internal shear forces on either side of  $x = 0$  must be in equilibrium. Thus, the two remaining boundary conditions of an infinite beam under moment excitation can be formulated as:

$$\frac{\partial^2 u_+(0)_{M_\infty}}{\partial x^2} - \frac{\partial^2 u_-(0)_{M_\infty}}{\partial x^2} = \frac{M_0}{EI}, \quad (5.13)$$

$$EI \frac{\partial^3 u_+(0)_{M_\infty}}{\partial x^3} = EI \frac{\partial^3 u_-(0)_{M_\infty}}{\partial x^3}. \quad (5.14)$$

A derivation of the wave amplitudes can be found in Appendix A8. From Appendix A8 the desired wave amplitudes are given by:

$$\begin{Bmatrix} A_+ \\ B_+ \\ C_- \\ D_- \end{Bmatrix} = \begin{Bmatrix} \frac{M_0}{4EI k^2} \\ -\frac{M_0}{4EI k^2} \\ -\frac{M_0}{4EI k^2} \\ \frac{M_0}{4EI k^2} \end{Bmatrix}. \quad (5.15)$$

Substituting equation (5.15) into (5.4) and (5.5), respectively the beam's response due to an applied moment may be defined as [103]:

$$u_+(x, t)_{M_\infty} = \frac{M_0}{4EI k^2} (e^{kx} - e^{-jkx}) e^{j\omega t}, \text{ for } x \geq 0, \quad (5.16)$$

$$u_-(x, t)_{M_\infty} = -\frac{M_0}{4EI k^2} (e^{kx} - e^{jkx}) e^{j\omega t}, \text{ for } x \leq 0. \quad (5.17)$$

### 5.3.2 Vibrational Input Power

In section 3.5 VIP expressions were presented. It has been shown that input power to a structure can be determined from the knowledge of the real part of the point mobility. Mobility functions are defined as the ratio of velocity response due to an applied load and the load itself. Mobility functions describe the dynamic response at any point in the structure due to the applied load. If the response at the excitation location is of interest, then point mobility functions are employed. If spatial positions away from the excitation location are of interest, then transfer mobility functions are employed. With the determined transverse beam displacement of the infinite beam the VIP due to point force and moment excitation can be found simply by substituting the point mobility of the respective structure into equation (3.23) and (3.24), respectively. Due to the energy balance of infinite structures the input power must be equal to the transmitted energy if internal losses are neglected.

#### 5.3.2.1 Point Force Excitation

Point mobility of a structure due to a harmonic point force at excitation location  $x_0$  is defined as:

$$Y_F = \frac{\frac{\partial u(x_0, t)_F}{\partial t}}{F_0 e^{j\omega t}}. \quad (5.18)$$

Substituting equation (5.11) and (5.12), respectively, into definition (5.18) and setting  $x_0 = 0$ , the point force mobility of an infinite beam can be written as:

$$Y_{F_\infty} = \frac{(1-j)\omega}{4EI k^3}. \quad (5.19)$$

Substituting equation (5.19) into equation (3.23) vibrational input power to an infinite beam is given as:

$$(P_{in})_{F_{\infty}} = \frac{F_0^2 \omega}{8EI k^3}. \quad (5.20)$$

### 5.3.2.2 Moment Excitation

Moment point mobility of a structure due to a harmonic moment at excitation location  $x_0$  is defined as:

$$Y_M = \frac{\frac{\partial^2 u(x_0, t)_M}{\partial t \partial x}}{M_0 e^{j\omega t}}. \quad (5.21)$$

Substituting equation (5.16) and (5.17), respectively, into expression (5.21) and setting  $x_0 = 0$ , the moment point mobility of an infinite beam can be written as:

$$Y_{M_{\infty}} = -\frac{(1+j)\omega}{4EI k}. \quad (5.22)$$

Note, the negative sign of equation (5.17) changes with clockwise moment excitation and is a result due to the employed sign convention. Since power input to a structure cannot be negative, the minus sign is neglected for input power definition. Substituting equation (5.22) into equation (3.24) VIP to an infinite beam due to moment excitation is given by:

$$(P_{in})_{M_{\infty}} = \frac{M_0^2 \omega}{8EI k}. \quad (5.23)$$

### 5.3.3 Transmitted Vibrational Energy

With the determined complex wave amplitudes the transmitted vibrational energy due to point force and moment excitation can be found simply by substituting the wave amplitudes into the general four-wave VEF equation derived in section 5.2. The right-hand side and the left-hand side of the beam are considered separately.

#### 5.3.3.1 Point Force Excitation

Substituting the wave amplitudes of equation (5.10) into equation (5.2) and setting  $B_- = A_- = 0$ , the active transmitted energy within a point force excited infinite beam to the right (+) and left (-) can be found to be:

$$(P_{x_a})_{F_\infty} = \pm \frac{F_0^2 \omega}{16EI k^3}. \quad (5.24)$$

Analogously, substituting the wave amplitudes given by (5.10) into equation (5.3) the reactive VEF to either sides (upper sign for  $x > 0$  and lower sign for  $x < 0$ ) of the infinite beam is given by:

$$(P_{x_r})_{F_\infty} = \frac{jF_0^2 \omega e^{\mp kx}}{16EI k^3} (\pm \cos(kx) + \sin(kx)). \quad (5.25)$$

#### 5.3.3.2 Moment Excitation

The same method, as described above, can be employed to find the transmitted vibrational power when applying an excitation moment simply by substituting the wave amplitudes given by equation (5.15) into equation (5.2). Thus, moment induced active VEF is given to the right side (+) and to the left side (-) of the infinite beam as:



$$(P_{x_a})_{M_\infty} = \pm \frac{M_0^2 \omega}{16EI k}. \quad (5.26)$$

Substituting the wave amplitudes of equation (5.15) into equation (5.3), the reactive VEF to both sides of a moment excited infinite beam is:

$$(P_{x_r})_{M_\infty} = \frac{jM_0^2 \omega e^{\mp kx}}{16EI k} (\sin(kx) \mp \cos(kx)). \quad (5.27)$$

## 5.4 Simply Supported Beam Analysis

In contrast to the infinite beam analysis, the response of a finite beam is dominated by reflections at the boundary locations. Since the boundaries of a finite beam are considered here to be lossless, internal dissipation of vibrational energy is the primary energy dissipation procedure.

The internal dissipation process is modelled within this work by a hysteretic damping approach [1, 103]. A hysteretic damping model employs a loss factor, which is defined as the ratio of dissipated energy (energy loss) and reversible energy and, thus, the loss factor indicates the amount of energy lost during one cycle of vibration [103]. To include damping the Young's modulus becomes a complex quantity. If one employs a wave-based approach, the wavenumber also changes into a complex quantity. Thus, exponential travelling waves, considered to be the primary energy transport component, are now multiplied by an evanescent wave component, which exponentially reduces the wave amplitude with increasing distance. Since the square of the wave amplitude is proportional to the vibrational energy transported through a volume, the VEF is diminished over distance too.

### 5.4.1 Forced Vibration

In this section, the VEF due to harmonic point force and moment excitation of a simply supported-simply supported beam is investigated. As mentioned before the boundaries of the simply supported beam are considered to be lossless. Also, the beam is assumed to be rectangular, uniform, and isotropic. At the time  $t = 0$ , the exciting load generates infinite wave components travelling away from the excitation location. If one considers the time within one cycle, i.e.  $0 \leq t < 2\pi/\omega$ , then the travelling infinite wave components are reflected at both ends of the beam causing a rise of reflected wave components, which are now travel towards each other and eventually superimpose, to create a so-called standing wave environment. If one assumes no internal material losses within the structure, consequently there is no net energy flow, since the superimposed wave field does not propagate.

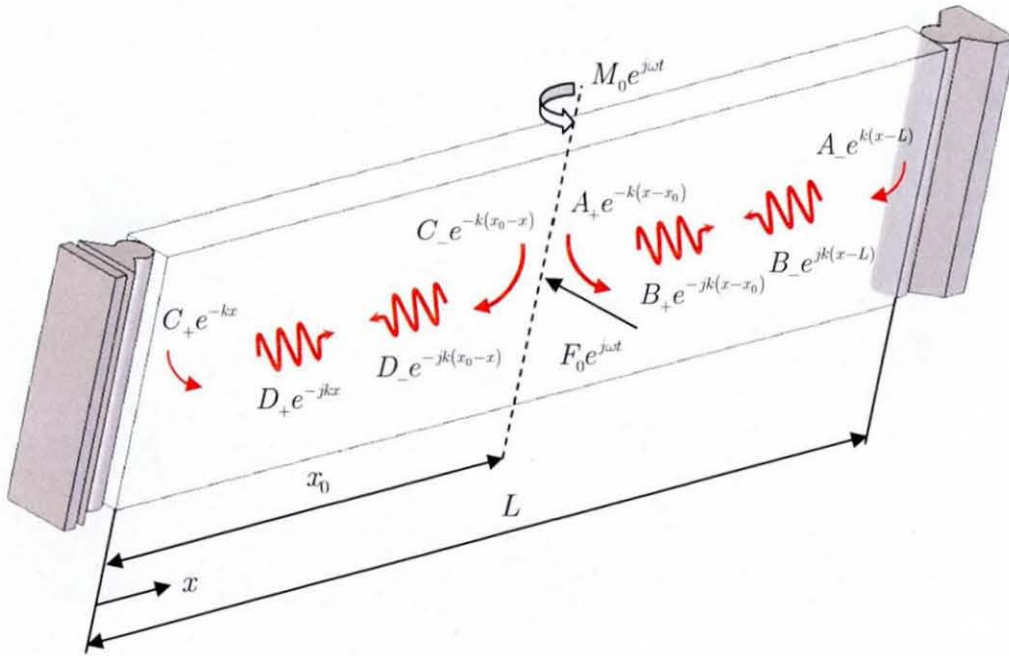


**Figure 5.4** Waves in a point force or moment excited simply supported beam.

Furthermore, no additional energy can be injected into the structure as soon as the second cycle commences, since the previous injected energy is still

stored within the beam. Thus, if one analyses a finite structure by neglecting internal material losses the point mobility of it is purely imaginary. Hence, according to equations (3.23) and (3.24), no energy can be injected into the structure because the VIP equations employ the real part of the point mobility only. It is clear from here on that damping must be included in order to account for real finite beam behaviour. When adopting a hysteretic damping model a complex Young's modulus,  $\underline{E} = E(1 + j\eta)$ , is employed. This complex modulus results in a complex, flexural wavenumber as:

$$\underline{k} = \left( \frac{\rho A \omega^2}{EI(1 + j\eta)} \right)^{\frac{1}{4}} \quad (5.28)$$

A good approximate solution to the fourth root of the denominator in equation (5.28) can be found by assuming a small loss factor, i.e.  $\eta < 0.25$ . The four roots may then be approximated by  $k(1 - j\eta/4)$ ,  $-k(1 - j\eta/4)$ ,  $k(\eta/4 + j)$  and  $-k(\eta/4 + j)$ , where  $k$  is the real positive wavenumber [1]. From the four possible solutions the complex wavenumber used in this thesis is defined as:

$$\underline{k} \approx k \left( 1 - j \frac{\eta}{4} \right) = k(1 - j\bar{\eta}). \quad (5.29)$$

If one substitutes equation (5.29) into the general wave equation of a finite beam equation, as shown by equation (5.30), it can be realised that the exponential travelling components will now also decay exponentially to some extent while travelling and the exponential decaying components will now also propagate to some extent while decaying. Due to the exponential decay of the travelling waves the net energy flow within the structure is not zero anymore. Energy can now be injected during each cycle, which is equal to the energy dissipated within the structure during that cycle. It can also be realised that the energy relations are much more complex, since both type of waves may transport vibrational energy.

#### 5.4.1.1 Point Force Excitation

The transverse beam displacement is considered herein as a superposition of an infinite beam displacement and reflections caused by the beam's simply supported boundaries. Thus, the wave model is formed by an infinite beam response and the reactions at the beam's end. Mathematically the transverse finite beam displacement may be expressed as [1]:

$$u(x, t) = \left( u(x)_\infty + B_- e^{jk(x-L)} + A_- e^{k(x-L)} + D_+ e^{-jkx} + C_+ e^{-kx} \right) e^{j\omega t}. \quad (5.30)$$

The infinite beam displacement is related to a finite beam in dependency upon the position  $x$  and the excitation location  $x_0$  and is given by [1]:

$$u(x)_{F_\infty} = \sum_{n=1}^2 K_n e^{-\underline{k}_n |x_0 - x|}. \quad (5.31)$$

Herein,  $K_n$  is the nearfield wave amplitude for  $n = 1$  and the farfield amplitude for  $n = 2$ . Furthermore,  $\underline{k}_1 = \underline{k}$  and  $\underline{k}_2 = j\underline{k}$ . The reason why only two wave amplitudes are employed is that they are identical for the left- and right-hand side of the excitation location. It is more convenient to relate the infinite beam response in finite structures by using equation (5.31).

As mentioned before the beam displacement is a superposition of infinite waves and reflection waves that occur at  $x = 0$  and  $x = L$ . A complete derivation of the transverse finite beam response can be found in Appendix A9 The boundary conditions at the excitation location are exactly the same, as shown by equations (5.6) to (5.9). The remaining boundary conditions at  $x = 0$  can be found to be:

$$u(0)_{ss} = 0, \quad (5.32)$$

$$\underline{EI} \frac{\partial^2 u(0)_{ss}}{\partial x^2} = 0. \quad (5.33)$$

Analogously, the boundary conditions at  $x = L$  can be written as:

$$u(L)_{ss} = 0 , \quad (5.34)$$

$$\underline{EI} \frac{\partial^2 u(L)_{ss}}{\partial x^2} = 0 . \quad (5.35)$$

Equations (5.32) to (5.35) display the classical simply supported boundary conditions of zero displacement and zero bending moment, respectively. By substituting the general wave-based solution shown by equation (5.30) into the above given boundary equations one may create a matrix equation as demonstrated in Appendix A9. Here, equation (5.31) is regarded. The solution of this matrix equation yields to the exponential wave amplitudes of a simply supported point force excited beam. Thus:

$$\begin{bmatrix} A_+ \\ B_+ \\ B_- \\ A_- \\ C_- \\ D_- \\ D_+ \\ C_+ \end{bmatrix} = \frac{F_0}{4\underline{EI}k^3} \begin{bmatrix} -1 \\ -j \\ \frac{j(e^{-jk(L+x_0)} - e^{-jk(L-x_0)})}{(e^{-2jkL} - 1)} \\ \frac{(e^{-jk(L+x_0)} - e^{-jk(L-x_0)})}{(e^{-2jkL} - 1)} \\ -1 \\ -j \\ \frac{j(e^{-jk(2L-x_0)} - e^{-jkx_0})}{(e^{-2jkL} - 1)} \\ \frac{(e^{-jk(2L-x_0)} - e^{-jkx_0})}{(e^{-2jkL} - 1)} \end{bmatrix} . \quad (5.36)$$

If one substitutes the complex wave amplitudes (5.36) into equation (5.30) under consideration of equation (5.31), the transverse displacement of a point force excited simply supported beam can be written as:

$$u(x, t)_{F_s} = -\frac{F_0 e^{j\omega t}}{4EI\bar{k}^3} \left( \begin{aligned} & e^{-\bar{k}|x_0-x|} + j e^{-j\bar{k}|x_0-x|} - \\ & \frac{j(e^{-j\bar{k}(L+x_0)} - e^{-j\bar{k}(L-x_0)})}{(e^{-2j\bar{k}L} - 1)} e^{j\bar{k}(x-L)} - \\ & \frac{(e^{-\bar{k}(L+x_0)} - e^{-\bar{k}(L-x_0)})}{(e^{-2\bar{k}L} - 1)} e^{\bar{k}(x-L)} - \\ & \frac{j(e^{-j\bar{k}(2L-x_0)} - e^{-j\bar{k}x_0})}{(e^{-2j\bar{k}L} - 1)} e^{-j\bar{k}x} - \\ & \frac{(e^{-\bar{k}(2L-x_0)} - e^{-\bar{k}x_0})}{(e^{-2\bar{k}L} - 1)} e^{-\bar{k}x} \end{aligned} \right). \quad (5.37)$$

#### 5.4.1.2 Moment Excitation

As shown in equation (5.15) the right-hand side and the left-hand side amplitudes are equal in magnitude but different in sign. Thus, the infinite beam displacement of a moment excited beam, related to the finite beam vibration, may be written as:

$$u(x)_{M_\infty} = \sum_{n=1}^2 (-1)^{n-1} \text{sig}(x-x_0) F_n e^{-\bar{k}_n|x_0-x|}. \quad (5.38)$$

Herein,  $\text{sig}(x-x_0)$  is a function similar to the well known signum function  $\text{sig}(x)$ . However,  $\text{sig}(x-x_0)$  is defined in this work as:

$$\text{sig}(x-x_0) = \begin{cases} 1 & \text{for } x \geq x_0 \\ -1 & \text{for } x \leq x_0 \end{cases}. \quad (5.39)$$

Here,  $F_n$  is the nearfield wave amplitude for  $n = 1$  and the farfield amplitude for  $n = 2$ . Furthermore, the wavenumber relations are  $\bar{k}_1 = \bar{k}$  and  $\bar{k}_2 = j\bar{k}$ .

From Appendix A10, the complex, exponential wave amplitudes are given by:

$$\begin{bmatrix} A_+ \\ B_+ \\ B_- \\ A_- \\ C_- \\ D_- \\ D_+ \\ C_+ \end{bmatrix} = \frac{M_0}{4EI\bar{k}^2} \begin{bmatrix} 1 \\ -1 \\ \frac{(e^{-jk(L+x_0)} + e^{-jk(L-x_0)})}{(e^{-2jkL} - 1)} \\ \frac{(e^{-k(L+x_0)} + e^{-k(L-x_0)})}{(e^{-2kL} - 1)} \\ -1 \\ 1 \\ \frac{(e^{-jk(2L-x_0)} + e^{-jkx_0})}{(e^{-2jkL} - 1)} \\ -\frac{(e^{-k(2L-x_0)} + e^{-kx_0})}{(e^{-2kL} - 1)} \end{bmatrix} \quad (5.40)$$

A complete derivation of the moment excited beam response is given in Appendix A10. The boundary conditions, when exciting by a moment, were satisfied by equations (5.10) and (5.12), equations (5.13) and (5.14), and equations (5.32) to (5.35). Substituting equation (5.40) into equation (5.30) under consideration of equation (5.38), the beam response was found to be:

$$u(x, t)_{M_0} = \frac{M_0 e^{j\omega t}}{4EI\bar{k}^2} \begin{bmatrix} \text{sig}(x_0 - x) \left( e^{-k|x_0-x|} - e^{-jk|x_0-x|} \right) - \\ \frac{(e^{-jk(L+x_0)} + e^{-jk(L-x_0)})}{(e^{-2jkL} - 1)} e^{jk(x-L)} + \\ \frac{(e^{-jk(2L-x_0)} + e^{-jkx_0})}{(e^{-2jkL} - 1)} e^{-jkx} + \\ \frac{(e^{-k(L+x_0)} + e^{-k(L-x_0)})}{(e^{-2kL} - 1)} e^{k(x-L)} - \\ \frac{(e^{-k(2L-x_0)} + e^{-kx_0})}{(e^{-2kL} - 1)} e^{-kx} \end{bmatrix} \quad (5.41)$$

## 5.4.2 Vibrational Input Power

### 5.4.2.1 Point Force Excitation

The derivation of the point mobility of a point force excited simply supported beam is given in Appendix A11. From there the point mobility  $Y_{F_s}$  is given by:

$$Y_{F_s} = \frac{j\omega}{4EI\bar{k}^3} \left[ \left( \frac{\sin(2\bar{k}x_0) + \sin(2\bar{k}(L - x_0)) - \sin(2\bar{k}L)}{1 - \cos(2\bar{k}L)} \right) - \left( \frac{\sinh(2\bar{k}x_0) + \sinh(2\bar{k}(L - x_0)) - \sinh(2\bar{k}L)}{1 - \cosh(2\bar{k}L)} \right) \right]. \quad (5.42)$$

It can be seen that  $Y_{F_s}$  is a rather complicated complex expression with complex arguments in each sinusoidal and hyperbolic term. Any further rearrangement of equation (5.42) into real and imaginary components would yield to a large expression that will not be shown in this work. If one substitutes equation (5.42) into equation (3.23), time-averaged VIP to a hysteretically damped simply supported beam excited by a point force is defined as:

$$(P_{in})_{F_s} = \frac{F_0^2 \omega}{8I} \Re \left[ \frac{j}{E\bar{k}^3} \left[ \left( \frac{\sin(2\bar{k}x_0) + \sin(2\bar{k}(L - x_0)) - \sin(2\bar{k}L)}{1 - \cos(2\bar{k}L)} \right) - \left( \frac{\sinh(2\bar{k}x_0) + \sinh(2\bar{k}(L - x_0)) - \sinh(2\bar{k}L)}{1 - \cosh(2\bar{k}L)} \right) \right] \right]. \quad (5.43)$$

Without damping the first fraction of equation (5.43) denotes travelling wave components and the second fraction denotes evanescent wave components, which are purely imaginary in that case (see equation (A11.7) in Appendix A11). However, due to the hysteretic damping each argument is now complex and, thus, undamped pure imaginary terms become complex by having a real part, which allows for power input. As mentioned previously, if one neglects



internal damping the energy input to a beam is zero, since the point mobility, given by equation (A11.7), is purely imaginary.

#### 5.4.2.2 Moment Excitation

Vibrational power input of a moment excited simply supported beam can be derived, as shown above. From Appendix A12 the moment point mobility is given as:

$$Y_{M_u} = \frac{j\omega}{4EI\bar{k}} \left[ \left( \frac{\sin(2\bar{k}x_0) + \sin(2\bar{k}(L - x_0)) + \sin(2\bar{k}L)}{1 - \cos(2\bar{k}L)} \right) + \left( \frac{\sinh(2\bar{k}x_0) + \sinh(2\bar{k}(L - x_0)) + \sinh(2\bar{k}L)}{1 - \cosh(2\bar{k}L)} \right) \right]. \quad (5.44)$$

Substituting equation (5.44) into the input power equation (3.24), time-averaged VIP of a moment excited simply supported beam can be found as:

$$(P_m)_{M_u} = \frac{M_0^2 \omega}{8I} \Re \left\{ \frac{j}{\bar{k}} \left[ \left( \frac{\sin(2\bar{k}x_0) + \sin(2\bar{k}(L - x_0)) + \sin(2\bar{k}L)}{1 - \cos(2\bar{k}L)} \right) + \left( \frac{\sinh(2\bar{k}x_0) + \sinh(2\bar{k}(L - x_0)) + \sinh(2\bar{k}L)}{1 - \cosh(2\bar{k}L)} \right) \right] \right\}. \quad (5.45)$$

Also here, the input power term is a rather complicated expression. It can be seen from equation (5.45) that the argument of each sinusoidal and hyperbolic term is fully complex. Thus, each term allows energy input to some extent.

#### 5.4.3 Transmitted Vibrational Energy

Since the beam displacement of a finite beam is composed of the infinite beam response and its reflections, it can be realised that VEF in a finite beam is formed by infinite waves and reflection waves. The simply supported

beam displacement as the summation of both wave groups simply can be written as:

$$u(x, t) = (u(x)_{\infty} + u(x)_r) e^{j\omega t}. \quad (5.46)$$

Herein,  $u(x)_{\infty}$  is the infinite waves response and  $u(x)_r$  is the reflection waves response. If one substitutes equation (5.46) into the shear force term of expression (3.33), the following shear force term can be obtained:

$$P_{x_s} = \frac{EI}{2} \left[ \frac{\partial^3 u(x, t)_{\infty}}{\partial x^3} \left( \frac{\partial u(x, t)_{\infty}}{\partial t} \right)^* + \frac{\partial^3 u(x, t)_r}{\partial x^3} \left( \frac{\partial u(x, t)_{\infty}}{\partial t} \right)^* + \frac{\partial^3 u(x, t)_{\infty}}{\partial x^3} \left( \frac{\partial u(x, t)_r}{\partial t} \right)^* + \frac{\partial^3 u(x, t)_r}{\partial x^3} \left( \frac{\partial u(x, t)_r}{\partial t} \right)^* \right]. \quad (5.47)$$

Analogously, the time-averaged bending moment VEF component can be found by substituting equation (5.46) into the bending moment term of equation (3.33):

$$P_{x_M} = -\frac{EI}{2} \left[ \frac{\partial^2 u(x, t)_{\infty}}{\partial x^2} \left( \frac{\partial^2 u(x, t)_{\infty}}{\partial x \partial t} \right)^* + \frac{\partial^2 u(x, t)_r}{\partial x^2} \left( \frac{\partial^2 u(x, t)_{\infty}}{\partial x \partial t} \right)^* + \frac{\partial^2 u(x, t)_{\infty}}{\partial x^2} \left( \frac{\partial^2 u(x, t)_r}{\partial x \partial t} \right)^* + \frac{\partial^2 u(x, t)_r}{\partial x^2} \left( \frac{\partial^2 u(x, t)_r}{\partial x \partial t} \right)^* \right]. \quad (5.48)$$

From equations (5.47) and (5.48) it can be seen that two uncoupled and two coupled VEF terms arise. The uncoupled VEF terms occur due to a pure VEF product of each wave group and they are denoted as  $(P_x)_{\infty}$  and  $(P_x)_r$ .

The coupling arises due to a mixed VEF product between both wave groups. Thus, coupling is defined as the VEF product of the shear force or bending moment component of the infinite waves group and its appropriate velocities components of the reflection waves group, denoted as  $(P_x)_{\infty, r}$  and  $(P_x)_{r, \infty}$ , respectively.

Thus, the VEF within a finite beam can be defined as:

$$(P_x) = (P_x)_\infty + (P_x)_r + (P_x)_c. \quad (5.49)$$

Here, the coupled term is given by:

$$(P_x)_c = (P_x)_{r,\infty} + (P_x)_{\infty,r}. \quad (5.50)$$

#### 5.4.3.1 Four-Wave Vibrational Energy Flow Including Damping

The uncoupled transmitted energy  $(P_x)_\infty$  and  $(P_x)_r$ , respectively can be determined simply by substituting the respective wave group into the general four-wave VEF expression. However, the expressions given in section 5.2 do not include damping. From section 5.2 the damped four-wave VEF can be obtained simply by substituting a complex wavenumber into equation (5.1) and using this definition to derive VEF due to the four wave presence. The derivation of this procedure is given in Appendix A13. Using the following simplifications:

$$D_{B_+A_+}^\pm = \Re\{B_+A_+^*\} \pm \Im\{B_+A_+^*\}, \quad (5.51)$$

$$D_{A_+B_-}^\pm = \Re\{A_+B_-^*\} \pm \Im\{A_+B_-^*\}, \quad (5.52)$$

$$D_{B_+A_-}^\pm = \Re\{B_+A_-^*\} \pm \Im\{B_+A_-^*\}, \quad (5.53)$$

$$D_{A_-B_-}^\pm = \Re\{A_-B_-^*\} \pm \Im\{A_-B_-^*\}, \quad (5.54)$$

the four-wave-based VEF of a hysteretically damped beam is given by:

$$(P_x)_{4W} = C_{4W} \left[ \begin{aligned} & (1 + j\bar{\eta})(B_+ B_+^* e^{-2kx\bar{\eta}} - B_- B_-^* e^{2k\tilde{x}\bar{\eta}}) + \\ & 2(\bar{\eta} + j\bar{\eta}^2) e^{-k\bar{\eta}(x+\tilde{x})} \left[ \begin{aligned} & \cos(k(x+\tilde{x})) \Im \{B_+ B_-^*\} - \\ & \sin(k(x+\tilde{x})) \Re \{B_+ B_-^*\} \end{aligned} \right] - \\ & 2(1 + j\bar{\eta}) e^{-k(x-\tilde{x})} \cos(k\tilde{x}\bar{\eta}) \left[ \begin{aligned} & \cos(kx\bar{\eta}) \Im \{A_+ A_-^*\} + \\ & \sin(kx\bar{\eta}) \Re \{A_+ A_-^*\} \end{aligned} \right] + \\ & 2(\bar{\eta} - j) e^{-k(x-\tilde{x})} \sin(k\tilde{x}\bar{\eta}) \left[ \begin{aligned} & \cos(kx\bar{\eta}) \Im \{A_+ A_-^*\} + \\ & \sin(kx\bar{\eta}) \Re \{A_+ A_-^*\} \end{aligned} \right] + \\ & (\bar{\eta} + j\bar{\eta}^2)(A_+ A_+^* e^{-2kx} - A_- A_-^* e^{2k\tilde{x}}) + \\ & (\bar{\eta} - j) e^{-kx} \left[ \begin{aligned} & e^{-kx\bar{\eta}} (\bar{\eta} - 1) \left[ \begin{aligned} & D_{B_+ A_+}^+ \cos(kx(1 + \bar{\eta})) - \\ & D_{B_+ A_+}^- \sin(kx(1 + \bar{\eta})) \end{aligned} \right] + \\ & e^{k\tilde{x}\bar{\eta}} (\bar{\eta} + 1) \left[ \begin{aligned} & D_{A_+ B_-}^- \sin(k(\tilde{x} - x\bar{\eta})) - \\ & D_{A_+ B_-}^+ \cos(k(\tilde{x} - x\bar{\eta})) \end{aligned} \right] \end{aligned} \right] + \\ & (\bar{\eta} - j) e^{k\tilde{x}} \left[ \begin{aligned} & e^{-kx\bar{\eta}} (\bar{\eta} + 1) \left[ \begin{aligned} & D_{B_+ A_-}^- \cos(k(x - \tilde{x}\bar{\eta})) + \\ & D_{B_+ A_-}^+ \sin(k(x - \tilde{x}\bar{\eta})) \end{aligned} \right] - \\ & e^{k\tilde{x}\bar{\eta}} (\bar{\eta} - 1) \left[ \begin{aligned} & D_{A_- B_-}^- \cos(k\tilde{x}(1 + \bar{\eta})) + \\ & D_{A_- B_-}^+ \sin(k\tilde{x}(1 + \bar{\eta})) \end{aligned} \right] \end{aligned} \right] \end{aligned} \right]. \quad (5.55)$$

Here, the simplification  $\tilde{x} = (x - L)$  is employed and the constant  $C_{4W}$  is defined as:

$$C_{4W} = \frac{EI k^3 \omega (1 - j\bar{\eta})^3}{1 + \bar{\eta}^2}. \quad (5.56)$$

If no damping is included, expression (5.55) may be reduced to equations (5.2) and (5.3). From (5.55) it can be seen that the damped VEF is a much more complex expression. This is due to the fact that each exponential VEF

term in equation (5.1) is now fully complex and contains travelling as well as evanescent parts.

To derive VEF expressions of a simply supported beam the infinite beam response  $u(x)_\infty$  is defined in this work as:

$$u(x)_\infty = C_1 e^{k\bar{x}} + C_2 e^{-jk\bar{x}}. \quad (5.57)$$

Herein, the simplification  $\bar{x} = |x_0 - x|$  is used. The near- and farfield wave amplitudes of the infinite beam response are  $C_1$  and  $C_2$ , respectively. The infinite waves amplitude are given by equation (5.10) and (5.15), respectively for both types of excitation. Note, equation (5.31) and (5.38), respectively need to be applied when employing the infinite beam response in the simply supported beam VEF analysis.

The reflection waves beam response  $u(x)_r$  is given as:

$$u(x)_r = D_+ e^{-jkx} + C_+ e^{-kx} + B_- e^{jkx} + A_- e^{kx}. \quad (5.58)$$

To derive VEF due to the infinite waves, two wave components need to be substituted into equation (5.55), only. To derive VEF due to the reflection waves, four wave components need to be substituted into equation (5.55).

### 5.4.3.2 Coupled Vibrational Energy Flow Including Damping

As shown in equations (5.47) and (5.48) two different forms of coupled VEF arise in a finite beam given by:

$$(P_x)_c = (P_x)_{r,\infty} + (P_x)_{\infty,r}. \quad (5.48)$$

As mentioned previously  $(P_x)_{r,\infty}$  appears due to the complex product of internal shear force and bending moment of the reflection waves and the appropriate infinite wave velocity components given by:

$$(P_x)_{r,\infty} = \frac{EI}{2} \left( \frac{\partial^3 u(x,t)_r}{\partial x^3} \left( \frac{\partial u(x,t)_\infty}{\partial t} \right)^* + \frac{\partial^2 u(x,t)_r}{\partial x^2} \left( \frac{\partial^2 u(x,t)_\infty}{\partial x \partial t} \right)^* \right). \quad (5.59)$$

Vice versa, the complex product of internal shear force and bending moment of the infinite waves and the appropriate reflection wave velocity components may be written as:

$$(P_x)_{\infty,r} = \frac{EI}{2} \left( \frac{\partial^3 u(x,t)_\infty}{\partial x^3} \left( \frac{\partial u(x,t)_r}{\partial t} \right)^* + \frac{\partial^2 u(x,t)_\infty}{\partial x^2} \left( \frac{\partial^2 u(x,t)_r}{\partial x \partial t} \right)^* \right). \quad (5.60)$$

A complete derivation of both quantities is presented in Appendix A14 for the damped and undamped case. Usually only travelling waves transmit energy across the beam. However, as mentioned before in the case of damping each wave component is now capable of transmitting energy to some extent because each exponent in the exponential definition is complex having a real part (evanescent component) and an imaginary part (travelling component). Thus, it can be realised that the definition of transmitted energy in a finite beam is fairly complicated, since all eight wave combinations are included. From Appendix A14 the coupled VEF  $(P_x)_c$  can be written as:

$$(P_x)_c = \frac{EI k^3 \omega}{1 + \bar{\eta}^2} \left[ \begin{aligned} & (1 + j\bar{\eta}) e^{-k\bar{\eta}(\bar{x}+x)} \left[ \begin{aligned} & \left( \text{sig}(\hat{x}) + 1 \right) \begin{pmatrix} \cos(k(x-\bar{x})) \Re \{C_2^* D_+\} + \\ \sin(k(x-\bar{x})) \Im \{C_2^* D_+\} \end{pmatrix} - \\ & \bar{\eta} (\text{sig}(\hat{x}) - 1) \begin{pmatrix} \cos(k(x-\bar{x})) \Im \{C_2^* D_+\} - \\ \sin(k(x-\bar{x})) \Re \{C_2^* D_+\} \end{pmatrix} \end{aligned} \right] + \\ & (1 + j\bar{\eta}) e^{-k\bar{\eta}(\bar{x}-\hat{x})} \left[ \begin{aligned} & \left( \text{sig}(\hat{x}) - 1 \right) \begin{pmatrix} \cos(k(\bar{x}+\hat{x})) \Re \{C_2^* B_-\} - \\ \sin(k(\bar{x}+\hat{x})) \Im \{C_2^* B_-\} \end{pmatrix} - \\ & \bar{\eta} (\text{sig}(\hat{x}) + 1) \begin{pmatrix} \cos(k(\bar{x}+\hat{x})) \Im \{C_2^* B_-\} + \\ \sin(k(\bar{x}+\hat{x})) \Re \{C_2^* B_-\} \end{pmatrix} \end{aligned} \right] + \\ & (1 + j\bar{\eta}) e^{-k(\bar{x}-\hat{x})} \left[ \begin{aligned} & \bar{\eta} (\text{sig}(\hat{x}) - 1) \begin{pmatrix} \cos(k\bar{\eta}(\bar{x}+\hat{x})) \Re \{C_1^* A_-\} + \\ \sin(k\bar{\eta}(\bar{x}+\hat{x})) \Im \{C_1^* A_-\} \end{pmatrix} + \\ & (\text{sig}(\hat{x}) + 1) \begin{pmatrix} \cos(k\bar{\eta}(\bar{x}+\hat{x})) \Im \{C_1^* A_-\} - \\ \sin(k\bar{\eta}(\bar{x}+\hat{x})) \Re \{C_1^* A_-\} \end{pmatrix} \end{aligned} \right] + \\ & (1 + j\bar{\eta}) e^{-k(x+\bar{x})} \left[ \begin{aligned} & \bar{\eta} (\text{sig}(\hat{x}) + 1) \begin{pmatrix} \cos(k\bar{\eta}(x-\bar{x})) \Re \{C_1^* C_+\} - \\ \sin(k\bar{\eta}(x-\bar{x})) \Im \{C_1^* C_+\} \end{pmatrix} - \\ & (1 - \text{sig}(\hat{x})) \begin{pmatrix} \cos(k\bar{\eta}(x-\bar{x})) \Im \{C_1^* C_+\} + \\ \sin(k\bar{\eta}(x-\bar{x})) \Re \{C_1^* C_+\} \end{pmatrix} \end{aligned} \right] + \\ & (\bar{\eta} - j) e^{-k(\bar{x}+x\bar{\eta})} \left[ \begin{aligned} & (\bar{\eta} - \text{sig}(\hat{x})) \begin{pmatrix} \cos(k(x+x\bar{\eta})) \Re \{C_1^* D_+\} + \\ \sin(k(x+x\bar{\eta})) \Im \{C_1^* D_+\} \end{pmatrix} - \\ & (1 - \text{sig}(\hat{x})\bar{\eta}) \begin{pmatrix} \cos(k(x+x\bar{\eta})) \Im \{C_1^* D_+\} - \\ \sin(k(x+x\bar{\eta})) \Re \{C_1^* D_+\} \end{pmatrix} \end{aligned} \right] - \\ & (\bar{\eta} - j) e^{-k(\bar{x}-\hat{x}\bar{\eta})} \left[ \begin{aligned} & (\text{sig}(\hat{x}) + \bar{\eta}) \begin{pmatrix} \cos(k(\hat{x}-\bar{x}\bar{\eta})) \Re \{C_1^* B_-\} - \\ \sin(k(\hat{x}-\bar{x}\bar{\eta})) \Im \{C_1^* B_-\} \end{pmatrix} - \\ & (\text{sig}(\hat{x})\bar{\eta} + 1) \begin{pmatrix} \cos(k(\hat{x}-\bar{x}\bar{\eta})) \Im \{C_1^* B_-\} + \\ \sin(k(\hat{x}-\bar{x}\bar{\eta})) \Re \{C_1^* B_-\} \end{pmatrix} \end{aligned} \right] + \\ & (\bar{\eta} - j) e^{-k(x+x\bar{\eta})} \left[ \begin{aligned} & (\text{sig}(\hat{x})\bar{\eta} - 1) \begin{pmatrix} \cos(k(\bar{x}+x\bar{\eta})) \Re \{C_2^* C_+\} - \\ \sin(k(\bar{x}+x\bar{\eta})) \Im \{C_2^* C_+\} \end{pmatrix} - \\ & (\bar{\eta} - \text{sig}(\hat{x})) \begin{pmatrix} \cos(k(\bar{x}+x\bar{\eta})) \Im \{C_2^* C_+\} + \\ \sin(k(\bar{x}+x\bar{\eta})) \Re \{C_2^* C_+\} \end{pmatrix} \end{aligned} \right] + \\ & (\bar{\eta} - j) e^{k(\bar{x}-\bar{x}\bar{\eta})} \left[ \begin{aligned} & (\text{sig}(\hat{x})\bar{\eta} + 1) \begin{pmatrix} \cos(k(\bar{x}-\hat{x}\bar{\eta})) \Re \{C_2^* A_-\} - \\ \sin(k(\bar{x}-\hat{x}\bar{\eta})) \Im \{C_2^* A_-\} \end{pmatrix} + \\ & (\text{sig}(\hat{x}) + \bar{\eta}) \begin{pmatrix} \cos(k(\bar{x}-\hat{x}\bar{\eta})) \Im \{C_2^* A_-\} + \\ \sin(k(\bar{x}-\hat{x}\bar{\eta})) \Re \{C_2^* A_-\} \end{pmatrix} \end{aligned} \right] \end{aligned} \right] \quad (5.61)$$

Here, the simplification  $\hat{x} = (x - x_0)$  is applied. A much simpler expression can be found in the undamped case of  $\bar{\eta} = 0$ . In that case expression (5.61) can be reduced to a real part (active VEF) as:

$$(P_x)_{c_a} = EI k^3 \omega \left( \begin{aligned} & \left( \text{sig}(\hat{x}) + 1 \right) \begin{pmatrix} \Re \{C_2^* D_+\} \cos(k(x - \bar{x})) + \\ \Im \{C_2^* D_+\} \sin(k(x - \bar{x})) \end{pmatrix} + \\ & \left( \text{sig}(\hat{x}) - 1 \right) \begin{pmatrix} \Re \{C_2^* B_-\} \cos(k(\tilde{x} + \bar{x})) - \\ \Im \{C_2^* B_-\} \sin(k(\tilde{x} + \bar{x})) \end{pmatrix} + \\ & e^{-k\bar{x}} \begin{pmatrix} e^{k\tilde{x}} (1 + \text{sig}(\hat{x})) \Im \{C_1^* A_-\} - \\ e^{k\tilde{x}} (1 - \text{sig}(\hat{x})) \Im \{C_1^* C_+\} \end{pmatrix} \end{aligned} \right). \quad (5.62)$$

The imaginary part of the simplification of equation (5.61) (reactive VEF) is given by:

$$(P_x)_{c_r} = jEI k^3 \omega \left( \begin{aligned} & e^{-k\bar{x}} \begin{pmatrix} \Re \{C_1^* D_+\} (\text{sig}(\hat{x}) \cos(kx) - \sin(kx)) + \\ \Im \{C_1^* D_+\} (\cos(kx) + \text{sig}(\hat{x}) \sin(kx)) + \\ \Re \{C_1^* B_-\} (\text{sig}(\hat{x}) \cos(k\tilde{x}) - \sin(k\tilde{x})) - \\ \Im \{C_1^* B_-\} (\cos(k\tilde{x}) + \text{sig}(\hat{x}) \sin(k\tilde{x})) \end{pmatrix} + \\ & e^{-k\bar{x}} \begin{pmatrix} \Re \{C_2^* C_+\} (\cos(k\bar{x}) - \text{sig}(\hat{x}) \sin(k\bar{x})) - \\ \Im \{C_2^* C_+\} (\text{sig}(\hat{x}) \cos(k\bar{x}) + \sin(k\bar{x})) \end{pmatrix} - \\ & e^{k\tilde{x}} \begin{pmatrix} \Re \{C_2^* A_-\} (\cos(k\bar{x}) + \text{sig}(\hat{x}) \sin(k\bar{x})) + \\ \Im \{C_2^* A_-\} (\text{sig}(\hat{x}) \cos(k\bar{x}) - \sin(k\bar{x})) \end{pmatrix} \end{aligned} \right). \quad (5.63)$$

### 5.4.3.3 Point Force Excitation

VEF in a simply supported beam is the sum of three terms given by:

$$(P_x)_{F_s} = (P_x)_{F_\infty} + (P_x)_{F_r} + (P_x)_{F_c}. \quad (5.64)$$



Herein,  $(P_x)_\infty$  is the uncoupled transmitted energy due to the infinite waves,  $(P_x)_r$  is the uncoupled transmitted vibrational energy due to the reflection waves, and  $(P_x)_c$  is the coupled transmitted energy due to coupling of both wave groups. To derive transmitted infinite wave energy flow within a hysteretically damped simply supported beam the damped infinite wave amplitudes given in equation (5.36) may be substituted into equation (5.55) by setting  $A_-$  and  $B_-$  equal to zero. Thus, equation (5.55) reduces to:

$$(P_x)_\infty = \frac{EI k^3 \omega (1 - j\bar{\eta})^3}{1 + \bar{\eta}^2} \left[ \frac{(1 + j\bar{\eta}) B_+ B_+^* e^{-2k\bar{x}\bar{\eta}} + (\bar{\eta} + j\bar{\eta}^2) A_+ A_+^* e^{-2k\bar{x}} +}{(\bar{\eta} - j) e^{-k\bar{x}(1 + \bar{\eta})} (\bar{\eta} - 1)} \left( \frac{D_{B_+ A_+}^+ \cos(k\bar{x}(1 + \bar{\eta})) -}{D_{B_+ A_+}^- \sin(k\bar{x}(1 + \bar{\eta}))} \right) \right]. \quad (5.65)$$

By setting  $A_- = 0$  and  $B_- = 0$  the active VEF is given by:

$$(P_{x_a})_{F_\infty} = \frac{\text{sig}(\hat{x}) C_{F_\infty}}{(1 + \bar{\eta}^2)} (A_{F_\infty} + 4\bar{\eta} B_{F_\infty}). \quad (5.66)$$

The reactive VEF can be found to be:

$$(P_{x_r})_{F_\infty} = j \frac{\text{sig}(\hat{x}) C_{F_\infty}}{(1 + \bar{\eta}^2)} (4\bar{\eta} A_{F_\infty} - B_{F_\infty}). \quad (5.67)$$

In equations (5.66) and (5.67) the following substitutions are used:

$$A_{F_\infty} = \left[ \frac{\frac{1 - \bar{\eta}^2}{(1 + \bar{\eta}^2)^2} e^{-2k\bar{x}\bar{\eta}} + \frac{\bar{\eta} - \bar{\eta}^3}{(1 + \bar{\eta}^2)^2} e^{-2k\bar{x}} -}{\frac{2(\bar{\eta}^2 + 1)(\bar{\eta}^2 - \bar{\eta}) e^{-k\bar{x}(1 + \bar{\eta})}}{(1 - 3\bar{\eta}^2)^2 + (3\bar{\eta} - \bar{\eta}^3)^2} \left( \cos(k\bar{x}(1 + \bar{\eta})) + \right)} \right], \quad (5.68)$$

$$B_{F_\infty} = \left( \frac{\frac{2\bar{\eta}}{(1+\bar{\eta}^2)^2} e^{-2k\bar{x}\bar{\eta}} + \frac{2\bar{\eta}^2}{(1+\bar{\eta}^2)^2} e^{-2k\bar{x}} - \frac{(\bar{\eta}+1)(\bar{\eta}-1)^2(\bar{\eta}^2+1)e^{-k\bar{x}(1+\bar{\eta})}}{(1-3\bar{\eta}^2)^2 + (3\bar{\eta}-\bar{\eta}^3)^2} \left( \cos(k\bar{x}(1+\bar{\eta})) + \sin(k\bar{x}(1+\bar{\eta})) \right) \right). \quad (5.69)$$

Note, to obtain positive VEF to the right and negative VEF to the left of the excitation location the sig function is employed and  $x$  is substituted by  $\bar{x} = |x_0 - x|$ . The factor  $C_{F_\infty}$  is given as:

$$C_{F_\infty} = \frac{F_0^2 \omega}{16Elk^3(1+16\bar{\eta}^2)}. \quad (5.70)$$

If no damping is considered, equations (5.66) and (5.67) and its substitutions reduce to equation (5.24) and (5.25), respectively, by having the same

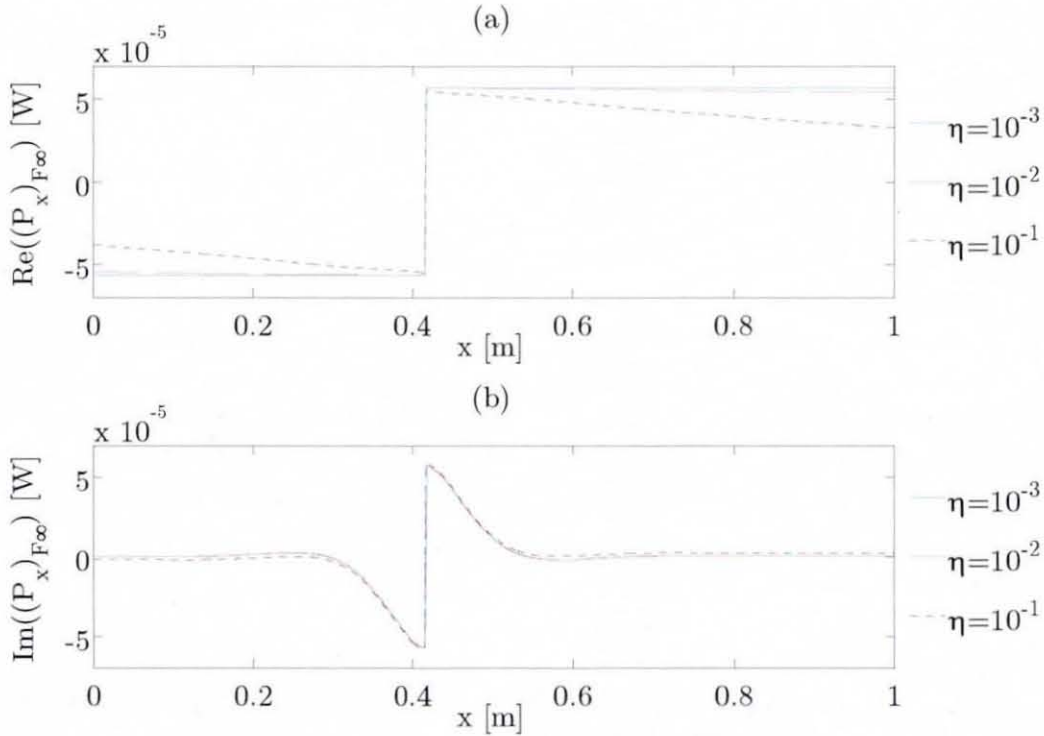


**Figure 5.5** Transmitted infinite wave energy along a force excited simply supported beam at different damping levels: (a) active VEF, (b) reactive VEF.

magnitude, as shown in equation (5.70), without the damping term included. It can be realised that the expression that includes damping is much more complicated. The first bracket term in equation (5.66) is the square of the travelling wave amplitude  $B_+$ , which is here exponentially decayed by  $e^{-2kx\bar{\eta}}$ . Also, the decaying wave products, as shown by the second and third bracket terms in equation (5.68), contribute to energy transmission, something that does not occur in the undamped case. Vice versa the travelling term also contributes reactive energy transmission. Thus, it has been demonstrated that each wave component contributes to active and reactive energy transmission but to a different extent. Figure 5.5 displays the infinite wave VEF of a simply supported beam at different levels of structural damping. Here,  $x$  is denoted as the beam length. The geometrical and material properties of the beam used are shown in Table 5.1.

Young's modulus	$E = 2.07 \cdot 10^{11} \text{ N/m}^2$
mass density	$\rho = 7.85 \cdot 10^3 \text{ kg/m}^3$
beam width	$b = 50 \cdot 10^{-3} \text{ m}$
beam thickness	$t = 10 \cdot 10^{-3} \text{ m}$
beam length	$L = 1 \text{ m}$

**Table 5.1** Simply supported beam properties.

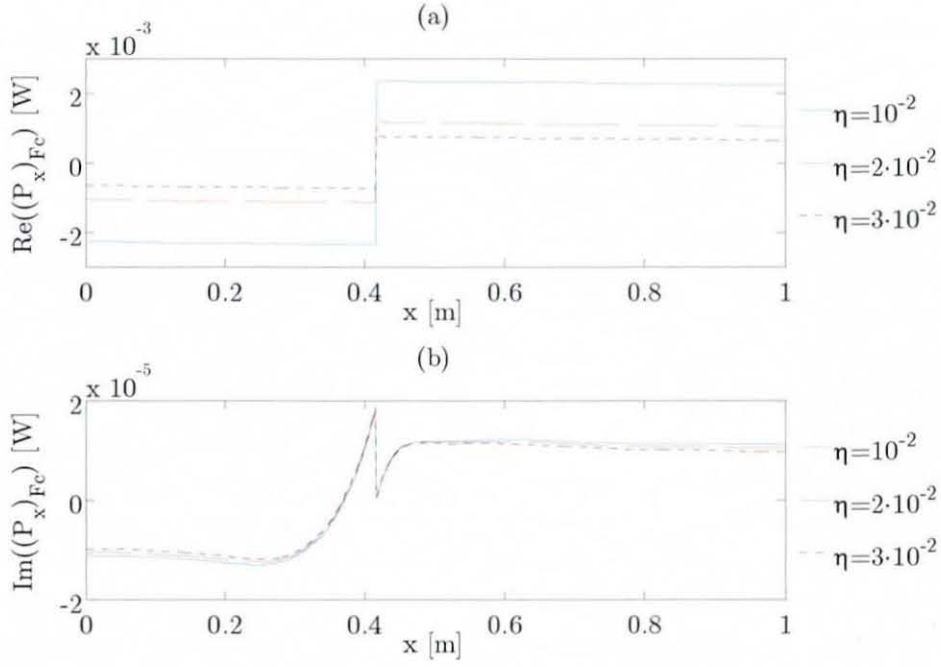
The beam was excited at the 6<sup>th</sup> mode at the undamped natural frequency of  $f_0 = 838.3 \text{ Hz}$  at a location of  $x_0 = 0.4167 \text{ m}$ . This excitation location is exactly at the peak amplitude of the mode shape and, thus, a maximum amount of energy can be injected into the beam. The material used was mild steel. A unity excitation force has been applied, away from the mid-length location of the beam. It can be seen that in a range of  $10^{-3} \leq \eta \leq 10^{-2}$  the damped transmitted vibrational energy is not significantly affected by damping. A horizontal line to either side in Figure 5.5(a) would symbolise undamped VEF. It can be seen from Figure 5.5(a) that effects of infinite waves damping take place only at very high levels of damping ( $\eta > 10^{-1}$ ). The

Figure 5.6 displays the VEF due to the reflection waves for different damping settings. It can be seen that a slight increase in damping strongly reduces the transmitted energy due to the reflection waves. However, the reactive transmitted energy stays nearly unaltered. As expected the VEF due to reflection waves is at most at the boundaries, and zero at the excitation location.

The coupled transmitted energy of a simply supported beam can be found by substituting the complex wave amplitudes, given by equation (5.36) into equation (5.61) by using the amplitude substitutions  $C_1 = A_+$  and  $C_2 = B_+$ . Figure 5.7 displays the energy in a simply supported beam due to the coupling of infinite waves and reflection waves. It can be seen that the energy transmission due to wave coupling is similar in shape to the energy transmission due to the infinite waves.

Finally the total VEF in a simply supported beam is shown in Figure 5.8. It can be seen in Figure 5.8 that the active VEF is zero at both ends due to a zero displacement and the assumption of non-dissipative boundaries. Further, due to an applied off-centre excitation the right-going energy is slightly higher than the left-going energy. The reason of this behaviour is that the longer right-hand beam side dissipates more vibrational energy and, thus, more injected energy is flowing to the right-hand side. This difference increases with decreasing  $x_0$ . It can also be realised from Figure 5.8 that there is a reactive energy flow however, occurs only at the excitation location. Further, the magnitude of reactive VEF is much smaller than the active VEF magnitude.

It can be realised from the above shown VEF figures that the reflection waves and the coupled waves are the dominant wave groups for total active energy transmission, whereas the infinite waves are the dominant wave group for total reactive energy transmission.



**Figure 5.7** Transmitted coupled wave energy along a force excited simply supported beam at different damping levels: (a) active VEF, (b) reactive VEF.

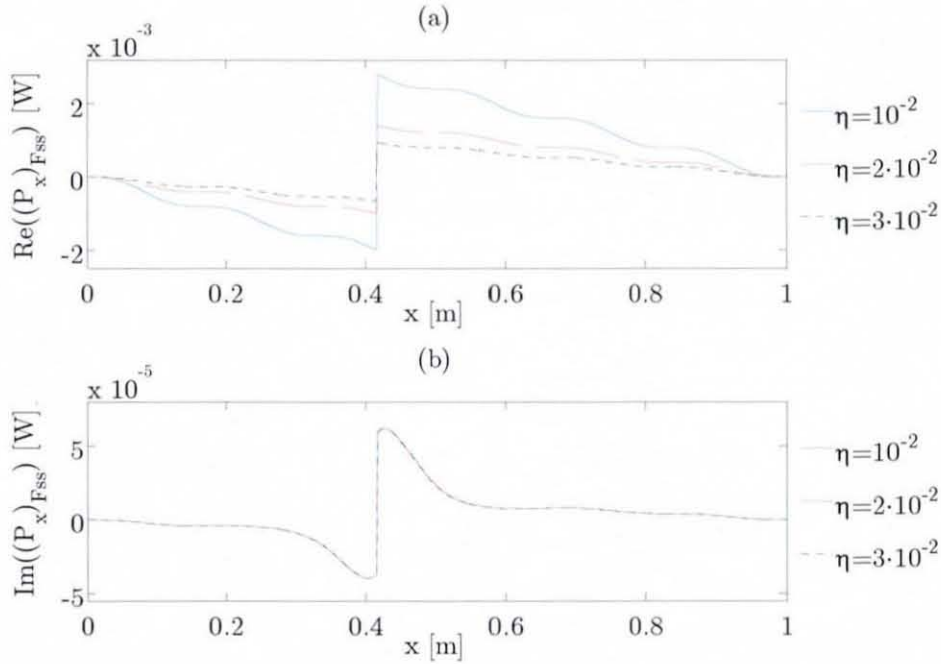


**Figure 5.8** Transmitted total wave energy along a force excited simply supported beam at different damping levels: (a) active VEF, (b) reactive VEF.

#### 5.4.3.4 Moment Excitation

VEF due to a harmonic moment excitation can be determined in the same way, as described above. VEF due to moment excitation within a simply supported beam can be written generally as:

$$(P_x)_{M_{ss}} = (P_x)_{M_{\infty}} + (P_x)_{M_r} + (P_x)_{M_e}. \quad (5.71)$$

Also here, the expressions for the reflection and coupled waves energy transmission are too comprehensive to be presented in this work. VEF equations of the undamped energy transmission are given in Appendix A16. If one substitutes the infinite wave amplitudes  $A_+$  and  $B_+$ , given in equation (5.40), into equation (5.65) and sets  $A_-$  and  $B_-$  equal to zero, one may obtain the active infinite waves VEF in a simply supported moment excited beam as:

$$(\underline{P}_{x_a})_{M_{\infty}} = \frac{\text{sig}(\hat{x})C_{M_{\infty}}}{(1 + \bar{\eta}^2)}(A_{M_{\infty}} + 4\bar{\eta}B_{M_{\infty}}). \quad (5.72)$$

The reactive infinite wave energy flow is given by:

$$(\underline{P}_{x_r})_{M_{\infty}} = j \frac{\text{sig}(\hat{x})C_{M_{\infty}}}{(1 + \bar{\eta}^2)}(4\bar{\eta}A_{M_{\infty}} - B_{M_{\infty}}). \quad (5.73)$$

In equations (5.72) and (5.73) the following abbreviations are used:

$$A_{M_{\infty}} = \left( \frac{\frac{1 - \bar{\eta}^2}{1 + \bar{\eta}^2} e^{-2k\bar{x}\bar{\eta}} + \frac{\bar{\eta} - \bar{\eta}^3}{1 + \bar{\eta}^2} e^{-2k\bar{x}} + \frac{2(\bar{\eta}^2 + 1)(\bar{\eta}^2 - \bar{\eta})e^{-k\bar{x}(1 + \bar{\eta})} \left( \cos(k\bar{x}(1 + \bar{\eta})) - \sin(k\bar{x}(1 + \bar{\eta})) \right)}{(1 - \bar{\eta}^2)^2 + 4\bar{\eta}^2} \right), \quad (5.74)$$



$$B_{M_\infty} = \left( \frac{\frac{2\bar{\eta}}{1+\bar{\eta}^2} e^{-2k\bar{x}\bar{\eta}} + \frac{2\bar{\eta}^2}{1+\bar{\eta}^2} e^{-2k\bar{x}} + \frac{(\bar{\eta}+1)(\bar{\eta}-1)^2(\bar{\eta}^2+1)e^{-k\bar{x}(1+\bar{\eta})}}{(1-\bar{\eta}^2)^2+4\bar{\eta}^2} \left( \cos(k\bar{x}(1+\bar{\eta})) - \sin(k\bar{x}(1+\bar{\eta})) \right) \right). \quad (5.75)$$

The constant  $C_{M_\infty}$  can be found to be:

$$C_{M_\infty} = \frac{M_0^2 \omega}{16EI k (1 + 16\bar{\eta}^2)}. \quad (5.76)$$

Also here,  $\bar{\eta} = 0$  reduces equations (5.72) and (5.73) including their substitutions (5.74) and (5.75) to equation (5.26) and (5.27), respectively. It can be seen from equations (5.72) and (5.73) that both expressions are fairly similar indicating that each wave form contributes to active and reactive energy transport, however, with a different level of strength. The first bracket term in equation (5.72) is the main contributor to active energy transmission in the beam, whereas the remaining terms contribute less energy flow. In terms of reactive energy transmission the last bracket term in equation (5.73) contributes the most.

In Figure 5.9 active and reactive infinite wave energy transmission due to moment excitation is shown. Also here, the same geometrical and material beam properties, as shown in Table 5.1, were used. The harmonic moment, as applied at  $x_0 = 0.45$  m, drives the beam at the 6<sup>th</sup> mode. It can be seen from Figure 5.9 that the beam behaves similar to point force excitation however, there is a sign change in reactive energy flow. It is evident from Figure 5.9 that an equal amount of energy is flowing to the right and to the left of the beam independent upon the amount of damping and the excitation location. This behaviour is also true for infinite wave energy transmission within point force excited beams.

The moment induced energy transport within the beam due to the reflection waves can be found by substituting the wave amplitudes  $A_-$ ,  $B_-$ ,  $C_+$  and  $D_+$  of equation (5.40) into the damped four-wave definition given by

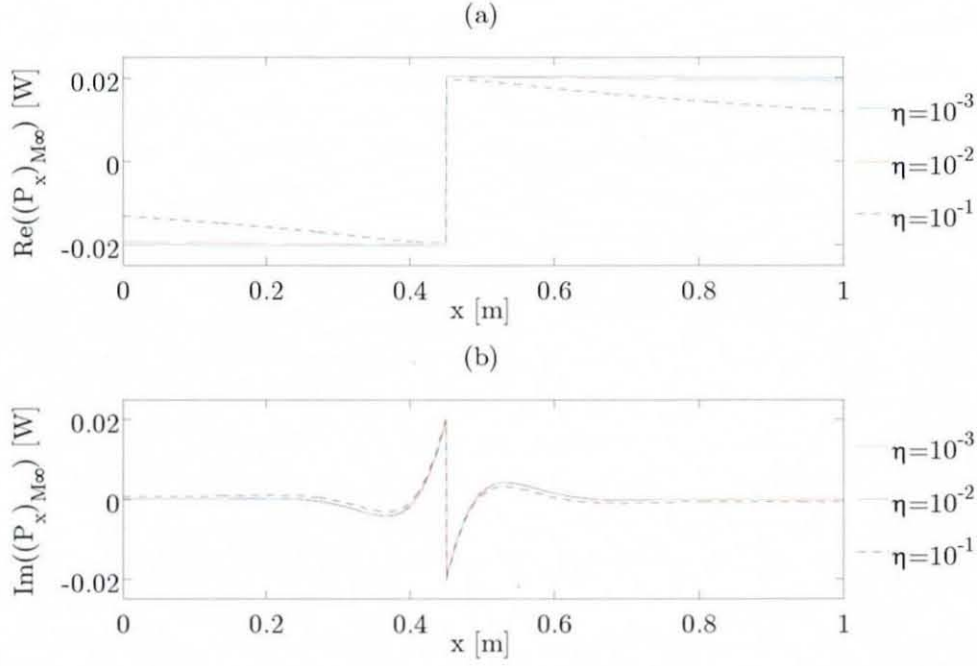


**Figure 5.9** Transmitted infinite wave energy along a moment excited simply supported beam at different damping levels: (a) active VEF, (b) reactive VEF.

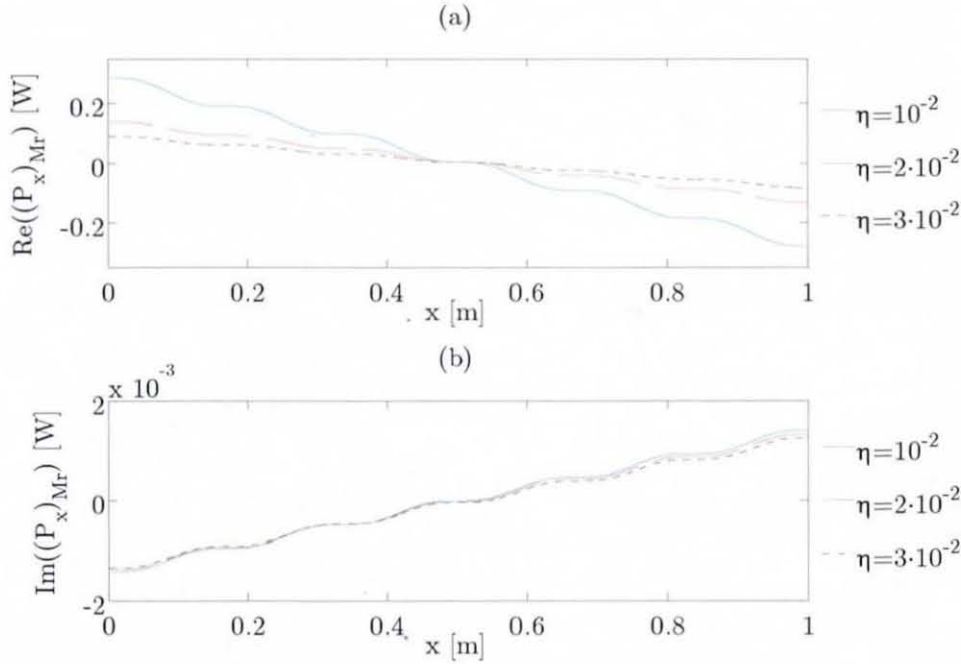


**Figure 5.10** Transmitted reflected wave energy along a moment excited simply supported beam at different damping levels: (a) active VEF, (b) reactive VEF.



equation (5.55). However, here the substitutions  $A_+ = C_+$  and  $B_+ = D_+$  need to be taken into account. The result of this computation is shown in Figure 5.10.

The coupled wave energy flow can be found by substituting the wave amplitudes given in (5.40) into equation (5.61). The infinite wave amplitudes

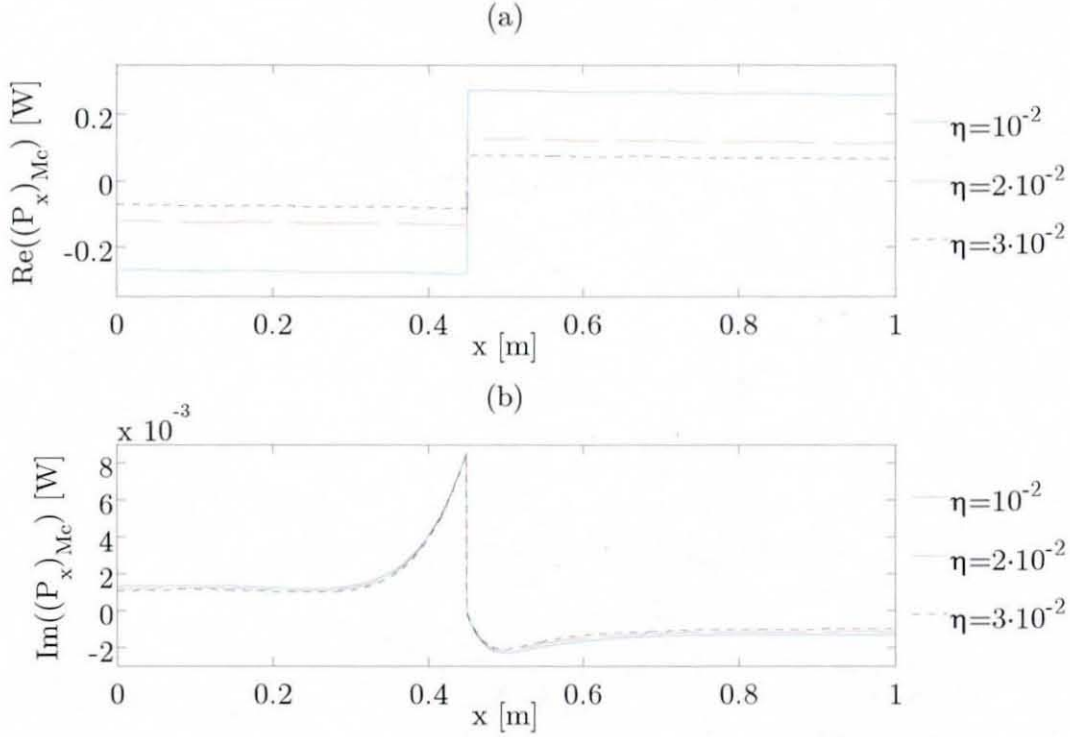


**Figure 5.11** Transmitted coupled wave energy along a beam excited simply supported beam at different damping levels: (a) active VEF, (b) reactive VEF.

are regarded as  $C_1 = \text{sig}(\hat{x})A_+$  and  $C_2 = \text{sig}(\hat{x})B_+$ . This result is shown in Figure 5.11.

Finally, the total vibrational energy transport regarded as the sum of infinite wave energy flow, reflection waves energy flow and coupled waves energy flow is shown in Figure 5.12. It can be seen from Figure 5.12 that the total moment induced transmitted vibrational energy behaviour is similar to the point force excited case. Also here, the active energy flow is much higher than the reactive energy flow and the energy input to the right is higher at excitation location than the energy input to the left.

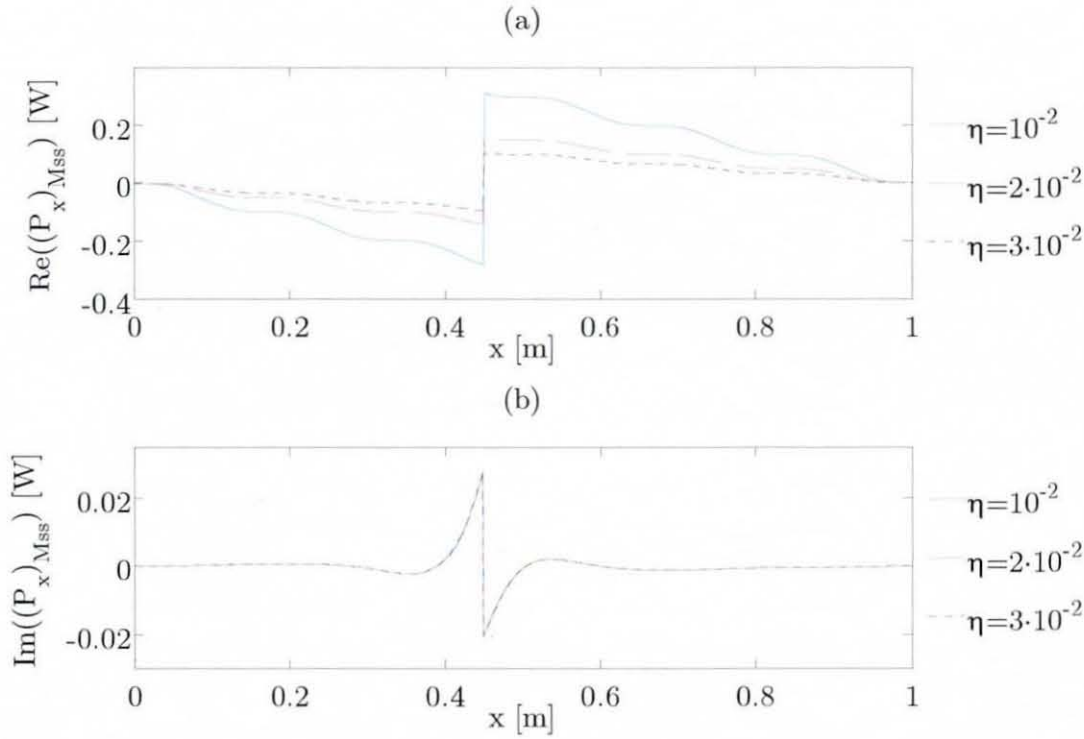


**Figure 5.12** Transmitted total wave energy along a moment excited simply supported beam at different damping levels: (a) active VEF, (b) reactive VEF.

Note, all the above presented VEF quantities are functions of the circular frequency  $\omega$ . However, due to shortage of notation reasons the more correct mathematical notation  $P(\omega)$  is neglected within this work. This procedure is also employed with the VIP quantities, which are also a function of frequency.

## 5.5 Unconstrained Layer Damping

Attenuation of the resonant vibration amplitude of a beam can be achieved by attaching a viscoelastic polymeric damping layer on the surface of the structure. Hence, overall damping will be increased. The initial form of the beam's complex bending stiffness  $EI$  alters due to the attachment of a damping layer. Figure 5.13 displays the cross-section of a beam attached by an unconstrained viscoelastic damping layer. The subscript  $B$  denotes beam

properties and the subscript  $D$  denotes damping layer properties. Due to the layer attachment the neutral axis of bending is set apart by the distance  $z_B$  from the middle line of the beam. This distance can be found by taking moments of the products  $EA$  about the neutral axis [1]. Due to this offset the

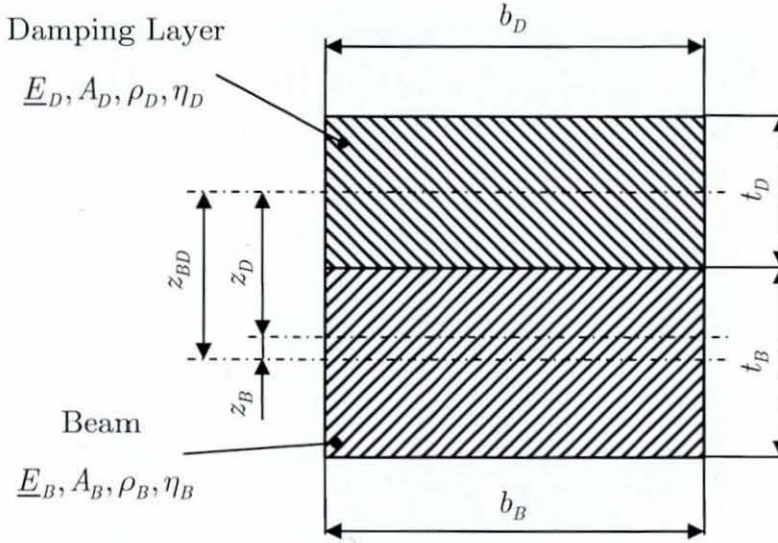


**Figure 5.13.** Unconstrained damping layer attached to a beam.

second moment of area  $I$  of both structures must be determined under consideration of the parallel axis theorem. Because the Young's modulus of beam and layer is complex the offset  $z_B$  is a complex quantity too. Thus, the second moments of area for both structures change into complex quantities. However, for  $(\eta_D - \eta_B)^2 \ll 1$  it can be shown that  $\Re\{I\} \gg \Im\{I\}$  and, hence, the imaginary parts of the complex second moment of area can be ignored. A thorough derivation of the combined complex beam-damping layer stiffness is given in Appendix A17.

From Appendix A17 the total bending stiffness due to the attached damping layer is given as:

$$(\underline{EI})_{BD} = (EI)_{BD} (1 + j\eta_{BD}). \quad (5.77)$$

The real part of the total bending stiffness  $(EI)_{BD}$  is given by:

$$(EI)_{BD} = (E_B I_B + E_D I_D). \quad (5.78)$$

Note, that in equation (5.78) the second moment of area  $I$  incorporates the offset from the neutral axis of bending by employing the parallel axis theorem. The combined linear hysteretic loss factor due to the layer attachment is defined as:

$$\eta_{BD} = \eta_B \left( 1 - \frac{E_D I_D}{E_B I_B + E_D I_D} \right) + \eta_D \left( 1 - \frac{E_B I_B}{E_B I_B + E_D I_D} \right). \quad (5.79)$$

If one neglects the internal damping of the beam ( $\eta_B = 0$ ) because  $\eta_D \gg \eta_B$ , the above given equations can be reduced to the expressions derived in reference [1]. The derivation of vibrational energy in a beam damped by an attached unconstrained damping layer can be carried out, as shown in the previous sections. However, the bending stiffness  $(EI)_{BD}$  needs to be employed instead along with the complex wavenumber that is given by:

$$\underline{k}_{BD} = \left( \frac{(\rho_B A_B + \rho_D A_D) \omega^2}{(EI)_{BD} (1 + j\eta_{BD})} \right)^{\frac{1}{4}}. \quad (5.80)$$

The approximate roots for  $\eta_{BD} < 0.25$  are given by:

$$\underline{k}_{BD} \approx k \left( 1 - j \frac{\eta_{BD}}{4} \right) = k (1 - j\bar{\eta}_{BD}). \quad (5.81)$$

Figure 5.14 displays a logarithmic plot of the combined linear hysteretic loss factor  $\eta_{BD}$  in dependency on the thickness ratio  $t_D/t_B$ . The loss factor of the damping layer was  $\eta_D = 0.12$ . The loss factor of the beam was obtained from an experimental modal analysis undertaken on the undamped beam used for



later experimental work. For the 6<sup>th</sup> mode vibration the modal loss factor was measured to be  $\eta_B = 6.34 \cdot 10^{-3}$ . It can be noted from Figure 5.14 that neglecting the beam's hysteretic loss factor produces differences in the computed combined loss factor up to a thickness ratio of approximately 5. It can also be seen from Figure 5.14 that a substantial change in damping can

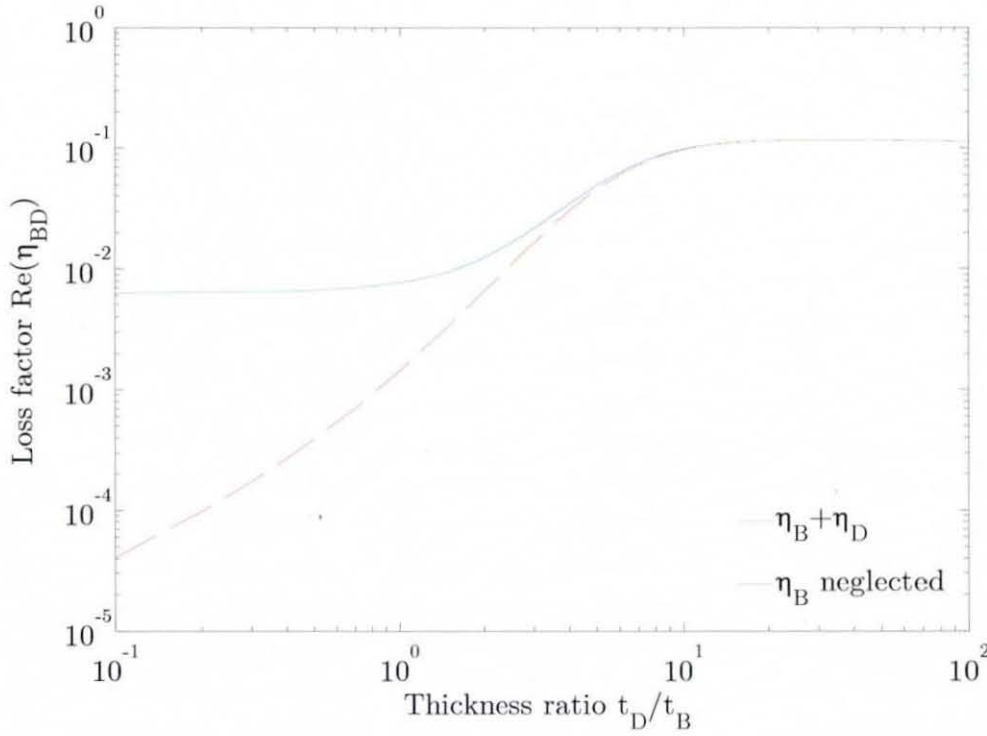


**Figure 5.14.** Combined linear hysteretic loss factor of an unconstrained layer damped beam in dependency on the thickness ratio  $t_D/t_B$ .

only be achieved in the range of  $1.5 \leq t_D/t_B \leq 10$ . At low thickness ratios  $0 \leq t_D/t_B \leq 1$  the combined hysteretic loss factor is approximately equal to the beam's hysteretic loss factor. Thus, when employing an experimental simply supported beam with a thickness of 10 mm at least a 15 mm thick layer should be attached to the beam in order to achieve a noticeable increase in damping. However, in practice this is not realisable. It can be realised that unconstrained layer damping of a beam does not produce a substantial increase in damping unless unrealistically thick damping layers are attached. Figure 5.15 displays the change in flexural or bending stiffness due to a

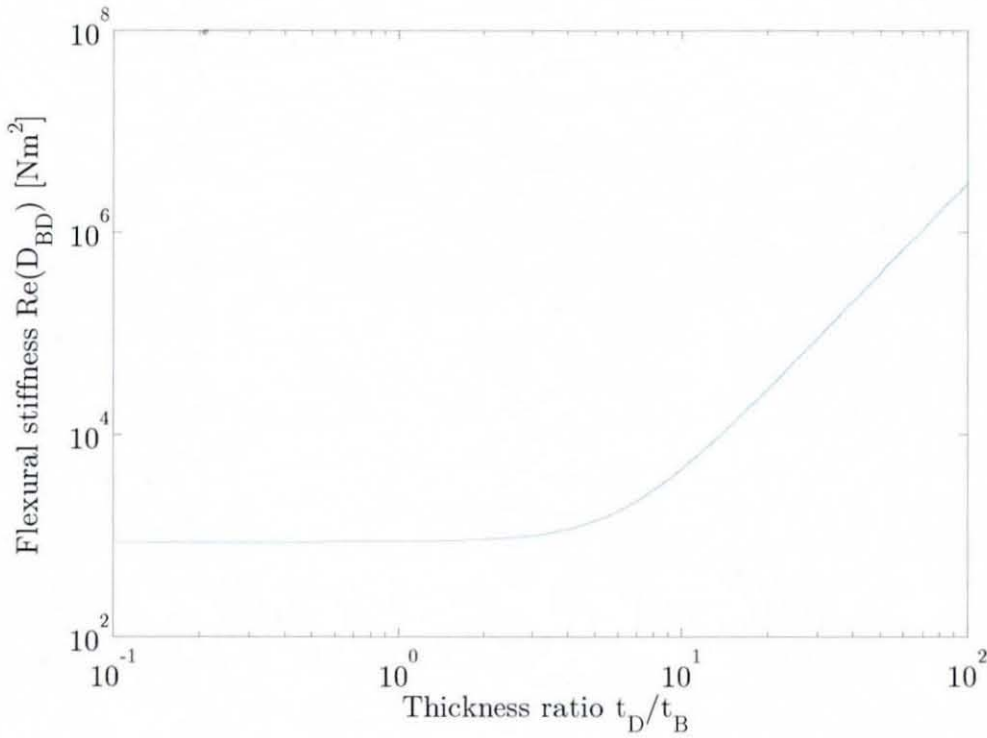


**Figure 5.15.** Combined flexural stiffness of an unconstrained layer damped beam in dependency on the thickness ratio  $t_D/t_B$ .

mineral filled viscoelastic polymer layer attachment. It is evident from Figure 5.15 that the beam's flexural stiffness is approximately constant up to a thickness ratio of  $t_D/t_B \approx 1$ . At higher thickness ratios the combined flexural stiffness of the beam must be taken into account.

## 5.6 Discussion

Displacement solutions to the forced beam's partial differential equation of motion have been presented for infinite and finite, simply supported beams by using a wave-based approach. Point force and moment excitations were considered. A four-wave-based VEF equation has been derived that can be used as a general tool to derive VEF in transversally vibrating beams. Within the VEF analysis (VEFA) the real part of any energy transmission equation is the most interesting part, since it physically represents the energy flow

within the structure. It is evident from equation (5.2) that if four wave components are present within the beam the net VEF is proportional to the difference of the squared magnitude of the travelling waves,  $|B_+|^2 - |B_-|^2$ . It has also been shown that the two nearfield components may contribute to energy transmission. However, due to the exponential decaying term  $2e^{-kL}$  this is only influential if the beam is acoustically short. Further, the nearfield wave amplitudes need to have an imaginary part. The reactive energy transmission based on 4 waves in a beam is a much more complex expression, as shown in equation (5.3). Due to multiplication of the shear force and the bending moment with their respective velocity components a multiple combination of cosine and sine functions occurred. However, each sinusoidal expression is multiplied by an exponential decaying function and, thus, only at the excitation location reactive nearfield energy transmission becomes influential assuming the wave amplitudes are complex.

The four-wave VEF equation has been derived in order to gain a simple understanding of the nature of active and reactive VEF in beams. The respective wave groups responsible for energy transfer can be identified easily, something that is not very conclusive when interpreting special solutions of VEF in infinite and finite beams.

The four-wave VEF equation was then applied to a simple semi-infinite beam displacement to define active and reactive VEF from prior determined complex wave amplitudes for point force excitation and moment excitation. It has been demonstrated that at a single excitation frequency active VEF in an infinite beam is constantly distributed along the beam length depending on the magnitude of the travelling wave component and the excitation frequency.

VIP expressions for both excitation forms have shown that the transmitted vibrational energy is half the magnitude of the input power. Thus, in infinite beams the usual assumption that half of the energy supply is flowing to the right and half of the energy supply is flowing to the left can be verified.

If one substitutes the flexural wavenumber  $k = (\rho A \omega^2 / (EI))^{1/4}$  into the denominator of equation (5.20) and (5.23), respectively, one can find that for



force excitation the input power is proportional to  $1/\sqrt{\omega}$  and for moment excitation the input power is proportional to  $\sqrt{\omega}$ . Thus, moment excited structures can transmit much more energy in higher frequency regions than force excited structures. The cross over point is at  $\omega = 1$ .

The derivation of VEF in a simply supported beam is more complex, as demonstrated in section 5.4. Within this work the boundaries are assumed to be adiabatic. Energy supplied by an external load cannot flow out of the beam structure and, thus, the vibrational energy net flow within the beam is zero. However, real finite structures dissipate some energy within the structure, denoted here as internal losses. In order to regard internal beam losses a hysteretic damping model was adopted. This model uses a complex, elastic modulus. Since the elastic modulus is incorporated in the flexural wavenumber definition, a complex wavenumber occurs in the calculation. It was demonstrated by equations (A11.7) and (A12.4) that the point mobility of an undamped simply supported beam is a purely imaginary quantity. Thus, undamped finite structures cannot absorb vibrational energy from the outside once they enter the second cycle because the real part of the point mobility is zero. Employing a complex, flexural wavenumber the point mobility of the hysteretically damped simply supported beam now becomes complex and, thus, energy can be supplied continuously to the simply supported beam. The amount of energy supply and, thus, internal net energy flow is controlled by the hysteretic loss factor.

The simply supported beam displacement was modelled using a superposition of infinite beam waves and reflection waves arising at both the simply supported boundaries due to infinite wave impingement. The undamped and forced simply supported beam displacement approaches infinite amplitude at the resonant frequencies. However, the use of a loss factor allowed for a finite forced simply supported beam displacement at resonant excitation frequencies. The complex, flexural wavenumber complicates the VEF expression enormously. Usually the displacement is formed by pure travelling waves and pure evanescent waves. However, due to the use of a complex wavenumber the evanescent waves now contain a travelling component and the travelling waves contain an evanescent



component controlled by the magnitude of the loss factor. Thus, the evanescent wave components also contribute to energy transmission to some extent.

It has been shown that VEF in a simply supported beam is composed of energy flow due to the infinite waves, the reflection waves and a coupling between both wave groups. This relation can be applied to each finite beam structure. Because hysteretic damping was considered the four-wave VEF equation had to be reformulated in order to account for damping. General VEF expressions of infinite wave energy flow, reflected wave energy flow and coupled waves energy flow were presented. The two uncoupled energy transmission mechanism can be calculated from the presented damped four-wave VEF equation. However, the coupled energy transmission needed to be derived separately, using a specially derived coupled VEF equation.

Due to its long expressions analytical VEF equations of a hysteretically damped, simply supported beam under point force and moment excitation was not given. However, numerical solutions were presented by numerically evaluating equations (5.64) and (5.71). It can be seen from Figures 5.5 and 5.9 that the active infinite wave VEF is spatially decreasing only at high damping, i.e.  $\eta > 10^{-1}$ . At lower damping values, i.e.  $\eta > 10^{-2}$  the energy flow is almost constant and, thus, can be neglected. Reactive VEF is only present at the excitation location. However, it has approximately the same peak value as the active VEF.

The active reflected VEF is more sensitive towards damping, as shown in Figures 5.6 and 5.10, where a significant change in VEF occurs for a small change in the range of loss factor values. The reactive energy flow has less damping sensitivity and is much smaller than the active reflected VEF component.

The active total transmitted coupled wave energy, as shown in Figures 5.7 and 5.11, is also damping sensitive. Interestingly, the reactive energy component is not approaching zero towards the beam ends.

Finally, the VEF of a simply supported beam excited by a point force (Figure 5.8) and a moment (Figure 5.12) reveals that the active energy flow is decreasing with increasing distance away from excitation location. At the

beam ends the flow is zero due to the adiabatic boundaries. In contrast to the infinite beam, the energy flow from the excitation location is not half the input energy if off-centre excitation is applied. In fact more energy is flowing to the right of the beam and less energy is flowing to the left. Of course the absolute active VEF amplitude at the excitation location is equal to the energy injected into the beam. Further, it was shown that for total active VEF the coupled and reflection waves are the dominant wave groups, whereas for total reactive VEF the infinite waves are the dominant wave group.

## 6 NUMERICAL ANALYSIS OF VIBRATIONAL ENERGY IN BEAMS

### 6.1 Introduction

This chapter investigates the numerical application of the vibrational energy flow determination using electronic speckle pattern interferometry (VEFESPI) method introduced in chapter 4 for infinite and simply supported beams. The results obtained herein for synthetic ESPI displacement data are then compared with the exact analytical vibrational energy flow (VEF) solutions presented in chapter 5. The numerical derivation of spatial partial derivatives is carried out in this work by the application of the  $k$ -space derivation (KSD) method. Thus, the strengths and weaknesses of this method are investigated thoroughly when applied to harmonic beam vibration.

To unveil the effect of filtering the VEFESPI method is subjected to artificially generated beam displacement signals contaminated by normally distributed noise. Thus, an error analysis investigating the effect of altering different filter parameters is undertaken. The added noise has different magnitude levels in order to investigate the behaviour of the VEFESPI method in low, medium, and high noise environments.

To find optimum filter parameters when analysing the recorded ESPI displacement data later in chapter 9, the artificial generated beam displacement signals are contaminated by measured optical noise that is extracted from the respective electronic speckle pattern interferometry (ESPI) data. This procedure is carried out for both beam structures. Thus,



filter parameters are determined, which can then be applied when analysing the acquired ESPI data.

Additional to the problem of signal contamination through noise the issue of non-periodic data is investigated too. Hence, three techniques are introduced in order to diminish the effect of spectral leakage when determining VEF in structures from non-periodic sets of data. This procedure becomes also helpful when analysing odd-numbered mode shaped finite beam vibration.

Although vibrational energy transmission in a beam is of one-dimensional nature the theoretical beam displacement here is numerically evaluated two-dimensionally, since the ESPI system provides two-dimensional information. In the past VEF predictions from ESPI acquired data has been computed by extracting a single line from the ESPI displacement data [63, 64]. As an extension to this VEF computation of beams is carried out herein using a two-dimensional displacement input, i.e. including the whole beam width of data. However, since the VEF results do not vary over beam width and for better visibility the results are presented in a one-dimensional way.

## **6.2 Numerical Infinite Beam Analysis**

This section deals with the numerical computation of VEF in an infinite beam by employing the VEFESPI method introduced in chapter 4. Here, the KSD method is employed in order to determine spatial derivatives from tabulated data. Obtained numerical results are then compared with the exact analytical solutions presented in section 5.3.

### **6.2.1 Non-Periodic Data Input**

In practice acquired data are often recorded with a non-integer number of periods. Further, the occurrence of nearfields due to evanescent waves makes periodic data often non-periodic due to its exponentially decaying properties with distance. Since the KSD method employs the spatial Fourier transform

(SFT), a periodic set of data is essential otherwise leakage will falsify the computation of the spatial derivatives and, hence, the accuracy of the computed VEF [51]. One could manipulate one-dimensional beam data by truncating the recorded data to an integer number of waves. This procedure however, often excludes the nearfield component and, thus, evanescent waves from the VEF analysis. Further, when analysing odd-numbered mode shapes periodisation of data is desired. Within this work three techniques are introduced and investigated that deal with the non-periodic data problem. Two of them utilise different mirroring and reversing techniques of the original data in order to obtain a periodic data sequence. The third technique, proposed by the author, simply manipulates the VEF result.

Kochersberger et al. proposed a periodisation technique, which mirrors reverses and shears (translational and rotational signal manipulation) the original non-periodic data [115, 116]. This method is addressed in this work as mirror-reverse-shear (MRS) periodisation technique. Its procedure can be followed by Figure 6.1. From there it can be seen that an image of the original signal, as shown in Figure 6.1(a), is mirrored, reversed, and connected to the original sequence, as illustrated in 6.1(b). To ensure a periodic sequence the combined signal is finally sheared simply by subtracting the shear line (dotted line in 6.1(b)) from the combined signal. Thus, the signal is now zero at both ends and, hence, periodic in space.

A second periodisation technique employed in this research was proposed by Pascal et al. [51]. However, since this method is not described clearly in reference [51], the author has altered its procedure to his own understanding. This method will be addressed in this work as mirror-processing (MP) technique. The procedure is illustrated in Figure 6.2. From Figure 6.2 it can be realised that the original set of data, shown in Figure 6.1(a), is mirrored about the  $x$ -axis and truncated by half. The half sized two mirror signals are then connected to both ends of the original signal, as shown in Figure 6.2(b). It can be noticed from Figure 6.2(b) that the connection between the original signal and its mirrored counterparts is not perfect as there appears a gap at both ends. This gap is closed herein by altering the left-hand side and right-hand side mirrored image with a cosine

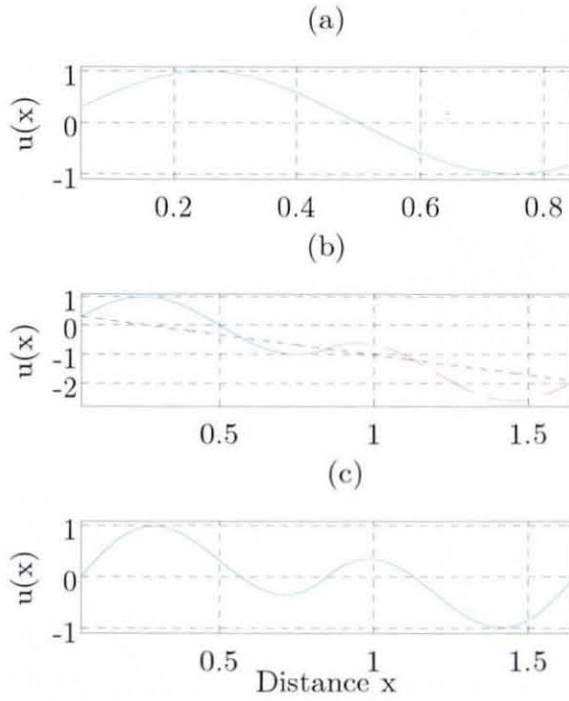


**Figure 6.1** Periodisation of a non-periodic sinusoidal signal using the MRS periodisation technique: (a) original signal, (b) original signal + mirrored and reversed signal, (c) sheared original + mirrored and reversed signal.

link function. The left-hand side link function  $S_L(n)_{left}$  for  $n = 1, 2, 3, \dots, N/2$  is given by:

$$S_L(n)_{left} = S_{mirr}(n)_{left} + \left( S(1) - S_{mirr}\left(\frac{N}{2}\right)_{left} \right) \frac{1}{2} \left( 1 - \cos\left(\frac{n\pi}{\frac{N}{2} - 1}\right) \right). \quad (6.1)$$

Herein,  $S_{mirr}(n)_{left}$  is the left-hand side mirror image of the original signal  $S$ . Similarly, the right-hand side is given as:

$$S_L(n)_{right} = S_{mirr}(n)_{right} + \left( S(N) - S_{mirr}(1)_{right} \right) \frac{1}{2} \left( 1 - \cos\left(\frac{n\pi}{\frac{N}{2} - 1}\right) \right)_{flip}. \quad (6.2)$$



Here,  $S_L(n)_{right}$  is the modified right-hand side link function,  $S_{mirr}(n)_{right}$  is the right-hand side mirror image of the original signal  $S$ ,  $N$  is the number of data points of the original signal and  $n$  is an integer number. Note, the left bracket that contains the cosine function needs to be permuted. The new continuous periodic signal is shown in Figure 6.2(c). It can be seen that due

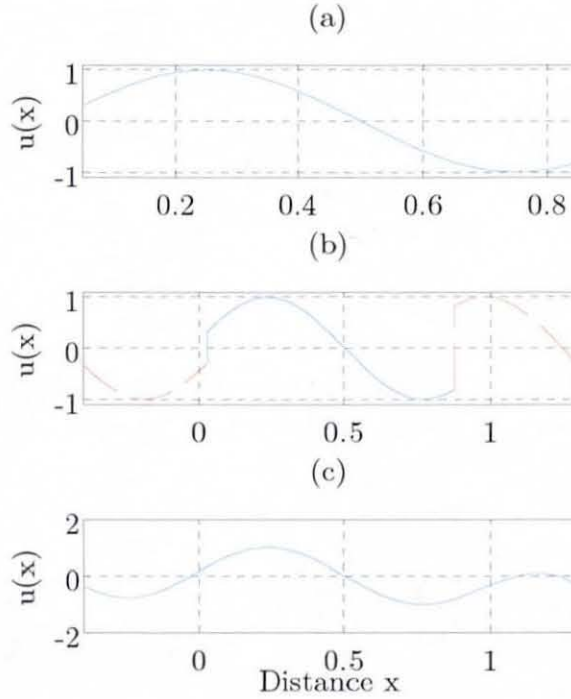


**Figure 6.2** Periodisation of a non-periodic sinusoidal signal using the MP periodisation technique: (a) original signal, (b) truncated mirrored signals + original signal, (c) continuously linked mirrored signals + original signal.

to the mirrored signal manipulation the initial gap at both ends of the original sequence is closed. The reason a cosine function is employed is that for higher spatial derivatives continuity of the link function derivatives must be ensured. Due to the mirroring process two redundant points needs to be deleted and, thus, both techniques increase the number of data points from  $N$  to  $2(N-1)$ .

### 6.2.2 Vibrational Energy Flow Excluding Noise

As mentioned before the VEF of a beam is calculated in this work using two-dimensional displacement input. All routines were implemented in the software environment MATLAB®. From there one-dimensional VEF solutions are extracted simply by taking out data from the middle line of the beam width. In the following sections VEF computation within an infinite beam is investigated numerically. It has been shown in section 5.3 that the evanescent waves do not contribute vibrational energy flow when an infinite beam is excited in the middle. However, to investigate the influence of the nearfield in numerical VEF analysis the nearfield is included here. The material properties of the beam are shown in Table 6.1. These are the same properties as the experimental “infinite” beam introduced in chapter 7.

Young's modulus	$E = 2.07 \cdot 10^{11} \text{ N/m}^2$
mass density	$\rho = 7.85 \cdot 10^3 \text{ kg/m}^3$
beam width	$b = 60 \cdot 10^{-3} \text{ m}$
beam thickness	$t = 10 \cdot 10^{-3} \text{ m}$

**Table 6.1** “Infinite” beam properties.

The complex, infinite beam displacement to the right is generated by numerical evaluation of equation (5.11) using a number of data points in the  $x$  direction of  $N_x = 150$  and in the  $y$  direction of  $N_y = 50$ . A unity excitation force of  $F_0 = 1 \text{ N}$  and an excitation frequency of  $f = 838.3 \text{ Hz}$  ( $k = 6\pi \text{ rad/m}$ ) was applied. Figure 6.3 displays the complex displacement of a point force excited infinite beam. Here,  $x$  is the beam length,  $u(x, y)$  is the two-dimensional transverse beam displacement and  $u(x)$  is the one-dimensional transverse beam displacement, extracted from the middle line of  $u(x, y)$ .

It can be noticed from Figure 6.3 that the real part of the displacement  $u(x)$  becomes non-periodic, with respect to the wavelength  $\lambda = 1/3 \text{ m}$ , due to the presence of evanescent waves arising at the excitation



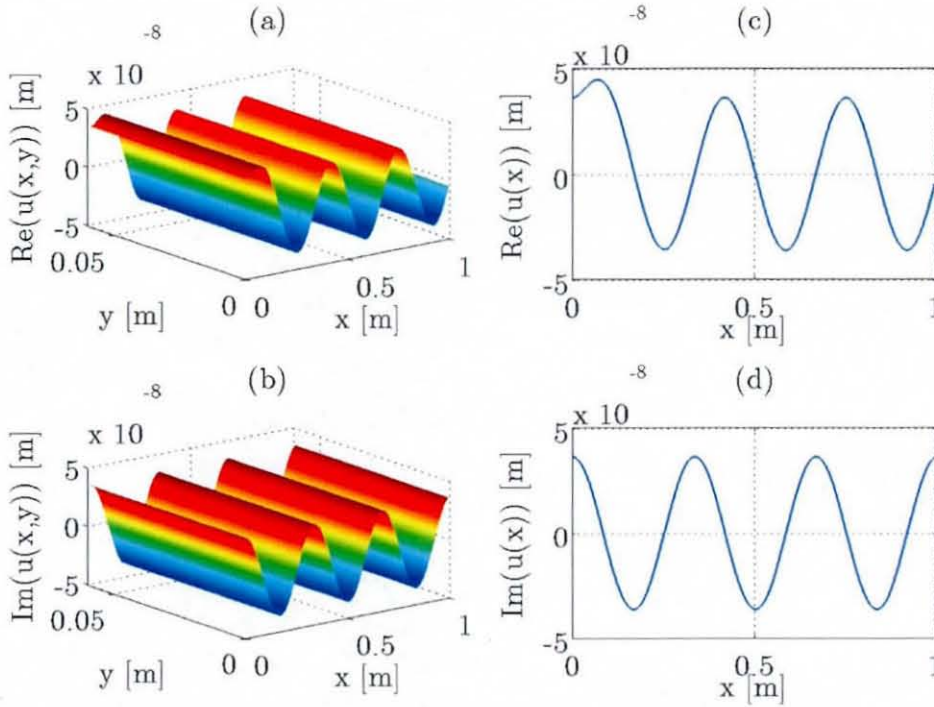


**Figure 6.3** Complex infinite beam displacement to the right: (a) 2D real part, (b) 2D imaginary part, (c) 1D real part, (d) 1D imaginary part.

location  $x_0 = 0$ . Since this nearfield wave is purely real (see equation (5.11)), the imaginary part does not include a nearfield component and, thus, an integer number of waves are present in the imaginary part.

If one would determine VEF straight from this displacement, the VEF would oscillate heavily around the true value, as shown in Figure 6.6. The reason for this behaviour is due to the presence of a nearfield component and subsequent consequences during the wavenumber multiplication process in order to obtain spatial derivatives. Figure 6.4 displays the real and imaginary part of the wavenumber spectrum of the infinite beam displacement to the right of the excitation location. If one substitutes equation (5.11) into equation (4.5) by setting  $k_y = 0$  and changes the factor in front of equation (4.5) to  $1/2\pi$ , one may obtain the Fourier spectrum of  $u(x)_{x>0}$  as:

$$F\{u(x)_{x>0}\} = \frac{F_0}{8\pi EI k_x^3} \left( \frac{k_{x_0}}{k_{x_0}^2 + k_x^2} + j \left( 2\pi \delta(k_x + k_{x_0}) - \frac{k_x}{k_{x_0}^2 + k_x^2} \right) \right). \quad (6.3)$$

Here,  $k_{x_0}$  is the excitation wavenumber,  $k_x$  is the wavenumber,  $\delta$  is the Dirac delta function. Note, to obtain the true amplitude of the spatial nearfield and farfield equation (6.3) needs to be multiplied by  $2\pi$ . It can be seen from

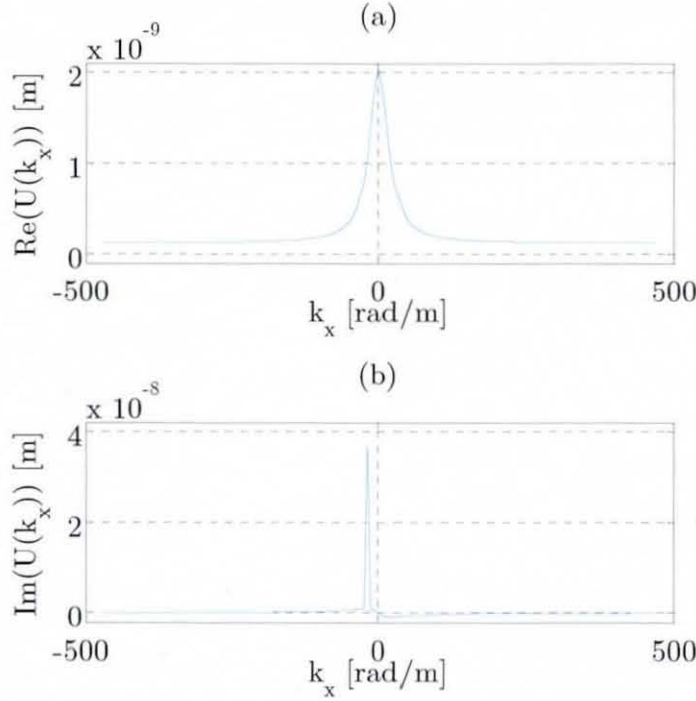


**Figure 6.4** Wavenumber spectrum of the infinite beam displacement shown in Figure 6.3: (a) real part, (b) imaginary part.

equation (6.3) and Figure 6.4 that the real part appears solely due to the evanescent wave, which is approximately  $20 \times$  less than the travelling wave amplitude. The imaginary part of the wavenumber spectrum is composed of travelling and evanescent wave spectra. Although the evanescent spectrum decreases with increasing wavenumber, as shown by the denominator in equation (6.3), a small fraction still remains in the spectrum for the real and imaginary part. During the spectral derivation process, this fraction is amplified by high wavenumber values especially for higher order derivatives.

Figure 6.5 displays the 3<sup>rd</sup> spectral derivative of  $U(k_x)$  for  $x > 0$  when using the VEFESPI method and also its exact value computed from analytical data. It can be realised that due to the multiplication process of

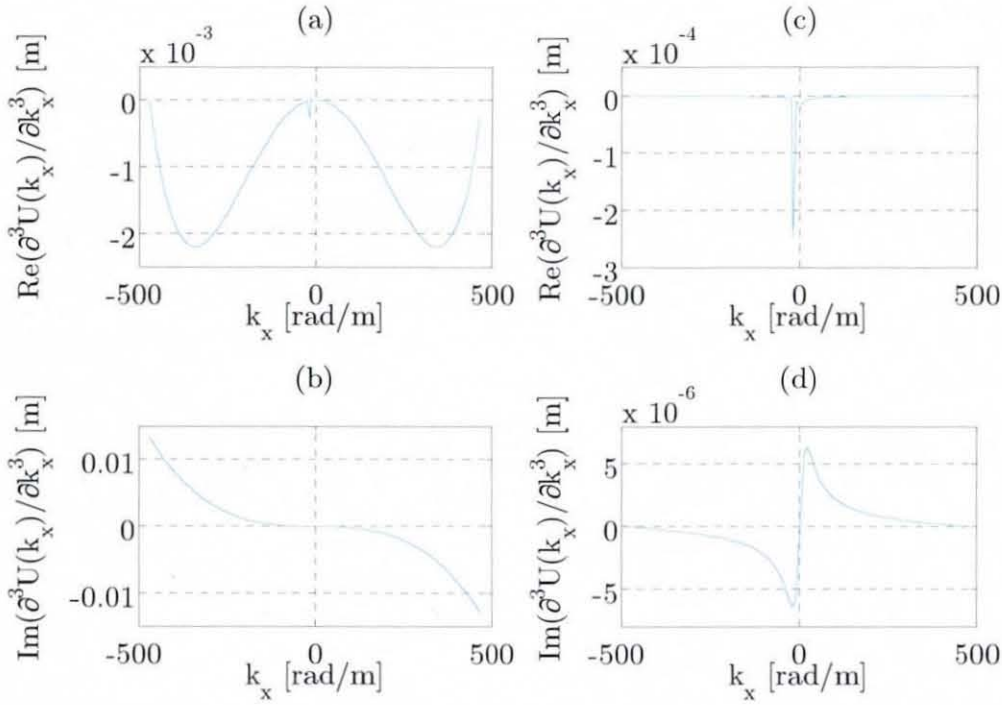


**Figure 6.5** KSD determined and exact solution of the 3<sup>rd</sup> spectral derivative of the displacement shown in Figure 6.3: (a) real part using KSD, (b) imaginary part using KSD, (c) real part exact solution, (d) imaginary part exact solution.

$K_x^3$  the initial curve shape of the spectral nearfield part has altered drastically and the amplitude, especially at high wavenumber components is amplified strongly. The spectral travelling component, shown as a spike in Figure 6.5(a), is almost hidden due to the spectral nearfield amplification. It can be realised that the same problem appears if a non-integer number of waves is included in the signal. Then spectral leakage occurs and the leakage amplification results in undesired spectral amplitudes especially at high wavenumbers. Thus, the KSD method has difficulties to produce accurate spatial derivatives and therewith sufficiently accurate spatial derivative information to calculate VEF if the displacement signal is irregular. This signal irregularity can be due to a presence of a strong nearfield or a non-integer wavelength inclusion or both. Of course one could argue that due to the nearfield component the displacement signal is non-periodic at least in the real part. But as shown later, the same phenomenon appears in a



vibrating simply supported beam excited at an even-numbered mode frequency where an integer number of waves are included in the signal.

Figure 6.6 displays the resulting VEF when the complex displacement, as shown in Figure 6.3, is analysed. As mentioned beforehand the active and reactive energy flow is oscillating about the true VEF value, which was calculated from equation (5.24) and (5.25), respectively. It can be realised

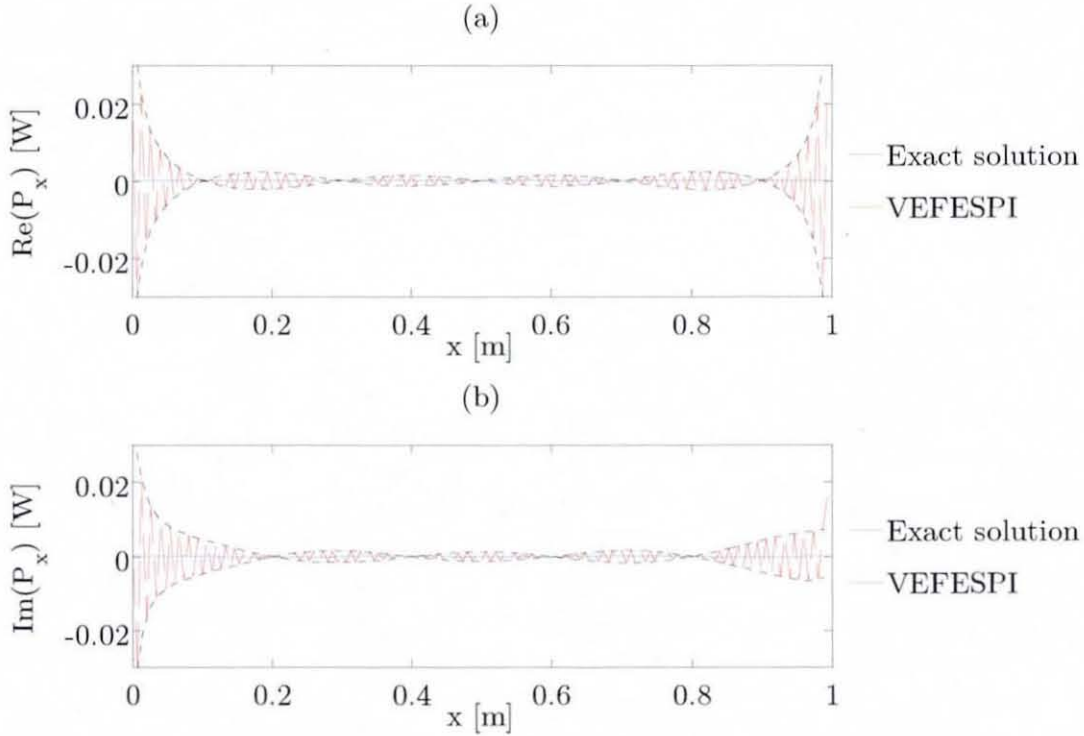


**Figure 6.6** Exact and VEFESPI determined energy flow of the infinite beam displacement shown in Figure 6.3: (a) active energy flow, (b) reactive energy flow.

from Figure 6.6 that two wrapping curves can be constructed, which enclose the oscillating energy flow (see black dotted curves). One curve includes all the odd-numbered VEF samples and the other includes all the even-numbered VEF samples. The sample size of both curves is half the sample size of the original VEF curve.

If one interpolates both curves in order to obtain the original sample size of the determined VEF curve and calculates the mean of both curves, an approximate energy flow,  $(P_x)_{app}$  can be found simply as:

$$(P_x)_{app} = \frac{1}{2} \left( (\tilde{P}_x)_{odd} + (\tilde{P}_x)_{even} \right). \quad (6.4)$$

Herein,  $(\tilde{P}_x)_{odd}$  is the interpolated odd-numbered curve wrap and  $(\tilde{P}_x)_{even}$  is the interpolated even-numbered curve wrap. This method is addressed in this work as the curve wrap (CW) method and can be used as a simple approximation of oscillating energy flux due to signal irregularities. To demonstrate the effect of diminishing VEF oscillations due to signal

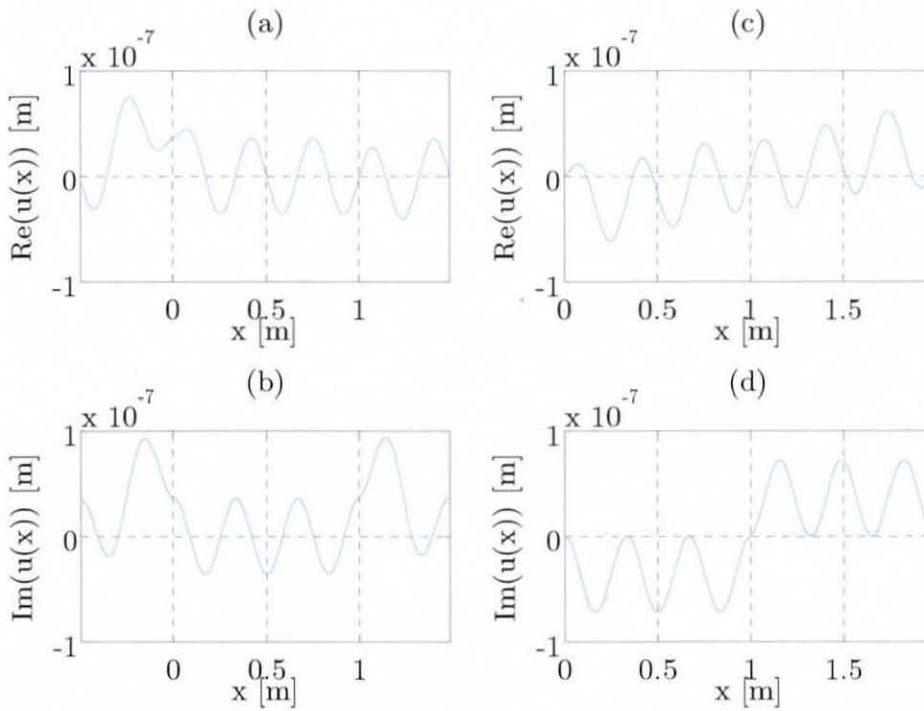


**Figure 6.7** Periodised infinite beam displacement shown in Figure 6.3: (a) real part MP method, (b) imaginary part MP method, (c) real part MRS method, (d) imaginary part MRS method.

irregularities all three techniques were incorporated into VEF analysis and the same numerical VEF procedure, as shown above, was carried out. Figure 6.7 displays the use of the MP and the MRS techniques to periodise spatially sampled displacement data. It can be noticed that the real part is now periodic in space.

Inserting the above shown two periodised complex displacements into the VEFESPI model and approximating the VEF from the non-periodised complex displacement by the CW technique one may find the VEF results, as shown in Figure 6.8. From there it can be realised that there is still some oscillation of VEF from the numerical computed data at both ends of the signal. However, in a range of  $0.1 \text{ m} < x < 0.9 \text{ m}$  all three techniques achieve

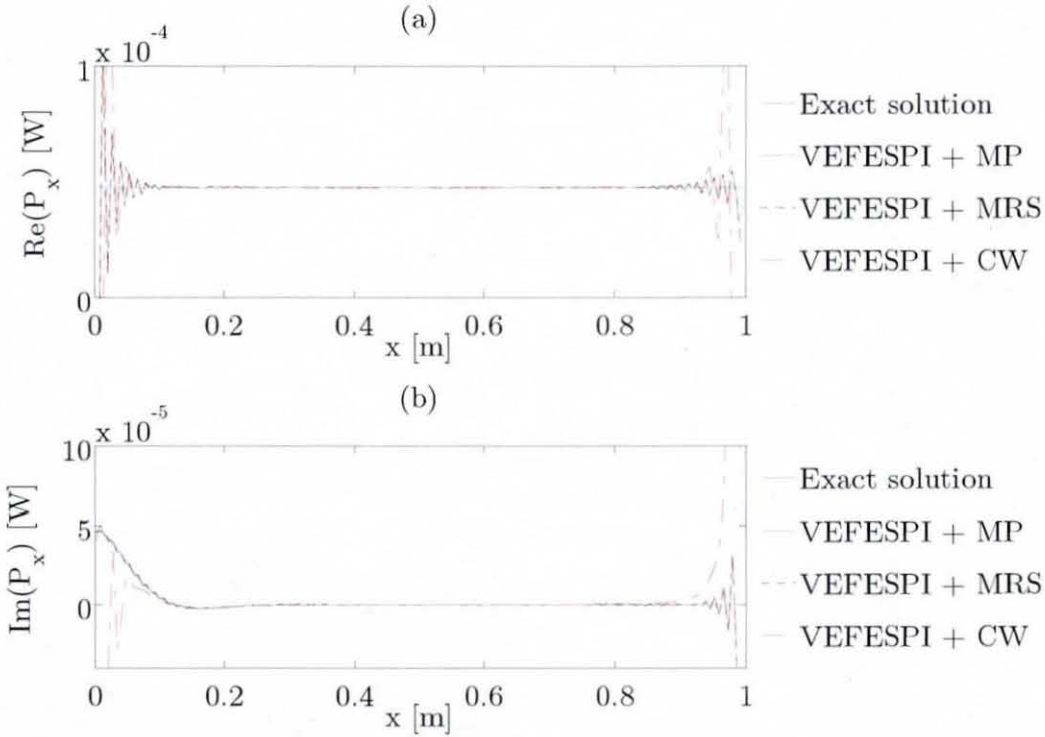


**Figure 6.8** Exact and VEFESPI determined energy flow of the infinite beam displacement shown in Figures 6.3 and 6.7: (a) active energy flow, (b) reactive energy flow.

acceptably good active VEF results. Unfortunately, an acceptably good reactive VEF result is only met by the VEFESPI + MP and VEFESPI + MRS procedure, as it can be seen in Figure 6.8. There, in the nearfield region, near the origin  $x = 0$ , the CW approximation method fails.

Due to the periodisation of the infinite beam displacement a relatively sharp connection of the original signal and mirrored parts is produced. It can be realised by zooming into Figure 6.8 that due to that sharp connections of the original displacement data the VEFESPI + MP and VEFESPI + MRS

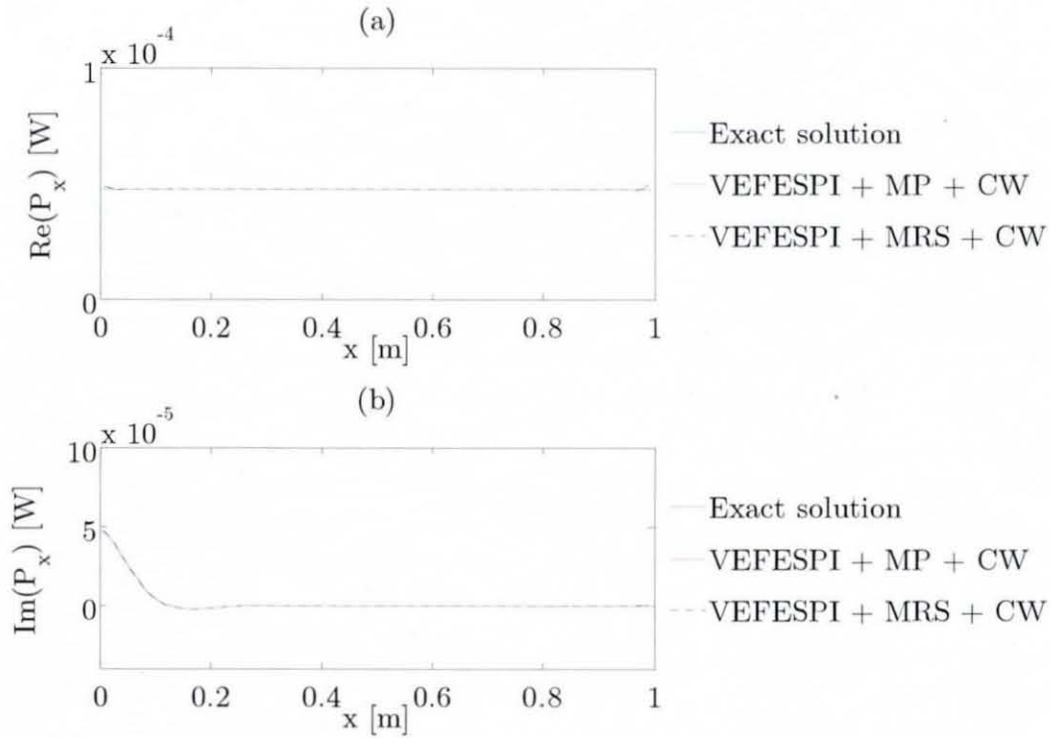


**Figure 6.9** Exact and VEFESPI determined energy flow of the infinite beam displacement shown in Figure 6.7: (a) active energy flow, (b) reactive energy flow.

technique still produces some energy flow oscillations. This effect can be diminished by applying the CW approximation to both techniques. The result of this procedure is shown in Figure 6.9. Despite some minor deviation at both ends of the signal it can be shown that the initial oscillations are diminished substantially and, thus, a sufficiently accurate active and reactive VEF of an infinite beam can be determined numerically using the VEFESPI method.

Figure 6.10 displays the relative error made, determined from VEFESPI computed VEF and exact VEF. Here, the VEFESPI method in combination with the MP + CW and MRS + CW technique, respectively, was considered only. It can be realised that both periodisation techniques in combination with the CW method produced good active and reactive VEF results. The reason for showing a different axis length of the relative imaginary error is that the imaginary values are approaching zero outside the nearfield region and, thus, zero division produces meaningless results. The



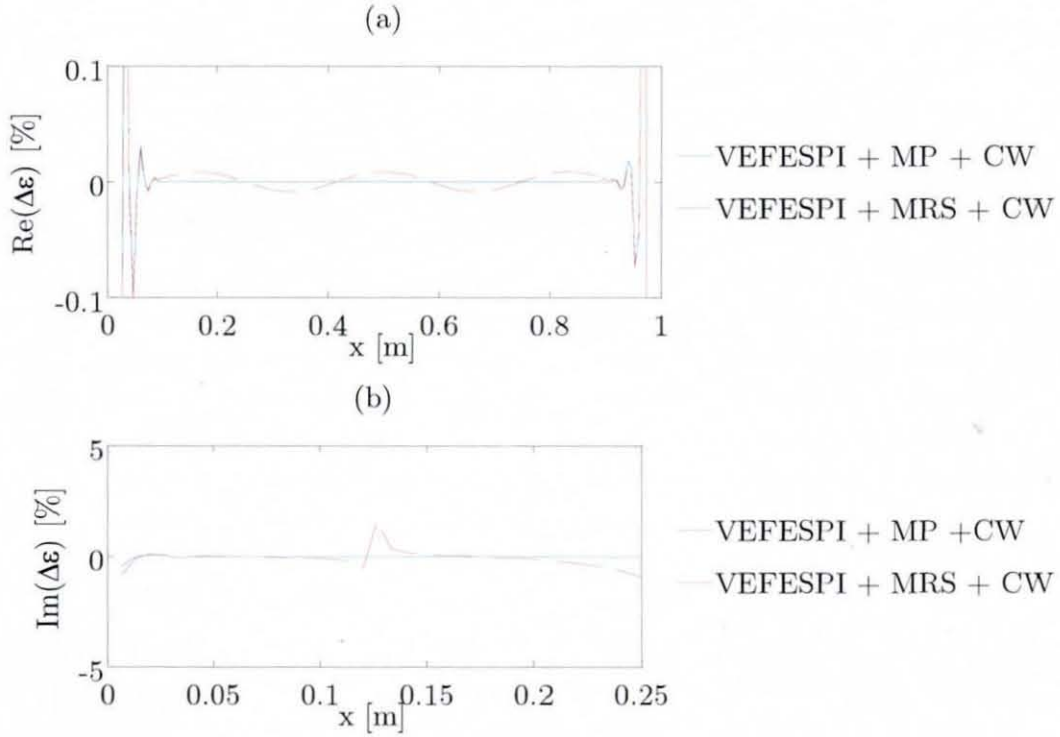


**Figure 6.10** Relative error of VEFESPI determined energy flow and exact solution of the infinite beam displacement shown in Figure 6.7: (a) relative active flow error, (b) relative reactive flow error.

magnitude of the energy flow oscillations, as shown in Figure 6.8, is depending upon the number of data points and also, the number of waves included in the signal. The spectral resolution  $\Delta k_x$  is given by:

$$\Delta k_x = \frac{2\pi}{\Delta x N_x} = \frac{2\pi}{L_x}. \quad (6.5)$$

Herein,  $\Delta x$  is the spatial resolution, i.e. the distance between the spatially sampled points and  $N_x$  is the number of spatially sampled points within the signal length  $L_x$ . To obtain the wavenumber vector  $K_x$  equation (6.5) is multiplied by:

$$K_x = \Delta k_x \{N\}_x. \quad (6.6)$$



Here,  $\{N\}_x = (0, 1, 2, \dots, N_x - 1)$ . To reduce the VEF oscillations the magnitude of  $K_x$  needs to be reduced. Hence, less amplification takes place during the spectral derivation process of the KSD method. From equation (6.6) it can be realised that there are mainly two ways in reducing the magnitude of  $K_x$ . Either the number of data points  $N_x$  is reduced or the spectral resolution  $\Delta k_x$  is decreased. By employing the first option one can reduce  $N_x$  by keeping  $L_x$  constant. The second option can be employed by increasing  $L_x$  and keeping  $N_x$  constant. However, both procedures result in an increase in the spatial sampling resolution  $\Delta x$  and, thus, both principles cannot be extended to infinity, since at least two sample points per flexural wavelength need to be included in the signal.

With the prior shown relations it can be realised that a much better result of the CW method may be shown if a lesser number of data points were used in the example given above. However, recorded ESPI data are usually spatially dense. Reducing the number of data points, by employing a re-sampling and interpolation technique, results in an undesired data manipulation. Thus, it is more desirable to find appropriate ways that deal with the actual recorded number of data points. Hence, the author has employed the MP and MRS technique that despite reducing the spectral resolution  $\Delta k_x$  by half the same wavenumber vector  $K_x$  is used, since the number of data points is almost doubled. However, since the spectral resolution  $\Delta k_x$  is reduced by half, the spectral nearfield component is multiplied only by half the wavenumber magnitude and therefore, the nearfield amplification, as shown in Figure 6.5, is reduced by half. Thus, one may conclude that the MP and MRS technique yield to better results, especially in reactive VEF computation by producing a more useful wavenumber spectrum.

Another desired spectrum alteration can be achieved due to an increase of the number of waves that are included in a signal simply by exciting the structure at higher excitation frequencies. Thus, the ratio of evanescent waves and travelling waves will change and the influence of the relatively dominant nearfield in the real part of the spectrum will be

diminished during the multiplication process, since the travelling part is multiplied by a higher wavenumber magnitude. Therefore, high frequency displacement signals are more useful for VEFESPI analysis using the KSD technique.

Finally it is worth to mention that the whole strength of the MP and MRS method lies in the analysis of non-periodic data where the CW technique on its own fails due to leakage in the wavenumber spectrum and, thus, wrong signal amplitude detection.

### **6.2.3 Vibrational Energy Flow Including Noise**

The previous section investigated the performance of the VEFESPI method when signal irregularities, such as nearfield waves, are present. There is another major factor, which needs to be considered when measuring VEF from recorded ESPI data. Thus, this section investigates the effect of noise on the VEFESPI method.

As introduced in section 4.3.2 two two-dimensional filter types are used in this work, an ideal 2D filter and an oval 2D Butterworth filter, to remove noise in the wavenumber domain that will be amplified otherwise. This noise amplification process introduces erroneous signal components into the analysis and, thus, falsifies the VEF determination. The oval 2D Butterworth filter is a low pass filter. This filter type can be adjusted to select an appropriate cut-off wavenumber as well as an appropriate filter slope. The ideal 2D filter, which is also employed in the wavenumber domain, works as a comparison algorithm, which sets wavenumber components equal to zero if they satisfy a certain condition.

Despite removing unwanted noise components in the wavenumber domain, the question arises how much noise needs to be filtered out in order to achieve an optimum filtering process. Thus, the two different filter types are investigated here thoroughly in relation to the error made when determining VEF from filtered data.

### 6.2.3.1 Ideal 2D Spectral Filtering

In this section the effect of filtering when using the 2D ideal filter to compute VEF is investigated. The same displacement, as shown in section 6.2.2, is used. However, the signal is contaminated by a fairly large amount of normally distributed noise. The amount of noise is defined by the signal-to-noise ratio (SNR) introduced in Appendix A18. If the SNR is approaching infinity the signal is not contaminated by noise at all. If the SNR is approaching zero noise is included only. Thus, the less the SNR the more noise contaminates the signal. Figure 6.11 displays the complex, two and one-dimensional beam displacement contaminated by a fairly large amount of noise. As usual the middle line is extracted for further analysis. It can be realised from Figure 6.11 that the noise will have high wavenumber components in the wavenumber domain that are amplified due to the

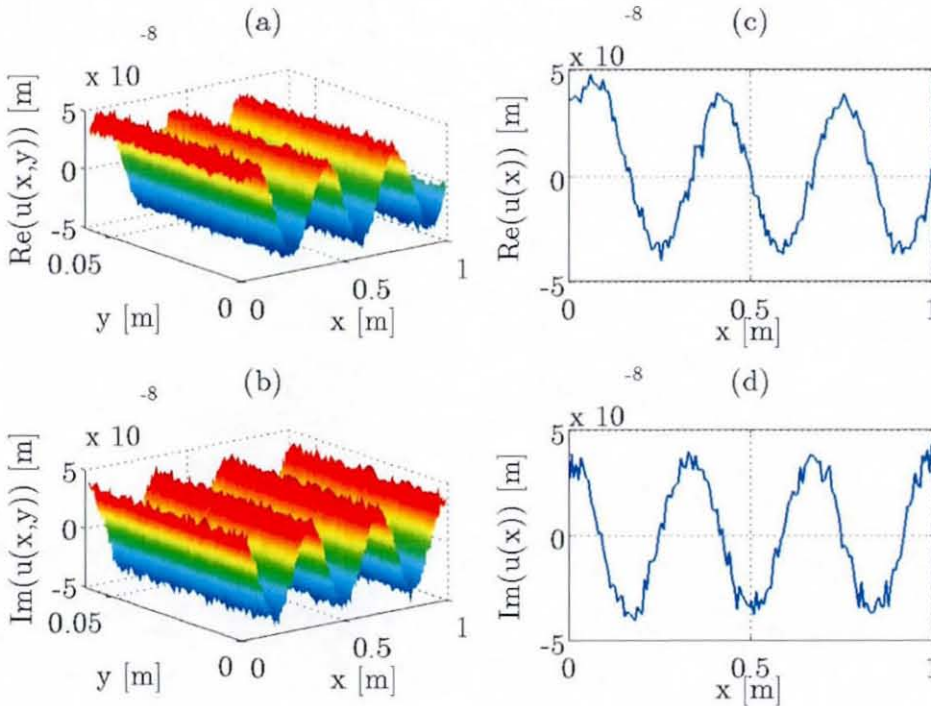


**Figure 6.11** Infinite complex beam displacement to the right of the excitation location contaminated by normally distributed noise with SNR = 108.2: (a) 2D real part, (b) 2D imaginary part, (c) 1D real part, (d) 1D imaginary part.



wavenumber multiplication process when calculating spectral derivatives. The transformed signal components can be seen in Figure 6.12. The reason why the imaginary noise components are almost invisible is that they are small in

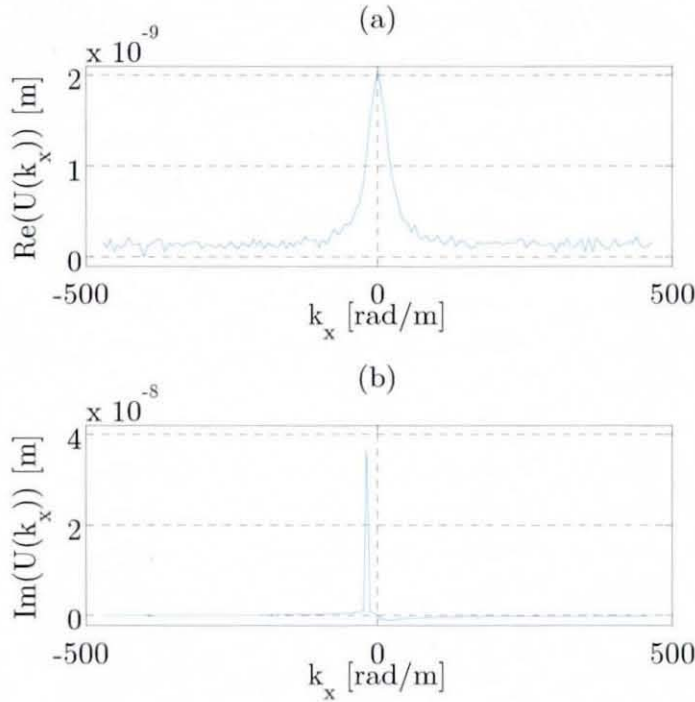


**Figure 6.12** Wavenumber spectrum of the infinite beam displacement shown in Figure 6.11: (a) real part, (b) imaginary part.

comparison to the travelling wave amplitude. To avoid this unwanted noise amplification, the wavenumber data need to be filtered.

The ideal filtering process applied in this work is a filtering algorithm applicable within the wavenumber domain. The noise contaminated discrete spectral matrix is searched element wise for components that are smaller or equal to a given number. If they satisfy this simple condition, the spectral matrix component is simply set to zero. Thus, this filtering process acts like a multiplication of the spectral matrix with zeros and ones at specifically defined locations. The given number is a certain amount of the travelling wave amplitude given in percent. Thus, the question arises at what percentage of the travelling wave amplitude is the error made due to the

filtering process at minimum? To answer this question a relative mean squared error (MSE) function is used in this work as [38]:

$$\Pi = \frac{1}{N_x} \sum_{i=1}^{N_x} \left( 1 - \frac{(P_{x_i})_{VEFESPI}}{(P_{x_i})_{exact}} \right)^2. \quad (6.7)$$

Here,  $(P_{x_i})_{VEFESPI}$  is the VEFESPI computed VEF and  $(P_{x_i})_{exact}$  is the exact VEF calculated by equation (5.24) and (5.25), respectively. Equation (6.7) is applied to different percentages of the magnitude of the travelling wave amplitude,  $|B_+|$ . This result is shown in Figure 6.13 for the original data and the MP and MRS periodised data. Note, the imaginary part of the relative

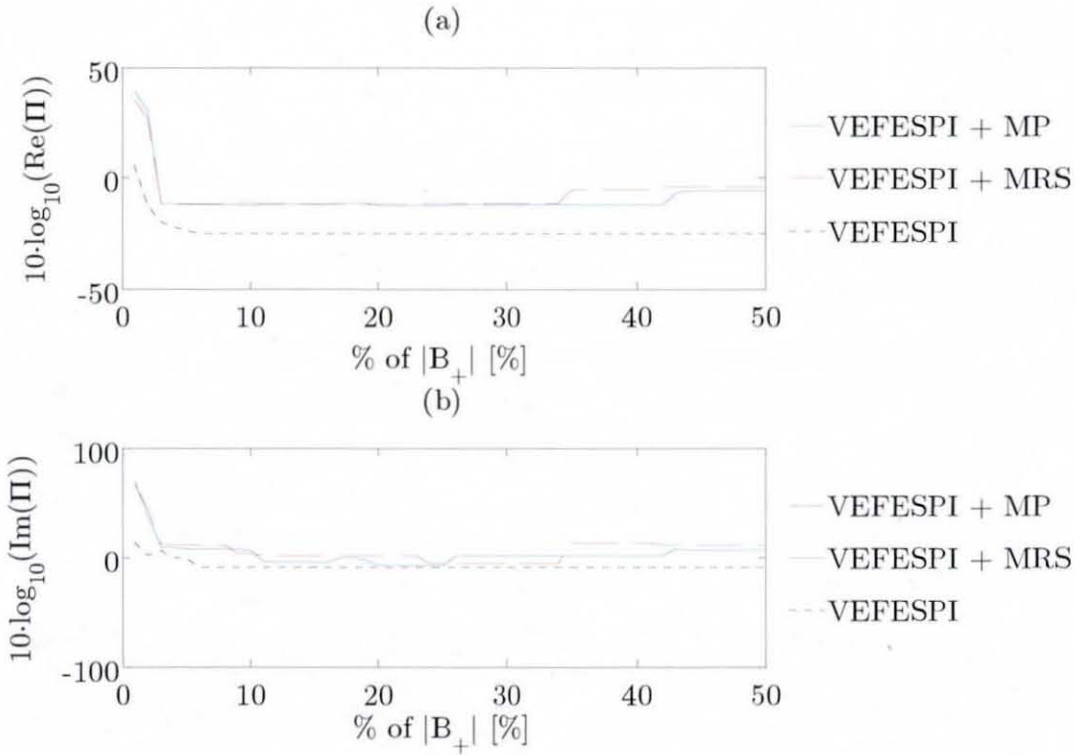


**Figure 6.13** Relative MSE of the infinite beam displacement shown in Figure 6.11 using ideal filtering: (a) real MSE, (b) imaginary MSE.

MSE is calculated only for locations within the nearfield region, since the imaginary part of VEF outside the nearfield approaches zero and subsequent

zero division will yield to meaningless results. It can be noticed from Figure 6.13 that at a certain % of  $|B_+|$ , i.e.  $|B_+| > 3\%$ , no improvement in MSE reduction can be made. This lies in the nature of the filtering algorithm because all noise components now satisfy the condition, which states that wavenumber components that are not bigger than a certain amount of the travelling wave amplitude are set to zero. It can also be seen from Figure 6.13 that the MP and MRS treated displacements yield to larger MSE than from analysing the original non-periodised data.

Figure 6.14 displays the VEF where every spectral matrix component below the optimum percentage of  $|B_+|$  is filtered out. Thus, the real and imaginary optimum cut-off points were taken out from the result shown in Figure 6.13 to compute the optimum filtered active and reactive VEF. It can be seen from Figure 6.14 that the ideal filtered active VEF computed from the non-periodised beam displacement is a straight line that deviates about

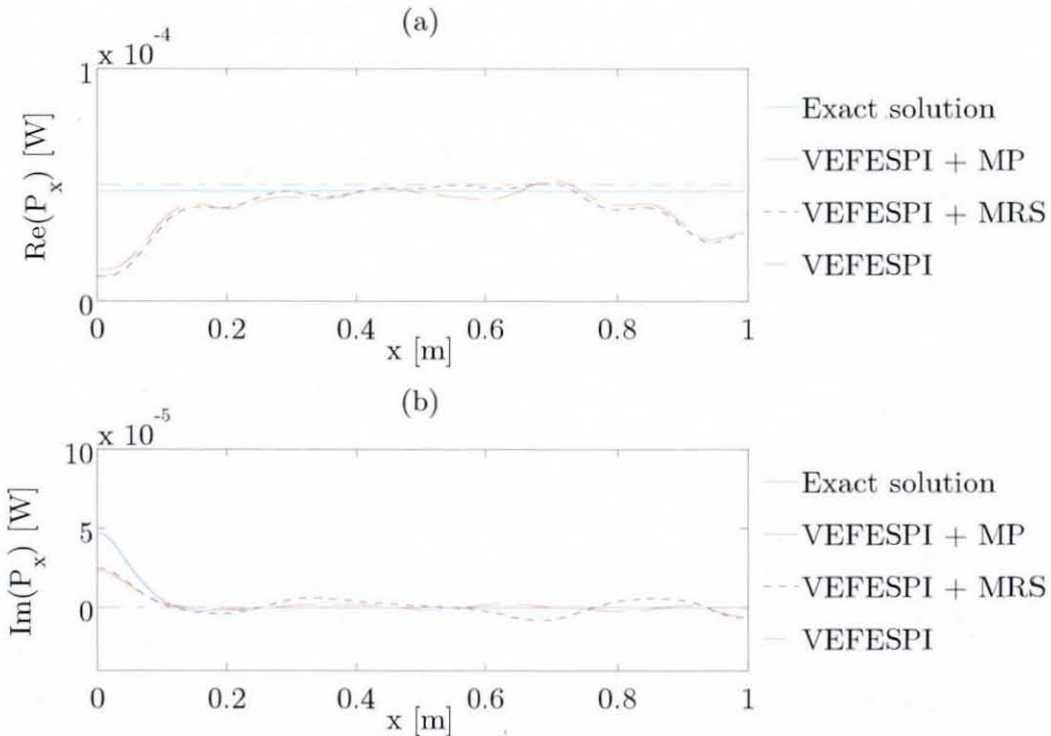


**Figure 6.14** Exact and ideal filtered VEF of the infinite beam displacement shown in Figure 6.11 using ideal filtering at optimum cut-off points: (a) active energy flow, (b) reactive energy flow.



5% from the true active VEF value. The reason of the 5% deviation is that the amplitude in the wavenumber spectrum is not met exactly due to superposition of farfield and nearfield spectra. It can be recognised from Figure 6.4 and to some extent in Figure 6.12 that the imaginary nearfield and farfield wavenumber spectra are superimposed. This means that at the spatial excitation frequency of  $k_0 = 6\pi$  the true travelling wave amplitude and the nearfield wave amplitude are superimposed. Due to the superposition, the travelling wave amplitude erroneously increases and, thus, a higher VEF is computed. Further, the active ideal filtered VEF from the original non-periodised displacement data delivers the best result. It fails however, when detecting reactive VEF due to filtering out some of the nearfield information in the wavenumber spectrum. Thus, this filter method is best applied if one determines VEF in the farfield only due to its sharp removal of noise in the wavenumber domain.

Finally, a sensitivity study is presented, which investigates the effect of noise on the ideal filtering technique when computing VEF from an infinite noise contaminated beam displacement. Here, four different levels of noise contamination, stretching from a high noise environment (SNR = 13.7) to a low noise environment (SNR = 6116.3) were analysed. The results of this study are shown in Table 6.2 however, due to brevity reasons only for the original non-periodised complex beam displacement. Note, the travelling wave amplitude is denoted as  $B_+$ .

$F_0 = 1 \text{ N}; f_0 = 838.3 \text{ Hz}; \text{ non-periodised data}$				
SNR	13.7	108.9	1003	6116.3
Optimum (% of $ B_+ _{\text{real}}$ [%])	6	6	6	6
MSE, $\Re(10 \cdot \log_{10}(II))$	-24.35	-25.05	-25.22	-25.36
Optimum (% of $ B_+ _{\text{imag}}$ [%])	6	6	6	6
MSE, $\Im(10 \cdot \log_{10}(II))$	-8.75	-8.75	-8.75	-8.75

**Table 6.2** Noise sensitivity study of non-periodised beam displacement data filtered with an ideal 2D filter.

It can be noticed from Table 6.2 that the relative MSE  $\Pi$  made during the filtering process is largely independent on the magnitude of the SNR and, thus, the ideal filtering method is insensitive towards different magnitudes of noise when computing VEF from infinite beam displacements.

### 6.2.3.2 Oval 2D Spectral Butterworth Filtering

The oval 2D Butterworth filter is a more commonly used filter. It allows for adjustments of the cut-off wavenumber  $k_c$  and of the filter slope in the wavenumber domain. The cut-off wavenumber  $k_c$  is the point in the wavenumber domain where the filter starts to remove spectral components. Also here, the question arises at which cut-off wavenumber can an optimum filtering process be achieved? Furthermore, what filter slope is the best in order to keep the error in VEF determination process as low as possible? Figure 6.15 displays the relative MSE made when filtering the beam displacement by an oval 2D Butterworth filter. Here, the wavenumber ratio

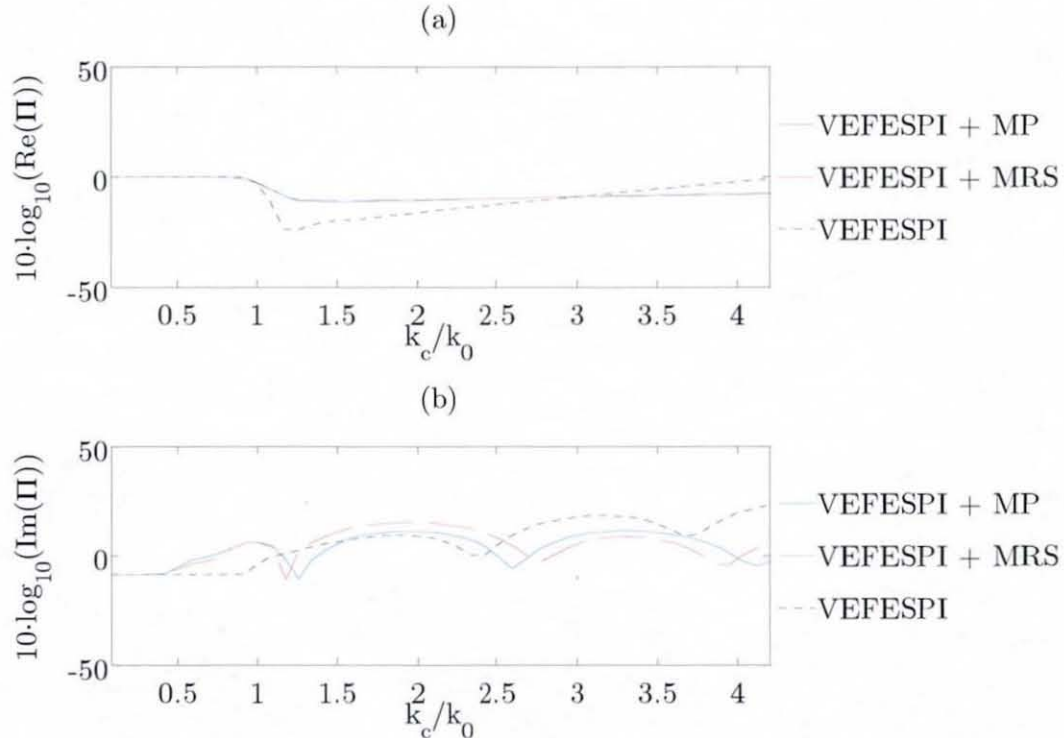


**Figure 6.15** Relative MSE of the infinite beam displacement shown in Figure 6.11 using a Butterworth filter: (a) real MSE, (b) imaginary MSE.



$k_e/k_0$  is shown on the  $x$ -axis, where  $k_0$  is the wavenumber of the excited beam. It can be seen from Figure 6.15 that the filtered original non-periodised displacement will produce the best active VEF result. The order of the filter slope employed was 5. The SNR was 108.6. The optimum cut-off wavenumber of the non-periodised data for active VEF computation is around  $1.25 \cdot k_0$  and for the periodised data around  $1.51 \cdot k_0$ . It can also be realised that the periodisation techniques produced a better reactive VEF result where the cut-off wavenumbers were located in the lower regions  $(0.83, 1.17, 1.25) \cdot k_0$ .

Figure 6.16 displays the active and reactive energy flow filtered at the optimum cut-off wavenumbers for each method in order to obtain the optimum active and reactive energy flow. From Figure 6.16 it can be noticed that the filtered active VEF of the MP and MRS treated displacements varies around the true VEF value. In contrast, the filtered active VEF of the

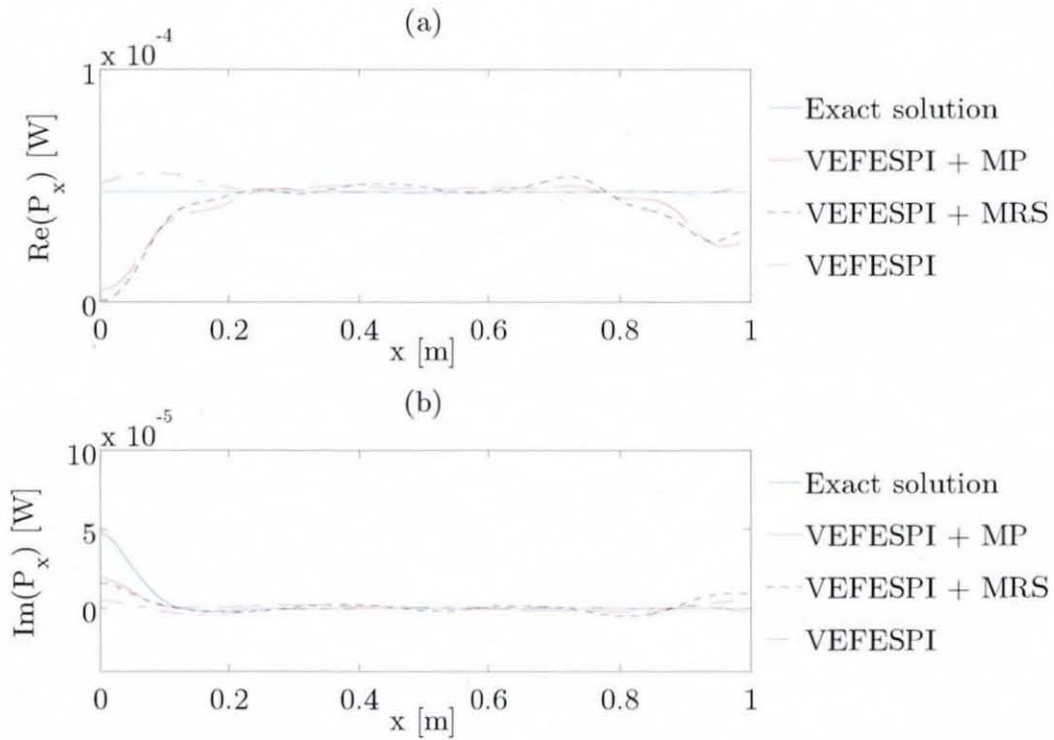


**Figure 6.16** Exact and Butterworth filtered VEF of the infinite beam displacement shown in Figure 6.11 using a Butterworth filter at optimum cut-off wavenumbers: (a) active energy flow, (b) reactive energy flow.

original data is much smoother. By comparing Figure 6.16 with Figure 6.14, it can also be seen that the reactive VEF of the Butterworth filtered data is slightly more accurate than the ideal filtered reactive VEF. This may be due to the fact that the 2D Butterworth filter includes more nearfield information within the filter, since the filter works as a true low-pass filter. However, also here the reactive VEF cannot be determined within an acceptable accuracy range. The MP and MRS altered displacement data achieve better reactive VEF results than the reactive VEF analysis of the non-periodic beam displacement.

Finally, a sensitivity study is carried out in order to investigate the error made due to altering the filter slope and the SNR. Again, for brevity reasons only the original non-periodised beam displacement will be employed in the investigation. Table 6.3 displays the error made when using different filter slope orders. As expected, the optimum cut-off wavenumber decreases with increasing filter slope order. However, there is only a slight improvement in the relative MSE made when calculating the active VEF. Only, a negligible reactive energy flow change can be achieved by altering the filter slope.

$F_0 = 1 \text{ N}; f_0 = 838.3 \text{ Hz}; \text{non-periodised data}; \text{SNR} = 108.6$				
Filter slope order	2	4	8	12
Optimum $(k_c)_{\text{real}} [\text{rad/m}]$	$1.50 \cdot k_0$	$1.25 \cdot k_0$	$1.17 \cdot k_0$	$1.08 \cdot k_0$
MSE, $\Re(10 \cdot \log_{10}(II))$	-22.14	-25.04	-23.59	-25.13
Optimum $(k_c)_{\text{imag}} [\text{rad/m}]$	$0.67 \cdot k_0$	$0.75 \cdot k_0$	$0.83 \cdot k_0$	$0.92 \cdot k_0$
MSE, $\Im(10 \cdot \log_{10}(II))$	-8.83	-8.81	-8.80	-8.82

**Table 6.3** Filter slope sensitivity study of non-periodised beam displacement data filtered with an oval 2D Butterworth filter.

Table 6.4 shows that the oval 2D Butterworth filter is insensitive to magnitudes of noise when computing VEF from infinite beam displacements. It has been demonstrated by the above given noise sensitivity study that

VEF can be computed in infinite beam structures, even then when a high noise contamination is present. The reason of the low sensitivity of the VEFESPI method may be due to the high ratio of the travelling wave magnitude and the noise floor magnitude.

$F_0 = 1 \text{ N}; f_0 = 838.3 \text{ Hz}; \text{non-periodised data; filter slope order} = 12$				
SNR	15.2	102.9	1037.3	6051.8
Optimum $(k_c)_{\text{real}} [\text{rad/m}]$	$1.08 \cdot k_0$	$1.08 \cdot k_0$	$1.08 \cdot k_0$	$1.08 \cdot k_0$
MSE, $\Re(10 \cdot \log_{10}(\Pi))$	-24.77	-25.14	-25.08	-25.23
Optimum $(k_c)_{\text{imag}} [\text{rad/m}]$	$0.92 \cdot k_0$	$0.92 \cdot k_0$	$0.92 \cdot k_0$	$0.92 \cdot k_0$
MSE, $\Im(10 \cdot \log_{10}(\Pi))$	-8.82	-8.81	-8.82	-8.82

**Table 6.4** Noise sensitivity study of non-periodised beam displacement data filtered with an oval 2D Butterworth filter.

#### 6.2.4 Vibrational Energy Flow Including ESPI Noise

In this section optimum filter parameters, VEF and the MSE made when filtering an ESPI noise contaminated synthetically generated infinite beam displacement are presented.

Figure 6.17 displays the real part of optical noise and the real part of normally distributed noise spatially varying over the measurement area. It can be seen that the optical noise form differs to the randomly generated normally distributed noise used in the previous sections. ESPI measurements of VEF of an infinite beam have been made in the farfield only. Thus, the nearfield will be excluded here.

Table 6.5 displays the vibration parameters extracted from the ESPI measurement. The shown excitation forces and excitation frequencies are used in order to predict VEF from artificially generated displacement data that has been contaminated by real ESPI noise. The ESPI noise was extracted within the wavenumber domain simply by deleting the travelling



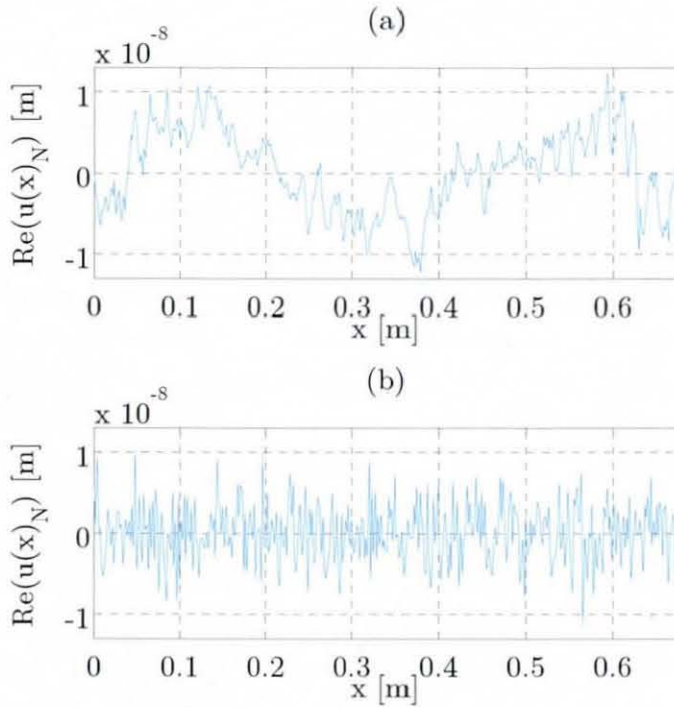


**Figure 6.17** Comparison of noise: (a) extracted ESPI noise of 801 Hz vibration, (b) normally distributed artificially generated noise.

wave information therein. After applying an inverse FFT of the manipulated wavenumber spectrum, the spatial distribution of the ESPI noise was then obtained. The SNR was predicted using equation (A18.1). Thus, a VEF prediction is given for each excitation frequency used during the experimental work reported later. In section 6.2.2 the problem of spectrum alteration due to the wavenumber multiplication process, used in order to derive spectral derivatives, was demonstrated (see Figure 6.5) when the displacement signal was composed of evanescent and travelling waves. In this section only travelling waves are present in the displacement signal and, thus, spectral alteration due to nearfield presence can be neglected. However, since the signal contains noise components, a spectral alteration due to multiplication of the wavenumber components with the noise components can be expected.

Figure 6.18 displays the spectrum alteration due to the presence of noise in the signal. It can be realised that especially at high wavenumbers spectral noise components are strongly amplified. Clearly, the spectrally

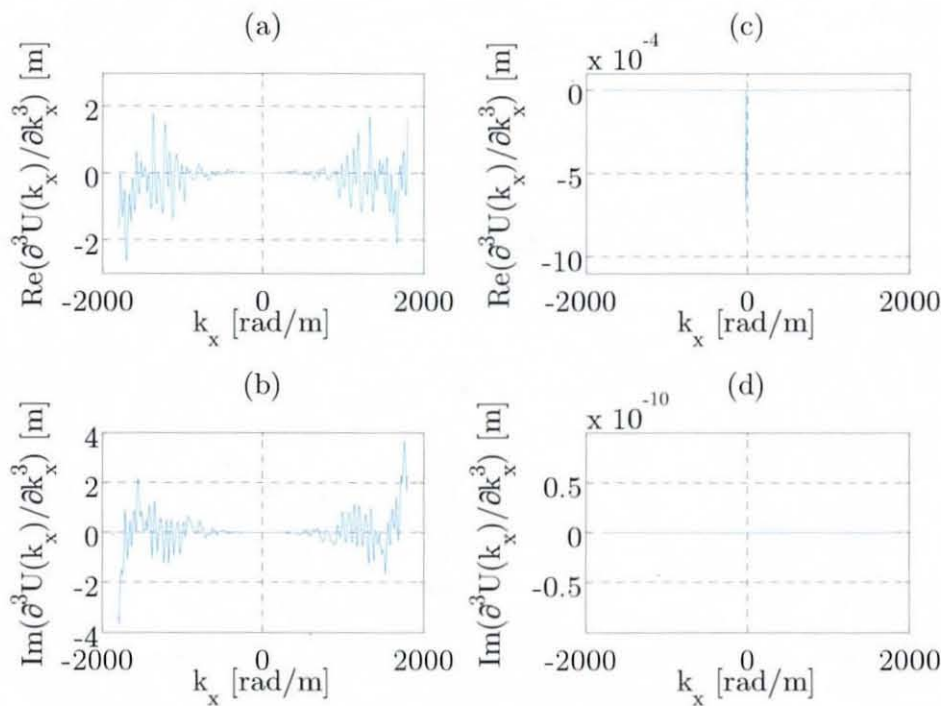


**Figure 6.18** KSD determined and exact solution of the 3<sup>rd</sup> spectral derivative of the ESPI noise contaminated infinite beam displacement at 801 Hz: (a) real part using KSD, (b) imaginary part using KSD, (c) real part exact solution, (d) imaginary part exact solution.

travelling wave component in Figure 6.18(a) is not visible. Additional to this the imaginary part now contains high spectral components although this part of the spectrum should be zero. It can be realised that the presence of noise causes substantial problems and, thus, filtering is indispensable. Of course the problem increases even further if a nearfield is present in the displacement signal.

Excitation frequency	801 Hz	1112 Hz	1146 Hz
Excitation force	3.281 N	2.645 N	5.897 N
SNR	60.2	264.4	135.05

**Table 6.5** Vibrational parameters of “infinite” beam.

Figure 6.19 shows the real part of the relative MSE made when analysing the 801 Hz beam vibration. Since in the farfield the reactive energy flow is approaching zero, it was neglected. Compared to Figures 6.13 and 6.15 it can be recognised that VEF can be analysed with much less error when neglecting the nearfield. It can also be realised from Figure 6.19 that the ideal

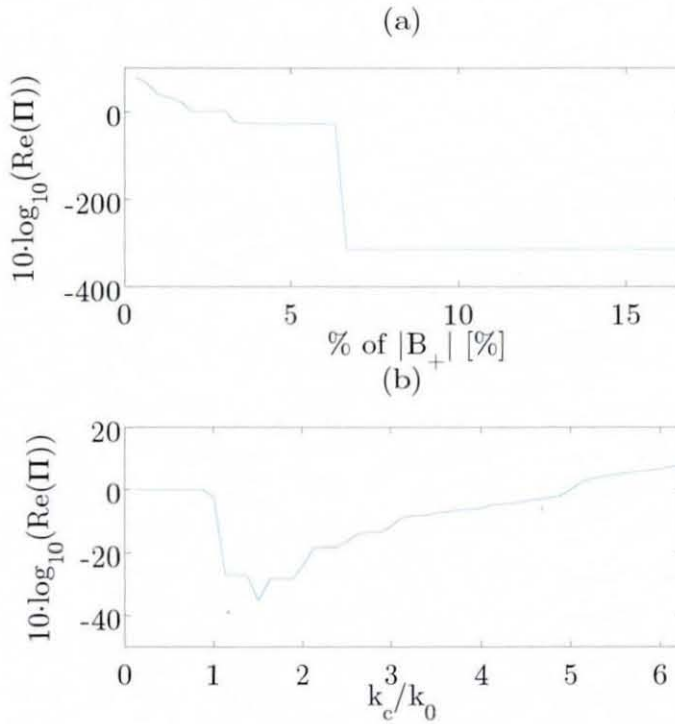


**Figure 6.19** Real relative MSE of the ESPI noise contaminated infinite beam displacement at 801 Hz using different types of filter: (a) ideal filter, (b) Butterworth filter.

filter produced better results when the farfield only is considered. No periodisation technique has been used, since the signal was restricted to two integer wavelengths.

Figure 6.20 displays the determined VEF of both filter types and the relative error in percent made when using them. It can be realised that the ideal filtered VEF is exactly the same as the true VEF. The oval 2D Butterworth filter has minor deviations which, however, are still in an acceptable range. The reason for the minor deviation is due to the low-pass technique that allows noise components to pass through at low wavenumbers.

It can be seen from Figure 6.20 that the ideal filter is perfect to filter displacements that include an integer number of farfield waves. Table 6.6 displays the optimum cut-off points at each excitation frequency for both

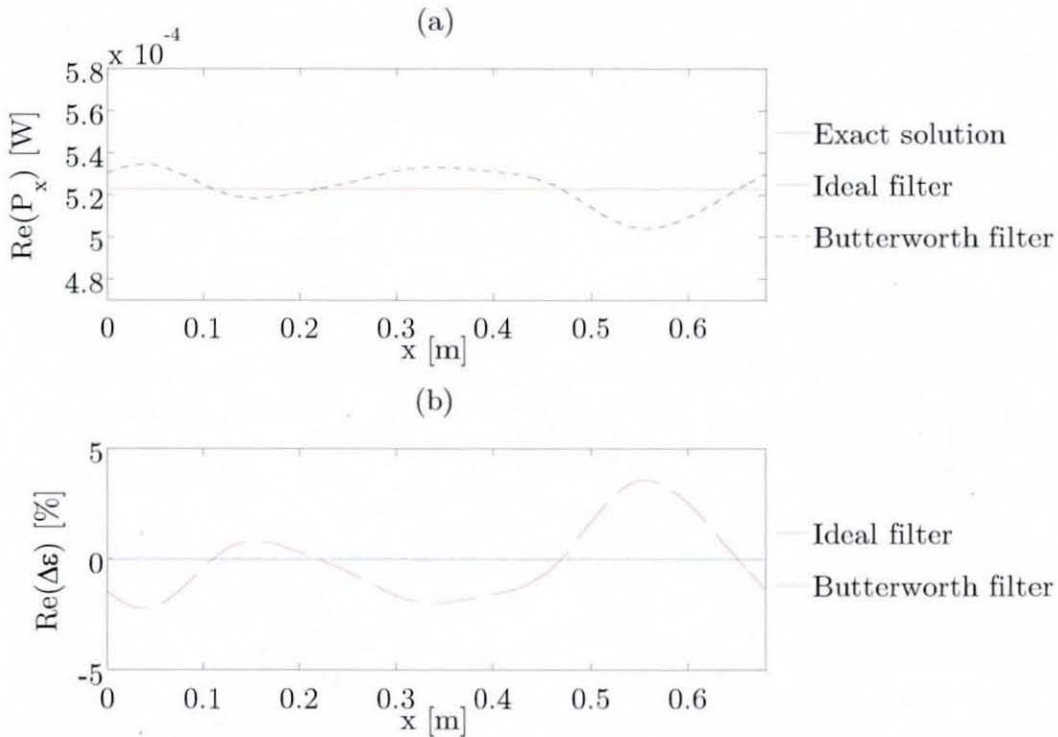


**Figure 6.20** Exact and filtered VEF of the ESPI noise contaminated infinite beam displacement at 801 Hz: (a) real part of active energy flow, (b) real part of relative error.

filter types. Also in Table 6.6, a prediction of the active VEF at each excitation frequency is given that can be compared later on with the measured VEF data. Note, the VEF due to the application of the oval 2D Butterworth filter is spatially-averaged over the beam distance, since this value varies with beam distance. It can be realised from Table 6.6 that both VEF values are close together. It is intended that the given optimum cut-off points are employed in chapter 9. Note, the predicted VEF values are the mean of the spatially varying VEF (see Figure 6.20(a)).



Excitation frequency $f_0$ [Hz]	801	1112	1146
Optimum (% of $ B_+ _{real}$ [%])	6.67	2.33	5.67
MSE, $\Re(10 \cdot \log_{10}(\Pi))$	-315.0	-303.21	-308.43
VEF, $(P_x)_{ideal}$ [W]	$5.23 \cdot 10^{-4}$	$2.88 \cdot 10^{-4}$	$1.41 \cdot 10^{-3}$
Optimum $(k_c)_{real}$ [rad/m]	$1.5 \cdot k_0$	$1.25 \cdot k_0$	$1.25 \cdot k_0$
MSE, $\Re(10 \cdot \log_{10}(\Pi))$	-35.4	-38.18	-40.86
Mean of VEF, $1/N_x \sum \Re\{(P_x)_{butter}\}$ [W]	$5.23 \cdot 10^{-4}$	$2.88 \cdot 10^{-4}$	$1.41 \cdot 10^{-3}$

**Table 6.6** Optimum “infinite” beam cut-off points and predicted VEF.

### 6.3 Numerical Simply Supported Beam Analysis

This section investigates the effects of numerical energy flow computation in a simply supported beam using the VEFESPI method. In the previous sections it was shown that the presence of a nearfield, the presence of noise or the presence of both can cause spectral deviation problems, which then yield to VEF computation errors. The reason an infinite beam has been presented first is that the cause of the problems can be easily understood, since the infinite beam was modelled by a simple two wave model only.

Young’s modulus	$E = 2.07 \cdot 10^{11} \text{ N/m}^2$
mass density	$\rho = 7.85 \cdot 10^3 \text{ kg/m}^3$
beam width	$b = 50 \cdot 10^{-3} \text{ m}$
beam thickness	$t = 10 \cdot 10^{-3} \text{ m}$
beam length	$L = 1 \text{ m}$

**Table 6.7** Simply supported beam properties.



Thus, the problems revealed in the infinite beam section can also be related to the finite beam analysis although here the beam displacement modelling is much more complex. The material properties of the beam are shown in Table 6.7. Again, these are the same properties as the experimental simply supported beam, used during the experiment.

### **6.3.1 Vibrational Energy Flow Excluding Noise**

#### **6.3.1.1 Vibrational Energy Flow Using the VEFESPI Method**

In section 5.4.1 it has been shown that the simply supported beam displacement is formed by a superposition of infinite beam waves and reflection waves. Both wave groups contain evanescent waves and travelling waves. Due to the application of hysteretic damping to solve the problem of infinite wave amplitudes at resonant excitation frequencies both wave types break into evanescent and travelling waves. Thus, the initial evanescent waves break into a large fraction of evanescent waves and a small fraction of travelling waves driven by the hysteretic loss factor. The initial travelling waves break into a large fraction of travelling waves and a small fraction of evanescent waves. Both wave types contribute to energy transfer and both wave types also contribute to spectral deviation due to nearfield components.

Figure 6.21 displays the frequency dependent magnitude of all complex wave amplitudes arising to the right of the excitation location of a transversally vibrating simply supported beam at different hysteretic loss factors. Independent upon the excitation location the left-going and right-going infinite wave amplitudes are the same. However, the left and right-going reflection wave amplitudes differ slightly from each other if off-centre excitation is employed. The excitation location applied here was off-centre at  $x_0 = 0.4167$  m. A unity force of  $F_0 = 1$  N was applied. From Figure 6.21 it is noticeable that hysteretic damping mostly affects the travelling reflection waves only, since the magnitude decreases clearly with increasing hysteretic loss factor. It can also be noticed from Figure 6.21 that the evanescent reflection wave amplitudes are smaller than the travelling reflection wave

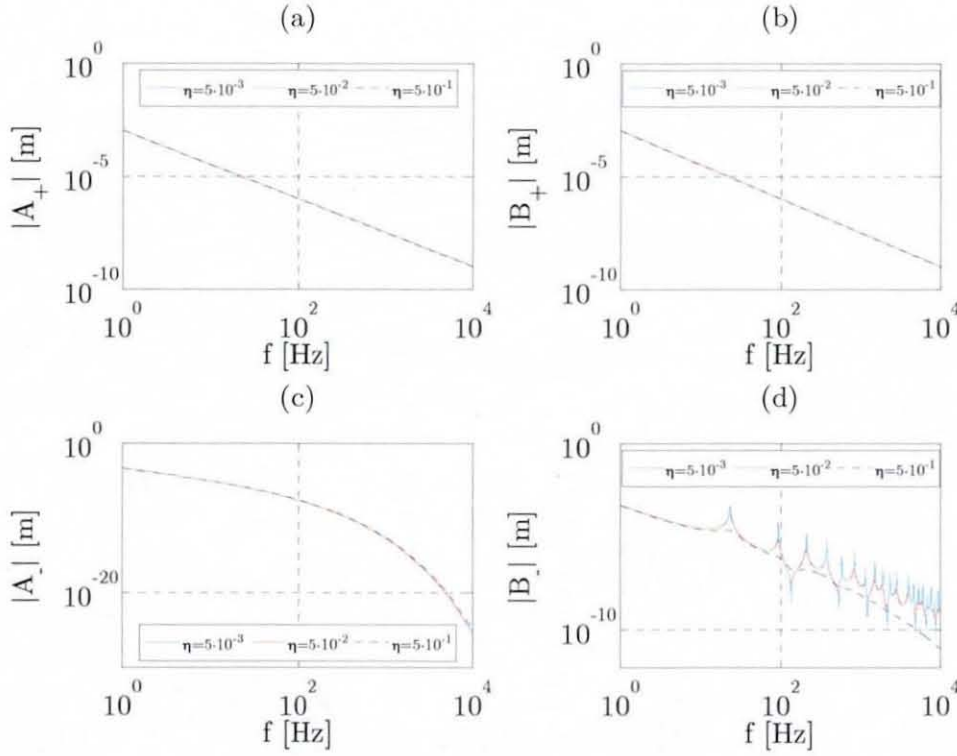


**Figure 6.21** Magnitude of complex wave amplitudes to the right of the excitation location for different loss factors: (a) infinite evanescent wave, (b) infinite travelling wave, (c) reflecting evanescent wave, (d) reflecting travelling wave.

amplitudes. Further, the amplitude ratio  $|B_-|/|A_-|$  is increasing exponentially with increasing excitation frequency. Thus, the influence of the reflection wave nearfield components decreases with increasing frequencies.

Figure 6.22 displays the steady state complex, infinite waves displacement and the complex, reflection waves displacement. The beam was excited at its natural undamped frequency of the 6<sup>th</sup> mode with  $f_0 = 838.3$  Hz using a unity force at three different hysteretic damping settings. Figure 6.22 shows that with increasing damping mainly the reflection wave amplitudes were decreased. The amplitude reduction of the infinite waves displacement is hardly noticeable over the range of different damping applied. At  $\eta = 5 \cdot 10^{-3}$ , the reflection waves displacement is about 60 times larger than the infinite waves displacement. However, at  $\eta = 5 \cdot 10^{-2}$  the reflection waves displacement is only about 10 times larger. Thus, with increasing damping the infinite waves displacement becomes a more dominant displacement part and, thus,

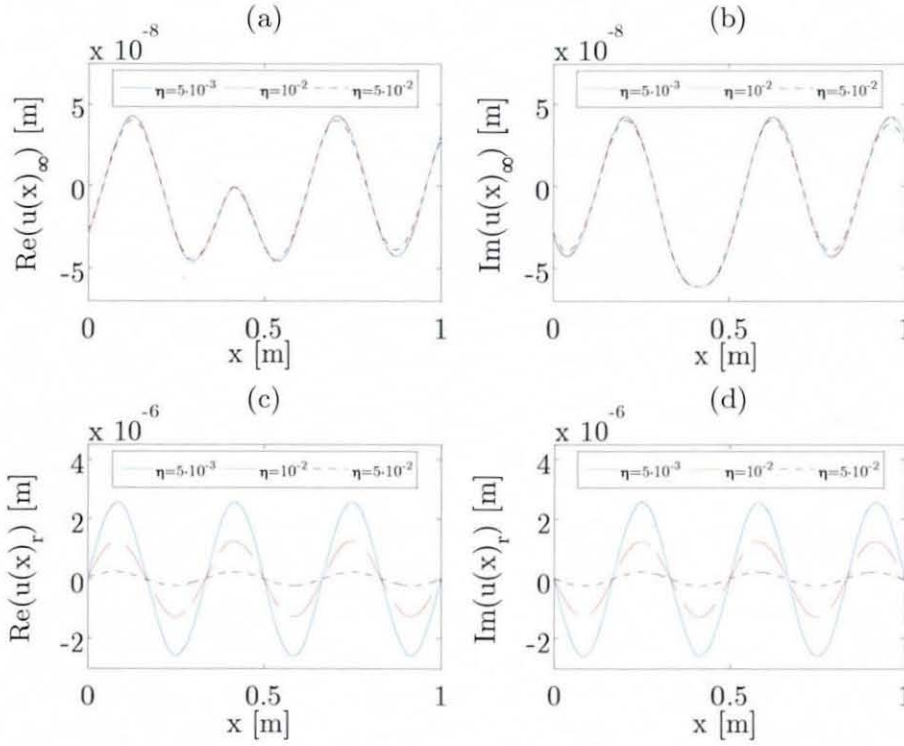


**Figure 6.22** Infinite waves and reflection waves beam displacement of a simply supported beam: (a) real part infinite waves, (b) imaginary part infinite waves, (c) real part reflection waves, (d) imaginary part reflection waves.

more leakage can be expected in the wavenumber domain when computing VEF from finite beam displacements. This is easy comprehensible, since at higher damping the reflected travelling waves are more spatially damped.

Figure 6.23 displays the two-dimensional simply supported beam displacement and the one-dimensional row extracted from the middle of the beam width. The beam was excited at the 6<sup>th</sup> mode with an excitation frequency of  $f_0 = 838.3$  Hz using a unity force and a hysteretic loss factor of  $\eta = 5 \cdot 10^{-2}$ . The reason such a high hysteretic loss factor is employed is to investigate numerical VEF computation when a low infinite wave to reflection wave ratio is present. The displacement is generated by evaluating equation (5.37) numerically using a number of data points in  $x$  direction of  $N_x = 256$ , and in  $y$  direction of  $N_y = 64$ . It can be realised from Figure 6.23 that an integer number of 3 waves is included in the spatial displacement signal.

Figure 6.24 displays the 3<sup>rd</sup> spatial derivative computed by the KSD



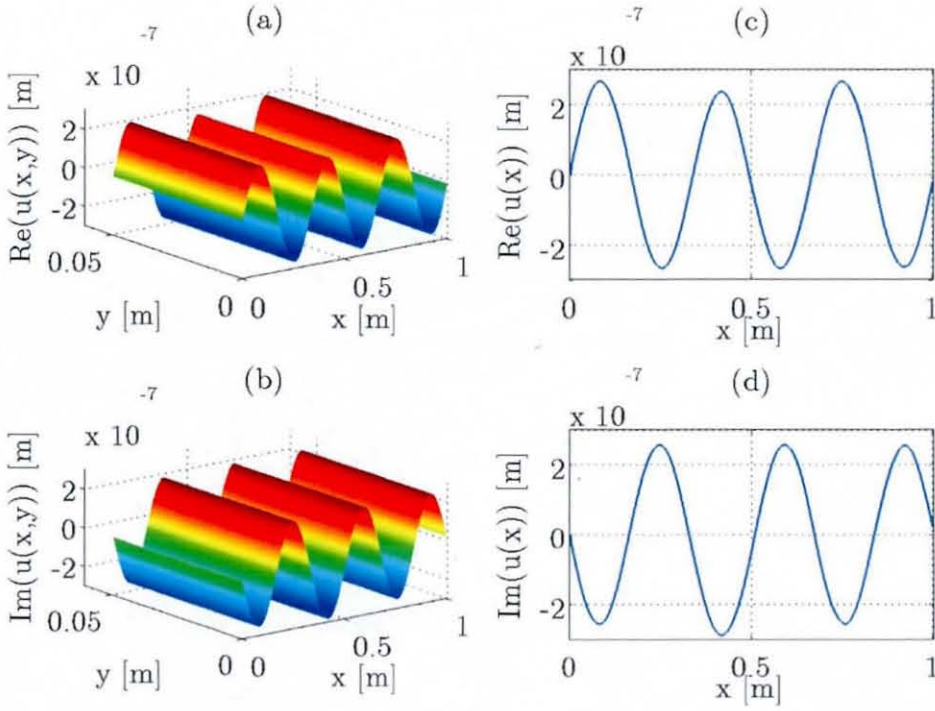


**Figure 6.23** Complex and hysteretically damped simply supported beam displacement at the 6<sup>th</sup> mode: (a) 2D real part, (b) 2D imaginary part, (c) 1D real part, (d) 1D imaginary part.

method plus the exact analytical 3<sup>rd</sup> order spatial derivative. From Figure 6.24 it can also be seen here that a spectral deviation between the determined 3<sup>rd</sup> order spatial derivative and the exact 3<sup>rd</sup> order spatial derivative is present. The reason of this deviation can be found when considering a few points. As mentioned before the infinite wave displacement contains a non-integer number of waves in the displacement signal. Although the infinite wave displacement is about 6 times smaller than the reflection wave displacement a small fraction of leakage appears in the wavenumber spectrum. Furthermore, each wave group contains nearfield waves and these components are detected in the wavenumber spectrum. Both the infinite wave leakage and the nearfield components of each wave result in spectral deviation especially at high wavenumbers. The reason of the smaller spectral deviation compared to the infinite beam, is that the nearfield components are much smaller than the travelling wave components. Since the infinite wave

displacement becomes more dominant with increasing damping, the spectral deviations will become larger too. From Figure 6.24 it can also be seen that the exact spectrum shows some spectral components away from the excitation wavenumber. This is due to the fact that with increasing damping the spatial derivatives of the infinite beam displacement start to develop a

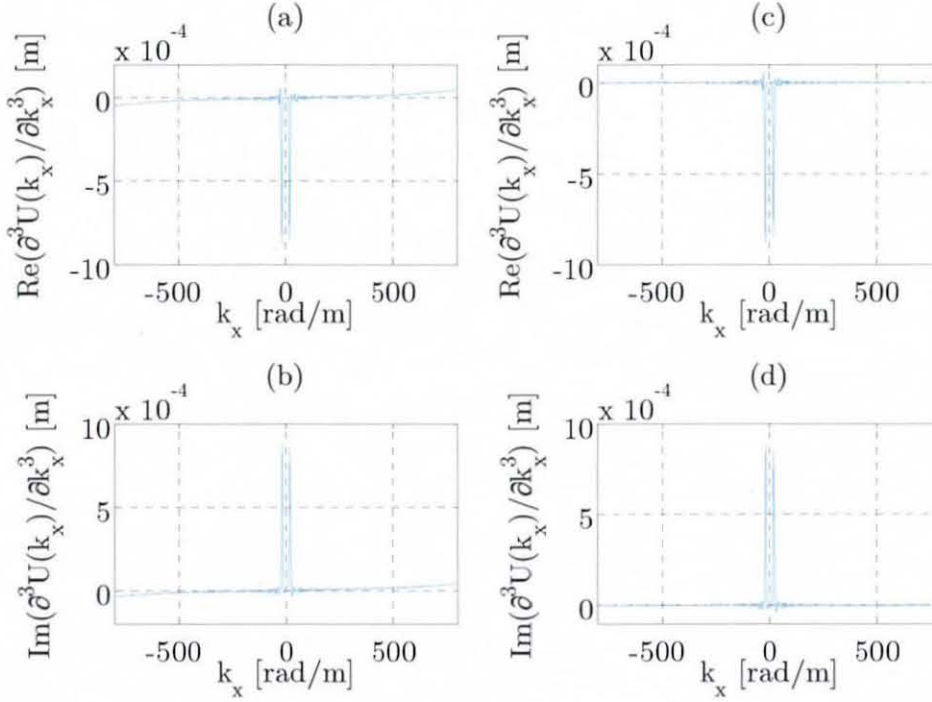


**Figure 6.24** KSD determined and exact solution of the 3<sup>rd</sup> spectral derivative of the beam displacement shown in Figure 6.23: (a) real part using KSD, (b) imaginary part using KSD, (c) real part exact solution, (d) imaginary part exact solution.

discontinuity at excitation location. Thus, the spectrum shown in Figures 6.24(c) and 6.24(d), respectively exhibits some spectral amplitude components due to the spatial Fourier transform of that discontinuity at excitation location (Gibb's phenomenon).

If one computes VEF within the simply supported beam using the displacement, as shown in Figure 6.23, one would obtain an active and reactive energy flow within the beam as displayed in Figure 6.25. The exact active and reactive VEF was calculated from equation (5.64). From Figure 6.25 it can be realised that the exact active and reactive VEF is zero at the

simply supported boundaries because the displacement is zero at these points and the boundaries were assumed to be non-dissipative. It can also be noticed that the active energy flow is maximum at excitation location and that the absolute value of the right-hand side energy flow at that point is larger than at the absolute value of the left-hand side. This means more energy is flowing

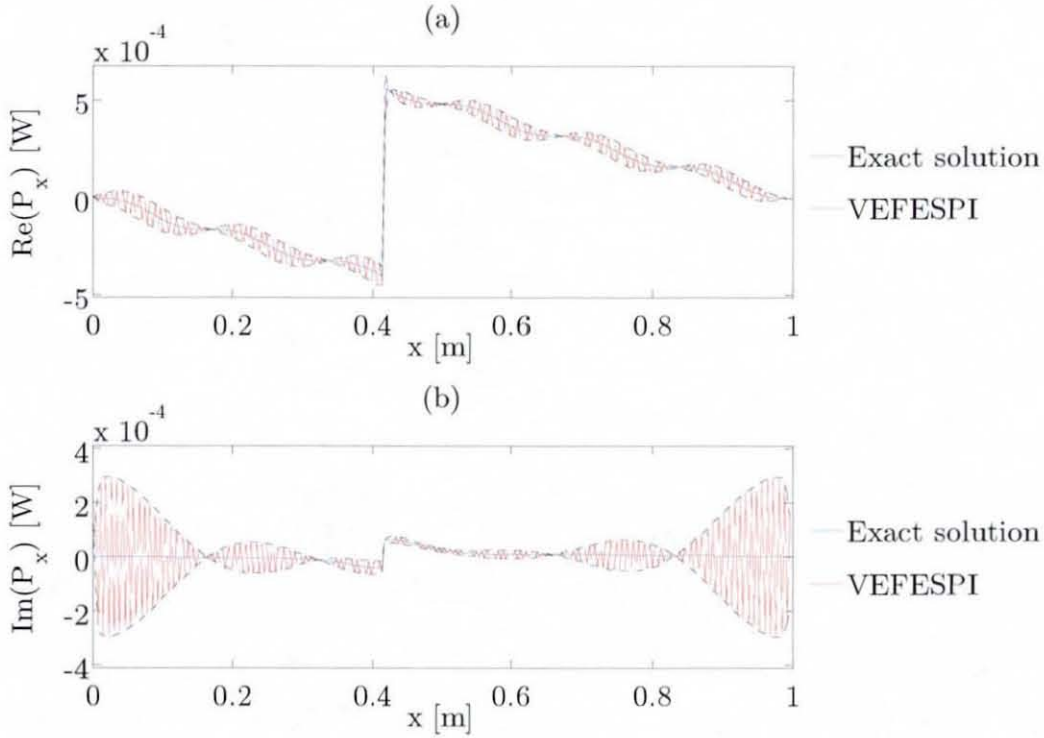


**Figure 6.25** Exact and determined VEF of the simply supported beam displacement shown in Figure 6.23: (a) active energy flow, (b) reactive energy flow.

to the right of the excitation location than to the left. Further, the sum of both absolute energy flow values at excitation location is equal to the input energy. The off-centre excitation location of  $x_0 = 0.4167$  m was chosen to be at a peak of the complex beam displacement. This ensures maximum energy to be injected into the beam.

As expected, the computed VEF oscillates around the exact value due to the above mentioned reason. If one would simply apply the CW technique in order to compensate the VEF fluctuation as demonstrated in section 6.2, one would obtain a fairly smooth computed energy flow within the simply



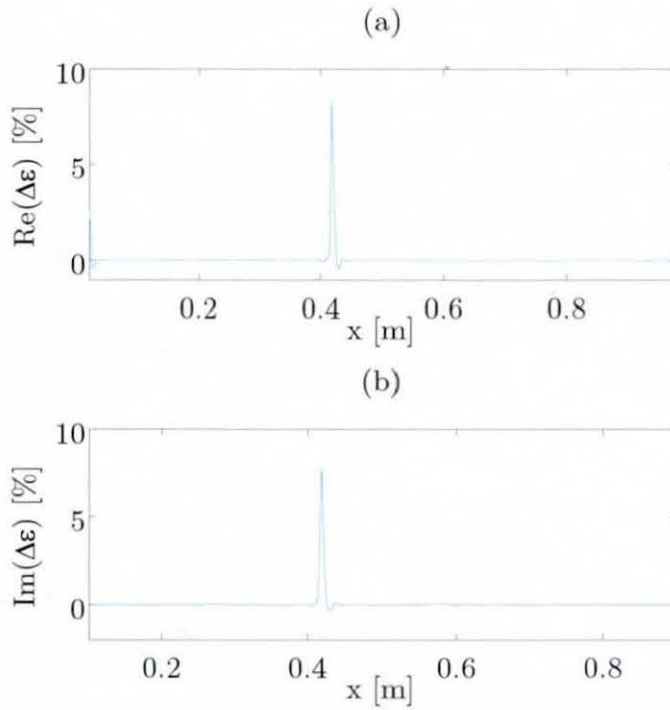


**Figure 6.26** Relative error of determined VEF of the simply supported beam displacement shown in Figure 6.23: (a) relative active flow error, (b) relative reactive flow error.

supported beam. Figure 6.26 displays the relative error made when applying the CW technique in order to compensate for VEF oscillations. Also here, the relative error between the VEFESPI determined VEF and the exact VEF solution of the simply supported beam was computed. Because the reactive VEF is approaching zero close to the beam's boundaries this region is not been shown due to zero division. It can be recognised from Figure 6.26 that the error made is almost neglectable except around the excitation location where the CW technique has some problems to approximate the sharp VEF discontinuity. However, compared to the numerical infinite beam analysis the CW technique compensates energy flow oscillations for the simply supported beam much better.

The above analysed beam displacement contained 3 waves within the displacement signal, since the beam was excited at the even 6<sup>th</sup> mode. However, if one excites the beam at odd-numbered mode shapes, such as the

7<sup>th</sup> mode, a non-integer number ( $3.5\lambda$ ) of waves will be included in the displacement signal. Thus, a considerable amount of spectral leakage will occur. Therefore, the 7<sup>th</sup> mode shape of the beam is investigated next using the periodisation techniques introduced in section 6.1 in order to diminish the effect of spectral leakage. Figure 6.27 displays the 7<sup>th</sup> mode simply supported beam displacement. The excitation frequency was  $f_0 = 1141$  Hz and the excitation location was  $x_0 = 0.3571$  m. The excitation location was changed

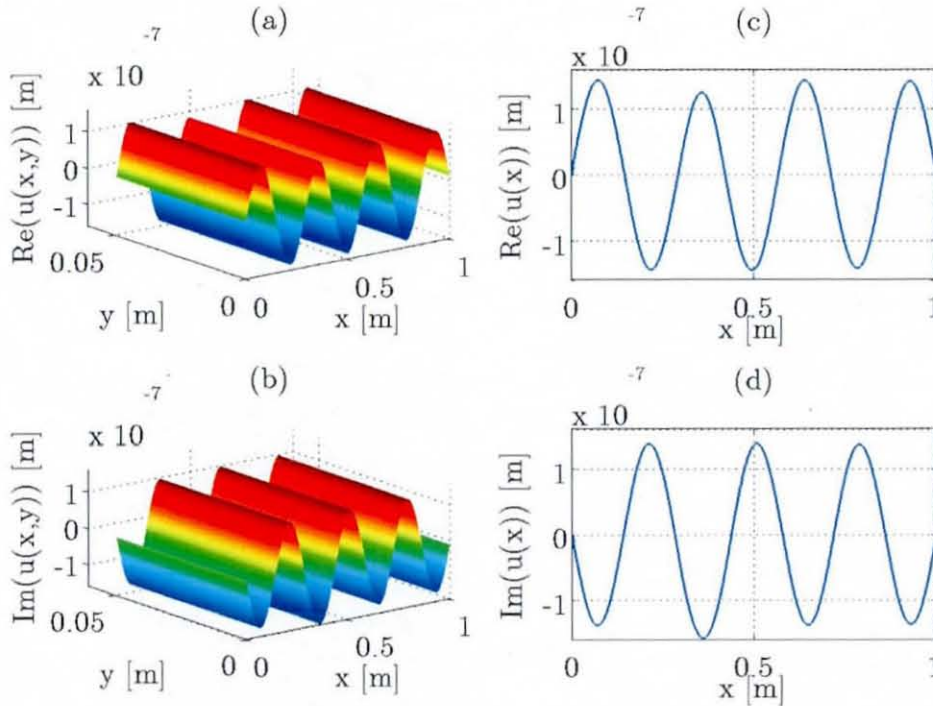


**Figure 6.27** Complex and hysteretically damped simply supported beam displacement at the 7<sup>th</sup> mode: (a) 2D real part, (b) 2D imaginary part, (c) 1D real part, (d) 1D imaginary part.

to the peak location of the 7<sup>th</sup> mode. Also here, a unity force was applied and the selected hysteretic loss factor was  $\eta = 5 \cdot 10^{-2}$ . If one would compute VEF when the beam is vibrating at its 7<sup>th</sup> mode using the MP and MRS technique to periodise the displacement, one would still obtain some undesired energy oscillations. As shown in section 6.2, the determined VEF from the periodised displacement is approximate further by using the CW technique. The computed energy flow of this procedure is shown in Figure 6.28. From there



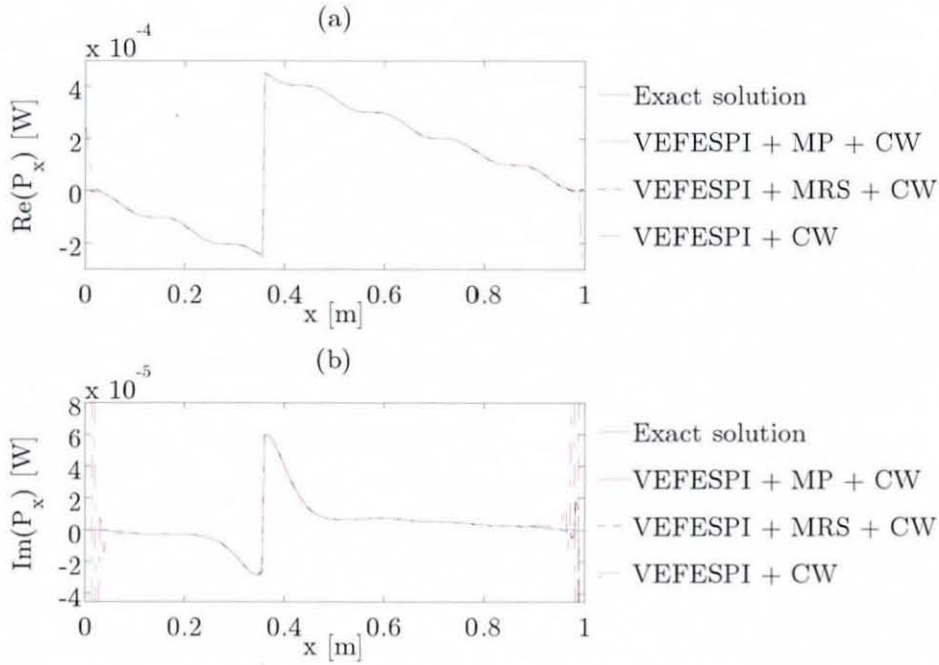


**Figure 6.28** Exact and VEFESI determined VEF of the simply supported beam displacement shown in Figure 6.27: (a) active energy flow, (b) reactive energy flow.

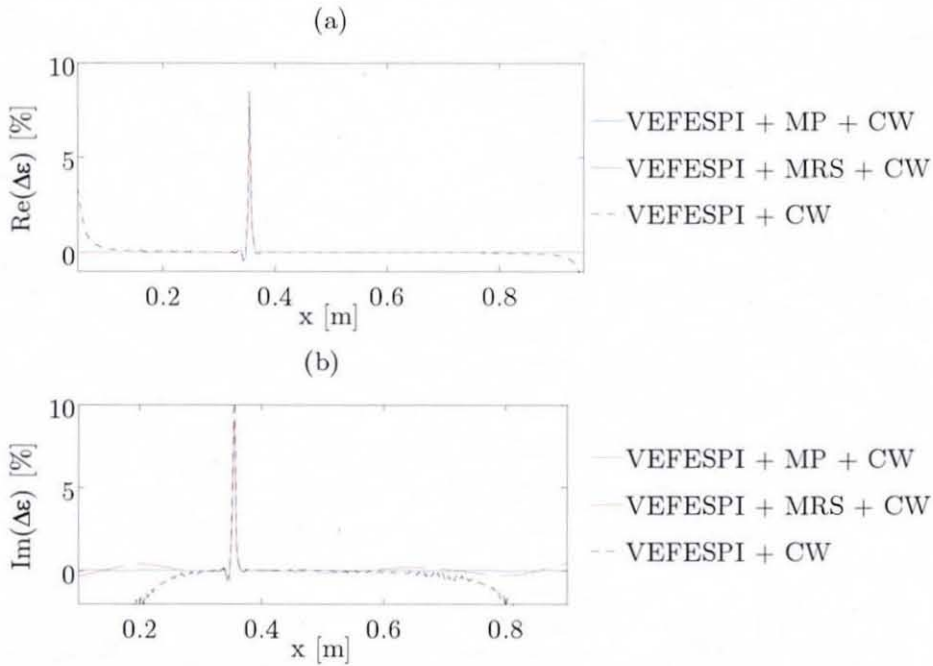


**Figure 6.29** Relative error of determined VEF of the simply supported beam displacement shown in Figure 6.27: (a) relative active flow error, (b) relative reactive flow error.

it can be realised that the periodisation techniques work well in order to determine VEF from the periodised beam displacement. As a comparison the VEF approximated by the CW technique is displayed too. It can be seen that the reactive VEFESPI+CW energy flow is less accurate at the beam's ends. However, all three computed active VEF agree well with the exact value.

Figure 6.29 displays the relative error made when analysing VEF with any of the three techniques. It can be seen that the VEF computed from the VEFESPI+CW technique increases in error towards the beam's ends. Especially the reactive energy flow cannot be approximated sufficiently accurate enough. However, VEF determined from the MP periodised displacement shows a very good agreement with the exact value. All three techniques have some problems to detect the sharp energy flow discontinuity at excitation location. This means that the input energy cannot be calculated without introducing errors.

#### **6.3.1.2 Vibrational Energy Flow from Energetic Quantities**

Within the beam analysis a second alternative approach is employed to compute VEF in finite beam structures from measured energy densities. Equation (3.39) displays the energy balance within a finite beam. It can be realised from (3.39) that the real part of the time-averaged complex input power is proportional to the product of circular frequency, hysteretic loss factor, and potential energy density. The imaginary input power is proportional to the product of circular frequency and Lagrangian density.

Definite integration of the energy densities along the beam length transfers the local energy densities into global energy quantities and, thus, an energy balance between local energy quantities and complex VIP can be carried out. However, indefinite integration of the potential and Lagrangian energy density may be employed in order to obtain spatial VEF information of the finite beam. Because the indefinite energy density integration is undertaken in this work in an incremental numerical way, this method will be addressed as incremental energy density integration method (IEDI). Thus, active VEF information from the potential energy density may be

numerically determined by an incremental integration of the potential energy as:

$$\Re \{P(x_n)\} = 2\omega\eta \int_{x_1}^{x_n} \langle e_{pot}(x) \rangle_t dx. \quad (6.8)$$

Here,  $n = 2, 3, 4, \dots, N_x$ . Analogously, the reactive VEF may be incrementally integrated using the Lagrangian energy density as:

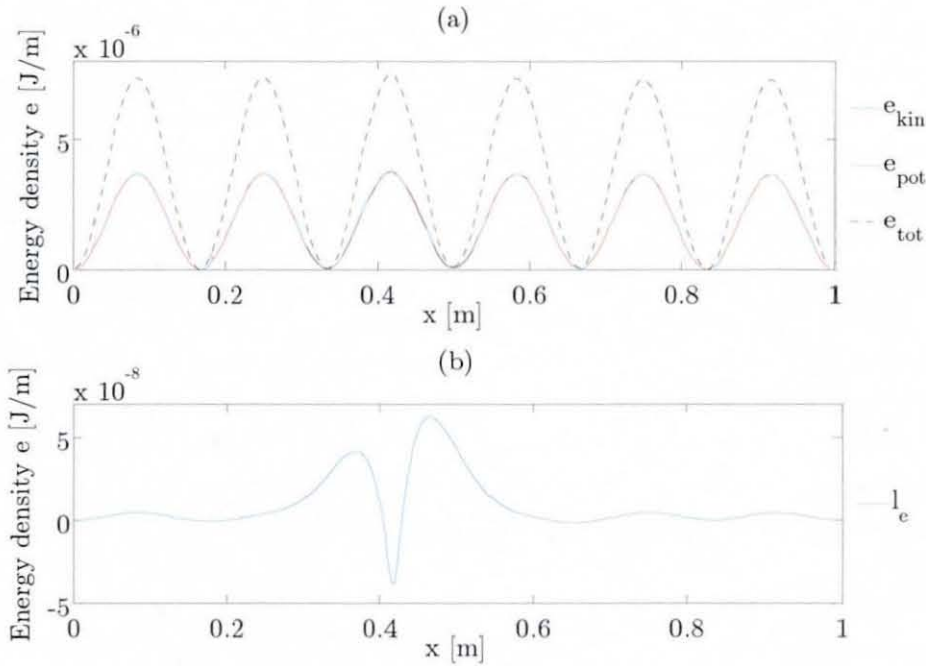
$$\Im \{P(x_n)\} = 2j\omega \int_{x_1}^{x_n} (\langle e_{kin}(x) \rangle_t - \langle e_{pot}(x) \rangle_t) dx. \quad (6.9)$$

By employing the method proposed by equations (6.8) and (6.9) the VEF determination that originally relied on the computation of spatial derivatives up to the third order, as shown in equation (3.33), is now reduced to a second order spatial derivative equation, as evident from equation (3.36).

Figure 6.30 displays the energy densities of the 6<sup>th</sup> mode displacement, as shown in Figure 6.23. It can be realised that the kinetic and potential energy densities are almost identical except at the excitation location. Herein,  $e_{kin}$  is denoted as the kinetic energy density,  $e_{pot}$  is denoted as the potential energy density,  $e_{tot}$  is denoted as the total energy density, and  $l_e$  is denoted as the Lagrangian energy density. The difference of both can be seen by Figure 6.30(b). This difference is proportional to reactive energy flow.

Figure 6.31 displays the numerical integrated VEF present within the simply supported beam by numerically evaluating equations (6.8) and (6.9). Here, a stepwise numerical integration of the potential and Lagrangian energy densities along the beam length was carried out. It is shown by Figure 6.31 that the numerically integrated energy flow matches well with the exact solution. Note, here the VEF oscillations of the spatial derivatives due to the nearfield components of the displacement were compensated by the CW technique. However, only very small VEF oscillations occurred, since only up to second order spatial derivatives were employed.

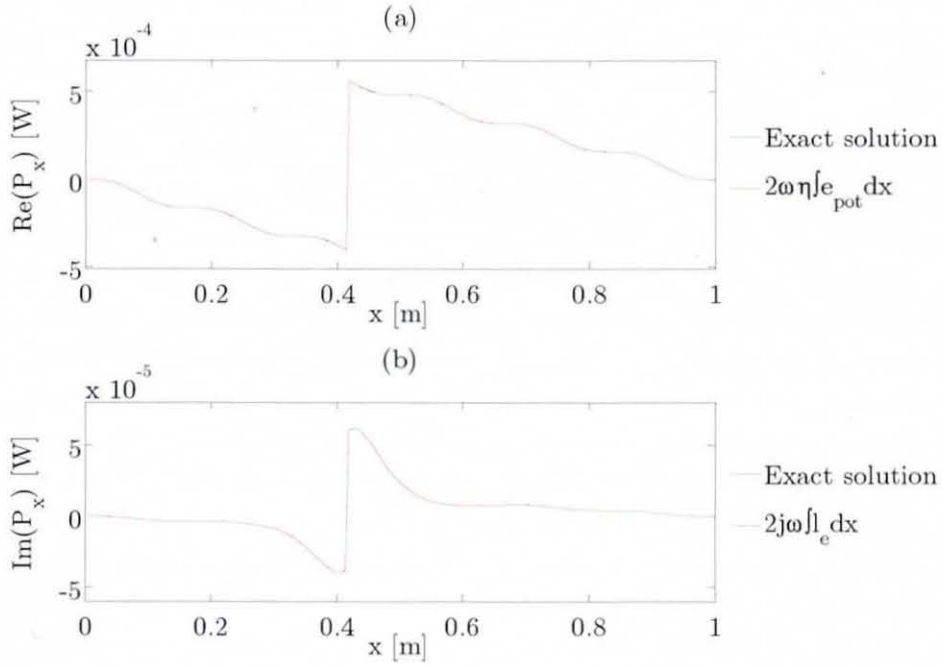




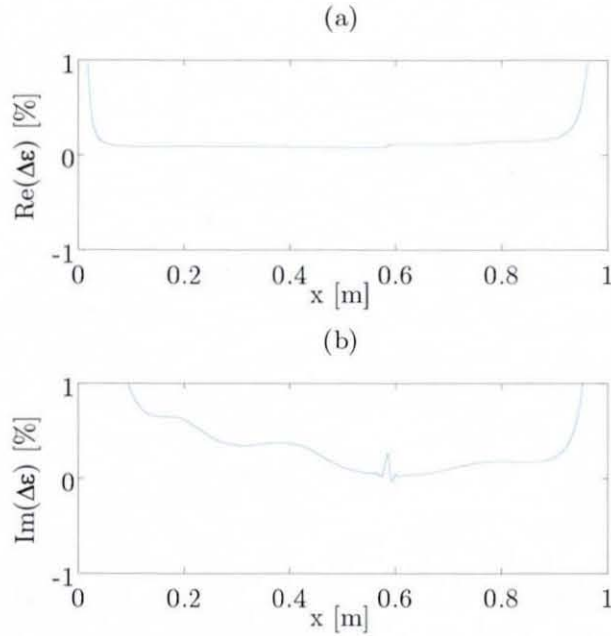
**Figure 6.30** Energy densities of the simply supported beam displacement shown in Figure 6.23: (a) kinetic, potential, and total energy density, (b) Lagrangian energy density.

Figure 6.32 displays the relative error made when determining VEF by using equation (6.8) and (6.9), respectively. It can be seen from Figure 6.32 that the relative error made, when applying the incremental energy density integration technique in combination with the KSD method is small. It can also be noticed from Figure 6.32 that in comparison to the result of the conventional method, as shown in Figure 6.26, the VEF error at excitation location was reduced substantially and, thus, the sharp VEF discontinuity at excitation location was computed much better. The deviation towards the beam's ends can be related to zero division within the relative error computation procedure that occurs at the beam's ends due to the exact VEF approaching zero.

Figure 6.33 illustrates the relative error made when employing different amount of hysteretic damping. It is evident from this analysis that with increasing damping the error of the active and reactive VEF increases slightly. However, at a very high structural damping of  $\eta = 10^{-1}$  the error of



**Figure 6.31** Exact and determined VEF from the incremental energy density integration method of the simply supported beam displacement shown in Figure 6.23: (a) active energy flow, (b) reactive energy flow.



**Figure 6.32** Relative error of determined VEF from the incremental energy density integration method of the simply supported beam displacement shown in Figure 6.23: (a) relative active flow error, (b) relative reactive flow error.

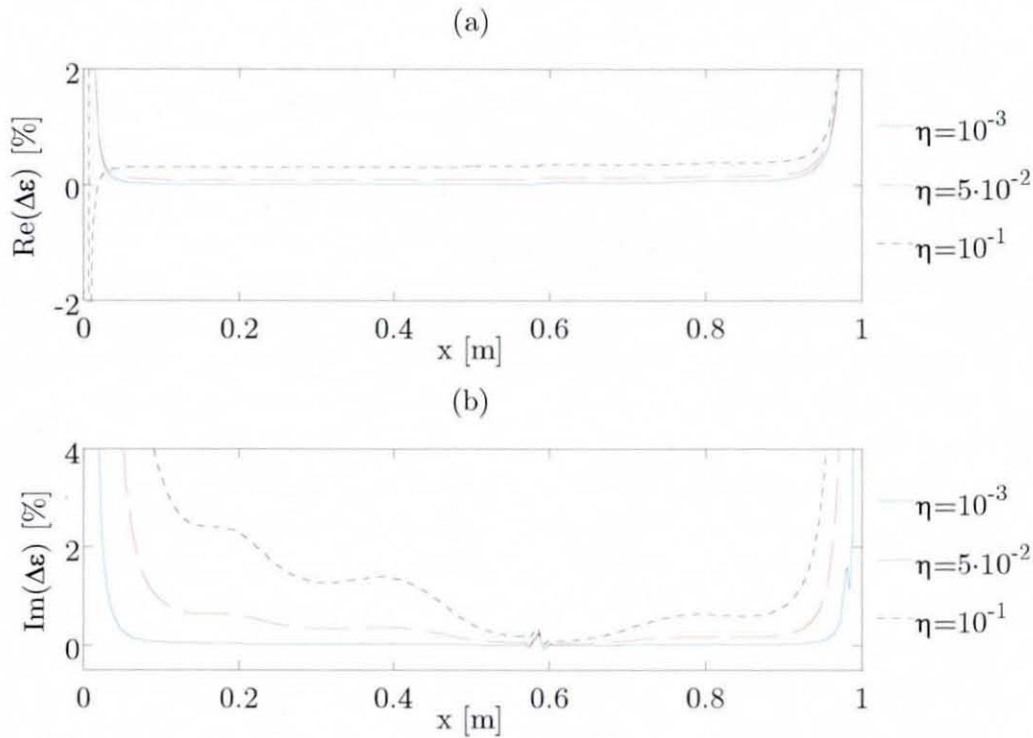


**Figure 6.33** Relative error of determined VEF from the incremental energy density integration method of the simply supported beam displacement shown in Figure 6.23 for different levels of damping: (a) relative active flow error, (b) relative reactive flow error.

computed VEF is still acceptable. Thus, VEF in a simply supported beam can be computed very well from the incremental integration of the energy densities.

In case of odd-numbered mode shape vibration (non-periodic beam displacement) the above introduced method can be applied in combination with the MP and MRS periodisation technique.

Figure 6.34 displays the integrated VEF of the 7<sup>th</sup> mode beam displacement, as shown in Figure 6.27. As expected, the periodised displacements show a much better result. The relative reactive VEF error made when analysing the non-periodised beam displacement is outside the plotting area, as evident from Figure 6.34(b). The analysis of the non-periodised beam displacement resulted in a potential energy density not being zero at the beam's ends and, thus, causing deviations. This problem is

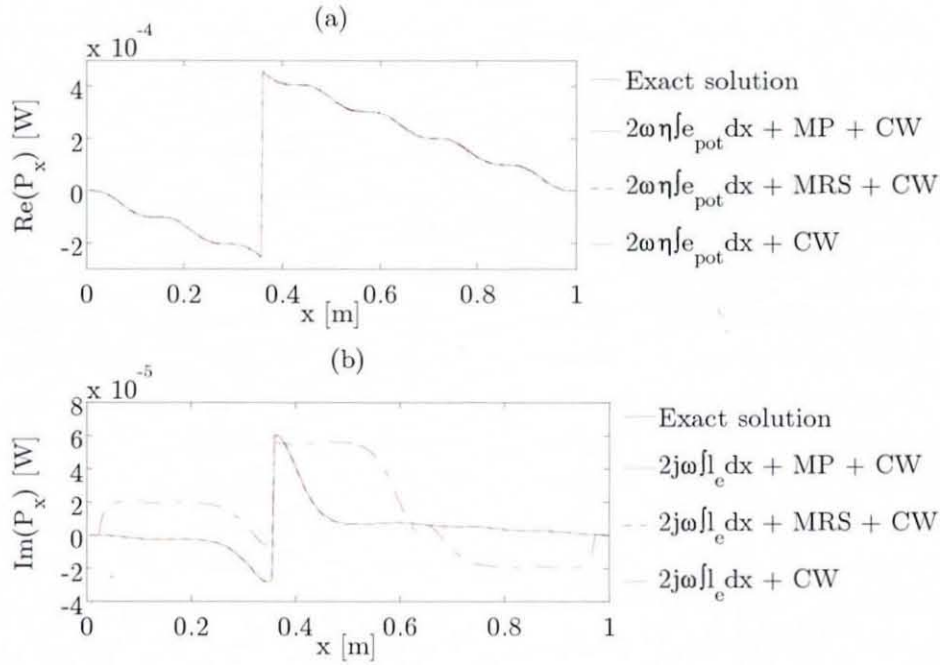


**Figure 6.34** Exact and determined VEF from the incremental energy density integration method of the simply supported beam displacement shown in Figure 6.27: (a) active energy flow, (b) reactive energy flow.

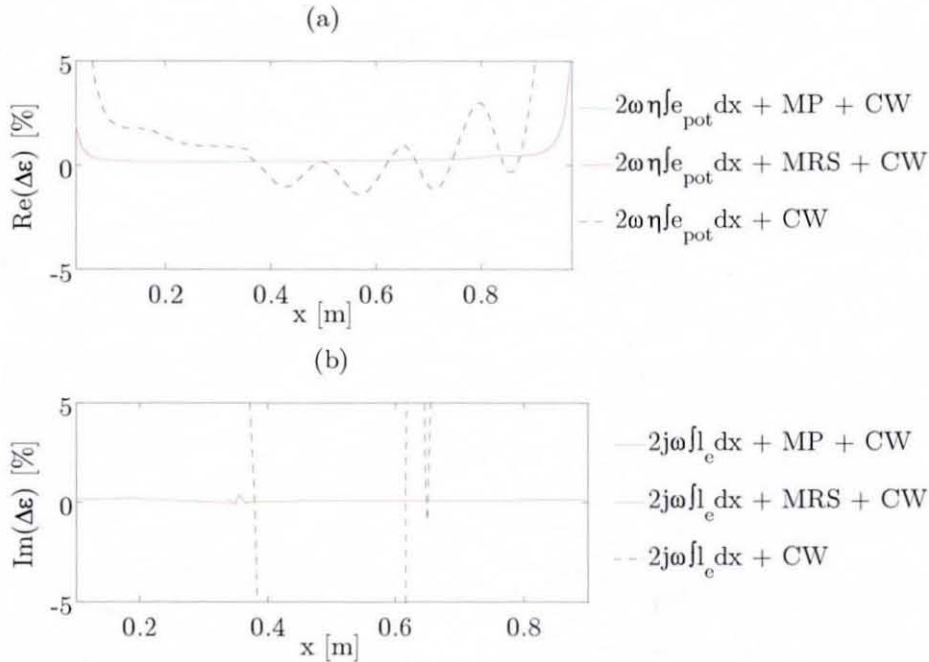


**Figure 6.35** Relative error of determined VEF from the incremental energy density integration method of the simply supported beam displacement shown in Figure 6.27: (a) relative active flow error, (b) relative reactive flow error.



diminished simply by integrating from the left-hand side and the right-hand side of the beam separately, rather than integrating from one beam side only as carried out with the periodised beam displacements. The relative error made by the periodised beam displacement is within an acceptable range, however, increases towards the beam's ends due to zero division.

### 6.3.2 Vibrational Energy Flow Including Noise

This section deals with the analysis of VEF in a simply supported beam when noise contamination is present. As carried out in section 6.2.3 normally distributed random noise will be added to the synthetic simply supported beam displacement signal. Both, the ideal 2D filter and the oval 2D Butterworth filter will be investigated.

It was shown in chapter 3 that VEF within a finite structure depends on the internal energy dissipation process only if non-dissipative boundaries are assumed and losses due to sound radiation are neglected. Thus, in contrast to VEF within an infinite structure, vibrational energy can only be injected into a finite structure if the injected energy will be dissipated somewhere in the structure. VEF within a damped finite beam is also a function of the loss factor  $\eta$ , as demonstrated in section 5.4.3, and VEF can only be computed if damping is included, since in a pure standing wave environment no net energy flow occurs. Hence, the amount of damping controls the amount of vibrational energy to be dissipated or transmitted within the volume of interest. In a simply supported structure the transmitted energy is at most at the excitation location and zero at the non-dissipative boundaries. The dissipated vibrational energy behaves vice versa. Thus, one can build a hypothetical model relating the VEF within finite structures to decaying travelling waves, which cause a decaying energy flow. It can be realised that these hypothetical decaying travelling waves are very small compared to the total standing wave displacement. If the total displacement signal is contaminated by noise then the ratio of the noise floor to the amplitude of the hypothetical decaying travelling waves is crucial to the accuracy of the VEF computation of the finite structure. If the level of



noise within the displacement signal is the same or even more than the amplitude of the decaying travelling waves, VEF within a finite structure cannot be computed. VEF computation is only feasible when the amount of noise is less than the decaying wave amplitude.

For this reason, a sensitivity study on the numerical VEF computation of noise contaminated simply supported beam displacements at different levels of damping and noise is carried out. To assess the sensitivity of the VEFESPI method an indicator is introduced, which allows for the assessment of the ratio between structural damping and noise contamination. This indicator is the product of the loss factor and the SNR, i.e.  $\eta \times \text{SNR}$ .

Two different levels of damping and noise will be considered. These levels are similar to the amount of damping and noise to be expected during the simply supported beam experiment. Different levels of damping are represented herein by different loss factors and different levels of noise are represented herein by different SNR's. Thus, VEF is computed at a loss factor setting of  $\eta = 5 \cdot 10^{-3}$  and  $\eta = 2.5 \cdot 10^{-2}$  and at a SNR setting of approximately  $\text{SNR} \approx 50$  and  $\text{SNR} \approx 1000$ .

### 6.3.2.1 Ideal 2D Spectral Filtering

As demonstrated in section 6.2.2 filtering of noise contaminated data is indispensable if one computes VEF from measured displacements. As mentioned, the effect of spectral noise amplification in the wavenumber domain needs to be reduced. Also here, the relative MSE function, as given in equation 6.7, is employed in order to compute optimum filter parameters.

Figure 6.36 displays the 6<sup>th</sup> mode displacement of a simply supported beam displacement that was noise contaminated by a SNR of 50. The beam was excited at the 6<sup>th</sup> mode with an excitation frequency of  $f_0 = 838.3$  Hz using a unity force and a hysteretic loss factor of  $\eta = 5 \cdot 10^{-3}$ . The excitation location was applied off-centre at  $x_0 = 0.4167$  m. Figure 6.37 displays the respective wavenumber spectrum. Clearly, two spikes representing the superposition of right travelling infinite wave and right travelling reflected wave and analogously for the left-hand side can be seen.

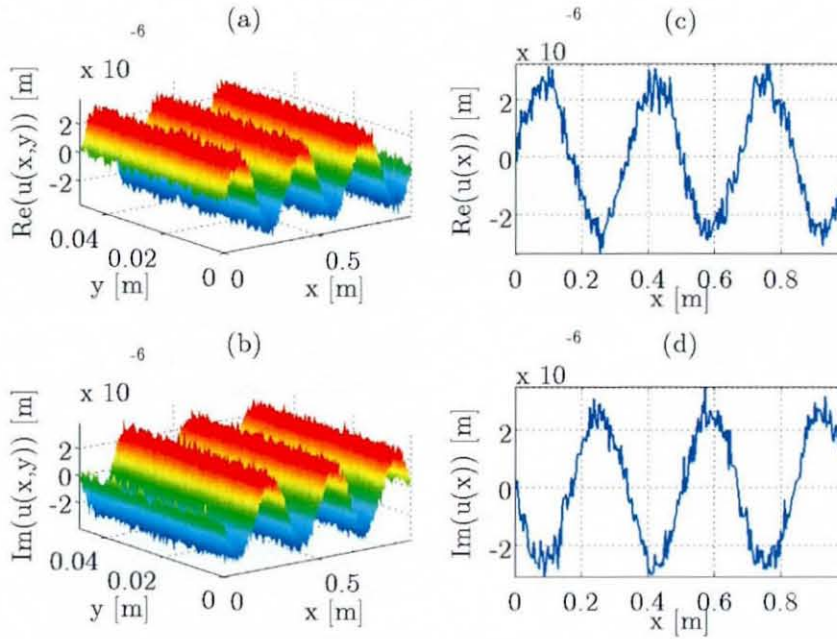


**Figure 6.36** Noise contaminated displacement of Figure 6.23 with  $\text{SNR} = 50$  &  $\eta = 5 \cdot 10^{-3}$ : (a) 2D real part, (b) 2D imaginary part, (c) 1D real part, (d) 1D imaginary part.

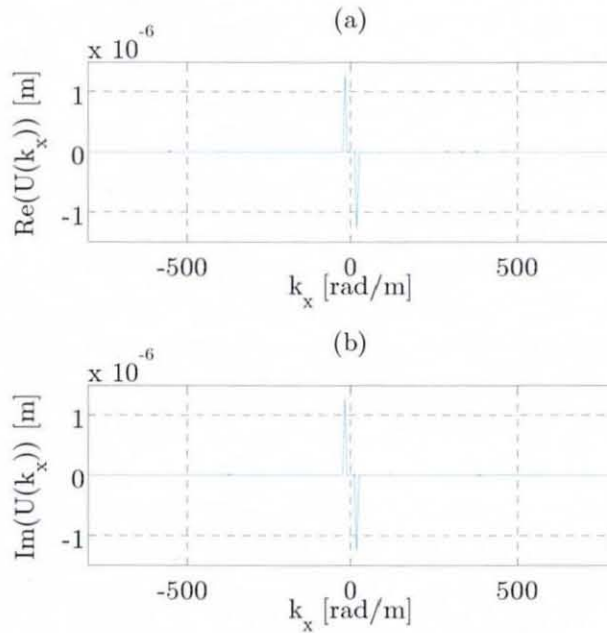


**Figure 6.37** Wavenumber spectrum of the displacement shown in Figure 6.36: (a) real part, (b) imaginary part.

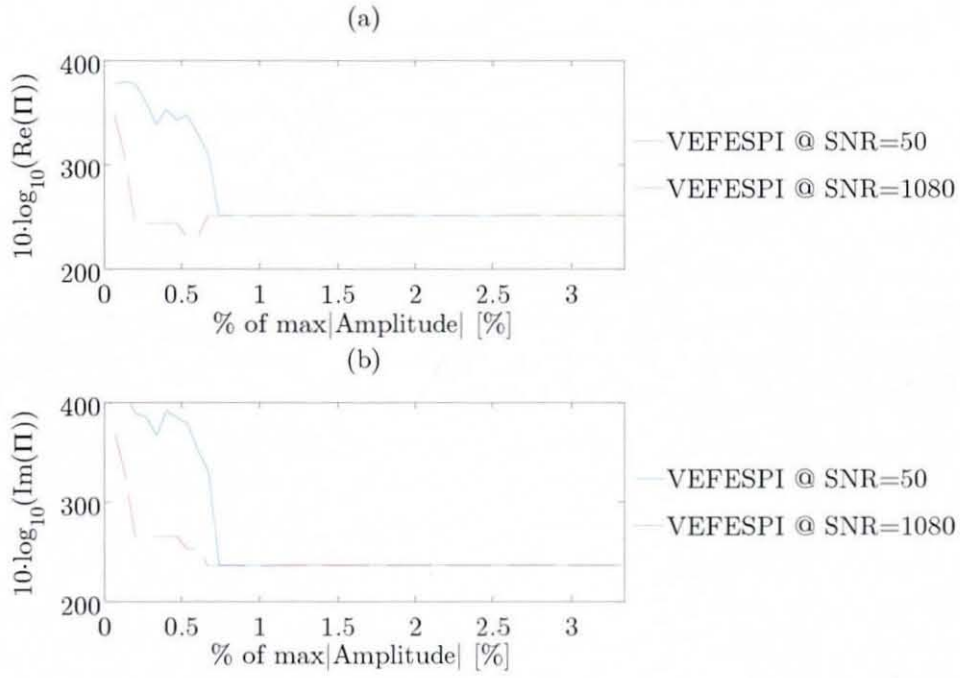
Figure 6.38 displays the complex relative MSE obtained when determining VEF of the noise contaminated 6<sup>th</sup> mode displacement at two different levels of noise by using the ideal filter. It can be seen in comparison to the infinite beam MSE that a much larger error occurs when filtering the simply supported beam spectrum. As expected the optimum filter cut-off point, % of  $\max|\text{Amplitude}|$ , decreases with increasing product of  $\eta \times \text{SNR}$ , since the level of noise decreases.

Figure 6.39 displays the ideal filtered VEF at the optimum cut-off points. It is evident from Figure 6.39 that the filtered transmitted energy cannot be computed at  $\eta \times \text{SNR} \approx 0.25$  where a straight line occurs. At  $\eta \times \text{SNR} \approx 5.4$  some improvement in VEF computation can be realised however, the sharp VEF discontinuity at excitation location cannot be computed. The reactive VEF cannot be computed for both settings of  $\eta \times \text{SNR}$ .

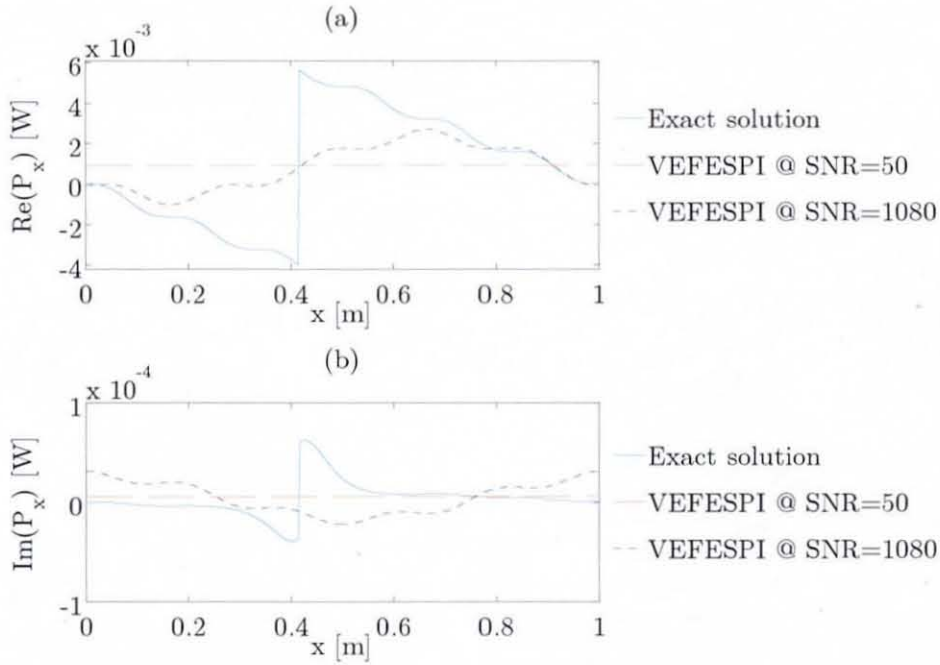
Figure 6.40 displays the complex relative MSE made when computing VEF from a beam displacement, as shown in Figure 3.36, however, damped with  $\eta = 2.5 \cdot 10^{-2}$ . It can be seen from Figure 6.40 that the MSE has slightly decreased when comparing to Figure 6.38.

Figure 6.41 shows the ideal filtered active and reactive VEF. It is evident from this figure that with increasing damping the sensitivity of the VEFESPI method decreases. At  $\eta = 2.5 \cdot 10^{-2}$  &  $\text{SNR} = 59$  ( $\eta \times \text{SNR} \approx 1.5$ ) a much better match in active VEF could be computed than at  $\eta = 5 \cdot 10^{-3}$  &  $\text{SNR} = 1080$  ( $\eta \times \text{SNR} \approx 5.4$ ), despite the latter combination was determined at a higher product of  $\eta \times \text{SNR}$ . Unfortunately also here, the reactive VEF cannot be computed well from noise contaminated simply supported beam displacements when filtering by an ideal 2D filter. This might be due to the fact that the noise floor amplitude is still much higher than the amplitude of the decaying nearfield waves. However, a further increase in structural damping ( $\eta = 5 \cdot 10^{-2}$ ) revealed that the reactive energy flow may be computed with a much better match than shown in Figures 6.39 and 6.41.





**Figure 6.38** Relative MSE of ideal filtered VEF of the simply supported beam displacement shown in Figure 6.36 at  $\eta = 5 \cdot 10^{-3}$ : (a) real MSE, (b) imaginary MSE.



**Figure 6.39** Exact and ideal filtered VEF of the simply supported beam displacement shown in Figure 6.36 at  $\eta = 5 \cdot 10^{-3}$ : (a) active energy flow, (b) reactive energy flow.

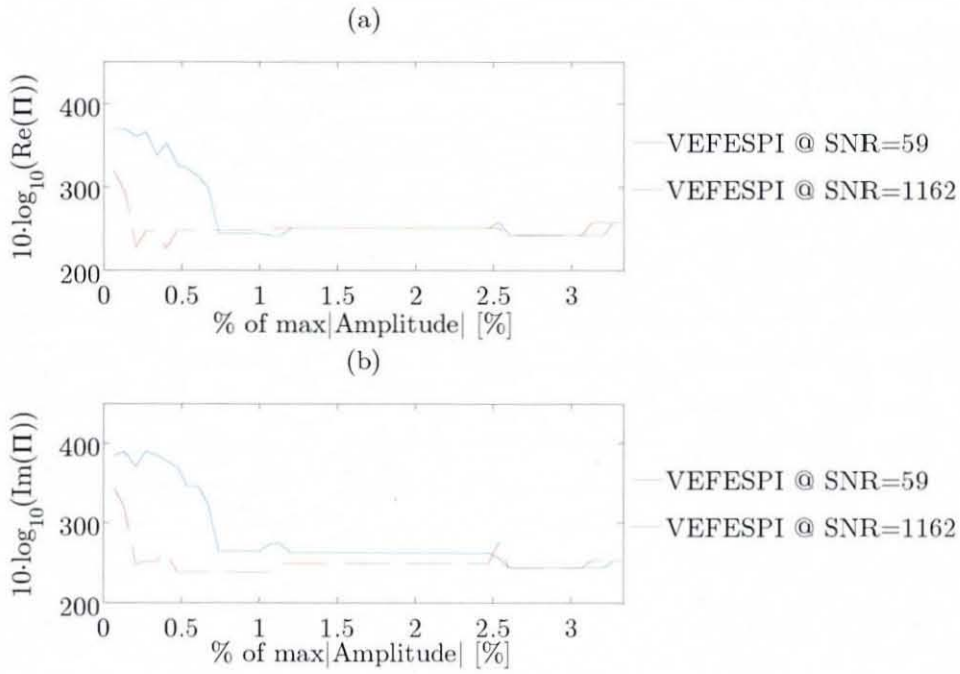


**Figure 6.40** Relative MSE of ideal filtered VEF of the simply supported beam displacement shown in Figure 6.36 at  $\eta = 2.5 \cdot 10^{-2}$ : (a) real MSE, (b) imaginary MSE.

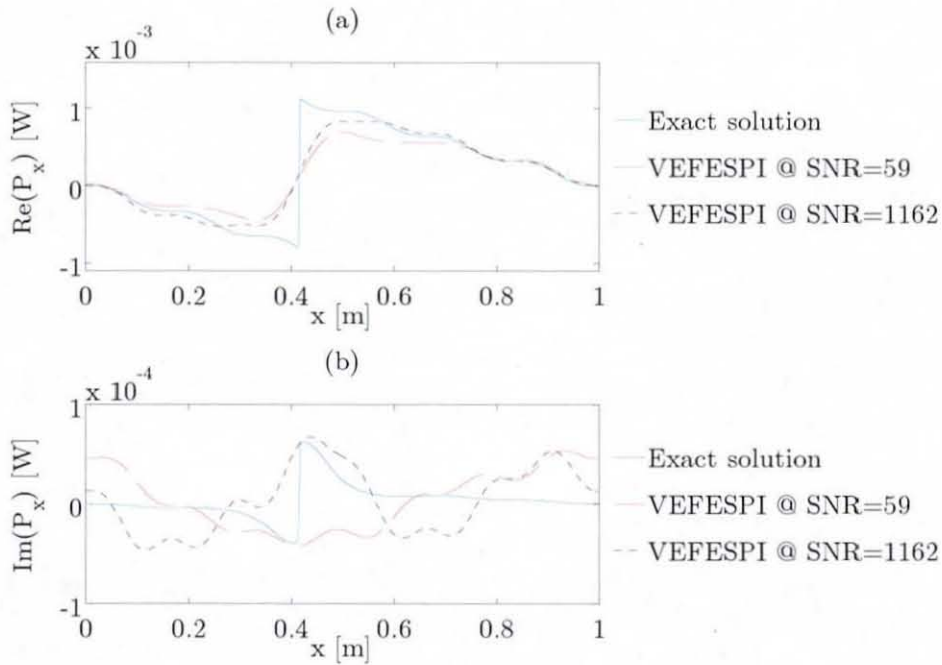


**Figure 6.41** Exact and ideal filtered VEF of the simply supported beam displacement shown in Figure 6.36 at  $\eta = 2.5 \cdot 10^{-2}$ : (a) active energy flow, (b) reactive energy flow.

In the previous section it was shown that odd-numbered mode shapes cause spectral leakage. Thus, wrong spatial frequencies appear in the wavenumber spectrum. It has also been shown that in the case of non-noisy data this effect can be diminished by applying one of the periodisation techniques, introduced earlier. The question, how the periodisation techniques have an effect on the VEF computation of noise contaminated and periodised odd-numbered mode shapes will be investigated next. Thus, a simply supported beam displacement, as shown in Figure 6.27, contaminated by normally distributed noise with a SNR of 109.9 and damped at  $\eta = 2.5 \cdot 10^{-2}$  is studied. The odd-numbered mode displacement is periodised by the MP and MRS method in order to reduce spatial leakage. The result of the periodisation is shown in Figure 6.42. Ideal filtered VEF of these periodised displacements is determined and compared with VEF computed straight from the 7<sup>th</sup> mode displacement without applying a periodisation. Figure 6.43 displays the

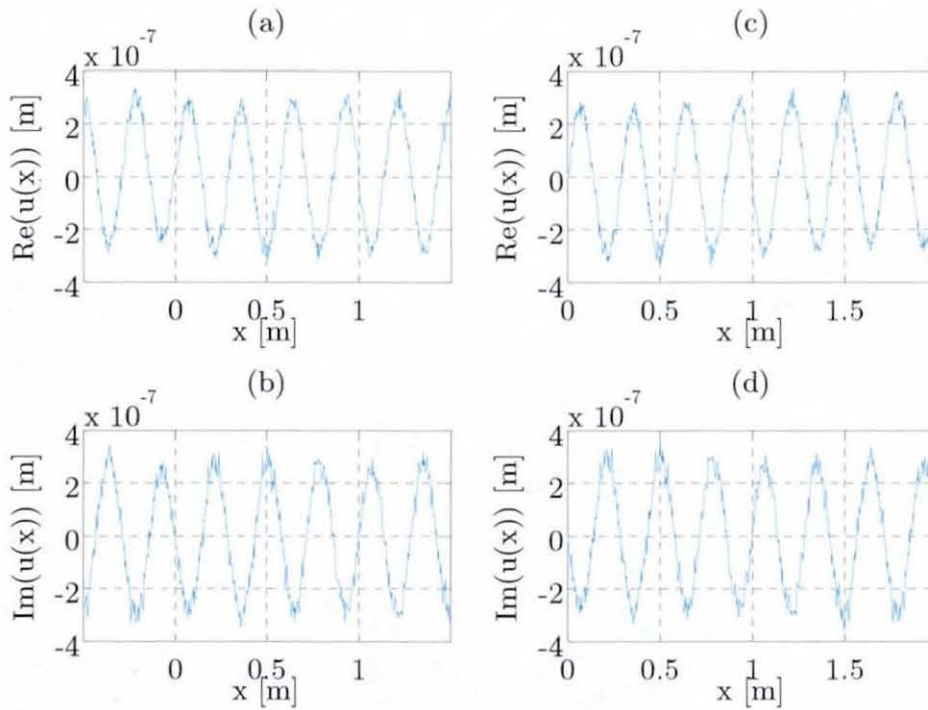


**Figure 6.42** MP and MRS periodised noise contaminated beam displacement shown in Figure 6.27: (a) real part MP, (b) imaginary part MP, (c) real part MRS, (d) imaginary part MRS.

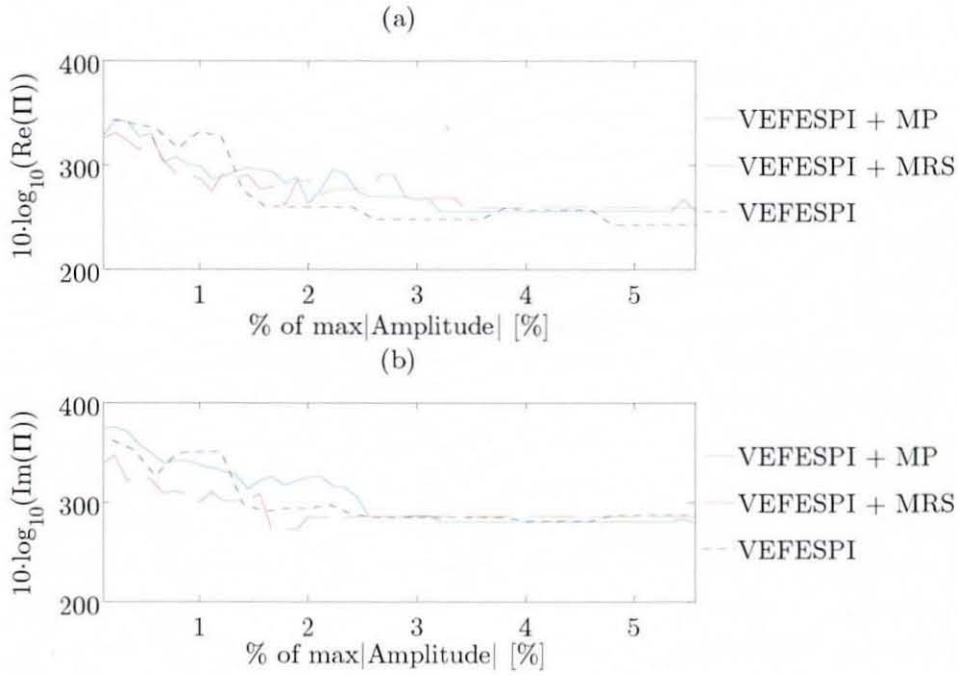


**Figure 6.43** Relative MSE of ideal filtered VEF of the simply supported beam displacement shown in Figure 6.42: (a) active MSE, (b) reactive MSE ( $\eta = 2.5 \cdot 10^{-2}$ ).

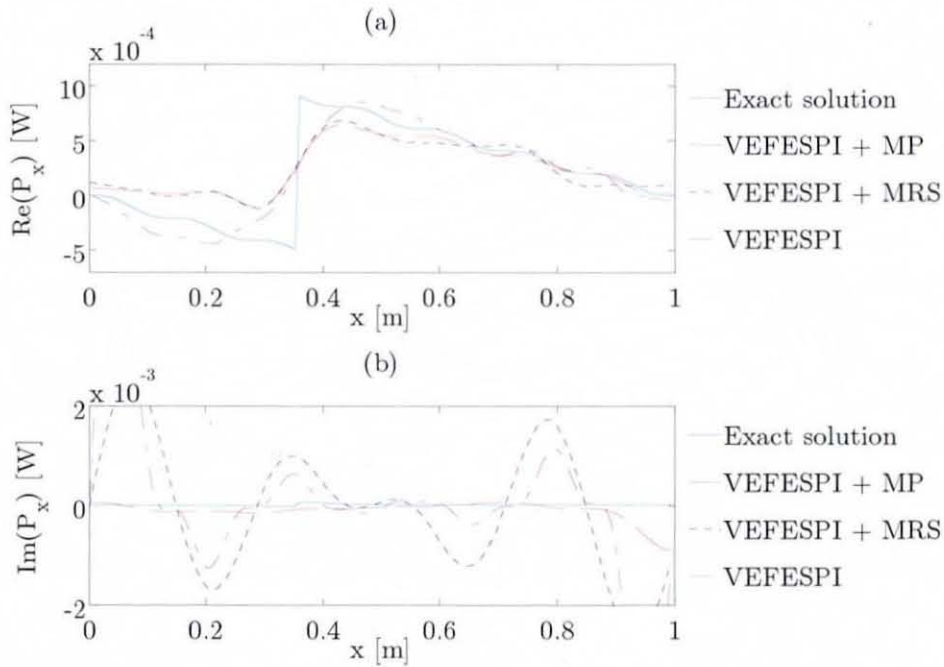


**Figure 6.44** Exact and ideal filtered VEF of the simply supported beam displacement shown in Figure 6.42: (a) active energy flow, (b) reactive energy flow ( $\eta = 2.5 \cdot 10^{-2}$ ).



complex relative MSE made when numerically computing VEF. In comparison to Figure 6.40 it can be seen that the relative MSE of the reactive VEF is much larger than analysing even-numbered mode shapes.

Figure 6.44 shows the real and imaginary energy flow. It can be noticed that odd-numbered mode shape displacements cause a larger error in the transmitted energy analysis than the analysis of even-numbered mode shape displacements. Especially the reactive energy cannot be detected with a great deal of accuracy. It can also be realised that the periodisation of the non-periodic beam displacement and subsequent ideal filtering does not yield to significant improvement, as initially expected. Interestingly, the error made when analysing the non-periodic and odd-numbered mode shape displacement is less than the error made using the periodisation techniques.

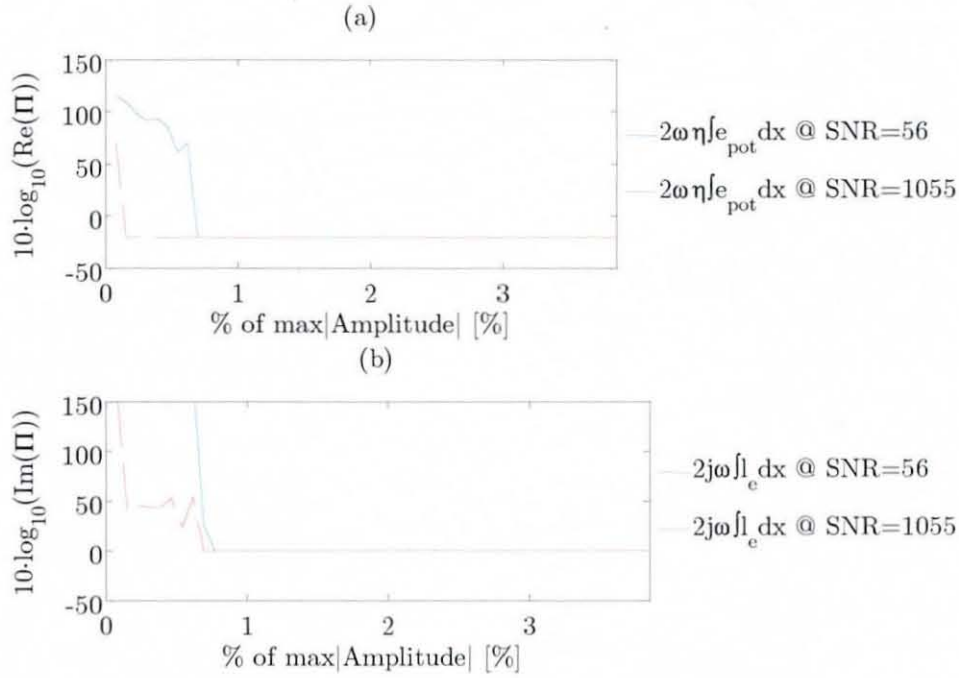
Finally, the above investigated 6<sup>th</sup> and 7<sup>th</sup> mode beam displacements are also used to compute VEF by using the incremental energy density integration method, as shown by equations (6.8) and (6.9). Also here, a sensitivity study is carried out by employing different damping and SNR settings.

Figure 6.45 displays the relative MSE made when computing VEF within a low damped simply supported beam displacement, as shown in Figure 6.36, which was contaminated by two different levels of noise. The IEDI method was employed. It can be seen that the active MSE is much less than the active MSE shown in Figure 6.38.

Figure 6.46 shows the IEDI computed VEF of the beam displacement shown in Figure 6.36. It is evident from this figure that the integrated active energy flow matches very well with the exact solution at each noise level. This surprising result can be explained by the fact that the IEDI method utilises 2<sup>nd</sup> order spatial derivatives, whereas the conventional VEFESPI method utilises spatial derivatives up to the 3<sup>rd</sup> order as defined by equation (3.33). Unfortunately, the computed reactive VEF is not a good match to the exact reactive VEF, but in close region.

Figures 6.47 and 6.48 display the MSE made and the IEDI computed VEF, respectively, when analysing the 6<sup>th</sup> mode beam displacement, as shown in Figure 6.36, however, damped with  $\eta = 2.5 \cdot 10^{-2}$ . It can be seen that the





**Figure 6.45** Relative MSE of ideal filtered VEF from the incremental energy density integration method of the beam displacement shown in Figure 6.36 at  $\eta = 5 \cdot 10^{-3}$ : (a) real MSE, (b) imaginary MSE.

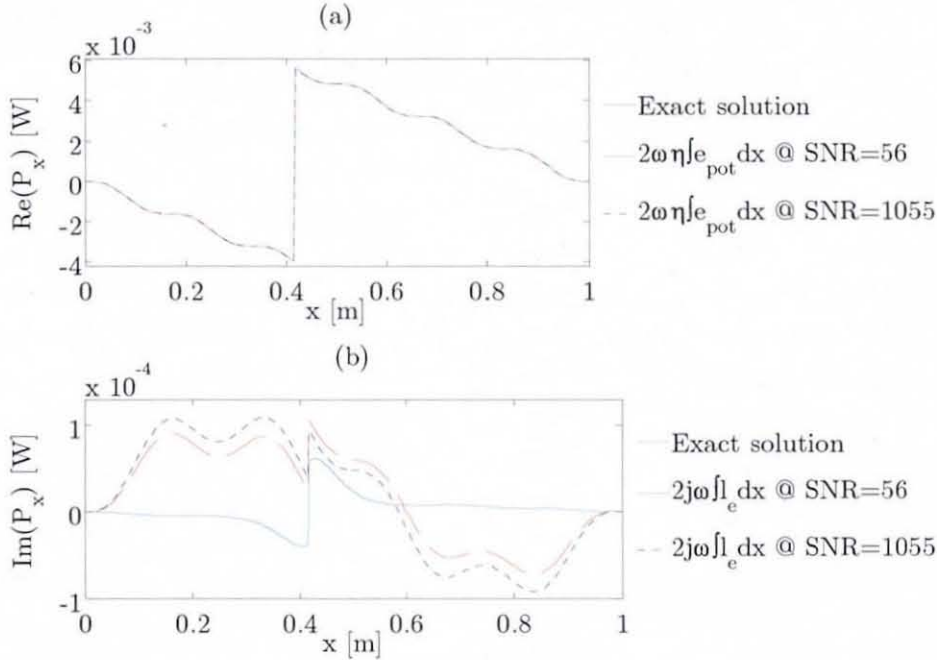


**Figure 6.46** Exact VEF and ideal filtered VEF from the incremental energy density integration method of the beam displacement shown in Figure 6.36 at  $\eta = 5 \cdot 10^{-3}$ : (a) active energy flow, (b) reactive energy flow.

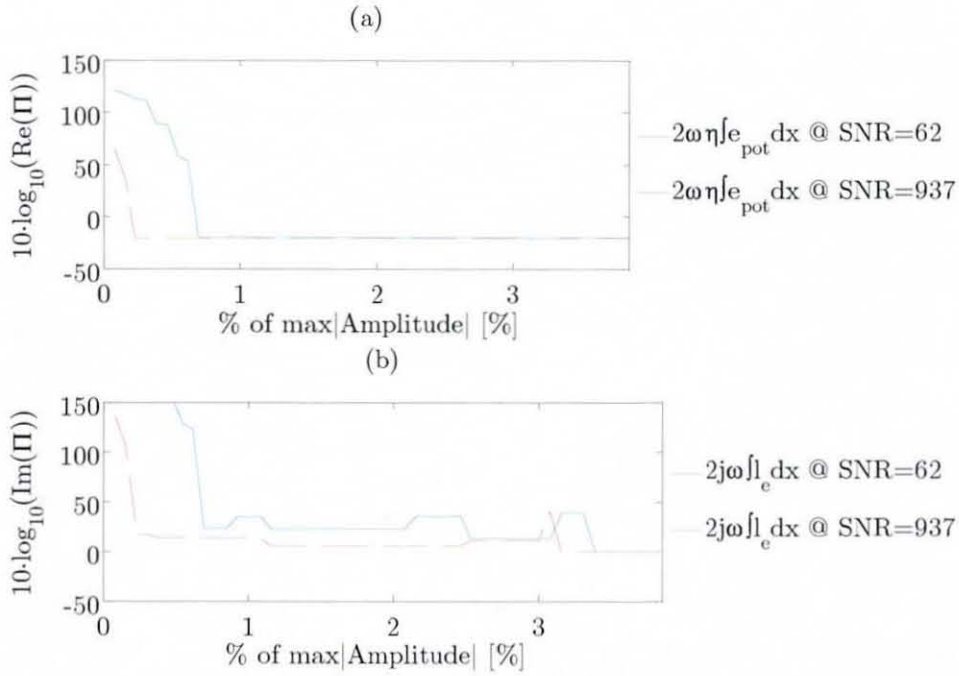


**Figure 6.47** Relative MSE of ideal filtered VEF from the incremental energy density integration method of the beam displacement shown in Figure 6.36 at  $\eta = 2.5 \cdot 10^{-2}$ : (a) real MSE, (b) imaginary MSE.

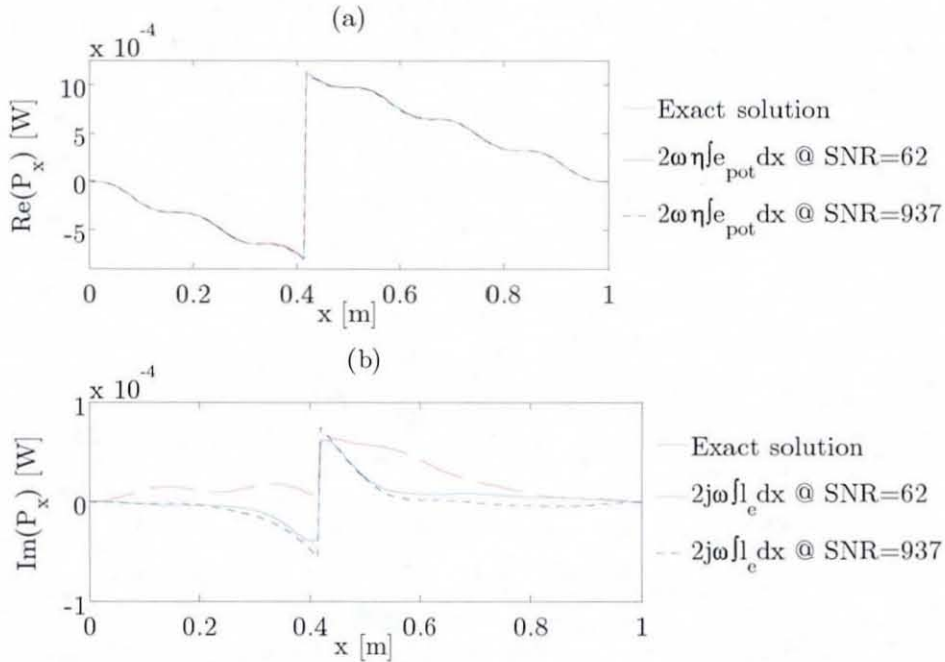


**Figure 6.48** Exact VEF and ideal filtered VEF from the incremental energy density integration method of the beam displacement shown in Figure 6.36 at  $\eta = 2.5 \cdot 10^{-2}$ : (a) active energy flow, (b) reactive energy flow.

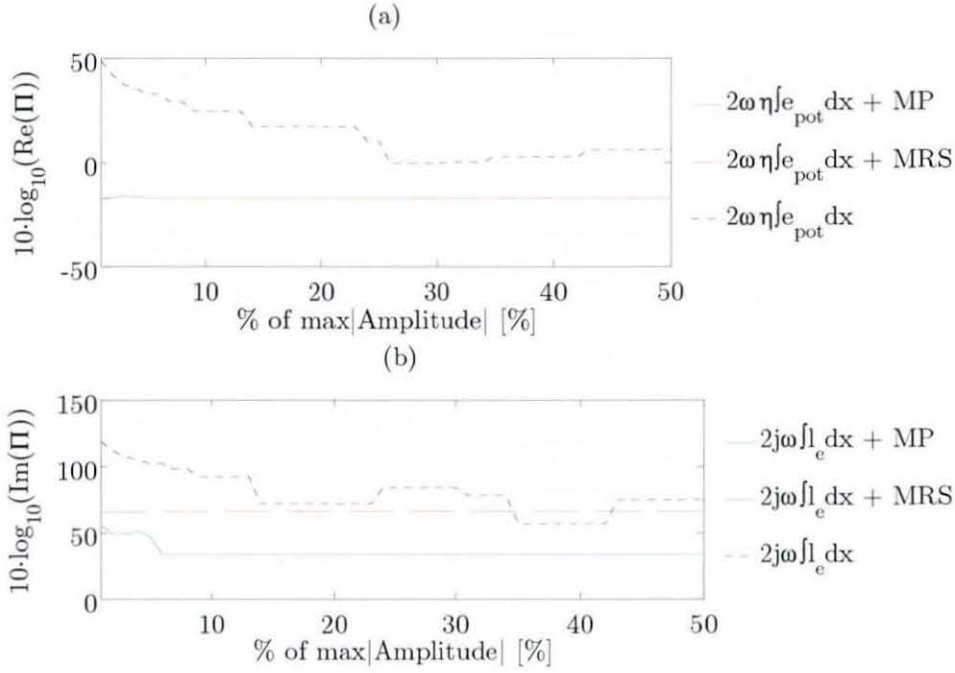
active and reactive energy flow computation has improved significantly. Even at the very high noise contaminated beam displacement, the reactive VEF could be computed within a reasonable range of accuracy. Also here, the active VEF was computed very accurately at both levels of noise contamination. Thus, the reactive flow sensitivity of the IEDI method decreases with increasing structural damping. However, the active flow sensitivity of the IEDI method is always very low. At each combination of damping and noise excellent matches of active VEF could be obtained. Here, the conventional VEFESPI method failed to provide acceptable results.

The IEDI method was also applied to the computation of VEF from odd-numbered mode shape displacement, as shown in Figure 6.27, however, contaminated by normally distributed noise. Analogously to the previous given example, the MP and MRS periodisation techniques were employed. The 7<sup>th</sup> mode simply supported beam displacement was noise contaminated with a SNR of 109.9 and the structural damping considered was  $\eta = 2.5 \cdot 10^{-2}$ .

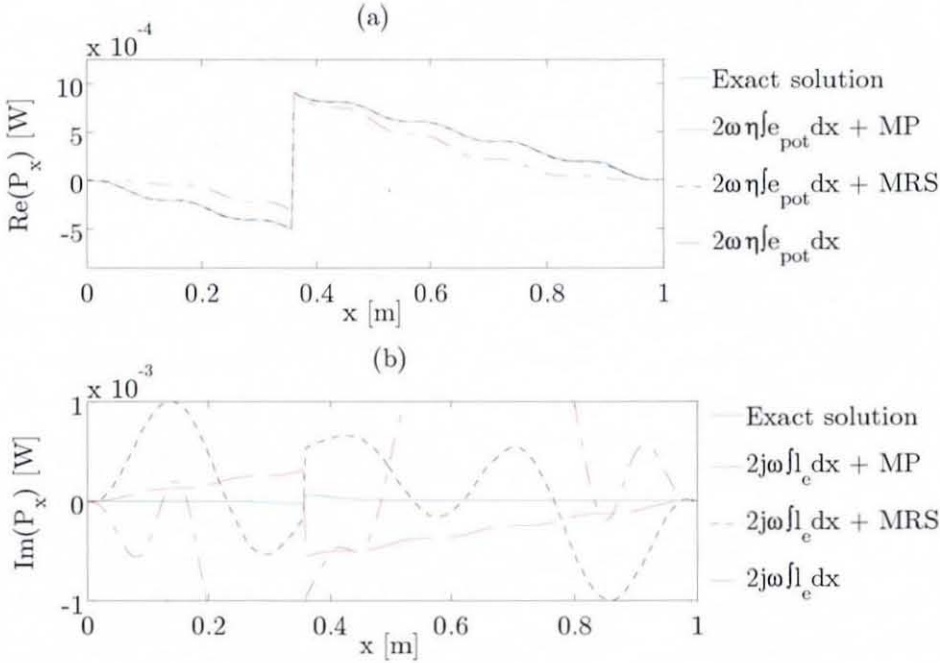
Figure 6.49 displays the complex relative MSE made when computing VEF from a noisy, non-periodic simply supported beam displacement. It can be realised from Figure 6.49 that the MP and MRS periodisation techniques reduce the active MSE. It can be seen further from Figure 6.49 that the MP technique produced the lowest reactive MSE.

Figure 6.50 displays the ideal filtered VEF when using the IEDI method. It can be noticed from Figure 6.50 that the periodisation techniques improve the computation of active VEF enormously. In comparison to Figure 6.44 periodisation of the beam displacement does yield to a more accurate active VEF computation when employing the IEDI method. Unfortunately, the computation of reactive VEF cannot be undertaken within an acceptable range of accuracy for all three techniques employed.

Interestingly, the application of the IEDI method reduced the sensitivity of the VEF computation. It should be mentioned that the IEDI method is part of the VEFESPI method, since spatial derivatives up to the 2<sup>nd</sup> order are used. However, subsequently the VEF is computed from incremental energy density integration along the beam axis rather than employing equation (3.33).



**Figure 6.49** Relative MSE of ideal filtered VEF from the incremental energy density integration method of the simply supported beam displacement shown in Figure 6.42: (a) active MSE, (b) reactive MSE ( $\eta = 2.5 \cdot 10^{-2}$ ).



**Figure 6.50** Exact VEF and ideal filtered VEF from the incremental energy density integration method of the simply supported beam displacement shown in Figure 6.42: (a) active energy flow, (b) reactive energy flow ( $\eta = 2.5 \cdot 10^{-2}$ ).



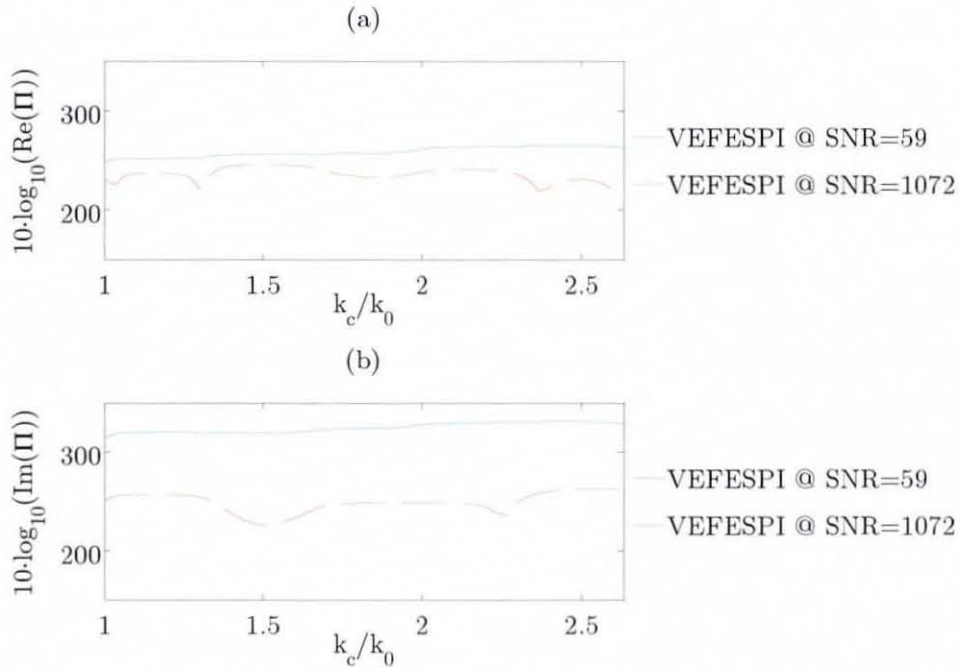
### 6.3.2.2 Oval 2D Spectral Butterworth Filtering

To study the effect of Butterworth filtering on the computation of VEF within noise contaminated simply supported beams, the same displacements as used in the previous section are analysed.

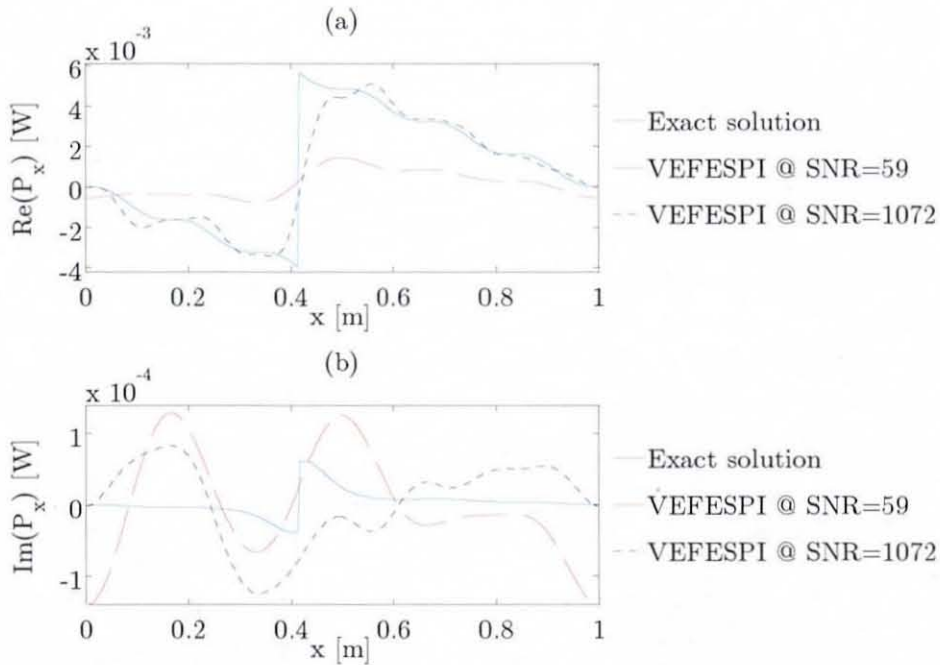
Figure 6.51 displays the complex relative MSE of the noise contaminated 6<sup>th</sup> mode beam displacement, as shown in Figure 6.36, at different levels of noise and damped with  $\eta = 5 \cdot 10^{-3}$ . Here, an oval 2D Butterworth filter was applied in the wavenumber domain. It can be noticed that the active MSE made is slightly less than the active MSE made when filtering by the ideal filter. The reason that only cut-off wavenumbers above  $1.0 \cdot k_0$  are shown is that below  $1.0 \cdot k_0$  the MSE approaches zero. Since an automatic detecting algorithm was employed in the code, minimum cut-off wavenumbers below  $1.0 \cdot k_0$  would have been detected. This is a disadvantage of the logarithmic MSE, which needs additional care if positive MSE's occur. Furthermore, due to strong variations in MSE computation only a small plausible normalised cut-off wavenumber range was investigated.

Figure 6.52 displays the respective active and reactive Butterworth filtered VEF at  $\eta = 5 \cdot 10^{-3}$ . When comparing Figure 6.52 with Figure 6.39 it can be noticed that the Butterworth filter produces a better filtered active energy flow than the ideal filter. This is due to the fact that the Butterworth filter includes the whole spectral nearfield information below the cut-off, wavenumber, whereas the ideal filter filters out some spectral nearfield points, which are located at low wavenumbers. However, a good agreement of transmitted energy at excitation location cannot be obtained. Also, the filtered reactive energy flow at excitation location is not in a good agreement with the exact solution. However, moving the cut-off frequency to lower locations might improve the reactive VEF curve shape.

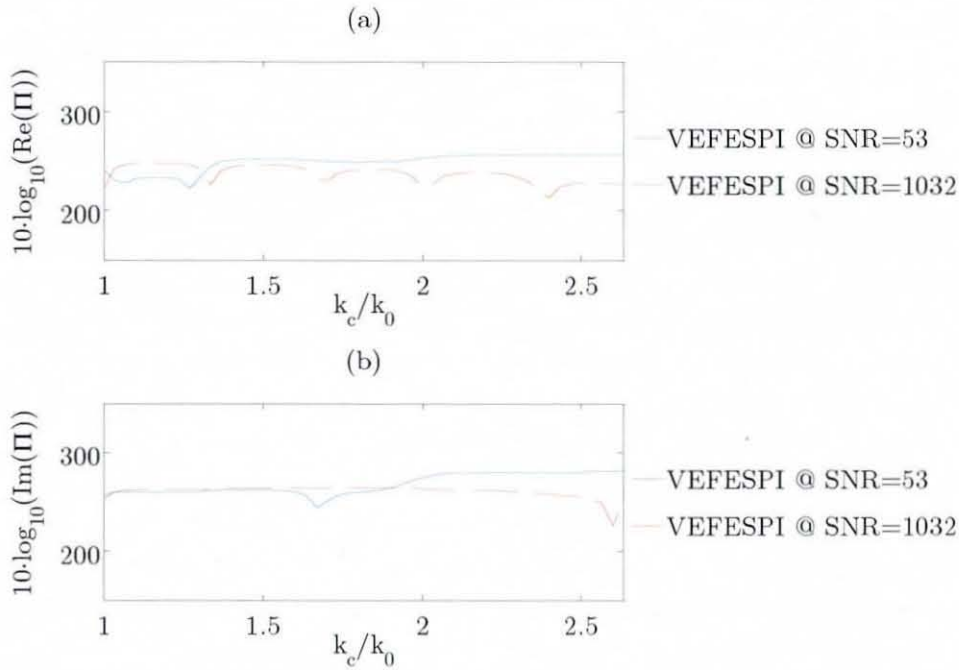
Figure 6.53 displays the relative MSE made when computing VEF from the noise contaminated 6<sup>th</sup> mode simply supported beam displacement, damped at  $\eta = 2.5 \cdot 10^{-2}$ . It can be seen that at the increased level of damping, the complex relative MSE decreases. Also, the optimum cut-off wavenumber has moved to higher wavenumber locations.



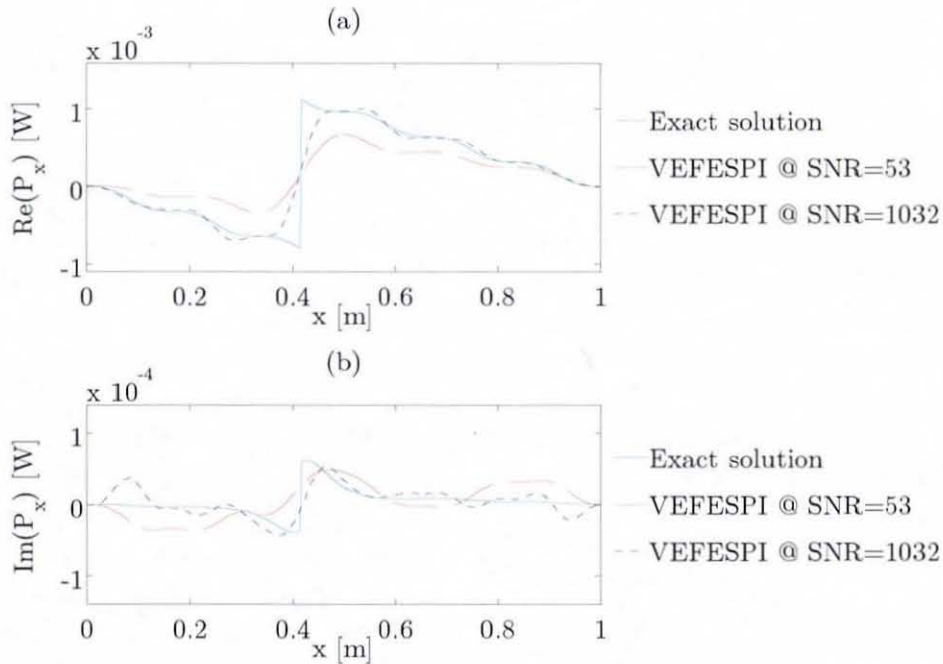
**Figure 6.51** Relative MSE of Butterworth filtered VEF of the simply supported beam displacement shown in Figure 6.36 at  $\eta = 5 \cdot 10^{-3}$ : (a) real MSE, (b) imaginary MSE.



**Figure 6.52** Exact and Butterworth filtered VEF of the simply supported beam displacement shown in Figure 6.36 at  $\eta = 5 \cdot 10^{-3}$ : (a) active energy flow, (b) reactive energy flow.



**Figure 6.53** Relative MSE of Butterworth filtered VEF of the simply supported beam displacement shown in Figure 6.36 at  $\eta = 2.5 \cdot 10^{-2}$ : (a) real MSE, (b) imaginary MSE.



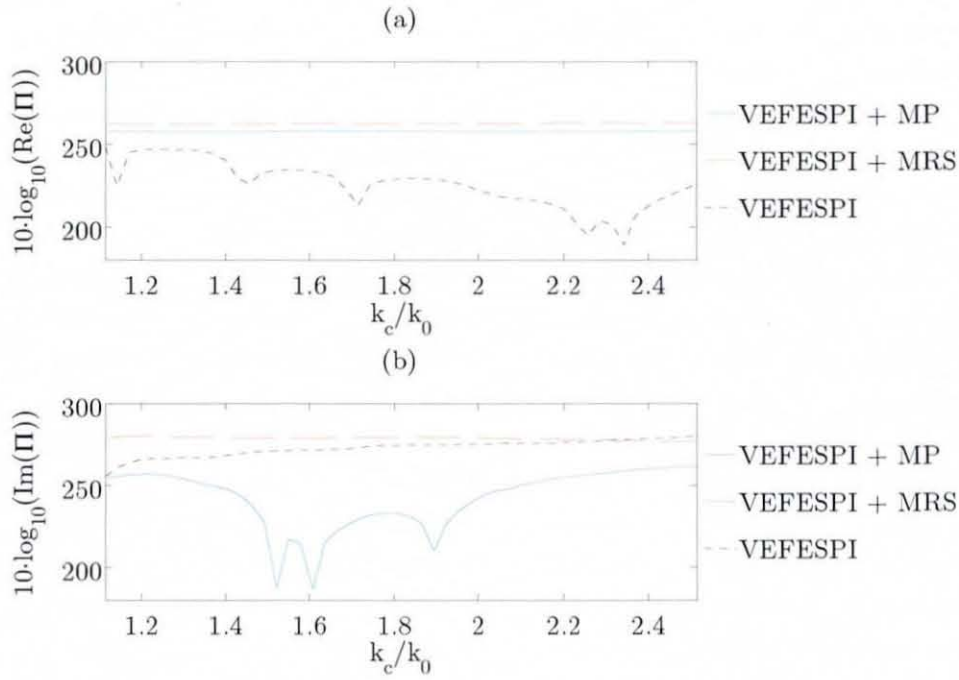
**Figure 6.54** Exact and Butterworth filtered VEF of the simply supported beam displacement shown in Figure 6.36 at  $\eta = 2.5 \cdot 10^{-2}$ : (a) active energy flow, (b) reactive energy flow.



Figure 6.54 displays the respective Butterworth filtered VEF. It can be realised that with increasing  $\eta \times \text{SNR}$  the VEF computation accuracy increases. Interestingly, a much better match between exact reactive and computed reactive VEF occurs, at both levels of damping. It should be mentioned that at  $\text{SNR} = 59$  and  $\eta = 2.5 \cdot 10^{-2}$  a better curve shape match between the exact VEF curve and the computed active VEF curve can be obtained, simply by moving the cut-off wavenumber to a higher position. However, the relative MSE made will increase. In general, it can be realised that the oval 2D Butterworth filter allows for a more accurate VEF computation within a simply supported beam. As expected, the sensitivity of the VEFESPI method decreases with increasing damping.

The noise contaminated 7<sup>th</sup> mode simply supported beam displacement, as partly shown in Figure 6.42, will also be investigated. Here, a SNR of 100.6 and a loss factor of  $\eta = 2.5 \cdot 10^{-2}$  were employed. As usual periodisation is carried out using the MP and MRS periodisation techniques. Figure 6.55 displays the relative MSE made when filtering by an oval 2D Butterworth filter.

Figure 6.56 exhibits the active and reactive transmitted energy within the simply supported beam that vibrated transversely at the 7<sup>th</sup> mode. It can be seen that a slight improvement of the Butterworth filtered active energy flow compared to the ideal filtered VEF could be achieved. However, still the reactive energy flow is in no good agreement with the exact value. This is due to the fact that spectral filtering erases valuable nearfield information in the wavenumber domain especially at  $k_x > k_c$ . Also, the sharp VEF discontinuity at the excitation location cannot be computed accurately. This means an accurate comparison to input energy measurements is hardly possible. The use of the periodisation techniques did not yield to any significant improvement in active VEF computation if filtering is included. This result is in contrast to the conclusions of reference [51]. Of course the leakage effect will be greater with fewer waves included in the signal. However, the spectral filtering process erased some spectral leakage components in the wavenumber domain. Thus, the effect of the periodisation techniques prior to filtering was less drastically.



**Figure 6.55** Relative MSE of Butterworth filtered VEF of the simply supported beam displacement shown in Figure 6.42: (a) active MSE, (b) reactive MSE ( $\eta = 2.5 \cdot 10^{-2}$ ).

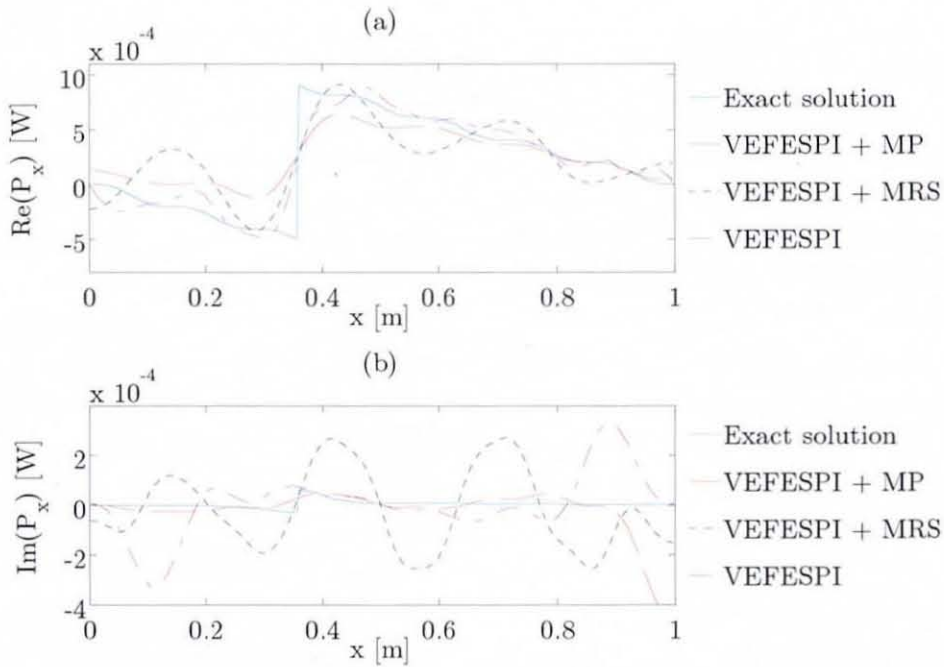


**Figure 6.56** Exact and Butterworth filtered VEF of the simply supported beam displacement shown in Figure 6.42: (a) active energy flow, (b) reactive energy flow ( $\eta = 2.5 \cdot 10^{-2}$ ).

Finally, the method of incremental energy density integration is also applied to the Butterworth filtered 6<sup>th</sup> and 7<sup>th</sup> mode displacements. Due to completeness reasons, a sensitivity study is also carried out by employing different damping and SNR settings.

Figures 6.57 and 6.59 show the complex relative MSE made when analysing the Butterworth filtered 6<sup>th</sup> mode simply supported beam displacement by the IEDI method at different levels of noise and damping. It is evident from both figures that the relative MSE made is much less than employing the conventional VEFESPI method (see Figures 6.51 and 6.53). Especially the active VEF error reduces drastically for all products of  $\eta \times \text{SNR}$ . The IEDI computed energy flows are shown in Figure 6.58 and 6.60, respectively. It can be noticed that at each product of  $\eta \times \text{SNR}$  good agreements between the exact active VEF and the computed active VEF can be achieved. The reactive VEF at  $\eta = 5 \cdot 10^{-3}$  &  $\text{SNR} = 59$  ( $\eta \times \text{SNR} \approx 0.295$ ) strongly deviates from the exact solution. However, at the remaining products of  $\eta \times \text{SNR}$  a relatively low erroneous reactive energy flow could be computed.

In the following, the IEDI method will also be applied to the computation of VEF from a non-periodic 7<sup>th</sup> mode simply supported beam displacement, partially shown in Figure 6.42.

If one compares Figures 6.61 and 6.62 with Figures 6.55 and 6.56, it can be realised that the IEDI method in combination with one of the periodisation techniques reduces the relative active MSE and, thus, improves the VEF computation of odd-numbered mode shape beam displacements. This could not be achieved by using the conventional VEF computation method where the direct analysis of the non-periodised beam displacement yielded to almost the same result as applying one of the periodisation techniques. However, the reactive energy flow is hard to compute, as shown by Figure 6.62(b).

It was shown herein that the application of the IEDI method reduced the noise sensitivity when computing VEF from noise contaminated simply supported beam displacements drastically. Especially the computation of active VEF is rather noise insensitive.



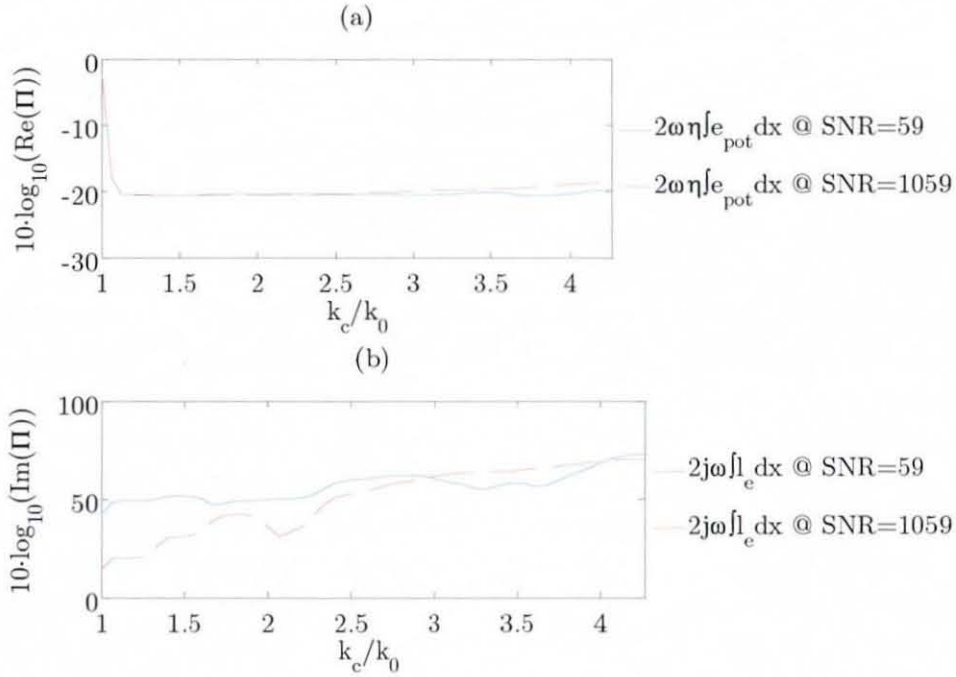


**Figure 6.57** Relative MSE of Butterworth filtered VEF from the incremental energy density integration method of the beam displacement shown in Figure 6.36 at  $\eta = 5 \cdot 10^{-3}$ ; (a) real MSE, (b) imaginary MSE.

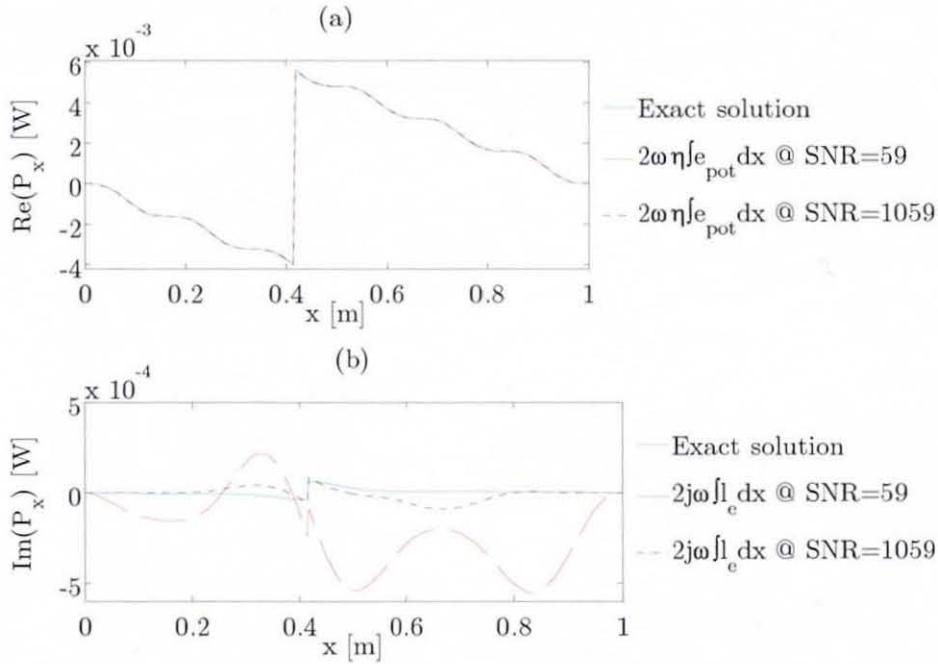


**Figure 6.58** Exact VEF and Butterworth filtered VEF from the incremental energy density integration method of the beam displacement shown in Figure 6.36 at  $\eta = 5 \cdot 10^{-3}$ ; (a) active energy flow, (b) reactive energy flow.

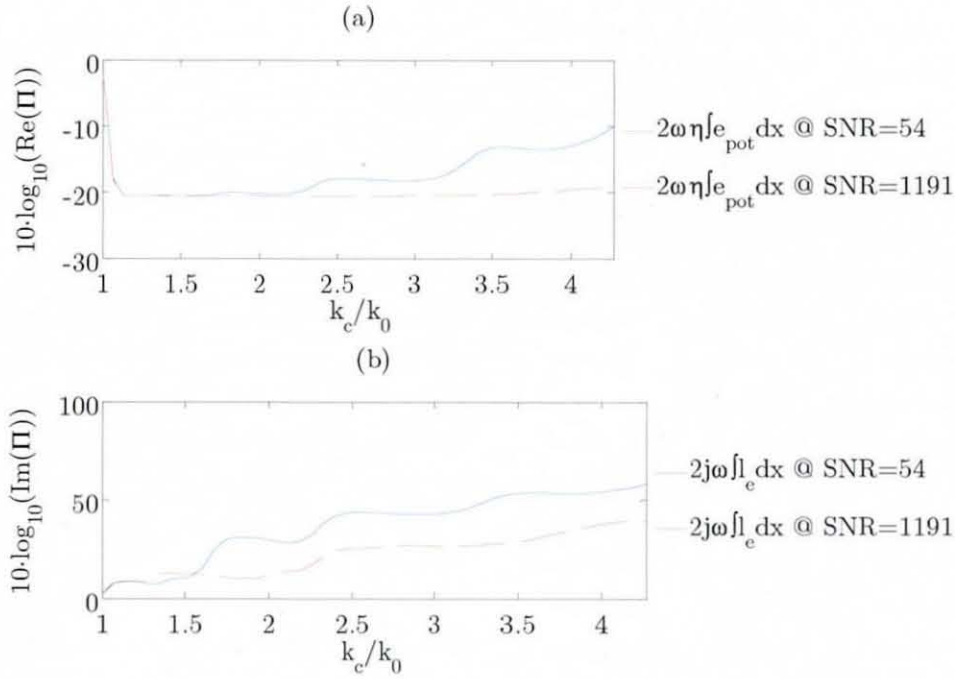


**Figure 6.59** Relative MSE of Butterworth filtered VEF from the incremental energy density integration method of the beam displacement shown in Figure 6.36 at  $\eta = 2.5 \cdot 10^{-2}$ : (a) real MSE, (b) imaginary MSE.

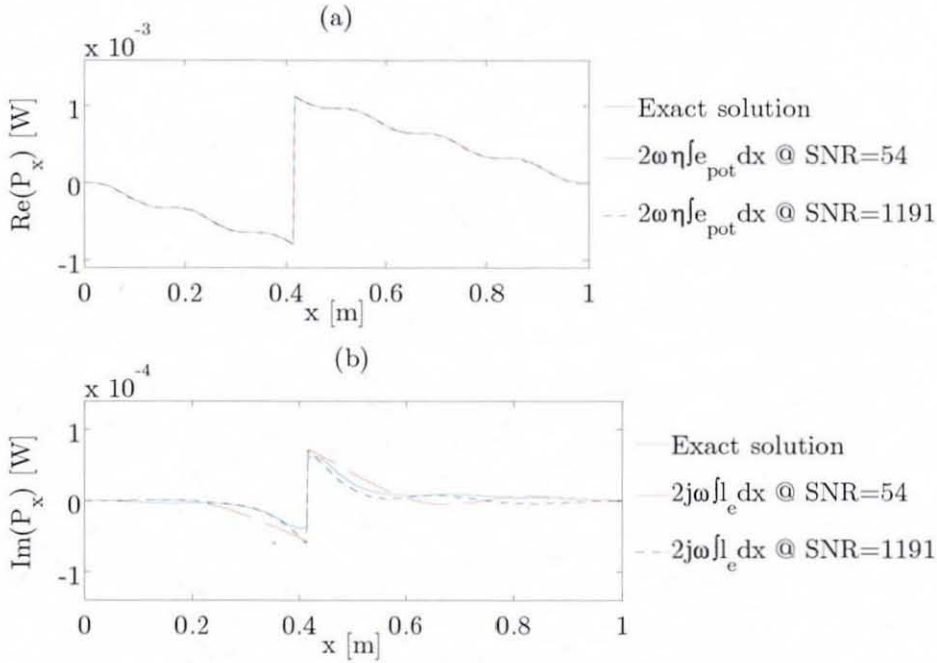


**Figure 6.60** Exact VEF and Butterworth filtered VEF from the incremental energy density integration method of the beam displacement shown in Figure 6.36 at  $\eta = 2.5 \cdot 10^{-2}$ : (a) active energy flow, (b) reactive energy flow.

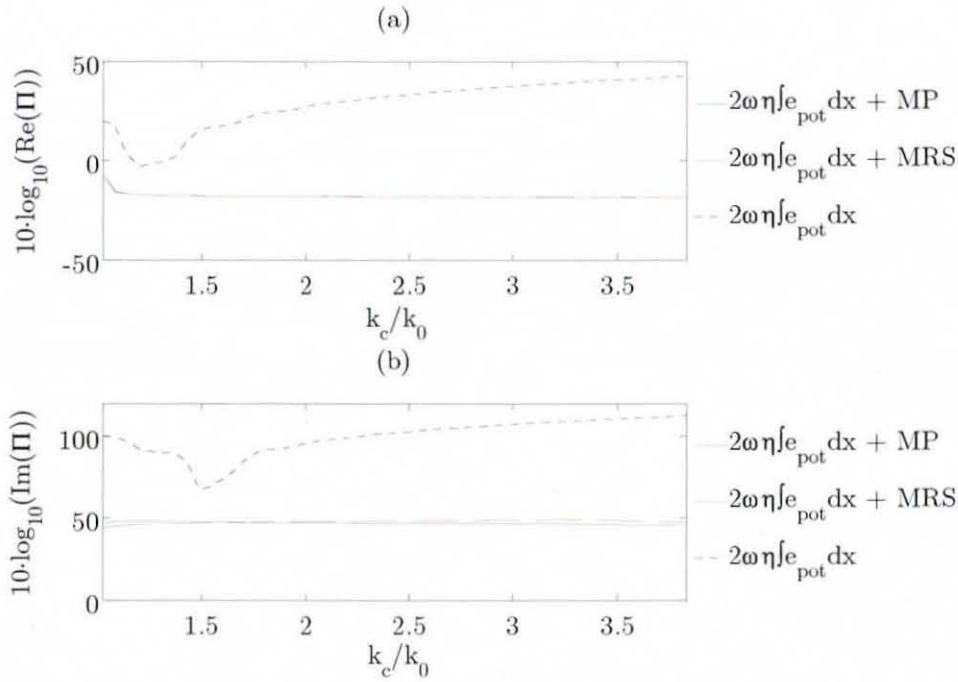


**Figure 6.61** Relative MSE of Butterworth filtered VEF from the incremental energy density integration method of the simply supported beam displacement shown in Figure 6.42: (a) active MSE, (b) reactive MSE ( $\eta = 2.5 \cdot 10^{-2}$ ).

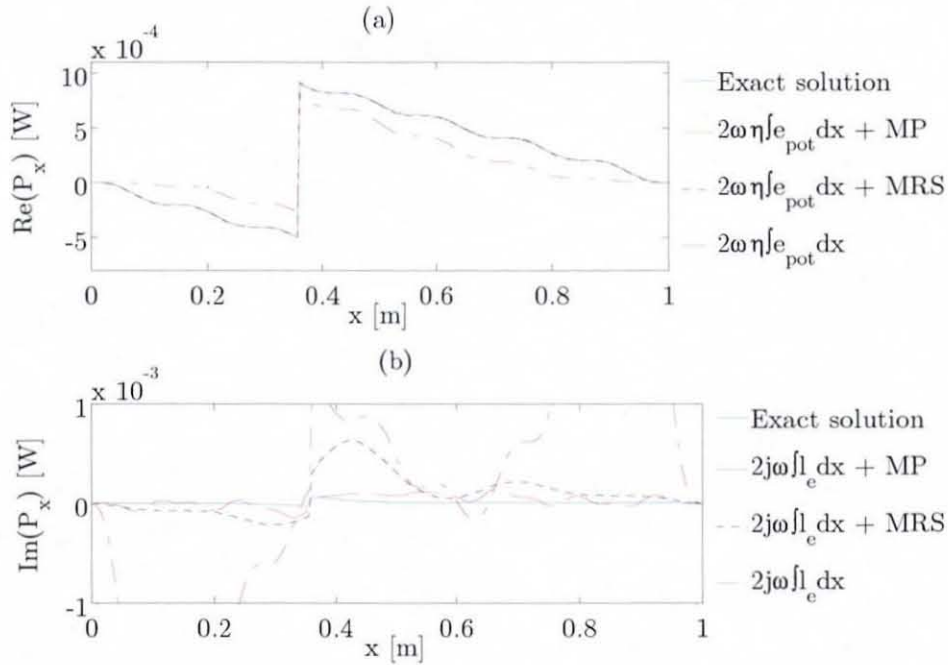


**Figure 6.62** Exact VEF and Butterworth filtered VEF from the incremental energy density integration method of the simply supported beam displacement shown in Figure 6.42: (a) active energy flow, (b) reactive energy flow ( $\eta = 2.5 \cdot 10^{-2}$ ).

### 6.3.3 Vibrational Energy Flow Including ESPI Noise

In section 6.2.4 it was shown that optical noise acquired by the ESPI system differs to artificial generated normally distributed noise. Also here, the MSE of computed VEF of the experimental simply supported beam structures will be predicted and possible optimum filter cut-off points are given. The MSE prediction and the optimum filter parameters for each excitation frequency are computed by superimposing extracted measured ESPI noise with an synthetically generated beam displacement as given by equation (5.37). Details about the beam experiment are presented in chapter 7. The measurement parameters are shown in the tables below.

$n$	6	8	9	11
$f_{0n}$	857 Hz	1467.5 Hz	1874 Hz	2772 Hz
$F_{0n}$	0.133 N	0.361 N	0.339 N	0.482 N
SNR	230.4	367.1	33.8	69.3
$\eta_n$	$6.337 \cdot 10^{-3}$	$8.705 \cdot 10^{-3}$	$8.295 \cdot 10^{-3}$	$1.405 \cdot 10^{-2}$

**Table 6.8** Vibration parameters of experimental non-layer damped simply supported beam.

The excitation location of all three beam structures was the same as applied during the ESPI experiment at  $x_0 = 0.583$  m. In Tables 6.8 to 6.10 the mode  $n$ , the excitation frequency of the ESPI experiment  $f_{0n}$ , the measured force magnitude, of the ESPI experiment  $F_{0n}$ , the SNR and the modal hysteretic loss factor  $\eta_n$  are given for each beam damping configuration. Herein, the beam was excited with the excitation frequency used during the ESPI experiment. The modal loss factor has been acquired from an experimental modal analysis applied at each beam structure using 10 measurement points that were equally distributed over the beam length [127].



$n$	6	8	9	11
$f_{0n}$	833.5 Hz	1441 Hz	1830.5 Hz	2745 Hz
$F_{0n}$	0.096 N	0.292 N	0.484 N	2.279 N
SNR	92.8	231.5	201.8	485.6
$\eta_n$	$1.657 \cdot 10^{-2}$	$9.231 \cdot 10^{-3}$	$9.394 \cdot 10^{-3}$	$1.252 \cdot 10^{-2}$

**Table 6.9** Vibration parameters of experimental single-layer damped simply supported beam.

$n$	6	8	9	11
$f_{0n}$	821 Hz	1426 Hz	1797	2682 Hz
$F_{0n}$	0.195 N	0.282 N	0.391 N	1.911 N
SNR	95.0	50.3	26.8	47.1
$\eta_n$	$1.874 \cdot 10^{-2}$	$1.982 \cdot 10^{-2}$	$1.421 \cdot 10^{-2}$	$2.576 \cdot 10^{-2}$

**Table 6.10** Vibrational parameters of experimental double-layer damped simply supported beam.

It can be seen from Tables 6.8 to 6.10 that measurements at four frequencies (two even-numbered mode shapes, two odd-numbered mode shapes) of three differently damped beam structures were carried out. The calculation of VEF when using the IEDI method requires the knowledge of the hysteretic loss factor. Usually the loss factor is depending upon the mode of vibration and may spatially vary across the beam structure. In chapter 7 it has been shown that the simply supported beam rig was designed having pins at one side and rollers at the other. Because of the roller configuration the complete beam displacement could not be recorded by the ESPI system. Due to this incomplete displacement recording it was decided to truncate each recorded beam displacement down to an integer number of waves located within the ESPI window. Thus, the even-numbered mode displacements are short one

wavelength and the odd-numbered mode displacements are short half a wavelength of full spatial information.

As demonstrated in section 6.2.4, ESPI noise was extracted from the recorded ESPI data and superimposed with an artificially generated simply supported beam displacement (equation 5.37) using the measured force magnitude acquired during the ESPI experiment. The measured SNR is shown in Tables 6.8 to 6.10. Two methods were employed to compute VEF. The first method is the conventional VEFESPI method by evaluating equation (3.33). The second method, addressed as the IEDI method and described earlier on, uses energy densities provided by the VEFESPI method. This procedure is defined by equations (6.8) and (6.9). The recommended computed cut-off points obtained from this analysis are shown in Appendix A19. These can be employed when computing VEF from the measured ESPI beam displacements.

In the following two figures are presented, which display the optimum filtered VEF of the double-layer damped 11<sup>th</sup> mode beam displacement computed by the VEFESPI method and computed by the IEDI method. Both, the ideal and the Butterworth filter were employed to remove spectral noise components. The unconstrained layer attachment was modelled according to the unconstrained layer theory introduced in section 5.5. It can be seen from Figures 6.63(a) and 6.64(a) that the IEDI method produced a much better VEF result than the conventional VEFESPI computation method. This can also be noticed by the relative active MSE made from the respective tables given in Appendix 19. However, the reactive energy flow cannot be computed accurately enough when employing both techniques.

It is shown by Figure 6.63(b) and Figure 6.64(b) that wavenumber domain filtering falsifies reactive energy flow computation. This might be due to the spectral removal of nearfield components in the high wavenumber region at  $k_x > k_c$  and the passing of low wavenumber noise components at  $k_x < k_c$ .

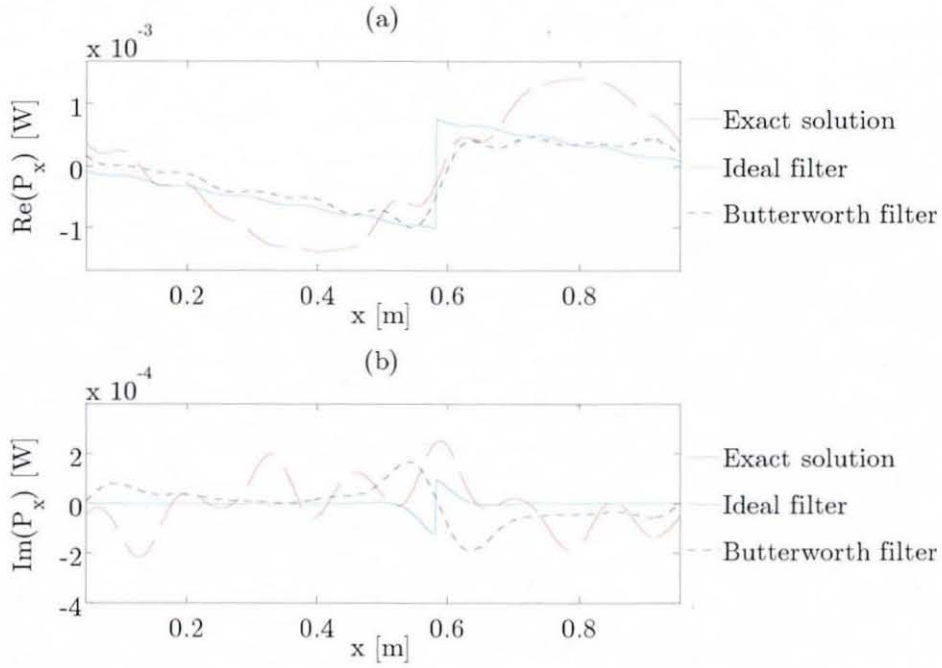


**Figure 6.63** VEF of ESPI noise contaminated 11<sup>th</sup> mode beam displacement using the VEFESPI method: (a) active flow, (b) reactive flow.

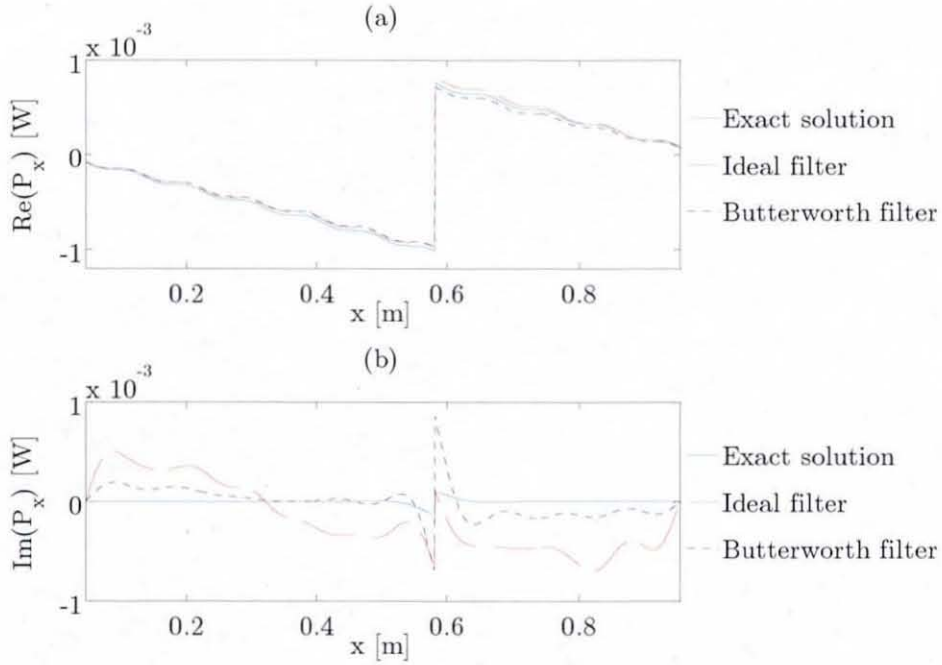


**Figure 6.64** VEF of ESPI noise contaminated 11<sup>th</sup> mode beam displacement using integrated energy densities: (a) active flow, (b) reactive flow.



## 6.4 Discussion and Summary

This chapter has investigated the numerical computation of VEF in infinite and simply supported beams. The KSD technique was employed to compute spatial derivatives from a complex matrix that contained spatial information of the structure's displacement.

It was shown above that the displacement of flexural vibrating structures is composed of nearfield and farfield wave components. The nearfield wave components are exponential decaying waves and the farfield wave components are sinusoidal travelling waves. Because the spatial Fourier transform is used as part of the KSD technique the transformed nearfield wave components resulted in broadband spectral components. This nearfield wavenumber spectrum was then amplified during the spectral derivation process by the wavenumber multiplication of the KSD method, as shown by equation (4.9). The spectral amplification is most significant at the high wavenumbers. If one computes spatial derivatives from the spectral wavenumber derivatives by employing an inverse Fourier transform, the back transformed spectral amplification will result in erroneous spatial derivatives. Further, these erroneous spatial derivatives caused errors in the VEF computation. The error made depended on the strength of the nearfield wave components present in the signal. If the nearfield wave amplitude is of the same magnitude as the travelling wave amplitude (e.g. infinite beam), a large deviation in the VEF calculation can be expected. Analogously, the structural damping dependent, relatively small wave amplitude of the simply supported beam caused less VEF deviations.

The same phenomenon occurred when the spatial signal to be analysed was non-periodic in space or contaminated by spatial noise. In both cases spectral amplification took place and, thus, erroneous VEF computation (oscillations) could not be avoided. Non-periodic signal consequences can be diminished by periodisation techniques, which artificially periodise the non-periodic displacement. Two were introduced here, addressed as the MP and MRS method. Noise contaminated signals were treated by employing a wavenumber domain filtering process in order to remove wavenumber noise

components at  $k_x > k_c$  that otherwise were amplified during the spectral derivation process. Two filtering techniques were introduced, a 2D ideal filtering process and an oval 2D Butterworth filter. The first filter type was perfect when filtering displacement signals containing only travelling wave components. The latter one is more applicable to displacement signals also containing nearfield wave components. However, in cases where the nearfield is not contributing to the active energy flow the application of the ideal filtering process will yield better active energy flow results.

It can be argued that due to the nearfield wave component the displacement signal becomes non-periodic in space and, thus, a form of leakage appears in the wavenumber domain. The application of the periodisation techniques yielded to better results than analysing the non-periodic beam displacement when the displacement was not noise contaminated. This can be explained by the fact that the periodisation techniques produced, for the KSD method, a better suited wavenumber spectrum by reducing leakage. Further, the spectral resolution  $\Delta k_x$  was reduced by half due to a double signal length  $L_x$  and, thus, less wavenumber domain amplification appeared, as shown by equation (6.6).

VEF oscillations due to spectral amplification can be compensated by the CW technique that was proposed by the author. This technique is simple to implement. However, in practice data acquired by a measurement system will contain noise. Thus, filtering is indispensable and the CW technique does not need to be employed. Due to the filtering process the wavenumber spectrum was altered. For an infinite beam it has been shown that the wavenumber spectral filtering was independent on the amount of noise assuming the noise amplitudes are in a realistic range, encountered in normal measurements. Also, due to the filtering of the wavenumber spectrum the spectral nearfield components in particular were altered. Hence, the computation of the spatial derivatives will deviate from the exact solution and therefore, the computed VEF is erroneous. However, the spectral amplification process is much less than when analysing non-noisy beam displacements.



It was shown in the previous sections that for noise contaminated beam displacements the computation of the reactive energy flow from spectral filtered data is not satisfactory. Especially for the wavenumber domain filtering of finite beam structures where the nearfield wave components also contribute to the active energy flow.

The numerical analysis of the simply supported beam revealed that the computation of VEF from noise contaminated simply supported beam displacements caused some problems. Two methods were proposed to compute VEF. One method was the conventional VEFESPI technique, also used to compute VEF in infinite beams. The second method, addressed here as the IEDI method, relied on the incremental integration of the respective energy densities. It was shown that the VEFESPI method is much more noise sensitive than the IEDI method. This noise sensitivity decreased with increasing damping. The product of loss factor and SNR was introduced as an indicator satisfactory VEF computation can be carried out. As shown in Figure 6.52, the product of loss factor and SNR should be at least 5, i.e.  $\eta \times \text{SNR} \geq 5$  when low structural damping is present, e.g.  $\eta = 5 \cdot 10^{-3}$ . At higher structural damping this number can decrease to one assuming the Butterworth filter is employed.

With the results obtained on the numerical VEF computation using the VEFESPI method it can be concluded that an accurate energy flow computation from the spatial derivatives up to the 3<sup>rd</sup> order is fairly difficult. To reduce the order of spatial derivatives the IEDI method was proposed, which can be seen as a part of the VEFESPI method. As mentioned, the computation of active energy flow within the simply supported beam was carried out by the incremental integration of the potential energy density. Reactive VEF was determined from the incremental integration of the Lagrangian energy density. Both energy density quantities were provided by the VEFESPI method. It has been shown that this method produced a much better active energy flow computation from noise contaminated data. Interestingly, it was found that the IEDI method is much less noise sensitive than the VEFESPI method when numerically computing VEF. This

surprising result may be related to the fact that the IEDI method utilises spatial derivatives up to the 2<sup>nd</sup> order only.

It was also shown that the oval 2D Butterworth filter produced better results than the ideal 2D filter, when computing VEF from noise contaminated simply supported beam displacements.

Finally some comments on the analysis of the complete simply supported beam displacement will be given. One could argue that it is better to divide the simply supported beam displacement into a left-hand side and right-hand side part, separated at excitation location because the infinite wave components will then be more appropriately better Fourier transformed. However, in practice dividing the simply supported beam displacement in this way would not help much. Although in principle, the infinite beam displacement is better analysed separately due to the sign change in the exponents  $jkx$  and  $-jkx$  the displacement cannot be truncated to an integer number of waves if the whole beam needs to be covered. Extra programming effort is necessary. Additional to this, the nearfield component still causes problems. Also, with increasing damping the infinite beam displacement is then not pure sinusoidal any more. Although the complete analysis of the simply supported beam caused errors due to an inclusion of non-periodic infinite wave components, the amplitude of the infinite waves are at least ten times less than the reflection wave amplitudes, as shown by Figure 6.22. Thus, due to the amplitude difference and a much easier computational implementation the separation of beam displacement was neglected here.



# **7 MEASUREMENT OF VIBRATIONAL ENERGY IN BEAMS: EXPERIMENTAL APPARATUS**

## **7.1 Introduction**

This chapter presents the experimental beam apparatus and the measurement setup used to measure vibrational energy flow (VEF) in an experimental “infinite” beam and an experimental simply supported beam. During the beam experiments, VEF within a force excited “infinite” and a force excited simply supported beam was measured using electronic speckle pattern interferometry (ESPI). Furthermore, measured moment induced point mobility and energy input to an “infinite” beam was also measured.

For the sake of completeness a brief introduction to ESPI and its principle is given. The ESPI measurement system used within this research is also introduced briefly.

## **7.2 Electronic Speckle Pattern Interferometry**

Electronic speckle pattern interferometry, also known as TV holography, is derived from holographic interferometry (HI). Both techniques are used to measure deformations of vibrating structures using monochromatic laser light. Employing laser based techniques enables fast, feasible and highly

accurate deformation measurements on a structure surface. In comparison to accelerometer based measurements ESPI provides a non-contacting and non-destructive technique with the influence of vibration alteration due to added masses being avoided.

The simplest form of laser based measurements in VEF is the use of laser Doppler vibrometry (LDV), which is a single point measurement technique that scans the surface point by point. The displacement or velocity field is then constructed employing post processing techniques [42].

ESPI is a whole-field measurement technique that provides two-dimensional vibration field information straight from the measurement data. In contrast, when employing HI the measured data are recorded on a photo plate and need to be post processed in order to obtain the displacement or velocity information.

### **7.2.1 Principle of Electronic Speckle Pattern Interferometry**

Holographic interferometry and electronic speckle pattern interferometry are described in detail in reference [117]. ESPI will be introduced here only briefly. ESPI was firstly demonstrated by Butters and Leendertz in 1971 [118]. With increasing performance of computational technology and digital recording technology, ESPI has become a widely used tool in surface deformation measurements.

A rough surface, illuminated by a laser, exhibits a granular light pattern, known as the speckle effect. The height variations of the surface roughness has to be of the order or greater than the wavelength of the illuminating laser light. The speckle effect is then a result of random interference, resulting from the numerous reflections occurring on the optical rough surface. Figure 7.1 displays the speckle pattern of an illuminated object. Its randomly varying light intensity appearance can be seen clearly. The minimum speckle size is typically in the range of 5 to 100  $\mu\text{m}$  [119,120]. The optical rough illuminated surface scatters a speckle pattern. Each pixel can be seen as a single Michelson interferometer. If the scattered light is superimposed with a reference beam, each surface pixel interferes with the

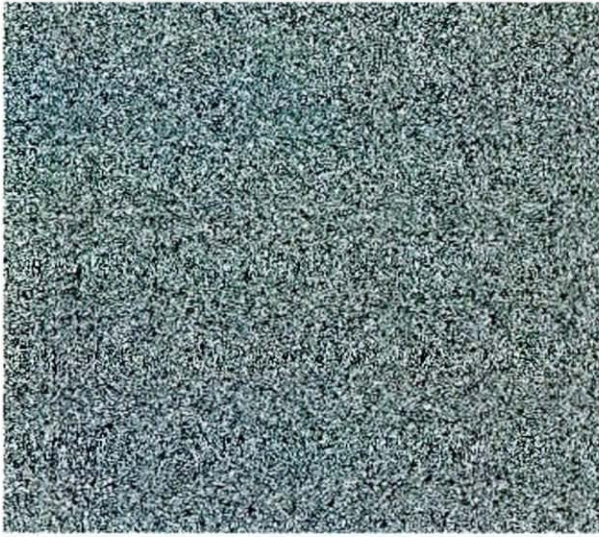


**Figure 7.1** Speckle effect on a laser illuminated surface.

reference beam light. Locating at the point of interference a charge coupled device (CCD) camera where the aperture is adjusted in a way that the speckle size is comparable to the resolution of the camera, the speckle effect can be recorded electronically. Information of surface deformation may then be obtained in consideration of two different images, recorded and stored

electronically at two different instants in time.

The successive images may be video-signal-added, video-signal-subtracted, or post processed by the so-called amplitude-fluctuation method [124]. In this work the signals coming from the CCD camera are subtracted. Using conventional continuous laser illumination, zero order Bessel functions may be used to describe the light intensity fringes. The time-averaging procedure is applied to obtain time-averaged correlation fringes. It is important that the exposure time should be equal to the vibration period or its integer multiple to describe exactly the light intensity  $I$  by a zero order Bessel function. Single frequency excitation is assumed. The modified output voltage of the two subtracted video signals can be written as [121]:

$$V_{im} = \frac{4N\alpha\pi}{\omega} \sqrt{I_0 I_r} \left[ (J_0(h_i) - 1)^2 \cos^2(\varphi) \right]^{\frac{1}{2}}. \quad (7.1)$$

Herein,  $J_0$  is the zero order Bessel function,  $N$  is the number of cycles,  $\alpha$  is the slope of the CCD camera sensitivity,  $\omega$  is the angular excitation frequency,  $I_0$  is the object light beam intensity, and  $I_r$  is the reference light



beam intensity. The random phase resulting from surface roughness is denoted by  $\varphi$ . The inner product of the Bessel function  $h_i$  is given by [121]:

$$h_i = \frac{2A\pi(1 + \cos(\theta))}{\lambda}. \quad (7.2)$$

The illumination angle of the object light is denoted as  $\theta$  and  $\lambda$  is the wavelength of the laser beam. The amplitude  $A$  can be found as [121]:

$$A = \frac{\lambda \zeta_i^*}{2\pi(1 + \cos(\theta))}. \quad (7.3)$$

The value  $\zeta_i^*$  needs to be taken out of a special table. This value can locally minimise the brightness equations of the monitor brightness.

### 7.2.2 ESPI Measurement System

The ESPI measurement system employed in this work, is composed of a laser generation unit and the so-called optical head, as shown in Figure 7.2. From the laser-generating unit an armoured fibre cable transmitted the laser light to the optical head. This has the advantage of carrying out measurements independently of the position of the laser generation unit. The directional coupler divided the laser light into an object and a reference beam. The scattered object light was focused by the SLR lens and interfered with the reference beam light at a CCD camera, producing interference fringes. A  $768 \times 768$  pixel low light monochrome Kodak high speed CCD camera captured the ESPI image operating with 25 frames per second. The aspect ratio of the CCD camera was 4:3.

Conventional ESPI systems have the effect of integrating out the phase information due to time-averaging of the correlation fringes [119]. Thus, the amplitude is recorded only, as described by equation (7.3). However, for VEF calculations measured transverse displacements need to be described by amplitude and phase information. To obtain phase

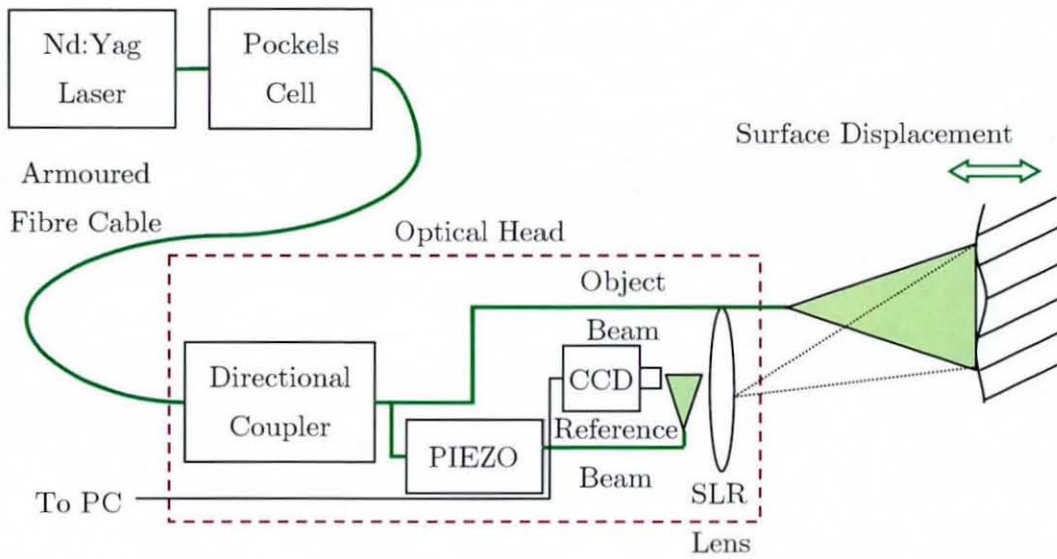


**Figure 7.2** ESPI system employed in this work for vibration measurements.

information stroboscopic illumination of continuous laser light in combination with a phase stepping algorithm is employed. The stroboscopic illumination is achieved by employing a Pockels cell working as a beam light shutter. The triggering process of the Pockels cell is controlled by a PC, which also stores the recorded ESPI image for further post signal processing. The strobe pulses have to be synchronised exactly to the excitation frequency of the vibrating structure to be measured.

The phase stepping algorithm utilises a cylindrical piezo-electrical transducer (PZT) [119,122]. The continuous 150 mW frequency doubled Nd:Yag laser is applied by a stroboscopic pulse that is synchronised to the excitation frequency of the structure. Newer systems already employ pulsed ruby lasers. A single mode fibre of the reference beam coming from the fibre coupler (see Figure 7.2) is wrapped around the PZT. Applying a voltage to the PZT results in an expansion of the crystal and, hence, the fibre strains. Therefore, the phase of the reference beam can be altered as the optical path length changes. Usually an applied voltage of approximately 5 V results in a phase change of  $2\pi$ . Two sets of strobe pulses are used in the phase stepping algorithm, which are denoted here as subscripts  $\alpha$  and  $\beta$ . Figure 7.3 displays

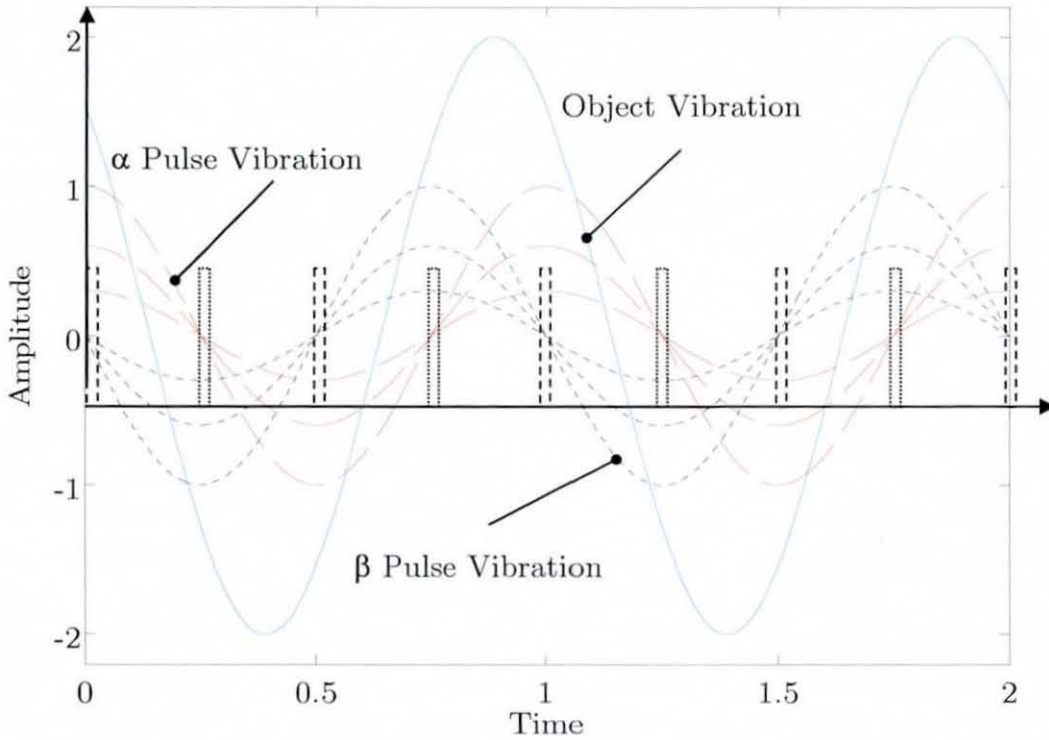


**Figure 7.3** Timing of stroboscopic illumination (modified from [119]).

the timing of the stroboscopic pulse illumination. Each rectangle symbolises a strobe pulse with very short duration time in comparison to the object's vibration period. The correlation fringe function  $I_\alpha$  of the intensity due to the  $\alpha$  pulse can be written as [119]:

$$I_\alpha = I_{\text{mod}} \sqrt{\cos(2K_1 A_v(x, y) \cos(\phi_v(x, y))) - 2K_2 A_r} + 1. \quad (7.4)$$

Here,  $I_\alpha$  is the intensity at coordinate  $x$  and  $y$  in the recorded fringe pattern,  $I_{\text{mod}}$  is the modulation intensity of the observed speckle,  $A_v$  is the amplitude of the vibrating object at position  $x$  and  $y$ ,  $A_r$  is the amplitude of the reference beam and  $\phi_v$  is the phase of the vibrating object at position  $x$  and  $y$ . Capital  $K$ 's are constants, defined as  $K_1 = 4\pi/\lambda$  and  $K_2 = 2\pi/\lambda$ , whereas  $\lambda$  is the wavelength of the laser beam.



Similarly, the intensity correlation function  $I_\beta$  is given by [119]:

$$I_\beta = I_{\text{mod}} \sqrt{\cos(2K_1 A_v(x, y) \sin(\phi_v(x, y)) + 2K_2 A_r) + 1}. \quad (7.5)$$

The phase of the reference beam is locked, thus, its vibration is coupled with the excitation frequency and strobe pulse. Adjusting now the amplitude term  $2K_2 A_r$  of the above displayed equations a phase step alteration can be applied to each correlation fringe function. Employing phase steps of  $\pi/2$  two sets of strobe data yield to eight correlation fringe functions, four of each set are being used to calculate a wrapped phase map. The phase map  $\phi_\alpha$  is defined as [119]:

$$\phi_\alpha = 2K_1 A_v(x, y) \cos(\phi_v(x, y)) = \tan^{-1} \left( \frac{I_{\alpha 270}^2 - I_{\alpha 90}^2}{I_{\alpha 0}^2 - I_{\alpha 180}^2} \right). \quad (7.6)$$

The phase map  $\phi_\beta$  is given by [119]:

$$\phi_\beta = 2K_1 A_v(x, y) \sin(\phi_v(x, y)) = \tan^{-1} \left( \frac{I_{\beta 270}^2 - I_{\beta 90}^2}{I_{\beta 0}^2 - I_{\beta 180}^2} \right). \quad (7.7)$$

The wrapped phase maps  $\phi_\alpha$  and  $\phi_\beta$  must both now be unwrapped relative to some known point, which is usually a nodal line with zero amplitude, since the arctangent function delivers results in the range of  $\pm \pi$ . Figure 7.4 displays the modulation intensities controlled by the piezo crystal. Carrying out the unwrapping process the phase of the vibrating object can be written as [119]:

$$\phi_v(x, y) = \tan^{-1} \left( \frac{\phi_\beta}{\phi_\alpha} \right). \quad (7.8)$$



The vibration amplitude  $A_v$  is given by [119]:

$$A_v(x, y) = \frac{\lambda \cdot (\phi_\alpha^2 + \phi_\beta^2)^{\frac{1}{2}}}{8\pi}. \quad (7.9)$$

It can be seen that the shift in phase is  $\pi/2$  of the four intensities. At points, where  $I_{270}$  is equal to  $I_{90}$ , the phase of the vibrating object becomes zero.

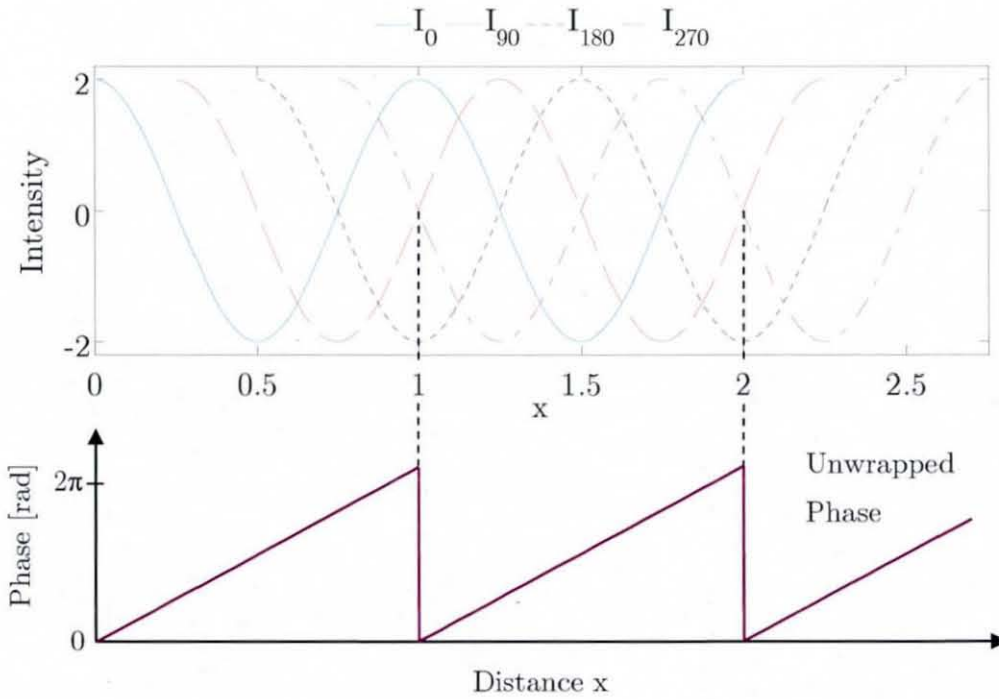


**Figure 7.4** Modulation intensities and unwrapped phase.

### 7.3 Experimental Beam Apparatus

Two different beam apparatus were used to simulate an infinite beam and a finite simply supported beam, respectively. In addition to this, a moment actuator was designed to apply moment excitation to an experimental

“infinite” beam. As mentioned earlier, VEF of the force excited “infinite” beam and the simply supported beam using the VEFESPI method as well as the point mobility and the input energy of a moment excited “infinite” beam was measured.

### 7.3.1 “Infinite” Beam Rig

#### 7.3.1.1 Force Excited “Infinite” Beam Setup

Infinite beams are simulated in practice using a finite beam that is highly damped at both ends. The high damping at both ends is achieved using

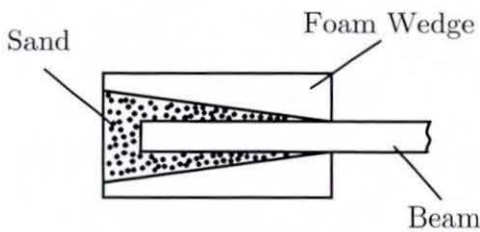


**Figure 7.5** Anechoic termination.

anechoic terminations that consist of foam wedges and sand inserted in a box. The foam wedges are employed to ensure the sand is dissipating vibrational energy at all frequencies. Due to the high damping very low reflection at the beam’s end can be achieved and, thus, the finite beam is

approximated to infinite beam behaviour. Figure 7.5 displays a schematic sketch of the anechoic termination. With this anechoic termination setup reflection coefficients of approximately 0.1 can be achieved [64].

Figure 7.6 shows the experimental “infinite” beam setup to measure force excited energy flow under use of ESPI [64]. A 6 m long, 60 mm by 10 mm cross-section mild steel beam was embedded in two 1 m long boxes containing foam wedges and sand to achieve anechoic termination at both ends. The beam was suspended on two thin wires and was excited in the middle by an electrodynamic shaker. To compare injected vibrational energy with transmitted farfield energy (energy balance) energy input to the beam structure has been measured by placing a force transducer and an accelerometer at the excitation location. The vibration amplitude and phase

was recorded to the right of the excitation location in an area that was at least  $\frac{3}{4}$  of a wavelength away from discontinuities. This region is called farfield and it is assumed that the spatially decaying nearfield wave has already vanished there. Further, to compare ESPI measured VEF with transmitted energy measured by the traditional two-accelerometer technique [28] a pair of light-weight accelerometers were placed within the ESPI

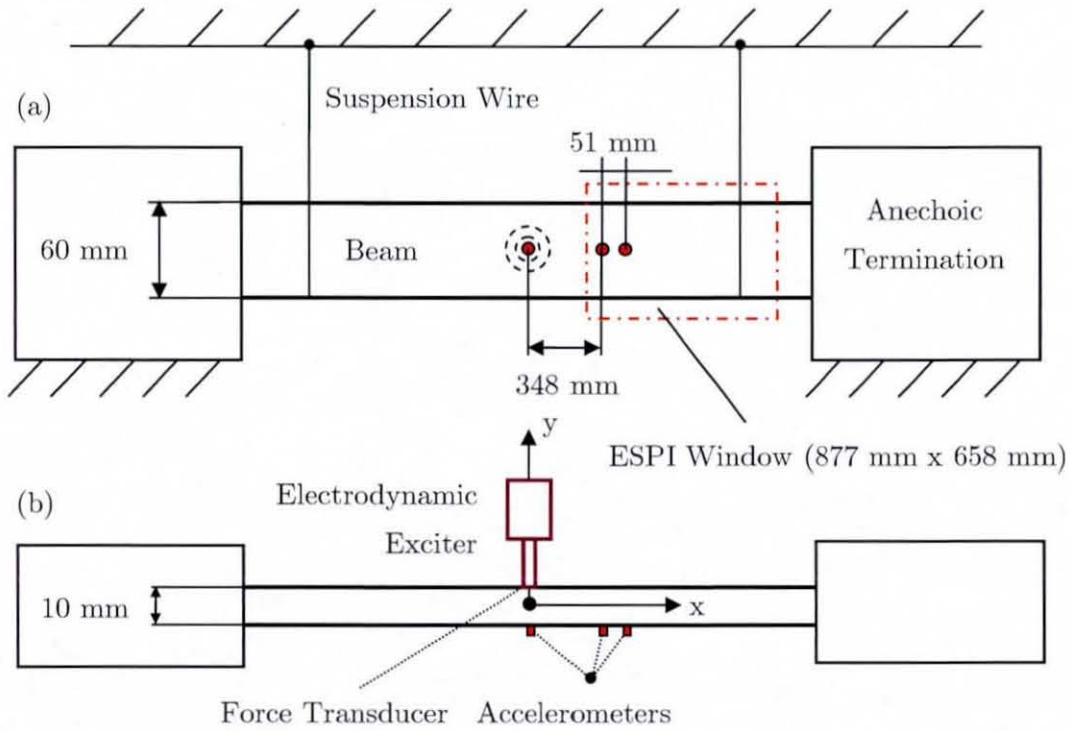


**Figure 7.6** Force excited experimental “infinite” beam setup: (a) side view, (b) top view.

window spaced 51 mm apart from each other. The spacing  $\Delta x$  was chosen to be between 0.15 and 0.2 of a wavelength of the excitation frequency. All four signals were recorded on a multi-channel spectrum analyser that provided the auto spectral and cross spectral data necessary to calculate conventionally measured vibrational input energy and transmitted energy.

### 7.3.1.2 Moment Excited “Infinite” Beam Setup

In addition to the ESPI measured VEF, moment induced point mobility and vibrational energy input was also measured in an “infinite” beam. For this reason the “infinite” beam subjected to moment excitation was set up similar to the setup, as shown in Figure 7.6. However, here different beam and anechoic termination dimensions were employed. The moment excited “infinite” beam setup is shown in Figure 7.7 where it can be seen that two moment arms 60 mm in length, 50 mm deep and 6 mm thick were welded at the centre of the beam. To apply an excitation moment the two moment

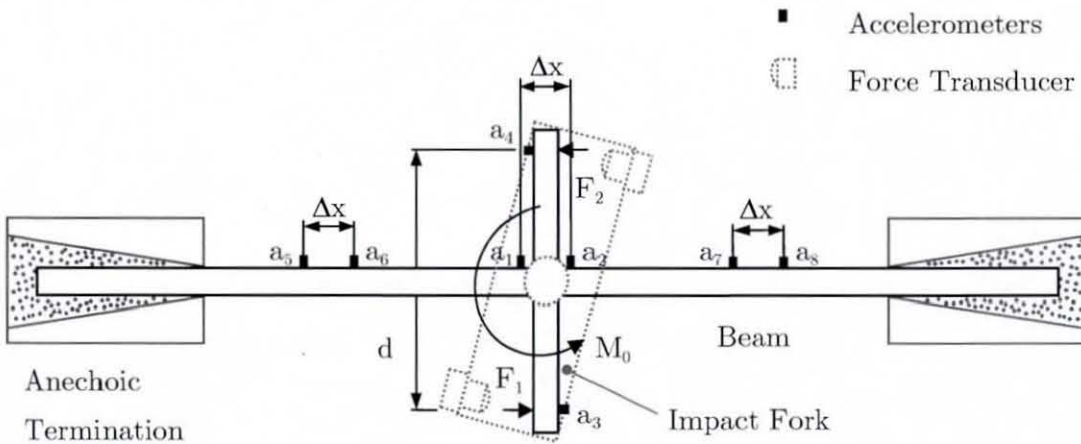


**Figure 7.7** Moment excited “infinite” beam setup: top view (not to scale).

arms were struck simultaneously by the so-called impact fork. The impact fork was suspended within the moment actuator mechanism, as shown in Figure 7.8. Input energy and transmitted energy at different locations on the beam were measured. Accelerometers  $a_1$  and  $a_2$  were used to measure the rotational velocity and, thus, the point mobility and input energy due to the applied moment. For comparison reasons accelerometers  $a_3$  and  $a_4$  were employed to measure the energy injected straight into the moment arms that was later compared to the moment induced energy input. Accelerometers  $a_5$  to  $a_8$  were used to measure transmitted energy in the farfield region using the two-accelerator technique to compare transmitted energy with the moment



induced input energy (energy balance). Also here, the accelerometer spacing  $\Delta x = 28$  mm was chosen to be between 0.15 and 0.2 of the wavelength of the highest frequency to be measured, in this case 1.6 kHz. All 8 signals were recorded on a multi-channel spectrum analyser. The length of the anechoic termination restricted the lowest frequency to be measured to approximately 100 Hz.

To apply the moment a specially designed moment actuator that was based on previous investigations [123, 124] was constructed. A photograph of the moment actuator is shown in Figure 7.8. This rig is predominately made from 1 inch square steel bar to ensure the rig has sufficient mass to avoid any undesired movement when impacting the beam. The impact fork was welded to a shaft, which runs in bearing units. The use of an impacter held within a static frame ensured that the direction of application of the impact forces was consistent between tests, something, which posed difficulty when using an impact hammer. The two arms of the impact fork were offset slightly to

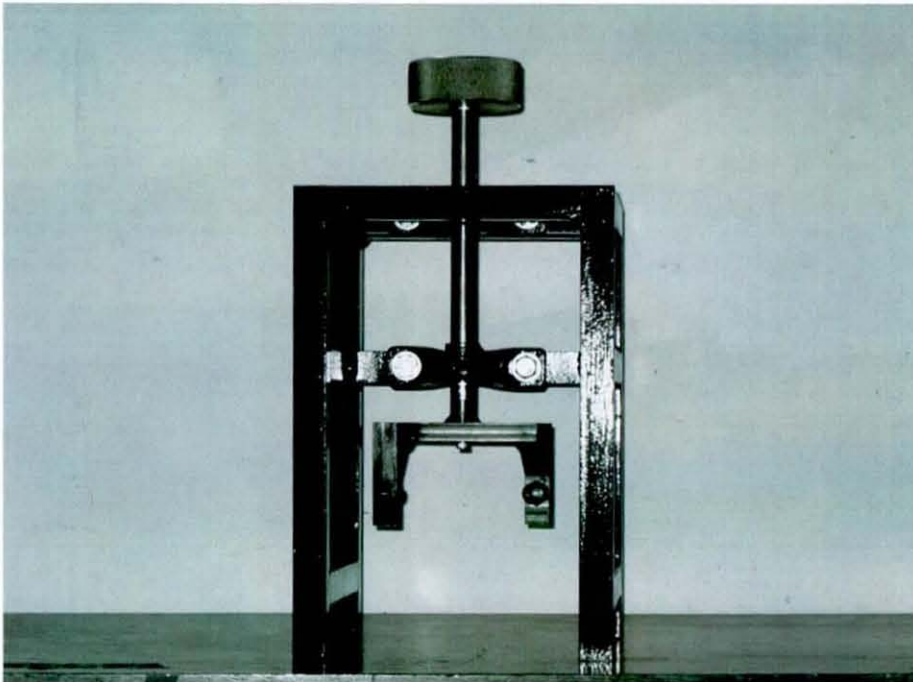


**Figure 7.8** Photograph of the moment actuator.

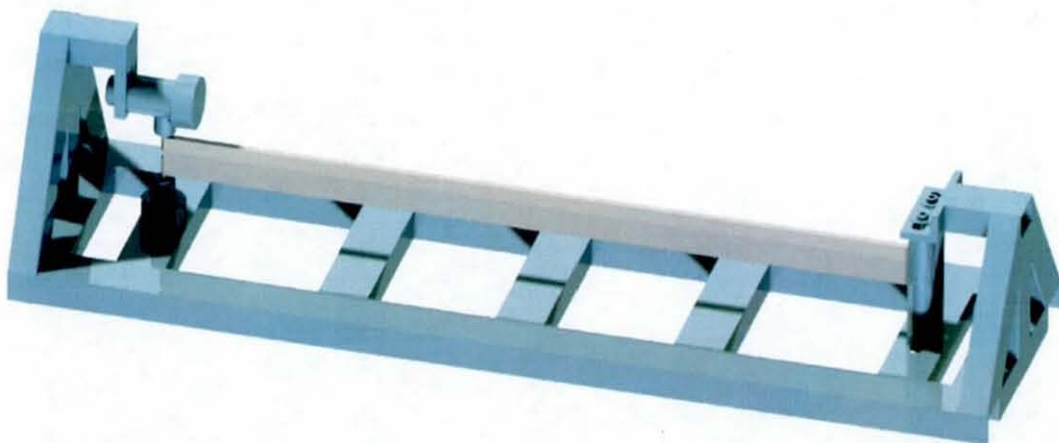
ensure perpendicular impact of the fork's arms onto the moment arms of the beam. One force transducer was placed on each of the fork's arms to measure the applied forces. Steel tips, screwed onto the force transducers, allowed point force impact onto the moment arms of the beam and provided an even distribution of the force over the force transducer [107].

### 7.3.2 Simply Supported Beam Rig

As an extension to the initial “infinite” beam measurements, force excited measurements on a simply supported beam rig were also carried out. The beam rig can be employed for both force and moment measurement types of excitation. However, in the case of moment excitation it needs to be combined with the moment actuator. Therefore, a simply supported beam rig was designed in order to meet simply supported boundary conditions for both types of excitation.

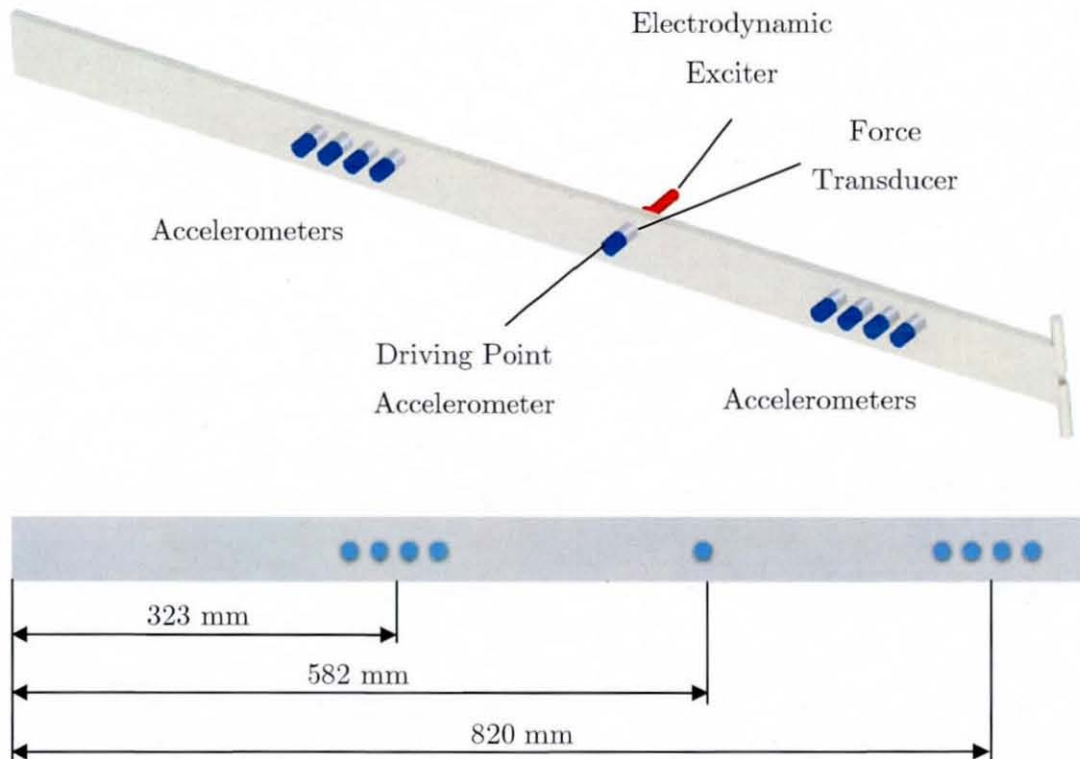
#### 7.3.2.1 Force Excited Simply Supported Beam Setup

Figure 7.9 shows the assembly of the simply supported beam rig. It can be realised from Figure 7.9 that the rig is welded from different standard steel



**Figure 7.9** Simply supported beam rig including the ESPI beam.

profiles. The beam is suspended on the left-hand side by two pins pivoting in two bushes and on the right-hand side by two rollers. The two rollers allowed for length variations of the beam. The pin design has been chosen to fix the beam's position at one side and allow fast beam changes during measurement of different specimens. The beams were made from mild steel, 1000 mm in length, 50 mm deep, and 10 mm thick. In order to measure beam structures having a different amount of damping non-layer damped, single unconstrained layer damped and double unconstrained layer damped beam specimens have been prepared. The thickness of the damping layers was 2.5 mm and 5 mm, respectively, covering one entire side of the beam. A mineral filled viscoelastic polymer layer material was used. The rig was constructed to ensure that its vibration was not interfering with the transverse beam vibration. The rig was loaded with additional weights to ensure a stationary



**Figure 7.10** Transducer locations on the simply supported ESPI beam.



rig position during measurement. As carried out during the “infinite” beam measurements, conventional accelerometer based input and transmitted energy measurements were undertaken in order to compare with measured ESPI energy flow. Figure 7.10 displays the locations of the accelerometers mounted on the beam. It can be followed from Figure 7.10 that the beam was excited by an off-centre force, located at  $x_0 = 0.582$  m. Further, transmitted energy was measured at the left and the right of the excitation location using the well known four-accelerator technique [30]. The reason four accelerometers have been employed is that the nearfield waves were included in the measurements.

### 7.3.2.2 Moment Excited Simply Supported Beam Setup

Based on the experience gathered during the moment excitation measurements of the “infinite” beam a redesigned impact fork may be employed in order to measure point mobility and input energy of a simply supported beam subjected to moment excitation. Due to the altered impact fork the moment arms needed also to be shortened in order to increase stiffness and, thus, increase the frequency range of application. Figure 7.11

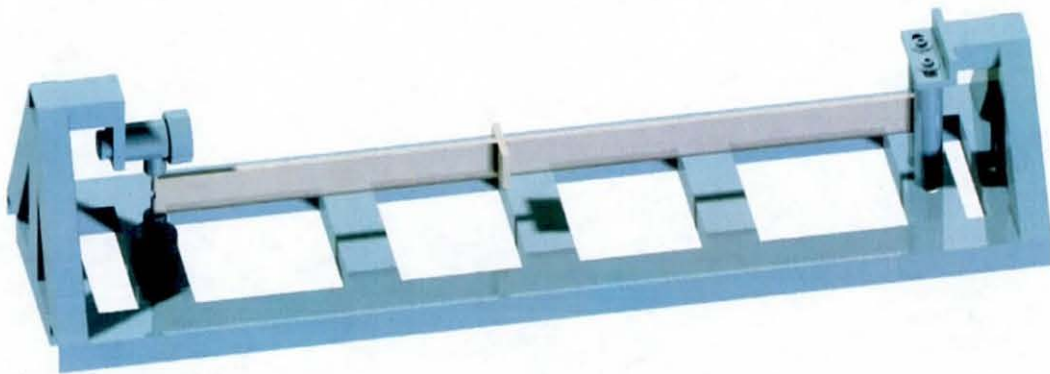


**Figure 7.11** Simply supported beam rig including the moment excitation beam.

displays the simply supported beam rig including the beam specimen with the moment arms. Also here, the beam was made from mild steel, 1000 mm in length, 50 mm deep, and 10 mm thick. The moment arms were attached off-centre at a location of  $x = 450\text{mm}$  from the pin side. The moment arms were machined from mild steel 33 mm in length, 50 mm deep, and 10 mm thick. Unfortunately, due to time pressure no moment induced simply supported beam experiments were conducted.

## 7.4 Summary

This chapter has introduced the different experimental beam apparatus used through this work. “Infinite” and finite beam structures were measured in order to investigate different VEF scenarios. Thus, a high energy transmission environment (“infinite” beam) and low energy transmission environment (simply supported beam) were simulated. Both force and moment excitation measurements were carried out. Force excited beam structures were used to measure VEF with the aid of ESPI. Moment excited structures were employed to measure moment point mobility and input power. To measure moment excited beam structures the respective beam rig was combined with a specially designed moment actuator that enabled moment impact on the beam’s moment arms.

The “infinite” beam rig consisted of two anechoic termination boxes containing foam wedges and sand, the beam specimen itself and wires that suspended the beam within the anechoic termination boxes.

The simply supported beam rig was constructed from simple standard profiles that were welded together. A pin-roller combination was chosen in order to meet simply supported boundaries. The pin at one side fixes the position of the beam and the roller at the other side allows for length variation of the beam during measurement.

In addition to the beam’s apparatus employed here, a brief introduction to ESPI and its principle has been given. The amount of literature on this subject is quite vast. Since it is not the objective of this

research to investigate the performance of the ESPI technique itself, a more thorough survey was omitted. The applied ESPI measurement system used in this work has also been introduced briefly where special focus has been given to the phase stepping algorithm applied in order to measure the vibration phase.

The author would like to thank Mr. Martin Dale who kindly supported this research with the provision of the ESPI system at Land Rover, Gaydon where the entire ESPI based measurements were undertaken under the direction of the author.

# 8 MEASUREMENT OF VIBRATIONAL ENERGY IN BEAMS: MEASUREMENT METHODS

## 8.1 Introduction

The aim of this chapter is to introduce the methods of measuring point mobility, vibrational input power (VIP) and vibrational energy flow (VEF) in beams. In order to justify the accuracy of the measurement of VEF using electronic speckle pattern interferometry (ESPI), conventional transducer based measurements have been carried out to compare VEF from both conventional and ESPI measurement techniques.

A novel method to measure moment point mobility at the excitation location and moment induced input energy is also presented in the moment excitation section. Therefore, the theoretical background of the proposed method as well as the practical implementation is given. This includes the approximation of the measured angular velocity by a first order finite-difference approximation and its practical measurement implementation using measured spectral density quantities. Also, two error appraisal functions are presented in order to judge the accuracy of the proposed moment excitation method. Some of the information presented herein was extracted from references [64] and [107], especially the description of the moment measurement method. As throughout this work, flexural beam motion is assumed.

## 8.2 Force Excited Beam Measurements

### 8.2.1 Point Mobility Measurements

Point mobility at the excitation location is measured throughout this work using a force transducer and an accelerometer at the excitation location. Employing the well known  $H_1(f)$  estimator point mobility is measured as:

$$Y_F = \frac{1}{j2\pi f} \frac{G(F_0, a_0)}{G(F_0, F_0)}. \quad (8.1)$$

Here,  $G(F_0, a_0)$  is the cross-spectral density between excitation force and driving point acceleration and  $G(F_0, F_0)$  is the auto power spectral density of the excitation force. The factor  $1/(j2\pi f)$ , where  $f$  is the frequency, accounts for integration of the acceleration in order to obtain velocity. The spectral density ratio of equation (8.1) is acquired as a spectrally-averaged frequency response function (FRF) using a multi-channel spectrum analyser.

### 8.2.2 Vibrational Input Power Measurements

Measurements of VEF using ESPI has been carried out on a force excited “infinite” and simply supported beam. To carry out simple energy balance analysis the measurement of vibrational energy injected into a vibrating structure is essential. In section 3.5 general VIP expressions were presented distinguishing between definitions based on the theoretical point mobility and the use of spectral density quantities, such as auto spectral density and cross-spectral density. This section presents the accelerometer and force transducer based measurements of VIP using both approaches.

VIP based on the theoretical point mobility of the respective force excited beam structures is given for infinite beams by equation (5.20). Using the geometrical and material “infinite” beam properties, VIP of an infinite beam can also be written as:

$$(P_{in})_{F_\infty} = \frac{F_0^2}{8A\rho\sqrt{2\pi f}} \sqrt{\frac{A\rho}{EI}}. \quad (8.2)$$

Here,  $F_0$  is the magnitude of the excitation force,  $A$  is the beam's cross-sectional area,  $\rho$  is the mass density of the beam,  $E$  is the Young's modulus, and  $I$  is the second moment of area. VIP of a point force excited hysteretically damped simply supported beam using the theoretical point mobility was given as:

$$(P_{in})_{F_\infty} = \frac{F_0^2 \pi f}{4I} \Re \left\{ \frac{j}{Ek^3} \left[ \left( \frac{\sin(2kx_0) + \sin(2k(L-x_0)) - \sin(2kL)}{1 - \cos(2kL)} \right) - \left( \frac{\sinh(2kx_0) + \sinh(2k(L-x_0)) - \sinh(2kL)}{1 - \cosh(2kL)} \right) \right] \right\}. \quad (5.43)$$

Unfortunately, a more simple expression of VIP for a simply supported beam cannot be given because of the occurring complex arguments in the sinusoidal and hyperbolic functions due to the complex, flexural wavenumber  $k$ . Nevertheless, the real part of the force excited hysteretically damped simply supported beam's driving point mobility can be computed easily using common software packages.

An alternative method to determine VIP from measured force and acceleration is the use of the imaginary part of the measured one-sided cross-spectral density, displayed again in equation (3.27) as:

$$(P_{in})_F = \frac{1}{2\pi f} \Im \{ G(F_0, a_0) \}. \quad (3.27)$$

Here,  $G(F_0, a_0)$  is the cross-spectral density between the driving force and the resulting acceleration. This expression is generally valid for each beam structure, is independent on the beam's boundaries and is considered to be more accurate than the use of the theoretical driving mobility due to variations between the actual and the theoretical point mobility.



### 8.2.3 Accelerometer Based Transmitted Vibrational Energy Measurements

In chapter 4, Figure 4.1 displays a typical one-dimensional four accelerometer setup. It has been outlined in section 3.6.1 that transmitted vibrational energy in a beam is composed of shear force and bending moment energy transmission components. If one substitutes the respective approximated spatial derivatives given by equations (4.1) to (4.4) into equation (3.33) and takes into account that  $v = a/j\omega$  and,  $G(v,v) = G(a,a)/\omega^2$ , then the complex, transmitted vibrational energy can be measured with the aid of four accelerometers as [30]:

$$P_{tr_4} = \frac{EI}{j(2\pi f)^3 \Delta x^3} \left( (G(a_2, a_2) - G(a_3, a_3)) + j4\Im\{G(a_3, a_2)\} + \right. \\ \left. G(a_2, a_4) - G(a_3, a_1) \right). \quad (8.3)$$

Here,  $\Delta x$  is the spacing between any two accelerometers,  $a_x$  is the measured transverse acceleration at locations 1 to 4,  $v$  is the transverse velocity,  $G(x,x)$  is the measured auto spectral density, and  $G(x,y)$  is the measured cross-spectral density between the accelerometer signals. Equation (8.3) enables the measurement of VEF in the near and farfield. The real part of equation (8.3) represents net energy flow through the accelerometer location. This technique is called the four-accelerometer technique.

The nearfield waves in a beam usually do not contribute to VEF. Thus, VEF can be measured in the farfield, i.e. at least  $\frac{3}{4}$  of a wavelength away from discontinuities, by employing only two accelerometers. This method is addressed as the two-accelerometer technique and utilises the measured cross-spectral density between the two accelerometers,  $G(a_1, a_2)$  as [30]:

$$P_{tr_2} = \frac{\sqrt{\rho AEI}}{2\pi^2 \Delta x} \frac{\Im\{G(a_1, a_2)\}}{f^2}. \quad (8.4)$$

Here,  $a_1$  and  $a_2$  are a pair of accelerometers, set apart by  $\Delta x$  and are located in the farfield. To compensate for the first order finite-difference approximation error, a correction factor  $k\Delta x/\sin(k\Delta x)$  may be applied [28]. The corrected transmitted vibrational energy  $(P_{tr_2})_{cr}$  is then given as:

$$(P_{tr_2})_{cr} = P_{tr_2} \left( \frac{k\Delta x}{\sin(k\Delta x)} \right). \quad (8.5)$$

The accelerometer based measurement of VEF in the “infinite” beam is carried out using equation (8.5), since ESPI based VEF has been recorded in the farfield only. Due to the presence of a nearfield at the left and right-hand side of the excitation location, especially at low excitation frequencies, accelerometer based VEF in a simply supported beam was measured by employing equation (8.3). The entire auto spectral and cross-spectral densities were recorded by a multi-channel FFT analyser using a spectral averaging of 50 measurements.

#### 8.2.4 Vibrational Energy Flow Measurements Using ESPI

It was shown in chapter 7 that the ESPI system provides vibration amplitude and vibration phase information. These two quantities are used herein to generate a measured time-averaged complex ESPI beam displacement as:

$$u(x, y)_{ESPI} = A(x, y)e^{j\phi(x, y)}. \quad (8.6)$$

Herein,  $A(x, y)$  is the measured two-dimensional ESPI amplitude and,  $\phi(x, y)$  is the measured two-dimensional ESPI phase. The generated beam displacement, as shown by equation (8.6), is used as the input to the VEFESPI method, as displayed in Figure 4.6 in chapter 4.

### 8.2.5 Application of the Measurement Methods to a Beam

The point mobility of the force excited beam is calculated from the measured FRF, as displayed by equation (8.1). The FRF function is recorded on a multi-channel spectrum analyser employing a spectral averaging of 50 measurements.

VIP to the force excited “infinite” ESPI beam was measured using equations (8.2) and (3.27). Since equation (8.2) represents the theoretical VIP due to a certain measured magnitude of the excitation force, this equation is considered to be only an approximation to the real input power. Equation (3.27) is seen to be a more accurate calculation of VIP to a beam. VIP to the simply supported ESPI beam was measured using equation (3.27).

The measurement of accelerometer based VEF in the force excited “infinite” ESPI beam was carried out by employing equation (8.5). Measured accelerometer based VEF in the force excited simply supported ESPI beam was carried out by employing equations (8.3) and (8.5).

The desired complex, “infinite” and simply supported ESPI beam displacement was generated by using equation (8.6). Unfortunately, within the ESPI signal window regions away from the beam were also recorded that contained only optical noise information. These regions needed to be truncated out of the ESPI displacement signal. After the data truncation the  $k$ -space derivation (KSD) method was applied. The truncated ESPI data were transformed into the  $k$ -space domain, by numerically applying a 2D Fast Fourier transform (FFT) according to equation (4.5). Within the wavenumber domain a spectral filtering process was carried out to remove unwanted noise components. Within this work two filtering techniques were used. An ideal 2D filtering process given by equation (4.13) and an oval 2D Butterworth filter defined by equation (4.15) were implemented to remove spectral noise. From the filtered spectral displacement data sets, different spectral wavenumber derivatives up to the 4<sup>th</sup> order were determined using the right-hand side of equation (4.9). These spectral derivatives were transformed back into the spatial domain by applying an inverse FFT by numerically evaluating equation (4.6). The determined respective spatial

derivatives were then substituted into equation (3.33) to determine VEF in the “infinite” and simply supported ESPI beam. The energy related quantities have been determined by substituting the respective spatial derivative components into equations (3.34) to (3.37).

### 8.3 Moment Excited Beam Measurements

Additional to the ESPI based VEF measurements, a novel method to measure the point mobility and vibrational input energy to a beam that is subjected to moment excitation was developed in references [107] and [125]. The presented method utilises a finite-difference approximation to calculate the rotational motion of the beam at the point of excitation. Moment excitation was induced by a specially designed impact rig, which applied two equal and opposite forces on two moment arms that were perpendicularly attached to the beam.

#### 8.3.1 Finite-Difference Approximation of the Angular Velocity

The novelty of the proposed method is the use of the finite-difference approximation to approximate the angular velocity at the driving point in combination with a specially designed impact rig. Figure 7.7 displayed again below shows the setup of the “infinite” beam. Herein, the angular velocity is not directly measured but approximated by using a finite-difference technique. In the proposed method, the measured accelerations  $a_1$  and  $a_2$  from two closely spaced accelerometers around the point of moment impact are used to estimate the translational acceleration  $a_0$  at a point midway between these two accelerometers. The approximation of the angular velocity from two translational acceleration points under assumption that  $a_1$  and  $a_2$  are complex quantities is given as:

$$\frac{\partial \theta_0}{\partial t} \approx \Re \left\{ \frac{1}{j\omega} \left( \frac{a_2 - a_1}{\Delta x} \right) \right\}. \quad (8.7)$$

### 8.3.2 Moment Point Mobility Measurements

$$Y_M = \frac{G\left(M, \frac{\partial \theta}{\partial t}\right)}{G(M, M)}. \quad (8.8)$$
$$M = \frac{d}{2}(F_1 + F_2). \quad (8.9)$$

If it is assumed that the magnitudes of both forces of the applied moment are equal, i.e.  $F_1 = F_2 = F$ , then the power spectral density of the applied moment is given by:

$$G(M, M) = d^2 G(F, F). \quad (8.10)$$

Thus, the cross-spectral density between the applied moment and the resulting rotational velocity  $G(M, \partial\theta/\partial t)$  at the excitation location can be calculated using the cross-spectral density between the applied forces and the resulting velocity  $\partial\theta/\partial t$ . Hence:

$$G\left(M, \frac{\partial\theta}{\partial t}\right) = dG\left(F, \frac{\partial\theta}{\partial t}\right). \quad (8.11)$$

In the approach adopted in this work the rotational velocity  $\partial\theta/\partial t$  is estimated using a finite-difference approximation between two closely spaced accelerometers, as given by equation (8.7). Applying equation (8.7) to equation (8.11) above, gives:

$$G\left(M, \frac{\partial\theta}{\partial t}\right) = \frac{d}{j2\pi f \Delta x} \{G(F, a_2) - G(F, a_1)\}. \quad (8.12)$$

In the experimental method described later on, the cross-spectral density functions are calculated using the physically closest force transducer to each response accelerometer. Thus:

$$G\left(M, \frac{\partial\theta}{\partial t}\right) = \frac{d}{j2\pi f \Delta x} \{G(F_2, a_2) - G(F_1, a_1)\}. \quad (8.13)$$

The moment point mobility is then estimated by substituting equations (8.10) and (8.13) into equation (8.8) to give:



$$Y_M = \frac{1}{j2\pi fd\Delta x} \frac{\{G(F_2, a_2) - G(F_1, a_1)\}}{G(F, F)}. \quad (8.14)$$

One error when using the finite-difference approximation is the underestimation of the true value due to the first spatial derivative of the transverse acceleration  $a$ . In reference [28], a correction factor for accelerometer based VEF measurements  $k\Delta x/\sin(k\Delta x)$  is suggested, which compensates for the finite-difference approximation error. When applied to equation (8.14), this correction factor leads then to the following expression for a corrected measurement of the moment point mobility:

$$(Y_M)_{cr} = \frac{k}{j2\pi fd \sin(k\Delta x)} \frac{\{G(F_2, a_2) - G(F_1, a_1)\}}{G(F, F)}. \quad (8.15)$$

### 8.3.3 Input Energy Measurements

In order to measure energy input to a beam under moment excitation of the structure the applied moment and rotational velocity at the excitation location need to be taken into account. Analogously to the input energy of a force excited beam given by equation (3.27), the energy input to a beam by moment excitation can be calculated by taking the real part of equation (8.11) as:

$$(P_{in})_M = \Re \left\{ G \left( M, \frac{\partial \theta}{\partial t} \right) \right\} \quad (8.16)$$

Applying the finite-difference correction factor  $k\Delta x/\sin(k\Delta x)$  equation (8.16) can be written as:

$$(P_{in})_{M_{cr}} = \Re \left\{ \frac{kd}{j2\pi f \sin(k\Delta x)} \{G(F_2, a_2) - G(F_1, a_1)\} \right\} \quad (8.17)$$

### 8.3.4 Consideration of Moment Arm Inertia

The mass of the moment arms was kept to a minimum to avoid bias errors in measuring the moment mobility when using an I-shaped exciter configuration [93, 98]. It was shown in references [93] and [98] that an I-shaped exciter configuration will induce additional force and moment contributions at the excitation location due to the translational and the rotational inertia of the I-piece. Hence, the true moment  $M_{cr}$  applied at the excitation location  $x_0$  was shown to consist of the measured force couple  $M$  given by equation (8.9) less a contribution from a rotary inertia term  $J\partial^2\theta/\partial t^2$ . Thus:

$$M_{cr} = M - J \frac{\partial^2\theta}{\partial t^2}. \quad (8.18)$$

Here,  $J$  is the rotary inertia of the I-piece. In references [93] and [98] this correction was applied directly. However, an alternative approach adopted in this work is to calculate the magnitude of this proposed correction using the finite-difference and spectral density techniques outlined in sections 8.3.1 and 8.3.2 and, hence, determine the frequency range where the measured moment  $M$  is a good approximation to the actual moment  $M_{cr}$ . Thus, from equation (8.18) the following ratio can be formed:

$$\frac{M_{cr}}{M} = 1 - \frac{J}{M} \frac{\partial^2\theta}{\partial t^2} \quad (8.19)$$

The quantity  $(\partial^2\theta/\partial t^2)/M$  is now evaluated using the  $H_1(f)$  estimator with the rotational acceleration approximated using the finite-difference expression given by the bracket term in equation (8.7). Hence, since equation (8.14) represents  $(\partial\theta/\partial t)/M$ , the quantity  $(\partial^2\theta/\partial t^2)/M$  can be calculated by multiplying equation (8.14) by  $j2\pi f$ . The ratio of actual moment to measured moment  $M_{cr}/M$  is formed using equation (8.19). This ratio is employed to assess the likely error in using the measured moment  $M$  as an approximation for the actual moment  $M_{cr}$ .

To achieve moment excitation, the moment excitation rig is aligned carefully such that the moment arms are struck by the impact fork at the same point in time, ensuring that the impact forces are equal and simultaneous. The outline of the impact fork is shown in dotted outline over the moment arms of the beam in Figure 7.7. The I-shape exciter arrangement has advantage over the T-shape exciter that any extraneous force due to an impure force couple is in the direction of low mobility. This advantage also applies when comparing excitation via the moment arms with direct application of the force couple onto the beam.

### 8.3.5 Application of the Measurement Methods to a Beam

Measurement of the moment point mobility of the beam was undertaken by implementing equation (8.15) using the transducer signals  $F_1$ ,  $F_2$ ,  $a_1$  and  $a_2$ , as shown in Figure 7.7. The accelerometer spacing  $\Delta x$  was chosen to be  $0.15\lambda$ , where  $\lambda$  was the wavelength of the highest frequency to be measured, in this case, 1.6 kHz. It can be shown that the theoretical cross mobility of a force and moment excited infinite beam will be zero [103]. However, in general a moment mobility measurement formed by measuring  $(\partial\theta/\partial t)/M$ , as implemented in equation (8.15), will contain errors due to a non-zero cross mobility and extraneous force  $F$  because of the rotary inertia of the I-piece. Therefore, a calculation of the force to moment ratio  $F/M$  will indicate the quality of the applied moment [92, 93, 98].

Assuming that any extraneous force due to an impure force couple acts in the longitudinal direction of the beam and, thus, can be neglected, the unwanted force  $F$  acting in the transverse direction at the measurement location  $x_0$  will be due solely to the translational inertia of the I-piece [93, 98]. Hence:

$$F = m \frac{\partial^2 u}{\partial t^2}. \quad (8.20)$$

Here,  $m$  is the mass of the I-piece. Thus, the force to moment ratio  $F/M$  is given by:

$$\frac{F}{M} = \frac{m}{M} \frac{\partial^2 u}{\partial t^2}. \quad (8.21)$$

The transverse acceleration  $\partial^2 u / \partial t^2$  can be calculated using the finite-difference approximation as:

$$\frac{\partial^2 u}{\partial t^2} \approx \frac{a_2 + a_1}{2}. \quad (8.22)$$

Thus, the transverse acceleration to moment ratio  $(\partial^2 u / \partial t^2) / M$  can be calculated using the  $H_1(f)$  estimator in a manner analogous to that described in 8.3.1 and 8.3.2 for the rotational velocity to moment ratio  $(\partial \theta / \partial t) / M$  as:

$$\frac{\left( \frac{\partial^2 u}{\partial t^2} \right)}{M} = \frac{1}{2d} \frac{\{G(F_2, a_2) + G(F_1, a_1)\}}{G(F, F)} \quad (8.23)$$

The force to moment ratio  $F/M$  can be calculated using equation (8.21).

Measurement of the energy input to the structure was calculated between the applied moment and resulting rotational velocity using equation (8.17). To verify the moment input energy measurement two accelerometers  $a_3$  and  $a_4$  were also placed opposite the force impact points on the moment arms, as shown in Figure 7.7. The energy input to the moment arms was then calculated using the measured force and resulting transverse velocity on the tip of the moment arms by employing equation (3.27). Two accelerometer pairs  $(a_5, a_6)$  and  $(a_7, a_8)$  were also placed in the vibrational farfield of the beam shown also in Figure 7.7. These pairs of accelerometers were used to measure transmitted energy along the beam by employing the two-accelerometer power flow technique implemented in equations (8.4) and (8.5).

The acquired signals were processed using a multi-channel spectrum analyser with the FFT folding frequency set at 1.6 kHz. The record length used for each acquired signal was 2 seconds and an average of 10 impacts was used to form the relevant auto and cross-power spectral density functions, which had a frequency resolution bandwidth of 0.5 Hz. Thus, the spectral density data presented in section 9.3 were scaled by the record length and the resolution bandwidth to obtain energy data in units of Joule/Hz [126].

## 8.4 Summary

This chapter has described the measurement method of previously defined VEF and energy based expressions for force excited and moment excited beam structures. Force excitation has been applied to “infinite” and simply supported beams. ESPI is employed here to acquire the complex beam displacement for the force excited beams. The ESPI recorded complex beam displacement was then used as an input to the VEFESPI method in order to determine VEF from the ESPI displacement measurement. To carry out a simple energy balance check VIP was measured using an accelerometer and force transducer at the driving point. To compare ESPI measured VEF with measured accelerometer based VEF the well known two-accelerometer (“infinite” ESPI beam) and four-accelerometer VEF (simply supported ESPI beam) techniques were implemented.

A novel measurement method to measure the point mobility and energy input of a moment excited beam was introduced. The method utilised a first order finite-difference approximation to determine the rotational velocity measured by a pair of accelerometers located at the excitation location in combination with a specially designed moment excitation rig. Due to the attachment of the I-piece an additional undesired force and moment contribution occurs due to the moment arm inertia. These erroneous forces and moments were described using an actual moment to measured moment ratio, as given by equation (8.19), and a transverse force to moment ratio, as given by equation (8.21). Thus, an error appraisal is feasible.

## **9 MEASUREMENT OF VIBRATIONAL ENERGY IN BEAMS: EXPERIMENTAL RESULTS**

### **9.1 Introduction**

This chapter presents results obtained from experimental beam measurements. Within this research force excited and moment excited structures were investigated. Force excitation is used to measure vibrational energy flow (VEF) and energetic quantities under use of electronic speckle pattern interferometry (ESPI) for “infinite” and simply supported beam structures.

Moment excitation of beams was the second major objective of this research. Within this chapter experimental results of a moment excited “infinite” beam are presented under use of a novel measurement technique introduced in section 8.3. Thus, recorded moment point mobility and input energy results are shown.

### **9.2 Force Excited Beam Measurements**

This section is divided into two parts. Section 9.2.1 contains the experimental results obtained on an ESPI measured “infinite” beam that was recorded during the work of reference [62]. Continulative from [62] the analysis is



extended here to a two-dimensional analysis, whereas in reference [62] one-dimensional VEF analysis only was considered. Section 9.2.2 contains experimental results obtained from the measured simply supported ESPI beams. Here, the measured VEF and measured energetic quantities are presented.

## 9.2.1 “Infinite” Beam Measurements

### 9.2.1.1 Point Mobility, Vibrational Input Power and Accelerometer Based Transmitted Vibrational Energy Measurements

The point mobility of the “infinite” beam was measured using the frequency response function (FRF) between the acceleration and the force at the driving point. Substituting this quantity into equation (8.1), resulted in the measured point mobility, as shown in Figure 9.1. Herein,  $f$  shown on the  $x$ -axis is the frequency. It can be seen from Figure 9.1(a) that the magnitude of

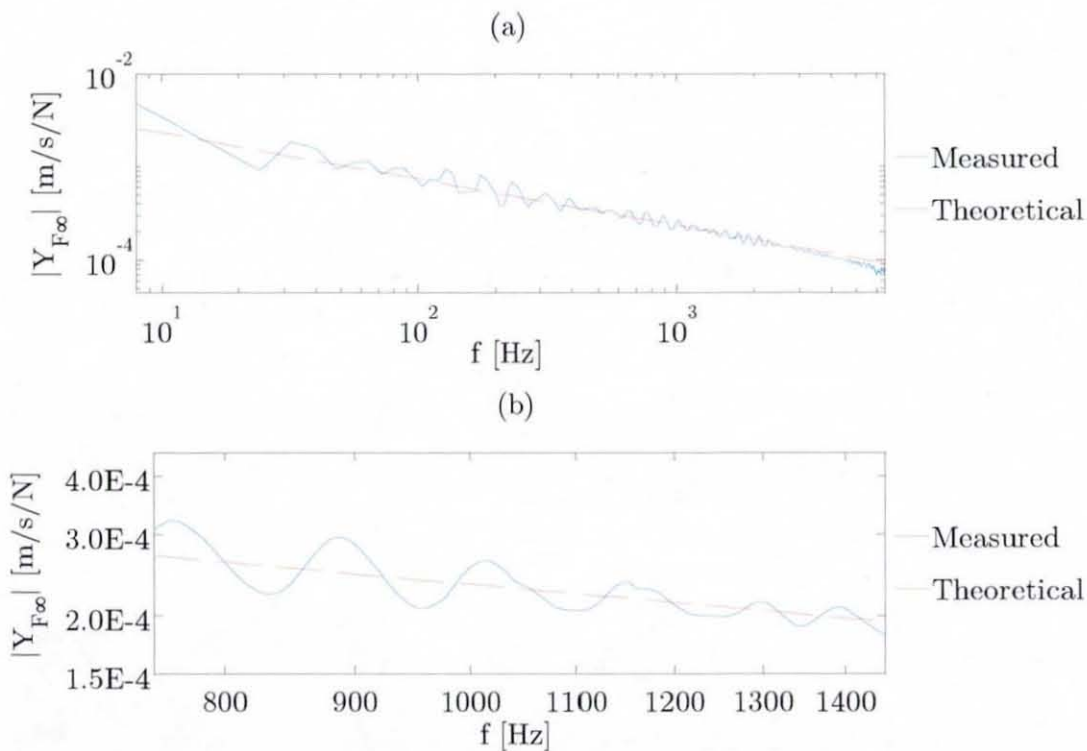


**Figure 9.1** Modulus of the measured and theoretical point mobility of the force excited “infinite” ESPI beam: (a) 10 Hz-6.4 kHz, (b) 750-1450 Hz.

the measured point mobility  $|Y_{F_\infty}|$  of the “infinite” ESPI beam varies around the theoretical point mobility of the equivalent infinite structure, indicating that there is still some modal behaviour within the “infinite” beam structure despite the anechoic termination. Nevertheless, a good approximation of infinite beam behaviour was achieved. Figure 9.1(b) displays the measured and theoretical point mobility in a frequency range of 750-1450 Hz. Three excitation frequencies, 801 Hz, 1112 Hz and 1146 Hz were selected out of that frequency range. As it can be seen from Figure 9.1(b), these frequencies were chosen to represent a local minimum in the FRF at 1112 Hz, a local maximum in the FRF at 1146 Hz and a frequency close to the theoretical infinite beam response at 801 Hz. Table 6.1 displays again the assumed properties of the experimental ESPI beam.

Young's modulus	$E = 2.07 \cdot 10^{11} \text{ N/m}^2$
mass density	$\rho = 7.85 \cdot 10^3 \text{ kg/m}^3$
beam width	$b = 60 \cdot 10^{-3} \text{ m}$
beam thickness	$t = 10 \cdot 10^{-3} \text{ m}$

**Table 6.1** (repeated) “Infinite” ESPI beam properties.

Table 9.1 displays the vibrational input power (VIP) values measured at the driving point for all three frequencies. The theoretical point mobility based VIP  $(P_m)_{FP}$  was calculated from equation (8.2). The more accurate VIP obtained from the measured cross-spectral density between force and acceleration at the driving point  $(P_m)_{Fa}$  was calculated from equation (3.27). It has been shown in sections 5.3.2 and 5.3.3 that the transmitted vibrational energy of an infinite beam is half the energy injected into the beam. Thus, in Table 9.1 half the input power values are given, since transmitted vibrational energy has been measured at one side of the beam only. The transmitted vibrational energy values were measured within the ESPI window, which was located in the farfield of the beam (see Figure 7.6). Equation (8.4) was employed to calculate the two-accelerometer based farfield transmitted

energy  $P_{tr_2}$ . Equation (8.5) was used to correct  $P_{tr_2}$  in order to account for the finite-difference approximation error.

Power quantity [W]	801 Hz	1112 Hz	1146 Hz
Half input power, $(P_m)_{FP}$	$5.23 \cdot 10^{-4}$	$2.88 \cdot 10^{-4}$	$1.41 \cdot 10^{-3}$
Half input power, $(P_m)_{Fa}$	$4.04 \cdot 10^{-4}$	$2.45 \cdot 10^{-4}$	$1.58 \cdot 10^{-3}$
Transmitted energy, $P_{tr_2}$	$3.46 \cdot 10^{-4}$	$2.26 \cdot 10^{-4}$	$1.20 \cdot 10^{-3}$
Corrected transmitted energy, $(P_{tr_2})_{cr}$	$4.03 \cdot 10^{-4}$	$2.80 \cdot 10^{-4}$	$1.49 \cdot 10^{-3}$

**Table 9.1** Measured input power and transmitted energy (all values given in Watts).

#### 9.2.1.2 Vibrational Energy Flow Measurements Using ESPI

The force excited “infinite” ESPI beam experiment was conducted in reference [62] and results were later published in references [63, 64]. Figure 9.2 displays the measured amplitude and phase of the “infinite” beam at 801 Hz, as provided by the ESPI system. With the measured amplitude and phase a beam displacement was generated by employing equation (8.6). It can be seen from Figure 9.2 that the measured “infinite” beam displacement is a two-dimensional  $N_x \times N_y$  matrix containing the complex, “infinite” beam displacement information.

It can also be seen from Figure 9.2 that within the amplitude and phase data matrices some blank regions occur indicating locations of low laser light illumination and, thus, missing information about the spatial distribution of amplitude and phase at these points. To avoid blank regions, only regions with fully valid information were used in references [63, 64] by truncating the generated ESPI displacement down to one measured wavelength only. Further, in references [63, 64] single rows along the  $x$ -axis were extracted out of the two-dimensional ESPI displacement matrix in order to determine ESPI based VEF using a single-row and multi-row analysis. This was a quite cumbersome process.



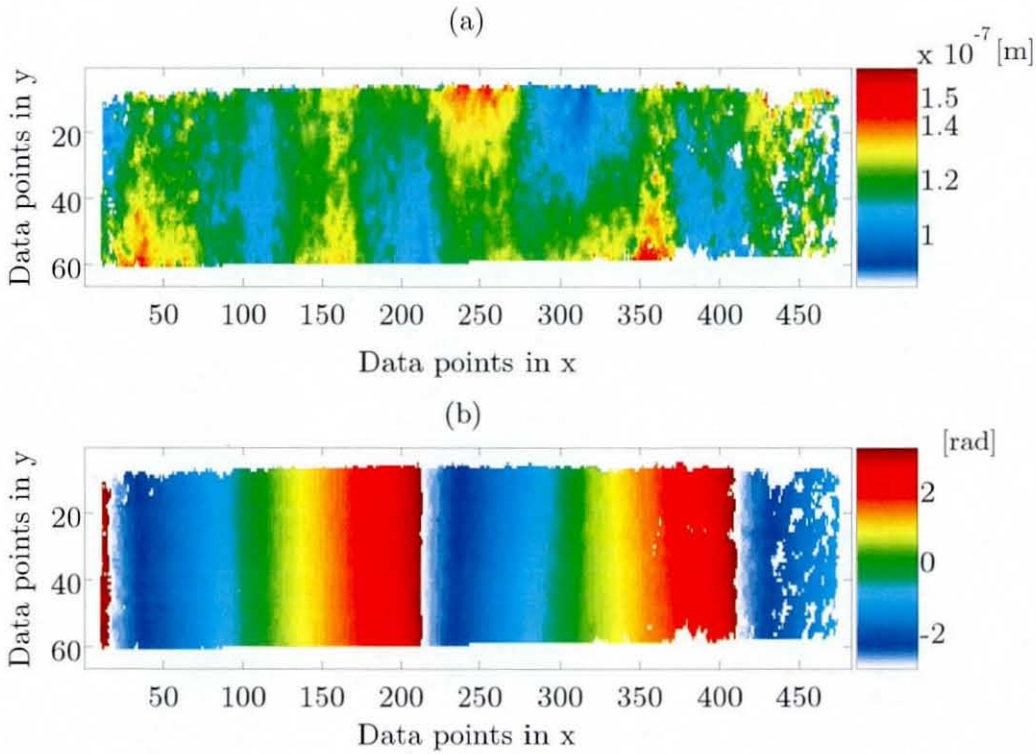


**Figure 9.2** ESPI image of measured beam displacement at 801 Hz: (a) amplitude, (b) phase.

However, the study herein has been extended by analysing the data two-dimensionally rather than extracting single rows out of the ESPI displacement matrix. Further, beam regions containing pockets of blank data were also included within the analysis. Thus, the spatial range of the generated ESPI displacement was increased to two wavelengths.

Figure 9.3 displays the ESPI displacement of the 801 Hz “infinite” beam displacement. Here,  $u(x,y)$  is the ESPI measured two-dimensional beam displacement and  $x$  is the beam length. The ESPI measurement window was truncated at the beam edges to include data within the beam width only. It was also truncated along the beam length to include an integer number of waves, a requirement of the Fast Fourier Transform (FFT), to avoid leakage effects. The one-dimensional displacement shown in Figure 9.3(c) and Figure 9.3(d) is the extracted row at  $y = 25 \cdot 10^{-3}$  m. It can be seen from Figure 9.3 that especially at the beginning and the end of the ESPI window many blank regions occur. Since these locations contain zero information, the

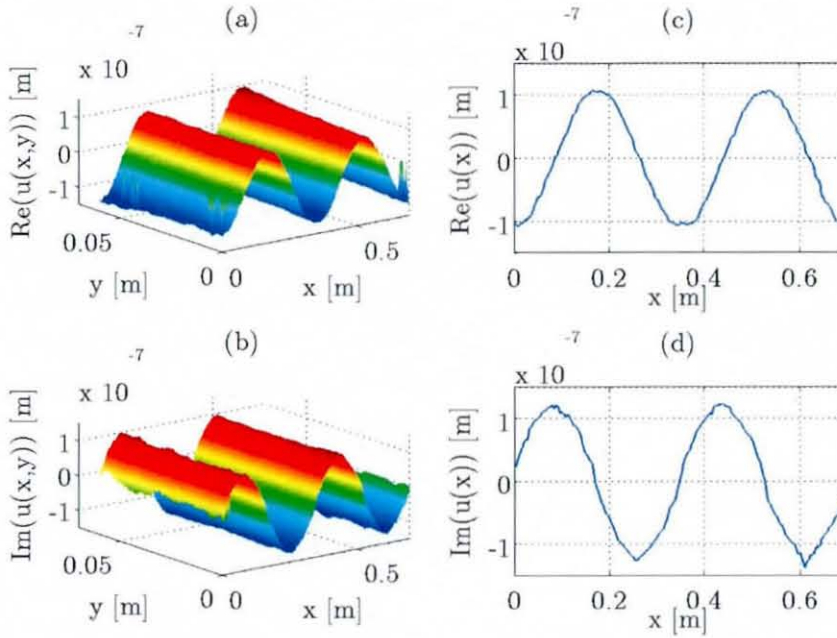


**Figure 9.3** Complex and truncated ESPI displacement of the “infinite” beam at 801 Hz: (a) 2D real part, (b) 2D imaginary part, (c) 1D real part, (d) 1D imaginary part.

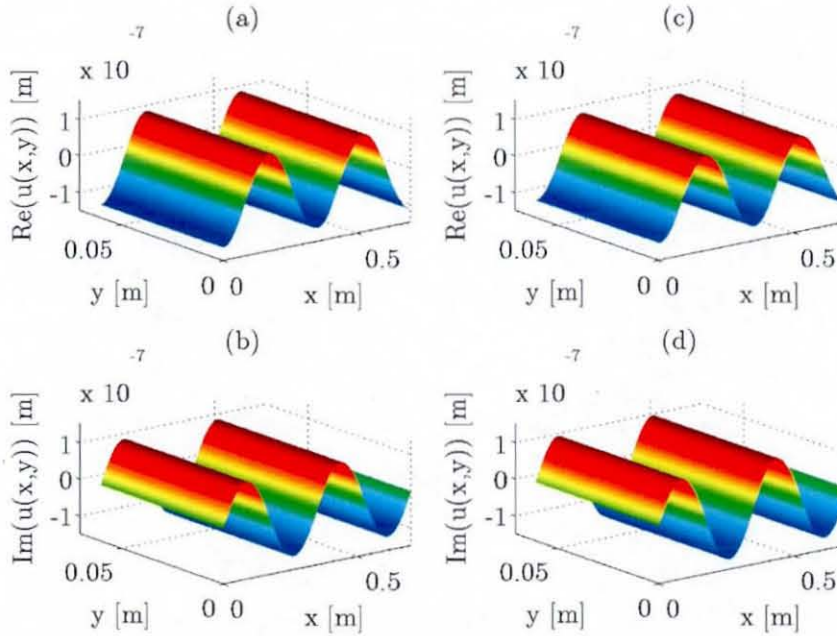


**Figure 9.4** Complex filtered and truncated ESPI displacement of the “infinite” beam at 801 Hz: (a)-(b) 2D ideal filtered, (c)-(d) 2D Butterworth filtered.

ESPI displacement is further contaminated by noise that is not relatable to the beam vibration process. The complex, two-dimensional ESPI beam displacement, as exhibited by Figures 9.3(a) and 9.3(b), is taken as input to the VEFESPI method, as shown by Figure 4.6. Thus, spatial derivatives of the measured and  $k$ -space filtered ESPI beam displacement were determined and substituted into equation (3.33). Figure 9.4 displays the complex and filtered displacement. It can be noticed that the wavenumber filtering process removes most of the unwanted noise components. Further, as it can be seen from Figure 9.4(a) that unwanted torsional motion of the beam was also removed. This torsional motion occurs from the fact that the electrodynamic exciter could not be attached exactly in the middle of the beam. Figure 9.5 displays the active VEF of the 801 Hz excited “infinite” beam. Here, the

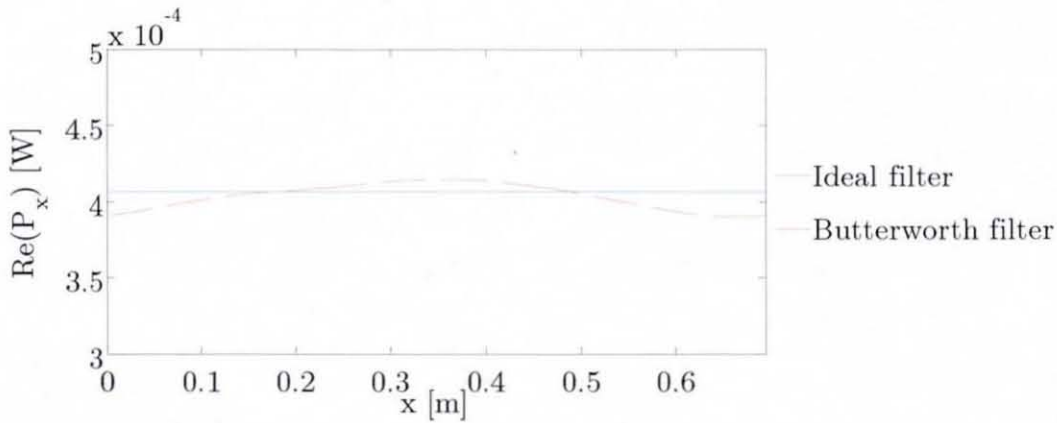


**Figure 9.5** Active VEF of the “infinite” ESPI beam at 801 Hz filtered with the ideal filter and Butterworth filter.

middle line of the two-dimensional VEF matrix is shown only, since the filtered VEF is constantly distributed across the beam width. The imaginary part is not shown, since this part is zero due to measurements taken in the farfield only. The filter cut-off points were employed from Table 6.6. It is noticeable from Figure 9.5 that the ideal filter produces a straight line and, thus, a constant VEF value, whereas the Butterworth filtered VEF is varying over the beam’s distance due to a low frequency noise component passing through the low pass filter.



### 9.2.1.3 Energy Balance

Simple energy balance within the “infinite” beam structure allows for a general assessment about the accuracy of the measurement. As explained previously, VIP at driving point and also VEF within the ESPI window was measured using charge type transducers. These measurement techniques are widely accepted as single point measurement techniques. Equation (3.38) displays the simple energy balance within the infinite beam. From equations (3.38), (5.20), and (5.24) it can be realised that half of the VIP should be equal to the transmitted energy. This simple energy balance is used to investigate the accuracy of the “infinite” ESPI beam measurements. Figure 9.6 shows the comparison of half of the measured VIP  $(P_{in})_{Fa}$ , the measured corrected transmitted energy  $(P_{tr2})_{cr}$  and the ESPI measured ideal filtered

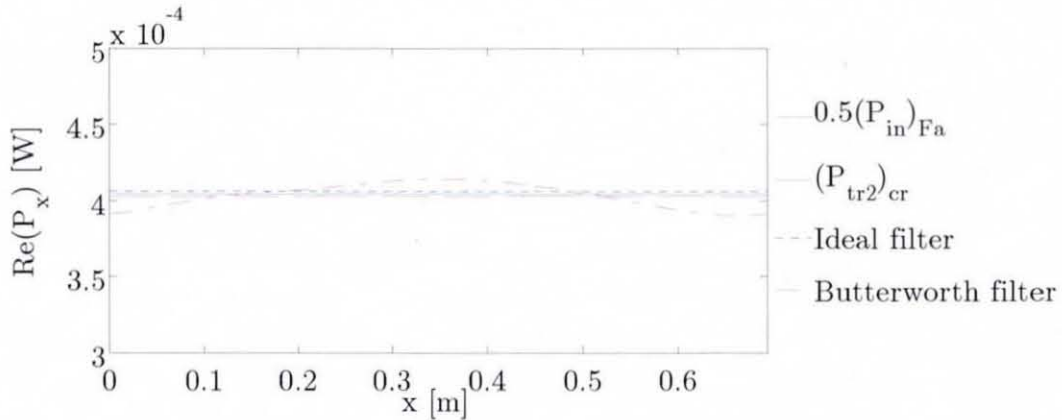


**Figure 9.6** Comparison of measured input power  $(P_{in})_{Fa}$ , measured corrected transmitted energy  $(P_{tr2})_{cr}$  and measured ESPI based energy flow at 801 Hz.

and Butterworth filtered VEF. Note,  $(P_{in})_{Fa}$  and  $(P_{tr2})_{cr}$  are single values. However, for better visibility they are shown against the beam length. It can be seen from Figure 9.6 that the ideal filtered and Butterworth filtered ESPI based energy values within the experimental “infinite” beam are very close to the transducer measured energy values.

Figure 9.7 displays the relative difference between the ESPI measured VEF and the transducer measured VIP and VEF values. The deviation



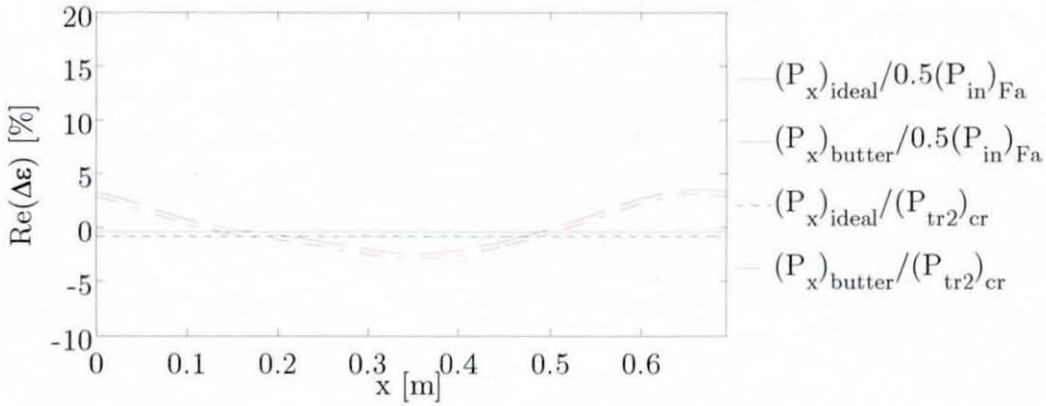


**Figure 9.7** Relative difference in percent between ESPI measured VEF and transducer measured energy values.

between the ideal filtered ESPI based VEF and transducer based energy values is less than 1%. The mean value of the Butterworth filter VEF is less than 0.3%. Table 9.2 summarises the VEF results and the relative deviation of each “infinite” beam measurement at 801, 1112 and 1146 Hz. The corresponding figures of the truncated displacements and energy balances of the 1112 Hz and 1146 Hz measurements are shown in Appendix A20. From there and from Table 9.2 it can be seen that the deviations of the 1112 Hz and 1146 Hz ESPI measurements are higher than the 801 Hz ESPI measurement. Especially for the 1146 Hz result, which deviates about 25% compared to the corresponding accelerometer based transmitted energy measurement.

#### 9.2.1.4 Discussion

The results shown in the previous section and in Appendix A20 indicate some deviation between the measured ESPI VEF and the measured accelerometer based power values. It can be seen from Table 9.2 that the transmitted energy  $(P_{tr2})_{cr}$  is not always equal to half the VIP  $(P_{in})_{Fa}$ . The approximation that half the input energy is flowing to the right and half the input energy is flowing to the left of the beam is not always true, since it assumes that both anechoic termination ends are dissipating the same amount of energy.

Power quantity	801 Hz	1112 Hz	1146 Hz
Half input power, $(P_{in})_{FP}$	$5.23 \cdot 10^{-4}$	$2.88 \cdot 10^{-4}$	$1.41 \cdot 10^{-3}$
Half input power, $(P_{in})_{Fa}$	$4.04 \cdot 10^{-4}$	$2.45 \cdot 10^{-4}$	$1.58 \cdot 10^{-3}$
Transmitted power, $P_{tr2}$	$3.46 \cdot 10^{-4}$	$2.26 \cdot 10^{-4}$	$1.20 \cdot 10^{-3}$
Corrected transmitted power, $(P_{tr2})_{cr}$	$4.03 \cdot 10^{-4}$	$2.80 \cdot 10^{-4}$	$1.49 \cdot 10^{-3}$
Ideal filtered VEF, $\Re\{(P_x)_{ideal}\}$	$4.06 \cdot 10^{-4}$	$3.18 \cdot 10^{-4}$	$1.87 \cdot 10^{-3}$
Butterworth filtered VEF, $1/N_x \sum \Re\{(P_x)_{butter}\}$	$4.04 \cdot 10^{-4}$	$3.18 \cdot 10^{-4}$	$1.87 \cdot 10^{-3}$
$(\Delta \mathcal{E})$ of $\Re\{(P_x)_{ideal}\}/0.5(P_{in})_{FP}$	-0.4%	-29.8%	-18.4%
$(\Delta \mathcal{E})$ of $1/N_x \sum \Re\{(P_x)_{butter}\}/0.5(P_{in})_{FP}$	0.2%	-29.7%	-18.4%
$(\Delta \mathcal{E})$ of $\Re\{(P_x)_{ideal}\}/(P_{tr2})_{cr}$	-0.9%	-13.5%	-24.9%
$(\Delta \mathcal{E})$ of $1/N_x \sum \Re\{(P_x)_{butter}\}/(P_{tr2})_{cr}$	-0.3%	-13.5%	-24.9%

**Table 9.2** Measured input power and transmitted energy (all power values given in Watts).

It can be seen from Table 9.2 that the relative difference between active ESPI measured VEF  $P_x$  and corrected transmitted energy  $(P_{tr2})_{cr}$  is about 0.9% at 801 Hz, -13.5% at 1112 Hz and -25% at 1146 Hz revealing a overestimation especially at the latter two excitation frequencies. The 801 Hz measurement showed a very good agreement. It is evident from Figures A20.3 and A20.5 that the 1112 Hz and especially the 1146 Hz measurement were contaminated by a considerable amount of torsion due to off-centre shaker attachment. The torsional motion could be removed by the 2D filtering, as evident from Figure 9.4. The 2D filtering process determines a mean displacement between the lower and higher twisted beam sides. However, if the torsional motion is not exactly about the middle line of the beam width, the resulting displacement amplitude due to 2D filtering can be higher or lower than the actual amplitude due to purely flexural beam motion. Since the square of the displacement amplitude is proportional to VEF, an

unwanted off-centre torsional beam motion could be the reason for overestimating the ESPI VEF at 1112 Hz and 1146 Hz.

Another crucial point to consider is related to the spatial resolution of the ESPI measurements. The spatial resolution, or spatial sampling interval, is defined as the ratio of measure span  $L_x$  and the number of data points  $N_x$  included in the measure span, i.e.  $\Delta x = L_x / N_x$ . It has been shown by equation (6.5) that the wavenumber spectral resolution  $\Delta k_x$  is a function of  $\Delta x$  and  $L_x$ , respectively. Since the spectral resolution is used to define the wavenumber matrix  $K_x$ , as evident from equation (6.6), the determined amount of VEF is dependent upon the spectral resolution and, thus, the correct measuring span. Here, the spatial resolution of the ESPI system was defined by the number of infinite beam wavelengths included in the signal ( $2\lambda$ ) and the number of data points included in the truncated  $2\lambda$  signal length, i.e.  $\Delta x = 2\lambda / N_x$ .

Figure 9.8 displays the relation between the relative alterations of the ESPI measured active VEF  $\text{Re}(\Delta P_x)$  in dependency upon the relative change

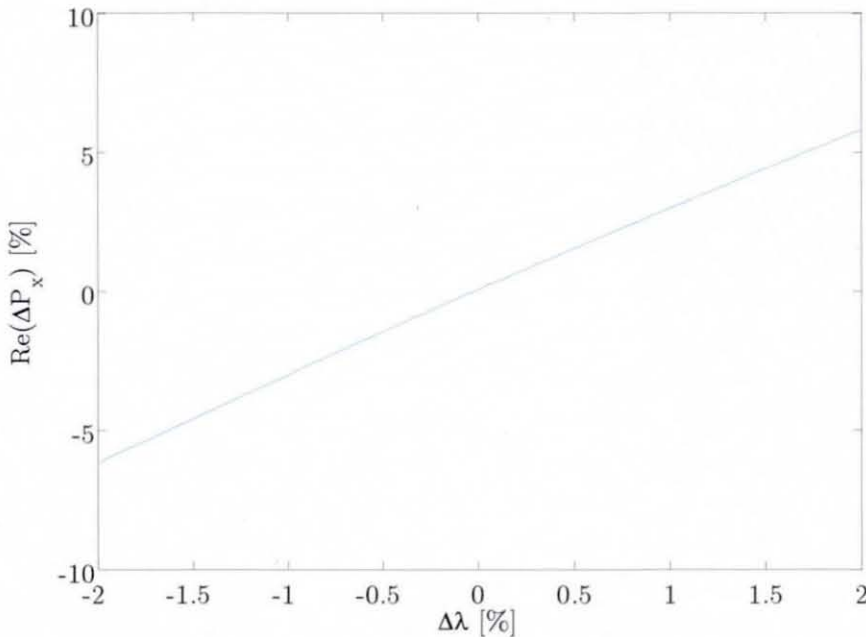


**Figure 9.8** Relative change of measured ESPI based VEF in dependency upon the relative change of wavelength span in percent of the ideal filtered ESPI based VEF measurement at 801 Hz.



in measure span  $\Delta\lambda$  of the 801 Hz ideal filtered measurement. Note, the relative change  $\Delta\lambda$  of the active Butterworth filtered VEF is identical. It can be seen that a relative change in measure span of 2% yields to a change in measured energy flow of 6%. By truncating the data by hand it is possible that the measure span can be below or above the theoretical value of  $2\lambda$ . Thus, care must be taken in order to determine the true spatial resolution of the measure span.

The comparison of the ESPI measured VEF to the accelerometer measured energy flow is seen only as an indicator how well the ESPI measured VEF matches the accelerometer based measurements, widely accepted in VEF analysis. It cannot be used entirely as a judgement in how accurate the ESPI measured VEF is, since errors of the accelerometer based measurements are likely to occur. It shall also be pointed out that a better energy balance may be employed on a semi-infinite structure because the measured VIP is then flowing to one side only and, thus, can be taken better into account.

The use of a 2D method rather than a 1D approach, as taken in reference [64], simplifies the application of the VEFESPI method enormously despite the fact that some truncation process still needs to be employed. Of course the application of a periodisation technique would diminish the truncation effort further. However, the number of data points to be analysed is then doubled and, thus, the computation time would increase further.

## **9.2.2 Simply Supported Beam Measurements**

### **9.2.2.1 Point Mobility, Vibrational Input Power and Accelerometer Based Transmitted Vibrational Energy Measurements**

ESPI based VEF measurements of simply supported beams were conducted in this work by employing three differently damped beam specimens. ESPI measured vibration amplitude and phase of a non-damping layer, single unconstrained damping layer and a double unconstrained damping layer beam structure were recorded. The thickness of the attached single layer was

2.5 mm and the thickness of the attached double layer was about 5 mm. Both layers were attached to one side only using a mineral filled viscoelastic polymer material. Figure 9.9 displays the measured point mobility computed from equation (8.1) for all three beam specimen. It can be seen from Figure 9.9 that the attachment of the unconstrained damping layers had little effect, since the peak amplitude at each resonant frequency was only reduced

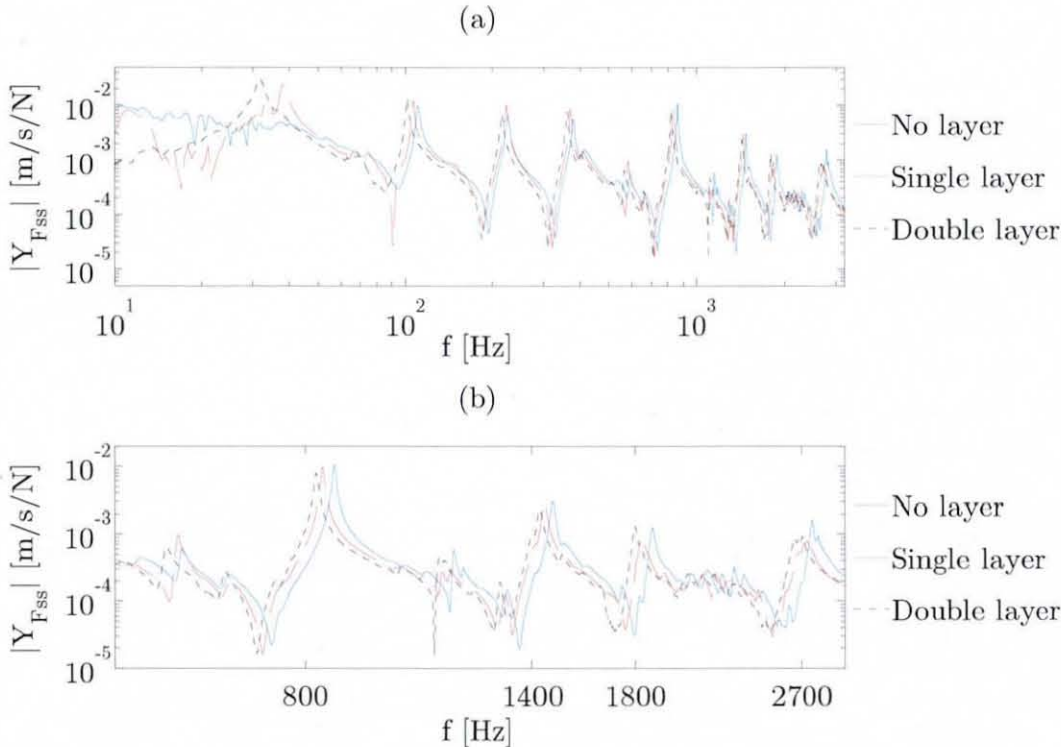


**Figure 9.9** Modulus of the measured point mobility of the force excited simply supported ESPI beams: (a) 10 Hz-3.2 kHz, (b) 500-3000 Hz.

slightly. This confirms the theoretical results obtained in section 5.5 concluding that a substantial damping can be achieved only within a thickness ratio range of  $1.5 \leq t_d/t_B \leq 10$ . Here,  $t_d/t_B$  was 0.25 and 0.5, respectively. From Figure 9.9(b) four resonant excitation frequencies were selected for each damping configuration. The frequencies were located at the resonant peak of the 6<sup>th</sup>, 8<sup>th</sup>, 9<sup>th</sup>, and 11<sup>th</sup> mode. Table 6.7 again displays the assumed material and geometric properties of the experimental ESPI beam.

Young's modulus	$E = 2.07 \cdot 10^{11} \text{ N/m}^2$
mass density	$\rho = 7.85 \cdot 10^3 \text{ kg/m}^3$
beam width	$b = 50 \cdot 10^{-3} \text{ m}$
beam thickness	$t = 10 \cdot 10^{-3} \text{ m}$
beam length	$L = 1 \text{ m}$

**Table 6.7** (repeated) Simply supported ESPI beam properties.

As shown in section 7.3.2.1 VIP at an off-centre excitation location of  $x_0 = 0.582 \text{ m}$  has been measured by substituting the measured cross-spectral density between the acceleration and force at the driving point into equation (3.27).

Transmitted vibrational energy was also measured on either side of the beam employing four-accelerometers and substituting the appropriate measured spectral densities into equation (8.3). Unfortunately, the applied accelerometer spacing of  $\Delta x = 3.25 \cdot 10^{-3} \text{ m}$  restricted the four-accelerometer method to a maximum frequency to be measured of the theoretical 5<sup>th</sup> mode only ( $\Delta x = 0.2\lambda = 80 \cdot 10^{-3} \text{ m}$ ) because a wrong spacing was applied during the measurement day. However, the two-accelerometer method can be applied instead using by equation (8.5). It was shown in Figure 6.21 that the nearfield of the infinite waves, which occurs at the excitation location, is much stronger than the two nearfields that occur at the simply supported boundaries. Hence, the nearfield at the excitation location is the most likely evanescent wave part that will have influence on the energy transmission measurements. One requirement of the two-accelerometer method is that the measurement should be carried out in the farfield. Farfield conditions are present at locations in the beam, which are at least  $\frac{3}{4}$  of a wavelength away from discontinuities, in this case the excitation location. The wavelength of the 6<sup>th</sup> mode was  $\lambda = 1/3 \text{ m}$ . Thus, the farfield is then  $0.25 \text{ m}$  away from the excitation location ( $0.75 \cdot \lambda$ ). The location of the accelerometer based measurements taken away from the excitation location was  $0.259 \text{ m}$  to the



left and 0.238 m to the right. Thus, the two-acceleration method can be used to measure transmitted energy with a little nearfield influence to be expected at the right-hand side of the 6<sup>th</sup> mode excitation only. The results of the four-accelerator and two-accelerator transmitted energy measurements are shown in Appendix A21. It can be seen from there that at some frequencies the total transmitted energy to the left and right of the excitation location is higher than the energy injected into the simply supported beam, e.g. 8<sup>th</sup> mode of the non-layer damped beam. Redman-White concluded in reference [28] that accelerometer based energy transmission measurements carried out on transverse beams that have standing wave ratios greater than 20:1 may yield to meaningless results. Thus, the accelerometer based measurements are believed not to be very trustworthy, since the simply supported beam structure was highly resonant with standing wave ratios much greater than 20:1.

#### **9.2.2.2 Vibrational Energy Flow Measurements Using ESPI**

As mentioned beforehand 12 measurements were taken from three differently damped simply supported beam structures. Due to shortage in space only one measured frequency will be shown here and the VEF results of the remaining frequencies are presented in Appendices A22 and A23, respectively. Figure 9.10 displays the complete measured ESPI amplitude and phase of the 11<sup>th</sup> mode single-layer damped beam. It can be seen from that figure that the ESPI signal contains some noise, as illustrated by coloured data points outside the beam area. The pin side here is on the right and the roller side is on the left of Figure 9.10. It is noticeable that on the right-hand side the displacement is approaching zero, whereas on the left-hand side non-zero deflection is present due to laser light occlusion by the rollers. Figure 9.11 displays the two-dimensional and one-dimensional truncated ESPI displacement generated from the measured ESPI amplitude and phase by numerically evaluating equation (8.6). As usual the one-dimensional beam displacement is extracted from the middle line of the beam's width. It can be seen that a quarter wave is truncated to either side of the beam reducing the



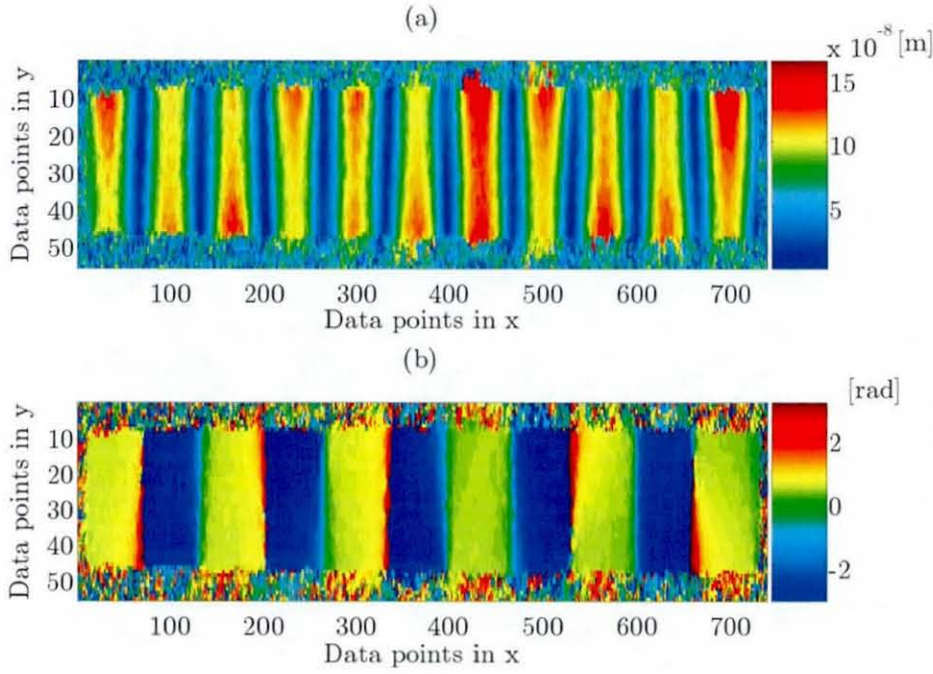


**Figure 9.10** ESPI image of the single-layer damped simply supported beam vibrating at the 11<sup>th</sup> mode and 2745 Hz: (a) amplitude, (b) phase.

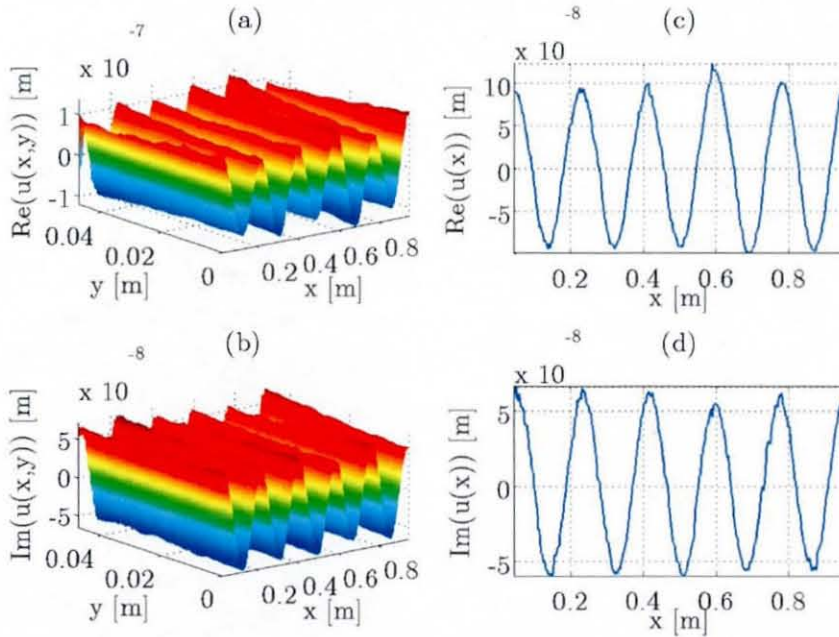


**Figure 9.11** Complex ESPI displacement of the single-layer damped simply supported beam vibrating at the 11<sup>th</sup> mode and 2745 Hz: (a) 2D real part, (b) 2D imaginary part, (c) 1D real part, (d) 1D imaginary part.

signal span in the  $x$  direction from 5.5 to 5 wavelengths. Further, it can be seen from Figures 9.11(a) and 9.11(b) that additionally to flexural vibration torsional motion is present in the measured ESPI displacement.

Figure 9.12 displays the ideal filtered and Butterworth filtered 11<sup>th</sup> mode single-layer damped beam displacement from which spatial derivatives were computed with aid of the KSD method. It is shown in Figure 9.12 that the initial torsional motion of the beam could be reduced (ideal filter) or completely filtered out (Butterworth filter). It can also be realised from

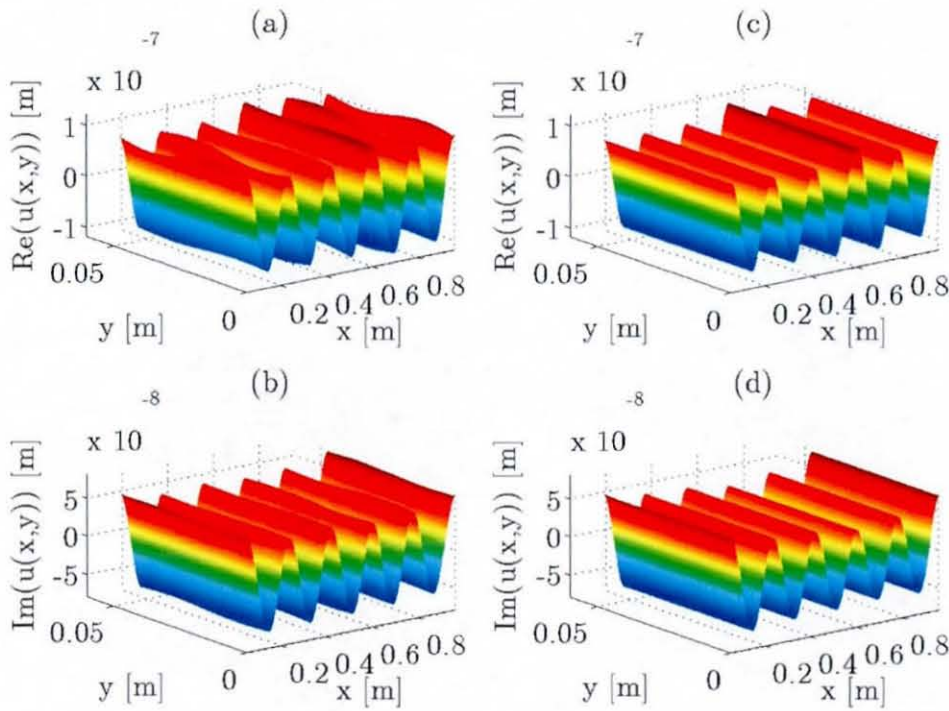


**Figure 9.12** Complex filtered ESPI displacement of the single-layer damped simply supported beam vibrating at the 11<sup>th</sup> mode and 2745 Hz: (a)-(b) 2D ideal filtered, (c)-(d) 2D Butterworth filtered.

Figure 9.12 that the oval 2D Butterworth filter removes the parasitic torsional beam motion much better than the 2D ideal filter because the cut-off wavenumber in the  $y$  direction can be adjusted more precisely. The truncated complex, two-dimensional ESPI displacement, as shown in Figures 9.11(a) and 9.11(b), was then taken as the input to the VEFESPI method.

Figure 9.13 exhibits the active and reactive VEF determined from the ideal filtered and Butterworth filtered 11<sup>th</sup> mode ESPI displacement data. It can be noticed from this figure that the discontinuity at the excitation location can be detected. There is a difference between ideal filtered and Butterworth filtered VEF. Also, a negative left-going flow (downstream) and positive-right going flow (upstream) was detected. However, as demonstrated in sections 6.3.2 and 6.3.3, the sharp discontinuity at the excitation location

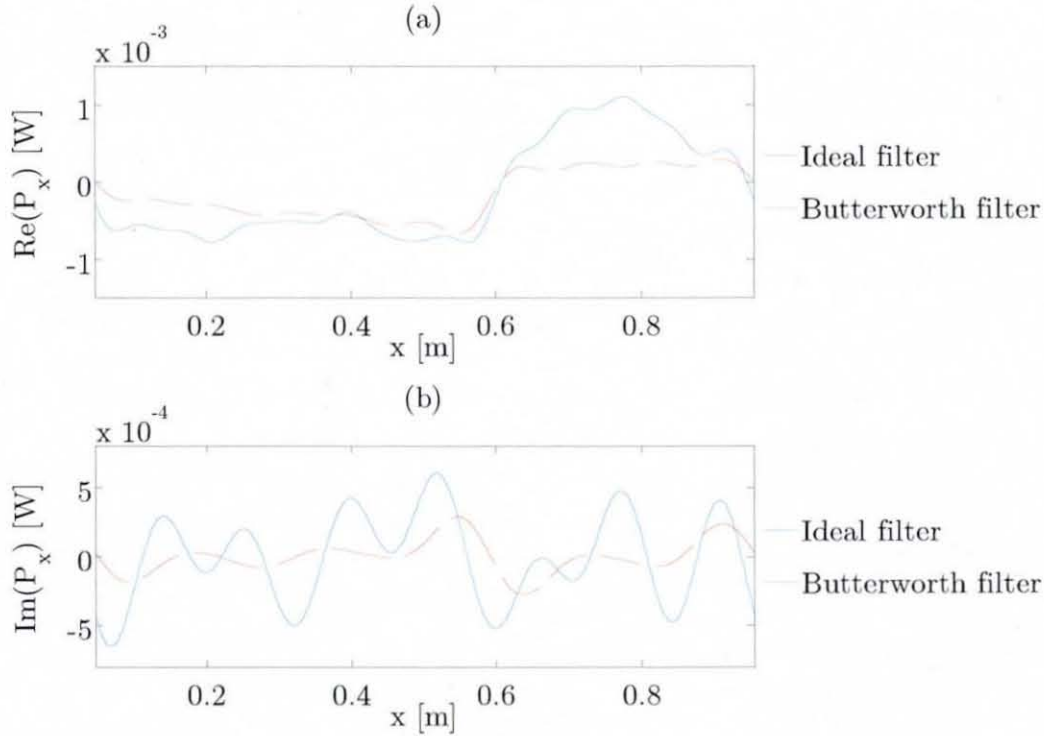


**Figure 9.13** ESPI measured VEF of the 11<sup>th</sup> mode single-layer damped beam displacement at 2745 Hz using the VEFESPI method: (a) active VEF, (b) reactive VEF.

cannot be determined in full detail. It can be seen from Figure 9.13(b) that the reactive energy flow curve shape strongly deviates from the theoretical curve shape, as shown in section 6.3.

In section 6.3 it was also demonstrated that the incremental integration of the potential energy density along the beam length led to better results in active VEF computation due to the use of more accurate second order derivatives only. Thus, the simply supported beam



displacement, as shown in Figure 9.11, is also analysed by the alternative incremental energy density integration (IEDI) method. The result of this analysis is shown in Figure 9.14. From there it can be seen that the computed active VEF curve is much closer to the theoretical VEF curve shape. The sharp energy flow discontinuity at the excitation location can be

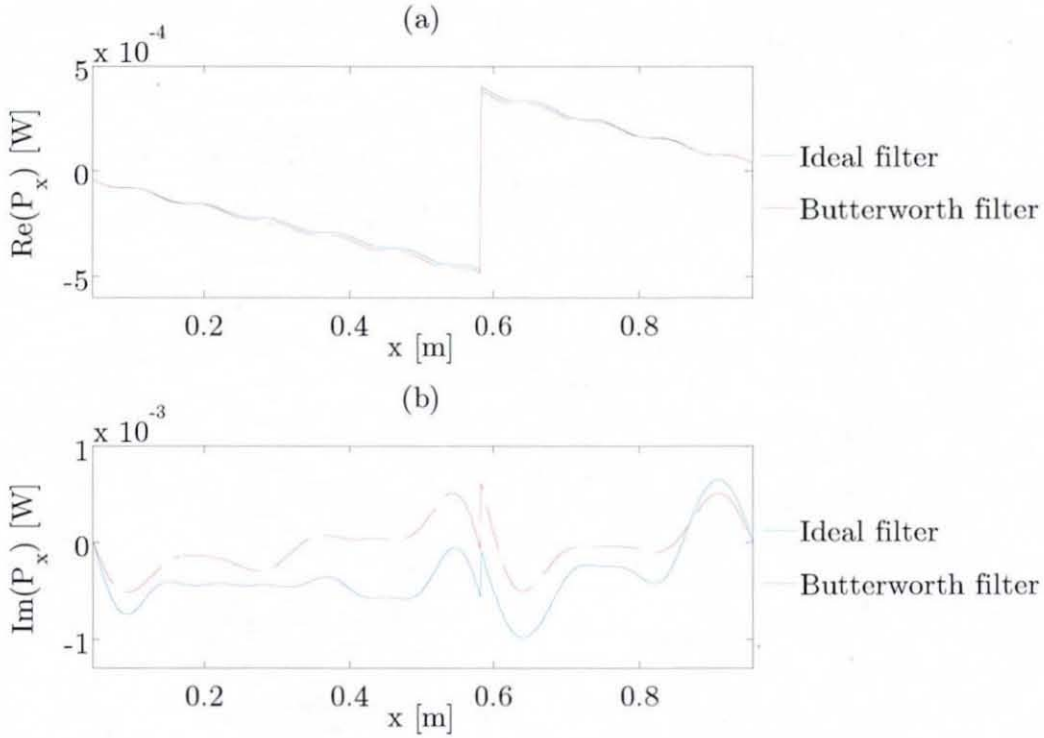


**Figure 9.14** ESPI measured VEF of the 11<sup>th</sup> mode single-layer damped simply supported beam at 2745 Hz using the IEDI method: (a) active VEF, (b) reactive VEF.

detected much better than using the conventional VEF determination method by evaluating equation (3.33). However, as already mentioned in section 6.3 the reactive energy flow cannot be computed very well. The VEF results of all frequencies are shown in Appendix A23. From there it can be seen that the IEDI computed active VEF from the measured ESPI displacements at all frequencies is very similar to the theoretical active VEF curve shape, whereas the reactive energy curve deviates in most cases.

### 9.2.2.3 Energy Balance

A simple energy balance, as employed in section 9.2.1.3, is not applicable to the simply supported beam, since the VEF is varying over space. However, an energy relationship between VIP and potential energy density was given by equation (3.40). This energy balance originally stated that the real part of the complex input energy density injected into the beam is proportional to the product of circular frequency, loss factor, and potential energy density. Since the input energy here is a global measure, the locally varying potential energy density needs to be integrated along the beam length. This is carried out in this work numerically. Figure 9.15 displays the ESPI measured potential energy density of the 11<sup>th</sup> mode single-layer damped beam displacement. It can be seen from Figure 9.15 that a quarter wave of potential energy density is missing on either side due to the initial truncation of the beam displacement. Thus, when integrating the potential energy

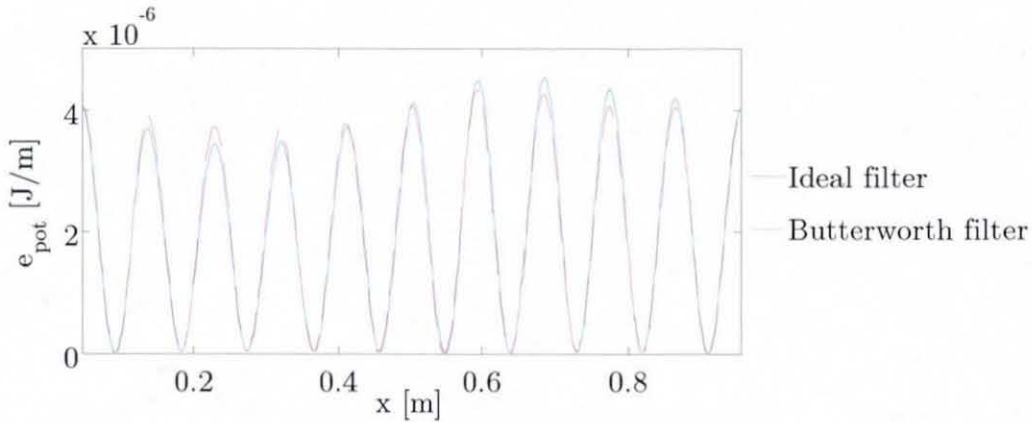


**Figure 9.15** Filtered ESPI measured potential energy density of the 11<sup>th</sup> mode single-layer damped beam displacement at 2745 Hz.

density along the beam length to compute the total transmitted vibrational energy (TTVE) from measured energetic data the missing energy density information to the left and right of the beam length need to be compensated for. To compute the active compensated TTVE from measured potential energy density it was assumed that 1/10 of the TTVE was missing and, thus, the integrated potential energy density was multiplied by 11/10. The

remaining frequencies were compensated accordingly to their ratio of number of wavelengths included in the signal and number of wavelengths missing due to the signal truncation. Also, the IEDI computed VEF curve shape from the ESPI measured energy densities, as shown in Figure 9.14, needed to be compensated because of the missing displacement information due to the truncation process. For the 11<sup>th</sup> mode displacement it was assumed that 1/10 of the TTVE was not regarded when integrating the potential energy density from the left-hand side of the beam, as shown in Figure 9.15. Further, 1/22 of the TTVE was not regarded when integrating the remaining potential energy density to the right-hand side of the beam's end. The remaining frequencies were compensated accordingly to their ratio of number of wavelengths included and number of wavelengths missing in the signal.

Note, when not considering the entire beam length in the energy balance, equation (3.3) has to be applied instead. However, the computation of the beam's VEF divergence relies on 4<sup>th</sup> order spatial derivatives, as shown by equation (3.34). Furthermore, the VIP has to be known as a density quantity. The 4<sup>th</sup> order spatial derivatives from measured data are considered to be very erroneous. Hence, the above described compensation procedure was used instead.

The Butterworth filtered TTVE results obtained from the integration of the ESPI based potential energy density along the beam length are shown in Tables 9.3 to 9.5 for each measured beam damping configuration. Note, the ideal filtered results are similar to the Butterworth filtered results.

$n$	6	8	9	11
$f_0$	857 Hz	1467.5 Hz	1874 Hz	2772 Hz
VIP, $(P_{in})_{Fa}$	$1.85 \cdot 10^{-4}$	$3.74 \cdot 10^{-4}$	$1.31 \cdot 10^{-4}$	$2.50 \cdot 10^{-4}$
TTVE, $(2\omega\eta[e_{pot} dx])_{butter}$	$1.19 \cdot 10^{-4}$	$2.16 \cdot 10^{-4}$	$4.53 \cdot 10^{-5}$	$1.52 \cdot 10^{-4}$
$(\Delta\epsilon)_{butter}$	35.7%	42.1%	65.5%	39.1%

**Table 9.3** Comparison of measured VIP and integrated ESPI measured potential energy density of the non-layer damped beam (all power values given in Watts).



$n$	6	8	9	11
$f_0$	833.5 Hz	1441 Hz	1830.5 Hz	2745 Hz
VIP, $(P_m)_{Fa}$	$9.08 \cdot 10^{-5}$	$2.48 \cdot 10^{-4}$	$2.10 \cdot 10^{-4}$	$1.95 \cdot 10^{-3}$
TTVE, $(2\omega \eta \int e_{pot} dx)_{butter}$	$1.40 \cdot 10^{-4}$	$1.46 \cdot 10^{-4}$	$8.50 \cdot 10^{-5}$	$9.19 \cdot 10^{-4}$
$(\Delta \varepsilon)_{butter}$	-53.6%	41.1%	59.6%	53%

**Table 9.4** Comparison of measured VIP and integrated ESPI measured potential energy density of the single-layer damped beam (all power values given in Watts).

$n$	6	8	9	11
$f_0$	821 Hz	1426 Hz	1797 Hz	2682 Hz
VIP, $(P_m)_{Fa}$	$2.86 \cdot 10^{-4}$	$1.67 \cdot 10^{-4}$	$1.90 \cdot 10^{-4}$	$2.65 \cdot 10^{-3}$
TTVE, $(2\omega \eta \int e_{pot} dx)_{butter}$	$3.77 \cdot 10^{-4}$	$2.16 \cdot 10^{-4}$	$1.83 \cdot 10^{-4}$	$2.16 \cdot 10^{-3}$
$(\Delta \varepsilon)_{butter}$	-31.7%	-29.4%	3.4%	18.5%

**Table 9.5** Comparison of measured VIP and integrated ESPI measured potential energy density of the double-layer damped beam (all power values given in Watts).

In Tables 9.3 to 9.5 the relative difference,  $\Delta \varepsilon = (1 - (P_m)_{Fa} / (2\omega \eta \int e_{pot} dx)) \cdot 100\%$ , between the Butterworth filtered TTVE and the accelerometer measured VIP  $(P_m)_{Fa}$  is shown. It can be seen that at 7 out of 12 frequencies the TTVE within the beam is less than the measured vibrational energy injected into the beam. It can also be seen from the tables above that at the double-layer damped beam the best agreement between ESPI measured TTVE and accelerometer measured VIP is obtained.

Tables 9.6 to 9.8 exhibit the accelerometer measured VEF and the Butterworth filtered VEF computed from the IEDI method at the location  $x_l = 0.323$  m and  $x_r = 0.82$  m. It can be seen from the tables below that the ESPI measured VEF is not at a close match to the accelerometer measured VEF. The initial presumption that the accelerometer based measurement of



transmitted energy in a high standing wave environment may yield to meaningless results can be validated by the results shown below.

$n$	6	8	9	11
$(P_{tr2})_{cr-left}$	$-8.45 \cdot 10^{-5}$	$-7.72 \cdot 10^{-5}$	$-1.02 \cdot 10^{-4}$	$-1.74 \cdot 10^{-4}$
$(P_{tr2})_{cr-right}$	$1.34 \cdot 10^{-4}$	$2.15 \cdot 10^{-4}$	$5.05 \cdot 10^{-5}$	$1.23 \cdot 10^{-4}$
$(P_x)_{butter-left}$	$-3.88 \cdot 10^{-5}$	$-7.22 \cdot 10^{-5}$	$-1.58 \cdot 10^{-5}$	$-5.03 \cdot 10^{-5}$
$(P_x)_{butter-right}$	$2.05 \cdot 10^{-5}$	$3.96 \cdot 10^{-5}$	$8.97 \cdot 10^{-6}$	$2.78 \cdot 10^{-5}$

**Table 9.6** Comparison of VEF measured by the two-accelerometer method and the IEDI method within the non-layer damped beam (all power values given in Watts).

$n$	6	8	9	11
$(P_{tr2})_{cr-left}$	$-1.74 \cdot 10^{-5}$	$-8.91 \cdot 10^{-6}$	$-5.19 \cdot 10^{-5}$	$-8.25 \cdot 10^{-4}$
$(P_{tr2})_{cr-right}$	$5.91 \cdot 10^{-5}$	$1.66 \cdot 10^{-4}$	$9.08 \cdot 10^{-5}$	$7.94 \cdot 10^{-4}$
$(P_x)_{butter-left}$	$-4.71 \cdot 10^{-5}$	$-4.86 \cdot 10^{-5}$	$-2.90 \cdot 10^{-5}$	$-2.95 \cdot 10^{-4}$
$(P_x)_{butter-right}$	$2.26 \cdot 10^{-5}$	$2.59 \cdot 10^{-5}$	$1.64 \cdot 10^{-5}$	$1.64 \cdot 10^{-4}$

**Table 9.7** Comparison of VEF measured by the two-accelerometer method and the IEDI method within the single-layer damped beam (all power values given in Watts).

$n$	6	8	9	11
$(P_{tr2})_{cr-left}$	$-4.73 \cdot 10^{-5}$	$-4.02 \cdot 10^{-5}$	$-5.44 \cdot 10^{-5}$	$-2.59 \cdot 10^{-3}$
$(P_{tr2})_{cr-right}$	$1.72 \cdot 10^{-4}$	$1.02 \cdot 10^{-4}$	$9.39 \cdot 10^{-5}$	$1.60 \cdot 10^{-3}$
$(P_x)_{butter-left}$	$-1.26 \cdot 10^{-4}$	$-7.29 \cdot 10^{-5}$	$-6.32 \cdot 10^{-5}$	$-6.93 \cdot 10^{-4}$
$(P_x)_{butter-right}$	$6.24 \cdot 10^{-5}$	$3.65 \cdot 10^{-5}$	$3.56 \cdot 10^{-5}$	$3.86 \cdot 10^{-4}$

**Table 9.8** Comparison of VEF measured by the two-accelerometer method and the IEDI method within the double-layer damped beam (all power values given in Watts).

#### 9.2.2.4 Discussion

The measurement of VEF within a high standing wave environment of a simply supported beam was reported above. It is evident that the herein applied thickness ratio range  $t_D/t_B$  of 0.25 and 0.5, respectively did not yield to a noticeable increase in structural damping within the beam. Thus, a structural damping scenario, as aimed for initially could not be experimentally achieved. The reason for the damping scenarios was to investigate the application of the VEFESPI method at different strong standing wave environments.

An energy balance was carried out herein in order to assess the accuracy of the ESPI measurements undertaken in this work. VIP was computed from the measured cross-spectral density of the driving force and acceleration response at the excitation location. In addition to the measurement of input power, transmitted vibrational energy was measured on the left-hand side and right-hand side of the excitation location using the two-accelerometer method. It is evident from Tables A21.4 to A21.6 that at four frequencies the total of the measured two-accelerometer based transmitted energy is higher than the transducer measured energy injected into the beam, which violates the conservation of energy law and, hence, indicates that transmitted energy measurements at these frequencies may be erroneous. Further, it can be realised that due to off-centre excitation of  $x_0 = 0.582$  m the energy flowing to the left (downstream) should be slightly higher than the energy flowing to the right (upstream) because more energy may be dissipated at the longer spatial left-hand side of the excitation location. The distances of the accelerometer measured transmitted energy were approximately the same with  $x_l = 0.259$  m and  $x_r = 0.238$  m from the excitation location. Thus, the accelerometer measured downstream energy should be higher than the upstream energy. However, as evident from Tables 9.6 to 9.8, the accelerometer measured downstream flow is at 7 frequencies lower than the measured upstream flow. Due to the experimental uncertainties of the transmitted energy flow and input power as well as upstream flows mostly being higher than downstream flows, the

accelerometer based transmitted energy measurements are considered not to be very trustworthy. In contrast to this and evident from Tables 9.6 to 9.8, it can be seen that the ESPI measured downstream flow is always larger than the upstream flow. However, a close match between both quantities could not be found.

Because of the accelerometer based transmitted energy uncertainties the energy balance, used as a measure for accuracy judgement of the ESPI based VEF measurements, was restricted to the comparison of measured accelerometer based input power and spatial integration of the ESPI measured potential energy density along the beam length. The comparison of transducer measured VIP and TTVE taken from the conventional VEFESPI method was neglected due to the fact that the sharp discontinuity at the excitation location could not be identified accurately enough, as evident from the VEF figures shown in Appendix A22. Also, as demonstrated in section 6.3.3, the accuracy of the IEDI method was expected to be higher than the accuracy of the conventional VEFESPI method.

The comparison between the transducer measured VIP and the TTVE, based on the potential energy density integration along the beam length, is shown by Tables 9.3 to 9.5 for each beam damping configuration. The quantity  $\Delta\epsilon$  in percent is used to indicate the relative difference between both measures where zero means no difference at all.

It can be seen from Tables 9.3 to 9.5 that the relative difference  $\Delta\epsilon$  between the VIP and TTVE at a first glance is fairly high, with best agreements achieved for the double-layer damped beam. However, in the following discussion it will be shown that these high relative differences  $\Delta\epsilon$  may be related to factors other than the accuracy of the VEFESPI measurement method.

From Tables 9.3 to 9.5 it can be noticed that except for three measurements the TTVE was always lower than the VIP. Assuming that a low error was made when measuring VIP with the aid of transducers some of the energy injected into the system must be lost by different mechanisms, other than the transverse beam vibration. It is visible from almost each measured ESPI displacement figure that during the ESPI experiment a



parasitic torsional contamination was present. This undesired parasitic torsional motion can be related to an unwanted off-centre attachment of the electrodynamic shaker during the experiment. Figure 9.16 displays the ESPI measured simply supported beam displacement of the non-layer damped beam vibrating at the 9<sup>th</sup> mode. It can be seen that here the transverse beam

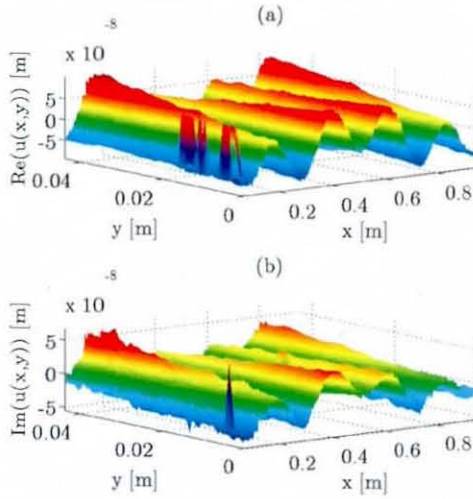


**Figure 9.16** Complex simply supported beam displacement of the 9<sup>th</sup> mode non-layer damped vibration: (a) real part, (b) imaginary part.

motion is strongly contaminated by a torsional motion. Therefore, vibrational energy injected into the beam at the excitation location can be balanced to the transverse beam motion as well as the torsional contamination and, thus, VIP is equal to the amount of TTVE plus the torsional fraction. However, this was not considered by the energy balance of equation (3.40) and, thus, a lower TTVE can be expected. Of course not every frequency was as strongly contaminated as the frequency shown in Figure 9.16. However, at

this particular frequency the highest relative difference of the experiment with 65.5% was obtained. It can be argued further that due to the 2D spectral filtering process the unwanted torsional contamination can be filtered out, as shown in Figure 9.13, but a lower VIP needs to be taken into account when comparing VIP and TTVE within the simply supported beam for the transverse wave motion only.

One disadvantage of the IEDI method is the requirement of the exact value of the hysteretic loss factor. This quantity may alter with frequency and may also be dependent upon the position within the beam. The spatial dependency of the loss factor was neglected here. A prior modal analysis was carried out to determine the loss factor of each mode measured during the ESPI experiment using the software package ME'scope 4 [127]. ME'scope 4

uses a least squared error curve fitting algorithm to compute an analytical description of the prior measured FRF. From this information the mode shape, the damped natural frequency and the modal damping were determined. The measured modal loss factor was employed here to compute both, the TTVE and VEF from the ESPI measured potential energy density. Measurements of the modal loss factor are often erroneous, with accuracies no better than about 20% due to the complicated, non-linear damping mechanism occurring in real vibrating structures [104]. For this reason a not neglectable relative difference between the transducer measured VIP and the TTVE can also be expected.

The simply supported beam rig was designed to use pins at one side and rollers at the other in order to simulate simply supported boundary conditions. However, at the higher excitation frequencies an increased boundary movement at the pin side could be observed where the complete left-hand side beam suspension was vibrating. Thus, it may have been that at the pin side the boundary was not entirely non-dissipative.

During the ESPI experiment the beam was generating a large audible amount of sound, especially at the higher frequencies. Although the beam due to its small area is less prone to sound radiation, and only small fractions of the VIP will be radiated away, some small losses due to sound radiation could have been occurred during the experiment.

Some additional sources of errors that might also have caused a relative difference between transducer measured VIP and ESPI measured TTVE will be mentioned next. As it can be seen by equation (3.27) the measured VIP is depending only on the measurement of the cross-spectral density. Material properties are not incorporated into the computation method. However, the computation of the TTVE from the measured energetic data required knowledge of the Young's modulus, the beam mass density and in the case of the unconstrained layer attachment, the Young's modulus of the layer, the mass density of the layer and the layer loss factor. These quantities were assumed herein and, thus, differences can be expected to the true values. The reason why a relative difference was employed is that



it cannot be ruled out that the transducer based VIP measurements are failure free and, thus, some error may also be expected here.

As mentioned before the ESPI displacement was not recorded entirely over the whole beam length. Further, to avoid spectral leakage when employing the KSD method, the ESPI measured beam displacement was truncated to an integer number of wavelengths. This procedure additionally reduced valuable spatial ESPI displacement information. Hence, the potential energy density of the beam was provided only partly because of the signal window used in the VEFESPI model. To compensate for the missing potential energy density beam sections, the integrated and truncated potential energy density was multiplied by a factor depending upon the ratio of number of wavelengths included in the signal and the number of wavelengths excluded due to signal truncation. Thus, the integrated 6<sup>th</sup> mode potential energy density was multiplied by  $3/2$  assuming that 50% of information was missing. This factor reduced with increasing modes to  $4/3$  for the 8<sup>th</sup> mode,  $9/8$  for the 9<sup>th</sup> mode and  $11/10$  for the 11<sup>th</sup> mode. With increasing mode numbers and especially at the odd-numbered modes much smaller factors were employed and, hence, a higher accuracy can be expected. It has been mentioned that at the 6<sup>th</sup> mode 50% of the spatial information was missing. The hysteretic damping mechanism causes a spatial decay of wave amplitudes away from excitation location. However, this decay was not regarded within the multiplication factor and, thus, a slight overestimation of VIP is unavoidable, decreasing with increasing mode numbers. Hence, the lower modes are sometimes in a lower agreement than the higher modes, as it can be seen in Tables 9.3 to 9.5.

It should also be noted here that the filter cut-off parameters used for the above presented analysis are taken from the theoretical mean squared error analysis carried out in section 6.3.3 and shown in Appendix A19. However, there is some difference between the true measured ESPI beam displacement and the numerically generated ESPI noise superimposed beam displacement due to a not exact extraction of the measured ESPI noise. Thus, employing a filter cut-off trial and error process, especially when using the Butterworth filter, could alter the relative difference further by up to 5%.

Further, the recorded ESPI displacements were partly heavily contaminated by optical noise with a product of  $\eta \times \text{SNR}$  of 0.28 at lowest and 6.1 at greatest. A reduction of the optical noise produced by the ESPI system would also lead to better agreements between measured VIP and measured TTVE.

As discussed above an energy balance, as defined by equation (3.40), is hard to accomplish when dealing with real structures. It was shown in section 6.3 that the active VEF can be measured successfully in theory. An error and sensitivity study showed that despite displacement non-periodicity and noise contamination, the energy balance according to equation (3.40) produced good results. However, as demonstrated in this section, a successful energy balance in real structures was depending on many factors that needed to be taking into account but were not incorporated in equation (3.40).

As demonstrated in section 6.3.3 and by the above given experimental findings the ESPI based measurement of the reactive VEF did not yield to satisfying results for both, the VEFESPI and IEDI computation method. It can be realised that due to the wavenumber spectral filtering procedure too much of the exponential decaying nearfield wave information was erased from the wavenumber spectrum that was then used to compute the spatial derivatives. Even the more insensitive incremental energy density integration method failed to compute an accurate reactive energy flow. It can be seen from Figure 6.30 that the Lagrangian density is highest around the excitation location and approximates towards zero at both of the simply supported beam boundaries. This very fine difference cannot be detected when filtering noisy measured ESPI data. Figure 9.17 displays the measured Lagrangian density of the 11<sup>th</sup> mode single-layer damped beam. It can be realised that due to the filtering there is also a difference between the potential and kinetic energy density away from excitation location and, thus, it is hardly possible to compute an accurate reactive energy flow.

Within this section it was experimentally validated that the incremental integration of the ESPI measured potential energy density is more suitable when measuring VEF in high standing wave environments of finite beams. The conventional VEFESPI method, given by equation (3.33), failed to produce an accurate VEF measurement over the beam length due to



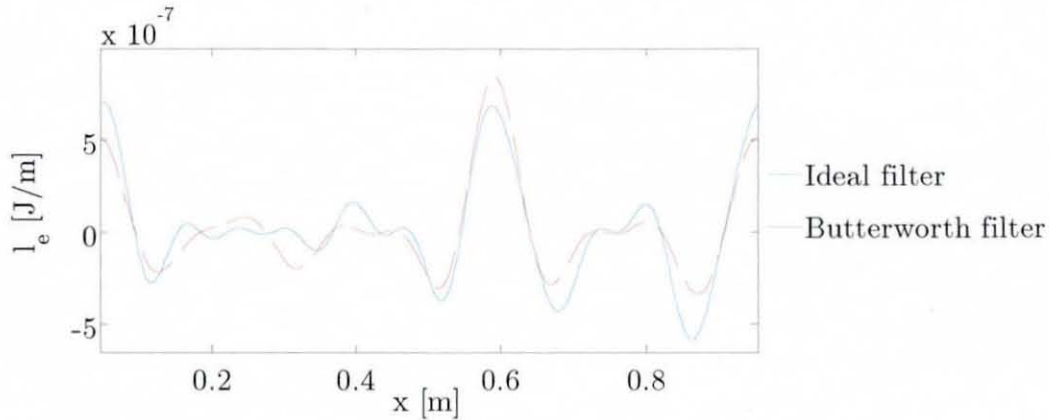


**Figure 9.17** Filtered ESPI measured Lagrangian energy density of the 11<sup>th</sup> mode single-layer damped beam displacement at 2745 Hz.

the employment of 3<sup>rd</sup> order spatial derivatives. In contrast, the IEDI method utilised a 2<sup>nd</sup> order spatial derivative only. The IEDI method was more insensitive towards noise contamination and, thus, produced a much more accurate VEF curve when measuring in high standing wave environments.

Though the relative differences between accelerometer measured VIP and potential energy integrated TTVE seemed to be fairly high at a first glance the author is convinced that due to the above discussed reasons the results obtained are reasonable. Unfortunately, there is no comparison to other methods in the literature that experimentally measured energy flows in high standing wave fields because no error analysis was carried out. It has been shown further that the accelerometer based measurement of VEF within the beam structure produced meaningless results within high standing wave environments.

## 9.3 Moment Excited Beam Measurements

### 9.3.1 “Infinite” Beam Measurements

Figure 9.18(a) shows typical time histories of the two measured force signals. It can be seen in Figure 9.18(a) that the force signals on each moment arm occur simultaneously and are of almost equal amplitude. Figure 9.18(b)

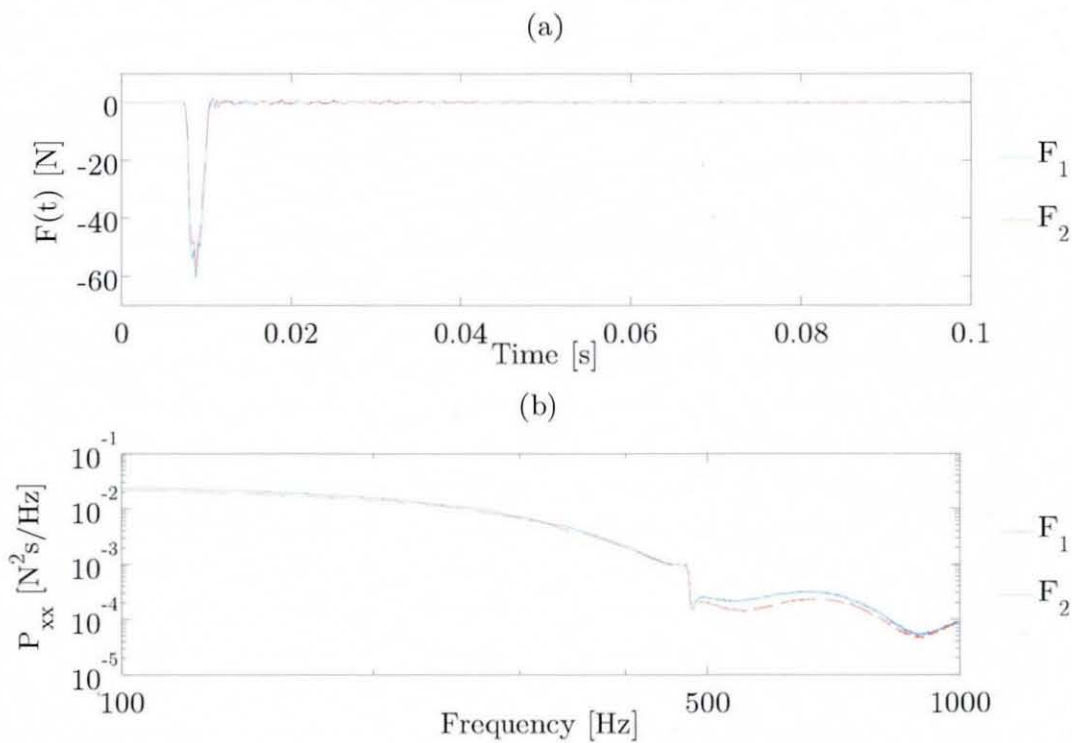


**Figure 9.18** Measured force signals: (a) time history, (b) auto spectral density.

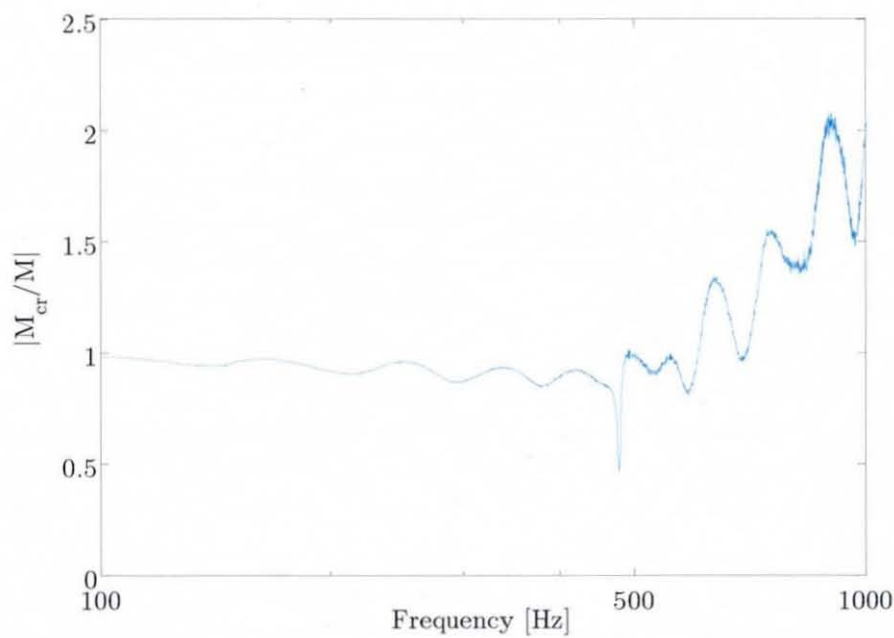


**Figure 9.19** Ratio of actual to measured moment signals.

shows the auto-spectral density of the two impact force signals  $F_1$  and  $F_2$ . It is evident from Figure 9.18(b) that the first zero in the applied force spectra occurs at approximately 470 Hz and that both force spectra are almost identical, particularly below the first zero frequency at 470 Hz.

Figure 9.19 displays on a logarithmic frequency scale from 100 Hz to 1000 Hz the amplitude ratio of actual moment to measured moment signals calculated using equation (8.19). It can be seen in Figure 9.19 that below the first zero in the applied force spectra, at 470 Hz, this ratio is approximately 1.0 indicating that the measured moment  $M$  is a good approximation to the actual moment  $M_{cr}$ . However, above 470 Hz, the trend is for the moment ratio to increase with increasing frequency. Thus, from equation (8.18) it is clear that as the impact forces shown in Figure 9.18(b) reduce in amplitude the applied moment  $M$  will reduce in amplitude and, hence, the rotary inertia  $J$  of the moment arms will become a more significant contributor to the actual moment  $M_{cr}$ .

### 9.3.1.1 Moment Point Mobility Measurements

Figure 9.20 displays logarithmically the modulus of the moment point mobility of the experimental “infinite” beam over the frequency range of interest, 100 Hz to 1000 Hz. The “corrected” measured point mobility data

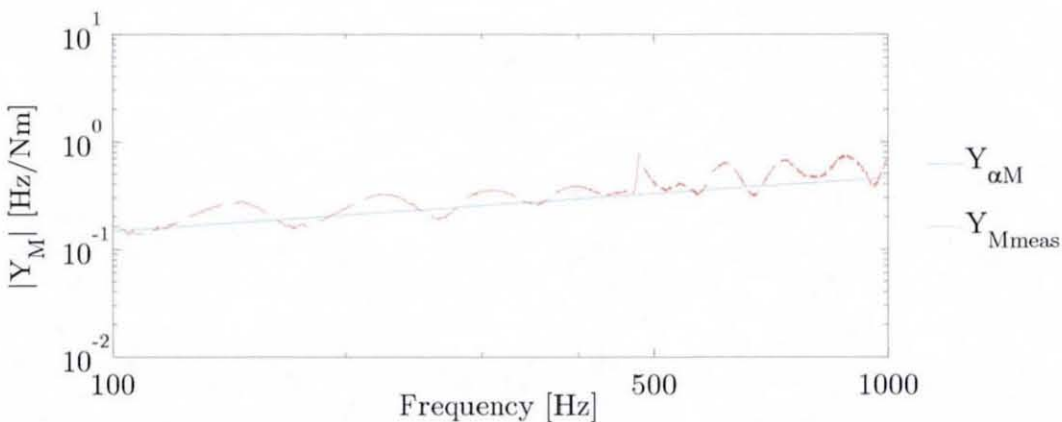


**Figure 9.20** Modulus of the measured and theoretical moment point mobility of the moment excited “infinite” beam.

calculated using equation (8.15)  $Y_{Mmeas}$  are shown as a solid line. Also shown in Figure 9.20 is the modulus of the moment point mobility  $Y_{\alpha M}$  calculated using equation (5.22). It can be seen that the measured point mobility data from the experimental beam follow the trend of the equivalent theoretical infinite structure. The fluctuations of the measured mobility curve over frequency are due to the fact that the experimental anechoic terminations do not work perfectly and, hence, there is some wave reflection from the ends of the beam. The measured moment point mobility data shown in Figure 9.20 appear to show a resonance at approximately 470 Hz. However, since this frequency coincides with the first zero frequency in the applied force signal, this effect is probably not due to a resonance in the structure but rather is attributable to the biasing effect of noise in the force signal when using the  $H_1(f)$  estimator.

### 9.3.1.2 Input Energy Measurements

Figure 9.21 shows the magnitude of amplitude ratio of extraneous force to

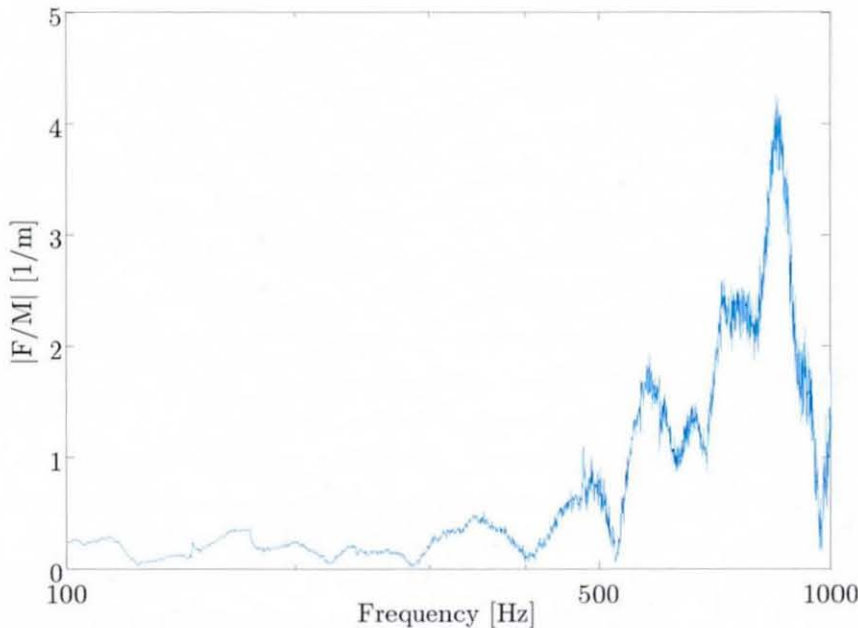


**Figure 9.21** Ratio of extraneous force to measured moment.



applied moment  $|F/M|$  calculated using equation (8.21). It can be seen in Figure 9.21 that this ratio remains less than 0.75 up to the first zero in the applied force signals at 470 Hz. From equation (8.21) it is clear that as the impact forces, and, hence, the measured moment  $M$  reduce in amplitude with increasing frequency then the transverse inertia term  $m\partial^2 u/\partial t^2$  will become increasingly significant compared to the measured moment. For the experimental “infinite” beam studied in this work the extraneous force  $F$  is assumed to have no effect upon the measured results, since the cross mobility of an infinite beam is zero. However, Figure 9.21 indicates that a correction to the measured moment mobility, as expressed in equation (3) of reference [107], may become necessary if the current technique is applied to practical finite structures with non-zero cross mobility terms.

Figure 9.22 shows a comparison between the vibrational energy input to the beam due to moment excitation  $(P_{in}(f))_{M_{cr}}$  calculated using equation (8.17), and the sum of direct vibrational energy input to the beam’s two moment arms by the two impact forces  $P_{in}(f)_{F1} + P_{in}(f)_{F2}$  calculated using the

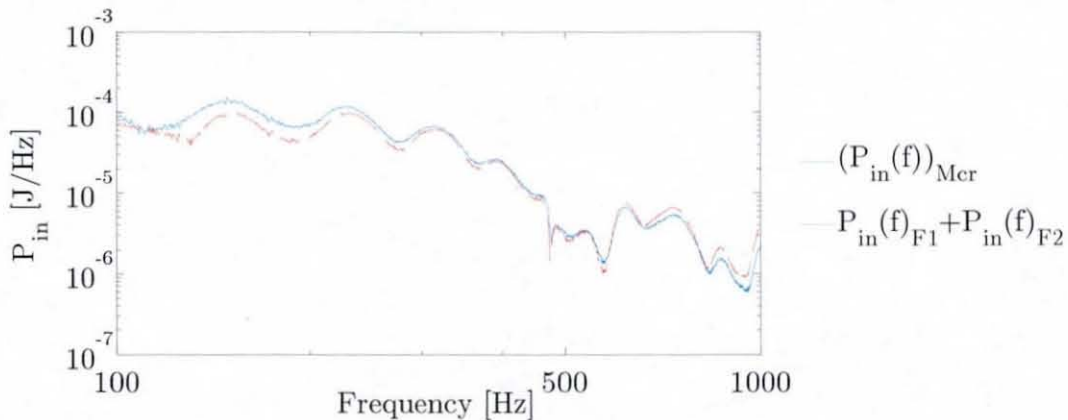


**Figure 9.22** Vibrational energy input to the experimental “infinite” beam measured using moment and rotational velocity compared with measured energy calculated using force and transverse velocity on the moment arms.

well known cross-spectral density method, equation (3.27), for both force signals. It can be seen in Figure 9.22 that both methods indicate similar values of input energy over a wide frequency range. Since both methods used

the same force signals and differ only in the response accelerometers employed, it can be assumed that the finite-difference approximation of the rotational velocity incorporated into equation (8.17) can be used to successfully measure the energy input to a beam by moment excitation.

### 9.3.1.3 Comparison of Input Energy and Transmitted Energy Measurements

Figure 9.23 shows a comparison of the measured input energy due to the moment excitation  $(P_{in}(f))_{Mcr}$  and the transmitted vibrational energy  $(P_{tr2}(f))_r + P_{tr2}(f))_l$  calculated using the two-accelerometer technique, equation (8.5). The transmitted energy was measured on both sides of the excitation location, as shown in Figure 7.7, and then summed to provide the total transmitted energy in the structure  $(P_{tr2}(f))_r + P_{tr2}(f))_l$ . Figure 9.23 indicates a close match between the measured input and transmitted energies below 470 Hz. The discrepancy between the energy values at approximately 470 Hz can be attributed to noise on the input force signal.

Above 470 Hz it can be seen in Figure 9.23 that the measured transmitted vibrational energy is slightly higher than the moment input energy, which is in conflict to the energy conservation law. One explanation may be that different accelerometers pairs were used on either side of the

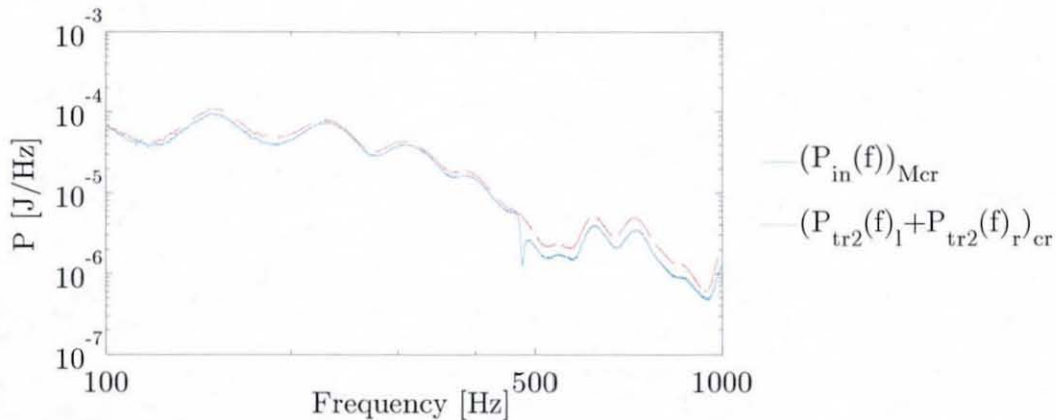


**Figure 9.23** Comparison of input and transmitted energies in the experimental “infinite” beam.



beam. During the experiment a pair of lightweight ICP accelerometers was employed to measure the energy flowing to the right of the excitation location however, a pair of conventional charge type accelerometers was used to measure the energy flowing to the left of the excitation location. The charge type accelerometers are much heavier than the ICP accelerometers and so may have mass loaded the structure. For these particular transducers the ICP accelerometers were a more closely phase matched pair than the charge type accelerometers. Hence, the ICP accelerometers can be expected to produce a more accurate measurement of transmitted energy. Assuming

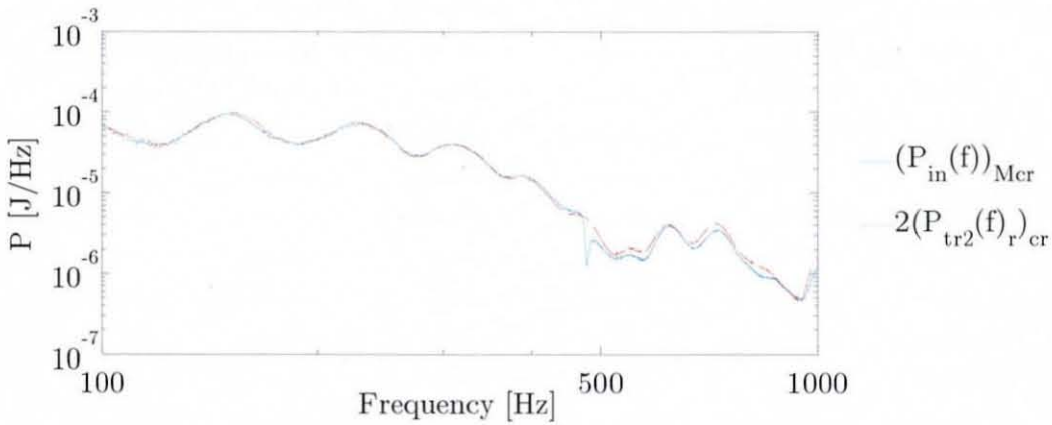


**Figure 9.24** Comparison of input and doubled transmitted energy to the right of the excitation location.

that the transmitted energy, flowing to either side of the excitation location is half the input energy, the doubled transmitted energy to the right of the beam  $2(P_{tr2}(f))_{r'cr}$  is shown versus the moment input energy in Figure 9.24. It can be seen that both sets of data are in excellent agreement with each other, particularly at frequencies below the first zero in the applied force spectrum at 470 Hz.

#### 9.3.1.4 Discussion

The above section has presented the experimental validation of a technique to measure the moment point mobility and energy input to an “infinite”

beam by moment excitation. The novelty of this technique is the use of a specially designed moment excitation rig to generate an impulsive moment combined with a finite difference based spectral density measurement method.

Preliminary measurements made upon an experimental "infinite" beam have shown this technique can be used to accurately measure the moment point mobility and energy input to the structure. In particular, the measured moment point mobility of the experimental "infinite" beam was seen to follow the trend line of the corresponding theoretical infinite structure. Further, the energy input to the beam by moment excitation measured with the new technique was shown to match (i) conventional input energy measurements made using the cross-spectral density between applied force and transverse acceleration signals at the points of impact on the moment arms of the beam; and (ii) conventional transmitted energy measurements made using the two accelerometer technique in the vibrational farfield of the beam.

However, it is clear that the duration of the moment impact should be kept as small as possible so as to avoid a zero in the force spectra at low frequencies. At frequencies above the first zero in the applied force spectra it was shown that the effect of translational inertia and rotational inertia due to the attachment of the moment arms becomes significant. A further disadvantage of the proposed technique is the requirement to rigidly attach a moment arm to the structure and the need for sufficient access to carefully locate the moment exciter.

Unfortunately, time pressure did not allow for further investigations of the moment measurement technique on a simply supported beam.

# 10 THEORY OF VIBRATIONAL ENERGY IN PLATES

## 10.1 Introduction

The aim of this chapter is to study vibrational energy relations of infinite and simply supported plates analytically. The plate structures are assumed to be uniform, linear-elastic and isotropic. The solutions presented herein are due to the application of a harmonic point force excitation. Within the analysis of infinite plates, it is further assumed that due to strong vibrational energy transmission, internal energy dissipation processes within the structure are neglectable. Within the analytical analysis of the simply supported plate a hysteretic damping model is employed in order to account for internal energy dissipation. Furthermore, the Euler-Bernoulli plate theory is applied when investigating infinite as well as simply supported plates.

Vibrational input power (VIP) and vibrational energy flow (VEF) expressions of an infinite plate and of a simply supported plate are presented. Most of these energy expressions were derived originally as they could not be found in any literature reference. Additionally, the presented unconstrained damping layer theory was extended herein by including the loss factor of the plate, which usually is neglected in the existing literature.

Section 10.2 presents the analysis of VEF and VIP in an infinite plate using the prior determined forced transverse displacement response of the plate. Analogously, section 10.3 presents the analysis of VEF and VIP of a simply supported plate from the prior defined transverse simply supported



plate response. Section 10.4 introduces the theory of an unconstrained layer attachment to a thin plate structure.

## 10.2 Infinite Plate Analysis

The analysis of an infinite structure enables vibrational energy studies under simplified conditions by ignoring rather complicated wave reflections at the plate's boundaries. Thus, the behaviour of structures with a high energy outflow from the excitation location can be studied. Since an infinite plate is extended to infinity and, thus, no travelling wave reflections occur that may form a standing wave field, the forced response of the infinite plate can be derived much easier. Practical "infinite" plate structures may be represented by finite plate structures with a very high amount of energy dissipation at the boundaries.

### 10.2.1 Point Force Excitation

The derivation of the complex, transverse, infinite plate displacement is given in Appendix A24. From there, the complex, polar, transverse response of the infinite plate to a harmonic point force excitation is given by [103]:

$$w(r, \theta, t) = \frac{F_0}{j8Dk^2} (H_0^{(2)}(kr) - H_0^{(2)}(-jkr)) e^{j\omega t}. \quad (10.1)$$

Here,  $D$  is the flexural rigidity given as  $Eh^3 / (12(1 - \nu^2))$ , where  $E$  is the Young's modulus and  $h$  is the plate's thickness. Furthermore,  $F_0$  is the magnitude of the excitation force,  $\nu$  is the Poisson ratio,  $k$  is the plate's flexural wavenumber and  $r$  is the radial distance from the excitation location. It can be seen from equation (10.1) that the displacement is formed by the difference of two Hankel functions of second kind and of zeroth order. In contrast to the arguments of the exponential wave-based beam displacements, the real argument  $kr$  of the Hankel function  $H_0^{(2)}(kr)$

physically represents a travelling farfield and the imaginary argument  $-jkr$  of the Hankel function  $H_0^{(2)}(-jkr)$  represents a decaying nearfield around the excitation location.

The Hankel function itself is defined as a combination of Bessel functions of the first and second kind [128], whereas the Bessel functions can be defined by fairly complicated infinite sum definitions. It can be noticed that due to the energy conservation within the lossless infinite plate, the amplitude of the infinite plate displacement must decrease with increasing distance away from excitation location (Sommerfeld radiation condition).

### 10.2.2 Vibrational Input Power

Analogously to the procedure undertaken in sections 5.3.2 and 5.4.2, VIP of the infinite plate is also derived here by employing equation (3.23). If one substitutes the temporal derivative of equation (10.1) into equation (5.18), the point mobility of an infinite plate may be found to be [103]:

$$Y_{F_\infty} = \frac{\omega}{8Dk^2} = \frac{1}{8\sqrt{D\rho h}}. \quad (10.2)$$

Equation (10.2) reveals that the point mobility of an infinite plate is a pure real quantity and independent on frequency. Substituting equation (10.2) into equation (3.23), VIP to an infinite plate, when excited by a transverse harmonic point force, can be written as:

$$(P_m)_{F_\infty} = \frac{F_0^2 \omega}{16Dk^2} = \frac{F_0^2}{16\sqrt{D\rho h}}. \quad (10.3)$$

### 10.2.3 Transmitted Vibrational Energy Using Hankel Functions

Lande and Langley derived total transmitted vibrational energy (TTVE) expressions for cylindrical bending waves in plates [18]. The TTVE represents

the total integrated energy, which flows through a closed contour located around the excitation location. This quantity is independent upon the distance from the excitation point. In this study attention was focused on the effects of plate displacement modelling using either the modified Bessel functions or the Hankel functions. Furthermore, possible energetic interactions between travelling and evanescent waves were investigated when modelling with the previously mentioned functions. An ingoing wave with amplitude  $A_n$ , and an outgoing wave with amplitude  $B_n$  were considered. In cases where the travelling wave component of the plate was described by the second order Hankel function  $H_n^{(2)}(kr)$  it has been shown that the total transmitted energy is equal to the input power expression shown in (10.3).

#### 10.2.4 Transmitted Vibrational Energy Using Asymptotic Expansion Functions

In another method to compute VEF in an infinite plate, and to simplify the vibrational energy derivations, the Hankel function difference, as shown in equation (10.1), can be approximated by truncating the asymptotic expansions of the Hankel functions. Thus, for small arguments of  $|kr| \ll 1$  it can be shown that the Hankel function difference may be approximated by a natural logarithm difference as [129]:

$$H_0^{(2)}(kr) - H_0^{(2)}(-jkr) \approx -\frac{2j}{\pi} \left( \ln\left(\frac{kr}{2}\right) + 1 - \left( \ln\left(-j\frac{kr}{2}\right) + 1 \right) \right) = 1. \quad (10.4)$$

For large arguments  $|kr| \gg 1$  the Hankel function difference may be approximated exponentially by [103]:

$$H_0^{(2)}(kr) - H_0^{(2)}(-jkr) \approx \sqrt{\frac{2}{\pi kr}} \left( e^{-j\left(kr - \frac{\pi}{4}\right)} - je^{-kr} \right). \quad (10.5)$$



It can be seen from (10.4) that the approximation of the Hankel function difference at small values of  $|kr|$  is equal to one and, thus, the displacement at  $r = 0$  is equal to  $F_0 / (j8Dk^2)$ . However, expression (10.4) cannot be used to determine VEF in close vicinity to the excitation location, since this approximation is a constant value equal to the displacement amplitude at the excitation location. Thus, only the approximation of the Hankel function difference at  $|kr| \gg 1$  is employed in this work in order to determine VEF in an infinite plate analytically.

#### 10.2.4.1 Polar Expressions

If one substitutes equation (10.5) into equation (10.1), the polar approximation of the infinite plate displacement is given by [103]:

$$w(r, \theta, t) \approx \frac{F_0}{j8Dk^2} \sqrt{\frac{2}{\pi kr}} \left( e^{-j\left(kr - \frac{\pi}{4}\right)} - je^{-kr} \right) e^{j\omega t}. \quad (10.6)$$

As mentioned beforehand, equation (10.6) is valid for  $|kr| \gg 1$  only. In reference [103] it has been shown that from  $|kr| \geq 4$  very small errors can be expected. The first exponential bracket term in (10.6) represents a travelling wave component and the second exponential bracket term represents an evanescent wave component.

If one substitutes equation (10.6) into equations (3.68) and (3.69), VEF expressions of the infinite plate may be obtained. It can be realised that the infinite plate displacement has only radial and temporal dependency. The displacement does not alter angularly due to usage of the zeroth order Hankel function. Hence, the angular derivatives are expected to be zero. Thus, equation (3.69) and the angular derivatives in equation (3.68) can be neglected in the VEF analysis. A complete derivation of VEF from the truncated asymptotic expansion for large values of  $|kr|$  of an infinite plate is given in Appendix A25. From Appendix A25 the active VEF per unit length of the infinite plate  $(\overline{P}_{r_a})_{F_\infty} = \Re \left\{ (\overline{P}_{r_{evan}})_{F_\infty} + (\overline{P}_{r_{trav}})_{F_\infty} \right\}$  can be found to be:

$$(\overline{P}_a)_{F_\infty} = \frac{F_0^2 \omega}{512 D \pi} \left( \frac{16}{k^2 r} - \frac{4}{k^4 r^3} \right). \quad (10.7)$$

Note, here the overbar denotes VEF per unit length, the subscript  $a$  denotes an active quantity and the subscript  $r$  denotes a reactive quantity. It is evident from (A25.3) that the VEF due to the evanescent wave is a pure imaginary quantity and, thus, the evanescent wave contributes only to reactive energy flow. Analogously from Appendix A25, the reactive VEF per unit length of the infinite plate  $(\overline{P}_r)_{F_\infty} = \Im \left\{ (\overline{P}_{r \text{ evan}})_{F_\infty} + (\overline{P}_{r \text{ trav}})_{F_\infty} \right\}$  is given by:

$$(\overline{P}_r)_{F_\infty} = j \frac{F_0^2 \omega}{256 D \pi} \left( (1 + e^{-2kr}) \left( \frac{1 + \nu}{k^5 r^4} + \frac{4(\nu - 1)}{k^3 r^2} \right) + e^{-2kr} \frac{4(\nu - 1)}{k^4 r^3} \right). \quad (10.8)$$

Equations (10.7) and (10.8) display the active and reactive VEF of an infinite plate in dependency upon the radius  $r$  when modelling the point forced infinite plate response by equation (10.6). It can be seen that the polar definition of active VEF, equation (10.7), in an infinite plate is a fairly simple expression. Furthermore, only the travelling wave component is contributing to active energy flow, as evident when comparing equation (10.7) and equation (A25.6). The reactive energy transmission is a more complex expression. Interestingly, the reactive energy flow is composed of not only exponential decaying terms but also of travelling terms. However, it cannot be pointed out which term in equation (10.8) is the error caused by the truncated asymptotic expansion, as an exact reactive TTVE was not derived.

A simple energy balance can be computed for the infinite plate, as shown by equation (3.59). If one neglects the internal energy dissipation within the structure due to high energy boundary crossing (outflow) being present, it can be assumed that the integrated VEF per unit length of the infinite plate around a closed contour is equal to the real part of the complex, time-averaged VIP injected into the structure. Thus:

$$\Re \{ \langle \underline{P}_{in} \rangle_t \} = \oint_C (\overline{P}_a)_{F_\infty} dr. \quad (10.9)$$

It can be seen from (10.9) that at each location within the plate the conservation of energy demands equality between VIP and total transmitted active energy. Requirements for energy equality are a closed contour and a contour location around the excitation point. When dealing with polar expressions, ideally a circle may be chosen as the shape of the contour to be integrated. Because the circumference of the contour to be integrated increases with increasing radial distance from the excitation location, the spatial amplitude of the infinite plate displacement must decrease in order to ensure injected energy is equal to the total energy flux (TTVE) that flows perpendicular to the normal of the plate's surface across the boundaries of the closed contour. Figure 10.1 displays a circular and rectangular contour shape employed in this work. As mentioned before, polar expressions ideally

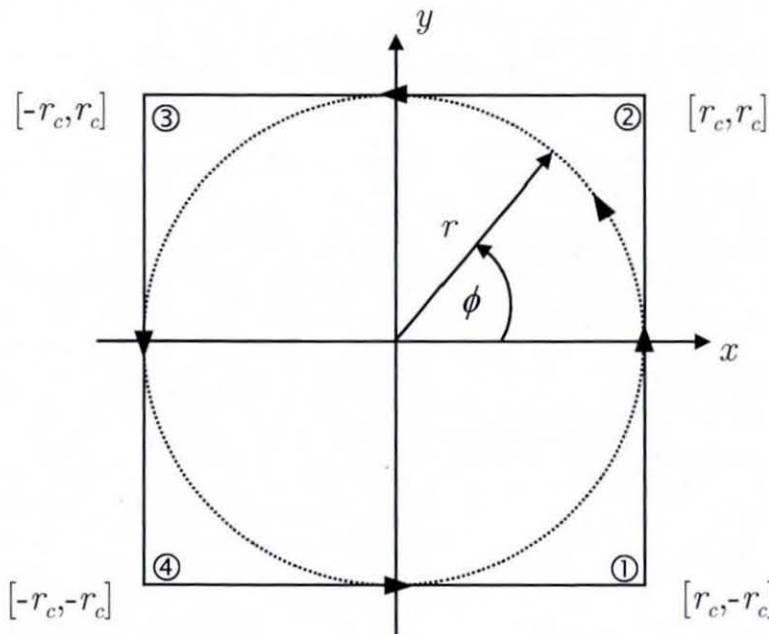


**Figure 10.1** Different integration contours in the VEF field of an infinite plate.

are integrated around a closed circle. If one substitutes the active VEF expression given by equation (10.7) into equation (10.9) and takes into account that  $dr = r d\phi$ , one may obtain the following integral expression:



$$(P_a)_{F_\infty} = \frac{F_0^2 \omega}{512 D \pi} \int_0^{2\pi} \left( \frac{16}{k^2} - \frac{4}{k^4 r^2} \right) d\phi. \quad (10.10)$$

By solving equation (10.10) the active TTVE is:

$$(P_a)_{F_\infty} = \frac{F_0^2 \omega}{16 D k^2} \left( 1 - \frac{1}{4 k^2 r^2} \right). \quad (10.11)$$

From equation (10.11) it can be noticed that the first term is equal to the VIP expression given by equation (10.3) and independent of the radius  $r$  as well as the circular frequency  $\omega$ , which can be cancelled out from (10.11). The second term can be identified as the error made when using the truncated exponential asymptotic expansions of the Hankel functions. However, it can also be seen from (10.11) that this error decreases quadratically with increasing radius  $r$  and rationally by  $1/\omega$ . Thus, for large arguments of  $|kr|$ , the error introduced by the approximation can be considered to be small.

#### 10.2.4.2 Cartesian Expressions

Using the relation  $r^2 = x^2 + y^2$  the polar displacement approximation of the infinite plate, as shown by equation (10.6), can be written in Cartesian coordinates as:

$$w(x, y, t) \approx \frac{F_0}{j 8 D k^2} \sqrt{\frac{2}{\pi k (x^2 + y^2)^{\frac{1}{2}}}} \left( e^{-j \left( k(x^2 + y^2)^{\frac{1}{2}} - \frac{\pi}{4} \right)} - j e^{-k(x^2 + y^2)^{\frac{1}{2}}} \right) e^{j \omega t}. \quad (10.12)$$

Time-averaged VEF in the  $x$  direction that is defined by Cartesian coordinates can be found by substituting equation (10.12) into equation (3.49). A complete derivation of VEF within the infinite plate, when using Cartesian coordinates, is given in Appendix A26. From there, the active VEF in the  $x$  direction only  $(\overline{P}_{x_a})_{F_\infty} = \Re \left\{ (\overline{P}_{x_{evan}})_{F_\infty} + (\overline{P}_{x_{trav}})_{F_\infty} \right\}$  is:

$$(\overline{P}_{x_a})_{F_\infty} = \frac{F_0^2 \omega x}{512 D \pi} \left( \frac{16}{k^2 (x^2 + y^2)} - \frac{4}{k^4 (x^2 + y^2)^2} \right). \quad (10.13)$$

Note, herein the quantity  $(\overline{P}_{x_a})_{F_\infty}$  is of two-dimensional nature. However, the mathematically more correct notation  $\overline{P}_{x_a}(x, y)_{F_\infty}$  is dropped for compaction. It can be noticed from equation (A26.5) that the VEF due to the evanescent wave is purely imaginary and, thus, the evanescent wave contributes only to reactive energy flow. Furthermore, equation (10.13) can easily be derived from equation (10.7) simply by substituting  $r = (x^2 + y^2)^{1/2}$  and  $x = \cos(\theta)r$  with  $\theta = 0$  into equation (10.7). The VEF of the infinite plate in the  $y$  direction is simply obtainable by interchanging the spatial variables  $x$  and  $y$ . It can be seen from equation (10.13) that only the  $x$  in front of the bracket term needs to be substituted by  $y$  in order to find the active VEF in the  $y$  direction. The reactive energy transmission in the  $x$  direction within the infinite plate based on Cartesian coordinates derived from the truncated asymptotic expansion of the Hankel function difference  $(\overline{P}_{x_r})_{F_\infty} = \Im \left\{ (\overline{P}_{x_{evan}})_{F_\infty} + (\overline{P}_{x_{trav}})_{F_\infty} \right\}$  may be written as:

$$(\overline{P}_{x_r})_{F_\infty} = j \frac{F_0^2 \omega x}{256 D \pi} \left( \left( 1 + e^{-2k(x^2 + y^2)^{1/2}} \right) \left( \frac{1 + \nu}{k^5 (x^2 + y^2)^{5/2}} + \frac{4(\nu - 1)}{k^3 (x^2 + y^2)^{3/2}} \right) + \frac{e^{-2k(x^2 + y^2)^{1/2}}}{k^4 (x^2 + y^2)^2} \frac{4(\nu - 1)}{k^4 (x^2 + y^2)^2} \right). \quad (10.14)$$

Also here, the reactive energy flow in the  $y$  direction can be found by substituting the variable  $x$  in front of the bracket term by  $y$ . Equations (10.13) and (10.14) represent the time-averaged two-dimensional active and reactive energy flow within the infinite plate in the  $x$  direction. As shown by the polar expression, the second bracket term in (10.13) is the error made when approximating the infinite plate displacement by equation (10.12).

The total transmitted active vibrational energy can be found by integrating expression (10.13) and its equivalent expression for the  $y$  direction

along a closed square contour, as shown by Figure 10.1. Integrating equation (10.13) from point 1,  $x = r_c$  and  $y = -r_c$ , to point 2,  $x = r_c$  and  $y = r_c$ , the following integral expression can be formed:

$$\left\{ (P_{x_a})_{F_\infty} \right\}_{1 \rightarrow 2} = \int_{x=r_c, y=-r_c}^{x=r_c, y=r_c} (\overline{P_{x_a}})_{F_\infty} dy = \frac{F_0^2 \omega}{128 D \pi} \left( \frac{2\pi}{k^2} - \frac{1}{2k^4 r_c^2} \left( 1 + \frac{\pi}{2} \right) \right). \quad (10.15)$$

It can be shown that equation (10.13) integrated from point 2,  $x = r_c$  and  $y = r_c$ , to point 3,  $x = -r_c$  and  $y = r_c$ , results in zero flow as:

$$\left\{ (P_{x_a})_{F_\infty} \right\}_{2 \rightarrow 3} = \int_{x=r_c, y=r_c}^{x=-r_c, y=r_c} (\overline{P_{x_a}})_{F_\infty} dx = 0. \quad (10.16)$$

Furthermore, it can also be shown that integrating equation (10.13) from point 3,  $x = -r_c$  and  $y = r_c$ , to point 4,  $x = -r_c$  and  $y = -r_c$ , will yield to:

$$\left\{ (P_{x_a})_{F_\infty} \right\}_{3 \rightarrow 4} = - \left\{ (P_{x_a})_{F_\infty} \right\}_{1 \rightarrow 2}. \quad (10.17)$$

If one takes the VEF in the  $y$  direction  $(\overline{P_{y_a}})_{F_\infty}$  into account and defines the active TTVE in the  $x$  and  $y$  directions as:

$$(P_a)_{F_\infty} = \left[ \int_{x=r_c, y=-r_c}^{x=r_c, y=r_c} (\overline{P_{x_a}})_{F_\infty} dy + \left| \int_{x=-r_c, y=r_c}^{x=-r_c, y=-r_c} (\overline{P_{x_a}})_{F_\infty} dy \right| + \left| \int_{x=-r_c, y=-r_c}^{x=r_c, y=-r_c} (\overline{P_{y_a}})_{F_\infty} dx \right| + \int_{x=r_c, y=r_c}^{x=-r_c, y=r_c} (\overline{P_{y_a}})_{F_\infty} dx \right], \quad (10.18)$$

it can be demonstrated that due to symmetrical properties of the Cartesian coordinate based VEF, the TTVE in the  $x$  and  $y$  directions is equal and,

$$\text{thus, } \left\{ (P_{x_a})_{F_\infty} \right\}_{1 \rightarrow 2} = \left\{ (P_{y_a})_{F_\infty} \right\}_{2 \rightarrow 3} \text{ and } \left| \left\{ (P_{x_a})_{F_\infty} \right\}_{3 \rightarrow 4} \right| = \left| \left\{ (P_{y_a})_{F_\infty} \right\}_{4 \rightarrow 1} \right|.$$



Note, a square contour integration was assumed. Hence, the total transmitted energy within the infinite plate can be determined by using equation (10.15) as:

$$(P_a)_{F_\infty} = 4 \int_{x=r_c, y=-r_c}^{x=r_c, y=r_c} (\overline{P_a})_{F_\infty} dy = \frac{F_0^2 \omega}{16Dk^2} \left( 1 - \frac{\pi}{4k^2 r_c^2} \left( 1 + \frac{\pi}{2} \right) \right). \quad (10.19)$$

It can be realised from equation (10.19) that the first term in this equation is equal to the injected VIP, as given by equation (10.3). The second term in equation (10.19) is the error made due to the asymptotic displacement approximation.

If one desires to determine transmitted vibrational energy from polar VEF expressions numerically, Cartesian coordinate based integration can be carried out only. Thus, due to straight line integration of a radial function an error will be introduced, which needs to be compensated for. If one substitutes the relation  $r^2 = x^2 + y^2$  into equation (10.7) and omits the second error term, which arises due to Hankel function approximation, one may find the following expression:

$$\overline{P_a}(x, y)_{F_\infty} = \frac{F_0^2 \omega}{32Dk^2 \pi} \frac{1}{\sqrt{x^2 + y^2}}. \quad (10.20)$$

Integrating equation (10.20) along a square contour in the same manner as described above to compute the total energy flow through that square contour one may obtain:

$$(P_a)_{F_\infty} = 4 \int_{-r_c}^{r_c} \overline{P_a}(x, y)_{F_\infty} dy = 4 \ln \left( \frac{\sqrt{2} + 1}{\sqrt{2} - 1} \right) \frac{F_0^2 \omega}{32Dk^2 \pi}. \quad (10.21)$$

With the result of equation (10.21) a compensation factor can be found to compensate the error made when integrating polar VEF along a square contour. If one divides the first term of equation (10.11) by the result of

equation (10.21), the following correction factor may be employed when integrating polar VEF of an infinite plate using a square contour as:

$$\frac{(P_a)_{F_\infty}}{\{(P_a)_{F_\infty}\}_{1 \rightarrow 4}} = \frac{\pi}{2 \ln \left( \frac{\sqrt{2} + 1}{\sqrt{2} - 1} \right)}. \quad (10.22)$$

### 10.3 Simply Supported Plate Analysis

In contrast to the infinite plate, the simply supported plate is considered here to be a closed rectangular system with adiabatic simply supported boundaries at its edges. It is assumed further, that the plate is simply supported on all four edges,  $x = 0$ ,  $x = L_x$ ,  $y = 0$  and  $y = L_y$ .

As shown in the previous section, the infinite plate responded to a harmonic point force excitation by creating radially symmetric waves, which travelled away from the excitation location towards infinity. It can be realised that similar to the standing wave displacement formation process of the finite beam the initially travelling infinite plate waves are eventually reflected at the rectangular edges of the finite plate. Furthermore, it can also be realised that this reflection process is much more complicated due to the radially two-dimensional incidence of the infinite travelling waves. Because of the previously mentioned complicated wave scattering process a modal approach, rather than a wave-based approach, is employed within this work in order to describe the simply supported plate response and, thus, vibrational energy.

Theoretically, a vibrating finite plate structure exhibits resonant behaviour on an infinite number of different frequencies. A resonant vibration situation occurs if the excitation frequency coincides with the eigenfrequency of the structure. This can be on single frequency excitation or broad band frequency excitation. The eigenfrequencies are dependent on the material

used, the geometric shape of the structure and the boundary conditions employed. Each resonant vibration situation is called a mode and each mode has its particular spatial distribution pattern. In the case of a two-dimensional structure mode shapes occur in both directions.

### 10.3.1 Point Force Excitation

The basic concept of the modal approach is that when a structure is excited by a certain excitation frequency, either single or broadband, each mode of the structure is contributing with different strength to the total response of the structure. Thus, the modal solution of the structural response must include all eigenfunctions, eigenfrequencies and the load applied to force the plate response. Employing the well known eigenfunction expansion theorem the forced spatial plate displacement  $w(x,y)$  is given by [129]:

$$w(x,y) = \sum_{n=1}^{\infty} \sum_{m=1}^{\infty} \frac{\phi_{mn}(x,y)}{\int_S \rho h \phi_{mn}^2(x,y) dx dy (\omega_{mn}^2 - \omega^2)} \int_S p(x,y) \phi_{mn}(x,y) dx dy. \quad (10.23)$$

In equation (10.23) the eigenfunctions are denoted as  $\phi_{mn}$ . Further,  $\omega_{mn}$  is the eigenfrequency,  $\omega$  is the excitation frequency and  $p(x,y)$  is the applied load. The integer variables,  $m$  and  $n$ , are the modal numbers in the  $x$  and  $y$  direction, respectively. The most important property of the eigenfunctions is their orthogonality. Furthermore, the eigenfunctions must satisfy the boundary conditions of the respective structure. It can be seen that the structural response, as shown in equation (10.23), is an infinite series of mode shapes contributing with different strength to the total plate response. If the excitation frequency  $\omega$  coincides with the eigenfrequency  $\omega_{mn}$  of a particular mode, this mode is then the dominant contributor to the total structural response.

In the case of simply supported rectangular boundaries with zero displacement and zero moment conditions at the edges, it can be shown that the following eigenfunctions satisfy the previously mentioned conditions [129]:



$$\phi_{mn}(x, y) = \sin\left(\frac{m\pi x}{L_x}\right) \sin\left(\frac{n\pi y}{L_y}\right). \quad (10.24)$$

The simply supported rectangular plate displacement can be found by substituting equation (10.24) into (10.23) and solving the integral expressions. The force integral on the right-hand side may be solved simply by employing a harmonic point force with  $p(x, y) dxdy = F_0 e^{j\omega t}$  at  $x = x_0$  and  $y = y_0$ . From equation (10.23), it can be seen that in case of  $\omega_{mn} = \omega$  the response of this particular mode tends towards infinity, which clearly is not the case in reality. Thus, internal damping needs to be included. Internal damping is considered here by employing a hysteretic damping process similar to the beam case. Taking internal damping effects into account, the point forced simply supported rectangular plate displacement can be written as [129]:

$$w(x, y, t) = \frac{4F_0 e^{j\omega t}}{\rho h L_x L_y} \sum_{m=1}^{\infty} \sum_{n=1}^{\infty} \frac{\sin\left(\frac{m\pi x}{L_x}\right) \sin\left(\frac{n\pi y}{L_y}\right) \sin\left(\frac{m\pi x_0}{L_x}\right) \sin\left(\frac{n\pi y_0}{L_y}\right)}{\omega_{mn}^2 (1 + j\eta) - \omega^2}. \quad (10.25)$$

From equation (10.25), it is not obvious how the denominator in (10.25) introduces structural damping similar to the exponential spatial decay of the wave-based approach. A good exploration of the duality between the modal approach and the wave-based approach of two-dimensional structures can be found in reference [130]. As an alternative to equation (10.25), a summation of plane exponential travelling waves is often used to model the response of finite plates [4]. However, this model is restricted to farfield vibration only.

### 10.3.2 Vibrational Input Power

Analogously to the previous sections, VIP of the simply supported plate is also derived here by employing equation (3.23). Using the temporal derivative of equation (10.25), and substituting the simply supported

rectangular plate velocity into equation (5.18), the point mobility of the simply supported plate is found to be:

$$Y_{F_{ss}} = \frac{4j\omega}{\rho h L_x L_y} \sum_{m=1}^{\infty} \sum_{n=1}^{\infty} \frac{\sin^2 \left( \frac{m\pi x_0}{L_x} \right) \sin^2 \left( \frac{n\pi y_0}{L_y} \right)}{\omega_{mn}^2 (1 + j\eta) - \omega^2}. \quad (10.26)$$

If one substitutes equation (10.26) into equation (3.23), the vibrational energy input to a simply supported rectangular plate, excited by a point force at excitation location  $x = x_0$  and  $y = y_0$ , is given by:

$$(P_m)_{F_{ss}} = \frac{2\omega F_0^2}{\rho h L_x L_y} \Re \left\{ j \sum_{m=1}^{\infty} \sum_{n=1}^{\infty} \frac{\sin^2 \left( \frac{m\pi x_0}{L_x} \right) \sin^2 \left( \frac{n\pi y_0}{L_y} \right)}{\omega_{mn}^2 (1 + j\eta) - \omega^2} \right\}. \quad (10.27)$$

### 10.3.3 Transmitted Vibrational Energy

Transmitted vibrational energy within the simply supported rectangular plate can be found by substituting the simply supported plate displacement, as shown in equation (10.25), into equation (3.49) and (3.50), respectively in order to calculate VEF into the  $x$  and  $y$  directions. A complete derivation of VEF, based on the eigenfunction expansion theorem, is given in Appendix A27. From there, the complex VEF in the  $x$  direction is given by:

$$\begin{aligned} (\overline{P_x})_{F_{ss}} = & \frac{j\omega \underline{DC}^2}{2} \sum_{m=1}^{\infty} \sum_{n=1}^{\infty} \sum_{k=1}^{\infty} \sum_{i=1}^{\infty} \frac{C_{m_0} C_{n_0} C_{k_0} C_{i_0}}{(\omega_{mn}^2 (1 + j\eta) - \omega^2)(\omega_{ki}^2 (1 - j\eta) - \omega^2)} \times \\ & \sin(C_m x) \sin(C_n y) \sin(C_k x) \sin(C_i y) \times \\ & \left( \cot(C_m x) (C_m^3 + C_m C_n^2) - \cot(C_k x) C_k (C_m^2 + \nu C_n^2) + \right. \\ & \left. (1 - \nu) \cot(C_m x) \cot(C_n y) \cot(C_i y) C_m C_n C_i \right). \end{aligned} \quad (10.28)$$

The complex energy flow in the  $y$  direction can be written as:

$$\begin{aligned}
 (\overline{P}_y)_{F_{ss}} = & \frac{j\omega \underline{D} C^2}{2} \sum_{m=1}^{\infty} \sum_{n=1}^{\infty} \sum_{k=1}^{\infty} \sum_{i=1}^{\infty} \frac{C_{m_0} C_{n_0} C_{k_0} C_{i_0}}{(\omega_{mn}^2 (1 + j\eta) - \omega^2)(\omega_{ki}^2 (1 - j\eta) - \omega^2)} \times \\
 & \sin(C_m x) \sin(C_n y) \sin(C_k x) \sin(C_i y) \times \\
 & \left( \cot(C_n y) (C_n^3 + C_n C_m^2) - \cot(C_i y) C_i (C_n^2 + \nu C_m^2) + \right. \\
 & \left. (1 - \nu) \cot(C_m x) \cot(C_n y) \cot(C_k x) C_m C_n C_k \right). \quad (10.29)
 \end{aligned}$$

Note, in equation (10.28) and equation (10.29) the under-bar denotes a complex, flexural rigidity  $\underline{D} = D(1 + j\eta)$ . It can also be realised from equations (10.28) and (10.29) that the employed products of sine functions and cotangent functions are not defined at the boundary location  $x = 0$ ,  $x = L_x$ ,  $y = 0$  and  $y = L_y$ , as well as at locations where the cotangent argument is equal to an integer product with  $\pi$ . This unfortunate problem occurs due to simplification of equations (A27.12) and (A27.15). However, the definition given in equations (A27.12) and (A27.15) are true for each location within the plate. Thus, when employing equations (10.28) and (10.29) it has to be assumed that VEF at the boundaries is zero due to zero transverse and twisting velocity, as well as zero bending moment. In equations (10.28) and (10.29) the following substitutions were used:

$$C = \frac{4F_0}{\rho h L_x L_y}, \quad (10.30)$$

$$C_m = \frac{m\pi}{L_x}, \quad (10.31)$$

$$C_k = \frac{k\pi}{L_x}, \quad (10.32)$$

$$C_n = \frac{n\pi}{L_y}, \quad (10.33)$$



$$C_i = \frac{i\pi}{L_y}, \quad (10.34)$$

$$C_{m_0} = \sin\left(\frac{m\pi x_0}{L_x}\right), \quad (10.35)$$

$$C_{k_0} = \sin\left(\frac{k\pi x_0}{L_x}\right), \quad (10.36)$$

$$C_{n_0} = \sin\left(\frac{n\pi y_0}{L_y}\right), \quad (10.37)$$

$$C_{i_0} = \sin\left(\frac{i\pi y_0}{L_y}\right). \quad (10.38)$$

It can be seen from equations (10.28) and (10.29) that VEF in a point forced simply supported plate is defined here by a fourfold infinite series containing products of trigonometric functions and the hysteretic damping approach. It can be noticed further that at  $\omega_{mn} = \omega$  and  $\omega_{ki} = \omega$ , the main contribution to VEF is given at this particular resonant mode. It is also clear from the above equations that modes at which  $\omega_{mn} \neq \omega$  and  $\omega_{ki} \neq \omega$ , contribute less energy transmission to the VEF. Thus, modes with eigenfrequencies much greater than the excitation frequency can be neglected. In practice, the numerical evaluation of equations (10.28) and (10.29) can be carried out by truncating the infinite series at a modal frequency of  $(\omega_{mn} = \omega_{ki}) \gg \omega$ .

## 10.4 Unconstrained Layer Damping

The attachment of an unconstrained damping layer onto the plate's surface causes a shift  $z_N$  of the neutral axis of bending. Thus, the neutral axis of bending shifts off the plate's middle plane towards the attached layer. Attenuation of the plate's resonant vibration amplitudes is then achieved by

dissipating vibrational energy due to bending of the viscoelastic polymeric damping layer. Unlike the unconstrained damping setup, a constrained damping layer attenuates resonant amplitudes by dissipating vibrational energy due to shear deformation of the viscoelastic polymeric damping material, which sometimes is considered to be more effective.

Due to the layer attachment, the original flexural plate rigidity alters. However, the original plate rigidity and the original layer rigidity cannot be simply added together, since the neutral axis of bending has moved. Thus, the combined plate-layer structure must be integrated together along the  $z$ -axis in order to obtain the combined flexural rigidity. The derivation of the combined flexural rigidity can be traced back to the work of Oberst in 1952 [131]. However, in reference [131] it was assumed that the width of the damping layer was small compared to the flexural wavelength and, thus, transversal contractions were neglected. Furthermore, it was also assumed that the hysteretic loss factor of the plate was much smaller than the loss factor of the damping layer and, hence, internal damping within the plate was neglected. Mead [1] derived a combined flexural rigidity of the plate-layer configuration by using the beam-layer configuration derivation

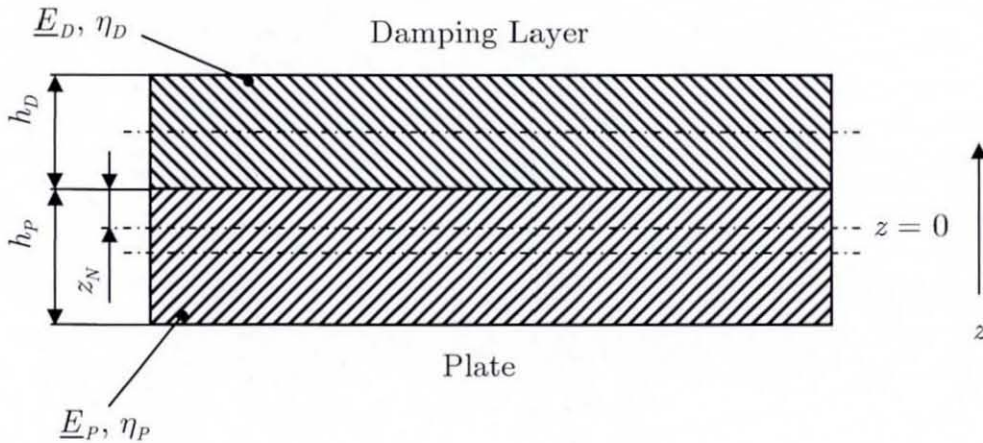


**Figure 10.2.** Unconstrained damping layer attached to a plate.

procedure (see section 5.5). It was assumed in reference [1] that the plate has a unity width. Also in reference [1], the internal plate damping was neglected. However, one-dimensional transversal contraction within the plate-layer compound was incorporated.

Within this section, the flexural rigidity required for VEF computation of the simply supported plate, attached by a uniform unconstrained viscoelastic polymeric damping layer, is presented. In contrast to the literature, internal damping within the plate is considered here. At lower thickness ratios  $h_D/h_P$  it will be shown that the inclusions of the plate's loss factor approximates the combined loss factor more accurately. The derived theory of the unconstrained layer damping of a plate-layer compound is presented in Appendix A28. The combined complex, flexural rigidity can be written in general form as:

$$\underline{D}_{PD} = D_{PD} (1 + j\eta_{PD}). \quad (10.39)$$

Herein,  $\underline{D}_{PD}$  is the combined complex, flexural rigidity,  $\eta_{DP}$  is the combined hysteretic loss factor due to plate-layer configuration and the under-bar denotes a complex quantity. From Appendix A28, the real part of the combined complex, flexural rigidity  $D_{PD}$  is given by:

$$D_{PD} = \frac{1}{12(1-\nu^2)} \frac{A_{PD}}{C_{PD}}. \quad (10.40)$$

Here, the numerator  $A_{PD}$  and denominator  $C_{PD}$  are defined as:

$$A_{PD} = \left[ B_{Eh} (A_{Eh} + E_P^2 h_P^4 + E_D^2 h_D^4) + 2\eta_P \eta_D (E_P^2 h_P^4 E_D h_D + E_D^2 h_D^4 E_P h_P) + \right. \\ \left. \eta_P^2 E_P h_P \left( \frac{A_{Eh} + 2E_P^2 h_P^4}{E_P h_P^3 B_{Eh}} - \right) + \eta_D^2 E_D h_D \left( \frac{A_{Eh} + 2E_D^2 h_D^4}{E_D h_D^3 B_{Eh}} - \right) \right], \quad (10.41)$$

$$C_{PD} = B_{Eh}^2 + (E_P h_P \eta_P + E_D h_D \eta_D)^2. \quad (10.42)$$



The abbreviations  $A_{Eh}$  and  $B_{Eh}$  employed in equations (10.41) and (10.42) are:

$$A_{Eh} = 2E_P h_P E_D h_D (2h_P^2 + 2h_D^2 + 3h_P h_D), \quad (10.43)$$

$$B_{Eh} = E_P h_P + E_D h_D. \quad (10.44)$$

The combined hysteretic loss factor  $\eta_{PD}$  of the plate-layer configuration can be written as:

$$\eta_{PD} = \frac{\left( \eta_P^2 \eta_D E_P h_P \left( \frac{A_{Eh} + E_P h_P^3 E_D h_D}{E_P h_P^3 E_D h_D} \right) + \eta_P \eta_D^2 E_D h_D \left( \frac{A_{Eh} + E_D h_D^3 E_P h_P}{E_D h_D^3 E_P h_P} \right) + \right.}{\left( B_{Eh} (A_{Eh} + E_P^2 h_P^4 + E_D^2 h_D^4) + 2\eta_P \eta_D (E_P^2 h_P^4 E_D h_D + E_D^2 h_D^4 E_P h_P) + \right.} \quad (10.45)$$

$$\left. \eta_D (E_P h_P (A_{Eh} - E_P h_P^3 E_D h_D) - E_D^2 h_D^4 (E_D h_D - 2B_{Eh})) + \right. \\ \left. \eta_P (E_D h_D (A_{Eh} - E_D h_D^3 E_P h_P) - E_P^2 h_P^4 (E_P h_P - 2B_{Eh})) + \right. \\ \left. \eta_P^3 E_P^3 h_P^5 + \eta_D^3 E_D^3 h_D^5 \right) \\ \left. \eta_P^2 E_P h_P \left( \frac{A_{Eh} + 2E_P^2 h_P^4 - E_P h_P^3 B_{Eh}}{E_P h_P^3 B_{Eh}} \right) + \eta_D^2 E_D h_D \left( \frac{A_{Eh} + 2E_D^2 h_D^4 - E_D h_D^3 B_{Eh}}{E_D h_D^3 B_{Eh}} \right) \right)$$

It can be seen from equation (10.45) that the loss factor of the plate and the loss factor of the layer form the combined loss factor expressions by building individual and cross products. If one neglects the plate's loss factor ( $\eta_P = 0$ ) because of  $\eta_D \gg \eta_P$ , expression (10.45) can be simplified further.

Figure 10.3 displays a logarithmic plot of the combined linear hysteretic loss factor  $\eta_{PD}$  in dependency upon the thickness ratio between plate and layer,  $h_D/h_P$ . The loss factor of the layer was  $\eta_D = 0.12$ . The loss factor of the plate used in this analysis was taken to be  $\eta_P = 5.32 \cdot 10^{-3}$ . Also here, the employed plate loss factor was obtained from an experimental modal analysis carried out on an undamped simply supported plate. In similarity to the result determined on the unconstrained layer damping of a beam, it can be seen from Figure 10.3 that an exclusion of the plate's

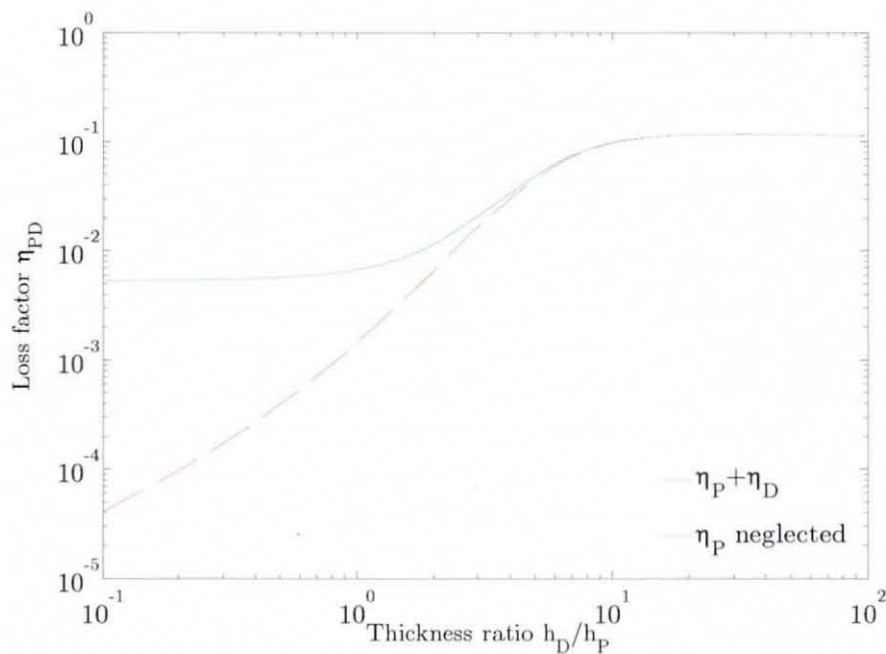


**Figure 10.3** Combined linear hysteretic loss factor of an unconstrained layer damped plate in dependency on the thickness ratio  $h_D/h_P$ .

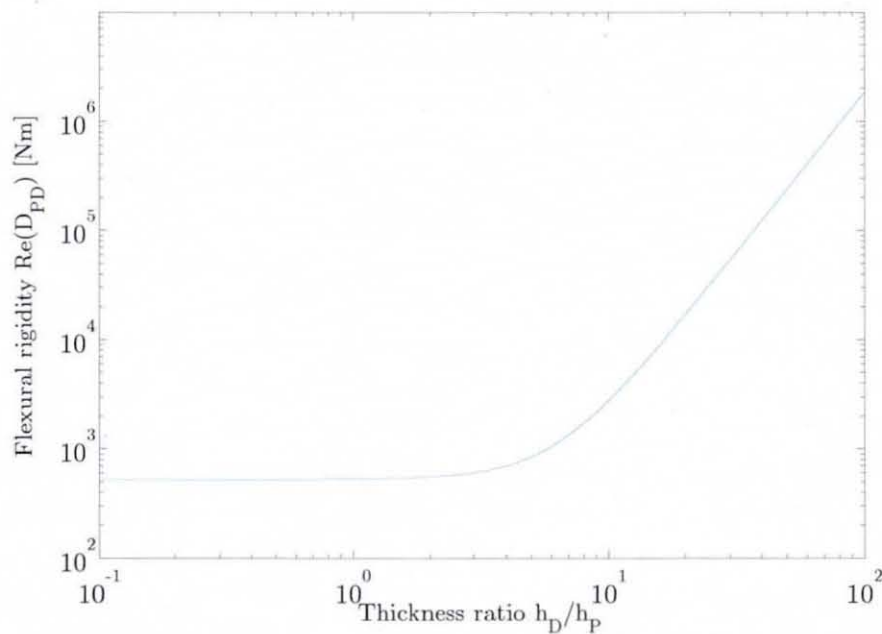


**Figure 10.4** Combined flexural rigidity of an unconstrained layer damped plate in dependency on the thickness ratio  $h_D/h_P$ .

hysteretic loss factor makes a difference in the combined loss factor computation. It can be noticed that up to a thickness ratio of  $h_D/h_P \approx 5$  the loss factor of the plate should not be neglected. Furthermore, as evident from Figure 10.3, a substantial increase in overall structural damping can only be achieved within a thickness ratio range of  $1.5 \leq h_D/h_P \leq 10$ . This result coincides with the unconstrained layer analysis of the beam. During the experimental work within this research, a 3 mm thick plate was employed and a 2.5 mm thick layer was attached to the plate's surface. It can be realised that the thickness ratio is about  $h_D/h_P \approx 0.83$ , which is higher than the thickness ratio employed during the simply supported beam experiment. Thus, a larger increase in structural damping is expected for the plate experiment.

Figure 10.4 displays the alteration in flexural rigidity occurring when an unconstrained layer is attached onto the plate. It can be realised from this figure that the increase in flexural rigidity can be neglected up to a thickness ratio of  $h_D/h_P \approx 1$ .

## 10.5 Discussion

This chapter presented the theoretical study of VEF in infinite and simply supported rectangular plates. VIP and transmitted energy expressions were originally derived for both plate structures based on the spatial partial derivatives of the prior derived infinite and simply supported plate displacements. Except for the polar coordinate based VIP and VEF expressions of the infinite plate [5], no literature sources were found that studied VIP and VEF of the plate structures considered herein. Thus, most of the VIP and VEF expressions were originally derived.

The vibrational energy analysis of the infinite plate was simplified by employing a truncated exponential asymptotic expansion expression in order to substitute for the Hankel function difference within the displacement equation. However, this procedure restricted the VEF analysis to locations in the plate where the product  $|kr|$  was greater than four. To ensure small VEF



analysis errors, the distance  $r$  from the excitation location should increase with increasing frequency. This means, the VEF analysis is increasingly restricted to the farfield region of the plate as the frequency is increased.

Since the wave propagation within an infinite plate is of a radially symmetric nature, polar VEF expressions were derived. It could be shown that the TTVE in an infinite plate is equal to the VIP. This relation is true at each location within the infinite plate assuming the internal vibrational energy losses are neglected. The TTVE is defined here as the integrated VEF per unit length over a closed contour.

Due to a comparison of the TTVE and the VIP, the error term of the derived active VEF could be identified. This was caused by using the truncated asymptotic expansion of the Hankel functions. Thus, the exact VEF within an infinite plate could be derived and was given by the first bracket term product of equation (10.7). However, when studying VEF within an infinite plate numerically, by employing the exponential asymptotic expansion of the Hankel function difference, errors have to be expected due to the approximation of the Hankel function difference.

When computing active TTVE within an infinite plate from polar expressions-based VEF fields by using a square contour integration, a correction factor needed to be employed in order to correct the erroneous TTVE. Thus, in equation (10.22) a correction factor was shown that compensated for the error made when integrating a polar quantity along a square contour.

VEF analysis of a simply supported rectangular plate was undertaken herein using a mode-based approach. This procedure can be considered as an alternative technique to the wave-based approach. Within a finite plate, multiple reflections of the initially outward travelling radially symmetric infinite wave occur at the plate's edges. It can be recognised that the modelling of this reflection process is rather complicated. Employing the eigenfunction expansion theorem for plates to form a modal displacement response yielded a rather more compact transmitted vibrational energy solution.

As mentioned, a modal VEF solution was presented for the simply supported rectangular plate. The use of the eigenfunction expansion theorem yielded a fourfold series using an infinite number of modes excited by the excitation frequency. It can be realised that the numerical implementation of this approach would lead to the consideration of an infinite number of modes. This is not feasible in reality. The infinite series has to be truncated at some point and, thus, errors to some extent will occur during the theoretical VEF calculations. Also, the implementation of a fourfold series is a fairly high computational effort.

At modes with eigenfrequencies of  $\omega_{mn} = \omega_{ik} = \omega$ , the denominator in equations (10.28) and (10.29) becomes the real quantity  $\omega^4 \eta^2$ . Without the inclusion of hysteretic damping, the denominator in equations (10.28) and (10.29) would be zero. However, by including the hysteretic damping and multiplying the denominator in equations (10.28) and (10.29) by the complex and constant fraction in front of equations (10.28) and (10.29), VEF at this particular mode is now a complex quantity. Note, it is assumed that the excitation location was selected in a way not to suppress this particular mode. Thus, active as well as reactive energy flow is present. Further, it can be realised that the active energy flow in comparison to the reactive VEF is reduced by the multiplication of the loss factor  $\eta$ .

# 11 NUMERICAL ANALYSIS OF VIBRATIONAL ENERGY IN PLATES

## 11.1 Introduction

The aim of this chapter is to investigate the numerical application of the vibrational energy flow determination using electronic speckle pattern interferometry (VEFESPI), as introduced in chapter 4. Here, the VEFESPI method will be applied to infinite and rectangular simply supported plate structures. The procedure is analogous to the procedure presented in chapter 6. The required spatial partial derivatives are computed by the  $k$ -space derivation (KSD) method. The strengths and weaknesses of this method were studied in chapter 6 for beam structures. The findings of the beam investigation are also valid for the plate's structural analysis. However, two dimensions need to be taken into account here.

To compute errors caused by the VEFESPI method the numerically determined vibrational energy flow (VEF) is compared to the exact VEF solutions that were presented in chapter 10. Therefore, a harmonically point force excited, two-dimensional and synthetic plate response signal is generated, which is then taken as an input to the VEFESPI computation model. The synthetic plate response can be seen as a substitute of the recorded electronic speckle pattern interferometry (ESPI) displacement signal.

Employing the KSD method may yield to computational accuracy problems when signal irregularities are present. These signal irregularities



may be caused by nearfields occurring at discontinuities (e.g. excitation location) or the analysis of odd-numbered mode shapes and, thus, non-periodic data. To ensure low VEF computation errors when applying the KSD method, periodisation of the displacement signal is desirable. Three periodisation techniques, which were introduced previously, will also be employed here.

The presence of noise in the displacement signal leads to substantial errors in VEF calculations due to spectral amplitude amplification of the Fourier transformed noise contaminated plate displacement. This problem was introduced in chapter 6. Analogously, the effects of spectral filtering of infinite and simply supported rectangular plate displacements will also be investigated here.

When computing VEF from measured ESPI displacement data optimum filter parameters are required in order to compute a low error VEF. To find optimum cut-off filter parameters, extracted optical noise from the measured ESPI data is superimposed with the artificially generated plate displacement. An error algorithm is then used to detect the optimum filter cut-off points where the error of VEF computation due to noise contamination is lowest.

It has been shown in chapter 6 that the presence of nearfield components, a non-periodic displacement input or noise contamination of the spatial signal causes VEF computation errors due to undesired amplification of spectral components in the wavenumber domain. Often a combination of the three error sources takes place. It is clear that these phenomena also occur when computing VEF in a plate. However, the problems are now related to two-dimensions. Thus, counteractive measures, as introduced in chapter 6 and applied to beams, are also employed here. However, the proposed techniques are extended into two dimensions.

Thus, this chapter presents a fundamental feasibility study of the numerical computation of VEF in plates. The novelty of the presented material is that an elaborate error and sensitivity analysis is undertaken, which highlights computational problems that may be expected when computing VEF in plates from measured ESPI displacement data.

## 11.2 Numerical Infinite Plate Analysis

This section investigates the numerical VEF determination of an infinite plate structure by inserting an artificially generated infinite plate displacement into the VEFESPI computation model. Effects of signal irregularity and noise contamination are studied and measures to increase VEF computation accuracy are introduced.

### 11.2.1 Vibrational Energy Flow Excluding Noise

As mentioned previously, the point force excited infinite plate response is a radially symmetric wave that is travelling away from the excitation location towards the infinite end. It has been shown in section 10.2 that the infinite plate displacement may be described by Hankel functions of second kind and zeroth order, representing a travelling farfield and a decaying nearfield. The numerical implementation of the Hankel function difference is problematic. To avoid this problem and to investigate the results given in section 10.2, the exponential asymptotic expansion of the Hankel functions, as introduced in section 10.2.4.1, is implemented herein instead using the software environment MATLAB<sup>®</sup>. The material properties of the infinite plate are shown in Table 11.1. These are the same properties as the experimental “infinite” plate used during the ESPI experiment.

Young's modulus	$E = 2.07 \cdot 10^{11} \text{ N/m}^2$
mass density	$\rho = 7.85 \cdot 10^3 \text{ kg/m}^3$
plate thickness	$h = 1 \cdot 10^{-3} \text{ m}$
Poisson ratio	$\nu = 0.33$

**Table 11.1** “Infinite” plate properties.

The forced infinite plate response is generated by numerically evaluating equation (10.12) using a number of data points in the  $x$  and  $y$  directions of  $N_x$

$= N_y = 128$ . As usual a unity excitation force of  $F_0 = 1$  N is applied. The infinite plate displacement is investigated within a window of  $L_x = L_y = 1$  m using an excitation frequency of  $f = 986.7$  Hz ( $k = 20\pi$  rad/m). As mentioned before, the exponential approximation of the Hankel function is very accurate from  $|kr| \geq 4$  on. Therefore, with locations greater than  $r = 1/5\pi$  m (6.4 cm) equation (10.12) is a very good displacement approximation.

Figure 11.1 displays the real and imaginary part of the two-dimensional infinite plate displacement as well as the one-dimensional curve in the  $x$  direction at  $y = 0$ . It can be noticed from Figures 11.1(c)-(d) that

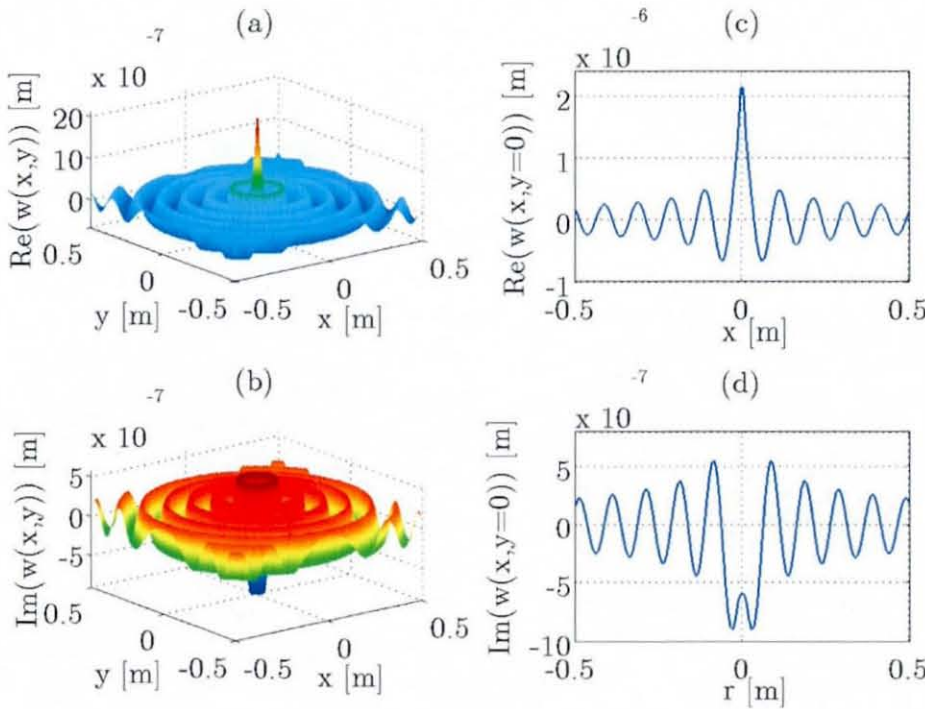


**Figure 11.1** Complex infinite plate displacement at  $f_0 = 986.7$  Hz: (a) 2D real part, (b) 2D imaginary part, (c) real part at  $y = 0$ , (d) imaginary part at  $y = 0$ .

the amplitude is decaying away from excitation location (Sommerfeld radiation condition). It is evident from the polar farfield approximation of equation (10.6) that at  $r = 0$  a singularity appears, i.e. the displacement approaches infinity. This singularity can be seen in Figure 11.1(a) by the sharp spike at the excitation location.



Figure 11.2 displays the top view image of the infinite plate displacement, as shown in Figure 11.1. The radial travelling nature of the displacement is clearly visible. To compute VEF using the KSD method, spectral derivatives of the infinite plate displacement need to be determined

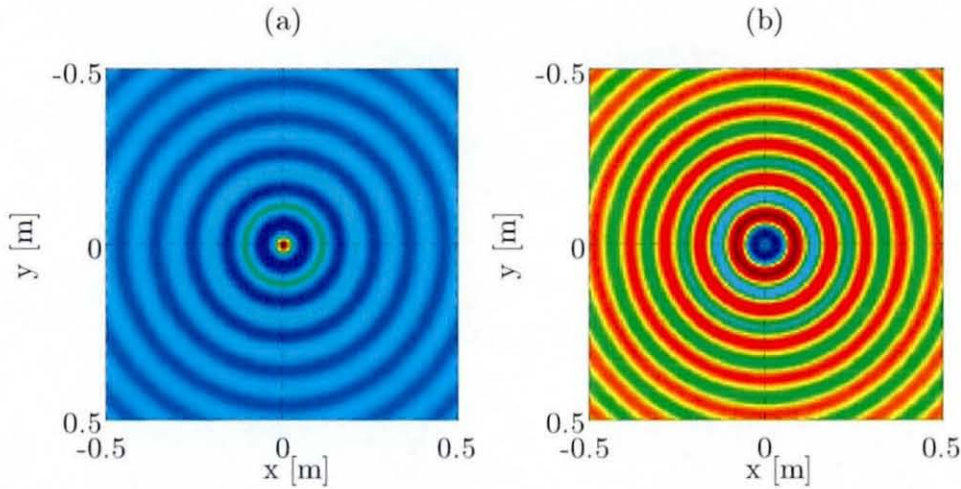


**Figure 11.2** Top view image of the complex infinite plate displacement shown in Figure 11.1: (a) real part, (b) imaginary part.

in order to obtain the required spatial partial derivatives of the infinite plate response.

It can be realised from equation (10.1) that the polar infinite plate displacement is a function of the radius  $r$  only. To compute the wavenumber spectrum of such a one-dimensional polar function the Hankel transform has to be applied [132]. The Hankel transform is the solution of an infinite integral expression containing the product of the spatial function  $w(r)$  to be transformed and a Bessel function in its kernel [132]. Its result is a one-dimensional wavenumber spectrum containing complex amplitudes at the radial wavenumber  $k_r$ . The solution of the integral kernel can be very complicated. Three main solution categories of Hankel transforms can be identified: the first class is based on a sinusoidal approximation of the Bessel function, using the asymptotic expansion of the Bessel function; the second class contains a Fourier transform based algorithm of the exponential substituted variables over an exponential constructed or sampled grid [133]; the third class computes the Hankel transform using the back projection or

the projection slice theorem. The projection slice theorem states that the two-dimensional Fourier transform can be computed by a two-dimensional Chebyshev or Abel transform followed by a one-dimensional Fourier transform [133, 134]. The back projection slice theorem states that the inverse two-dimensional Fourier transform can be evaluated by the one-dimensional inverse Fourier transform followed by the back projection operator [134].

However, the VEFESPI method as applied to two-dimensional structures requires two-dimensional spatial partial derivatives. It has been shown in reference [132] that the Hankel transform is equivalent to the two-dimensional Fourier transform. Thus, a two-dimensional Fourier transform can be employed in order to compute the wavenumber spectrum of the polar infinite plate displacement, evaluated in two dimensions, as shown in Figure 11.2.

Figure 11.3 displays the modulus of the wavenumber spectrum

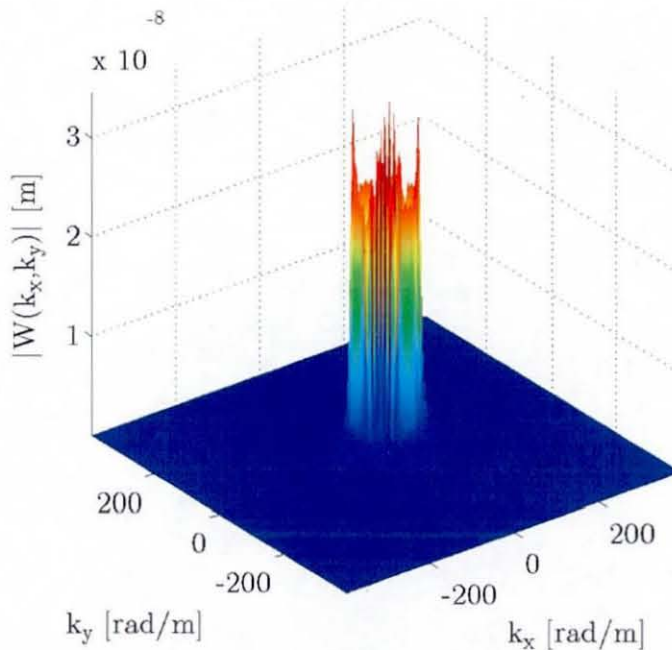


**Figure 11.3** Modulus of 2D FFT spectrum of the complex infinite plate displacement shown in Figure 11.1.

computed from the infinite plate displacement shown in Figures 11.1 and 11.2, respectively. It is noticeable that the spectrum is a cylindrical function having a radius of  $k_r^2 = k_x^2 + k_y^2$ , where  $k_r$  is the radial wavenumber,  $k_x$  is the wavenumber component in the  $x$  direction, and  $k_y$  is the wavenumber component in the  $y$  direction.

It is evident from Figure 11.2 that due to the radial nature of the displacement an integer number of waves cannot be included in the displacement signal due to Cartesian coordinate usage. Thus, the application of a non-periodic plate displacement cannot be avoided. Furthermore, as evident from equation (10.6), a nearfield component is also present. Because of these two reasons VEF computation errors due to undesired alteration of the spectral components in the wavenumber domain, when computing spectral derivatives, can be expected.

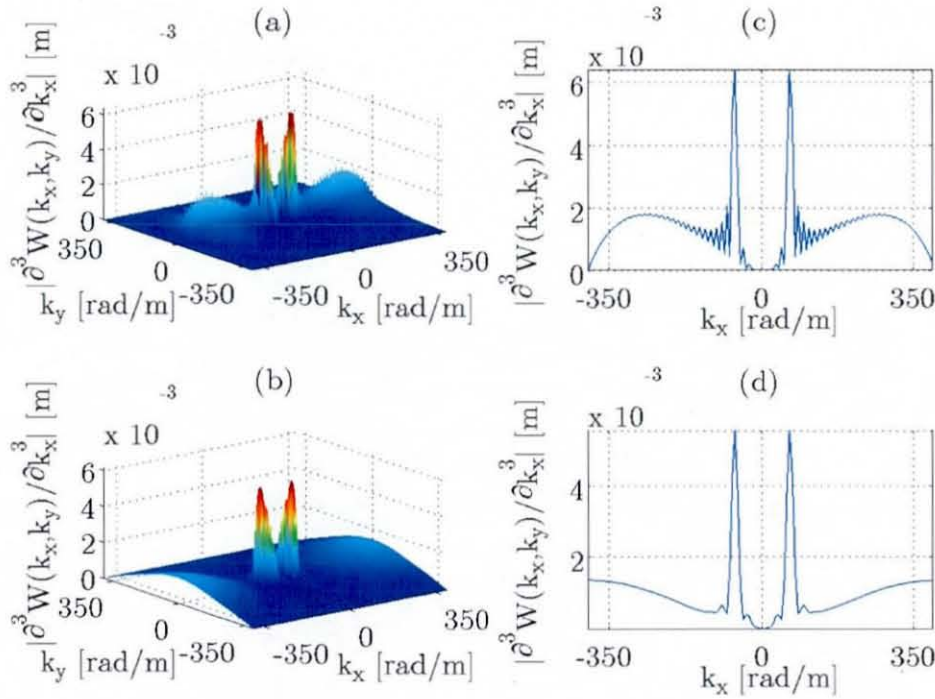


**Figure 11.4** VEFESPI determined and exact solution of the 3<sup>rd</sup> spectral derivative with respect to  $k_x$  of the displacement shown in Figure 11.1: (a) 2D modulus - VEFESPI, (b) 2D modulus - exact solution, (c) 1D modulus at  $k_y = 0$  - VEFESPI, (d) 1D modulus at  $k_y = 0$  - exact solution.



Figure 11.4 displays the modulus of the 3<sup>rd</sup> spectral derivative of the wavenumber displacement  $W(k_x, k_y)$  determined by the VEFESPI method and its exact value computed from analytical analysis. The two-dimensional derivative as well as the one-dimensional derivative curve at  $k_y = 0$  are shown.

Figure 11.5 displays the 3<sup>rd</sup> spatial derivative in the  $x$  direction of the infinite plate displacement  $w(x, y)$  obtained from the VEFESPI method and the exact solution. It can be seen from Figure 11.4 that oscillations are introduced to the spectral derivative  $\partial^3 W(k_x, k_y) / \partial k_x^3$  due to signal non-periodicity. These oscillations occurred due to spectral leakage amplification of the spectral multiplication process when computing spectral derivatives. When applying the inverse fast Fourier transform (FFT), these amplified oscillations, in addition to the amplified spectral nearfield components, also

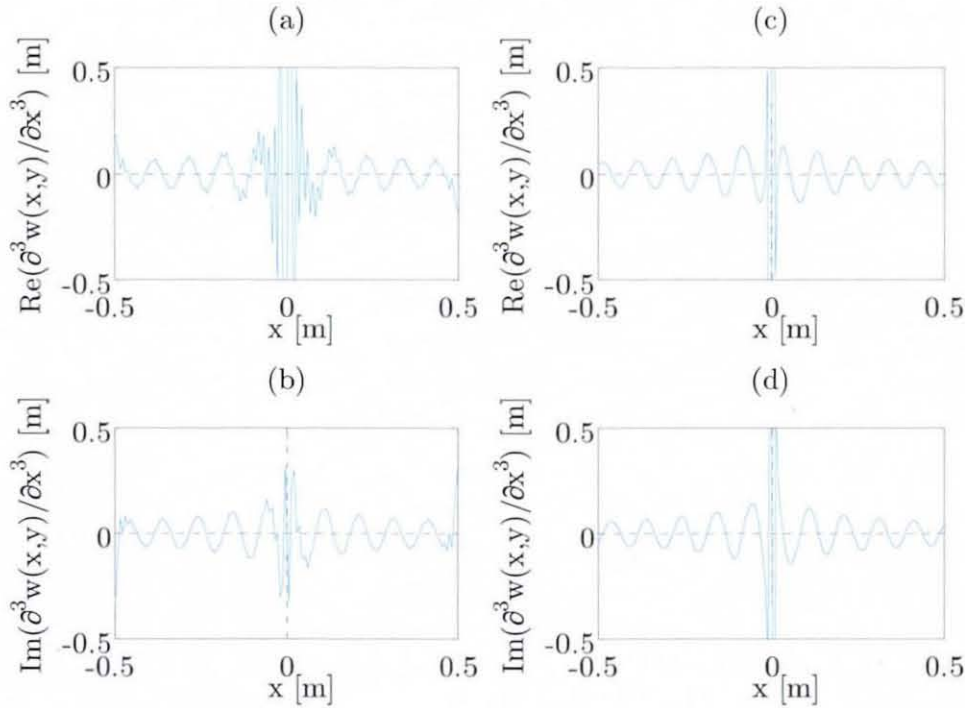
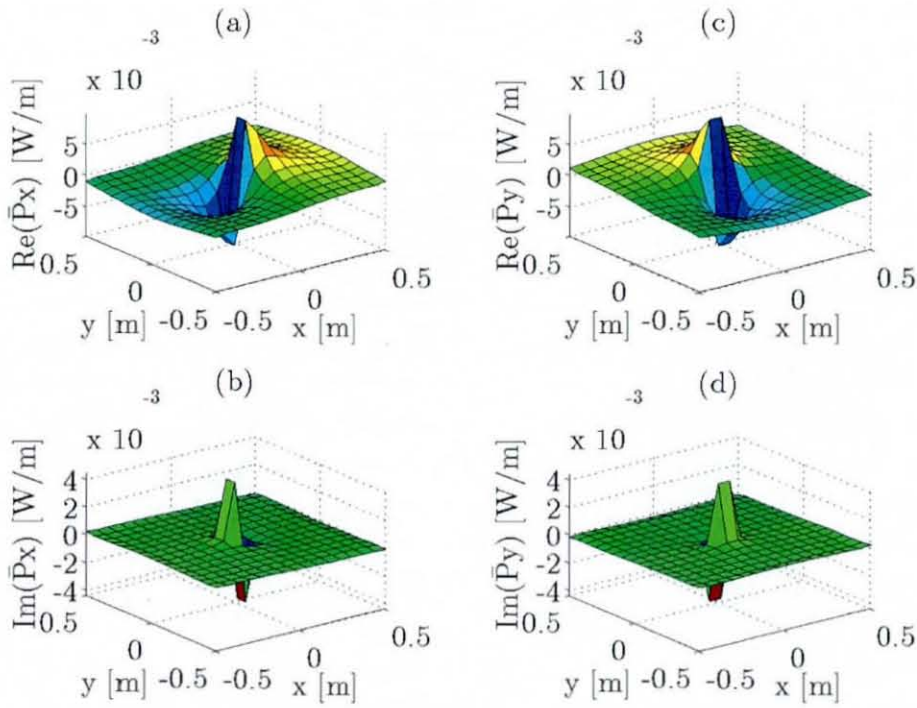


**Figure 11.5** VEFESPI determined and exact solution of the 3<sup>rd</sup> spatial derivative with respect to  $x$  of the displacement shown in Figure 11.1 at  $y = 0$ : (a) real part - VEFESPI, (b) imaginary part - VEFESPI, (c) real part - exact solution, (d) imaginary part - exact solution.

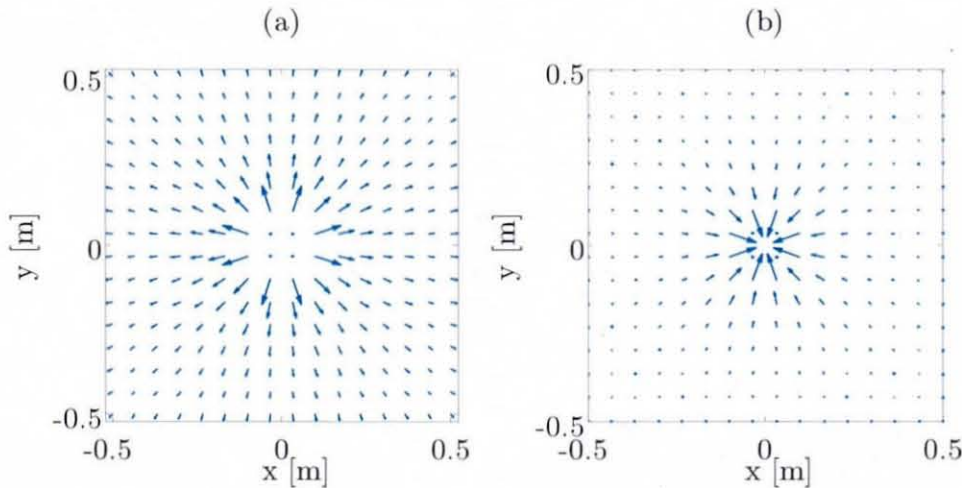
cause oscillations within the spatial derivative signal, as evident from Figure 11.5. However, the effect due to the nearfield is not as strong as in the case of the infinite beam analysis. Note, the figures of the spatial partial derivative  $\partial^3 w(x, y) / \partial x^3$  in Figures 11.5(a)-(d) are enlarged because of better oscillation illustration. Due to the above mentioned reasons the computation of VEF, when using the VEFESPI method, will result in errors. In chapter 6 VEF oscillations were diminished by either periodising the non-periodic beam displacement or computing a non-oscillating VEF by approximating the oscillating VEF curve using the curve wrap (CW) method. Two periodisation techniques were introduced, namely the mirror-reverse-shear (MRS) and mirror-processing (MP) technique, respectively. However, due to the radial nature of the infinite plate displacement the periodisation techniques cannot be employed when analysing the infinite plate displacement. Thus, VEF oscillations are reduced by applying the CW method only. However, this method is extended to a two-dimensional procedure by computing two-dimensional VEF curve wraps.

Figure 11.6 displays the Cartesian coordinate based VEF per unit width,  $\overline{P}_x$  and  $\overline{P}_y$ , of the infinite plate displacement, shown in Figure 11.1, computed by the VEFESPI method. VEF oscillations were reduced by employing the CW technique. It can be seen from Figure 11.6 that the active and reactive VEF per unit width,  $\overline{P}_x$  and  $\overline{P}_y$ , are orthogonal to each other. It has been shown in chapter 3 that the VEF per unit width,  $\overline{P}_x$  and  $\overline{P}_y$ , are complex, two-dimensional vector fields representing the two-dimensional flow of vibrational energy in the  $x$  and  $y$  direction, respectively. Thus, both components have to be used to construct an active and reactive VEF map, which contains arrows that represent the magnitude and direction of the energy flow within the plate.

Figure 11.7 displays the active and reactive VEF map of the infinite plate computed by the VEFESPI + CW method. For better illustration of Figures 11.6 and 11.7 the number of data points were reduced to  $N_x = N_y = 16$ , simply by averaging the original VEF flow maps over distance. Furthermore, the VEF arrows within the location of  $|kr| \leq 4$  were set to zero,



**Figure 11.6** Determined VEF in the  $x$  and  $y$  directions of the infinite plate displacement shown in Figure 11.1 using the VEFESPI + CW method: (a) active VEF in  $x$  direction, (b) reactive VEF in  $x$  direction, (c) active VEF in  $y$  direction, (d) reactive VEF in  $y$  direction.



**Figure 11.7** VEF maps of the infinite plate displacement shown in Figure 11.1 from the VEFESPI + CW method: (a) active VEF, (b) reactive VEF.



because for these regions, equation (10.6) is not valid. The magnitude of the energy flow arrows can be taken from Figure 11.6.

It can be seen from Figure 11.7(a) that the vibrational energy flows radially and symmetrically away from the excitation location towards infinity. It can also be noticed that with increasing distance  $r$  the magnitude of VEF is decreasing in order to obey the energy conservation law. Interestingly, the reactive energy is flowing towards the excitation location with relatively large magnitudes around the excitation location and very weak reactive flows in the farfield region. Thus, reactive energy flow occurs significantly around the excitation location within the infinite plate similar to the infinite beam.

To determine the accuracy of the VEFESPI method when computing VEF within infinite plates, a two-dimensional relative error distribution was calculated from the determined VEFESPI energy flow and the exact VEF as:

$$\Delta\varepsilon_x = \left( 1 - \frac{(\overline{P}_x)_{VEFESPI}}{(\overline{P}_x)_{exact}} \right) \cdot 100\%. \quad (11.1)$$

Note, the relative error  $\Delta\varepsilon_y$  is calculated accordingly simply by substituting subscript  $x$  with  $y$  in equation (11.1). Figure 11.8 displays the relative active and reactive VEF error distribution. Note, for better illustration the number of data points was reduced to  $N_x = N_y = 32$ . Furthermore, the VEF values within the region of  $|kr| \leq 4$  were also set to zero. It can be seen from Figure 11.8 that the relative error made when computing VEF by the VEFESPI method is very low, except at some points within the relative reactive error maps. Thus, the CW technique can be employed in order to reduce the effects of displacement non-periodicity and nearfield components arising within the infinite plate.

An alternative method to assess the accuracy of the VEFESPI + CW method is the numerical contour integration of the two-dimensional energy fields  $\overline{P}_x$  and  $\overline{P}_y$  (energy balance). It was shown by equation (10.9) that the integration of the active VEF around a closed contour is equal to the

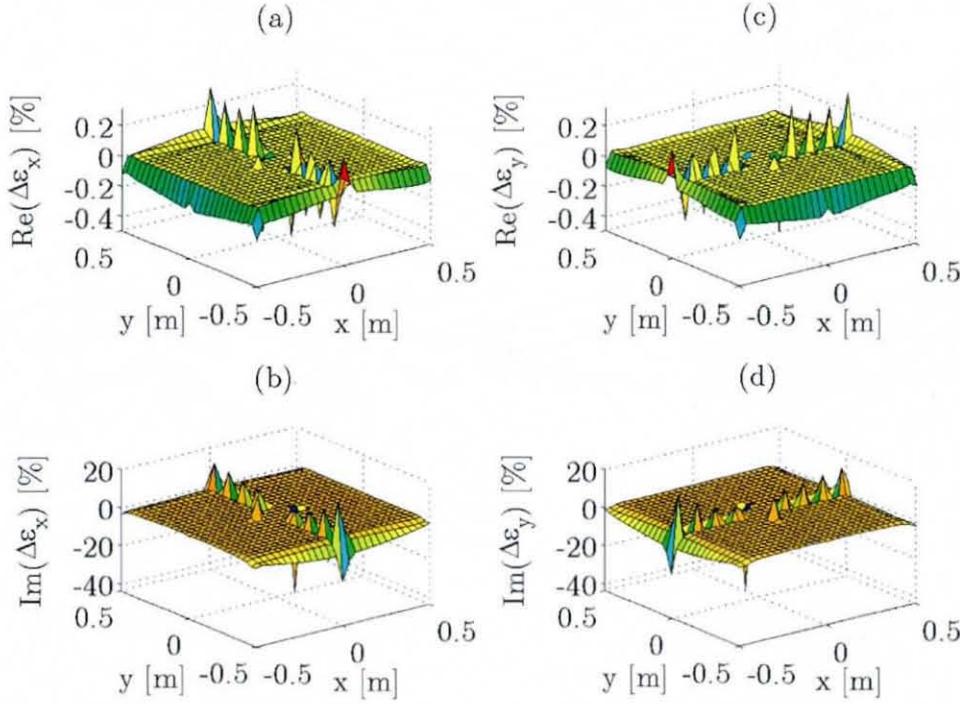


**Figure 11.8** Relative error of VEF of the infinite plate displacement shown in Figure 11.1: (a) relative active error in  $x$  direction, (b) relative reactive error in  $x$  direction, (c) relative active error in  $y$  direction, (d) relative reactive error in  $y$  direction.

vibrational input power (VIP) injected into the plate structure. This relation holds true for each location within the infinite plate.

Figure 11.9 displays the comparison of total transmitted vibrational energy (TTVE) and VIP. A quadratic Cartesian coordinate based numerical contour integration was carried out, as shown in Figure 10.1, for each numerical location  $|kr|$  by numerically evaluating equation (10.18). With a sample number of  $N_x = N_y = 128$ , 64 squares were integrated numerically. It can be seen from Figure 11.9 that around  $|kr| \approx 5$  the TTVE  $(P_a)_{F_\infty}$  within the infinite plate is approximately equal to the input power  $(P_m)_{F_\infty}$ . However, at lower locations of  $|kr|$  only a few points could be used to integrate  $\overline{P_x}$  and  $\overline{P_y}$  numerically. The accuracy therefore decreases at these locations. Taking this into account, it can be argued that the approximation of the infinite plate displacement, when using equation (10.6), results in low errors made within the range of  $|kr| \geq 4$ . Furthermore, the VEFESPI method in

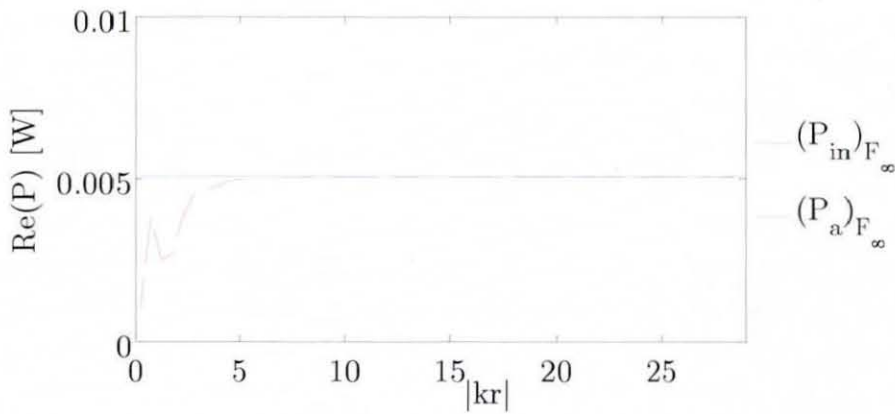


**Figure 11.9** Comparison of total transmitted active vibrational energy and vibrational input power of the infinite plate displacement shown in Figure 11.1.

combination with the CW technique produced very low errors when computing VEF within an infinite plate.

### 11.2.2 Vibrational Energy Flow Including Noise

This section investigates the effects of spectral filtering when computing VEF from an infinite plate displacement that is contaminated by normally distributed noise. As demonstrated previously in chapter 6, two types of filter are also employed herein, an ideal 2D filter and an oval 2D Butterworth filter. Both filter types are applied within the spectral domain prior to the spectral derivation process using the KSD method. The conclusions gained during the filter analysis in chapter 6 are also applicable to the filter analysis of the plate.

It has been shown in chapter 6 that the reactive energy cannot be computed accurately enough when dealing with noise contaminated beam displacement inputs due to the erasure of valuable nearfield wave information in the spectral domain. Thus, at this point attention is focused mostly on the computation of active VEF. To determine optimum filter parameters, a mean squared error (MSE) function similar to equation (6.7) is used here. However, the active TTVE  $(P_a)_{F_\infty}$  within the infinite plate at each numerical location  $|kr|$  is compared to the VIP  $(P_{in})_{F_\infty}$ , given by equation (10.3) as:



$$\Pi = \frac{1}{N} \sum_{i=1}^N \left( 1 - \frac{\left( P_{a_i} \right)_{F_\infty}}{\left( P_{m_i} \right)_{F_\infty}} \right)^2. \quad (11.2)$$

Here,  $N = N_x/2 = N_y/2$  is the number of points from each numerical contour integration along  $|kr|$ . It can be realised that the one-dimensional MSE function in equation (11.2) incorporates the two-dimensional energy fields,  $\overline{P_x}$  and  $\overline{P_y}$ , as shown in equation (10.18). Thus, the initial two-dimensional optimisation problem is now reduced to a one-dimensional problem, which can be implemented straightforwardly.

Figure 11.10 displays the infinite plate displacement, shown in Figure 11.1, however, contaminated by normally distributed noise with a signal-to-noise ratio (SNR) of 110.4. Note, here the SNR is a two-dimensionally integrated quantity and can be seen as an extension to the one-dimensional theory shown in Appendix A18. As demonstrated previously, the noise within

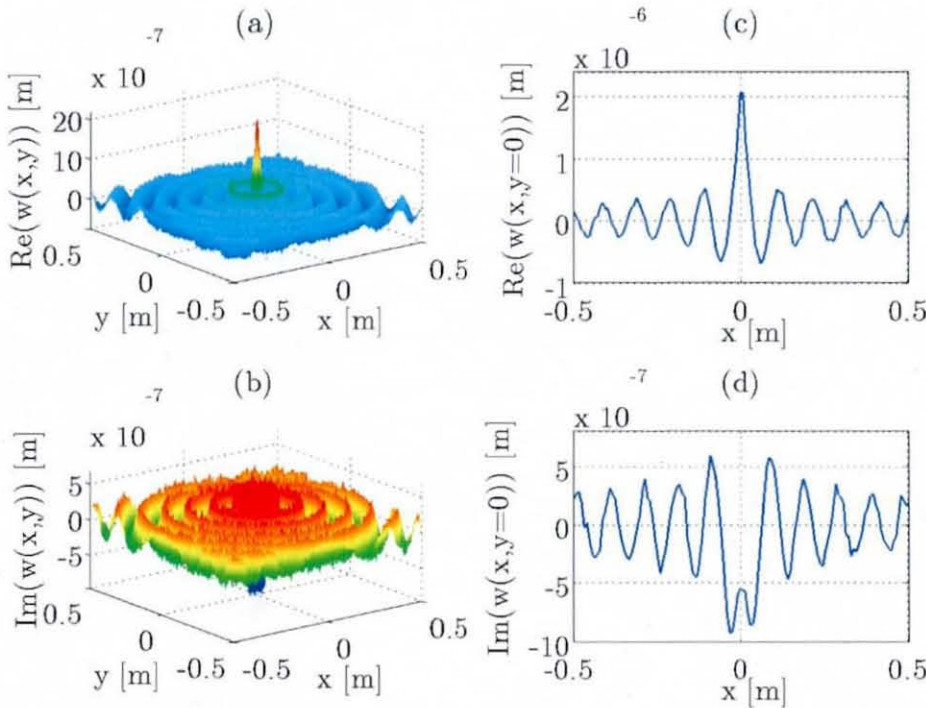


**Figure 11.10** Noise contaminated infinite plate displacement of Figure 11.1 with a  $\text{SNR} = 110.4$ : (a) 2D real part, (b) 2D imaginary part, (c) real part at  $y = 0$ , (d) imaginary part at  $y = 0$ .

the spatial displacement signal is transformed into the wavenumber domain and eventually the spectral amplitudes are then amplified when computing spectral derivatives, required for VEF computation. This procedure has most effect at the high wavenumber locations. To avoid the undesired spectral alteration process the noise contaminated wavenumber spectrum will be filtered by using an ideal 2D filter algorithm as well as an oval 2D Butterworth low-pass filter.

Figure 11.11 displays the Butterworth filtered 3<sup>rd</sup> order spectral derivative with respect to  $k_x$  of the wavenumber spectrum  $W(k_x, k_y)$  compared to the exact 3<sup>rd</sup> order spectral derivative. It can be noticed from Figure 11.11

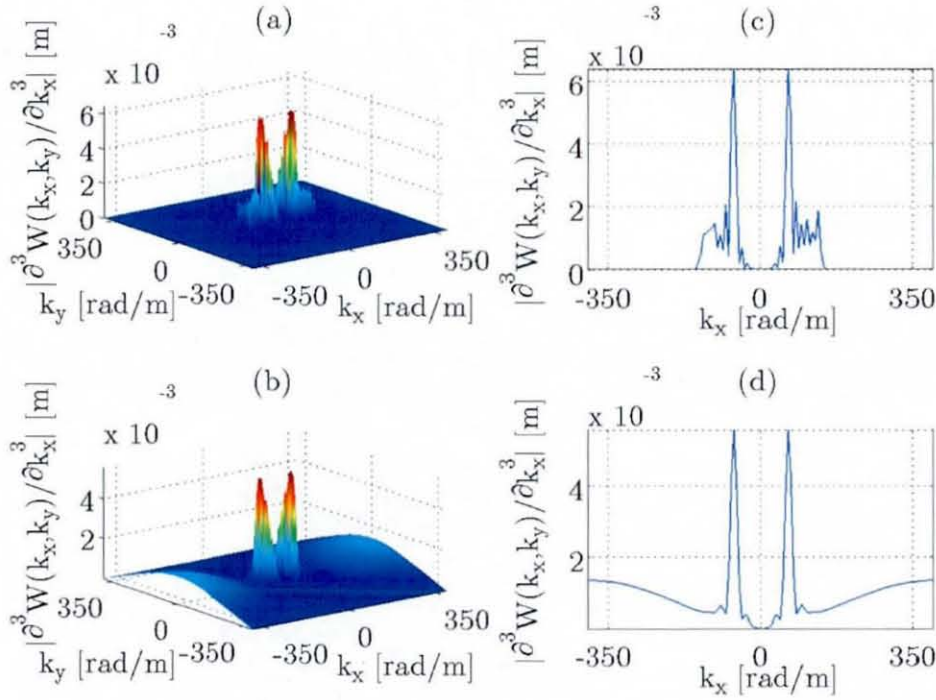


**Figure 11.11** Butterworth filtered and exact 3<sup>rd</sup> spectral derivative of the displacement shown in Figure 11.10: (a) 2D - VEFESPI, (b) 2D - exact solution, (c) 1D at  $k_y = 0$  - VEFESPI, (d) 1D at  $k_y = 0$  - exact solution.

that a small amount of noise remains within the spectrum up to the cut-off frequency point  $k_c$ . Note, the cut-off frequency  $k_c$  is related here to the radial wavenumber  $k_r$  as  $k_c = nk_r$ , where  $n$  is any real number.



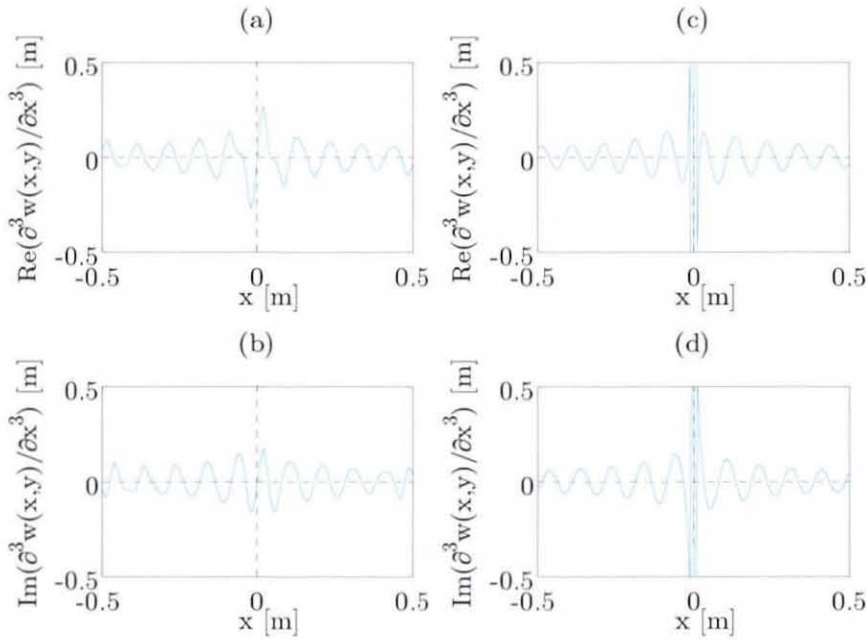
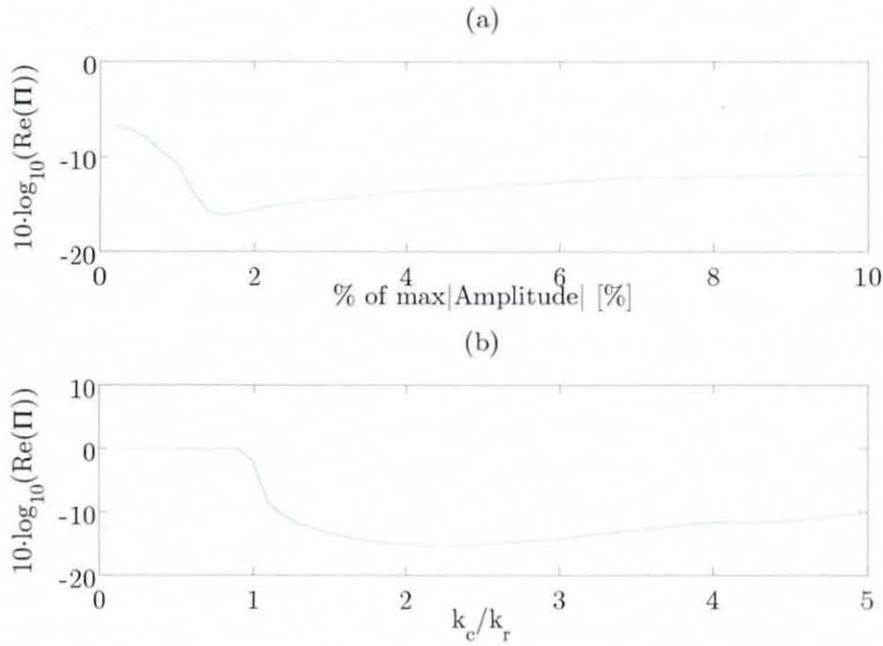


**Figure 11.12** Butterworth filtered and exact solution of the 3<sup>rd</sup> spatial derivative with respect to  $x$  of the displacement shown in Figure 11.10 at  $y = 0$ : (a) real part - VEFESPI, (b) imaginary part - VEFESPI, (c) real part - exact solution, (d) imaginary part - exact solution.

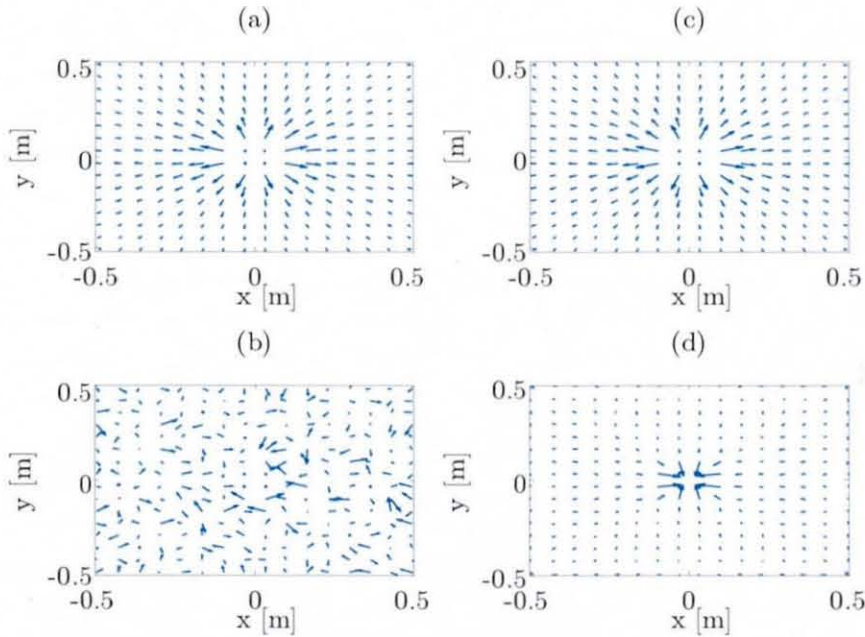
Figure 11.12 displays the comparison of the 3<sup>rd</sup> order spatial derivative. It can be realised from Figure 11.12 that, despite the filtering, a rather accurate spectral derivative result can be achieved.

Figure 11.13 displays the MSE made when filtering at different ascending cut-off points. It is clear from this that the ideal filter has an optimum filter cut-off point of about 2.4% of the maximum spectral amplitude modulus and the Butterworth filter produces best results at  $k_c = 2.2k_r$ . Note, these optimum cut-off points are determined for active energy flow only. Reactive filter cut-off points were determined by a trial and error process. Using the optimum filter cut-off points to determine active energy flow and the trial and error cut-off points to determine reactive energy flow, VEF is computed using the ideal filtered and Butterworth filtered infinite plate displacement.

From the active and reactive VEF maps for both types of filter, shown below in Figure 11.14, it can be clearly seen that the active VEF flow map



**Figure 11.13** Relative error of total transmitted energy flow of the infinite plate displacement shown in Figure 11.10: (a) active MSE ideal filter, (b) active MSE Butterworth filter.



**Figure 11.14** VEF maps of the infinite plate displacement shown in Figure 11.10: (a) active ideal filtered VEF, (b) reactive ideal filtered VEF, (c) active Butterworth filtered VEF, (d) reactive Butterworth filtered VEF.

displays a very accurate active energy flow pattern, very similar to the flow pattern shown in the analysis of the non-noise contaminated infinite plate. It can also be noticed from the Figures 11.14(b) and 11.14(d) that the reactive energy flow computation result is quite different when the ideal filter and Butterworth filter is employed. Here, the Butterworth filter seemed to produce a better result, due to the inclusion of more nearfield information at wavenumbers below the cut-off wavenumber.

To assess the accuracy of the active filtering process the active TTVE was computed from the filtered active VEF as described above by a square contour integration of  $\overline{P}_x$  and  $\overline{P}_y$ . This result is shown in Figure 11.15. It can be realised from Figure 11.15 that the oval 2D Butterworth filter produced a

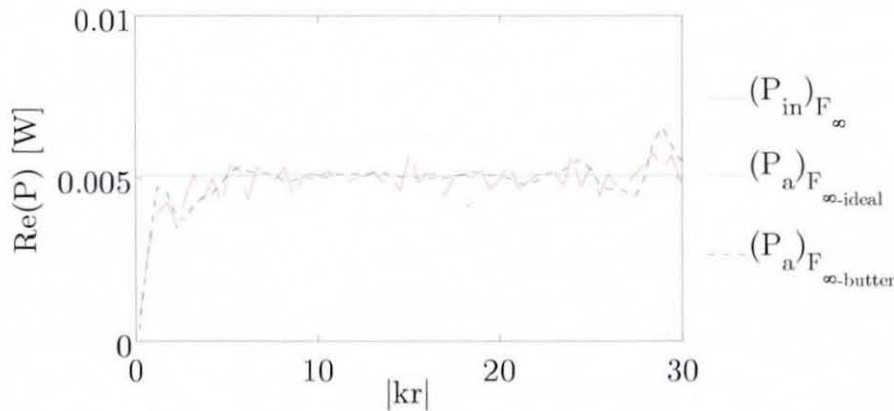


**Figure 11.15** Comparison of ideal filtered and Butterworth filtered total transmitted active vibrational energy and vibrational input power of the infinite plate displacement shown in Figure 11.10.

slightly better result than the ideal 2D filtering algorithm. However, both filter types can be employed in order to determine active VEF within an infinite plate.

### 11.2.3 Vibrational Energy Flow Including ESPI Noise

Within the experimental data analysis, it is desirable to compute VEF within the infinite plate from measured ESPI displacement data by the use of



optimum filter cut-off points. Thus, an optimisation process, by numerically evaluating equation (11.2), for a range of different ascending filter cut-off points is employed using extracted ESPI noise rather than synthetically generated and normally distributed noise. Extracted optical noise is used because it differs from normally distributed noise and, thus, it best approximates the measured displacement data. The optical noise was extracted from the measured ESPI displacement data simply by transforming the measured infinite plate displacement signal into the wavenumber domain by employing a 2D FFT. Within the wavenumber domain the travelling wave component was deleted. The spectral noise signal then back transformed is superimposed with a non-noise contaminated synthetically generated infinite plate displacement, using the measured force amplitude that was obtained during the ESPI experiment. Table 11.2 displays the vibration parameters of the infinite plate that were employed.

Excitation frequency	569.7 Hz	605.6 Hz	899.5 Hz	1194.4 Hz	1503.2 Hz
Excitation force	0.0529 N	0.0947 N	0.1802 N	0.2144 N	0.2099 N
SNR	89.5	92.9	79.1	96.6	75.1

**Table 11.2** Vibrational parameters of “infinite” plate.

Figure 11.16 shows the contaminated infinite plate displacement that was contaminated by optical noise, at an excitation frequency of  $f_0 = 1503.2$  Hz as well as the extracted ESPI noise. The displacement was generated within the same signal window as used when computing VEF from measured ESPI displacement data. It can be seen that approximately 2 wavelengths are included within the displacement signal. The complex, infinite plate displacement, as shown in Figures 11.16(a)-(b), is used as an input to the VEFESPI computation method. Optimised filter cut-off points of the ideal and Butterworth filtering process are then determined by computing VEF for a range of ascending filter cut-off points. The number of filter cut-off points used here was 50.

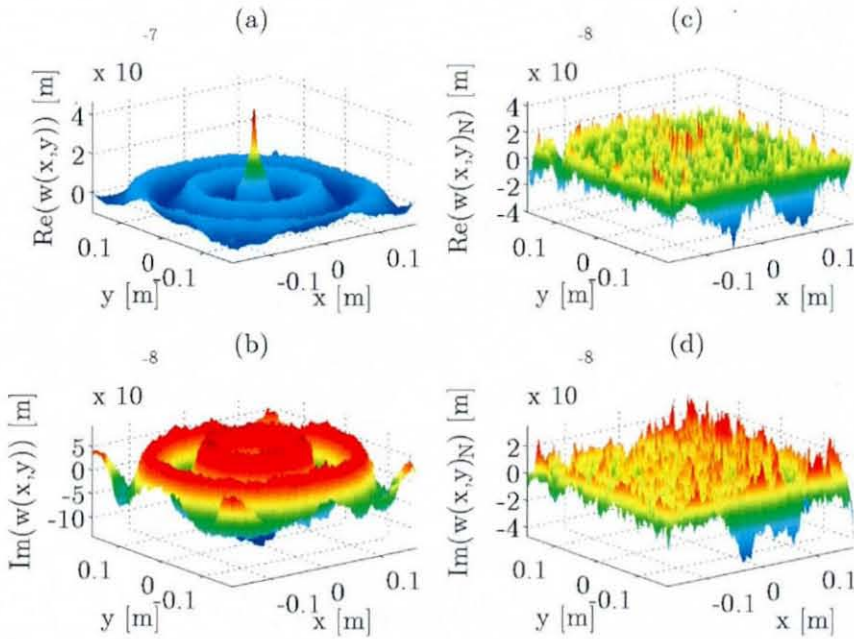


**Figure 11.16** Noise contaminated infinite plate displacement and extracted ESPI noise at 1503.2 Hz: (a) 2D real displacement part, (b) 2D imaginary displacement part, (c) 2D real noise part, (d) 2D imaginary noise part.

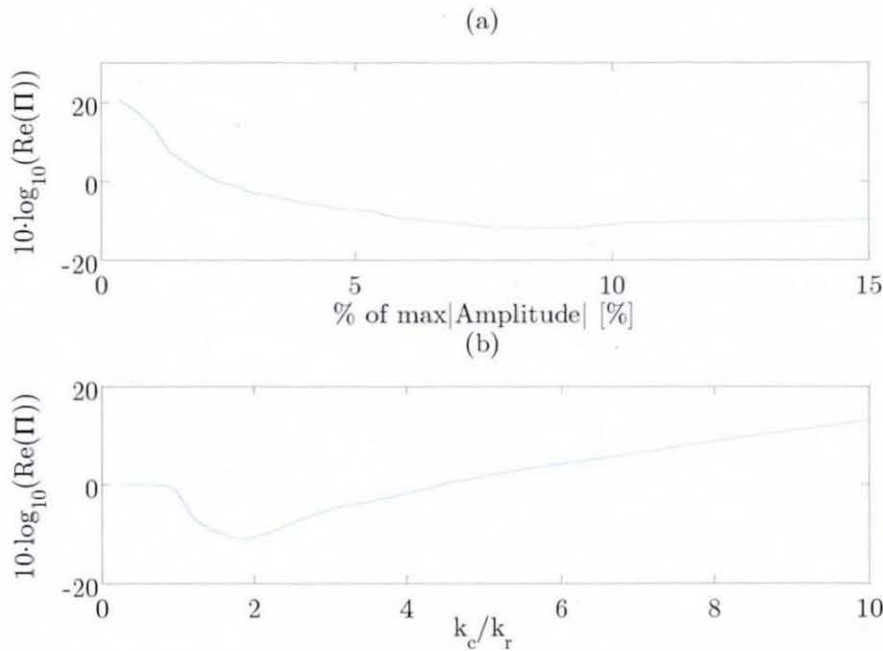


**Figure 11.17** Relative active error of total transmitted energy flow of the infinite plate displacement shown in Figure 11.16: (a) active MSE ideal filter, (b) active MSE Butterworth filter.



Figure 11.17 displays the MSE obtained at 50 different filter cut-off points of the 1503.2 Hz excited infinite plate displacement. It can be noticed from that figure that the optimum cut-off point for the ideal filter is about 7.7% of the modulus of maximum spectral displacement amplitude. The optimum spatial cut-off wavenumber of the Butterworth filter is about  $k_c = 2k_r$ . The optimum cut-off points when filtering the infinite plate displacement are slightly higher than the determined infinite beam cut-off points.

Figure 11.18 displays the computed VEF map by employing the optimum ideal filtered and Butterworth filtered cut-off points. Clearly, the

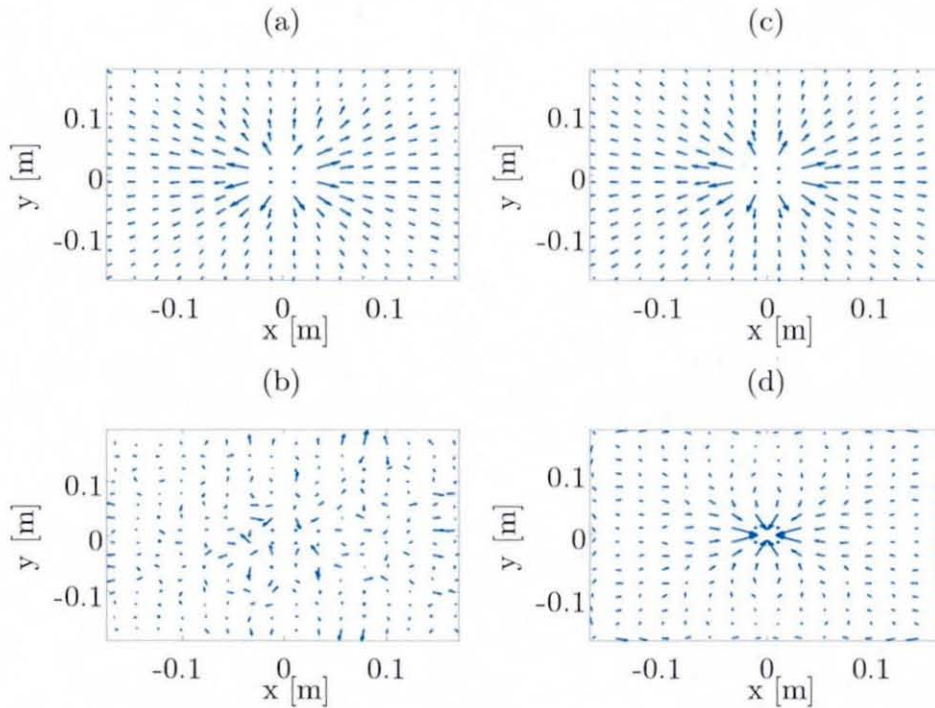


**Figure 11.18** VEF maps of the infinite plate displacement shown in Figure 11.16: (a) active ideal filtered VEF, (b) reactive ideal filtered VEF, (c) active Butterworth filtered VEF, (d) reactive Butterworth filtered VEF.

radially spreading active energy flow can be seen.

Figure 11.19 displays the comparison between the energy injected into the plate (VIP) and the TTVE computed from the square contour integration of  $\overline{P_x}$  and  $\overline{P_y}$ . The optimised filter cut-off points were employed. Figure 11.19 clearly shows that, at low  $|kr|$ , large deviations between input

power and total transmitted energy, as expected, are present. Also, at larger locations of  $|kr|$  some deviations between VIP and TTVE can be seen. It seems that the extracted optical noise caused more errors when computing VEF than the VEF computation with normally distributed noise. In contrast

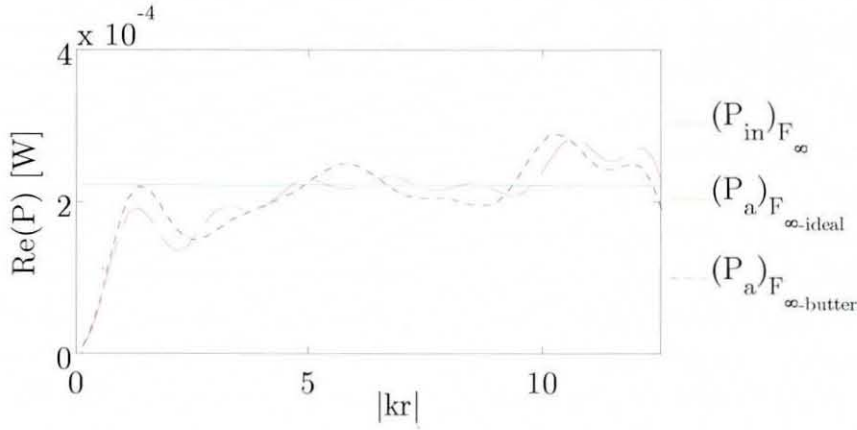


**Figure 11.19** Comparison of ideal filtered and Butterworth filtered total transmitted active vibrational energy and vibrational input power of the infinite plate displacement shown in Figure 11.16.

to the result obtained in the previous section, here, a reduced difference between ideal filtered and Butterworth filtered energy flow results was obtained.

Table 11.3 displays the optimum filter cut-off points for the ideal filter and Butterworth filter as well as the MSE that can be expected. It can be noticed from the displayed active MSE that the ideal filter worked as well as the Butterworth filter.

Excitation frequency $f_0$ [Hz]	569.7	605.6	899.5	1194.4	1503.2
Optimum (% of $ W(k_x, k_y) _{\max}$ ) [%]	13.33	12.33	8.0	8.0	8.67
Active MSE, $\Re(10 \cdot \log_{10}(\mathcal{I})_{\text{ideal}})$	-9.4	-10.2	-10.6	-11.0	-11.9
Optimum $(k_c)_{\text{real}}$ [rad/m]	1.9132	2.1568	1.8963	1.9352	1.9219
Active MSE, $\Re(10 \cdot \log_{10}(\mathcal{I})_{\text{butter}})$	-8.3	-8.6	-10.0	-10.9	-11.0

**Table 11.3** Optimum “infinite” plate cut-off points of square truncated data.

### 11.3 Numerical Simply Supported Plate Analysis

The aim of this section is to investigate the numerical application of the VEFESPI method when applied to simply supported plate structures. The transition from infinite plate structures to finite plate structures was made to study the ability of the VEFESPI method when computing VEF within two-dimensional high standing wave environments.

This is based on the assumption that the boundaries of the simply supported plate are non-dissipative. Analogously to the infinite plate section, effects of signal irregularities and noise contamination are studied and measures to increase VEF computation accuracy are introduced. Furthermore, a sensitivity and error analysis is carried out when computing VEF from noise contaminated simply supported beam displacements.

#### 11.3.1 Vibrational Energy Flow Excluding Noise

Within this work the simply supported plate displacement is defined by using a particular solution of the eigenfunction expansion theorem. From this modal definition of the forced, complex, simply supported plate displacement, VIP and VEF expressions are derived. In each solution hysteretic damping is incorporated using the hysteretic loss factor  $\eta$ .

Within this section the effects of numerical computation of VEF as well as the effects of a non-periodic plate displacement input are investigated. As carried out previously, numerically computed VEF is compared to exact solutions presented in section 10.3. Deviation to the exact VEF solution can be expected due to the wavenumber multiplication process in the spectral domain, especially at high wavenumbers, when employing the KSD method in order to compute spectral derivatives. This undesired effect occurs especially if nearfield components are present. Unfortunately, this effect is amplified even further, if a non-periodic plate displacement is used as an input to the VEFESPI method. The resulting spectral leakage will then be amplified.



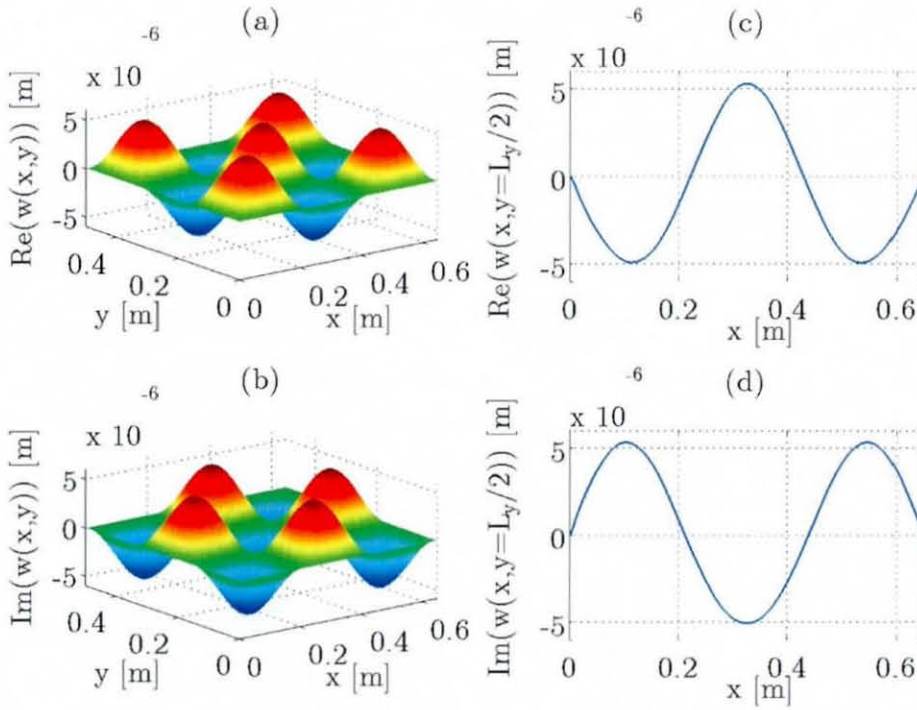
During the ESPI experiment reported in chapter 14, the simply supported plate was excited at the middle of the plate, e.g.  $L_x/2$  and  $L_y/2$  in order to reduce the number of modes at which the plate can be excited. Thus, only odd-numbered mode shape plate displacements were recorded. However, an odd-numbered mode shape displacement is non-periodic in space by half a wavelength. Hence, the effects of computing VEF from odd-numbered mode shape displacements are investigated here. It can be realised that the Fourier transform of an even-numbered mode shape displacement will produce no spectral leakage. Its VEF computation is then less critical, yielding to almost no VEF oscillations. Hence, the computation of VEF from even-numbered mode shape displacements is omitted here. It has been shown in section 6.3 that problems in the VEF computation occurred only when analysing odd-numbered mode shape displacements. This behaviour also holds true for two-dimensional plate structures.

Table 11.4 displays the material properties of the experimental simply supported plate employed during the ESPI experiment. All routines used here were written within the software environment MATLAB<sup>®</sup>.

Young's modulus	$E = 2.07 \cdot 10^{11} \text{ N/m}^2$
mass density	$\rho = 7.85 \cdot 10^3 \text{ kg/m}^3$
plate thickness	$h = 3 \cdot 10^{-3} \text{ m}$
plate length	$L_x = 0.646 \text{ m}$
plate width	$L_y = 0.496 \text{ m}$
Poisson ratio	$\nu = 0.33$

**Table 11.4** Simply supported plate properties.

Figure 11.20 displays the displacement of a simply supported plate generated by numerically evaluating equation (10.25). Here, a unity excitation force of  $F_0 = 1 \text{ N}$  was employed. The plate was excited in the middle at  $L_x/2$  and  $L_y/2$  by an excitation frequency of  $f_0 = 429.2 \text{ Hz}$ . The number of data points used here was  $N_x = 64$  and  $N_y = 64$ . The hysteretic



**Figure 11.20** Complex simply supported plate displacement: (a) 2D real part, (b) 2D imaginary part, (c) real part at  $y = L_y/2$ , (d) imaginary part at  $y = L_y/2$ .

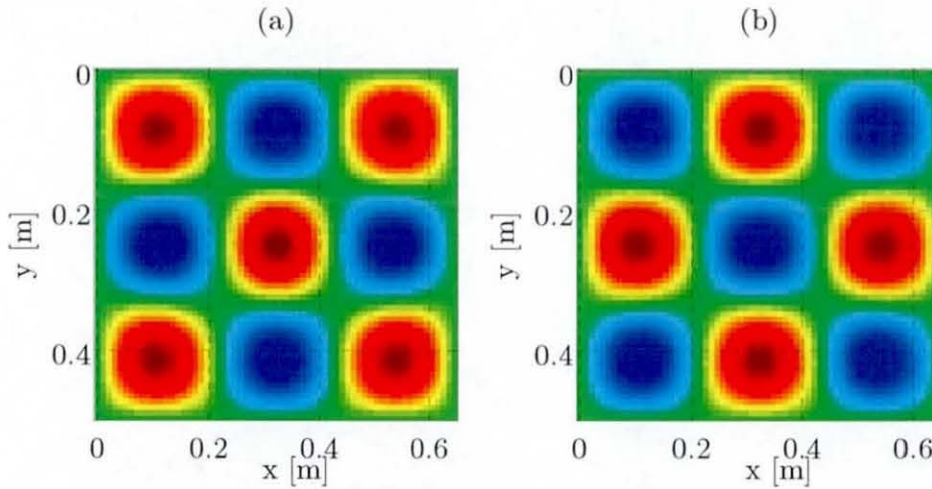


**Figure 11.21** Top view image of the complex simply supported plate displacement shown in Figure 11.20: (a) real part, (b) imaginary part.

loss factor employed was  $\eta = 10^{-2}$ . For the numerical computation of VEF by



using the equations presented in section 10.3, only 11 modes within the modal summation were considered.

Figure 11.21 displays the top view image of the simply supported beam displacement shown in Figure 11.20. It can be seen from both figures that the excitation frequency coincided with the undamped natural frequency of the mode (3,3). By the mode notation,  $(m,n)$ ,  $m/2$  wavelengths in the  $x$  direction and  $n/2$  wavelengths in the  $y$  direction occur. It can also be realised that a non-periodic number of wavelengths are included in the displacement signal. Hence, leakage will occur and spectral amplification within the wavenumber domain can be expected, when computing spectral derivatives using the KSD method.

Figure 11.22 displays the modulus of the wavenumber spectrum of the plate displacement shown in Figure 11.20 computed by employing a 2D FFT. It can be seen from this figure that four spikes occur within the wavenumber domain that can be interpreted as four travelling waves travelling away from

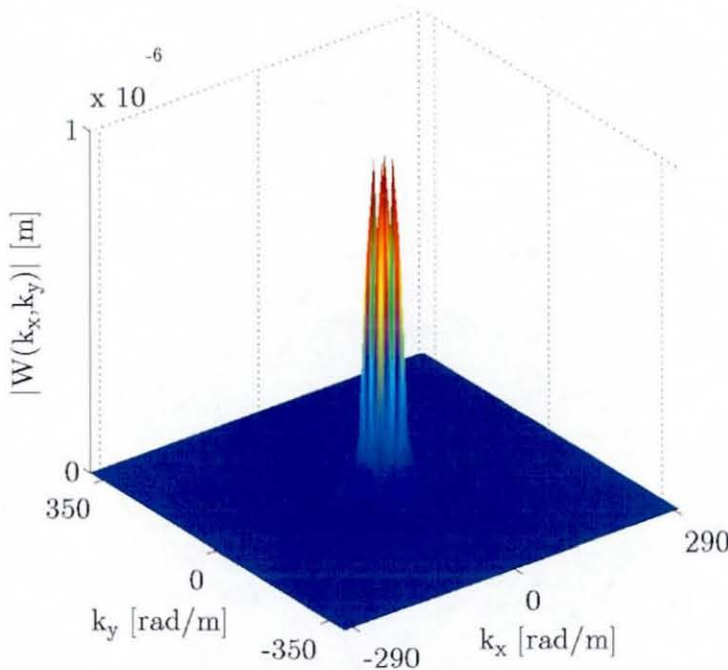


**Figure 11.22** Modulus of the 2D FFT spectrum of the complex simply supported plate displacement shown in Figure 11.20.

the excitation location at 90 degrees separation. Thus, the simply supported plate displacement may also be approximated by a plane-wave model that uses four travelling plane waves, which travel at  $\pm 45$  degrees away from the excitation location [4].

Figure 11.23 displays the modulus of the 3<sup>rd</sup> spectral derivative of the spectral displacement  $\partial^3 W(k_x, k_y) / \partial k_x^3$  computed by the KSD method and the exact solution by analytically differentiating equation (10.25). Clearly, the effect of spectral amplification, especially at high wavenumbers, can be

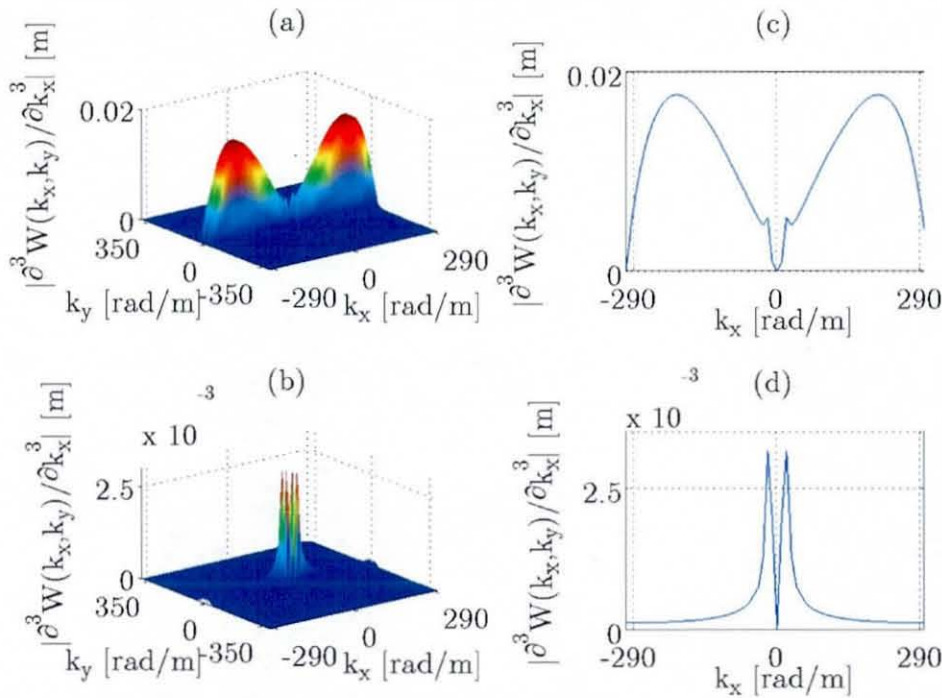


**Figure 11.23** VEFESPI determined and exact solution of the 3<sup>rd</sup> spectral derivative with respect to  $k_x$  of the displacement shown in Figure 11.20: (a) 2D modulus - VEFESPI, (b) 2D modulus - exact solution, (c) 1D modulus at  $k_y = 0$  - VEFESPI, (d) 1D modulus at  $k_y = 0$  - exact solution.

seen. If one employs an inverse 2D FFT, it can be realised that the spatial derivatives will also deviate from the exact solution.

Figure 11.24 displays the 3<sup>rd</sup> order spatial derivative  $\partial^3 w(x, y) / \partial x^3$  at  $y = 0$ , obtained by the VEFESPI method and the exact analytical solution. It can be seen from Figure 11.24 that oscillations due to the spectral

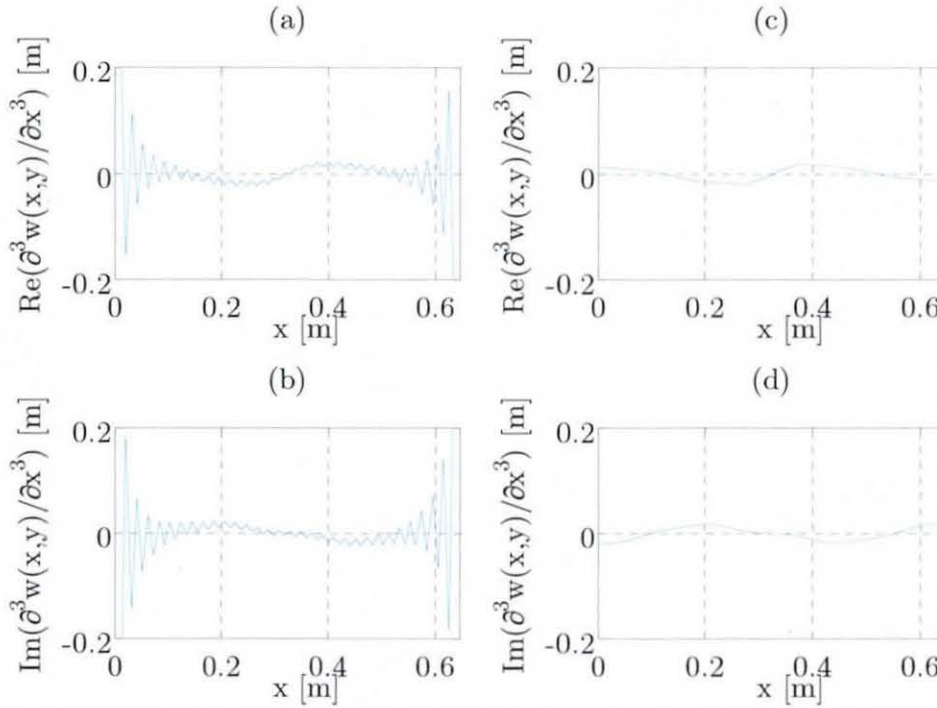


**Figure 11.24** VEFESPI determined and exact solution of the 3<sup>rd</sup> spatial derivative of the displacement shown in Figure 11.20 at  $y = 0$ : (a) real part - VEFESPI, (b) imaginary part - VEFESPI, (c) real part - exact solution, (d) imaginary part - exact solution.

alteration within the wavenumber domain occur as previously shown in chapter 6. However, here the problem is of a two-dimensional nature. It can be realised that the plate displacement needs to be periodised by employing the mirror-processing (MP) technique or the mirror-reverse-shear (MRS) technique. Alternatively, oscillations within the computed VEF  $\overline{P}_x$  and  $\overline{P}_y$  may be diminished by employing the curve-wrapping (CW) technique. As shown previously, all three methods led to a more accurate result when analysing VEF in a beam.

Figure 11.25 displays the time-averaged active and reactive energy flow within the simply supported plate in the  $x$  and  $y$  directions computed from the exact solution. It can be noticed that the active VEF in the  $x$  and  $y$  directions differs from each other due to the use of a rectangular plate. The use of a square plate in combination with centre excitation would produce an



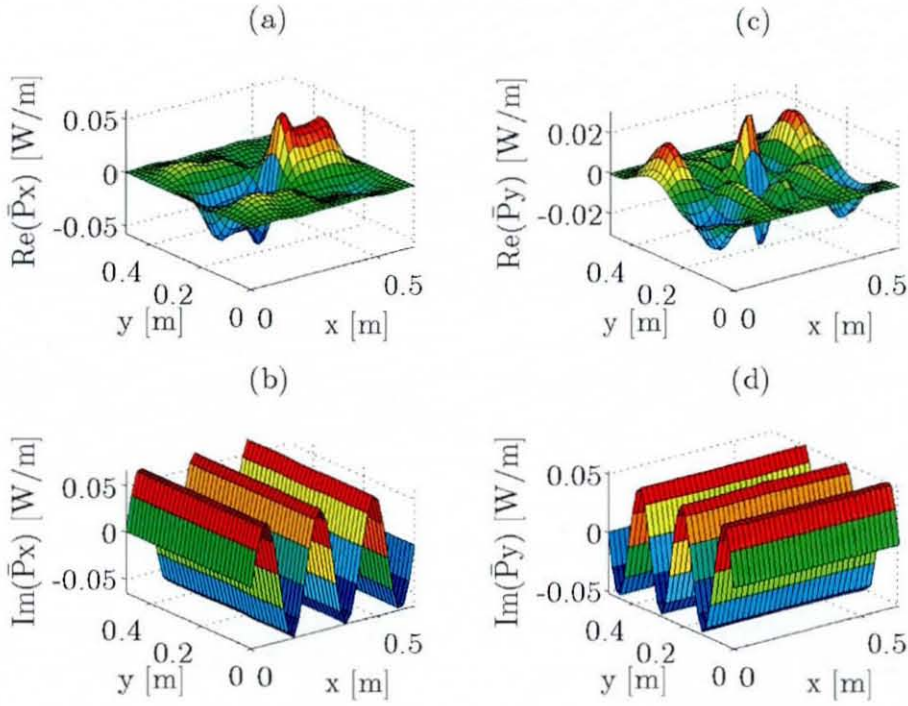


**Figure 11.25** Computed VEF in  $x$  and  $y$  direction of the simply supported plate displacement shown in Figure 11.20 from analytical data: (a) active VEF in  $x$  direction, (b) reactive VEF in  $x$  direction, (c) active VEF in  $y$  direction, (d) reactive VEF in  $y$  direction.

equal active energy flow in the  $x$  and  $y$  directions. Interestingly, the reactive energy shows the modal behaviour of the plate. Note, for better visibility the number of data points was reduced to  $N_x = N_y = 32$ .

As evident from Figure 11.24 undesired oscillations in VEF computation need to be reduced. This is accomplished here by periodising the non-periodic plate displacement prior to the spatial derivative computation using the MP and MRS technique, respectively. Further, the CW technique was also applied. Figures 11.26 (a)-(b) show the exact active and reactive VEF maps determined by numerically evaluating equation (10.28) and (10.29), respectively. For comparison purposes, computed VEF using the VEFESPI method in combination with the CW technique is shown in Figures 10.26 (c)-(d). It can be seen from these VEF maps that the VEFESPI + CW computed active VEF coincides well with the exact active VEF. It can also

be seen that the active vibrational energy flows mainly in the  $x$  direction away from excitation location by creating four flow vortices towards the

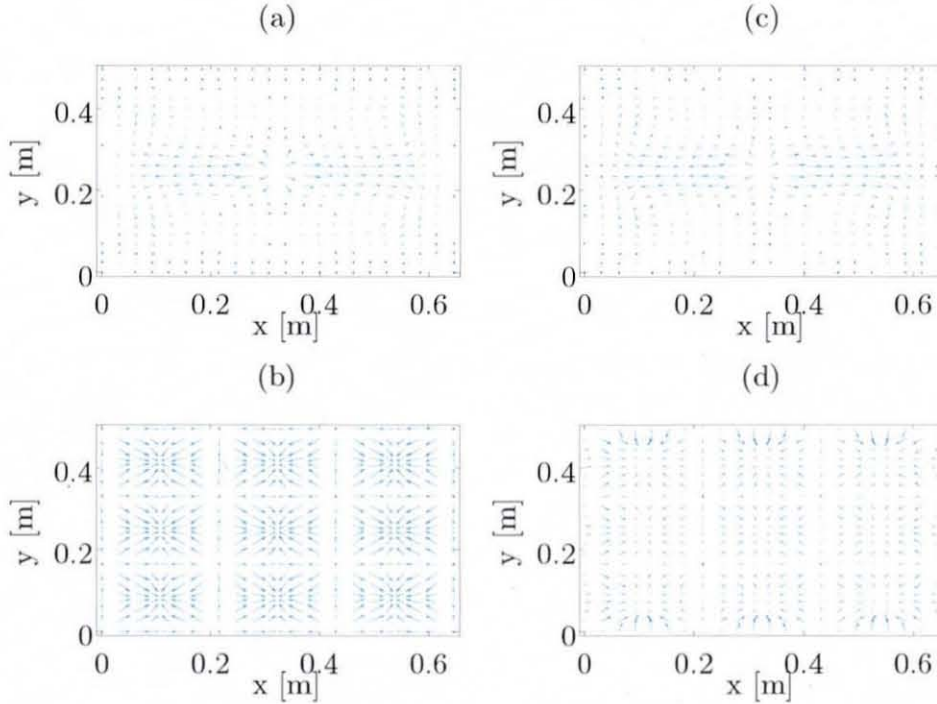


**Figure 11.26** VEF maps of the simply supported plate displacement shown in Figure 11.20: (a) exact active VEF, (b) exact reactive VEF, (c) active VEF - VEFESPI + CW, (d) reactive VEF - VEFESPI + CW.

plate's corners. Interestingly, the reactive energy flow map shows reactive energy nodal lines, which allows for mode identification. At the position of the peaks of the modal amplitudes the reactive energy is flowing towards the respective amplitude peaks creating something like energy sinks. It can also be seen that the reactive VEF oscillations could not be entirely diminished at the plate's boundaries and, hence, some deviations in the reactive energy flow computation from the VEFESPI + CW method occur. Note, for better visibility the number of data points was reduced to  $N_x = N_y = 22$ . In addition, two points were deleted in Figures 11.26(c) and 11.26(d) due to large VEF deviation at the boundaries.

Figure 11.27 displays the VEF maps computed from the periodised simply supported plate displacement using the MP and MRS periodisation



technique. It can be seen from Figure 11.27 that the reactive energy flow in particular better matches the exact solution. However, all three VEF

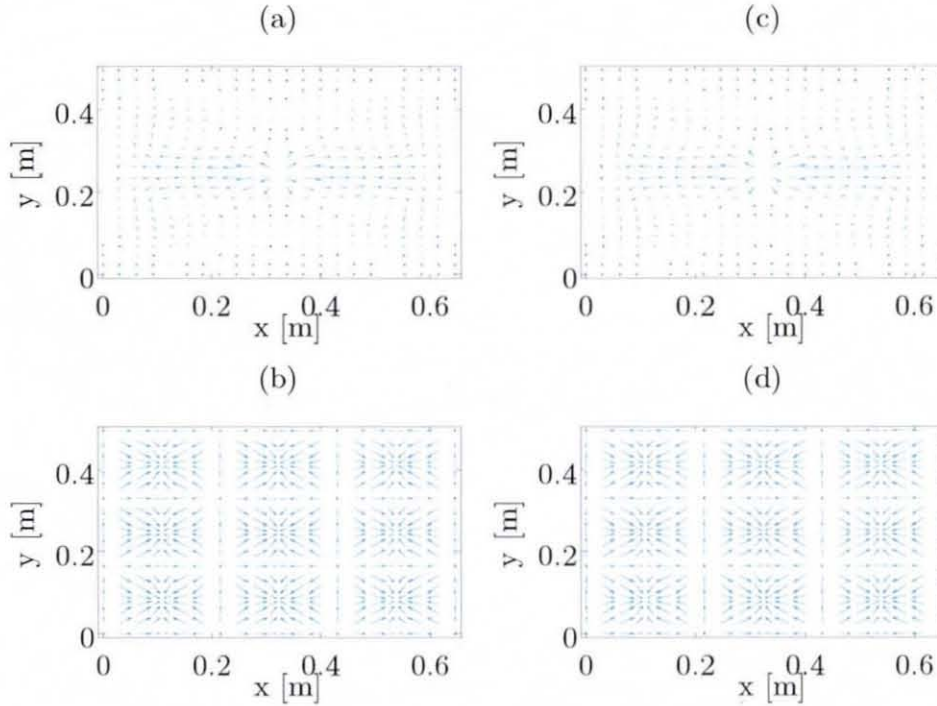


**Figure 11.27** VEF maps of the simply supported plate displacement shown in Figure 11.20: (a) active VEF - VEFESPI + MP, (b) reactive VEF - VEFESPI + MP, (c) active VEF - VEFESPI + MRS, (d) reactive VEF - VEFESPI + MRS.

oscillation reduction approaches produced a good match between exact active VEF and computed active VEF, as evident from Figures 11.26 and 11.27.

In section 11.2.1 a contour integration of the two-dimensional energy fields  $\overline{P}_x$  and  $\overline{P}_y$  was employed to determine the accuracy of the VEFESPI method when using the CW technique in order to reduce the effects of spectral amplification and, thus, VEF oscillations. The result of such a closed contour integration at each position  $|kr|$  was then compared to input power, since the energy outflow of each closed contour within the infinite plate was constant and equal to the energy injected into the structure. Thus, the initial two-dimensional error distribution problems, which had to be determined for both vector fields  $\overline{P}_x$  and  $\overline{P}_y$  were reduced to a one-dimensional problem due

to the inclusion of both energy fields in the contour integration process. Within this section a similar approach will be employed in order to reduce the computational effort when assessing the error made by the numerical computation of VEF in simply supported plates.

To assess the deviation between exact VEF and VEFESPI computed energy flow, the total flow of vibrational energy (TTVE) across perpendicular lines parallel to the plate's edges will be employed. The TTVE in the  $x$  direction across a perpendicular line is given by:

$$\phi_x = \int_0^{L_y} \overline{P}_x dy. \quad (11.3)$$

Note, the TTVE in the  $y$  direction across a perpendicular line can be found simply by interchanging  $x$  and  $y$ . Using equation (11.3), the relative error of TTVE in percent in the  $x$  direction is defined as:

$$\Delta\varepsilon_x = \left( 1 - \frac{(\phi_x)_{VEFESPI}}{(\phi_x)_{exact}} \right) \cdot 100\%. \quad (11.4)$$

The complex relative error of TTVE in the  $y$  direction can also be found here by substituting the variable  $y$  for  $x$ . Within this work the crossing of TTVE at perpendicular lines in the  $x$  and  $y$  directions is computed at each line along the plate width and plate length, respectively. Thus, employing an initial number of points of  $N_x = N_y = 64$ , 64 numerical integrations were carried out within the two-dimensional energy fields  $\overline{P}_x$  and  $\overline{P}_y$ .

The result of evaluating equations (11.3) and (11.4) for each perpendicular line is shown in Figures 11.28 and 11.29, respectively. Note, the units of the 2D energy flow fields  $\overline{P}_x$  and  $\overline{P}_y$  of the simply supported plate are in W/m. Integrating along a line perpendicular to the flow direction will yield to TTVE in units of Watts at that particular line position. It can be seen from Figures 11.28 and 11.29 that the curve shape of the total active transmitted energy  $\phi_x$  and  $\phi_y$  is fairly similar to the curve shape of active

VEF within a simply supported beam, as shown for instance in Figure 5.8, with a maximum energy transmission at the excitation location (here  $x_0 = 0.323$  m) and zero energy transmission at the non-dissipative boundaries. Interestingly, the reactive TTVE is varying sinusoidally along the plate width

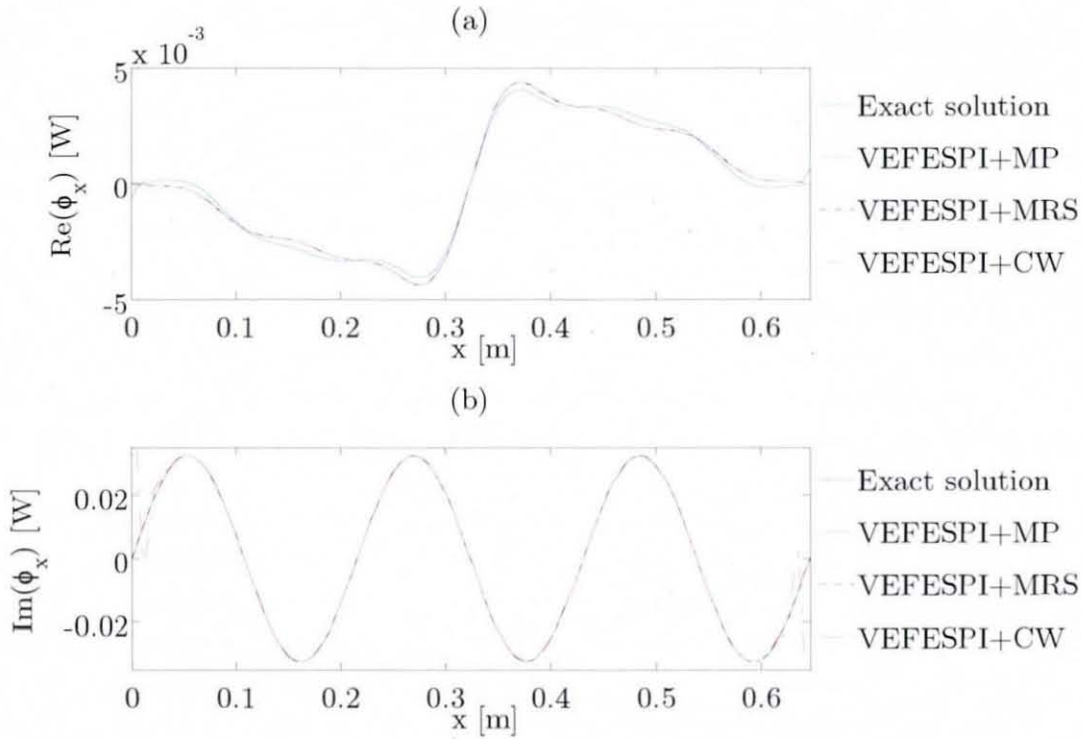


**Figure 11.28** Total transmitted vibrational energy  $\phi_x$  of the simply supported plate displacement shown in Figure 11.20: (a) active  $\phi_x$ , (b) reactive  $\phi_x$ .

and length, respectively, reflecting the modal behaviour of the structure. It can also be seen from Figures 11.28 and 11.29 that the VEFESPI method in combination with the MP, MRS, and CW technique produced good results when reducing VEF oscillations by these techniques. However, it can be noticed that the VEFESPI method in combination with the CW technique deviated at the boundaries compared to the exact solution. An energy balance according to equation (3.61) resulted in a very low relative error of  $-0.03\%$ . This relative error was determined between the theoretically computed VIP using equation (10.27) and the surface integrated potential



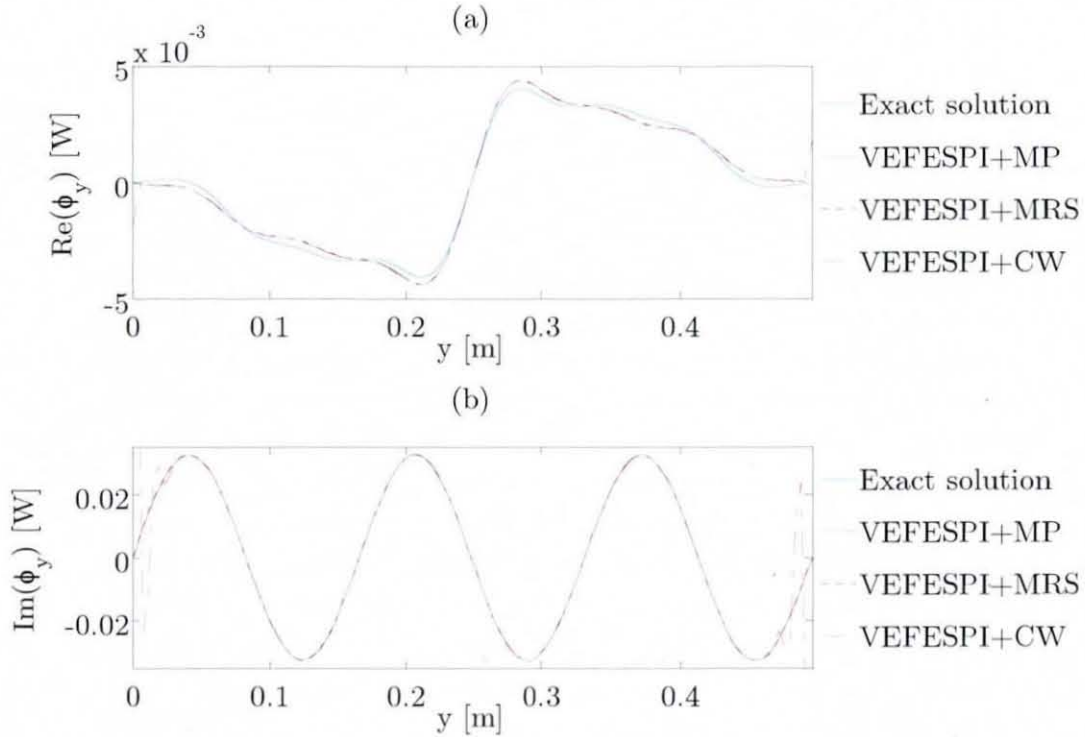


**Figure 11.29** Total transmitted vibrational energy  $\phi_y$  of the simply supported plate displacement shown in Figure 11.20: (a) active  $\phi_y$ , (b) reactive  $\phi_y$ .

energy density using the right-hand side of equation (3.61).

Figures 11.30 and 11.31 display the complex relative error made when computing VEF from an odd-numbered mode shape simply supported plate displacement by numerically evaluating equation (11.4). It can be realised that the resulting errors are very small. The computation of reactive energy flow is much more accurate than the computation of the active energy flow within a simply supported plate, something that did not occur at the simply supported beam analysis. However, there are some discontinuities in the relative active error curve shape. These discontinuities close to the boundaries are due to zero crossing of the exact TTVE value and, hence, zero division in equation (11.4). Thus, it has been shown that VEF oscillations, occurring during the VEF computation of odd-numbered mode shape displacements of simply supported plates, can be reduced by using the MP, MRS, and CW technique.

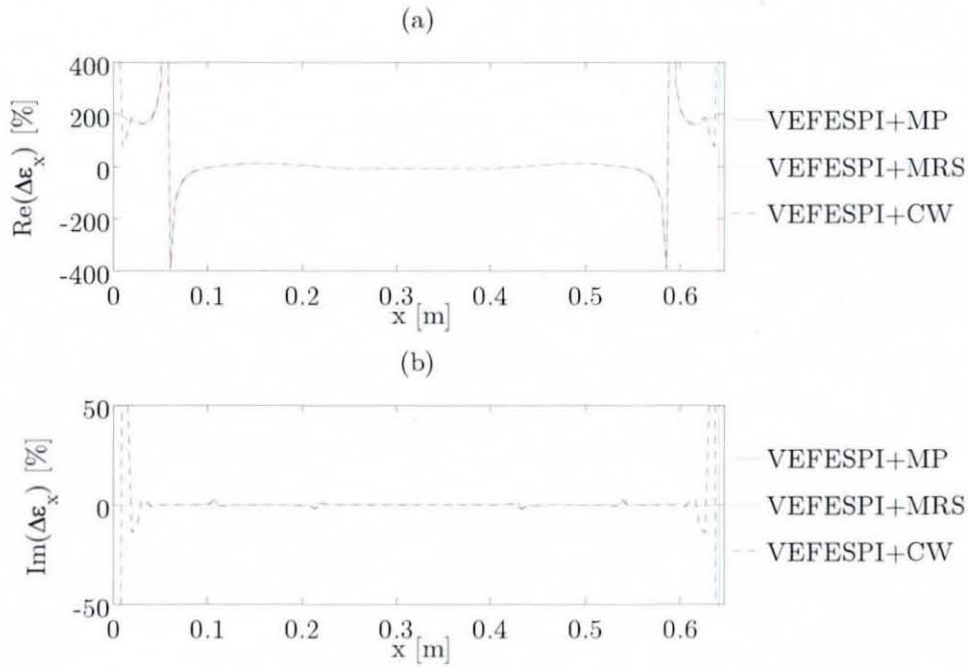


**Figure 11.30** Relative error  $\Delta\epsilon_x$  of the simply supported plate displacement shown in Figure 11.20: (a) relative active flow error, (b) relative reactive flow error.

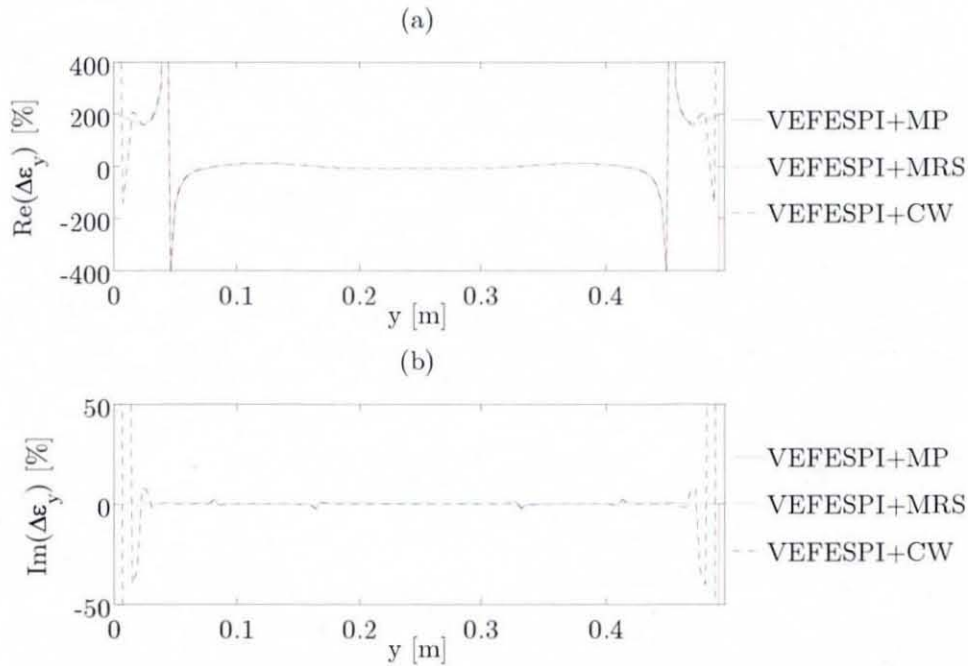


**Figure 11.31** Relative error  $\Delta\epsilon_y$  of the simply supported plate displacement shown in Figure 11.20: (a) relative active flow error, (b) relative reactive flow error.



### 11.3.2 Vibrational Energy Flow Including Noise

The aim of this section is to investigate the effect of spectral filtering when VEF is computed from noise contaminated, flexural, simply supported plate displacements. Thus, an artificially generated plate displacement is superimposed with normally distributed noise. As usual, filtered VEF is determined by using two types of filters, the ideal 2D filter and the oval 2D Butterworth filter. Only odd-numbered mode shapes are investigated, since even-numbered mode shapes were not measured during the ESPI experiment and they resulted in lesser VEF computation problems, as shown in chapter 6.

#### 11.3.2.1 Ideal 2D Spectral Filtering

As demonstrated in section 6.3.2, numerical computation of VEF from noise contaminated displacements of vibrating finite structures caused a decrease in VEF computation accuracy. It can be seen from Figure 11.20(c) that due to the employment of hysteretic damping, the plate's amplitude decreased with increasing distance from the excitation location. The amount of amplitude reduction also depends on the loss factor  $\eta$ , i.e. an increase in loss factor (structural damping) results in an increase in amplitude reduction and vice versa. VEF within a finite structure can be computed only if damping is included, since within a pure standing wave environment a zero net energy flow is present. Thus, the amount of damping controls the amount of vibrational energy to be dissipated or transmitted within the volume of interest. In a simply supported structure, the transmitted energy is greatest at the excitation location and zero at the non-dissipative boundaries. The reverse effect is obtained from the dissipated vibrational energy. Thus, one can build a hypothetical model relating the VEF within finite structures to decaying travelling waves, which cause a decaying energy flow within the structure. It can be realised that these notional decaying waves are very small compared to the total standing wave displacement. If the total displacement signal is contaminated by noise, then the ratio of the noise floor

to the amplitude of the notional decaying waves is crucial to the accuracy of the VEF computation within a finite structure. If the level of noise within the displacement signal is the same or even higher than the amplitude of the decaying travelling waves, VEF within a finite structure cannot be computed. VEF computation is only feasible, if the amount of noise is less than the decaying wave amplitude.

For this reason, numerical VEF computation from noise contaminated simply supported plate displacements will be shown here at two different levels of damping and noise. Different levels of damping are represented herein by different loss factors, and different levels of noise are represented by different SNR's. Thus, VEF is computed at loss factors of  $\eta = 10^{-3}$  and  $\eta = 10^{-2}$  for a simply supported plate, which is excited centrally by a unity force at an excitation frequency of  $f_0 = 714$  Hz, which is then equal to the undamped natural frequency of the  $(m = 5, n = 3)$  mode. The two hysteretic loss factors represent the boundaries of damping to be expected during the simply supported plate experiment. Figure 11.32 displays the plate displacement at  $\eta = 10^{-3}$  with an SNR of 119. Also here, the SNR is determined from the two-dimensional integration of the signal power and noise power matrix. It can be seen that the signal is very noisy, whereas an amplitude reduction is hardly noticeable. Figure 11.33 displays the top view image of the displacement shown in Figure 11.32. Also there, the noise contamination is clearly visible.

Analogously to the filtering procedures demonstrated previously, an error assessment function is employed herein using the relative MSE of the total flow of vibrational energy across perpendicular lines parallel to the plate's edges. The relative MSE is determined from the VEFESPI computed TTVE and from the exact computed TTVE in the  $x$  and  $y$  directions. Using equation (11.3), the relative MSE  $\Pi_x$  in the  $x$  direction is given by:

$$\Pi_x = \frac{1}{N_x} \sum_{i=1}^{N_x} \left( 1 - \frac{(\phi_{x_i})_{VEFESPI}}{(\phi_{x_i})_{exact}} \right)^2. \quad (11.5)$$

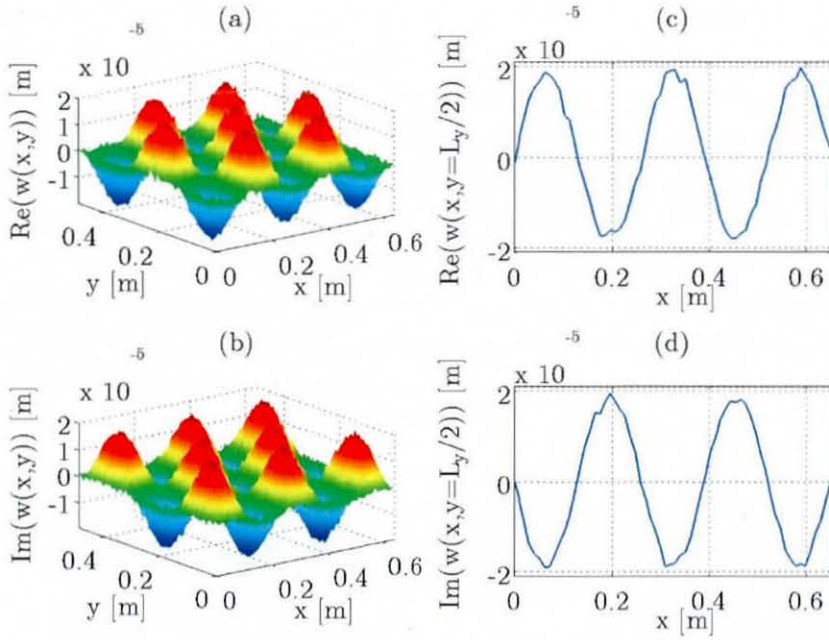


**Figure 11.32** Noise contaminated simply supported plate displacement: (a) 2D real part, (b) 2D imaginary part, (c) real part at  $y = L_y/2$ , (d) imaginary part at  $y = L_y/2$ , ( $\eta = 10^{-3}$ ).

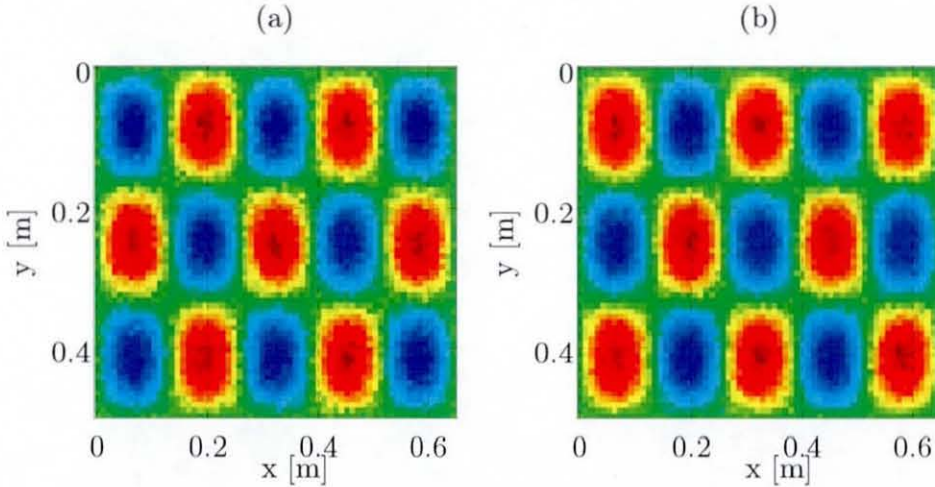


**Figure 11.33** Top view image of the complex simply supported plate displacement shown in Figure 11.32: (a) real part, (b) imaginary part, ( $\eta = 10^{-3}$ ).



Note, the relative MSE  $\Pi_y$  obtained from the total flow of vibrational energy across lines perpendicular to the  $x$ -axis can be found simply by interchanging the spatial variable  $x$  by  $y$ .

Figure 11.34 displays the relative MSE made when computing ideal filtered TTVE from the simply supported plate displacement, shown in

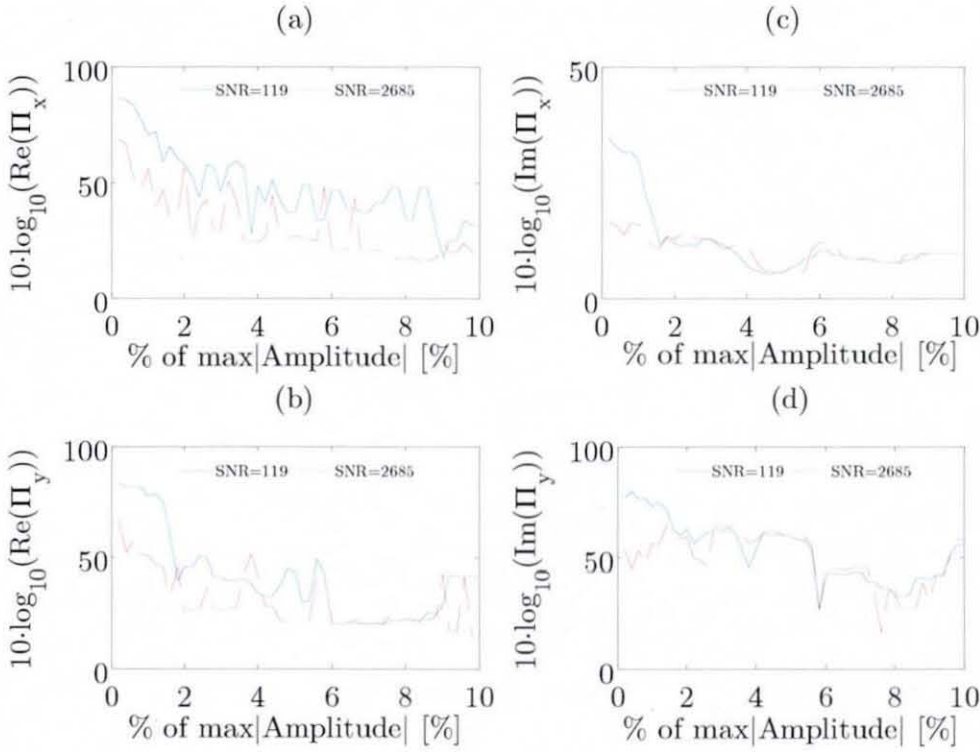


**Figure 11.34** Relative MSE of ideal filtered TTVE of the plate displacement shown in Figure 11.32: (a) active MSE in  $x$  direction, (b) active MSE in  $y$  direction, (c) reactive MSE in  $x$  direction, (d) reactive MSE in  $y$  direction, ( $\eta = 10^{-3}$ ).

Figure 11.32, at different filter cut-off points and different SNR's. It can be deduced that with a decreasing level of noise the active relative MSE decreases, whereas the reactive MSE stays approximately constant. It can also be realised that the computation accuracy of active VEF in finite structures strongly relies on the product of damping and noise, i.e.  $\eta \times \text{SNR}$ .

Figure 11.35 displays the optimum ideal filtered TTVE in the  $x$  direction. Note, the ideal filtered TTVE  $\phi_y$  (not shown) displays a similar curve shape however, with a lower MSE, as expected from Figure 11.34(b).

For reasons of brevity, this figure is excluded here. It can be seen from Figure 11.35 that at  $\eta \times \text{SNR} \approx 0.12$  large deviations between the active ideal filtered and the exact active TTVE are obtained, whereas at  $\eta \times \text{SNR} \approx 2.7$  a much better match between both quantities was realised. It is quite clear that the higher the product of  $\eta \times \text{SNR}$  the better the accuracy of the active

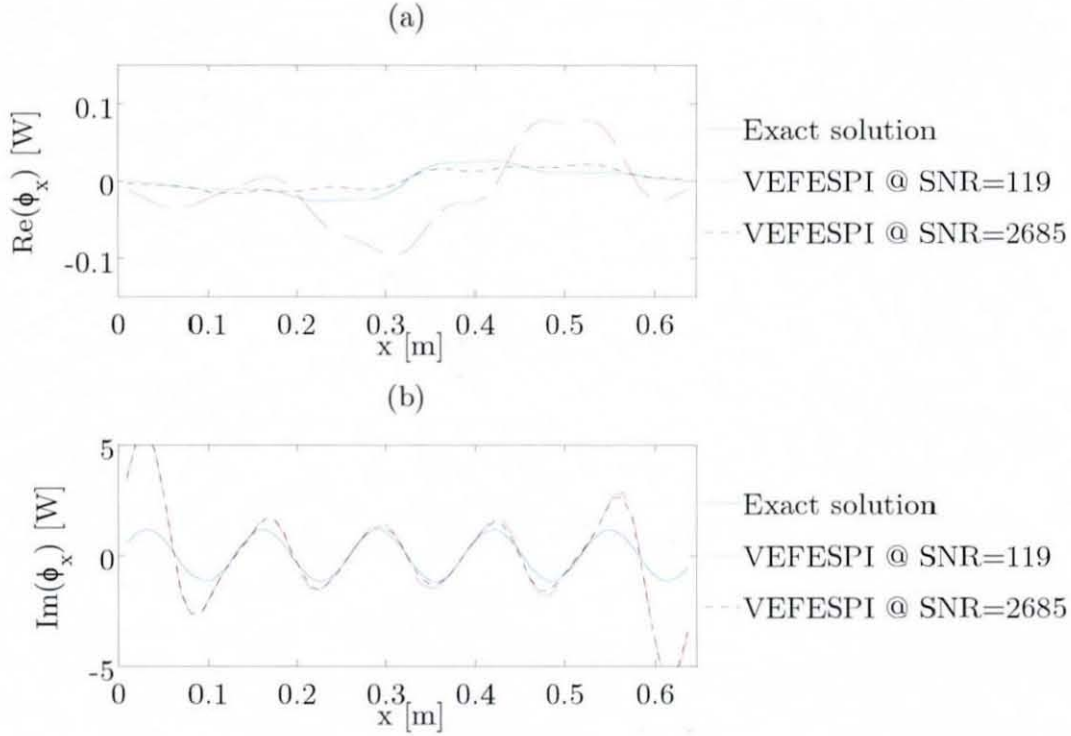


**Figure 11.35** Exact and ideal filtered total transmitted vibrational energy of the simply supported plate displacement shown in Figure 11.32: (a) active  $\phi_x$ , (b) reactive  $\phi_x$  ( $\eta = 10^{-3}$ ).

VEF computation. Interestingly, the computation of the reactive TTVE did not depend as strongly on the product of  $\eta \times \text{SNR}$ .

Analogously to the procedure shown above, the same numerical VEF computation is carried out for a simply supported plate with the same vibrational parameters but a difference in applied structural damping. Here, a ten times larger loss factor is employed, i.e.  $\eta = 10^{-2}$ . Figure 11.36 displays the relative MSE made when computing TTVE numerically using a loss factor of  $\eta = 10^{-2}$  at two different levels of noise. It can be noticed when



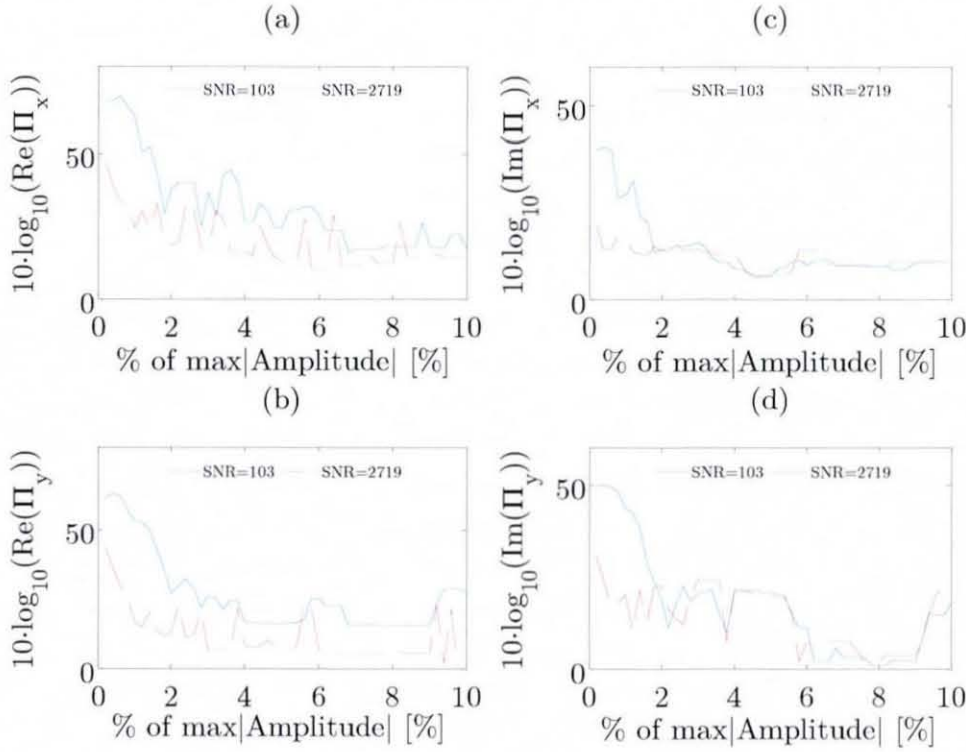


**Figure 11.36** Relative MSE of ideal filtered total transmitted energy of a simply supported plate: (a) active MSE in  $x$  direction, (b) active MSE in  $y$  direction, (c) reactive MSE in  $x$  direction, (d) reactive MSE in  $y$  direction, (mode (5,3),  $\eta = 10^{-2}$ ).

comparing Figure 11.36 with Figure 11.34 that the relative MSE is lower for each product of  $\eta \times \text{SNR}$  when the internal structural damping has increased.

Figure 11.37 displays the optimum ideal filtered TTVE  $\phi_x$ . The curve shape of the optimum ideal filtered TTVE  $\phi_y$  is rather similar and excluded due to brevity reasons. It can be seen from Figure 11.37 that the ideal filtered active TTVE matches much better with the exact solution at both noise levels. However, at a SNR of 124, which symbolises a heavily noise contaminated signal, the product of  $\eta \times \text{SNR}$  is approximately 1.24 and, thus, lower than at the same scenario of the previous example. At an SNR of 2719 the product of loss factor and SNR is  $\eta \times \text{SNR} \approx 27.2$ . It can be realised from Figure 11.37 that at the product of  $\eta \times \text{SNR} > 1$  a reasonable accurate VEF within a simply supported plate can be computed at a higher structural damping level. However, discrepancies to the exact solution are always present, even in the case where zero noise contaminates the signal ( $\text{SNR} = \infty$ )

because the spectral filtering procedure alters the wavenumber domain and with it the numerically determined spatial derivatives.

VEF maps of the exact solution, the ideal filtered VEF at  $\eta = 10^{-3}$  & SNR = 2685 and  $\eta = 10^{-2}$  & SNR = 103 are presented on the next page to

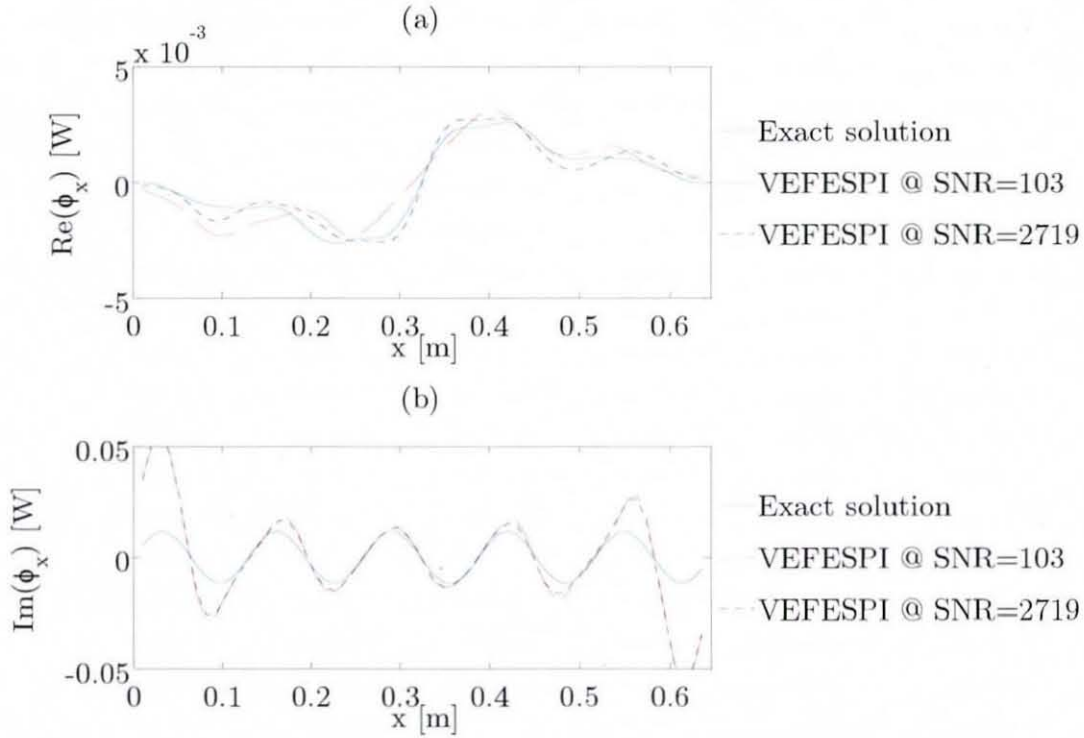


**Figure 11.37** Exact and ideal filtered total transmitted vibrational energy of a simply supported plate: (a) active  $\phi_x$ , (b) reactive  $\phi_x$  (mode (5,3),  $\eta = 10^{-2}$ ).

illustrate the effect of the relation between loss factor and SNR. It can be seen from Figures 11.38 and 11.39 that at  $\eta = 10^{-3}$  & SNR = 2685 and  $\eta = 10^{-2}$  & SNR = 103 a similar VEF pattern was computed. It can be realised that with increasing damping, the product  $\eta \times \text{SNR}$  may decrease in order to compute a useful VEF pattern, as shown in the figures above. Hence, with increasing internal damping within the simply supported plate, the noise sensitivity of the VEFESPI method decreases. If the plate is lightly damped ( $\eta \approx 10^{-3}$ ), the product of  $\eta \times \text{SNR}$  should at least be about 3, whereas at a structural damping of  $\eta \approx 10^{-2}$  the product of  $\eta \times \text{SNR}$  may be about 1. Interestingly, an energy balance according to equation (3.61) revealed that at

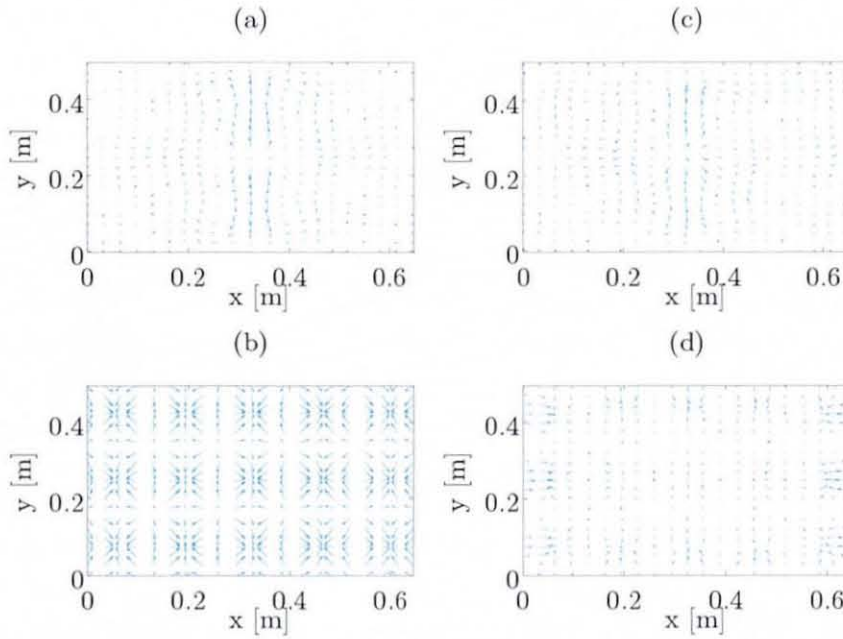


**Figure 11.38** Ideal filtered and exact VEF maps of the plate displacement shown in Figure 11.32: (a) exact active VEF, (b) exact reactive VEF, (c) active VEF - VEFESPI, (d) reactive VEF - VEFESPI, ( $\eta = 10^{-3}$  &  $\text{SNR} = 2685$ ).

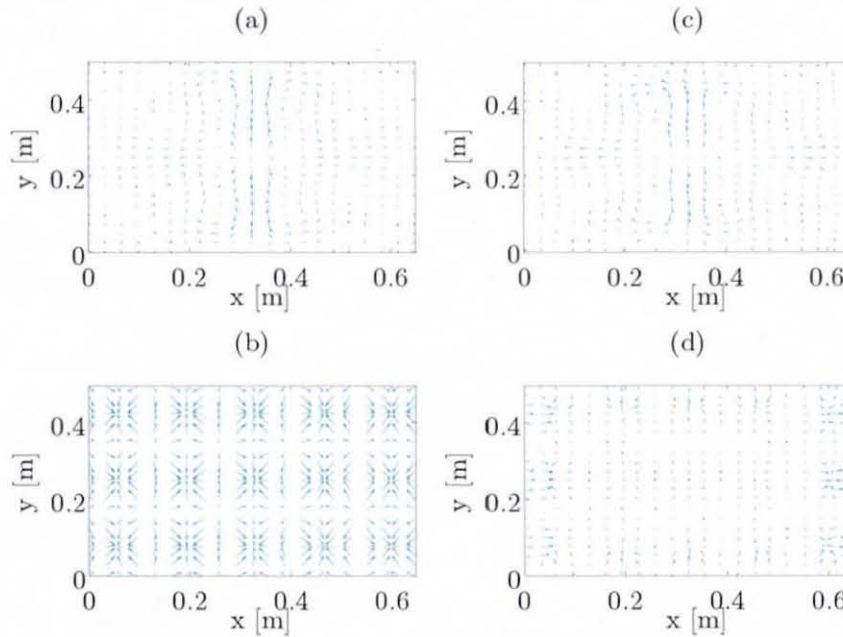


**Figure 11.39** Ideal filtered and exact VEF maps of a simply supported plate: (a) exact active VEF, (b) exact reactive VEF, (c) active VEF - VEFESPI, (d) reactive VEF - VEFESPI, ((mode (5,3) &  $\eta = 10^{-2}$  &  $\text{SNR} = 103$ )).

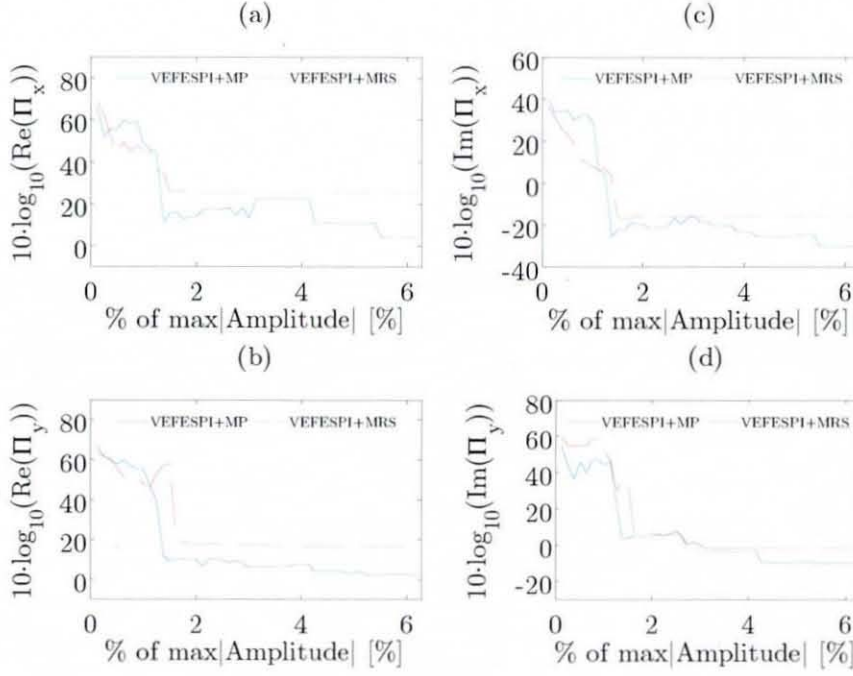


$\eta = 10^{-3}$  &  $\text{SNR} = 2685$  and at  $\eta = 10^{-2}$  &  $\text{SNR} = 103$  the total transmitted energy within the plate, obtained from the surface integration of the potential energy density, in comparison to the theoretical determined VIP was about 7.5 % and 9.1 %, respectively. Thus, the computation of the VEF pattern is much more noise sensitive than the computation of the active TTVE from the VEFESPI determined potential energy density.

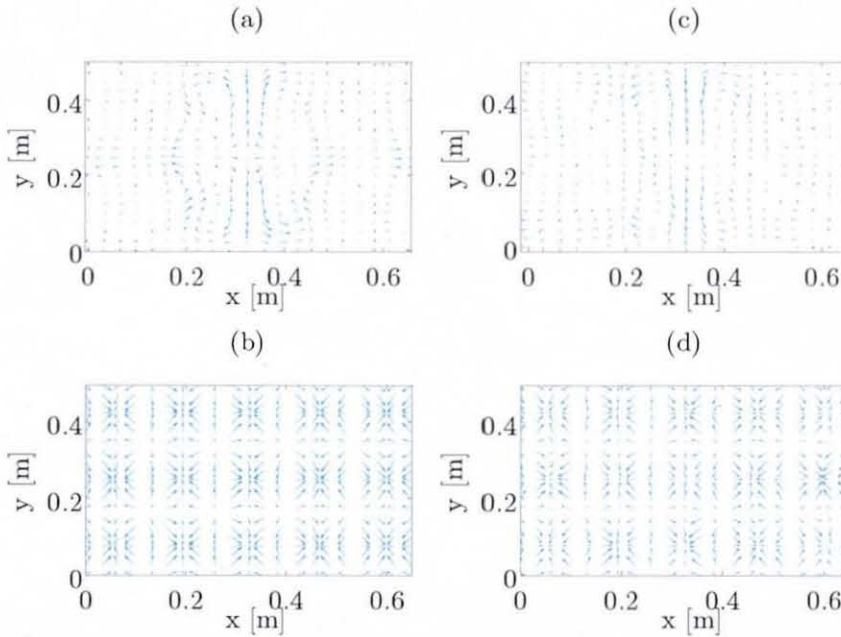
It can be seen from the filtered reactive energy figures, shown above, that the ideal filtered reactive VEF did not match well with the exact solution. The deviation of reactive energy flow can be explained by the analysis of an odd-numbered mode shape plate displacement, which causes leakage in the wavenumber spectrum and, thus, deviations in VEF computation. To reduce this effect the MP and MRS periodisation may be employed.

Figure 11.40 displays the relative MSE made when analysing a simply supported plate displacement, excited centrally by a unity force at an excitation frequency of  $f_0 = 714$  Hz, which forced the plate to a modal response of the mode (5,3). The plate was damped with  $\eta = 10^{-2}$  and the displacement was contaminated by normally distributed noise with an SNR of 94. Figures 11.40(c) and 11.40(d) show that the relative reactive MSE is lower than the reactive MSE shown in Figures 11.36(c) and 11.36(d). Interestingly, here the MSE of the reactive VEF in the  $x$  direction is lower than the MSE made when computing reactive energy flow in the  $y$  direction. This may be due to the inclusion of more waves in the  $x$  direction because the mode employed here was (5,3). However, both periodisation techniques produced a much better computed reactive energy flow map than the VEFESPI analysis of the non-periodised plate displacement, as evident from Figure 11.41.

Figure 11.41 displays the VEF maps computed from the MP and MRS periodised plate displacements. It can be seen from Figure 11.41(c) that the MRS based computation of active VEF is not as successful as the MP technique. Here, strong oscillations of the active TTVE occurred. Furthermore, the computation of active VEF from an MP periodised plate



**Figure 11.40** Relative MSE of ideal filtered total transmitted energy of a simply supported plate: (a) active MSE in  $x$  direction, (b) active MSE in  $y$  direction, (c) reactive MSE in  $x$  direction, (d) reactive MSE in  $y$  direction, ( $\eta = 10^{-2}$ ,  $\text{SNR} = 94$ ).



**Figure 11.41** Ideal filtered VEF maps of a simply supported plate: (a) active VEF - VEFESPI+MP, (b) reactive VEF - VEFESPI+MP, (c) active VEF - VEFESPI+MRS, (d) reactive VEF - VEFESPI+MRS, ( $\eta = 10^{-2}$  &  $\text{SNR} = 94$ ).



displacement did not produce a better result than the direct computation of active VEF from a non-periodised displacement.

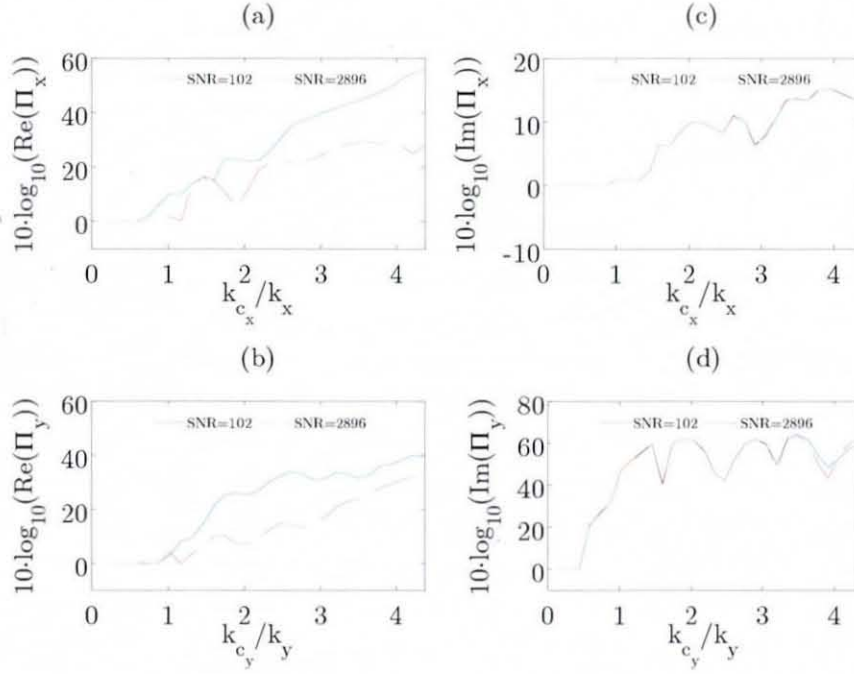
### 11.3.2.2 Oval 2D Spectral Butterworth Filtering

Analogously to the procedure demonstrated in the previous section, the effect of computing Butterworth filtered VEF from noise contaminated simply supported plate displacements is presented. Also here, four different combinations of high and low level noise contamination in combination with high and low structural damping are investigated. Thus, VEF is computed at a loss factor of  $\eta = 10^{-3}$  and  $\eta = 10^{-2}$  for a simply supported plate, which was excited centrally by a unity force at an excitation frequency of  $f_0 = 714$  Hz, which forced that plate to the modal shape of mode (5,3).

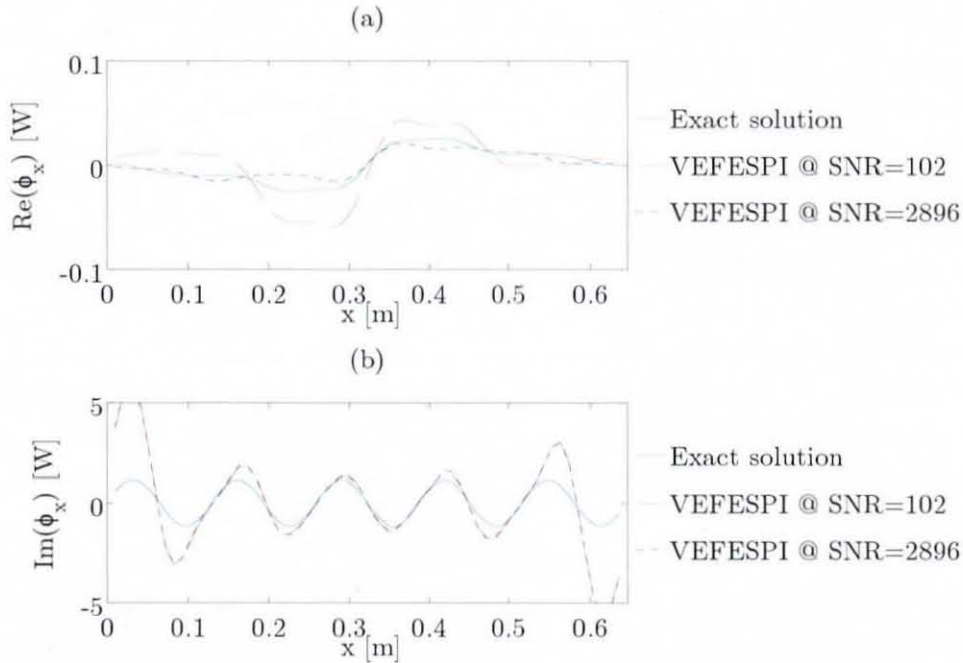
Figure 11.42 shows the relative MSE made when computing VEF from a simply supported plate displacement, as shown in Figure 11.32. Equation (11.5) was employed to determine the MSE. It can be seen from Figure 11.42 that the relative MSE of reactive TTVE does not alter with the variation of the SNR. However, the relative MSE of the active TTVE does alter with the variation of the SNR. In comparison to Figure 11.34, the Butterworth filtered active and reactive MSE is lower than the ideal filtered counterpart, especially at the higher noise level. In Figure 11.42 it can also be seen that the TTVE in the  $x$  and  $y$  directions has a separate cut-off frequency, denoted here as  $k_{c_x}$  and  $k_{c_y}$ , respectively. Due to the use of a non-symmetrical mode shape displacement (5,3) the spectral low pass-Butterworth has to be oval, as shown in Figure 4.5. Thus, different cut-off wavenumbers are required in the  $k_x$  and  $k_y$  direction, respectively.

Figure 11.43 displays the Butterworth filtered TTVE in the  $x$  direction. Also, due to similarity, the TTVE in the  $y$  direction is excluded. It can be seen from Figure 11.43 that with an increase of the product  $\eta \times \text{SNR}$  the accuracy of the VEF computation improves.

In the following a numerical VEF computation is carried using the same simply supported plate displacement parameters, with, however, a difference in applied structural damping, i.e.  $\eta = 10^{-2}$ .



**Figure 11.42** Relative MSE of Butterworth filtered total transmitted energy of a simply supported plate: (a) active MSE in  $x$  direction, (b) active MSE in  $y$  direction, (c) reactive MSE in  $x$  direction, (d) reactive MSE in  $y$  direction, (mode (5,3),  $\eta = 10^{-3}$ ).



**Figure 11.43** Exact and Butterworth filtered total transmitted vibrational energy of a simply supported plate: (a) active  $\phi_x$ , (b) reactive  $\phi_x$ , (mode (5,3),  $\eta = 10^{-3}$ ).

Figure 11.44 displays the relative MSE that is made when TTVE is computed from Butterworth filtered data. Here also, at a high noise floor an

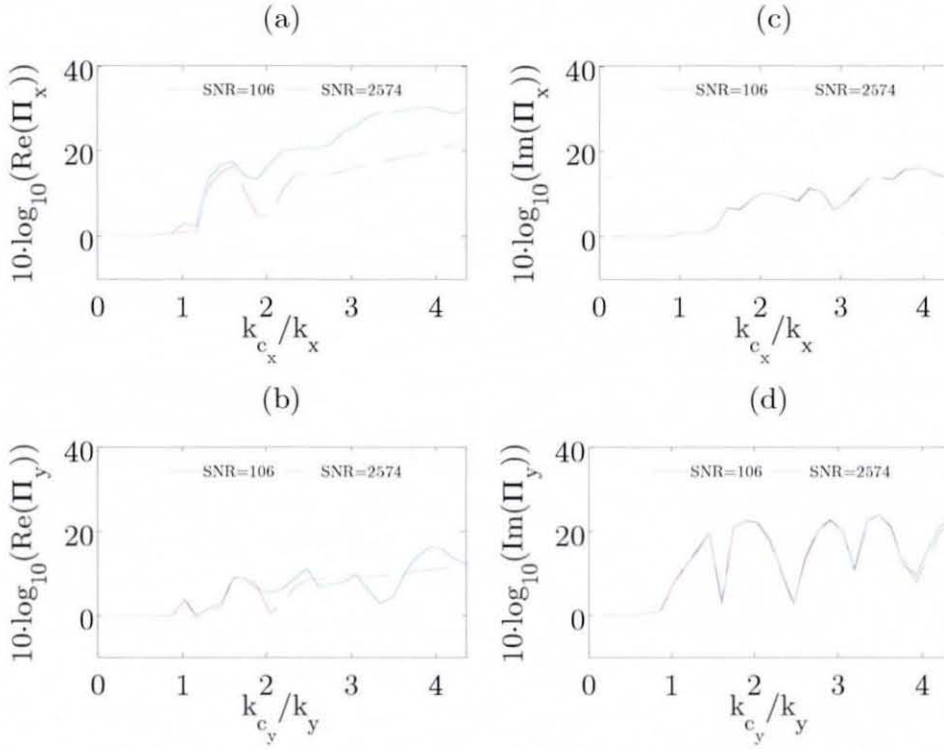


**Figure 11.44** Relative MSE of Butterworth filtered total transmitted energy of a simply supported plate: (a) active MSE in  $x$  direction, (b) active MSE in  $y$  direction, (c) reactive MSE in  $x$  direction, (d) reactive MSE in  $y$  direction, (mode (5,3),  $\eta = 10^{-2}$ ).

acceptable result can be obtained due to the increase in damping.

Figure 11.45 displays the Butterworth filtered TTVE in the  $x$  direction. It is evident from this figure that a reasonable VEF computation accuracy can be realised at  $\eta \times \text{SNR} \approx 1$ . Of course products of  $\eta \times \text{SNR} \gg 1$  are preferable. However, this quantity is driven by the plate's modal structural loss factor and the noise sensitivity of the measurement system, which records the two-dimensional displacement information. Thus, the product of  $\eta \times \text{SNR}$  cannot be influenced.

Figures 11.46 and 11.47 display the active and reactive VEF maps of the exact solution and the Butterworth filtered VEF computed at  $\eta = 10^{-3}$  &



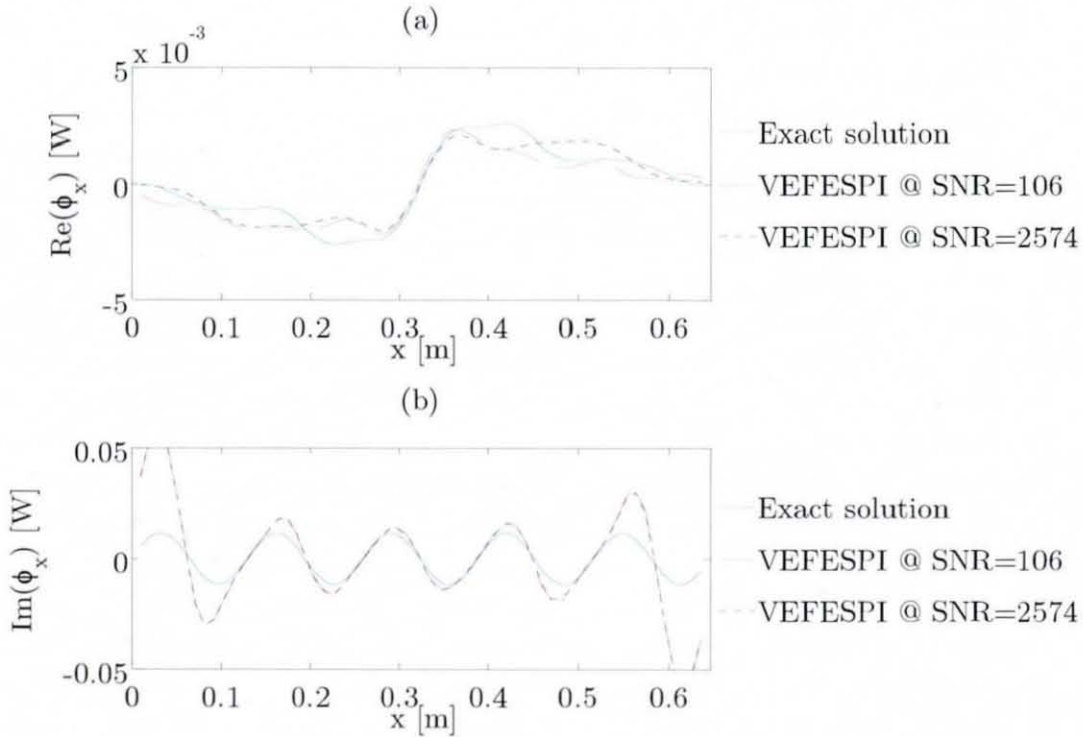


**Figure 11.45** Exact and Butterworth filtered total transmitted vibrational energy of a simply supported plate: (a) active  $\phi_x$ , (b) reactive  $\phi_x$ , (mode (5,3),  $\eta = 10^{-2}$ ).

SNR = 98 and  $\eta = 10^{-2}$  & SNR = 129, respectively. It can be seen from both figures that the Butterworth filtered active VEF at  $\eta = 10^{-3}$  & SNR = 2896 and  $\eta = 10^{-2}$  & SNR = 106 match well with the exact solution. This again indicates that with increasing damping within the structure, the noise sensitivity of the VEFESPI method decreases. Also here, an energy balance according to equation (3.61) revealed a very low relative error between the surface integrated potential energy density (TTVE within the plate) and the theoretical VIP of 0.35 % and -0.11 %, respectively. It seems the magnitude of the Butterworth filtered active VEF is more accurate than the ideal filtered magnitude of active VEF.

However, the computation of the Butterworth filtered reactive energy flow is also fairly erroneous. To reduce the error made when computing reactive energy flow, the non-periodic plate displacement was periodised by employing the MP and MRS technique. Figure 11.48 displays the relative MSE made when computing Butterworth filtered TTVE from a periodised

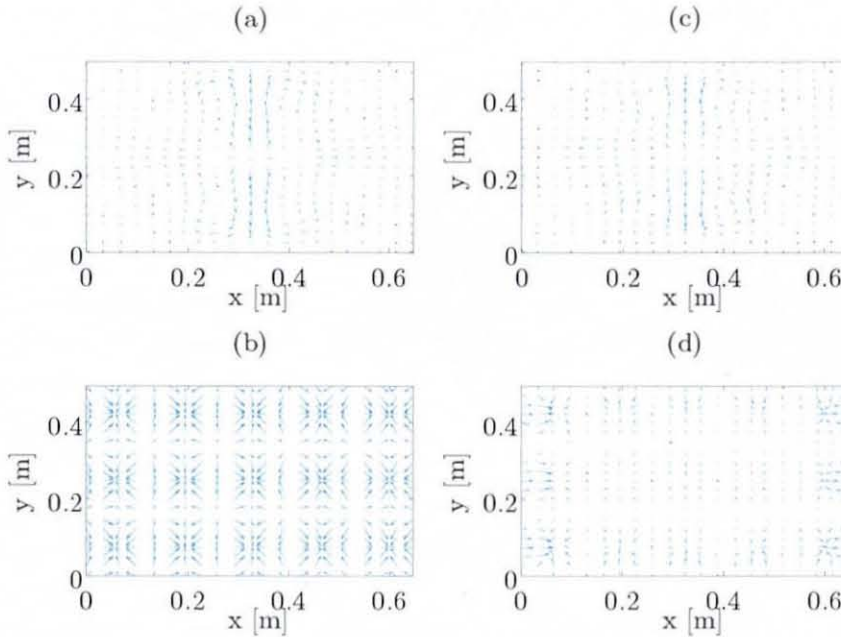


**Figure 11.46** Butterworth filtered and exact VEF maps of simply supported plate: (a) exact active VEF, (b) exact reactive VEF, (c) active VEF - VEFESPI, (d) reactive VEF - VEFESPI, ((mode (5,3) &  $\eta = 10^{-3}$  & SNR = 2896).

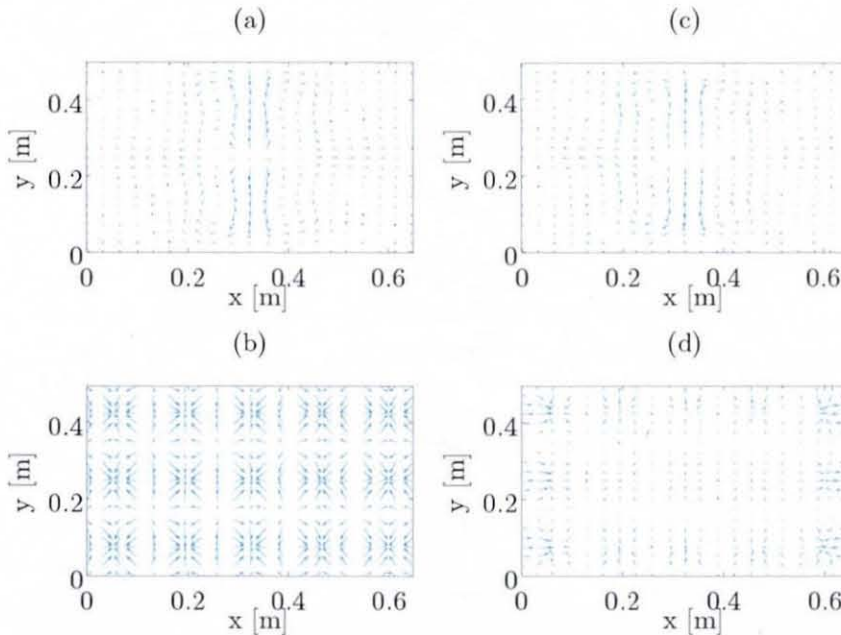


**Figure 11.47** Butterworth filtered and exact VEF maps of simply supported plate: (a) exact active VEF, (b) exact reactive VEF, (c) active VEF - VEFESPI, (d) reactive VEF - VEFESPI, ((mode (5,3) &  $\eta = 10^{-2}$  & SNR = 106).



simply supported plate displacement. Analogously to the procedure demonstrated above, a simply supported plate, excited centrally by a unity force at an excitation frequency of  $f_0 = 714$  Hz that is equal to the undamped natural frequency of the (5,3) mode was analysed. The loss factor of the plate

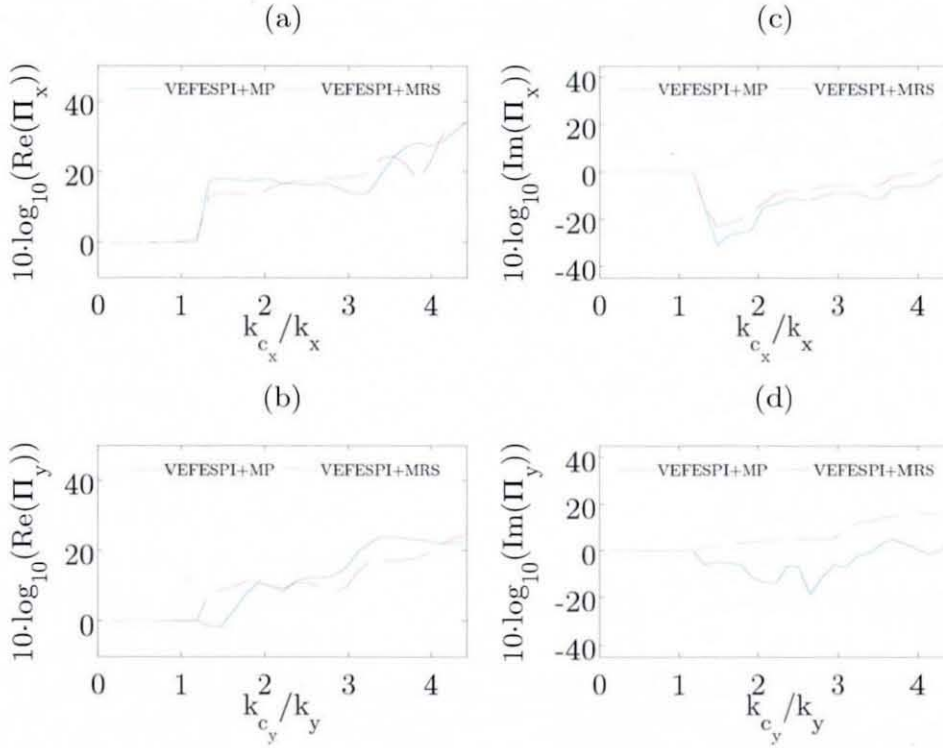


**Figure 11.48** Relative MSE of Butterworth filtered total transmitted energy of a simply supported plate: (a) active MSE in  $x$  direction, (b) active MSE in  $y$  direction, (c) reactive MSE in  $x$  direction, (d) reactive MSE in  $y$  direction, ( $\eta = 10^{-2}$  &  $\text{SNR} = 104$ ).

was chosen to be  $\eta = 10^{-2}$ . The displacement was contaminated by normally distributed noise with a SNR of 104. It can be seen from Figures 11.48(c) and 11.48(d) that the relative reactive MSE can be decreased when computing TTVE from Butterworth filtered periodised displacements. In addition, the MP periodisation technique produced best results.

Figure 11.49 displays the active and reactive VEF determined from the Butterworth filtered and periodised simply supported plate displacement. It is evident when comparing Figure 11.49 with the exact VEF solution

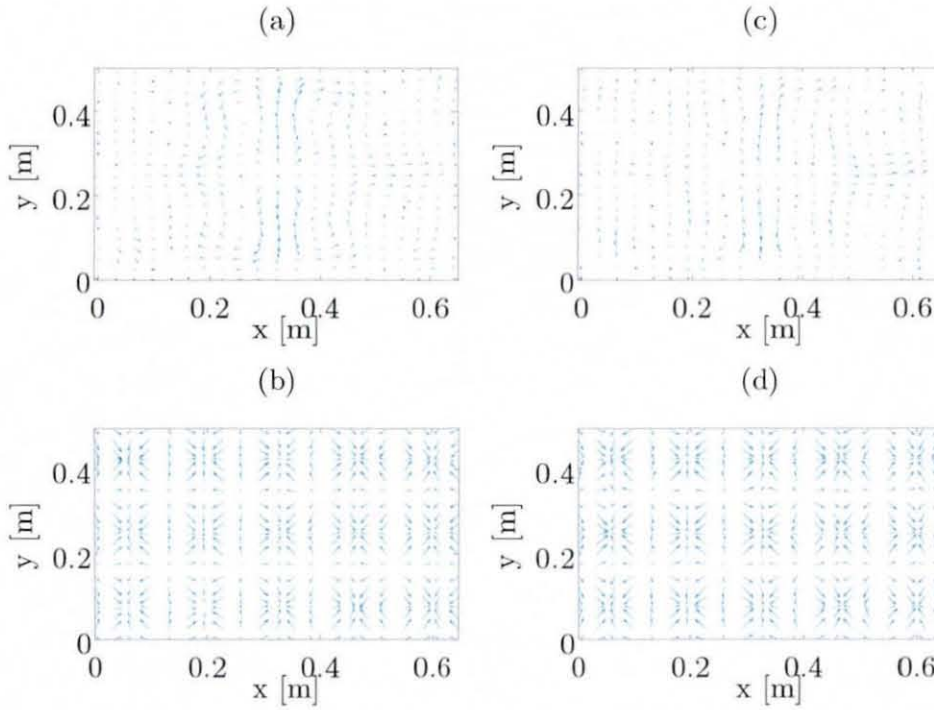


**Figure 11.49** Butterworth filtered VEF maps of a simply supported plate: (a) active VEF - VEFESPI+MP, (b) reactive VEF - VEFESPI+MP, (c) active VEF - VEFESPI+MRS, (d) reactive VEF - VEFESPI+MRS, ( $\eta = 10^{-2}$  &  $\text{SNR} = 104$ ).

displayed in Figure 11.46 that the reactive energy flow is a better match with the exact reactive VEF solution.

### 11.3.3 Vibrational Energy Flow Including ESPI Noise

The aim of this section is to provide optimised filter cut-off points, which may then be employed during the VEF analysis of the ESPI measured simply supported plate data. Therefore, ESPI noise was extracted within the wavenumber domain from the Fourier transformed and ESPI measured simply supported plate displacements. Tables 11.5 to 11.7 display the vibration parameters of the experimental simply supported plate structures obtained during the ESPI experiments.

mode	$f_0$	$F_0$	$\eta_{m,n}$	SNR
(3,3)	428.7 Hz	0.0139 N	$3.362 \cdot 10^{-3}$	75.6
(5,3)	711.6 Hz	0.0344 N	$3.445 \cdot 10^{-3}$	55.7
(1,5)	766.7 Hz	-	$6.954 \cdot 10^{-3}$	197.0
(7,1)	896.2 Hz	0.1509 N	$6.442 \cdot 10^{-3}$	495.1
(5,5)	1190.9 Hz	0.1275 N	$5.317 \cdot 10^{-3}$	98.4
(9,1)	1461.9 Hz	0.0817 N	$3.464 \cdot 10^{-3}$	81.7
(7,5)	1615.2 Hz	0.2215 N	$5.558 \cdot 10^{-3}$	96.0
(9,5)	2180.9 Hz	0.3060 N	$8.393 \cdot 10^{-3}$	25.2

**Table 11.5** Vibration parameters of the experimental non-layer damped simply supported plate.

mode	$f_0$	$F_0$	$\eta_{m,n}$	SNR
(3,3)	398.1 Hz	0.0994 N	$1.862 \cdot 10^{-2}$	21.3
(5,3)	660.7 Hz	0.1713 N	$1.904 \cdot 10^{-2}$	47.6
(7,1)	832.1 Hz	0.2562 N	$2.154 \cdot 10^{-2}$	65.6
(5,5)	1105.7 Hz	0.5560 N	$2.176 \cdot 10^{-2}$	52.2
(9,1)	1357.3 Hz	0.4173 N	$1.927 \cdot 10^{-2}$	52.4
(7,5)	1499.6 Hz	0.5398 N	$1.417 \cdot 10^{-2}$	136.2
(5,7)	1773.3 Hz	0.9970 N	$1.671 \cdot 10^{-2}$	145.0
(11,1)	2013.8 Hz	0.9520 N	$1.836 \cdot 10^{-2}$	78.0

**Table 11.6** Vibration parameters of the experimental single-layer damped simply supported plate.

mode	$f_0$	$F_0$	$\eta_{m,n}$	SNR
(3,3)	412.1 Hz	0.0525 N	$1.080 \cdot 10^{-2}$	35.5
(5,3)	684.0 Hz	0.1216 N	$1.070 \cdot 10^{-2}$	105.3
(7,1)	861.4 Hz	0.1239 N	$1.561 \cdot 10^{-2}$	126.0
(5,5)	1144.7 Hz	0.2576 N	$1.001 \cdot 10^{-2}$	159.2
(9,1)	1405.2 Hz	0.1700 N	$9.347 \cdot 10^{-3}$	69.6
(7,5)	1552.6 Hz	0.3844 N	$1.498 \cdot 10^{-2}$	61.8
(5,7)	1835.9 Hz	0.4784 N	$9.860 \cdot 10^{-3}$	152.5
(9,5)	2096.3 Hz	0.5983 N	$1.022 \cdot 10^{-2}$	96.3

**Table 11.7** Vibration parameters of the experimental checkerboard-layer damped simply supported plate.

It is shown in the tables above that the ESPI measured plate displacements were recorded on three differently damped and simply supported plate structures. To simulate different standing wave environments, a non-layer covered plate, a fully unconstrained layer covered plate, and a partially damped plate, covered with patches that were arranged in a checkerboard pattern layout, were measured. Eight ESPI measurements at different modes were recorded. As usual, the extracted ESPI noise was superimposed with a simply supported plate displacement that was synthetically generated. The plate was centrally excited by the force magnitude  $F_0$  as measured during the ESPI experiment. Here, the theoretical undamped natural frequency  $f_0$  of the respective mode was employed using the simply supported plate parameters, as shown in Table 11.4. The measured modal hysteretic loss factors  $\eta_{m,n}$ , shown in the tables above, were acquired from an experimental modal analysis applied for each plate structure using a 10×10 accelerometer measurement grid, which was evenly distributed over the plate's surface [127].

Due to the design of the simply supported plate rig, introduced later in section 12.2.2, the plate displacement could not be fully recorded and was

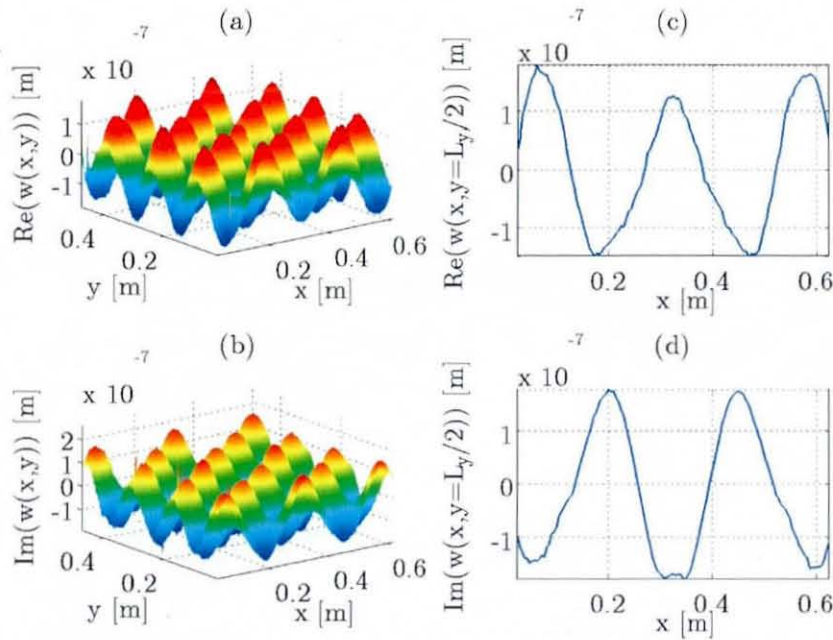


excluded approximately 2.5 cm around the edges. Hence, the displacement non-periodicity due to the excited odd-numbered mode shapes of the plate was increased even further. For this reason optimised filter cut-off points will also be determined for a simply supported plate displacement truncated to an integer number of wavelengths included in the signal. However, the truncation procedure will decrease the number of wavelengths to be analysed during the experimental analysis.

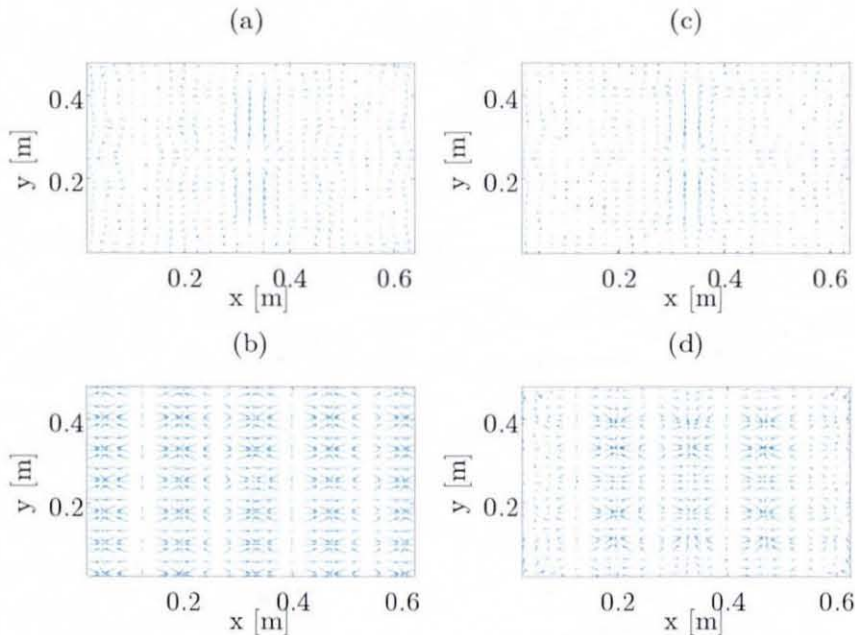
As mentioned previously, ESPI noise for each simply supported ESPI plate measurement was extracted within the wavenumber domain simply by deleting the travelling wave information of the computed wavenumber spectrum. After applying an inverse 2D FFT the spatial ESPI noise distribution was obtained. This noise displacement was then superimposed with a synthetic simply supported plate displacement by numerically evaluating equation (10.25). With this procedure, optimum filter cut-off points for each experimental excitation frequency were determined for the non-periodic and periodic plate displacements. The results of these analyses are shown in Appendix A29. In the following, two results of the VEF computations are presented for a non-periodic plate displacement and a plate displacement truncated to an integer number of wavelengths.

Figure 11.50 displays the non-periodic plate displacement as it would be in truncated form straight from the experimentally acquired ESPI data. The plate displacement was generated synthetically using equation (10.25) and superimposed by the extracted ESPI noise. The force amplitude employed here is equal to the force magnitude measured during the ESPI experiment and is shown in Tables 11.5 to 11.7. A single unconstrained damping layer was modelled simply by altering the complex, flexural plate rigidity according to the unconstrained damping layer theory introduced in section 10.4. The simply supported plate was excited by an excitation frequency of  $f_0 = 1773.3$  Hz forcing the plate to vibrate at its natural mode (5,7). The remaining vibration parameters are shown in Table 11.6. It can be seen from Figure 11.50 and from Table 11.6 that the displacement was contaminated by noise with an SNR of 145.





**Figure 11.50** ESPI noise contaminated, single layer damped, simply supported plate displacement: (a) 2D real part, (b) 2D imaginary part, (c) real part at  $y = L_y/2$ , (d) imaginary part at  $y = L_y/2$ , ((mode (5,7) &  $\eta = 1.67 \cdot 10^{-2}$  & SNR = 145).



**Figure 11.51** Butterworth filtered and exact VEF maps of the simply supported plate displacement shown in Figure 11.50: (a) exact active VEF, (b) exact reactive VEF, (c) active VEF - VEFESPI, (d) reactive VEF - VEFESPI.

Figure 11.51 displays the VEF pattern determined from the exact non-noise contaminated plate displacement and the Butterworth filtered ESPI noise contaminated plate displacement. Figure 11.52 shows the exact and filtered TTVE in the  $x$  direction. It can be seen from both figures that a good match between exact active VEF and filtered active VEF can be achieved despite

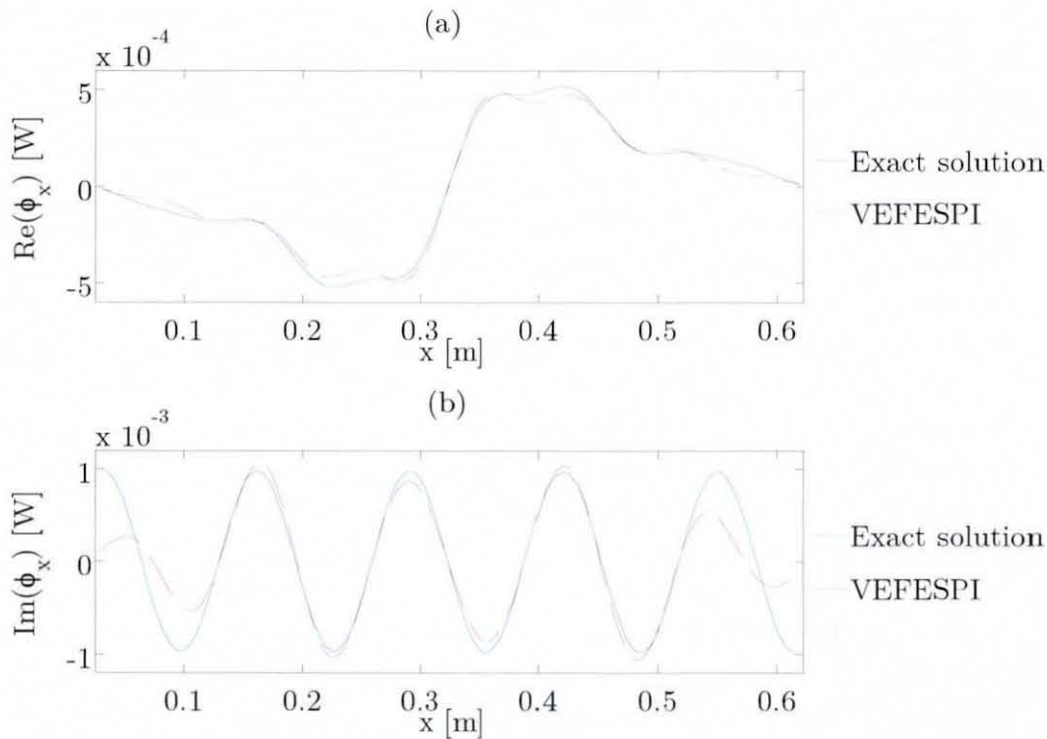
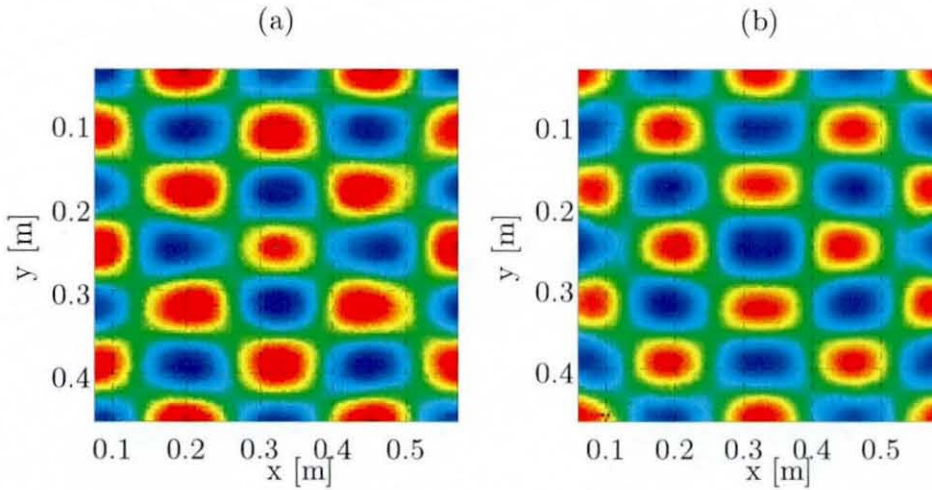


**Figure 11.52** Exact and Butterworth filtered total transmitted vibrational energy of the simply supported plate displacement shown in Figure 11.50: (a) active  $\phi_x$ , (b) reactive  $\phi_x$

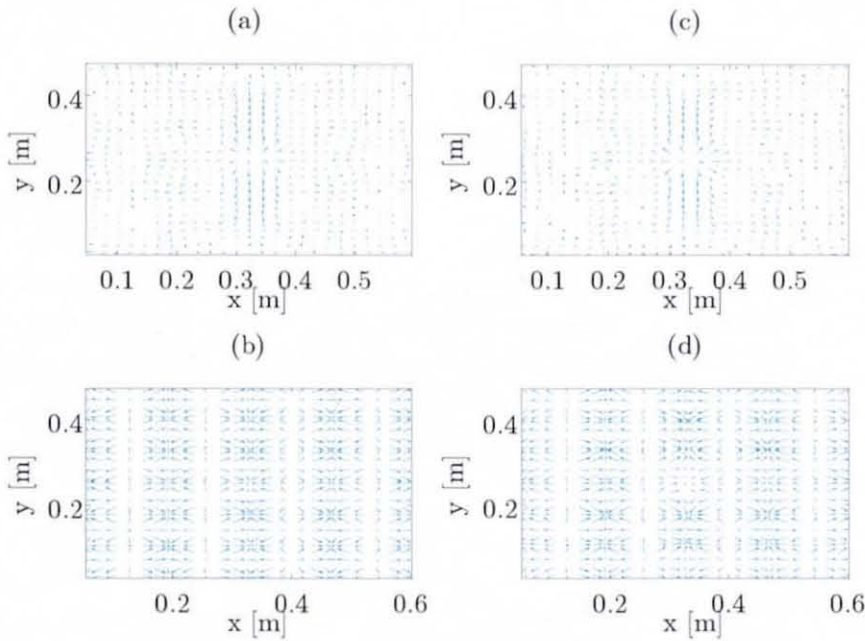
analysing the non-periodic plate displacement. However, the reactive energy flow pattern does not match well. This problem increases with decreasing number of modes. Thus, a truncation to an integer number of wavelengths within the plate displacement was carried out.

Figure 11.53 displays the integer wavelength truncation of the plate displacement shown in Figure 11.50. This procedure will also be employed when analysing the experimental simply supported plate data.

Figure 11.54 shows the VEF pattern of the exact solution and the Butterworth filtered VEF computed from the displacement shown in Figure



**Figure 11.53** Top view image of the simply supported plate displacement shown in Figure 11.50 however, truncated to an integer number of wavelengths: (a) real part, (b) imaginary part.



**Figure 11.54** Butterworth filtered and exact VEF maps of the simply supported plate displacement shown in Figure 11.53: (a) exact active VEF, (b) exact reactive VEF, (c) active VEF - VEFESPI, (d) reactive VEF - VEFESPI.



11.53. It can be noticed by comparing Figure 11.54(d) with Figure 11.51(d) that the Butterworth filtered reactive VEF matches much better with the exact solution. Also here, the active VEF patterns match well with each other.

Figure 11.55 displays the TTVE computed from the exact VEF and Butterworth filtered VEF of the periodically truncated simply supported plate displacement shown in Figure 11.53. It is evident that the computation of the reactive TTVE from ESPI noise contaminated displacement data that

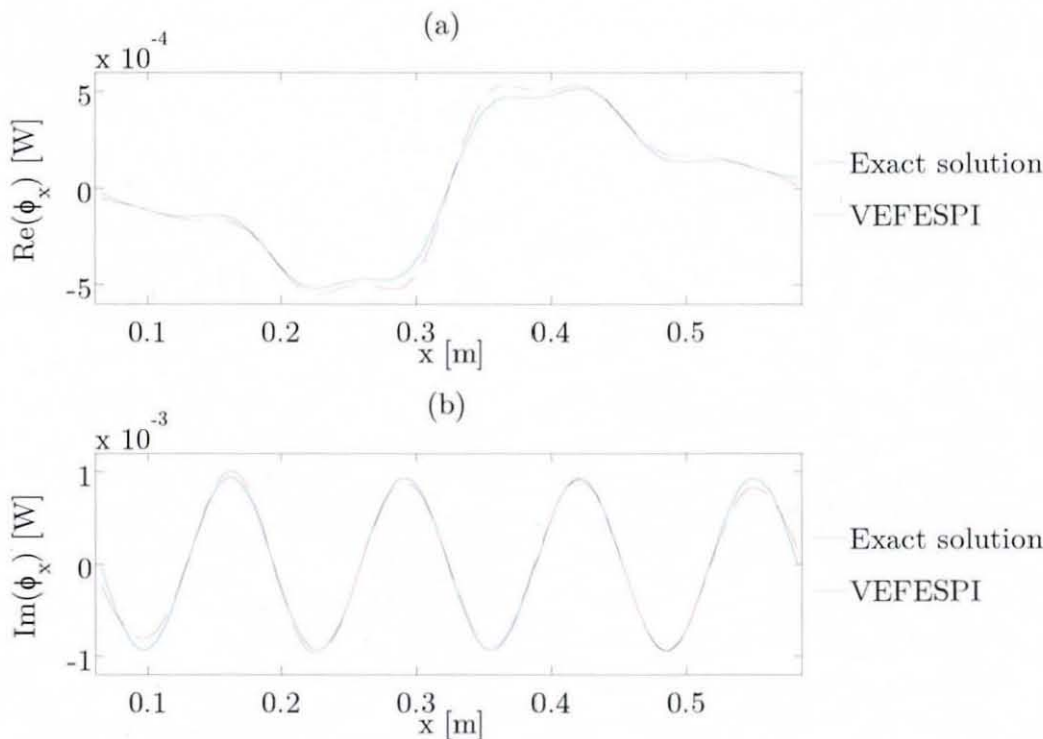


**Figure 11.55** Exact and Butterworth filtered total transmitted vibrational energy of the simply supported plate displacement shown in Figure 11.53: (a) active  $\phi_x$ , (b) reactive  $\phi_x$ .

are truncated to an integer number of wavelengths clearly increases in accuracy. Also, the accuracy of the active TTVE curve shape has slightly improved. Thus, the truncation of the ESPI recorded experimental simply supported plate displacement to an integer number of wavelengths is expected to increase the computation of energy flow. Note, the TTVE in the  $y$  direction has not been shown here due to a similar curve shape.

## 11.4 Discussion and Summary

Within this chapter the numerical computation of VEF and energy flow related quantities in infinite plates and finite simply supported plates was studied. VEF and energy flow related quantities were determined from synthetically generated plate displacements using the VEFESPI method. To assess the accuracy of the VEFESPI method under different circumstances, the numerically determined energy quantities have been compared to exact VEF solutions given in chapter 10. Spatial derivatives required for VEF computation were calculated using the KSD technique.

Because experimental data is contaminated by noise, the effect of spectral filtering has been investigated in detail. Furthermore, the reduction of leakage, occurring due to the analysis of non-periodic plate displacements, was taken into account.

In section 11.2 an infinite plate was investigated. The point force response of an infinite plate may be analytically described by a set of Hankel functions of second kind and zeroth order, representing a travelling farfield and a decaying nearfield. To simplify the VEF analysis, the Hankel functions were approximated by the exponential asymptotic expansion of the Hankel functions. The asymptotic expansion expressions are fairly accurate for locations of  $|kr|$  greater than 4.

The computation of VEF within an infinite plate from synthetic non-noise contaminated displacement data resulted in VEF oscillations due to the analysis of a non-periodic, radially symmetric, exponentially decaying displacement that was truncated to a Cartesian coordinate based displacement matrix. However, these undesired oscillations could be compensated for, using the CW technique as well as the MP and MRS periodisation techniques. It should be mentioned that although the MP and MRS technique delivered very good results, its application increased the computation time significantly. Thus, when dealing with a high number of data points during numerical VEF analysis, the CW technique performs much faster. Furthermore, the CW technique is also easier to implement within a software environment.



VEF within a plate structure is determined herein from two complex-valued VEF fields denoted as  $\overline{P}_x$  and  $\overline{P}_y$ , which contained the two-dimensional information of energy flow in the  $x$  and  $y$  direction, respectively. With this information it is possible to construct so-called VEF maps exhibiting the magnitude and direction of VEF within the plate structure.

Active VEF within an infinite plate travelled radially symmetrically away from the excitation location and decreased in amplitude with increasing distance from the excitation location (Figure 11.7). In contrast, reactive VEF travelled towards the excitation location.

Energy balances within the infinite plate were carried out by integrating the VEF fields in the  $x$  and  $y$  directions along a closed square contour that was located around the excitation location with distance of  $|kr|$ . It has been shown that the computed active TTVE obtained from the contour integration is constant at each radial distance away from the excitation location and equal to the VIP (Figure 11.9). The TTVE was also used here as a quantity to assess the error that was made during the numerical infinite plate VEF computation. This procedure had the advantage that the two VEF fields,  $\overline{P}_x$  and  $\overline{P}_y$ , could be combined with one error appraisal quantity only.

The effect of noise contamination on the computation of VEF within an infinite plate was also investigated. Thus, synthetic displacement data was superimposed with normally distributed noise and noise extracted from the experimental ESPI data. As usual, a spectral filtering was carried out by applying the ideal 2D filtering procedure as well as the oval 2D Butterworth filter. It has been shown that due to the alteration of the wavenumber domain during the spectral filtering, the VEF computation accuracy reduced. However, employing the optimised filter cut-off points could reduce the error to an acceptable range. Thus, as evident from the VEF maps of the spectral filtered infinite plate displacements, as shown in Figures 11.14 and 11.18, a good VEF pattern can still be reconstructed. However, the accuracy of the energy balance was reduced, as evident from Figures 11.15 and 11.19. This reduction in the accuracy of computation depended on the magnitude of the noise floor, which contaminated the displacement signal.

In contrast to the numerical infinite plate analysis, VEF within a finite structure, namely a simply supported plate, was also investigated numerically. The simply supported plate represented a finite structure that contained a high amount of standing waves. Due to the high standing wave ratio, very weak net energy flows could be expected and, thus, the effects of displacement discontinuities and especially noise contamination are much stronger when analysing a finite structure.

The simply supported plate displacement was synthetically generated by numerically evaluating equation (10.25). From there it can be realised that a modal approach was used to describe the simply supported plate response to a harmonic point force excitation by using an infinite number of excited modes contributing with a different amount of strength to the displacement formation. However, in practice only a finite number of modes can be considered. Thus, within this work only 11 modes ( $m = 11, n = 11$ ) were taken into account, to keep the computation time within a reasonable range.

The numerical computation of VEF from a non-noisy, non-periodic simply supported plate displacement also revealed VEF oscillations. These undesired VEF oscillations were caused by the spectral amplification of spectral leakage components especially at high wavenumber components. To reduce the effect of leakage due to signal irregularities three techniques, namely the CW, MP and MRS technique were employed. It has been shown that the VEF pattern as well as the TTVE within the plate could be computed with very high accuracy. The relative error, between the theoretical VIP and the integrated potential energy density (active TTVE), was about  $-0.03\%$  when employing the MP and MRS technique.

It can be realised from the VEF maps shown in Figures 11.26 and 11.27 that the reactive VEF pattern of a finite structure is much more distinctive than the reactive energy flow pattern of an infinite structure. Also, the amplitude of the total transmitted reactive energy is much higher than the active flow amplitude of an equivalent infinite plate structure. It can be seen from Figures 11.28 and 11.29 that the reactive TTVE in the  $x$  and  $y$  direction, respectively, is much higher than the active TTVE. Thus, finite



plate structures with a high standing wave ratio have a very high reactive VEF and a distinctive reactive VEF shape. Furthermore, it can be seen from these figures that the reactive VEF maps can be related to the modal shape of the displacement, whereas the active VEF pattern cannot be related to the modal displacement shape.

VEF oscillations from non-noisy, non-periodic simply supported plate displacements were reduced using the CW technique as well as the MP and MRS periodisation technique. The latter two techniques periodised the initial non-periodic plate displacement. It can be seen from Figures 11.30 and 11.31 that the MP and MRS technique produced better results. However, the CW technique is much easier to implement. Furthermore, the application of the MP and MRS technique increased the computation time.

The numerical computation of VEF within a finite plate from noise contaminated displacements revealed a large noise sensitivity of the VEFESPI method. Although not proven mathematically, a hypothetical model was introduced relating the net energy flow within finite structures to the spatial decay of the travelling waves. These notional decaying and travelling waves are very small compared to the total standing wave displacement. If the noise magnitude that contaminates the displacement signal is larger than the magnitude of the decaying waves, VEF cannot be computed. However, if the magnitude of the noise floor is less than the magnitude of the small travelling displacement part, VEF can be computed by the VEFESPI method.

To assess the computability of VEF from noisy, simply supported plate displacements, the product of loss factor and SNR, i.e.  $\eta \times \text{SNR}$  was suggested as an indicator to obtain VEF in pattern and magnitude by the VEFESPI method. It was shown that with increasing internal damping the noise sensitivity of the VEFESPI method decreased. Thus, active VEF could be computed at lower products of  $\eta \times \text{SNR}$ . The computation of reactive VEF was not strongly dependent on the noise floor. Problems occurred here but only due to non-periodicity of the initial plate displacement. An alternative indicator to assess the computability of VEF from noisy finite structure displacements may be the standing-wave ratio (SWR). However,

the product of  $\eta \times \text{SNR}$  was preferred here, since the loss factor was measured by an experimental modal analysis and wavenumber domain manipulation allowed for easy extraction of the ESPI noise.

Figure 11.56 displays the minimum MSE made when computing VEF from a simply supported plate displacement excited at the mode (3,3), noise contaminated by different levels of noise and structurally damped at  $\eta = 10^{-3}$  and  $\eta = 10^{-2}$ , respectively. The loss factor range employed in this analysis represents the range of the loss factor to be expected during the simply supported plate experiment. It is evident from Figure 11.56 that the higher the product of  $\eta \times \text{SNR}$  the lower the error made when computing VEF. The minimum MSE  $\Pi_x$  was computed using equation (11.5). It is evident from Figure 11.56(b) that computation of reactive VEF within a simply supported plate is less erroneous and more insensitive to noise contamination than the computation of active energy flow. Here, the computation accuracy increased

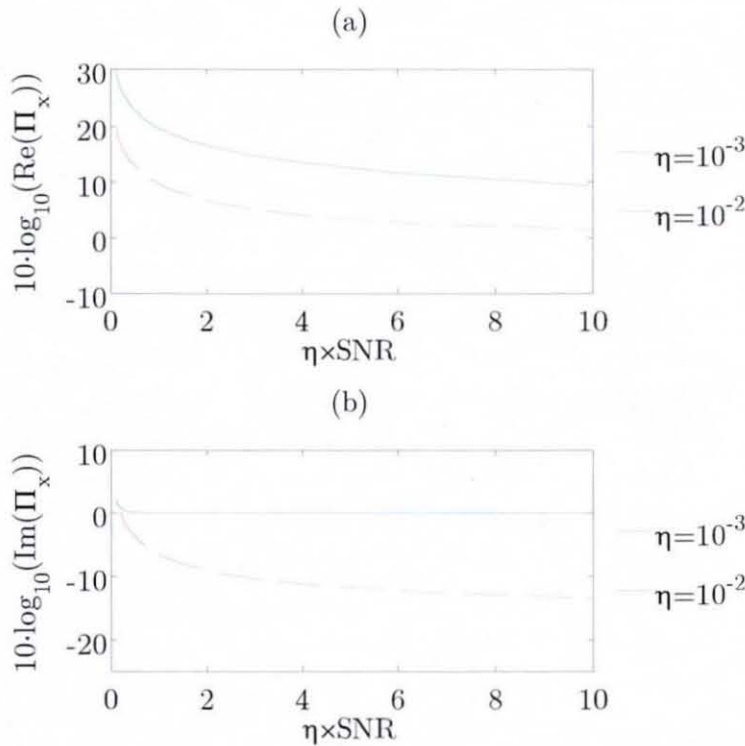


**Figure 11.56** Computed MSE of periodised simply supported plate displacement using the MP technique, excited at the natural (3,3) mode in dependency on the product of  $\eta \times \text{SNR}$ : (a) active MSE, (b) reactive MSE.

with increasing internal damping. From Figure 11.56(a) it can be seen that at a product of  $\eta \times \text{SNR} \geq 3$  no significant reduction in MSE can be achieved. Also, the computation accuracy increased with increasing loss factor and, thus, with increasing damping the sensitivity of the VEFESPI method decreased.

When computing VEF from simply supported plate displacements higher modes were more insensitive towards error due to the inclusion of more spatial information in the displacement signal.

Interestingly, the active TTVE curve shapes of a simply supported plate, as shown in the figures above, were similar to the VEF curves present in the simply supported beam with maximum energy transmitted at the excitation location and zero energy flow at the non-dissipative boundaries. As mentioned previously, this curve can be seen either as TTVE or energy dissipated within the structure.

Finally, an energy balance was carried out by using synthetic displacement data contaminated by extracted ESPI noise to predict the relative error that may be made when analysing the experimental simply supported plate data. The plate was centrally excited by a point force using the measured experimental force magnitude. To reduce the leakage effect, periodically truncated simply supported plate displacements were analysed only.

mode	$f_0$	$\eta \times \text{SNR}$	$(P_{in})_{F_{ss}}$	$2\omega\eta \int_S \langle e_{pot} \rangle_t dx dy$	$\Delta\epsilon$
(3,3)	428.7 Hz	0.25	$5.64 \cdot 10^{-6}$ W	$5.52 \cdot 10^{-6}$ W	2.16 %
(5,3)	711.6 Hz	0.19	$2.03 \cdot 10^{-5}$ W	$1.99 \cdot 10^{-5}$ W	2.07 %
(5,5)	1190.9 Hz	0.52	$1.08 \cdot 10^{-4}$ W	$1.06 \cdot 10^{-4}$ W	1.99 %
(7,5)	1615.2 Hz	0.53	$2.60 \cdot 10^{-4}$ W	$2.56 \cdot 10^{-4}$ W	1.53 %
(9,5)	2180.9 Hz	0.21	$2.97 \cdot 10^{-4}$ W	$3.09 \cdot 10^{-4}$ W	-4.13 %

**Table 11.8** Comparison of the theoretical input power  $(P_{in})_{F_{ss}}$  with the total transmitted energy within the plate computed from the integrated potential energy density of the non-layer damped simply supported plate.



mode	$f_0$	$\eta \times \text{SNR}$	$(P_{in})_{F_{ss}}$	$2\omega\eta \int_S \langle e_{pot} \rangle_t dx dy$	$\Delta\epsilon$
(3,3)	398.1 Hz	0.40	$4.85 \cdot 10^{-5}$ W	$4.80 \cdot 10^{-5}$ W	0.99 %
(5,3)	660.7 Hz	0.91	$8.58 \cdot 10^{-5}$ W	$8.49 \cdot 10^{-5}$ W	0.99 %
(5,5)	1105.7 Hz	1.14	$4.91 \cdot 10^{-4}$ W	$4.91 \cdot 10^{-4}$ W	0.01 %
(7,5)	1499.6 Hz	1.93	$7.48 \cdot 10^{-4}$ W	$7.65 \cdot 10^{-4}$ W	-2.17 %
(5,7)	1773.3 Hz	2.42	$1.24 \cdot 10^{-3}$ W	$1.23 \cdot 10^{-3}$ W	1.19 %

**Table 11.9** Comparison of the theoretical input power  $(P_{in})_{F_{ss}}$  with the total transmitted energy within the plate computed from the integrated potential energy density of the single-layer damped simply supported plate.

mode	$f_0$	$\eta \times \text{SNR}$	$(P_{in})_{F_{ss}}$	$2\omega\eta \int_S \langle e_{pot} \rangle_t dx dy$	$\Delta\epsilon$
(3,3)	412.1 Hz	0.38	$2.41 \cdot 10^{-5}$ W	$2.36 \cdot 10^{-5}$ W	1.97 %
(5,3)	684.0 Hz	1.13	$7.89 \cdot 10^{-5}$ W	$7.74 \cdot 10^{-5}$ W	1.96 %
(5,5)	1144.7 Hz	1.60	$2.26 \cdot 10^{-4}$ W	$2.21 \cdot 10^{-4}$ W	2.10 %
(7,5)	1552.6 Hz	0.93	$3.82 \cdot 10^{-4}$ W	$3.91 \cdot 10^{-4}$ W	-2.36 %
(5,7)	1835.9 Hz	1.50	$4.95 \cdot 10^{-4}$ W	$4.78 \cdot 10^{-4}$ W	3.41 %
(9,5)	2096.3 Hz	0.98	$9.60 \cdot 10^{-4}$ W	$1.01 \cdot 10^{-3}$ W	-5.55 %

**Table 11.10** Comparison of the theoretical input power  $(P_{in})_{F_{ss}}$  with the total transmitted energy within the plate computed from the integrated potential energy density of the checkerboard-layer damped simply supported plate.

Note, the damping layer attachment was modelled using the unconstrained layer theory introduced in section 10.4. Furthermore, also shown is the product of  $\eta \times \text{SNR}$  at which the relative errors may be expected.

The theoretical input power  $(P_{in})_{F_{ss}}$  was computed using equation (10.27). The potential energy density  $\langle e_{pot} \rangle_t$  was provided by the Butterworth filtered VEFESPI data. It can be seen from these tables above that the expected relative error computed as:

$$\Delta\varepsilon = \left( 1 - \frac{2\omega\eta \int_S \langle e_{pot} \rangle_t dx dy}{(P_{in})_{F_{ss}}} \right) \cdot 100\%, \quad (11.6)$$

is within a range of  $\pm 5\%$ . It can also be seen from the tables above that the energy balance within a plate is less sensitive towards noise contamination, since at different products of  $\eta \times \text{SNR}$  similar low errors were made. However, as shown in section 11.3.2, the computation of VEF pattern is much more sensitive towards the amount of noise contamination. Thus, the accuracy of the energy balance can be expected to be higher than the accuracy of the VEF pattern computation due to the use of second order spatial derivatives when integrating the potential energy density.

Finally, it can be concluded that VEF can be computed in plate structures even when a high standing wave environment or noise contamination is present. The computation of VEF from noise contaminated plate displacements that contained a low SWR was less critical. However, when dealing with noise contaminated plate displacements having a high SWR, the VEFESPI method was much more sensitive to noise. As expected, this sensitivity is a function of the structural damping  $\eta$  and the amount of noise contamination, i.e. SNR. Hence, the product of  $\eta \times \text{SNR}$  was suggested as an indicator of the VEF computability of the VEFESPI method. It was shown that the computation of the correct VEF direction was much more sensitive to the product of  $\eta \times \text{SNR}$  than the computation of TTVE.

# **12 MEASUREMENT OF VIBRATIONAL ENERGY IN PLATES: EXPERIMENTAL APPARATUS**

## **12.1 Introduction**

The aim of this chapter is to present the experimental plate apparatus used within this research to measure vibrational energy flow (VEF) in a force excited experimental “infinite” and a force excited experimental simply supported plate. Furthermore, the measurement setup employed during the experiment is introduced in detail. Also here, indirect vibrational energy measurements within the plate structures were carried out using conventional transducer based measurements as well as electronic speckle pattern interferometry (ESPI). Conventional transducer based measurements were undertaken to obtain energy based reference quantities, which are then used as a comparison measure to ESPI based VEF measurements. The ESPI measurement system employed during the plate experiments is the same as introduced in section 7.2.2.

## **12.2 Experimental Plate Apparatus**

In analogy to the beam measurements described previously, VEF in a force excited experimental “infinite” plate as well as a force excited experimental



simply supported plate were measured. The experimental “infinite” plate idealises finite structures with boundaries that dissipate almost all vibrational energy flowing towards the boundaries. Hence, large energy flows within the plate away from energy sources may be expected. In contrast, the experimental simply supported plate idealises a finite structure with almost no energy dissipation at the boundaries and, thus, very low net energy transmission within the plate may be expected due to the presence of a high standing wave environment.

### 12.2.1 “Infinite” Plate Rig

To measure VEF within a force excited experimental “infinite” plate a specially designed rig, as shown in Figure 12.1, was built. The rig was made predominately from high density fibreboard (HDF). The rig consisted of an upper and lower frame, which enclosed the rectangular plate specimen. The rectangular plate was made from mild steel, 1300 mm in length, 1100 mm in width and 1 mm in thickness. The upper and lower frame was further divided into an outer and an inner frame. The outer frame was 1500 mm in length,

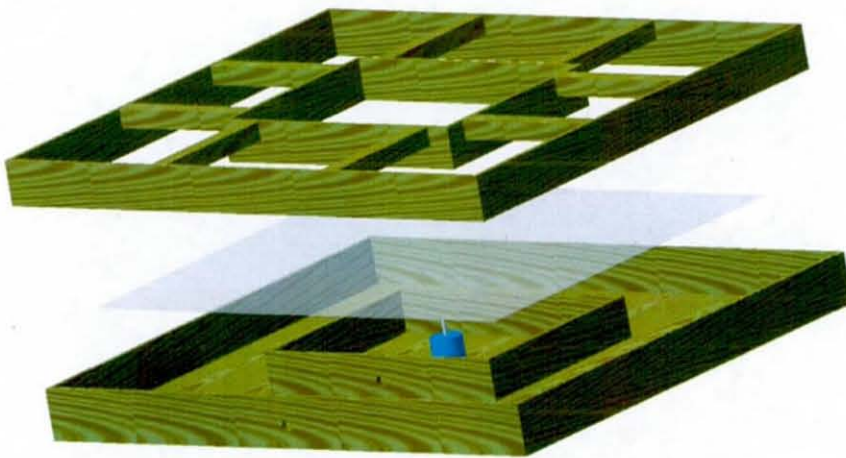


**Figure 12.1** Experimental “infinite” plate rig including the ESPI plate.

and 1300 mm in width and 120 mm in height. The inner frame had dimensions of 700 mm in length, 525 mm in width and 120 mm in height. Thus, a region of 700 mm by 525 mm of the plate was illuminated by the continuous 150 mW frequency doubled Nd:Yag laser addressed herein as ESPI window. During the experiment, the plate specimen was covered at one side by a reflection sheet to improve the reflection of the incident laser light. Between the inner and outer frames, kiln dried sand and foam wedges were inserted in order to provide an anechoic termination, as shown in Figure 7.5. The alignment of the foam wedges is shown in Figure 12.2. The ESPI plate was embedded between the inner and outer frame stretching 192 mm into the anechoic termination region. The length of 192 mm ensured that approximately one spatial wavelength of the lowest frequency to be measured was covered in sand. Usually half a wavelength embedding is required minimally. The lowest frequency to be measured was about 400 Hz due to limitations of the ESPI measurement system. The dimensions of the inner frame were chosen to be of a ratio of 4:3, exactly the same as the aspect ratio of the CCD camera. The rig was designed so that the ESPI displacement images of the “infinite” ESPI plate specimen were recorded from the top and

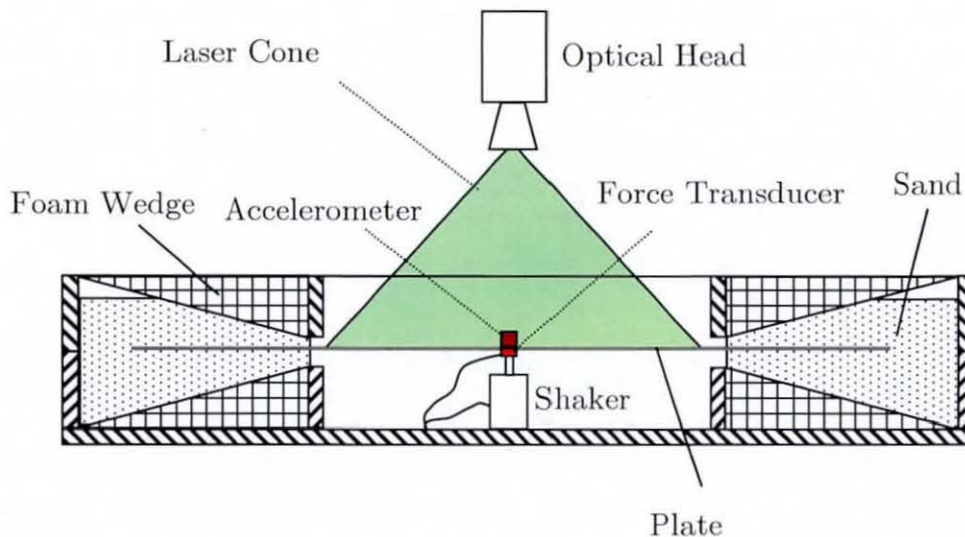


**Figure 12.2** Cross-sectional view of the force excited experimental “infinite” plate setup.



within the inner frame, as shown in Figure 12.2. This figure also displays the experimental setup of the “infinite” plate.

From Figure 12.2 it can be seen that the plate was excited at the bottom of the horizontally lying plate. The horizontal plate alignment ensured an effective anechoic termination process and easy access of the optical head to the plate specimen. However, connecting the electrodynamic shaker to the plate was rather complicated and time consuming. Also, checking was undertaken to ensure no vertical bending of the horizontal plate occurred due to its own weight, or the shaker attachment in its initial, non-excited position.

The plate was excited off-centre at a position  $x_0 = 550$  mm and  $y_0 = 600$  mm, measured from the left bottom corner of the plate. At the driving point (excitation location) vibrational input power (VIP) measurements were carried out in order to measure the energy injected into the plate using an accelerometer and a force transducer at that location. These signals were recorded on a multi-channel spectrum (LMS) analyser, which provided the required auto spectral and cross-spectral densities for further VIP computation.

### 12.2.2 Simply Supported Plate Rig

To achieve simply supported boundary conditions, a simply supported plate rig was designed that allowed rotational edge motion while restricting the plate's edge displacement. Figures 12.3, 12.4 and 12.5 display the simply supported plate rig at different views. The rig frame was predominately made from different standard steel profiles, ensuring a high mass compared to the plate specimen. It can be seen from Figures 12.4 and 12.5 that the plate was simply supported between two frames made from HDF material. The edges of the HDF frame are chamfered having a radius of 23.5 mm. A mild steel plate 647 mm in length, 497 mm in width and 3 mm in thickness was embedded horizontally. Also here, the forced plate displacement was recorded from the top by the ESPI system. The outer dimensions of the rig were 812 mm in length, 662 mm in width and 236 mm in height. During the experiment,

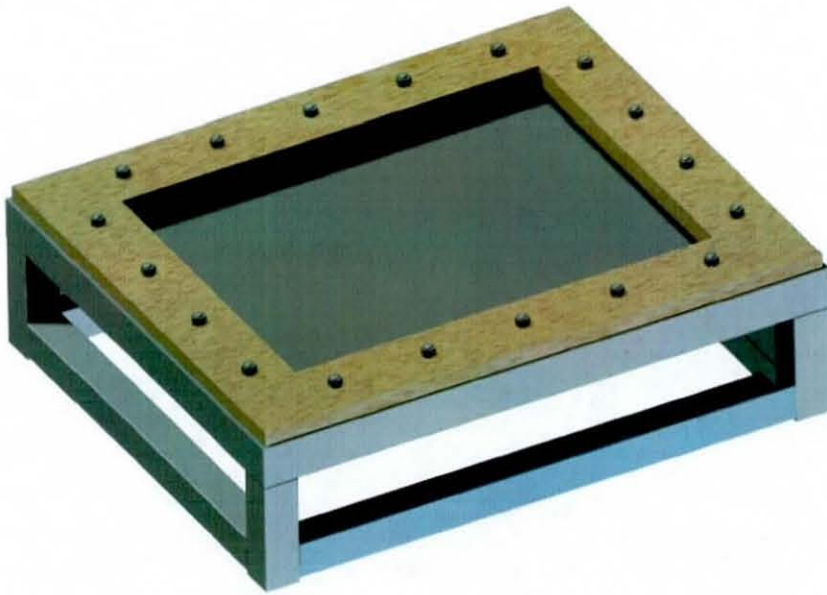


**Figure 12.3** Experimental simply supported plate rig including the ESPI plate.

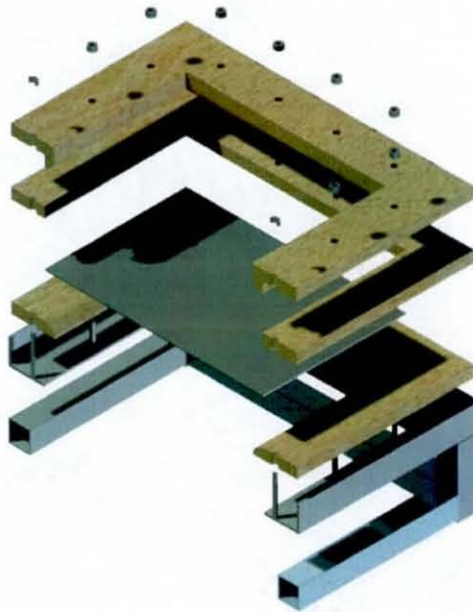


**Figure 12.4** Explosion view of half cut experimental simply supported plate rig including the ESPI plate.

transverse displacements of three differently damped plate specimens were measured. The damping was achieved by attaching an unconstrained damping layer to the plate's surface by using a mineral filled viscoelastic polymer layer. A non-layer damped plate, a single-layer damped plate, and a partially damped plate were measured. The surface of the single-layer damped plate was fully covered by the unconstrained damping layer. A checkerboard pattern of attached damping material patches was employed to partially reduce the vibration amplitude of the plate. Because the HDF frames were fastened by hexagon bolts, a fast plate change could be guaranteed. The plate was excited from the bottom, exactly at the centre of the plate. The centre excitation allowed even mode cancellation in order to reduce the selection of the excitation frequencies applied during the experiment. At the driving point an accelerometer and a force transducer

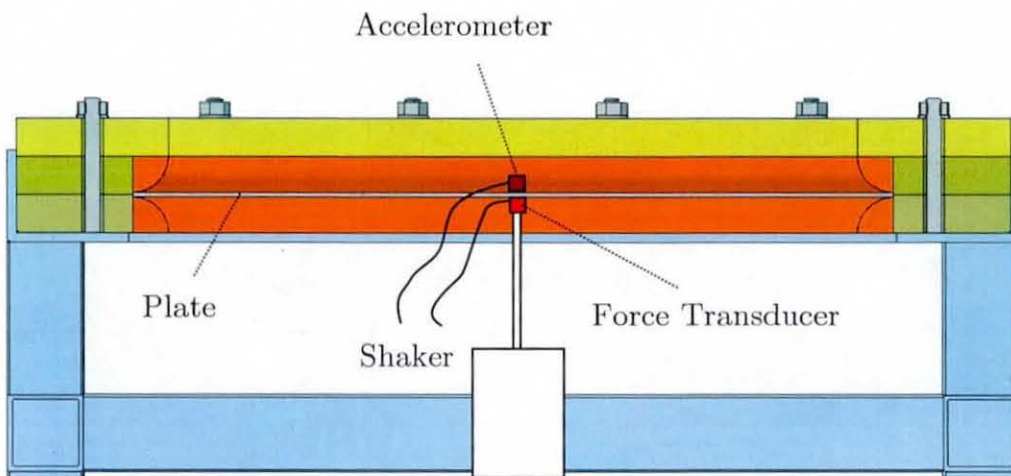


**Figure 12.5** Side view of half cut experimental simply supported plate rig including the ESPI plate.

were attached to measure the vibrational energy injected into the plate. These signals were recorded on a multi-channel spectrum (LMS) analyser that provided the required auto spectral and cross-spectral densities for further VIP computation. To ensure that the plate vibrations did not



interfere with an undesired rig vibration, the rig was loaded with additional weights at its corners to ensure a stationary position during the experiment.

### 12.3 Summary

This chapter has briefly presented the experimental equipment employed throughout the “infinite” plate and simply supported plate experiment. Herein, transverse plate displacements are recorded with the aid of an ESPI system.

The “infinite” plate rig was designed to embed the plate horizontally within an anechoic termination region, to dissipate vibrational energy injected into the plate with the aid of an electrodynamic shaker. During the experiment it had to be ensured that the non-excited plate was positioned in an exact horizontal and even level.

The simply supported rig was designed to also embed the plate specimen horizontally. However, here the simply supported boundary conditions were achieved by suspending the plate between two chamfered frames, made from HDF material. Furthermore, and in contrast to the “infinite” plate rig, the chamfered HDF frames had to ensure non-dissipative simply supported boundary conditions. The rig was designed to be rigid compared to the transverse vibration of the plate. Additional weights during the experiment were used to ensure a stationary experiment.

The author would like to acknowledge that the measurements were undertaken at the Applied Optics Laboratory at Land Rover at Gaydon under the direction of the author.

# **13 MEASUREMENT OF VIBRATIONAL ENERGY IN PLATES: MEASUREMENT METHODS**

## **13.1 Introduction**

The aim of this chapter is to introduce the methods of measuring point mobility, vibrational input power (VIP) and vibrational energy flow (VEF) in an experimental “infinite” plate and an experimental simply supported plate, using the apparatus introduced in chapter 12. Since the measurement methods employed during the plate experiments are similar to the methods employed during the beam experiments, a brief introduction will be given only.

During the plate experiments two-dimensional VEF was measured indirectly from the transverse out-of plane plate displacements that were recorded by an electronic speckle pattern interferometry (ESPI) system. To assess the accuracy of the ESPI based VEF measurement (VEFESPI) method, conventional transducer based VIP measurements at the excitation location were also carried out. The measured input power was then used as a reference quantity in a simple vibrational energy balance analysis carried out in combination with measured VEFESPI based quantities.



13.2 Force Excited Plate Measurements

13.2.1 Point Mobility Measurements

Measurement of the point mobility of plates is carried out in this research analogously to the measurement of point mobility of a beam by attaching a force transducer and an accelerometer at the excitation location and measuring the well known  $H_1(f)$  estimator. As shown in section 8.2.1, the measured point mobility of plates can be computed as:

$$Y_F = \frac{1}{j2\pi f} \frac{G(F_0, a_0)}{G(F_0, F_0)}.$$
 (8.1)

Here,  $G(F_0, a_0)$  is the cross-spectral density between the excitation force and driving point acceleration and  $G(F_0, F_0)$  is the auto power spectral density of the excitation force. The ratio  $G(F_0, a_0)/G(F_0, F_0)$  is measured by a multi-channel spectrum analyser using spectrally-averaged frequency response functions (FRF). Point mobility measurements can be used to compute VIP but can also be used to assess the operational range of the respective employed plate apparatus. Table 13.1 displays the operational parameters employed during the measurement of the point mobility in an “infinite” plate and a simply supported plate.

	“Infinite” plate	Simply supported plate
Frequency range	0 - 6400 Hz	0 - 4096 Hz
Frequency resolution	2 Hz	0.5 Hz
Number of averages	15	30

**Table 13.1** Operational parameters employed during the point mobility measurements.

### 13.2.2 Vibrational Input Power Measurements

One advantage of measuring VEF with an ESPI system is that two-dimensional energy flow information can be obtained for a large region within the plate. However, it is too cumbersome to make a VEF comparison between measured ESPI based VEF and measured accelerometer based transmitted energy.

To assess the accuracy, the measured ESPI based VEF is compared with conventional measured transducer based VIP. Thus, the measured amount of energy injected into the plate structure is used herein to assess the accuracy of the ESPI based VEF quantities using simple energy balance analysis for both structures, “infinite” plate and simply supported plate.

Usually, VIP is measured using the imaginary part of the measured one-sided cross-spectral density between the driving force and the resulting acceleration, as displayed by Equation (3.27). However, during the “infinite” plate experiment an erroneous force signal was recorded. Thus, the imaginary part of the measured one-sided cross-spectral density between the driving force and the resulting acceleration cannot be used to compute measured VIP. An alternative approach is employed instead using the impedance of the theoretical infinite beam. From equation (10.2) the theoretical point mobility of a point force excited infinite beam is given by:

$$Y_{F_\infty} = \frac{1}{8h^2} \sqrt{\frac{12(1-\nu^2)}{E\rho}}. \quad (13.1)$$

It is well known that the theoretical mechanical impedance is inverse proportional to the theoretical mechanical mobility [103]. Similarly to equation (3.23) and by employing the mechanical point impedance, VIP to a structure can be written as:

$$(P_m)_F = \frac{1}{2} |v_0|^2 \Re \{ Z_{F_0, \underline{v}_0} \}. \quad (13.2)$$

Here,  $v_0$  is the point velocity of the structure at the excitation location  $x_0$  and  $Z_{E_0,x_0}$  is the theoretical point impedance. Using equations (13.1) and (13.2) and taking into account that  $Y_{F_\infty} = (Z_{F_\infty})^{-1}$ , VIP to an infinite beam can be written as:

$$(P_m)_{F_\infty} = 4|v_0|^2 h^2 \sqrt{\frac{E\rho}{12(1-\nu^2)}}. \tag{13.3}$$

Equation (13.3) displays the equation to measure VIP of an “infinite” plate by using the measured point velocity  $v_0$  at the excitation location. This quantity is obtained from the measured auto spectral density of the driving point acceleration as  $|v_0|^2 = (j2\pi f)^{-1} G(a_0,a_0)$ , where  $G(a_0,a_0)$  is the auto power spectral density of the driving point acceleration.

VIP to the simply supported beam is measured herein by using equation (3.27) as:

$$(P_m)_F = \frac{1}{2\pi f} \Im \{G(F_0,a_0)\}. \tag{3.27}$$

Here,  $G(F_0,a_0)$  is the cross-spectral density of the driving force and driving acceleration. Table 13.2 displays the operational parameters employed during the VIP measurement.

	“Infinite” plate	Simply supported plate
Frequency range [Hz]	0 - 4096 Hz	0 - 4096 Hz
Frequency resolution [Hz]	0.25 Hz	0.5 Hz
Number of averages	50	30

**Table 13.2** Operational parameters employed during the input power measurements.



### 13.2.3 Vibrational Energy Flow Measurements Using ESPI

Analogously to the description given in section 8.2.4, the transverse time-averaged ESPI measured complex plate displacement is generated as:

$$w(x,y)_{ESPI} = A(x,y)e^{j\phi(x,y)}. \quad (13.4)$$

Herein,  $A(x,y)$  is the measured two-dimensional ESPI amplitude of the plate and  $\phi(x,y)$  is the measured two-dimensional ESPI phase of the plate. This generated complex plate displacement is then taken as the input to the VEFESPI method in order to determine spatial derivatives and subsequently, VEF from the ESPI recorded transverse plate displacement.

### 13.2.4 Application of the Measurement Methods to a Plate

The point mobility of the “infinite” and simply supported plate was measured by using equation (8.1). During the point mobility measurements of the “infinite” plate, problems occurred while using an electrodynamic shaker. The author believes that these problems may have occurred due the use of a very thin plate, lying horizontally in the rig. Thus, point mobility measurements of the “infinite” plate were carried out using an impact hammer rather than an electrodynamic shaker. The point mobility measurement of the simply supported plate was conducted using an electrodynamic shaker.

VIP to the force excited “infinite” plate was measured using equation (13.3). VIP to the force excited simply supported plate was measured using the well known cross-spectral density based expression shown by equation (3.27).

VEF within an “infinite” and simply supported plate is measured in this research indirectly by using ESPI recorded transverse plate displacements. Thus, the transverse ESPI plate displacement was generated by employing equation (13.4) from prior acquired ESPI amplitude and ESPI phase information. The generated complex, two-dimensional ESPI

displacement was then taken as the input to the VEFESPI method, as described in chapter 4. Unfortunately, the generated ESPI displacement contained recorded regions that included no displacement information due to a laser illumination larger than the ESPI window of the respective plate structure. These regions required spatial truncation. Further, the “infinite” plate data were truncated symmetrically around the off-centre excitation location to ensure a symmetric number of wavelengths included in the signal. After the displacement truncation, the  $k$ -space derivation (KSD) method was employed as a part of the VEFESPI method. Thus, spectral derivatives were computed by employing a 2D fast Fourier transform (FFT), according to equation (4.5), to transform the spatial displacement data into the wavenumber domain. The spectral derivation process within the wavenumber domain was carried out, as shown in the bracket term on the right-hand side of equation (4.9). Of course, spectral noise components were removed within the wavenumber domain prior to the spectral derivation process by employing either the ideal 2D filtering process or the oval 2D Butterworth filter. After applying the inverse 2D FFT of the filtered and spectrally derived wavenumber data, spatial derivative components of different orders were substituted into equation (3.49) and (3.50), respectively, to compute VEF of the “infinite” and simply supported plate in the  $x$  and  $y$  directions.

### 13.3 Summary

This chapter briefly presented the measurement methods used to measure point mobility, VIP and ESPI based VEF of “infinite” and simply supported plate structures. Transducer based VIP measurements were conducted to assess the accuracy of the VEFESPI method using simple energy balance analysis, as described in chapter 3. Point mobility measurements were carried out to assess the operational ranges of the respective plate apparatus. The ESPI recorded complex plate displacement was used as an input to the VEFESPI method in order to determine VEF indirectly from ESPI measured displacement information.



# **14 MEASUREMENT OF VIBRATIONAL ENERGY IN PLATES: EXPERIMENTAL RESULTS**

## **14.1 Introduction**

This chapter presents results obtained from the measurement of vibrational energy in a force excited experimental “infinite” plate and a force excited experimental simply supported plate. Vibrational energy flow (VEF) has been measured indirectly from electronic speckle pattern interferometry (ESPI) recorded plate displacements. Energy balances between ESPI measured energy quantities and transducer measured vibrational input power (VIP) quantities are carried out in order to assess the accuracy of the VEF measurement technique using ESPI (VEFESPI).

## **14.2 Force Excited Plate Measurements**

Analogously to section 9.2, this section is divided into two parts presenting results obtained from force excited plate measurements. Section 14.2.1 contains the results obtained on a force excited experimental “infinite” plate. Section 14.2.2 presents results obtained from the measurement of a force excited experimental simply supported plate. In both sections VEF maps from ESPI measured displacement data and energy balances are shown.

## 14.2.1 “Infinite” Plate Measurements

### 14.2.1.1 Point Mobility and Vibrational Input Power Measurements

As mentioned previously, problems occurred during the point mobility measurement of the “infinite” plate when using an electrodynamic shaker. Thus, an impact hammer was employed to measure point mobility of the “infinite” plate, instead of using an electrodynamic exciter to excite the structure. Figure 14.1 displays the theoretical point mobility computed from equation (10.2) and the measured point mobility computed from equation (8.1). Here,  $f$  shown on the  $x$ -axis is denoted as the frequency. It can be seen from Figure 14.1(a) that with increasing frequency the measured point

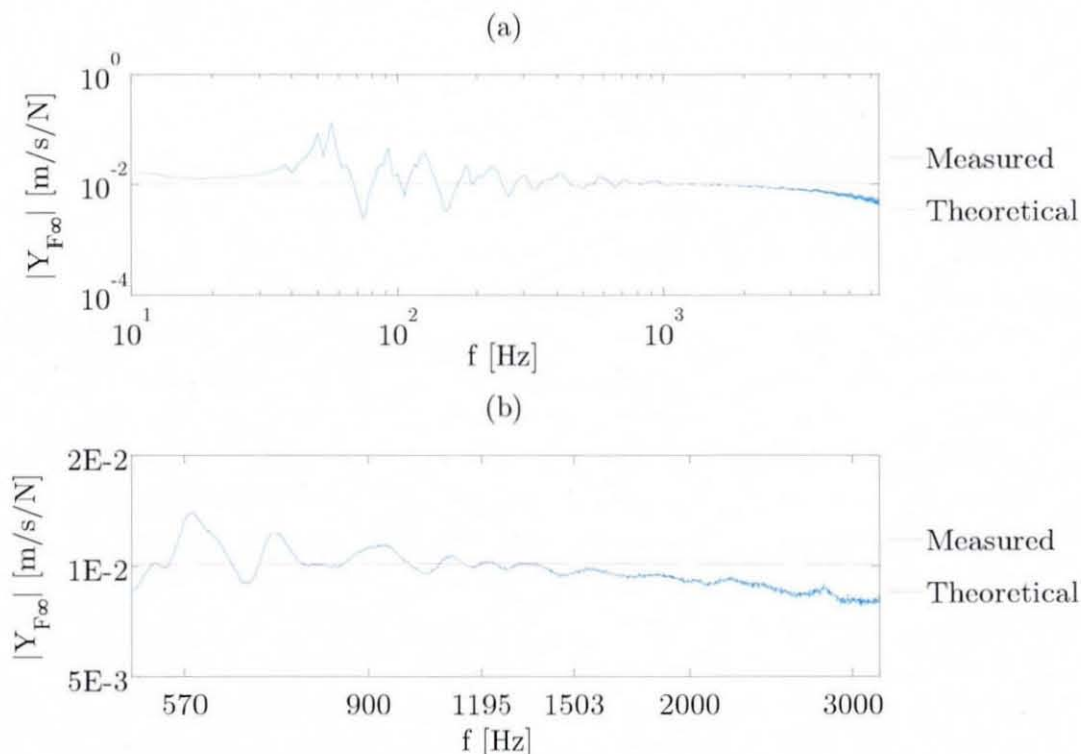


**Figure 14.1** Modulus of the measured and theoretical point mobility of the force excited “infinite” ESPI plate: (a) 10 Hz-6.4 kHz, (b) 500-3200 Hz.

mobility curve drops in amplitude compared to the theoretical point mobility solution. Since the accuracy of impact based measurements depends on the time of impact and, thus, the frequency location of the first zero in the

applied force spectra, impact measurements at high frequencies are considered to be not very accurate. From the theoretical solution it can be realised that the point mobility of an infinite plate is independent upon frequency. Also, at the lower frequencies some resonant plate behaviour is still present indicating a lower degree of damping achieved by the anechoic termination and, thus, undesired reflections occur on the plate's boundaries. However, this result is not surprising, since the rig was designed to effectively dissipate vibrational energy at frequencies greater than 400 Hz. This effect can be seen in Figure 14.1(b) where the theoretical infinite plate point mobility matches well with the measured "infinite" plate point mobility within the frequency range where the ESPI measurements were conducted. At five selected excitation frequencies,  $f_0$ , experimental "infinite" plate displacements were recorded using the ESPI system, introduced in section 7.2.2. The excitation frequencies  $f_0$  as well as the computed vibrational input power values are shown in Table 14.1.

$f_0$	569.7 Hz	605.6 Hz	899.5 Hz	1194.4 Hz	1503.2 Hz
$(P_m)_{F_\infty}$	$1.49 \cdot 10^{-5}$	$4.79 \cdot 10^{-5}$	$1.73 \cdot 10^{-4}$	$2.45 \cdot 10^{-4}$	$2.35 \cdot 10^{-4}$

**Table 14.1** Measured vibrational input power (all power values given in units of Watts).

It can be seen that the VIP quantities  $(P_m)_{F_\infty}$ , computed from equation (13.3), are very low power values especially at the lower frequencies, indicating a low vibrational energy input into the plate structure. Note, the measured point mobility, as shown in Figure 14.1, is not the point mobility measured during the ESPI experiment. During the ESPI experiment a shaker was attached to the experimental "infinite" plate and the measured point mobility curve constantly decreased with increasing frequency. This unexpected point mobility curve shape might be due to the attachment of a relatively large force transducer attachment area in relation to a very small plate thickness. The excitation frequency of the 569.7 Hz measurement was



selected to be located at a local minimum of the frequency response function (FRF). The excitation frequencies of 605.6 Hz and 899.5 Hz were selected to represent a local maximum of the FRF. The remaining two frequencies were located close to the theoretical infinite plate response. Table 11.1 displays again the assumed properties of the experimental ESPI plate.

Young's modulus	$E = 2.07 \cdot 10^{11} \text{ N/m}^2$
mass density	$\rho = 7.85 \cdot 10^3 \text{ kg/m}^3$
plate thickness	$h = 1 \cdot 10^{-3} \text{ m}$
Poisson ratio	$\nu = 0.33$

**Table 11.1** (repeated) “Infinite” ESPI plate properties.

#### 14.2.1.2 Vibrational Energy Flow Measurements Using ESPI

Due to shortage in thesis space the graphical results of the measurement of VEF within the “infinite” plate are presented for two excitation frequencies only. The entire measurement results of the “infinite” plate experiment are shown in Appendix A30.

Analogously to the ESPI based VEF computation procedure described in section 13.2.4, the ESPI measured amplitude and ESPI measured phase were used to generate the desired complex ESPI displacement of the experimental “infinite” plate, using equation (13.4). Figure 14.2 displays the amplitude and phase at 1503 Hz, as acquired and provided by the ESPI system. Here, it can be seen that within the ESPI window some blank regions appear (dark blue) indicating a low laser light illumination. Within these regions, transverse displacement information is missing and the initial recorded amplitude and phase matrices need to be truncated in order to provide the VEFESPI method with as much useful information as possible. Clearly, from the recorded ESPI phase shown in Figure 14.2(b), it can be realised that a radially symmetric wave is travelling away from the excitation

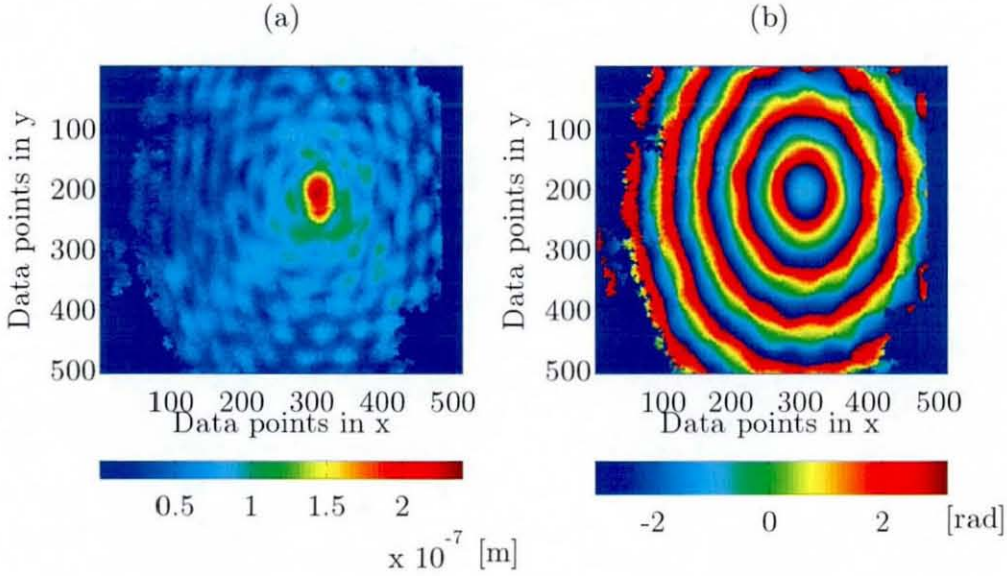


**Figure 14.2** ESPI image of the measured “infinite” plate displacement at 1503 Hz: (a) amplitude, (b) phase.

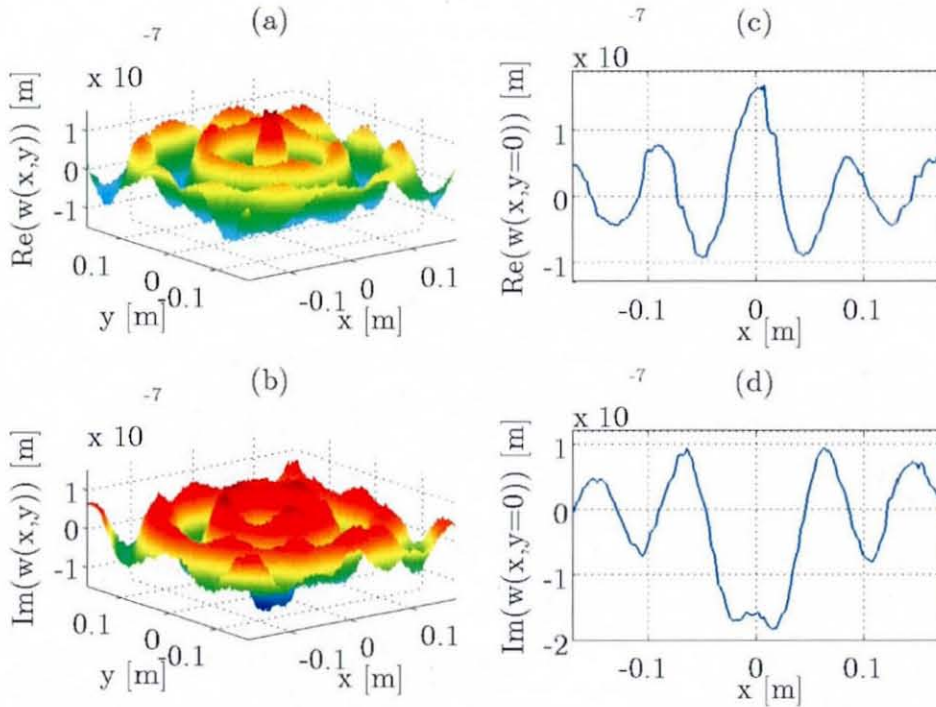


**Figure 14.3** ESPI image of the measured and truncated “infinite” plate displacement at 1503 Hz: (a) 2D real part, (b) 2D imaginary part, (c) real part at  $y = 0$ , (d) imaginary part at  $y = 0$ .



location. Thus, the rig worked well at this particular excitation frequency. It can be realised from the displacement figures shown in Appendix A30 that the operationability of the rig increased with increasing excitation frequency.

Figures 14.3(a)-(b) display the recorded and truncated two-dimensional transverse ESPI displacement. Figures 14.3(c)-(d) show a cross-section of the transverse ESPI displacement along  $y = 0$ . The one-dimensional displacement curve at  $y = 0$  is presented to point out the effect of optical noise, which clearly can be seen.

Figure 14.4 shows the top view ESPI image of the truncated ESPI displacement at 1503 Hz. It can be noticed that the displacement is symmetrically truncated around the excitation location. Furthermore,

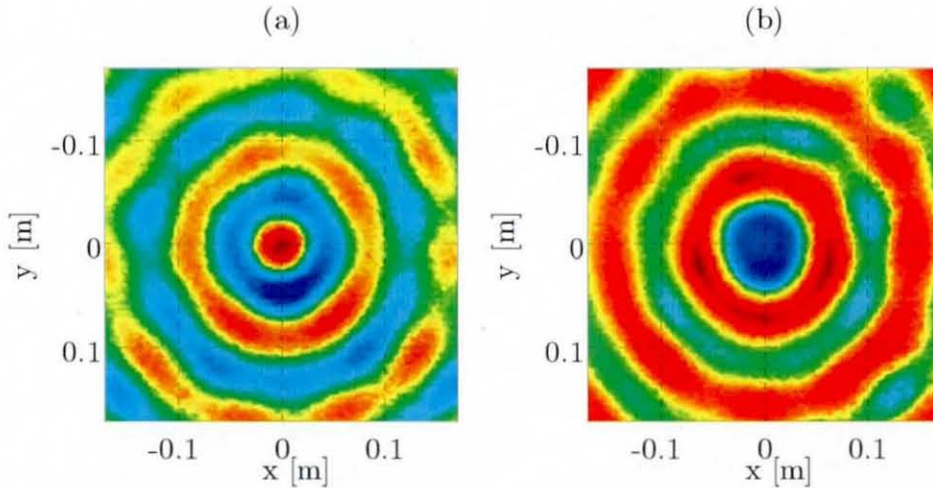


**Figure 14.4** Top view image of the complex “infinite” plate displacement shown in Figure 14.3: (a) real part, (b) imaginary part.

approximately two waves are included within the truncated ESPI signal. Also here, the radially symmetric wave propagation can be recognised.

The truncated plate displacement, as shown in Figures 14.3 and 14.4, is used as an input to the VEFESPI method. Thus, spatial derivatives were determined from measured data, which were then substituted into equation (3.49) and (3.50), respectively. Within the wavenumber domain, a spectral filtering of the plate displacement was carried out prior to the spectral derivation process, using the ideal 2D filtering process and the oval 2D

Butterworth filter. Figure 14.5 displays the complex, “infinite” plate displacement at 1503 Hz, filtered by the previously mentioned two filter types, using the optimum filter cut-off points shown in Table 11.3. It can be

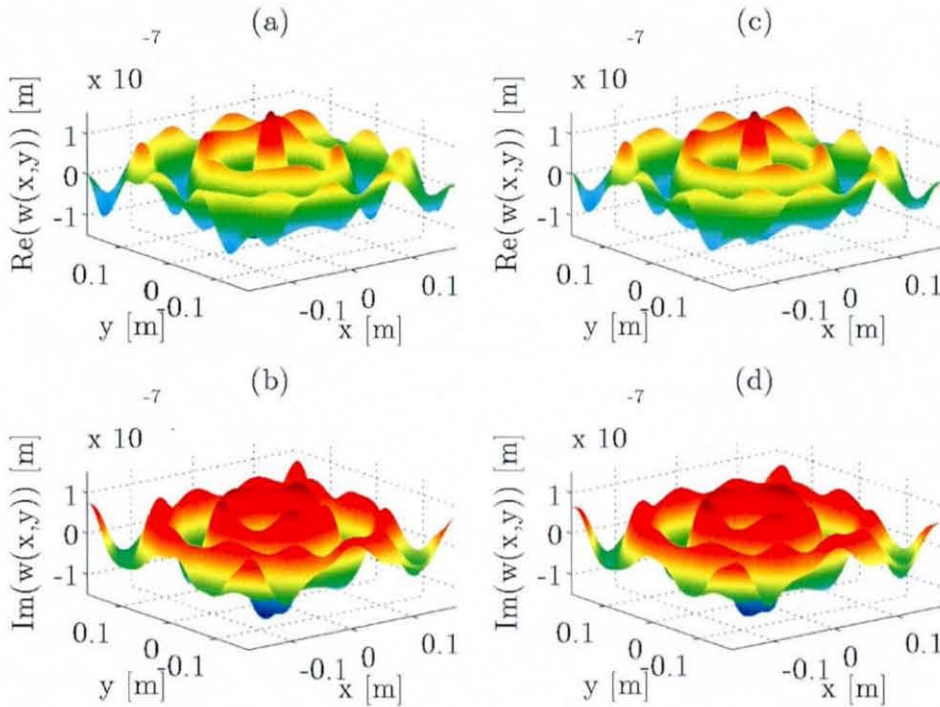
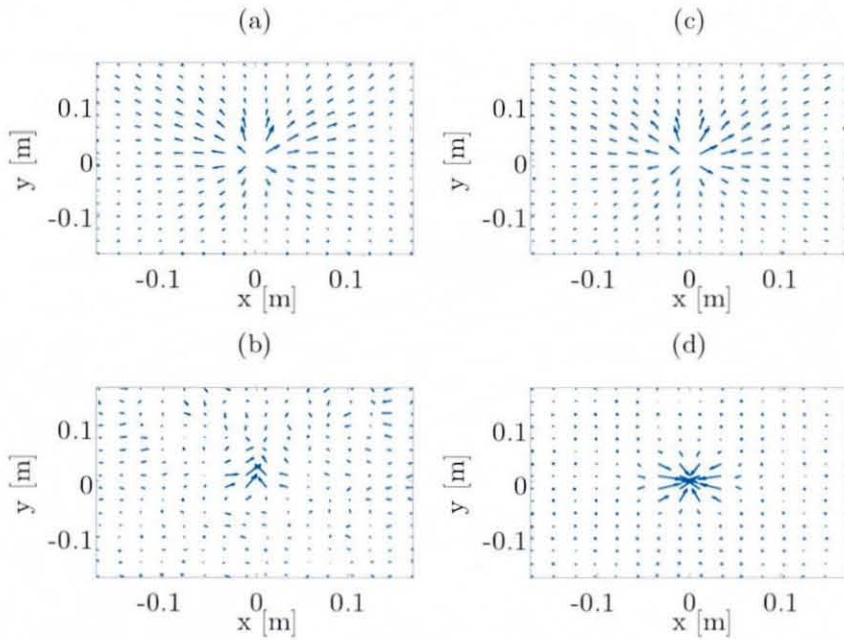


**Figure 14.5** Filtered complex “infinite” plate displacement at 1503 Hz: (a)-(b) ideal 2D filtered, (c)-(d) 2D Butterworth filtered.

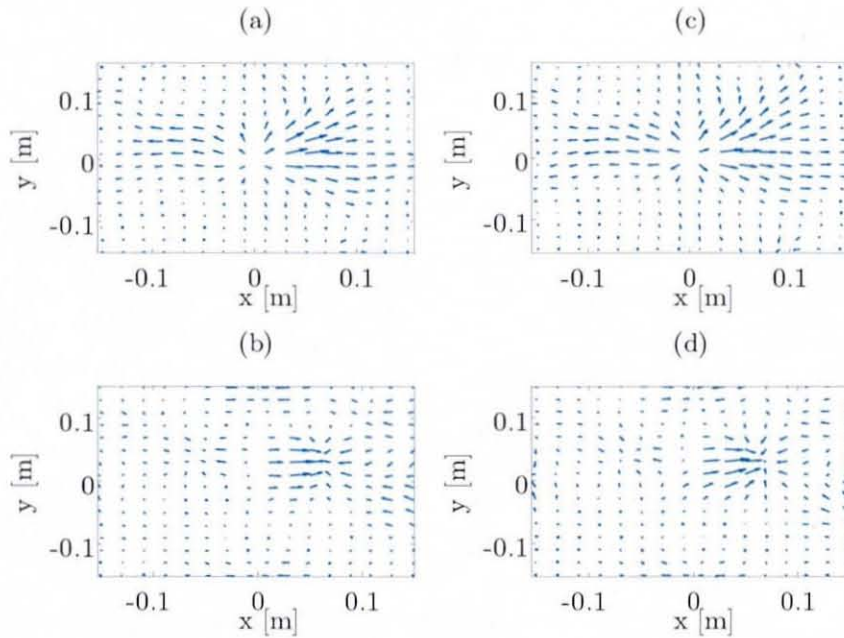
seen that the noise components are removed. Also, both types of filter produced similar results.

Figure 14.6 shows the filtered active and reactive VEF maps, as a result of applying the VEFESPI method to the 1503 Hz measurement. It can be noticed from this figure that the active energy flows radially away from the excitation location, as expected. Both filter types also produced similar VEF results. In contrast to the 1503 Hz measurement, the plate displacement recorded at 605.6 Hz contained reflections. These are visible in Figure A30.6.

Figure 14.7 displays the VEF maps obtained from the ESPI plate displacement recorded at 605.6 Hz. It can be noticed from Figure 14.7 that the active energy also flows radially away from the excitation location,



**Figure 14.6** Filtered VEF maps of the “infinite” plate displacement at 1503 Hz: (a) active VEF – ideal filter, (b) reactive VEF – ideal filter, (c) active VEF – Butterworth filter, (d) reactive VEF – Butterworth filter.



**Figure 14.7** Filtered VEF maps of the “infinite” plate displacement at 605.6 Hz: (a) active VEF – ideal filter, (b) reactive VEF – ideal filter, (c) active VEF – Butterworth filter, (d) reactive VEF – Butterworth filter.



however, with increasing distance some dominant energy flow paths arise where more vibrational energy travels towards the anechoic termination. Interestingly, the reactive VEF map is more distinctive than the reactive VEF map, as shown in Figure 14.6. This indicates that a certain amount of the initial travelling radial wave is reflected at the plate's boundaries and, thus, some standing waves were created within the experimental "infinite" plate. Also here, the ideal 2D filter and the oval 2D Butterworth filter produced similar VEF results. The filtering of the reactive VEF was undertaken using a trial and error procedure, since no parameter optimisation was carried out. Note, the number of data points in Figures 14.6 and 14.7 were reduced for better visibility.

#### 14.2.1.3 Energy Balance

The energy balance within the experimental "infinite" plate is carried out, as demonstrated in section 11.2. It is evident from equation (10.9) that the integration of the active VEF around a closed contour is equal to the VIP injected into the plate. Thus, here the ESPI measured VEF in the  $x$  and  $y$  directions is integrated around the excitation location for each location  $|kr|$ , by numerically evaluating equation (10.18). The result of such a contour integration is the total transmitted vibrational energy (TTVE) through this

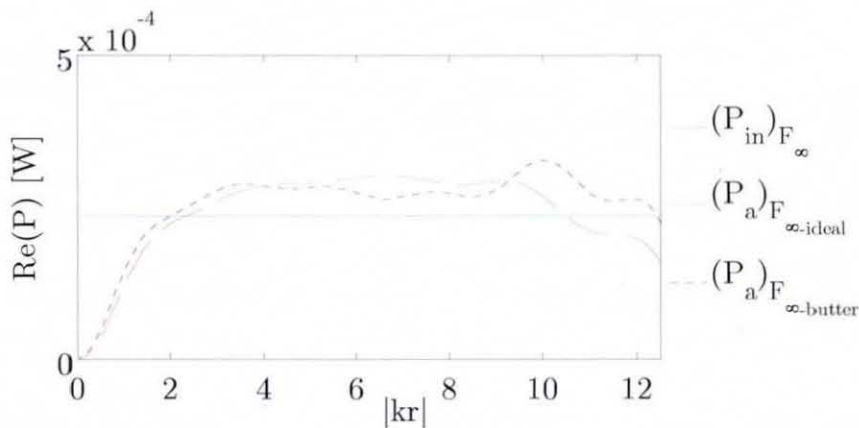


**Figure 14.8** Comparison of total transmitted ESPI measured active VEF and vibrational input power at 1503 Hz.

particular contour  $(P_a)_{F_\infty}$ . From equation (10.9) it is evident that  $\Re\{\langle P_{in} \rangle_t\} = (P_a)_{F_\infty}$ . Figure 14.8 displays the result of the contour integration carried out at each numerical location  $|kr|$  within the ESPI measured “infinite” plate, at 1503 Hz for both filters. It can be seen from Figure 14.8 that the TTVE is close to the measured VIP. Figure 14.9 displays the same

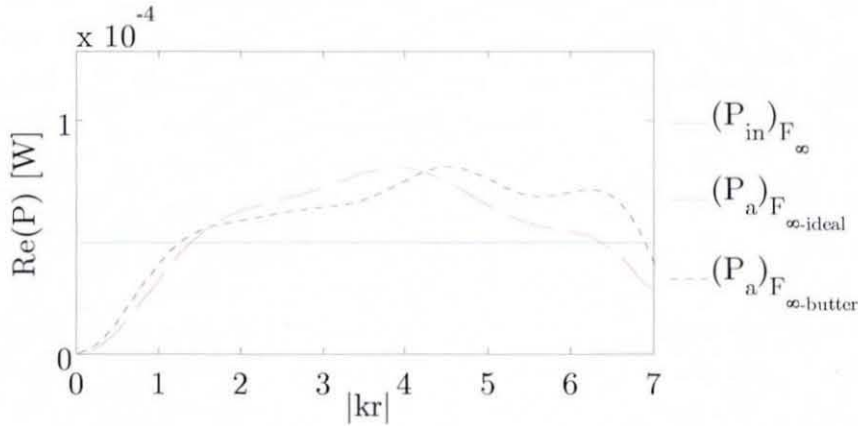


**Figure 14.9** Comparison of total transmitted ESPI measured active VEF and vibrational input power at 605.6 Hz.

properties for the 605.6 Hz measurement. It can be noticed from Figure 14.9 that the TTVE at each numerical location  $|kr|$  is also close to the VIP injected into the plate. At both measurements it can be realised that at the excitation location  $|kr| = 0$  the TTVE is equal to zero. This problem occurs

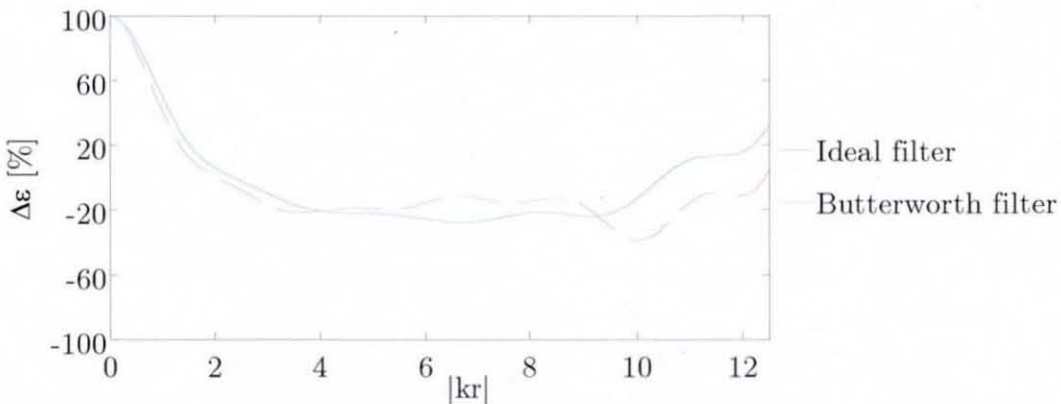


**Figure 14.10** Relative difference in percent between total transmitted ESPI measured power and measured VIP at 1503 Hz.



due to the numerical integration at the excitation location, since only four points were included. Thus, at close locations, i.e.  $|kr| < 1$ , the numerical integration process leads to large errors due to the inclusion of very few VEF

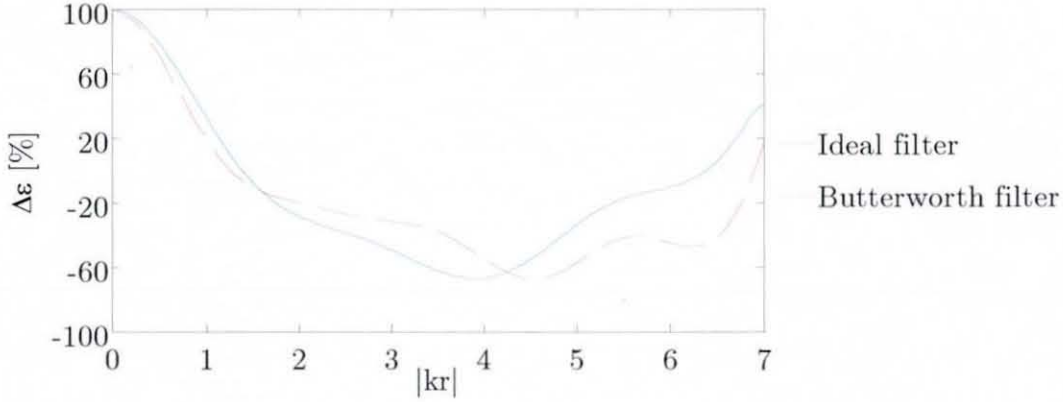


**Figure 14.11** Relative difference in percent between total transmitted ESPI measured power and measured VIP at 605.6 Hz.

points. However, in both figures it can be seen that the ESPI measured TTVE is close to the measured VIP. Figures 14.10 and 14.11 display the relative difference  $\Delta\varepsilon$  between the ESPI measured TTVE  $(P_a)_{F_\infty}$  and the measured VIP  $(P_m)_{F_\infty}$ , computed as:

$$\Delta\varepsilon = \left(1 - (P_a)_{F_\infty} / (P_m)_{F_\infty}\right) \cdot 100\%. \quad (14.1)$$

It can be noticed by comparing both figures that less difference between both quantities occurred at the higher excitation frequency. Note, the relative differences of all frequencies are shown in Appendix A30.

#### 14.2.1.4 Discussion

This section has reported on the computation of VEF within an experimental “infinite” plate. Five frequencies within a range of 570 Hz to 1503 Hz were analysed. The energy flow within the plate was computed from prior recorded “infinite” plate displacements, acquired with an ESPI system. Active and

reactive VEF maps were presented for two selected frequencies. VEF measurement results of all five frequencies are shown in Appendix A30.

From the point mobility plot of Figure 14.1, and the ESPI amplitude and ESPI phase maps shown in Appendix A30, it can be realised that the experimental “infinite” plate rig increased its anechoic efficiency with increasing frequency. At higher frequencies, infinite plate behaviour could be simulated much better and, thus, at the excitation frequencies of 899.5 Hz, 1194.4 Hz and 1503.2 Hz a good “infinite” plate response was recorded. However, at the excitation frequencies of 569.7 Hz and 605.6 Hz some reflections at the embedded plate’s edge created a mixture between infinite and finite plate response.

From the VEF map figures presented above and in Appendix A30, it can be realised that the active VEF radially flows away from the excitation location. However, at 569.7 Hz and 605.6 Hz some dominant paths can clearly be detected. These dominant paths are due to a higher amount of wave reflection at the plate’s boundaries or a different amount of energy dissipation within the anechoic termination region. This conclusion may be underlined by the consideration of the reactive VEF maps, which are more distinctive at these two frequencies. This reactive VEF behaviour is typical for finite plate structures. At the higher excitation frequencies a more symmetric radial active energy flow could be measured. This indicates that the experimental plate vibration was much closer to an infinite plate response. However, at all five frequencies very good VEF maps were computed with a determined VEF pattern, as expected.

The use of the ideal 2D filter and the oval 2D Butterworth filter yielded to similar VEF results in active energy flow computation. However, the reactive energy flow determination differed slightly from each other, whereas the ideal filter failed to detect the distinctive reactive energy sink about the excitation location at frequencies where the experimental plate response was close to the infinite plate response. At these frequencies the Butterworth filter delivered much better results.

To assess the accuracy of the ESPI measured VEF, the active VEF maps were integrated along a closed line by using a closed square contour

about the excitation location. This procedure was carried out at  $N/2$  numbers of closed contours about the excitation location, where  $N$  is the number of data points within the active VEF map. To relate the result of the line integrations to an axis, a quantity denoted as  $|kr|$  was introduced. This quantity can be seen as a non-dimensional spatial frequency similar to the Helmholtz number. The closed line integration resulted in the total vibrational energy transmitted through that particular contour. From equation (10.9) and (3.59), respectively, it was then assumed that the total transmitted energy is equal to the input power. This relation is true for all the contour integrations within the active VEF map.

Figures 14.8 and 14.9, as well as the figures in Appendix A.30, showed the comparison between the ESPI based TTVE and the transducer based VIP. In theory both lines should be constant over the  $|kr|$  range and equal in magnitude. It can be realised from these figures that at 899.5 Hz, 1194.4 Hz, and 1503.2 Hz a good agreement between both measures was achieved, with differences being in a range of  $\pm 20\%$ . However, at 569.7 Hz and 605.6 Hz larger deviations between both quantities were obtained. In the following some sources of errors that may have led to these differences will be explained.

From Figures A30.1 and A30.6 it can be realised that especially at 569.7 Hz and 605.6 Hz a larger amount of reflection within the experimental plate displacement occurred and, thus, a standing wave environment to some extent was present. However, equation (10.9) is only true for pure infinite wave motion. If larger reflections within the plate are present, equations (10.9) or (3.59) are not valid. Under this circumstance, the energy balance shown by equation (3.3) needs to be taken into account and the contour integrated TTVE is not equal to the VIP. This might be one reason for a larger difference between TTVE and VIP at these two frequencies.

The VIP measurement based on the theoretical infinite plate impedance is considered here not to be very accurate as it assumes pure infinite plate behaviour, something that is not true for an experimental "infinite" plate structure. As shown by Figure 14.1, it can be noticed that,



especially at the lower frequencies, deviations between the measured point mobility and theoretical point mobility occur.

Measured VIP has been computed here by using equation (13.3). It can be seen from equation (13.3) that material properties of the plate needed to be substituted into this expression. The material properties of the plate were assumed by the author within this work. Differences to the plate's true material properties can be expected.

Furthermore, as explained in section 9.2.1.4, the knowledge of the true spatial resolution or spatial sampling interval of the ESPI system employed during the ESPI experiment is crucial for VEF measurements. Here, the spatial resolution of the conducted ESPI measurements was determined from the length of the ESPI window and the number of data points included in it, i.e.  $\Delta x = L_x/N_x$ . Again spatial resolution errors are likely to be made by the simple assumption  $\Delta x = L_x/N_x$  and, as shown in Figure 9.8, deviation to the true ESPI measured VEF may be likely.

Due to a large number of blank regions present within the acquired ESPI amplitude and phase maps (see Appendix A.30), the usable spatial range of the measured plate displacement was restricted. This restriction was forced by truncating the data around the off centre excitation location. At the 569.7 Hz and 605.6 Hz measurements approximately one wavelength of displacement data could be included only. In particular, the 569.7 Hz measurement contained a very small spatial range of data, as shown in Figure A30.2. This small range of spatial data may have resulted in a further source of error, since at least one wavelength needed to be included when employing the Fourier transform. However, at 569.7 Hz a full wavelength of displacement data could not be identified clearly due to the large amount of standing waves present in the recorded ESPI displacement signal.

Finally, a few remarks will be given to the measurement of ESPI based VEF in "infinite" plates. It was demonstrated herein that VEF can be measured indirectly from ESPI acquired "infinite" plate displacements. The differences between the TTVE through a contour of interest and measured VIP are in good agreement at three frequencies (899.5 Hz, 1194.4 Hz, and 1503.2 Hz). The differences between both quantities are mainly related to the

reasons mentioned above. By measuring the input power, using the cross-spectral density between the driving force and its acceleration response, a better agreement could have been obtained. Also, the increase in usable spatial range of ESPI amplitude and phase data would have resulted in a more accurate VEF computation. Nevertheless, VEF from “infinite” plate displacements that include some standing waves, as present at the 569.7 Hz and 605.6 Hz measurements, can be analysed. However, simple energy balances, as carried out by evaluating equation (10.9) or (3.59), respectively, cannot be applied anymore in order to assess any difference between TTVE and energy injected into the plate.

### **14.2.2 Simply Supported Plate Measurements**

To measure differently damped simply supported plate structures, experimental measurements were conducted on a non-layer damped plate, a plate fully covered by an unconstrained layer, and a plate partially covered by unconstrained layer patches attached in a checkerboard pattern layout. A mineral filled viscoelastic polymer layer material was used. The thickness of the attached damping layer was 2.5 mm. To select resonant excitation frequencies, point mobility measurements of all three plate structures were carried out. To undertake energy balance comparisons, between transducer measured vibrational energy injected into the plate and ESPI measured total transmitted energy within the plate, VIP measurements were conducted for each selected excitation frequency.

#### **14.2.2.1 Point Mobility and Vibrational Input Power Measurements**

Figure 14.12 displays the measured point mobility for each simply supported plate structure. Also here,  $f$  shown on the  $x$ -axis is the frequency. The point mobility was computed from the measured FRF of each structure by using equation (8.1). It can be seen from Figure 14.12 that a reduction in resonant amplitude could be achieved by attaching an unconstrained layer onto the plate's surface. In contrast to the simply supported beam experiment where



almost no amplitude reduction was achieved, the increased thickness ratio of  $h_D/h_P = 0.833$  has improved the structural damping behaviour. Figure 14.12(b) displays an enlarged point mobility plot in the frequency range of  $350 \text{ Hz} \leq f \leq 2100 \text{ Hz}$ . From there the amplitude reduction due to the layer attachment can be seen clearly. The measured modal loss factors for each experimental plate structure, as displayed by Tables 11.15 to 11.17, confirm the herein shown damping behaviour. Further, the shift of the resonant frequencies due to the increase in damping and layer mass loading can clearly

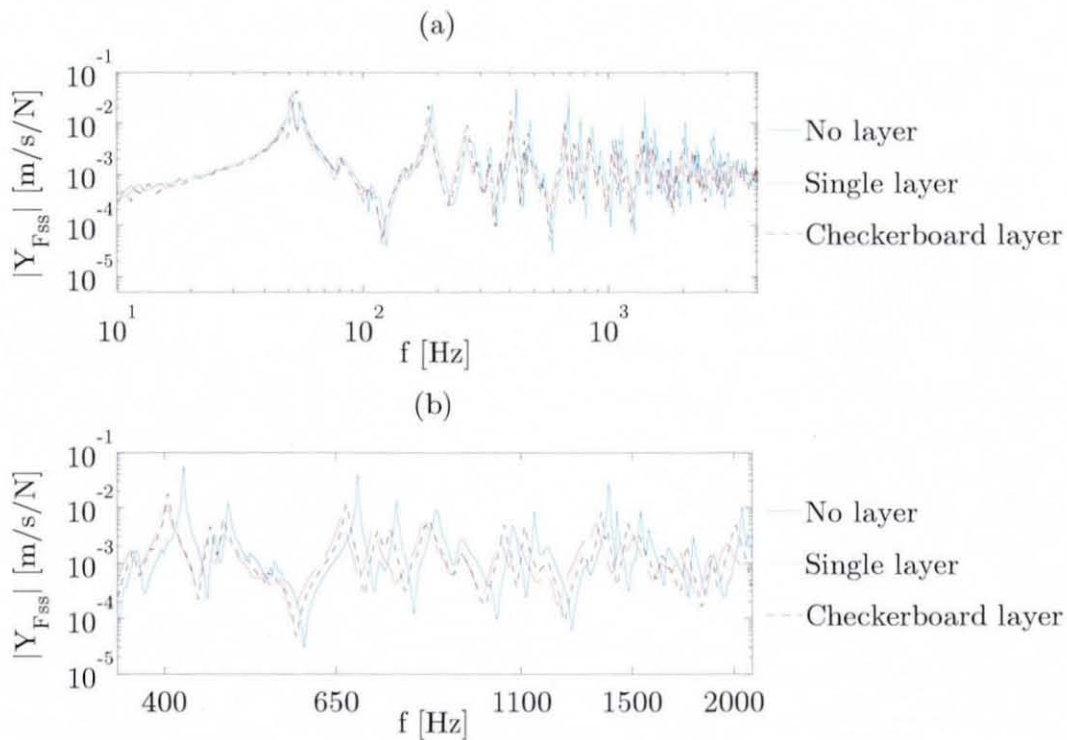


**Figure 14.12** Modulus of the measured point mobility of the force excited simply supported ESPI plates: (a) 10 Hz-3.2 kHz, (b) 350-2100 Hz.

be seen. From this figure, 8 resonant excitation frequencies were selected for each damping configuration. VIP has been computed using equation (3.27) from the measured cross-spectral density of the driving force and the driving point response acceleration. The results of the VIP measurements are given in the Appendix A31. The geometrical and material properties employed during the experimental analysis were the same, as assumed in Table 11.4.

### 14.2.2.2 Vibrational Energy Flow Measurements Using ESPI

As mentioned in the previous section, 24 ESPI amplitude and phase measurements of the experimental plate displacement were recorded from three differently damped experimental simply supported plate structures. Due to the excitation force located centrally, only odd-numbered mode shape displacements were recorded. The centre excitation location was applied to reduce the otherwise vast number of modes to be selected from the measured point mobility. Also here, only one frequency is presented in detail due to shortage in space. VEF maps of all the measured frequencies are shown in Appendix A32.

Figure 14.13 displays the ESPI measured two-dimensional amplitude and phase map of the plate that was damped by a fully covered unconstrained layer and excited at  $f_0 = 1459$  Hz. It can be seen from Figure 14.13 that the plate was excited at the natural damped mode of (7,5). It can

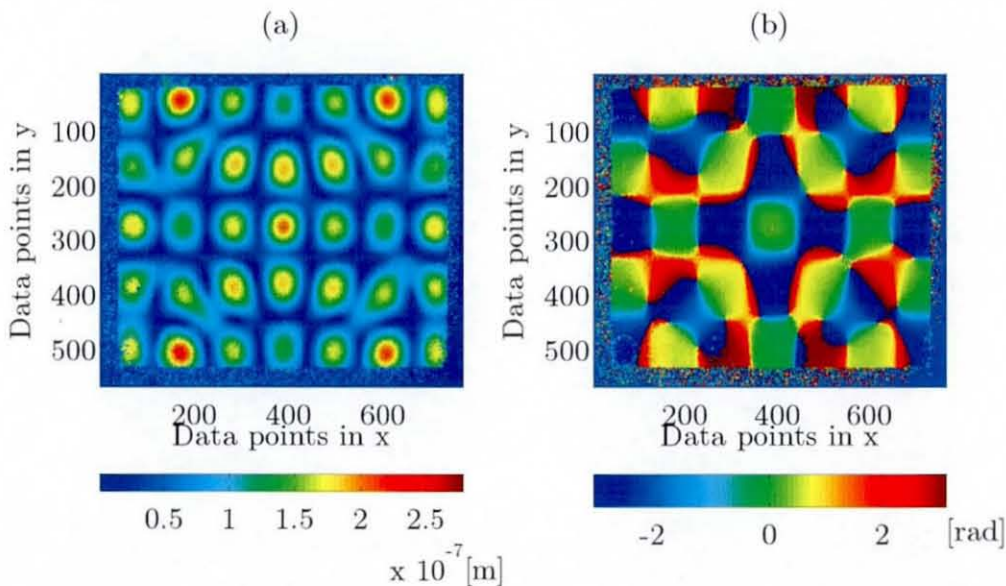


**Figure 14.13** ESPI image of the measured fully covered single-layer damped simply supported plate displacement at 1459 Hz & mode (7,5): (a) amplitude, (b) phase.

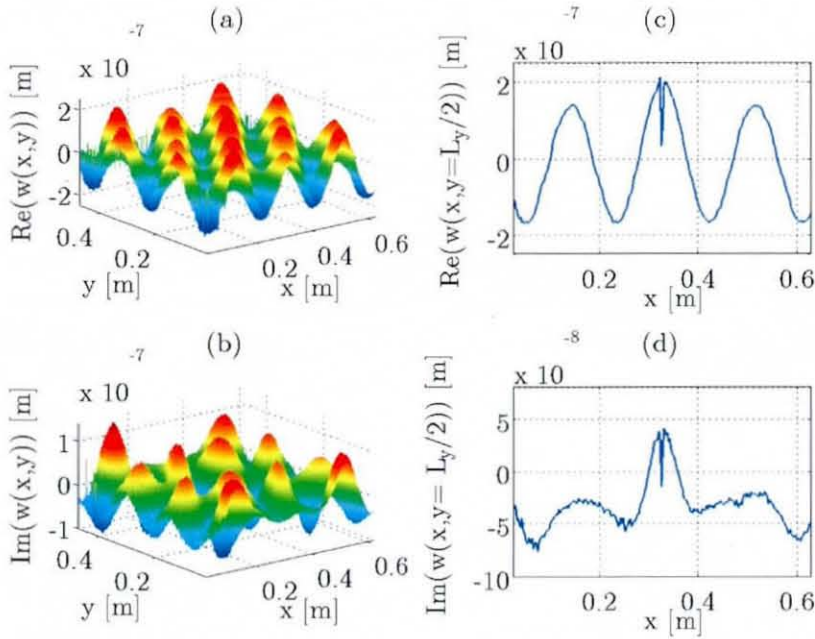
also be noticed that the entire plate displacement was not completely recorded due to the outer boundary design of the simply supported plate rig. Furthermore, missing data points due to insufficient laser light illumination,

as well as the effect of optical noise contamination, can also be seen from Figure 14.13. From the ESPI measured amplitude and phase information the complex, flexural plate displacement was generated using equation (13.4). It can be realised from Figure 14.13 that the recorded plate displacement needed to be truncated in order to exclude regions that did not include spatial displacement information. Within this work two differently truncated plate displacements were investigated. To include as much spatial information as possible, and enabling the analysis of mode shapes having only half a wavelength included within the ESPI window ( $m = 1, n = 1$ ), the initially recorded plate displacement was truncated to exactly the locations where the ESPI displacement recording took place. However, the non-periodicity of the odd-numbered mode shape displacements is increased even further. Thus, stronger spectral leakage within the wavenumber domain can be expected. Furthermore, when carrying out the energy balance within the plate the compensation of missing ESPI measured TTVE due to the displacement truncation is more complicated. Because of these reasons, the measured plate displacements with a mode shape number greater than 1 were also truncated in a way that only an integer number of wavelengths were included in the spatial signal. Therefore, leakage effects are reduced substantially and the compensation of ESPI measured TTVE due to displacement information exclusion can be realised much easier.

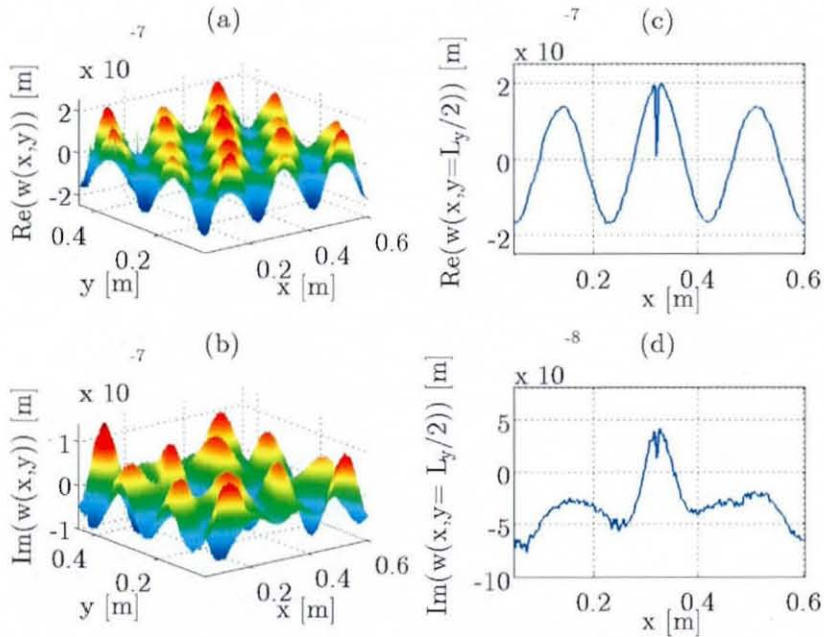
Figure 14.14 displays the ESPI measured simply supported plate displacement, generated from the ESPI measured amplitude and phase maps shown in Figure 14.13. The displacement is non-periodically truncated to include as much spatial displacement information as possible.

Figure 14.15 displays the same simply supported plate displacement however, truncated to an integer number of wavelengths. It can be realised from Figure 14.15 that the displacement is reduced by a quarter of a wavelength at each side. The sharp drop of displacement amplitude at the excitation location, as shown in Figures 14.14(c)-(d) and Figures 14.15(c)-(d), respectively, is mainly due to the attachment of the accelerometer at the driving point. Interestingly, the reduction in spatial amplitude due to the structural damping can be seen from the  $y$ -axis scale shown in Figures





**Figure 14.14** ESPI image of the measured and non-periodically truncated simply supported plate displacement at 1459 Hz & mode (7,5): (a) 2D real part, (b) 2D imaginary part, (c) real part at  $y = L_y/2$ , (d) imaginary part at  $y = L_y/2$ .



**Figure 14.15** ESPI image of the measured and periodically truncated simply supported plate displacement at 1459 Hz & mode (7,5): (a) 2D real part, (b) 2D imaginary part, (c) real part at  $y = L_y/2$ , (d) imaginary part at  $y = L_y/2$ .

14.14(c) and 14.15(c), respectively. Here, the experimentally determined modal loss factor was  $\eta_{7,5} = 1.42 \cdot 10^{-2}$ .

Figure 14.16 displays the top view image of the periodically truncated simply supported plate displacement, as shown in Figure 14.15. The periodic truncation process can be seen in better detail. Interestingly, the real

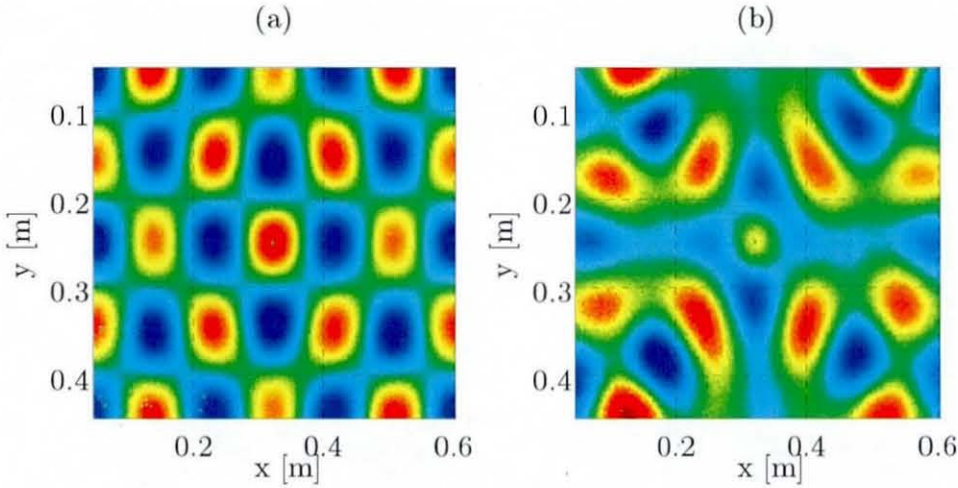


**Figure 14.16** Top view image of the complex simply supported periodically truncated plate displacement shown in Figure 14.15: (a) real part, (b) imaginary part.

displacement part and imaginary displacement part differ in amplitude and mode shape due to a phase difference recorded by the ESPI system. The complex, two-dimensional plate displacements shown in Figures 11.14(a)-(b) and Figures 11.15(a)-(b) were taken as the input to the VEFESPI method. Also here, the ideal 2D filtering process and the oval 2D Butterworth filter were employed. Thus, undesired spectral noise components were removed within the wavenumber domain. This procedure is necessary to avoid spectral amplification occurring during the spectral derivation process in order to compute the spatial derivatives required by the plate's VEF equations, shown in equations (3.49) and (3.50).

Figure 14.17 displays the complex plate displacement, as shown in Figure 14.15, however, filtered by the ideal filtering process and the Butterworth filter. It can be seen from this figure that the flexural plate displacement is substantially smoothed and, thus, most of the optical noise



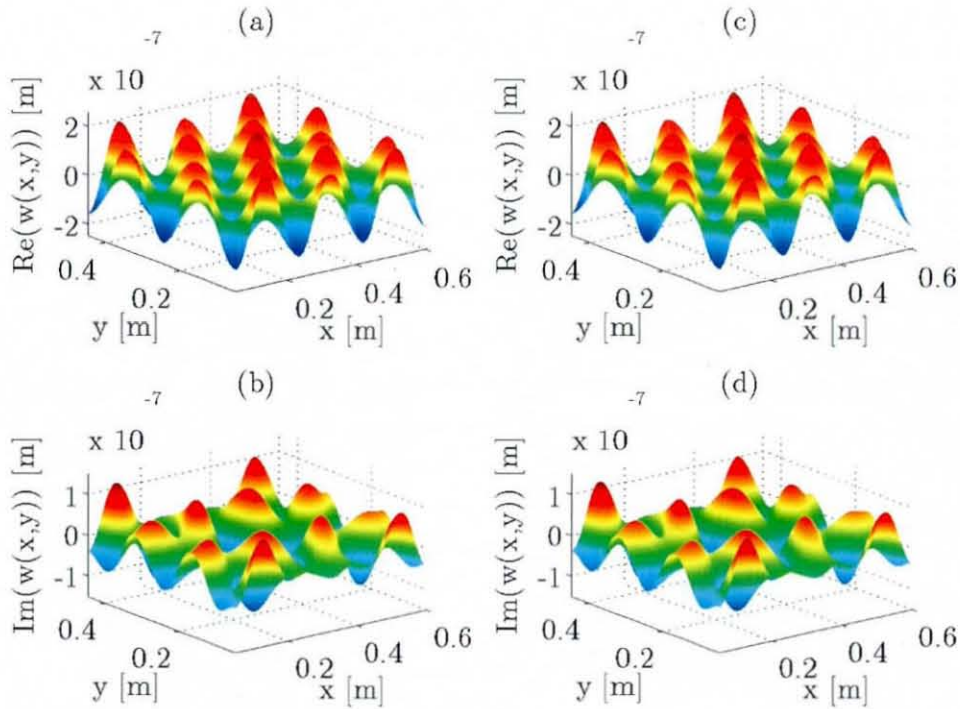


**Figure 14.17** Filtered and periodically truncated complex simply supported plate displacement at 1459 Hz & mode (7,5): (a)-(b) ideal 2D filtered, (c)-(d) oval 2D Butterworth filtered.

components were removed from the displacement signal. Furthermore, both the ideal filtering process and the Butterworth filter delivered similar results.

Figure 14.18 displays the VEF maps computed from the non-periodically truncated displacement shown in Figure 14.14, determined by the VEFESPI method. Figure 14.19 displays the same result. However, the VEF maps were computed from the periodically truncated simply supported plate displacement, as shown in Figure 14.15. Note, for better visibility the number of data points were reduced. It can be seen from Figures 14.18 to 14.21 that the periodic displacement truncation process affects mostly the computation of the reactive energy flow, which seems to have a more accurate VEF pattern when analysing the periodic plate displacement. The computation of the active VEF within the experimental plate is rather similar for both truncated displacements. However, it should be noted that the difference between both truncation procedures increased with decreasing number of

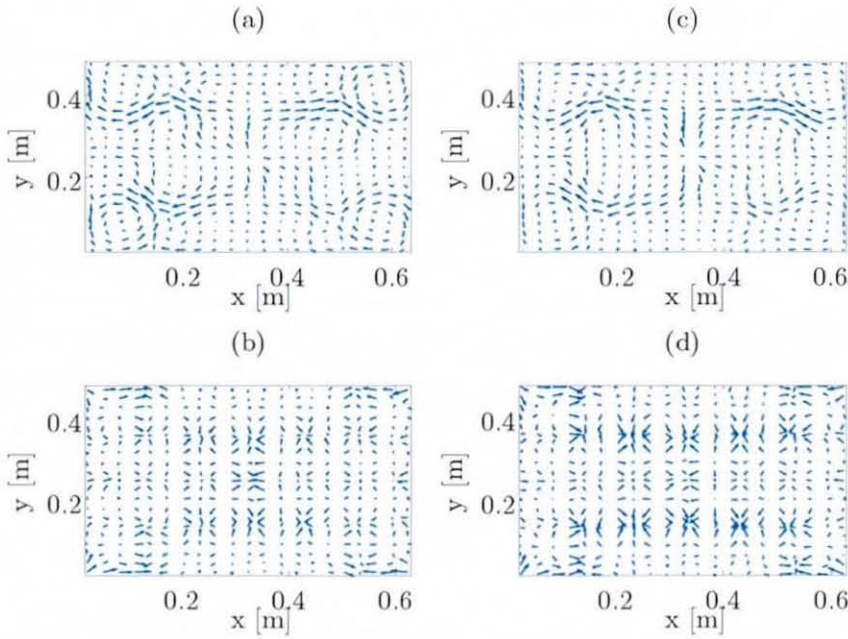


**Figure 14.18** Filtered VEF maps of the non-periodically truncated simply supported plate at 1459 Hz & mode (7,5): (a) active VEF - ideal filter, (b) reactive VEF - ideal filter, (c) active VEF - Butterworth filter, (d) reactive VEF - Butterworth filter.

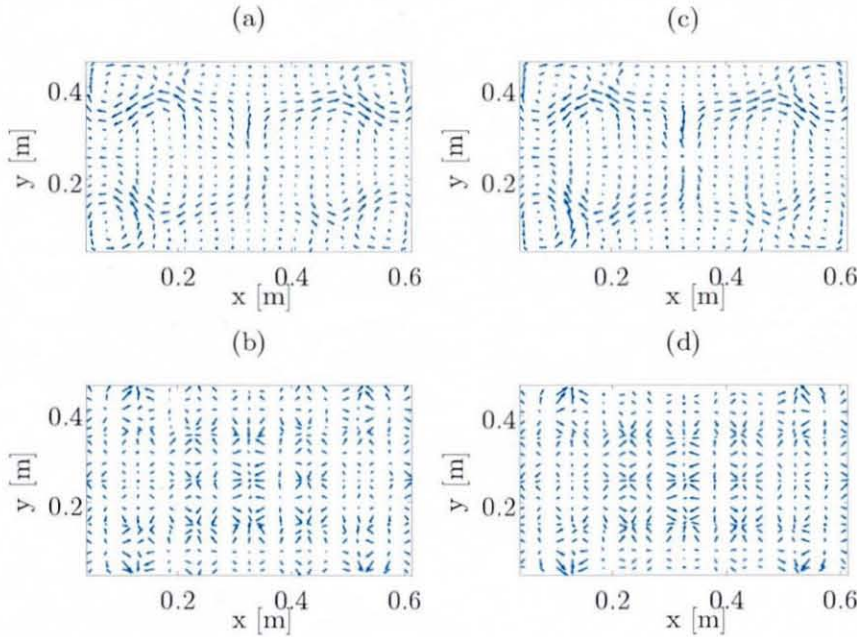


**Figure 14.19** Filtered VEF maps of the periodically truncated simply supported plate at 1459 Hz & mode (7,5): (a) active VEF - ideal filter, (b) reactive VEF - ideal filter, (c) active VEF - Butterworth filter, (d) reactive VEF - Butterworth filter.



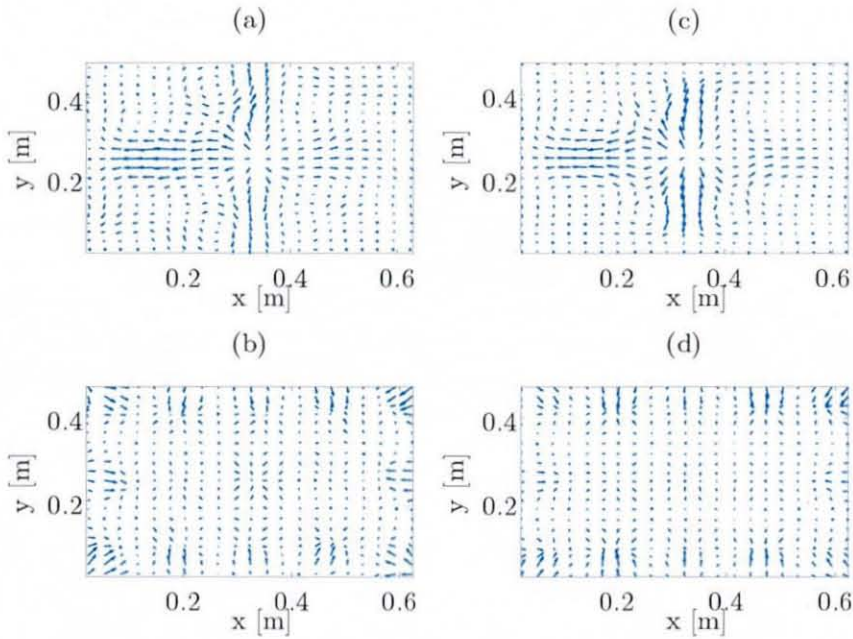


**Figure 14.20** Filtered VEF maps of the non-periodically truncated simply supported plate at 658 Hz & mode (5,3): (a) active VEF - ideal filter, (b) reactive VEF - ideal filter, (c) active VEF - Butterworth filter, (d) reactive VEF - Butterworth filter.

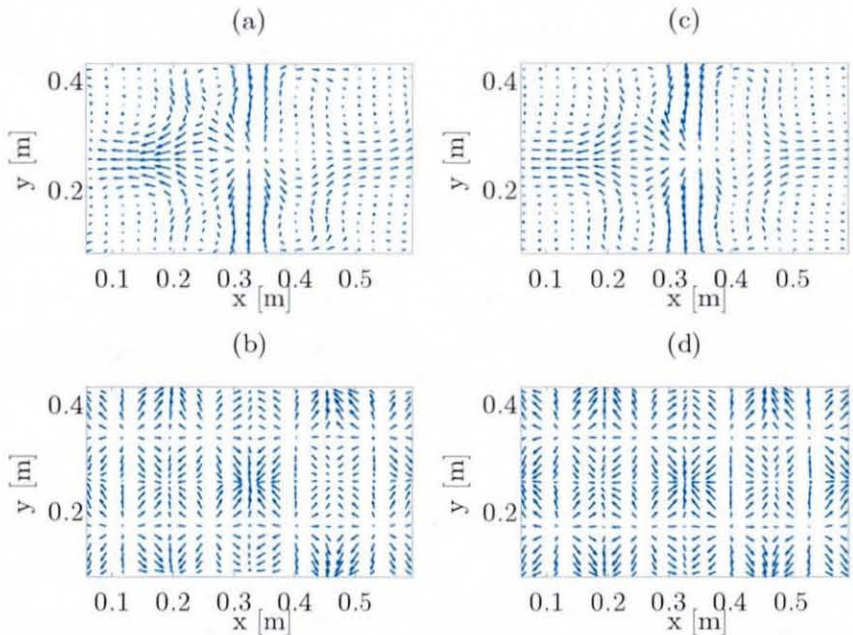


**Figure 14.21** Filtered VEF maps of the periodically truncated simply supported plate at 658 Hz & mode (5,3): (a) active VEF - ideal filter, (b) reactive VEF - ideal filter, (c) active VEF - Butterworth filter, (d) reactive VEF - Butterworth filter.

wavelengths included in the signal, as evident from Figures 14.20 and 14.21. These figures show the VEF maps of the non-periodically truncated and periodically truncated simply supported plate displacement that was excited at the mode (5,3). Also here, the plate was damped by a fully covered unconstrained layer and, the excitation frequency was  $f_0 = 658$  Hz. It can be seen from Figures 14.20 and 14.21 that in particular the computation of reactive energy flow improves at the lower modes, when truncating the ESPI measured simply supported plate displacement to an integer number of wavelengths. Furthermore, as evident from the VEF maps shown above, the active as well as the reactive VEF within an experimental simply supported plate can be measured when using an ESPI system to acquire the transverse plate displacements. Note, all VEF maps of the periodically truncated plate displacements are shown in Appendix A32.

#### 14.2.2.3 Energy Balance

In the previous chapter it was shown that the VEF pattern of an ESPI measured experimental simply supported plate can be measured by the VEFESPI method. However, the question of how accurate the shown magnitude of active and reactive energy flow is, still remains. This subject is investigated within this section by employing an energy balance. Thus, transducer measured VIP at the driving point is compared to TTVE obtained from spatial integration of the VEFESPI computed energy densities by numerically evaluating equation (3.61). The difference between transducer measured input power  $(P_{in})_{Fa}$  and the integrated potential energy density  $\langle e_{pot} \rangle_t$  is computed as:

$$\Delta\varepsilon = \left( 1 - (P_{in})_{Fa} / 2\omega\eta \int_S \langle e_{pot} \rangle_t dx dy \right) \cdot 100\%, \quad (14.2)$$

Note, only the periodically truncated displacements are analysed. In the previous section it has been shown that the ESPI displacement is truncated to either a non-periodic or a periodic spatial size. Thus, when employing an

energy balance, equation (3.60) is violated, since it assumes global energy values and, thus, the consideration of the entire plate. Because in this research time-averaged and truncated data are used, equation (3.3) should be employed instead. Equation (3.3) requires the knowledge of the input energy density. However, during the experiment total VIP was measured only. Furthermore, due to the use of the more erroneous 4<sup>th</sup> order spatial derivatives to compute the VEF divergence, equation (3.60) will still be employed. Hence, a compensation factor was computed here to account for the excluded potential energy density information due to the truncation process. Because a quarter of a wavelength of energy density information is truncated around the plate, the integrated energy density from the periodically truncated data are multiplied by  $1+1/(m-1)$  when integrating in the  $x$  direction and by  $1+1/(n-1)$  when integrating in the  $y$  direction, where

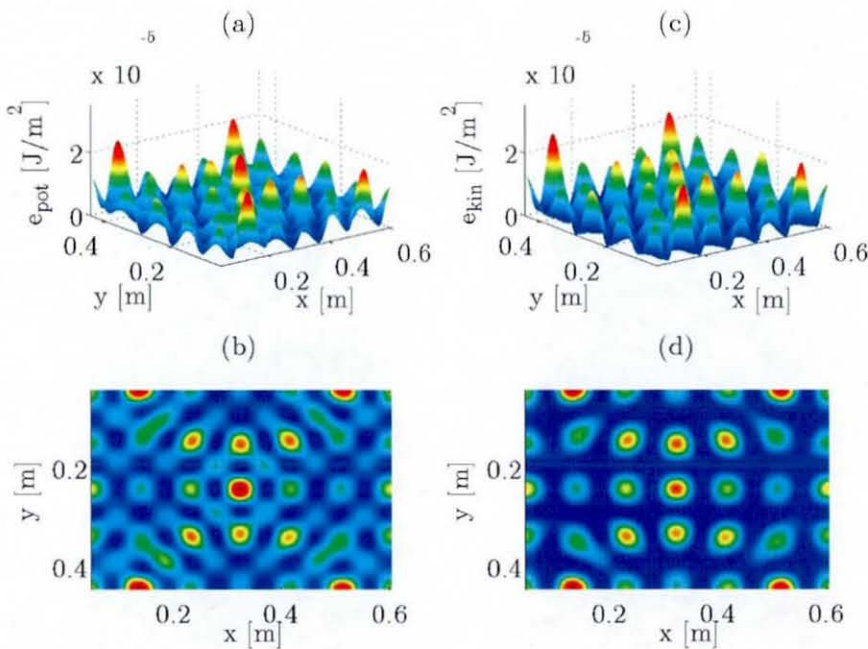


**Figure 14.22** Butterworth filtered energy densities of the periodically truncated, single-layer damped simply supported plate at 1459 Hz & mode (7,5): (a) 2D potential energy density, (b) top view image of  $e_{pot}$  (c) 2D kinetic energy density, (d) top view image of  $e_{kin}$ .



$m$  and  $n$  are the modal numbers. Because these simple compensation factors can be used, the periodically truncated data are analysed instead.

Figure 14.22 displays the potential and kinetic energy density computed from the ESPI recorded fully covered single-layer damped simply supported plate displacement, excited at 1459 Hz and mode (7,5). The potential energy density, shown in Figure 14.22(a), is used to compute the total transmitted energy within the plate by using the right-hand side of equation (3.61). Tables 14.2 to 14.4 display the results obtained when employing an energy balance according to equation (3.61). Note, only the Butterworth filtered data are shown, since the ideal filtered results are almost identical.

mode	$f_0$	$(P_m)_{Fa}$	$2\omega\eta\int_S\langle e_{pot}\rangle_t dx dy$	$\Delta\epsilon$
(3,3)	422.5 Hz	$1.39\cdot 10^{-5}$ W	$1.45\cdot 10^{-5}$ W	-3.8%
(5,3)	689 Hz	$4.77\cdot 10^{-5}$ W	$4.23\cdot 10^{-5}$ W	11.3%
(5,5)	1139 Hz	$1.37\cdot 10^{-4}$ W	$1.36\cdot 10^{-4}$ W	1.0%
(7,5)	1536 Hz	$4.39\cdot 10^{-4}$ W	$3.87\cdot 10^{-4}$ W	11.7%
(9,5)	2040.5 Hz	$9.22\cdot 10^{-4}$ W	$1.11\cdot 10^{-3}$ W	-20.2%

**Table 14.2** Comparison of transducer measured VIP and ESPI measured Butterworth filtered TTVE of the non-layer damped experimental simply supported plate.

It can be seen from Tables 14.2 to 14.4 that the relative difference  $\Delta\epsilon$ , between transducer measured VIP and ESPI measured TTVE, of most measurements is in the range of  $\pm 30\%$ . Here, the non-layer damped plate revealed the best agreement between both measures. A more detailed discussion about potential errors in the experiment is given in the next section.

mode	$f_0$	$(P_{in})_{Fa}$	$2\omega\eta\int_S\langle e_{pot}\rangle_t dxdy$	$\Delta\epsilon$
(3,3)	402 Hz	$1.08\cdot 10^{-4}$ W	$9.04\cdot 10^{-5}$ W	16.0%
(5,3)	658 Hz	$1.82\cdot 10^{-4}$ W	$1.52\cdot 10^{-4}$ W	16.4%
(5,5)	1086 Hz	$7.74\cdot 10^{-4}$ W	$6.33\cdot 10^{-4}$ W	18.2%
(7,5)	1459 Hz	$7.92\cdot 10^{-4}$ W	$4.66\cdot 10^{-4}$ W	41.1%
(5,7)	1716 Hz	$1.40\cdot 10^{-3}$ W	$8.93\cdot 10^{-4}$ W	36.3%

**Table 14.3** Comparison of transducer measured VIP and ESPI measured Butterworth filtered TTVE of the single-layer damped experimental simply supported plate.

mode	$f_0$	$(P_{in})_{Fa}$	$2\omega\eta\int_S\langle e_{pot}\rangle_t dxdy$	$\Delta\epsilon$
(3,3)	404.5 Hz	$4.80\cdot 10^{-5}$ W	$3.77\cdot 10^{-5}$ W	21.4%
(5,3)	669 Hz	$1.64\cdot 10^{-4}$ W	$1.40\cdot 10^{-4}$ W	14.3%
(5,5)	1111.5 Hz	$2.95\cdot 10^{-4}$ W	$2.40\cdot 10^{-4}$ W	18.7%
(7,5)	1486.5 Hz	$7.56\cdot 10^{-4}$ W	$7.19\cdot 10^{-4}$ W	4.8%
(5,7)	1750 Hz	$4.59\cdot 10^{-4}$ W	$3.37\cdot 10^{-4}$ W	26.5%
(9,5)	2005.5 Hz	$1.75\cdot 10^{-3}$ W	$1.10\cdot 10^{-3}$ W	38.8%

**Table 14.4** Comparison of transducer measured VIP and ESPI measured Butterworth filtered TTVE of the checkerboard pattern-layer damped experimental simply supported plate.

#### 14.2.2.4 Discussion

This section has reported on the measurement of VEF within simply supported plates, using ESPI to experimentally acquire two-dimensional, transverse simply supported plate displacements. 24 measurements were

recorded from three differently damped simply supported plate structures. During the experiment a non-layer damped plate, a fully covered and single-layer damped plate, as well as a checkerboard pattern-layer damped plate were used. Due to simplification in post measurement analysis, the ESPI recorded displacement data were truncated to a non-integer number of wavelengths as well as an integer number of wavelengths. The latter procedure was used during the energy balance analysis. Thus, the initial 24 measurements were reduced to 16 measurements, since recordings of mode shapes with half a wavelength, in either the  $x$  or  $y$  direction only, could not be truncated to an integer number of wavelengths.

The point mobility plot, as shown in Figure 14.12, displays that the attachment of an unconstrained layer reduced the modal amplitude of the flexural vibrating plate specimen. Thus, a damping scenario, as initially intended, could be achieved. However, the reduction of modal displacement is only small. This agrees with the results found in section 10.4. Due to the low thickness ratio of  $h_D/h_P \approx 0.83$ , only a small increase in damping could be achieved. From Figure 14.12(b) it is evident that the additional damping shifted the modal resonant frequency towards lower frequencies.

Within this work VEF in simply supported plates was computed indirectly from ESPI measured surface displacements by using the VEFESPI method. The displacement information was recorded two-dimensionally with a high spatial sampling density of  $768 \times 768$  data points. Because the plates were centrally excited, only odd-numbered mode shape displacements were recorded. Due to the design of the simply supported plate rig, the entire plate displacement could not be recorded, with sampling data missing from approximately 25 mm to each side of the plate's edges. To reduce the effect of spectral leakage due to displacement non-periodicity, the initial plate displacement was also truncated to an integer number of wavelengths. This procedure also had the advantage that a compensation factor, required for a later employed energy balance analysis, could be derived easily.

One of the main objectives of VEF analysis is the visualisation of VEF in structures. This procedure is essential to detect regions of high and low VEF. Thus, VEF maps were computed from the ESPI measured simply



supported plate displacements, using the VEFESPI method. It has been shown by Figures 14.18 to 14.21 and all of the VEF maps given in Appendix A32 that the flow of vibrational energy can be detected from most of the measured displacements. To compare the measured VEF pattern with the analytical computed VEF pattern, theoretically determined VEF maps were given in Appendix A33 for each mode excited during the experiment. It can be seen from the comparison of the spatial VEF distribution that some measurements are very close to the analytical VEF pattern. However, there are also some measured frequencies which are not close to each other. The differences in VEF pattern are mainly relatable to three points.

Firstly, real structures behave differently to theoretical structures. From some ESPI amplitude figures it can be seen that the strong symmetry of a certain theoretical mode shape could not be simulated precisely due to limitations of the simply supported rig, as evident from Figure 14.13. In these cases, the recorded modal displacement shapes differed from the analytical modal displacement shape and a difference in VEF pattern can be expected.

Secondly, some measurements were acquired at very low values of  $\eta \times \text{SNR}$ , especially the non-layer damped plate measurements. Here, at the modes (5,3) and (5,5) a low agreement in active spatial VEF distribution between experimental and analytical results was obtained despite a good ESPI recorded modal displacement shape. However, at the modes (3,3), (7,5) and (9,5) a good agreement was computed. As concluded in section 11.4, the sensitivity of the VEFESPI method decreases with increasing damping. Thus, with increasing damping lower values of  $\eta \times \text{SNR}$  may also lead to acceptable active VEF results. For this reason, some measurements of the non-layer damped plate showed a good active flow pattern agreement, whereas active flow pattern at the mode (5,3) with  $\eta \times \text{SNR} \approx 0.19$  and  $\eta = 3.5 \cdot 10^{-3}$  could not be measured satisfactory. The predicted values of  $\eta \times \text{SNR}$  are given in Tables 11.8 to 11.10 and the measured modal loss factors are given in Tables 11.5 to 11.7.

The agreement in active VEF between experimental and analytical results of the fully covered, single-layer damped plate and the checkerboard pattern-layer damped plate was good at each measured frequency. In

particular the single-layer damped plate at the modes (5,3), (5,5), (5,7) as well as the checkerboard pattern-layer damped plate at the modes (5,5), (5,7), (9,5) showed a good agreement.

As expected, the reactive energy flow pattern could be detected at all three plate structures within a satisfactory range. However, the agreement between experimental and analytical data diverged with increasing excitation frequency, since here more measured wavelengths were included in the signal to be analysed that differed from the theoretical modal shape.

Partial damping, as employed with one plate specimen, has influence on the spatial distribution of VEF. However, this was not regarded when computing the analytical VEF distribution. Thus, differences between the measured and analytical VEF of the checkerboard layer damped plate were present, as evident from the measurement of mode (5,3). Here, the primary shape of the analytical mode (5,3) can be seen. However, partial attachment of the unconstrained layer patches altered the pattern of the VEF.

Thirdly, the required spectral filtering also affected the computation of the measured VEF. In this work an ideal 2D filtering process and an oval 2D Butterworth filter were employed within the wavenumber domain, in order to remove undesired spectral noise components. Due to the filtering in the spectral domain, the subsequent computation of spatial derivatives, as required by the VEF computation, naturally produced altered spatial derivatives. Thus, differences in magnitude and direction of VEF can be expected. Interestingly, the two employed filter shapes produced almost identical results.

VEF measurements are used to measure vibrational energy in terms of flow direction and flow magnitude. It has already been shown that the direction of flow (spatial distribution of VEF) in finite structures can be measured using an ESPI system. To assess the accuracy of the flow magnitude an energy balance was carried out. Therefore, conventionally measured VIP was compared with the TTVE within the simply supported plate. Because the boundaries of the plate rig were considered as non-dissipative, the injected vibrational energy should be equal to the total dissipated vibrational energy within the plate. Thus, equation (3.61) was



employed. The TTVE within the plate was computed by evaluating a surface integration of the ESPI measured potential energy density. The measured VIP was computed from the accelerometer and force transducer measured cross-spectral density between the driving force and the driving point acceleration, as shown by equation (3.27).

Tables 14.2 to 14.4 display the result of such an energy balance computed for all three measured plate structures. The parameter  $\Delta\epsilon$  represents the relative difference between the transducer measured VIP and the ESPI measured TTVE. It can be seen that there is a relative difference of  $\pm 30\%$  for most of the measurements. However, at most measurements the TTVE is less than the VIP. It can be seen that the relative difference computed for the non-layer damped plate is lowest and in a very close range. This contradicts the results obtained from the computation of the VEF pattern where the non-layer damped plate produced less accurate VEF shapes. However, according to the conclusion obtained in section 11.3, the computation of the VEF pattern depends very much on the product of  $\eta \times \text{SNR}$  in combination with the level of damping, whereas the relative error made by balancing the VIP and the TTVE is less dependent upon the damping. From Tables 11.8 to 11.10, it can be seen that the non-layer damped plate experiment was conducted at very low values of  $\eta \times \text{SNR}$ . Further, the measured modal loss factors were lower than the respective measured modal loss-factors of the layer damped structures. This indicates that the sensitivity of the VEFESPI method can be expected to be higher when computing the VEF pattern. Thus, when balancing the measured VIP with the measured TTVE within the plate, differences are mainly caused by deviations due to the idealisation of equation (3.61) and the modelling of the damping layer attachment, which obviously was excluded when analysing the non-layer damped plate.

As mentioned before, a higher relative difference for the single-layer and checkerboard pattern-layer damped plate may be related to the layer attachment modelling. As shown in section 10.4 and Appendix A28, it was assumed, in order to simplify the modelling of the combined flexural rigidity, that the plate and the layer have the same Poisson ratio. Thus, in

combination with the assumed plate and damping layer properties, considerable computation errors can be expected when computing the combined flexural rigidity. This argument is strengthened by the fact that the combined modal loss factor computed was always considerably lower than the measured modal loss factor. Thus, it is assumed herein that the deviation in the combined flexural rigidity due to the layer attachment modelling is the main reason for a higher relative difference being present for the single-layer damped and checkerboard pattern-layer damped plate.

During the ESPI experiment, sound radiation of the excited experimental plate was clearly audible. At some modes, especially at the higher frequencies, a very loud sound was radiated by the vibrating plate. However, losses of the plate due to sound radiation are neglected in the energy balance, as defined by equation (3.61). Figure 14.23 displays the predicted theoretical VIP  $(P_{in})_{F_{ss}}$  and theoretical radiated sound power  $(P_{rad})_{F_{ss}}$  of a baffled non-layer damped simply supported plate. For the prediction, the same geometrical and material properties as the experimental plate were used. The analysis was carried out with a mean force magnitude

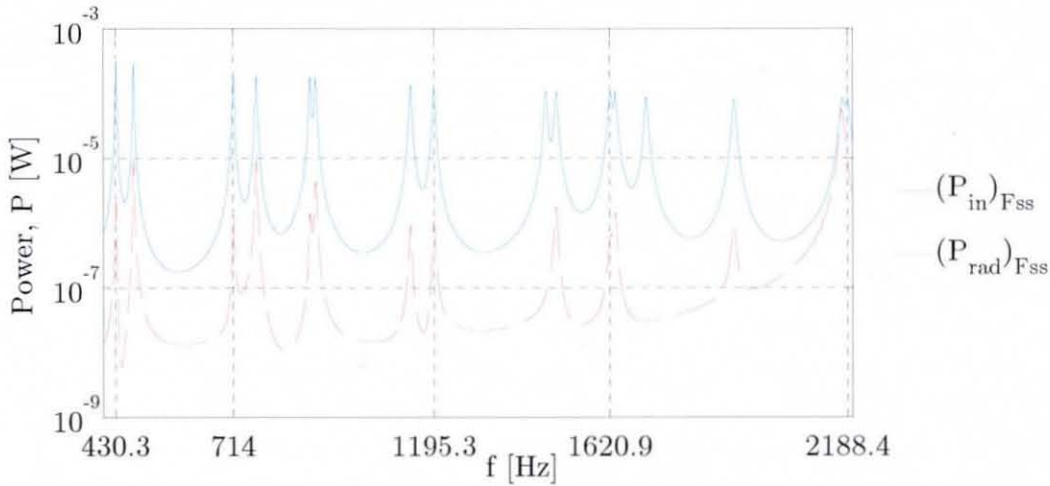


**Figure 14.23** Comparison of VIP and radiated sound power at both sides of a baffled non-layer damped simply supported plate using a force magnitude of  $F_0 = 0.141$  N and a loss factor of  $\eta = 5.22 \cdot 10^{-3}$ .

and a mean loss factor, averaged from the measured force magnitude and measured modal loss factor.

Figure 14.24 shows the radiation efficiency. From both figures it can be seen that the radiated sound power is more significant at the higher frequencies. Hence, losses due to sound radiation can be regarded as a potential reason for larger discrepancies occurring between the TTVE and VIP at the higher excitation frequencies. Thus, the higher relative differences

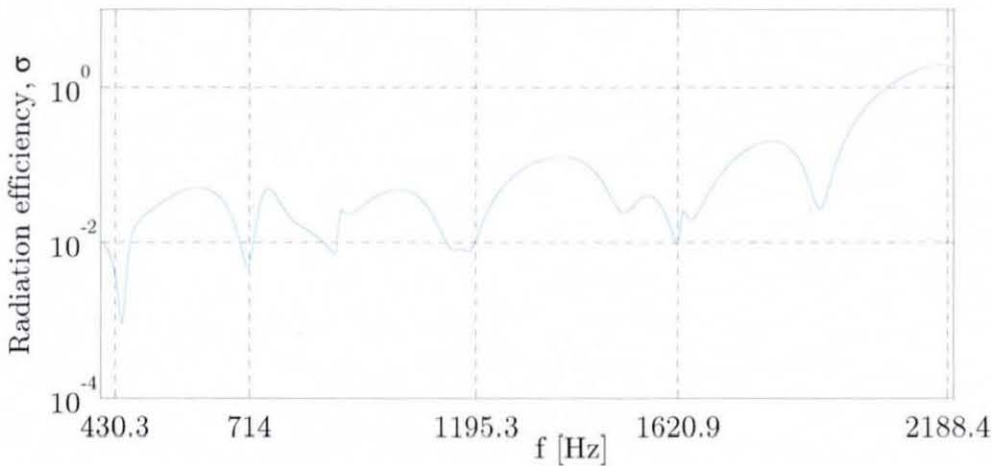


**Figure 14.24** Radiation efficiency of a baffled non-layer damped simply supported plate using a force magnitude of  $F_0 = 0.141$  N and a loss factor of  $\eta = 5.22 \cdot 10^{-3}$ .

between the measured VIP and measured TTVE of the single-layer damped and checkerboard pattern-layer damped plate may be related to some losses due to sound radiation. Of course the attachment of an unconstrained damping layer reduces the measured surface velocity and, hence, the sound power radiated. However, the trend that more injected energy is radiated at higher excitation frequencies remains.

Further, cognitions gained when discussing the simply supported beam results can also be related to the measurement of finite plates. The modal loss factor was measured here by an experimental modal analysis using a grid of  $10 \times 10$  FRF measurement points on the plate's surface [127]. It was noted in reference [104] that measurements of the modal loss factor are often erroneous with an accuracy no better than about  $\pm 20\%$  due to complicated,



non-linear damping mechanisms occurring in real vibrating structures. Furthermore, the material properties of the plate and especially the damping layer were assumed herein when calculating TTVE, whereas, material properties were not regarded when computing the VIP from the measured cross-spectral density. Although it was assumed that the boundaries of the rig are non-dissipative, there might have been some energy crossing at the boundaries. However, these energy losses are not regarded in equation (3.61). Finally, the truncation process and the subsequent compensation using a compensation factor may also have introduced errors.

Due to the above mentioned sources of potential errors, the energy balance according to equation (3.61), which worked well in theoretical analysis, cannot be applied in full practice in order to assess the exact accuracy of the VEFESPI method. However, it can be used to check if the measured VIP and measured TTVE are in a close range to each other. This certainly has been shown by Tables 14.2 to 14.4. Thus, it can be concluded that the magnitude, as well as the spatial distribution of the ESPI measured VEF within a simply supported plate, can be measured within an acceptable range of accuracy.

Also, some regards are given towards the relation of vibrational energy transmission and vibrational energy dissipation. The active VEF maps, as shown above and in Appendix A32, visualised the measured VEF within the simply supported plate. With the aid of the active VEF maps, the amount and direction of actual transmitted vibrational energy is shown. This quantity represents the true physical energy flow within the plate. It can be seen from Figures 14.18 to 14.21 that although the active spatial energy flow distribution is symmetrical within a simply supported plate, the active flow pattern cannot be related to the modal displacement shape of the plate and vice versa. However, modal information can be gained from the reactive VEF maps, simply by counting the number of reactive energy sinks.

Figures 14.18 and 14.19 displayed the VEF maps of the single-layer damped plate excited at 1459 Hz and mode (7,5). It can be seen that the vibrational energy flowed almost radially symmetrically away from the centre of the plate. However, energy vortices, typical for finite structures, occurred

within the plate showing a rotation of vibrational energy around a given location. The generation mechanisms of VEF vortices are explained in reference [135]. There, it was shown that vortices are generated due to interference of at least two modes, producing a so-called vortex generation block. However, sometimes the excitation location cannot be located this easily, especially when the excitation location is not known or a large number of energy sources and sinks appear within the VEF field. For a detection of energy sources and sinks, the divergence of VEF can be used, as also shown in reference [78].

Figure 14.25 displays the VEF divergence computed from the ESPI measured and periodically truncated single-layer damped simply supported plate displacement that was excited at 1459 Hz and mode (7,5). Equation (3.54) was used to compute the divergence from the two VEF fields  $\bar{P}_x$  and  $\bar{P}_y$ . The divergence of VEF within a plate is defined as the sum of the partial derivatives of the VEF fields  $\partial \bar{P}_x / \partial x + \partial \bar{P}_y / \partial y$ . Thus, the spatial rate of VEF change can be computed. As stated in section 3.2, a non-zero divergence of VEF indicates an increase in VEF if  $\nabla \bar{P} > 0$  and a decrease in VEF if  $\nabla \bar{P} < 0$ .  $\nabla \bar{P} = 0$  occurs at the non-dissipative simply supported boundary. Within the plate  $\nabla \bar{P}$  is usually non-zero due to energy supply and

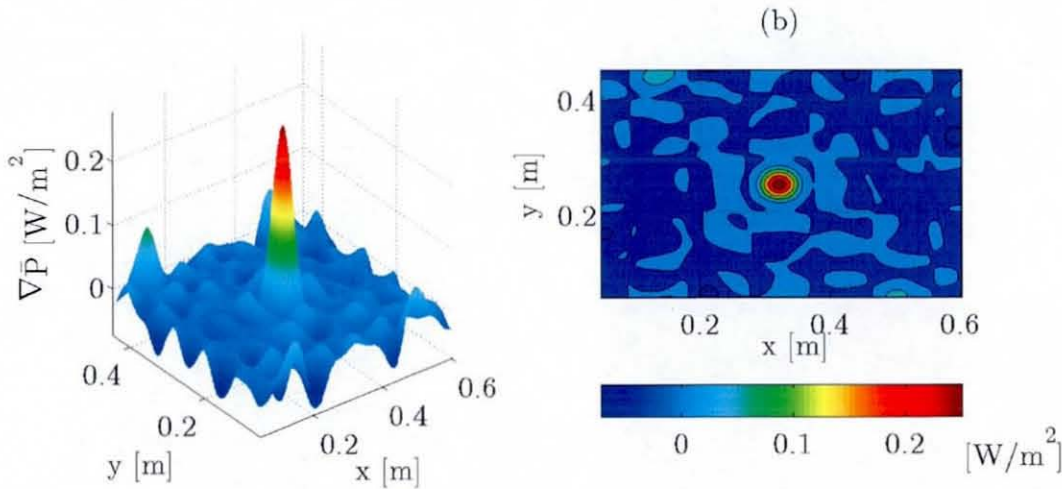


**Figure 14.25** Butterworth filtered VEF divergence of the periodically truncated, single-layer damped simply supported plate at 1459 Hz & mode (7,5): (a) 2D divergence of VEF, (b) contour plot of VEF divergence.



subsequent damping. An increase in VEF may occur due to energy injection. A decrease in VEF may occur due to energy dissipation. From Figure 14.25, the excitation location as an energy supply can be identified clearly in the centre of the plate, since this value is positive and largest.

Furthermore, regions of energy dissipation can also be identified from Figure 14.25(b) at locations, where  $\nabla \bar{P} < 0$ . Interestingly, the energy dissipation is rather oddly distributed over the plate. It can also be noticed from Figure 14.25 that the divergence of VEF is not zero at the edges. This is mainly due to the truncation of the experimental simply supported plate displacement. Hence, some energy dissipation is still in progress.

For comparison reason Figure 14.26 displays the contour plot of the divergence of the non-layer damped plate excited at 1536 Hz and mode (7,5). It can be seen from this figure that a more symmetrical modal pattern of

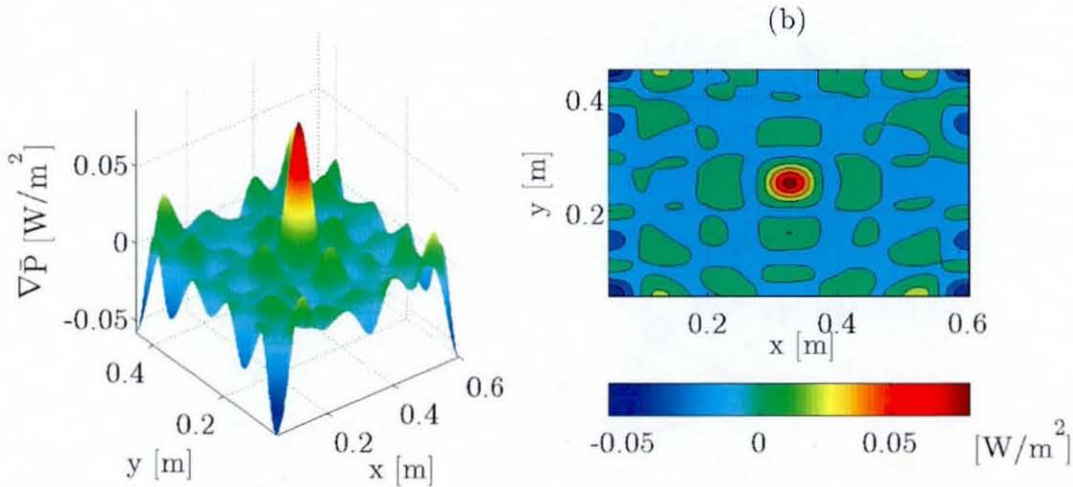


**Figure 14.26** Butterworth filtered VEF divergence of the periodically truncated non-layer damped simply supported plate at 1536 Hz & mode (7,5): (a) 2D divergence of VEF, (b) contour plot of VEF divergence.

energy dissipation occurs. It can be assumed that the attachment of a single unconstrained layer introduced asymmetric distributed energy dissipation.

Unfortunately, the computation of the divergence of VEF required 4<sup>th</sup> order spatial derivatives. It was shown previously that the computation error that occurred when determining the spatial derivatives by the KSD

technique, increased with increasing order. Thus, the computation of VEF divergence can be expected to some extent to be erroneous. The VEF divergence can be used to detect the excitation location as it was shown above. Another quantity to investigate the dissipation behaviour of the simply supported plate is the use of the right-hand side of equation (3.61). The total dissipated energy within the simply supported plate is proportional to the surface integral of the potential energy density. The proportional factor is  $2\omega\eta$ . Figure 14.27 displays the integrated potential energy density along the  $y$ -axis. This quantity represents the total dissipated energy in the  $x$  direction. Note, the curve shape of the equivalent quantity in the  $y$  direction looks similar, however, only 5 amplitude peaks would appear. Integration of the curve, as shown in Figure 14.27, along the  $x$ -axis would yield the TTVE within the plate. Since the boundaries are assumed to be non-dissipative, the TTVE is equal to the total dissipated vibrational energy.

From Figure 14.27 it is evident that the maximum energy in the  $x$  direction is dissipated at locations  $x = a\lambda_x/4$ , where  $a$  is positive integer.

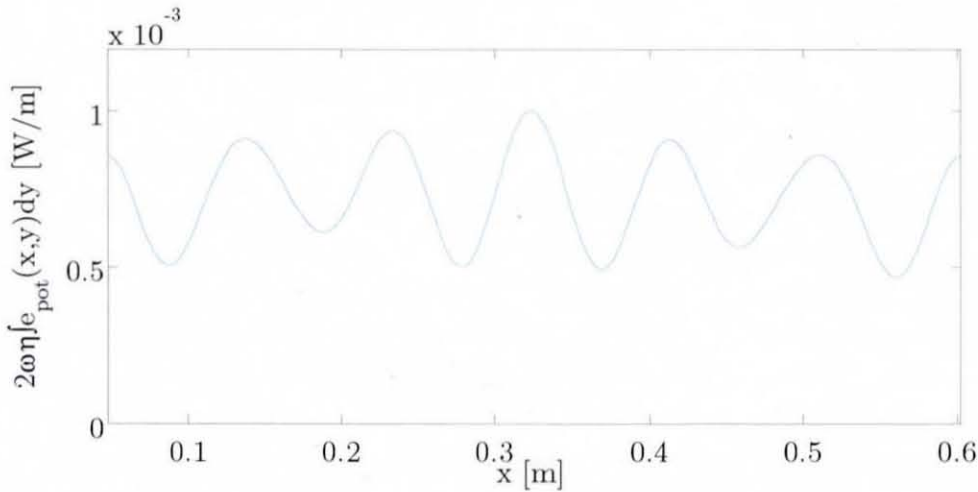


**Figure 14.27** Butterworth filtered total dissipated energy in the  $x$  direction of the periodically truncated single-layer damped simply supported plate at 1459 Hz & mode (7,5).

From Figure 14.16 it can be noticed that these points are located at the peaks of the modal simply supported plate displacement. Thus, energy

dissipation is at maximum at the peaks of the modal plate displacement. This information cannot be obtained from the active VEF maps.

Finally, it can be concluded that the measurements of VEF within differently damped simply supported plate structures were successfully conducted using an ESPI system. VEF pattern could be determined for all three damping structures, which mostly agreed well with their analytical counterpart. Also, the relative difference between the transducer measured VIP and ESPI measured TTVE were within a reasonable range. With the experimental results, presented in this section, the conclusions gained in section 11.3 could be confirmed. Thus, the sensitivity of the VEFESPI method increased with increasing damping and the energy balance within finite structures is less sensitive towards noise and damping.

# 15 CONCLUSIONS AND FUTURE WORK

## 15.1 General Conclusions

This chapter concludes the thesis with general results and cognitions obtained on the numerical computation of vibrational energy flow (VEF) and the measurement of VEF under use of electronic speckle pattern interferometry (ESPI) in beam and plate structures. In this dissertation, focus has been drawn to the theoretical and numerical computation of VEF in beam and plate structures. For validation purposes, ESPI based VEF measurements were undertaken for each structure considered in theory.

To assess the performance of the vibrational energy flow determination method using electronic speckle pattern interferometry (VEFESPI), infinite and finite structures were analysed. These two types represented structures containing very strong and very weak VEF fields. Generally, the numerical computation and measurement of VEF within infinite structures did not introduce as many problems as the application of the method to finite structures. VEF within infinite structures, or structures having a high amount of damping, can mostly be related to travelling waves. Thus, a high VEF may be expected and measured. Infinite structures were investigated, since the behaviour of the VEFESPI method could be investigated much easier and results obtained could partly be related to finite structures.

Due to the presence of high standing waves, VEF within finite structures is expected to be much weaker. VEF in lightly damped finite



structures can be related mostly to dissipation processes within the structure. However, even a very weak VEF within a finite structure may generate a considerable amount of sound, as experienced during the ESPI experiments. It is therefore important for each VEF measurement technique, to cope with the measurement of weak energy flows. The main problem with the VEF measurement within finite structures is that the magnitude of the generally weak travelling waves is within the same range as the magnitude of the noise floor that contaminates the displacement signal. Thus, a filtering due to noise contamination was indispensable and larger errors in VEF computation may be expected.

It has been demonstrated, with the aid of the numerical analysis of VEF in beams and plates, that the VEFESPI method worked well despite some potential sources of errors. To compute successfully VEF in beams and plates, attention should be drawn to the following points:

- Displacement irregularities, such as odd-numbered mode shape displacements, strong nearfields, or simple displacement non-periodicity may be compensated by applying periodisation techniques.
- Real measured ESPI data contain optical noise, which needs to be removed. However, filtering does affect the accuracy of the VEFESPI method due to erasing valuable displacement information. To obtain best results, an optimisation process of the filtering is advisable.
- When computing VEF in finite structures, the product of the loss factor  $\eta$  and the signal-to-noise ratio (SNR), i.e.  $\eta \times \text{SNR}$ , may be used as an indicator to assess the sensitivity of the VEFESPI method. Generally, the sensitivity of the VEFESPI method decreases with increasing structural damping.

In the chapters investigating the numerical computation of VEF in beam and plate structures, it was shown that VEF can be determined even when strong noise contaminated displacements were present. To validate the theoretical results, VEF was measured indirectly from ESPI recorded infinite and finite beam and plate displacements. It was shown that VEF in an “infinite” beam



and plate structure can be measured within an acceptable range of accuracy. Although some differences to conventional measured vibrational input power (VIP) was found, the results obtained on the measurement of VEF in finite beams and plates were good, since the VEF pattern and magnitude could be determined within a reasonable range of accuracy. However, the measurement accuracy of VEF within finite structures using ESPI could not be assessed as accurately due to the following points:

- The modal loss factor used to compute the total transmitted vibrational energy (TTVE) from the measured potential energy density was measured and, thus, may contain a measurement error of  $\pm 20\%$  or more.
- The spatial resolution of the ESPI system was predicted from theoretical wavelength computation and, thus, may vary in comparison with the real value. A correct knowledge of this quantity is essential due to a high sensitivity of the VEFESPI method towards the spatial resolution parameter. The attachment of a ruler on the structure to be measured prior to the measurement may be applied to determine the correct spatial resolution of the ESPI system.
- Material properties of the structure and the employed damping layer were assumed herein, whereas within the conventional measurement of VIP no information of material properties was needed.
- Sound radiation at higher frequencies, as well as VEF dissipation or VEF crossing at the rig boundaries, was not included in the energy balance.
- The combined flexural beam stiffness and the combined flexural plate rigidity, used throughout the VEF determination of the unconstrained layer damped structures, were computed from theory. Thus, variations to the real structure values may be expected.

The application of ESPI as a potential tool to measure VEF certainly has advantages over conventional measurement techniques. Firstly, the VEF information provided by the method is two-dimensional and spatially dense.

From the ESPI measurement system, the two-dimensional displacement information is provided digitally for further processing. Measurements can be undertaken fast and accurately, and for small scale structures, in situ. However, there is one drawback of the VEFESPI method. Unfortunately, a single frequency can be measured only. Therefore, the frequency range of such a system is limited and, thus, broadband frequency based vibrational phenomena cannot be measured with one measurement run. However, in combination with simple transducer based mobility measurements, critical frequencies may be identified conventionally. The ESPI system can then be used to measure a particular frequency. Also, the ESPI system provides spatial information only, since the displacement data are time-averaged. In particular modern scanning laser Doppler vibrometer (LDV) measurement systems provide both temporal and spatial displacement information that is recorded over a wide frequency range.

Finally, it can be concluded that the flow pattern and the magnitude of VEF in highly and weakly damped structures can be measured providing the noise contamination is within a reasonable relation to the damping of the structure. In this dissertation it has been demonstrated that in theory VEF can be indirectly measured from transverse structural displacements very well even when the displacements are contaminated by a considerable amount of noise or signal irregularities, such as displacement non-periodicity. The measurement of VEF in infinite structures is less sensitive to noise contamination. However, filtering of noise is also indispensable here. For every VEF measurement technique the measurement of VEF in weakly damped structures will cause more problems. It has been shown in theory that with the aid of the VEFESPI technique VEF can be measured in finite structures as long as the noise contamination is within a reasonable relation to the damping of the structure. The product of the loss factor  $\eta$  and the SNR, i.e.  $\eta \times \text{SNR}$ , was proposed as an indicator. Sometimes the loss factor and the SNR are not known, especially if commercial engineering structures are measured. In this case, both quantities may be extracted from the wavenumber domain prior to the VEF computation. Of course other indicators can be employed, such as the standing wave ratio. However, the



indicators should be available during the measurements. Further, since the sensitivity of the VEFESPI method decreased with increasing damping, the loss factor is therefore an obvious quantity to use.

In this research the measurement of moment point mobility and energy input to an “infinite” beam was also investigated. It was concluded in chapter 9.3.1.4 that this technique can be used to measure moment point mobility and energy input to an “infinite” beam. A precise adjustment of the moment actuator was essential. The adjustment of the moment actuator is slightly tedious. However, after the moment actuator is aligned correctly, sequential measurements can be undertaken. Further, it was decided not to hit the beam directly without the use of the attached moment arms to avoid local beam deformations at the point of impact. Also, the use of the moment arms ensured an evenly distributed moment across the beam width and undesired differences of the two opposite impact forces will act in longitudinal beam direction.

## 15.2 Future Work

The experimental validation of the results obtained in theory on the measurement of VEF revealed some differences between measured ESPI based VEF and measured transducer based VEF. The reasons were discussed in the respective sections. However, the accuracy of the measurement technique is most dependent on the ability of the ESPI measurement system to acquire accurate vibrational amplitude and phase information. Within this research, the error tolerance of the employed ESPI system was not known. Also, the ESPI measurements undertaken herein used an ESPI measurement system courtesy of Land Rover. This measurement system was one of the first among the practical application of ESPI on commercial engineering structures. However, modern more advanced ESPI systems may provide even more accurate amplitude and phase information, with potentially less noise contamination. Thus, the use of modern off-the-shelf systems may improve the feasibility of the VEFESPI technique even further.

Within this work the computation of spatial derivatives from measured data was an essential part of the VEFESPI method. The utilisation of the fast Fourier transform (FFT) within the  $k$ -space derivation (KSD) method and simultaneous spectral filtering caused some problems, especially as signal irregularities and noise contaminations were present. An interesting alternative to the KSD method could be the application of B-splines to determine spatial derivatives from measured displacement data by simultaneously filtering the data due to the smoothing properties of the B-spline approximation technique. The application of the B-spline technique may reduce the problems occurring with signal irregularities and spectral filtering, since spatial derivatives may be computed directly from the piecewise polynomials. Thus, non-periodic displacement data may be employed in order to measure VEF.

The time consuming process of data preparation and truncation may be automated by more intelligent software codes, able to provide the VEFESPI method with useful ESPI based displacement information straight from the recorded ESPI data. Apart from measuring VEF with the aid of the VEFESPI technique, this method can also very easily be incorporated into a theoretical and a numerical analysis of VEF in structures to predict VEF from analytical displacement computation.

Finally, the measurement of moment point mobility and energy input to a finite beam may be carried out to extend the herein proposed impact moment measurement method. In contrast to the measurement of an "infinite" beam structure, high standing waves and cross mobilities need to be taken into account when measuring the true moment mobility and input energy.

## REFERENCES

- [1] **Mead, D. J.** *Passive Vibration Control*. John Wiley & Sons Ltd, Chichester, 1998.
- [2] **Dobson, B. J., Pinnington, R. J. and White, R. G.** Vibrational Power Transmission Analysis of Machinery Installations in Ships with the Objective of Noise Reduction. *Institute of Sound and Vibration Research*, 91/38, Southampton, 1991.
- [3] **Mandal, N. K. and Biswas, S.** Vibration Power Flow: A Critical Review. *The Shock and Vibration Digest*, **37**(1), 2005, 3-11.
- [4] **Noiseux, D. U.** Measurement of Power Flow in Uniform Beams and Plates. *Journal of the Acoustical Society of America*, **47**, 1970, 238-243.
- [5] **Goyder, H. G. and White, R. G.** Vibrational Power Flow from Machines into Built-Up Structures, Part I: Introduction and Approximate Analyses of Beam and Plate-Like Foundations. *Journal of Sound and Vibration*, **68**(1), 1980, 59-75.
- [6] **Goyder, H. G. and White, R. G.** Vibrational Power Flow from Machines into Built-Up Structures, Part II: Wave Propagation and Power Flow in Beam-Stiffened Plates. *Journal of Sound and Vibration*, **68**(1), 1980, 77-96.
- [7] **Goyder, H. G. and White, R. G.** Vibrational Power Flow from Machines into Built-Up Structures, Part III: Power Flow Through Isolation Systems. *Journal of Sound and Vibration*, **68**(1), 1980, 77-96.
- [8] **Walsh, S. J. and White, R. G.** Vibrational Power Transmission in Curved Beams. *Journal of Sound and Vibration*, **233**(3), 2000, 455-488.



- 
- [9] Wohlever, J. C. and Bernhard, R. J. Mechanical Energy Flow Models of Rods and Beams. *Journal of Sound and Vibration*, **153**(1), 1992, 1-19.
- [10] Carcaterra, A. and Sestieri, A. Energy Density Equations and Power Flow in Structures. *Journal of Sound and Vibration*, **188**(2), 1995, 269-282.
- [11] Bouthier, O. M. and Bernhard, R. J. Simple Models of the Energetics of Transversely Vibrating Plates. *Journal of Sound and Vibration*, **182**(1), 1995, 149-166.
- [12] Park, D.-H., Hong, S.-Y. and Kil, H.-G. Power Flow Model of Flexural Waves in Finite Orthotropic Plates. *Journal of Sound and Vibration*, **264**(1), 2003, 203-204.
- [13] Bobrovnikskii, Y. I. Calculation of the Power Flow in Flexural Waves on Thin Plates. *Journal of Sound and Vibration*, **194**(1), 1996, 103-106.
- [14] Norris, A. N. and Vemula, C. Scattering of Flexural Waves on Thin Plates. *Journal of Sound and Vibration*, **181**(1), 1995, 115-125.
- [15] Bobrovnikskii, Y. I. On The Energy Flow in Evanescent Waves. *Journal of Sound and Vibration*, **152**(1), 1992, 175-176.
- [16] Kurze, U. J. Comments on "On the Energy Flow in Evanescent Waves" 1992. *Journal of Sound and Vibration*, **161**(2), 1993, 355-356.
- [17] Langley, R. S. and Shorter, P. J. Diffuse Wavefields in Cylindrical Coordinates. *Journal of the Acoustical Society of America*, **112**(4), 2002, 1465-1470.
- [18] Lande, R. and Langley, R. S. The Energetics of Cylindrical Bending Waves in a Thin Plate. *Journal of Sound and Vibration*, **279**(2), 2005, 513-518.
- [19] Xiong, Y.-P., Xing, J. T. and Price, W. G. A Power Flow Mode Theory Based on a System's Damping Distribution and Power Flow Design Approaches. *Proceedings of the Royal Society London A*, **461**, 2005, 3381-3411.
- [20] Ji, L., Mace, B. R. and Pinnington, R. J. A Power Mode Approach to Estimating Vibrational Power Transmitted By Multiple Sources. *Journal of Sound and Vibration*, **265**(2), 2003, 387-399.

- 
- [21] **Xing, J.-T. and Price, W. G.** A Power-Flow Analysis Based on Continuum Dynamics. *Proceedings of the Royal Society London A*, **455**, 1999, 401-436.
- [22] **Pavic, G.** The Role of Damping on Energy and Power in Vibrating Systems. *Journal of Sound and Vibration*, **281**(1), 2005, 45-71.
- [23] **Pavic, G.** Vibration Damping, Energy and Energy Flow in Rods and Beams: Governing Formulae and Semi-Infinite Systems. *Journal of Sound and Vibration*, **291**(4), 2006, 932-962.
- [24] **Pavic, G.** Numerical Study of Vibration Damping, Energy and Energy Flow in a Beam-Plate System. *Journal of Sound and Vibration*, **291**(4), 2006, 902-931.
- [25] **Pavic, G.** Measurement of Structural Borne Wave Intensity, Part I: Formulation of the Methods. *Journal of Sound and Vibration*, **49**(2), 1976, 221-230.
- [26] **Verheij, J. W.** Cross Spectral Density Methods for Measuring Structure Borne Power Flow in Beams and Pipes. *Journal of Sound and Vibration*, **70**(1), 1980, 133-139.
- [27] **Pinnington, R. J. and White, R. G.** Power Flow Through Machine Isolators to Resonant and Non-Resonant Beams. *Journal of Sound and Vibration*, **75**(2), 1981, 179-197.
- [28] **Redman-White, W.** The Experimental Measurement of Flexural Wave Power Flow in Structures. *2nd International Conference on Recent Advances in Structural Dynamics*, 1984, 467-474.
- [29] **Ming, R. S. and Craik, R. J.** Errors in the Measurement of Structure-Borne Power Flow Using Two-Accelerometer Techniques. *Journal of Sound and Vibration*, **204**(1), 1997, 59-71.
- [30] **Linjama, J. and Lahti, T.** Estimation of Bending Wave Intensity in Beams Using the Frequency Response Technique. *Journal of Sound and Vibration*, **153**(1), 1992, 21-36.
- [31] **Linjama, J. and Lahti, T.** Measurement of Bending Wave Reflection and Impedance in a Beam by the Structural Intensity Technique. *Journal of Sound and Vibration*, **161**(2), 1993, 317-331.

- 
- [32] **Bauman, P. D.** Measurement of Structural Intensity: Analytic and Experimental Evaluation of Various Techniques for the Case of Flexural Waves in One-Dimensional Structures. *Journal of Sound and Vibration*, **174**(5), 1993, 677-694.
- [33] **Walsh, S. J. and White, R. G.** Measurement of Vibrational Power Transmission in Curved Beams. *Journal of Sound and Vibration*, **241**(2), 2001, 157-183.
- [34] **Williams, E. G., Dardy, H. D. and Fink, R. G.** A Technique for Measurement of Structure-Borne Intensity in Plates. *Journal of the Acoustical Society of America*, **78**(6), 1985, 2061-2068.
- [35] **Williams, E. G. and Dardy, H. D.** SIMAP, Structural Intensity from the Measurement of Acoustic Pressure. *2nd International Congress on Acoustic Intensity*, 1985, 235-242.
- [36] **Maynard, J. D., Williams, E. G. and Lee, Y.** Nearfield Acoustic Holography: I. Theory of Generalized Holography and the Development of NAH. *Journal of the Acoustical Society of America*, **78**(4), 1985, 1395-1413.
- [37] **Unglenieks, R. J. and Bernhard, R. J.** Measurement of flexural Structural Intensity using Wavenumber Techniques. *4th International Congress on Intensity Techniques*, 1993, 305-311.
- [38] **Morikawa, R., Ueha, S. and Nakamura, K.** Error Evaluation of the Structural Intensity Measured with a Scanning Laser Doppler Vibrometer and a K-Space Signal Processing. *Journal of the Acoustical Society of America*, **99**(5), 1996, 2913-2921.
- [39] **Pascal, J.-C., Loyau, T. and Mann III, J. A.** Structural Intensity from Spatial Fourier Transformation and BAHIM Acoustical Holography Method. *3rd International Congress on Intensity Techniques*, 1990, 197-204.
- [40] **Hayek, S. I., Pechersky, M. J. and Suen, B. C.** Measurement and Analysis of Near and Far Field Structural Intensity by Scanning Laser Vibrometry. *3rd International Congress on Intensity Techniques*, 1990, 281-288.

- 
- [41] Kojima, N., Hirayu, T., Mikami, M. and Saito, M. Vibration Intensity Measurement on U-Shaped Shell Using Laser Vibrometers. *Inter Noise 98*, 1998.
- [42] Blotter, J. D. and West, R. L. Identification of Energy Sources and Sinks in Plates by Means of a Scanning Laser Doppler Vibrometer. *Noise Control Engineering Journal*, 44(1), 1996, 61-68.
- [43] Zhang, Y. and III, J. A. Measuring the Structural Intensity and Force Distribution in Plates. *Journal of the Acoustical Society of America*, 99(1), 1996, 345-353.
- [44] Romano, A. J., Abraham, P. B. and Williams, E. G. A Poynting Vector Formulation for thin Shells and Plates, and its Application to Structural Intensity Analysis and Source Localization. Part I: Theory. *Journal of the Acoustical Society of America*, 87(3), 1990, 1166-1175.
- [45] Mindlin, R. D. Influence of Rotatory Inertia and Shear on Flexural Motions of Isotropic, Elastic Plates. *Journal of Applied Mechanics*, 18, 1951, 31-38.
- [46] Nejade, A. and Singh, R. Flexural Intensity Measurements on Finite Plates using Modal Spectrum Ideal Filtering. *Journal of Sound and Vibration*, 256(1), 2002, 33-63.
- [47] Pascal, J.-C., Loyau, T. and Carniel, X. Complete Determination of Structural Intensity in Plates Using Laser Vibrometers. *Journal of Sound and Vibration*, 161(3), 1993, 527-531.
- [48] Pascal, J.-C., Carniel, X., Chalvidan, V. and Smigielski, P. Determination of Structural Intensity and Mechanical Excitation Using Holographic Interferometry. *4th International Congress on Intensity Techniques*, 1993, 137-144.
- [49] Pascal, J.-C., Carniel, X., Chalvidan, V. and Smigielski, P. Energy Flow Measurements in High Standing Vibration Fields by Holographic Interferometry. *Inter Noise 95*, 1995, 625-630.
- [50] Pascal, J.-C., Carniel, X., Chalvidan, V. and Smigielski, P. Determination of Phase and Magnitude of Vibration for Energy Flow

- Measurements in a Plate Using Holographic Interferometry. *Optics and Lasers in Engineering*, **25**, 1996, 343-360.
- [51] **Pascal, J.-C., Li, J. F. and Carniel, X.** Wavenumber Processing Techniques to Determine Structural Intensity and Its Divergence from Optical Measurements Without Leakage Effects. *Shock and Vibration*, **9**(1), 2002, 57-66.
- [52] **Mandal, N. K., Rahman, R. A. and Leong, M. S.** Estimation of Structure-Borne Noise in Plates for Far Field Conditions Using The Structural Intensity Method. *Inter Noise 98*, 1998.
- [53] **Mandal, N. K., Rahman, R. A. and Leong, M. S.** Structure-Borne Power Transmission in Thin Naturally Orthotropic Plates: General Case. *Journal of Vibration and Control*, **9**, 2003, 1189-1158.
- [54] **Mandal, N. K., Rahman, R. A. and Leong, M. S.** Experimental Investigation of Vibration Power Flow in Thin technical Orthotropic Plates by the Method of Vibration Intensity. *Journal of Sound and Vibration*, **285**(3), 2005, 669-695.
- [55] **Troitskey, M. S.** *Stiffened Plates: Bending, Stability and Vibration*. Elsevier Scientific Publishing Company, Amsterdam, 1976.
- [56] **Mandal, N. K.** Experimental Studies of Quasi-Longitudinal Waves Power Flow in Corrugated Plates. *Journal of Sound and Vibration*, **297**(2), 2006, 227-242.
- [57] **Petzing, J. N., Tyrer, J. R. and Pavic, G.** The Analysis of Structural Surface Intensity Using Wholefield Laser Speckle Techniques. *Inter Noise 96*, 1996, 1405-1410.
- [58] **Alves, P. S., Arruda, J. R., Gaul, L. and Hurlebaus, S.** Power Flow Estimation Using Pulse ESPI. *4th International Conference on Vibration Measurements by Laser Techniques: Advances and Applications*, 2000, 362-373.
- [59] **Arruda, J. R.** Surface Smoothing and Partial Spatial Derivatives Computation Using a Regressive Discrete Fourier Series. *Mechanical Systems and Signal Processing*, **6**(1), 1992, 41-50.



- 
- [60] Chambard, J. P., Chalvidan, V., Carniel, X. and Pascal, J.-C. Pulsed TV-Holography Recording for Vibration Analysis Applications. *Optics and Lasers in Engineering*, **38**, 2002, 131-143.
- [61] Carniel, X., Pascal, J.-C. and Li, J. F. Structural Intensity and Acoustic Radiation from optical Measurements: The VIPART Software. *Proceedings - SPIE The International Society For Optical Engineering*, 2000, 258-265.
- [62] Eck, T. Structural Intensity Measurements Using Electronic Speckle Pattern Interferometry – SIMESPI. *MSc Thesis, Loughborough University*, 2003.
- [63] Eck, T., Walsh, S. J., Dale, M. and Taylor, N. C. Structural Intensity Measurements Using Electronic Speckle Pattern Interferometry (SIMESPI). *Institute of Acoustics Spring Conference 2004*, 2004, 235-246.
- [64] Eck, T., Walsh, S. J., Dale, M. and Taylor, N. Vibrational Power Flow Measurements in a Beam Using Electronic Speckle Pattern Interferometry. *Acta Acustica United with Acustica*, **92**(5), 2006, 765-776.
- [65] Kwon, Y. I. and Ih, J.-G. Identification of Vibration Transmission Through Belt-Pulley Systems by Using the Structural Intensity Method. *Inter Noise 98*, 1998.
- [66] Lee, H.-J. and Kim, K.-J. Multi-Dimensional Vibration Power Flow Analysis of Compressor System Mounted in Outdoor Unit of an Air Conditioner. *Journal of Sound and Vibration*, **272**(3), 2004, 607-625.
- [67] Hussein, M. F. and Hunt, H. E. A Power Flow Method for Evaluating Vibration From Underground Railways. *Journal of Sound and Vibration*, **293**(4), 2006, 667-679.
- [68] Lee, S.-K. Identification of a Vibration Transmission Path in a Vehicle by Measuring Vibrational Power Flow. *Proceedings of the Inst. Mechanical Engineering, Part D*, **218**(1), 2004, 167-175.

- 
- [69] Hambric, S. A. Power Flow and Mechanical Intensity Calculations in Structural Finite Element Analysis. *Journal of Vibration and Acoustics*, **112**, 1990, 542-549.
- [70] Hambric, S. A. and Taylor, P. D. Comparison of Experimental and Finite Element Structure-Borne Flexural Power Measurements for a Straight Beam. *Journal of Sound and Vibration*, **170**(5), 1994, 595-605.
- [71] Gavric, L. and Pavic, G. A Finite Element Method For Computation of Structural Intensity by the Normal Mode Approach. *Journal of Sound and Vibration*, **164**(1), 1993, 29-43.
- [72] Li, Y. J. and Lai, J. C. Prediction of Surface Mobility of a Finite Plate with Uniform Force Excitation by Structural Intensity. *Applied Acoustics*, **60**(3), 2000, 371-383.
- [73] Xu, X. D., Lee, H. P. and Lu, C. Power Flow Paths in Stiffened Plates. *Journal of Sound and Vibration*, **282**(5), 2005, 1264-1272.
- [74] Mace, B. R. and Shorter, P. J. Energy Flow Models From Finite Element Analysis. *Journal of Sound and Vibration*, **233**(3), 2000, 369-389.
- [75] Khun, M. S., Lee, H. P. and Lim, S. P. Structural Intensity in Plates with Multiple Discrete and Distributed Spring-Dashpot Systems. *Journal of Sound and Vibration*, **276**(3), 2004, 627-648.
- [76] Lee, H. P., Lim, S. P. and Khun, M. S. Diversion of Energy Flow Near Crack Tips of a Vibrating Plate Using the Structural Intensity Technique. *Journal of Sound and Vibration*, **296**(3), 2006, 602-622.
- [77] Wang, C. Q., Ong, E. H., Quian, H. and Guo, N. Q. On the Application of B-Spline Approximation in Structural Intensity Measurements. *Journal of Sound and Vibration*, **290**(2), 2006, 508-518.
- [78] Alves, P. S. and Arruda, J. R. Energy Source Localization Using the Reactive Structural Intensity. *17th International Congress on Acoustics*, 2001.
- [79] Fuller, C. R. and Burdisso, R. A. A Wavenumber Domain Approach to the Active Control of Structure-Borne Sound. *Journal of Sound and Vibration*, **148**(2), 1991, 355-360.

- 
- [80] **Arruda, J. R. and Pereira, A. K.** Further Results on the Active Control of the Flexural Power Flow in Plates. *Inter Noise 98*, 1998.
- [81] **Mace, B. R. and Halkyard, C. R.** Real-Time Far-Field Estimation in Beams: A Wave Decomposition and Reconstruction Approach. *Inter Noise 98*, 1998.
- [82] **Mace, B. R., Halkyard, C. R. and El-Khatib, H. M.** Real-Time Measurement of Wave Components and Intensity in a Beam in the Presence of a Near Field. *Journal of Sound and Vibration*, **286**(3), 2005, 507-527.
- [83] **Liu, Z. S., Lee, H. P. and Lu, C.** Passive and Active Interior Noise Control of Box Structures Using the Structural Intensity Method. *Applied Acoustics*, **67**(2), 2006, 112-134.
- [84] **Wu, C. J. and White, R. G.** Vibrational Power Transmission in a Finite Multi-Supported Beam. *Journal of Sound and Vibration*, **181**(1), 1995, 99-114.
- [85] **Wu, C. J. and White, R. G.** Reduction of Vibrational Power in Periodically Supported Beams By Use of a Neutralizer. *Journal of Sound and Vibration*, **187**(2), 1995, 329-338.
- [86] **El-Khatib, H. M., Mace, B. R. and Brennan, M. J.** Suppression of Bending Waves in a Beam Using a Tuned Vibration Absorber. *Journal of Sound and Vibration*, **288**(5), 2005, 1157-1175.
- [87] **Wang, Z. H., Xing, J. T. and Price, W. G.** A Study of Power Flow in a Coupled Plate-Cylindrical Shell System. *Journal of Sound and Vibration*, **271**(4), 2004, 863-882.
- [88] **Koh, Y. K. and White, R. G.** Analysis and Control of Vibrational Power Transmission to Machinery Supporting Structures Subjected to a Multi-Excitation System, Part I: Driving Point Mobility Matrix of Beams and Rectangular Plates. *Journal of Sound and Vibration*, **196**(4), 1996, 469-493.
- [89] **Petersson, B. A.** Structural Acoustic Power Transmission by Point Moment and Force Excitation, Part I: Beam- and Frame-Like Structures. *Journal of Sound and Vibration*, **160**(1), 1993, 43-66.

- 
- [90] **Yap, S. H. and Gibbs, B. M.** Structure-Borne Sound Transmission From Machines in Buildings, Part 1: Indirect Measurement of Force at the Machine-Receiver Interface of a Single and Multi-Point Connected System by a Reciprocal Method. *Journal of Sound and Vibration*, **222**(1), 1999, 85-98.
- [91] **Yap, S. H. and Gibbs, B. M.** Structure-Borne Sound Transmission From Machines in Buildings, Part 2: Indirect Measurement of Force and Moment at the Machine-Receiver Interface of a Single Point Connected System by a Reciprocal Method. *Journal of Sound and Vibration*, **222**(1), 1999, 99-113.
- [92] **Jianxin, S. and Gibbs, B. M.** Measurement of Point Moment Mobility in the Presence of Non-Zero Cross Mobility. *Applied Acoustics*, **54**(1), 1998, 9-26.
- [93] **Sanderson, M. A. and Fredö, C. R.** Direct Measurement of Moment Mobility, Part I: A Theoretical Study. *Journal of Sound and Vibration*, **179**(4), 1995, 669-684.
- [94] **Petersson, B. A.** Structural Acoustic Power Transmission by Point Moment and Force Excitation, Part II: Plate-Like Structures. *Journal of Sound and Vibration*, **160**(1), 1993, 67-91.
- [95] **Petersson, B. A.** On the Use of Giant Magnetostrictive Devices for Moment Excitation. *Journal of Sound and Vibration*, **116**(1), 1987, 191-194.
- [96] **Koh, Y. K. and White, R. G.** Analysis and Control of Vibrational Power Transmission to Machinery Supporting Structures Subjected to a Multi-Excitation System, Part II: Vibrational Power Analysis and Control Schemes. *Journal of Sound and Vibration*, **196**(4), 1996, 495-508.
- [97] **Koh, Y. K. and White, R. G.** Analysis and Control of Vibrational Power Transmission to Machinery Supporting Structures Subjected to a Multi-Excitation System, Part III: Vibrational Power Cancellation and Control Experiments. *Journal of Sound and Vibration*, **196**(4), 1996, 509-522.

- 
- [98] Sanderson, M. A. Direct Measurement of Moment Mobility, Part II: An Experimental Study. *Journal of Sound and Vibration*, **179**(4), 1995, 685-696.
- [99] Champoux, Y., Cotroni, V., Paillard, B. and Beslin, O. Moment Excitation of Structures Using Synchronized Impact Hammers. *Journal of Sound and Vibration*, **263**(3), 2003, 515-533.
- [100] CETIM Structural Intensity and Vibrational Energy Flow. *Proceedings of the 4th International Congress on Intensity Techniques*, 1993.
- [101] Lase, Y., Ichchou, M. N. and Jezequel, L. Energy Flow Analysis of Bars and Beams: Theoretical Formulations. *Journal of Sound and Vibration*, **192**(1), 1996, 281-305.
- [102] Maysenhölder, W. *Körperschallenergie*. S. Hirzel Verlag, Stuttgart, 1994.
- [103] Cremer, L., Heckl, M. and Ungar, E. E. *Structure-Borne Sound - Structural Vibrations and Sound Radiation at Audio Frequencies*. Springer-Verlag, Berlin, 1988.
- [104] Lyon, R. H. and DeJong, R. G. *Theory and Application of Statistical Energy Analysis*. Butterworth-Heinemann, Boston, 1995.
- [105] Alfredsson, K. S. Active and Reactive Structural Energy Flow. *Journal of Vibration and Acoustics*, **119**(1), 1997, 70-79.
- [106] Pascal, J.-C., Carniel, X. and Li, J.-F. Characterisation of a Dissipative Assembly using Structural Intensity Measurements and Energy Conservation Equation. *Mechanical Systems and Signal Processing*, **20**(6), 2006, 1300-1311.
- [107] Eck, T., Walsh, S. J. and Horner, J. L. Measurement of Vibrational Energy and Point Mobility of a Beam Subjected to Moment Excitation Using a Finite-Difference Approximation. *Proceedings of the Inst. Mechanical Engineering, Part C: Journal of Mechanical Engineering Science*, **220**(6), 2006, 795-806.
- [108] Graff, K. F. *Wave Motion in Elastic Solids*. Clarendon Press, Oxford, 1975.



- 
- [109] **Rayleigh, J. W.** *The Theory of Sound*. Dover Publications, New York, 1945.
- [110] **Leissa, A. W.** *Vibration of Plates*. U.S. Government Printing Office, NASA SP-160, Washington, D.C., 1969.
- [111] **Cooley, J. W. and Tuckey, J. W.** An Algorithm for the Machine Calculation of Complex Fourier Series. *Mathematics of Computation*, **19**, 1965, 297-301.
- [112] **Dierckx, P.** *Curve and Surface Fitting with Splines*. Oxford University Press, Oxford, 1993.
- [113] **Boor, C. D.** *A Practical Guide to Splines*. Springer-Verlag, London, 1978.
- [114] **Warburton, G. B.** *The Dynamical Behaviour of Structures*. Pergamon Press Ltd., Oxford, 1976.
- [115] **Kochersberger, K., Mitchell, L. D. and Wicks, A. L.** Structural Angular Velocity Extraction Using DFT-IDFT Techniques. *The 9th International Modal Analysis Conference*, 1991, 657-663.
- [116] **Li, W. X., Mitchell, L. D. and Neumann, M. L.** Mapping Nonsquare and Unevenly Spaced 2-D SLDV Data of an Aircraft Fuselage by Using Spatial DFT-IDFT Techniques. *Shock and Vibration*, **3**(2), 1996, 135-140.
- [117] **Jones, R. and Wykes, C.** *Holographic and Speckle Interferometry - A Discussion of the Theory, Practice and Application of the Techniques*. Cambridge University Press, Cambridge, 1989.
- [118] **Butters, J. N. and Leendertz, J.** Speckle Pattern and Holographic Techniques in Engineering Metrology. *Optics and Laser Technology*, **3**, 1971, 26-30.
- [119] **Towers, D. P., Buckberry, C. H., Stockley, B. C. and Jones, M. P.** Measurement of Complex Vibrational Modes and Surface Form - a Combined System. *Measurement Science and Technology*, **6**, 1995, 1242-1249.
- [120] **Jones, J. D., Valera, J., Buckberry, C. H. and Towers, D. P.** Laser Measure up for the Car Industry. 1995.

- 
- [121] Wang, W. C., Hwang, C. H. and Lin, S. Y. Vibration Measurement by the Time-Averaged Electronic Speckle Pattern Interferometry. *Applied Optics*, **35**(22), 1996, 4502-4509.
- [122] Valera, J. D., Doval, A. and Jones, J. D. Vibration Phase Measurement by Fibre Optic Electronic Speckle Pattern Interferometry (ESPI) with Stroboscopic Illumination. *The 9th International Conference on Optical Fibre Sensors*, 1992, 381-384.
- [123] Morrell, C., Ranft, M. and Simms, S. Moment Excitation of an Infinite Beam: Response Measurement Using A Finite Difference Method. Final year group report, *Loughborough University*, 2004.
- [124] Morrish, I. Moment Excitation of Structures. *BEng Thesis, Loughborough University*, 2005.
- [125] Eck, T., Walsh, S. J. and Horner, J. L. Measurement of Point Mobility and Input Energy of a Beam Under Moment Excitation. *9th International Conference on Recent Advances in Structural Dynamics*, 2006.
- [126] Randall, R. B. *Frequency Analysis*. K. Larsen & Son A/S, Glostrup, 1987.
- [127] Kumaresan, P. P. Modal Analysis of Automotive Panels. *MSc Thesis, Loughborough University*, 2007.
- [128] Abramowitz, M. and Stegun, I. A. *Handbook of Mathematical Functions*. Dover Publications, New York, 1972.
- [129] Cremer, L., Heckl, M. and Petersson, B. A. *Structure-Borne Sound - Structural Vibrations and Sound Radiation at Audio Frequencies*. Springer-Verlag, Berlin Heidelberg, 2005.
- [130] Langley, R. S. Some Perspectives on Wave-Mode Duality in SEA. *Symposium on Statistical Energy Analysis*, 1997.
- [131] Oberst, H. and Frankenfeld, K. Über die Dämpfung der Biegeschwingungen Dünner Bleche Durch Fest Haftende Beläge. *Acustica, Akustische Beihefte*, **2**(Heft 4), 1952, 181-194.
- [132] Papoulis, A. *Systems and Transforms with Applications in Optics*. McGraw-Hill, Inc., New York, 1968.

- 
- [133] **Knockaert, L.** Fast Hankel Transform by Fast Sine and Cosine Transforms: The Mellin Connection. *IEEE Transactions on Signal Processing*, 48(6), 2000, 1695-1701.
  - [134] **Sutter, B. W.** Fast Nth-Order Hankel Transform Algorithm. *IEEE Transactions on Signal Processing*, 39(2), 1991, 532-536.
  - [135] **Tanaka, N., Kikushima, Y., Kuroda, M. and Snyder, S. D.** Structure-Borne Intensity Characteristics of an Actively Controlled Thin Plate. *4th International Congress on Intensity Techniques*, 1993, 273-280.
  - [136] **Wang, C. T.** *Applied Elasticity*. McGraw-Hill Book Company, New York, 1953.
  - [137] **Milne-Thomson, L. M.** *The Calculus of Finite Differences*. MacMillan & Company LTD, London, 1960.
  - [138] **Milne, W. E.** *Numerical Calculus*. Princeton University Press, Princeton, 1959.
  - [139] **Spiegel, M. R.** *Theory and Problems of Calculus of Finite Differences and Difference Equations*. McGraw-Hill, Inc., 1994.
  - [140] **Weller, F.** *Numerische Mathematik für Ingenieure und Naturwissenschaftler*. Vieweg, Braunschweig Wiesbaden, 1996.
  - [141] **Hildebrand, F. B.** *Finite-Difference Equation and Simulations*. Prentice-Hall, Inc., Englewood Cliffs, 1968.
  - [142] **Papoulis, A.** *Signal Analysis*. McGraw-Hill, Inc., London, 1984.
  - [143] **Kreyszig, E.** *Advanced Engineering Mathematics*. John Wiley & Sons, Inc., New York, 1999.

